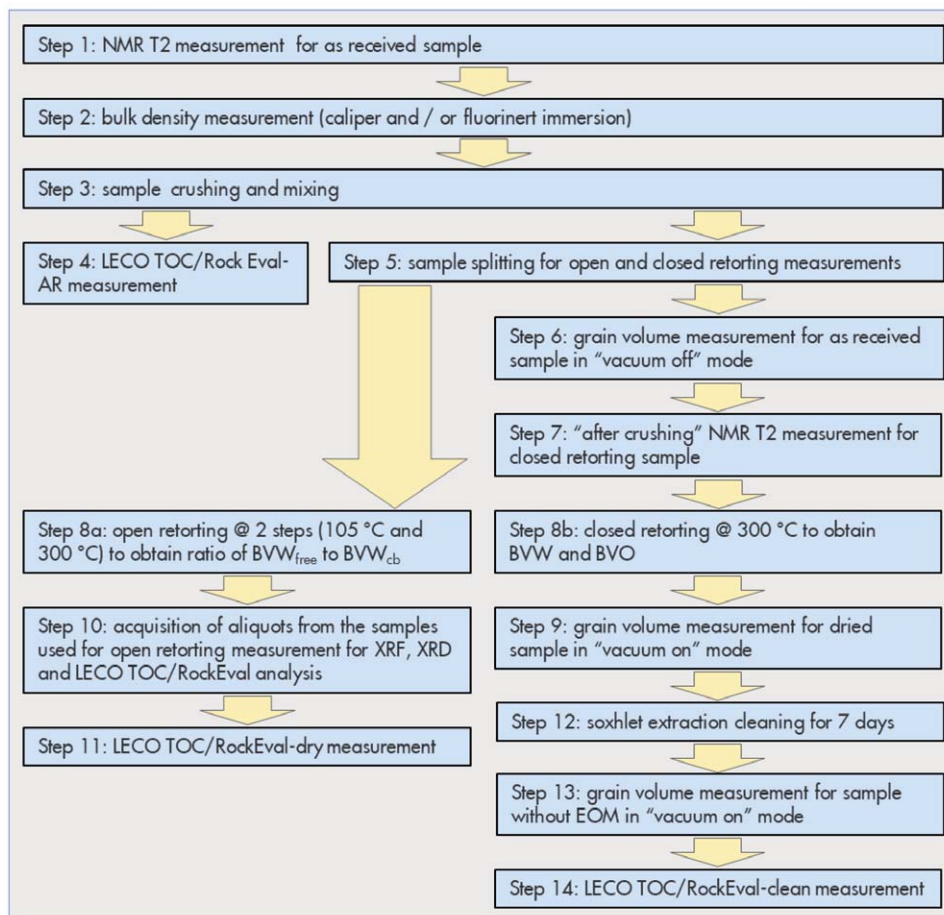
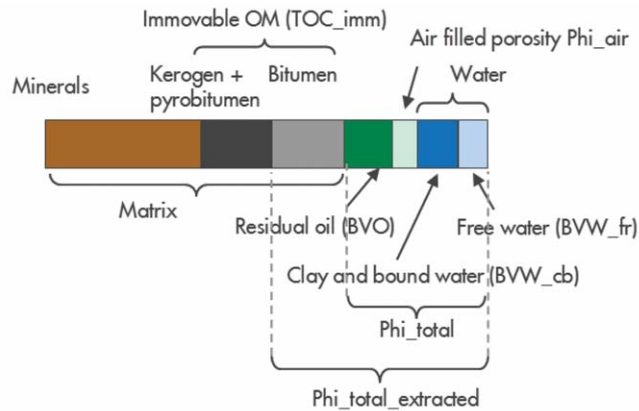
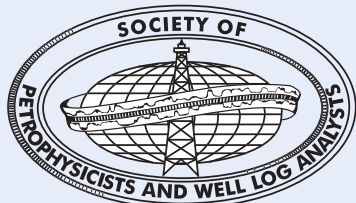


PETROPHYSICS

THE SPWLA JOURNAL OF FORMATION EVALUATION AND RESERVOIR DESCRIPTION





The Society of Petrophysicists and Well Log Analysts

8866 Gulf Freeway, Suite 320
Houston, TX 77017, USA
P: +1-713-947-8727
F: +1-713-947-7181
Email: Sharon@spwla.org
Membership@spwla.org
www.SPWLA.org

SPWLA Foundation. This fund supports scholarships in higher education and research in formation evaluation. Please send donations to: SPWLA, 8866 Gulf Freeway, Suite 320, Houston, TX 77017, USA

ISSN 1529-9074

PETROPHYSICS is published bimonthly by the Society of Petrophysicists and Well Log Analysts (SPWLA). Subscription is included in annual dues for members. Library Subscription cost is \$250 (6-issues, Feb, April, June, Aug, Oct, Dec) Send Subscription and member address changes to the SPWLA business office. Back issues if available are \$35 each to members and \$45 each to library subscribers.

ADVERTISING RATES: (based on one-time, full color) Full Page: \$1500, Half Page: \$1200, Quarter Page: \$1000. Additional fee for printing on covers. Media kits are available by contacting the SPWLA business office or by visiting the SPWLA website www.spwla.org. Responsibility: The statements and opinions expressed in PETROPHYSICS are those of the authors and should not be construed as an official action or opinion of the Society of Petrophysicists and Well Log Analysts, Inc. © Copyright 2019 by the Society of Petrophysicists and Well Log Analysts, Inc.

About the Cover

Obtaining representative core analysis in unconventional reservoirs continues to challenge our industry. In this issue, Nikitin et al. introduce an extension to the GRI protocol that aims to address many of the issues that current procedures encounter.

PRINTED IN USA ON ACID FREE PAPER

PETROPHYSICS

December Vol. 60, No. 6

Contents

695 From the Editor

ARTICLES - BEST OF THE 2019 SYMPOSIUM, PART 2

- 697 **Inversion of High-Resolution High-Quality Sonic Compressional and Shear Logs for Unconventional Reservoirs**
Ting Lei, Smaine Zeroug, Sandip Bose, Romain Prioul, and Adam Donald
- 712 **New 4.75-in. Ultrasonic LWD Technology Provides High-Resolution Caliper and Imaging in Oil-Based and Water-Based Muds**
Peng Li, Jonathan Lee, Richard Coates, Jing Jin, and Siong Ming Wong
- 733 **Deducing Electrical Permittivity of Formations From LWD Resistivity Measurements**
Stein Ottar Stalheim
- 755 **Crushed-Rock Analysis Workflow Based on Advanced Fluid Characterization for Improved Interpretation of Core Data**
Anton Nikitin, Melanie Durand, Adam McMullen, Aidan Blount, Brian Driskill, and Amie Hows

ARTICLES - REGULAR SUBMISSIONS

- 771 **NMR Evaluation of Light-Hydrocarbon Composition, Pore Size, and Tortuosity in Organic-Rich Chalks**
Zeliang Chen, Philip M. Singer, Xinglin Wang, Harold J. Vinegar, Scott V. Nguyen, and George J. Hirasaki
- 798 **Influence of Magnetic Susceptibility Contrast on NMR Studies—Experimental Analysis From Siliciclastic Reservoirs**
Partha Sarathi Sarkar, Soma Chatterjee, Mohan Lal, Manoj Kumar, and P.P. Deo
- 825 **New Robust Model to Estimate Formation Tops in Real Time Using Artificial Neural Networks (ANN)**
Salaheldin Elkhatay, Ahmed Al-AbdulJabbar, and Ahmed Abdulhamid Mahmoud
- 838 **A Comparative Study of Three Supervised Machine-Learning Algorithms for Classifying Carbonate Vuggy Facies in the Kansas Arbuckle Formation**
Tianqi Deng, Chicheng Xu, Dawn Jobe, and Rui Xu
- 854 **Joint Interpretation of Elastic and Electrical Data for Petrophysical Properties of Gas-Hydrate-Bearing Sediments Using Inverse Rock Physics Modeling Method**
Haojie Pan, Hongbing Li, Yan Zhang, Jingyi Chen, Shengjuan Cai, and Chao Geng
- 872 **Review of Micro/Nanofluidic Insights on Fluid Transport Controls in Tight Rocks**
Ayaz Mehmani, Shaina Kelly, and Carlos Torres-Verdin
- 891 **Corrigendum**
- 892 **Annual Index**

Full-Color versions of all technical articles are available in the digital edition of Petrophysics, which is free to SPWLA members and can be found at https://www.spwla.org/SPWLA/Publications/Journals/Recent_Petrophysics_Journals.aspx.

The Society of Petrophysicists and Well Log Analysts is dedicated to the advancement of the science of formation evaluation through well logging and other formation evaluation techniques. SPWLA is dedicated to the application of these techniques, to the exploration and exploitation of gas, oil and other minerals. PETROPHYSICS publishes original contributions on theoretical and applied aspects of formation evaluation; particularly well logging and petrophysics.

As of Vol. 46 (1) 2005,
Petrophysics [ISSN: 1529-9074]
is indexed and abstracted in
Thomson Reuters:
Scientific Citation Index Expanded
Journal Citation Report—Science
Current Contents—Physical, Chemical,
and Earth Sciences

PETROPHYSICS

Editor



Tom Neville
Asia-Pacific Formation Evaluation Services
tom.neville@formation-evaluation.asia
(+61) 416-672-392

Associate Editors



Acoustics and Rock Physics
Richard Coates, *Halliburton*



Core Analysis and Laboratory Petrophysics
Gary Beck, *Cardinal Geosciences*



Electromagnetics
Hui Xie, *Schlumberger*



Formation Testing
Melton Hows, *Shell*



Integrated Formation Evaluation
Chengbing Liu, *Saudi Aramco*
Haijing Wang, *Chevron*



Integrated Formation Evaluation and Case Studies
Hesham El-Sobky, *ConocoPhillips*



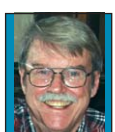
Magnetic Resonance
Lalitha Venkataraman, *Schlumberger*
Wim Looyestijn, *Shell*



Nuclear
Pingjun Guo, *ExxonMobil*



Petroleum Geochemistry
Drew Pomerantz, *Schlumberger*



Well and Reservoir Surveillance
Dale Fitz, *Consultant*



Data-Driven Analytics
Chicheng Xu, *Aramco Services*

The Society of Petrophysicists and Well Log Analysts Board of Directors 2019–2020



President
Jesus Salazar
Marathon Oil Company
Houston, TX, USA
(+1) 512-785-8979
President@spwla.org



**VP Finance, Secretary,
and Administration**
Doug Patterson
Baker Hughes, a GE Company
Houston, Texas, USA
(+1) 713 879-4056
VP-Finance@spwla.org



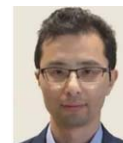
President-Elect
James Hemingway
Consultant
Manitou Springs, CO, USA
(+1) 281-433-5170
President-Elect@spwla.org



VP Publications
Tom Neville
Asia-Pacific Fm. Eval. Services
Brisbane, Australia
(+61) 416-672-392
VP-Publications@spwla.org



VP Technology
Michael O'Keefe
Schlumberger
Bucharest, Romania
(+40) 739-855-658
VP-Technology@spwla.org



VP IT
Lin Liang
Schlumberger-Doll Research
Cambridge, MA, USA
(+1) 617-335-4469
VP-InfoTech@spwla.org



VP Education
Katerina Yared
SM Energy
Highlands Ranch, CO, USA
(+1) 720-431-7482
VP-Education@spwla.org

REGIONAL DIRECTORS



N. America 1
Adam Haecker
Continental
Oklahoma City, OK, USA
(+1) 979-587-1061
Director-NA1@spwla.org



Middle East/Africa
Shouxiang (Mark) Ma
Saudi Aramco
Dhahran, Saudi Arabia
(+966) 3-874-5078
Director-MEA@spwla.org



N. America 2
Kelly Skuce
Core Petrophysical Consulting
Calgary, Canada
(+1) 587-228-0203
Director-NA2@spwla.org



Asia and Australia
Jennifer Market
MPC Kinetic
Perth, Australia
(+1) 713-302-8325
Director-Asia-Aus@spwla.org



Latin America
Nadege Bize-Forest
Schlumberger
Rio de Janeiro, Brazil
(+55) 21-97454-8772
Director-LA@spwla.org



Executive Director
Sharon Johnson
SPWLA
Houston, TX 77017
(+1) 713-947-8727
sharon@spwla.org



Europe
Craig Lindsay
Core Specialist Services Ltd.
Aberdeenshire, United
Kingdom
(+44) 7530-040117
Director-Europe@spwla.org



Managing Editor
Stephen Prenskey
(+1) 301-593-4966
sprenskey@gmail.com

Publication Manager
Anna Tarlton
InkSpot Printing
2301 S. Shaver
Pasadena, TX 77502, USA
(+1) 713-472-1100
orders@inkspotprinting.com

Welcome to the December 2019 edition of *Petrophysics*. In this issue you will find four papers to conclude our “Best of the 2019 Symposium” series, as selected by the 2019 Annual Symposium Technical Committee. Also included in this issue are six regular submissions to *Petrophysics*. There is quite a diverse range of topics represented in this month’s edition, and I hope that everyone will find something of interest to them.

As I mentioned in my previous columns in *Petrophysics*, as Vice President Publications for the SPWLA I have defined three high-level goals for this year. My third goal for the coming year is to improve the financial position of SPWLA publications.

‘Publications’ is one of the largest line items in the SPWLA annual operating budget. We prepare six issues of *Petrophysics* and six of *SPWLA Today* each year. To support this, we employ the skills of a Managing Editor, a publishing company, and a printing company to ensure that we continue to produce the highest quality publications that we can for the benefit of our membership.

Historically, the printing and distribution of *Petrophysics* in hard copy has been a major part of the publication costs. To reduce the overall cost of SPWLA publications, the decision was taken a couple of years ago to move to primarily electronic distribution, with *Petrophysics* in hard copy available as an additional subscription. This did have the intended effect of significantly reducing costs associated with the preparation of our publications, but an unintended consequence of this was a major decrease in the amount of advertising revenue our publications attracted. To address this, we are revamping our advertising strategy for SPWLA publications, positioning *SPWLA Today* as our primary platform for advertising. We are also continuing to look at our expenses relating to hard copy distribution of *Petrophysics*, with the aim of ultimately reaching a cost-neutral position on hard copy publications.

To further offset costs associated with the preparation of *Petrophysics*, a paper preparation fee was introduced at the beginning of 2019, replacing the historical color pages charges. Similar fees are levied by many of our sister professional societies, as well as other publishers of technical papers, and we do offer a waiver of this fee to those authors who are unable to pay it. However, such a fee can certainly act as a deterrent to those who may be considering submitting a paper to *Petrophysics*, which leads to my third goal for this year. This goal is to secure, through increased advertising and other sources, sufficient income so that we can do away with the paper preparation fee, and hence remove any roadblock for our potential contributors.

Since becoming Vice President Publications, I have probably received more correspondence related to the financial aspects of our publications than any other topic, particularly relating to the paper preparation fees. This is obviously an area of concern for many of our members. As readers of, and contributors to *Petrophysics*, I welcome your feedback and thoughts on this topic.

Tom Neville
Vice President Publications
tom.neville@formation-evaluation.asia

Best of the 2019 Symposium, Part 2

Inversion of High-Resolution High-Quality Sonic Compressional and Shear Logs for Unconventional Reservoirs¹

Ting Lei², Smaine Zeroug², Sandip Bose², Romain Prioul², and Adam Donald²

ABSTRACT

Interpretation of elastic properties honoring fine heterogeneity has garnered recognition recently in petrophysical analysis, bedding failure prediction, and hydraulic fracture job design for unconventional reservoirs. Traditional sonic log processing assumes homogeneity of the formation over a specific sonic tool receiver aperture length, e.g., at least 2 ft. This assumption may not be appropriate for highly laminated reservoirs. Additionally, shear slownesses extracted from low- and high-frequency processing are associated with different wavelengths and different rock volumes. Shear slowness logs from a high-frequency monopole transmitter and a low-frequency dipole flexural mode can exhibit different axial resolutions even when using the same receiver aperture length.

We developed a new interpretation algorithm to improve the layer slowness contrast for thinly laminated formations in vertical wells using borehole sonic data from array-based logging tools equipped with either a monopole, dipole, or a quadrupole transmitter. This novel interpretation method can yield high-quality high-resolution sonic compressional and shear logs. It is based on a robust deconvolution technique that jointly combines all logs processed at different array resolutions. This

method yields the sonic log with an optimal apparent resolution better than that estimated from the conventional 1-ft single-resolution subarray method. Finally, the residual is formulated to serve as a log quality-control flag and can be used to switch to more reliable low-resolution logs in depth intervals of poor-quality hole data.

The algorithm was validated with synthetic logs from finite-difference modeling and was then tested on a field dataset collected in a vertical well traversing a thinly laminated formation. The resolution of deconvolved compressional and shear logs from field measurements exceeds that from conventional processing, and is consistent with a higher resolution ultrasonic log from an ultrasonic imaging tool logged in the same well. The field-data application suggests that this deconvolution algorithm enhances the spatial resolution and more accurately captures the layer slowness contrast while removing outliers thereby improving the log quality.

The application of this method results in a superior characterization of the acoustic properties of thinly layered rocks relative to that from conventional processing. The estimated elastic moduli could improve stress profiling and rock-strength correlations for geomechanical modeling.

INTRODUCTION

Rock heterogeneity due to laminations plays a critical role in geomechanical analysis for unconventional reservoirs (Weng et al., 2018). Thinly laminated formations often display large contrast in elastic moduli between layers with implications for wellbore stability and fracture propagation (Xu et al., 2019). Borehole sonic logs are the most widely used technology for capturing such layer contrasts.

Figure 1 shows a borehole sonic logging device deployed in a vertical well. Part of the energy produced by either a monopole or dipole transmitter of the sonic logging

device propagates in a direction parallel to the borehole trajectory as headwaves. The propagating wave trains are then collected by an array of receivers placed a few feet above the transmitter. Processing the recorded array signals yields estimates of rock compressional and shear slownesses within the volume of receiver aperture. If a thin layer exists within the receiver aperture, the sonic signature can be complicated by reflections, mode conversion and phase change, depending on the layer contrast. Under the simple assumption of ray tracing, the measured slowness represents an averaged value of the slowness within the receiver aperture size.

Manuscript received by the Editor July 22, 2019; revised manuscript received October 23, 2019; manuscript accepted October 28, 2019.

¹Originally presented at the SPWLA 60th Annual Logging Symposium, The Woodlands, Texas, USA, June 17–19, 2019, Paper QQQ.

²Schlumberger-Doll Research, One Hampshire St., Cambridge, MA 02139, USA, tlei@slb.com; zeroug1@slb.com; bose1@slb.com; rprioul@slb.com; Schlumberger, 4-8 Nicolae Titulescu St., 011141 Bucharest, Romania; donalda1@slb.com

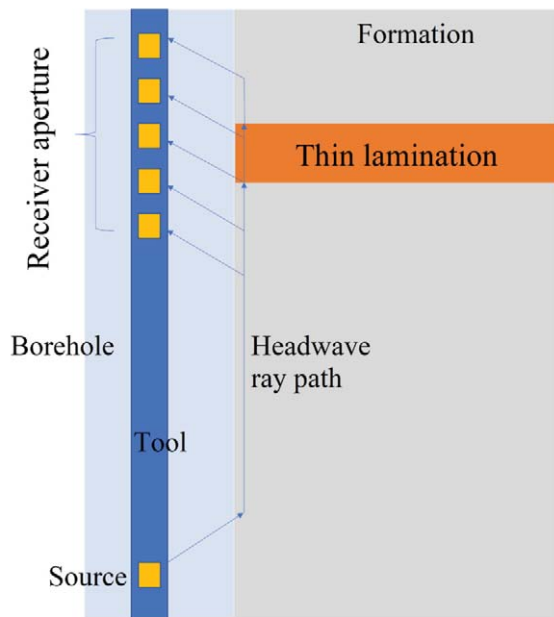


Fig. 1—Schematic view of an array sonic logging tool penetrating a thin lamination in a vertical well.

Obtaining high-resolution sonic logs for thinly laminated formations is not an easy task. Several subarray signal-processing methods have been proposed either in the time domain (Hsu and Chang, 1987; Tang et al., 1995; Valero et al., 2000; Tang and Patterson, 2001) or in the frequency domain (Sunaga et al., 2007; Wang et al., 2018; Sun et al., 2019). The time-domain methods, such as the multishot subarray slowness-time-coherence (STC) method (Kimball and Marzetta, 1984; Hsu and Chang, 1987), can yield higher layer contrast by reducing the number of subarray receivers (down to three). It might require several iterations to fine-tune processing parameters and relabel coherence peaks manually. Care must be taken in the manual relabeling work to make sure that the high-resolution sonic logs are not affected by the reduced signal/noise ratio associated with a smaller number of subarray receivers. Additionally, experience in sonic physics is often required to select a better sonic shear log when multiple processing options are available. Such a choice is usually based on the understanding of the physical characteristics of different sonic logging modes, i.e., the monopole and dipole borehole modes. In conclusion, there is no efficient way to automatically deliver quality-control (QC) logs for the processed answers.

Other approaches have also been proposed recently to enhance layer elastic contrast. For example, Huang and Torres-Verdín (2016) suggest a way to get high-resolution sonic logs using a nonlinear inversion method. Such an inversion gives a layer-by-layer estimation of compressional

and shear slownesses, although layer boundaries need to be accurately defined in advance. Khadhraoui et al. (2018) propose a way to automatically extract slowness by combining model-driven and data-driven approaches and thereby to stabilize the arrival times from the first arrival detection method they propose. A limitation of this method is that it can only get the compressional slowness.

Here, we propose a multiresolution based inversion algorithm that improves contrast and robustness of compressional and shear logs relative to traditional single-resolution approach. The new method outputs high-resolution sonic logs on a depth-by-depth basis and therefore does not require predefined layer boundaries. The robustness of this method is achieved by jointly deconvolving logs with different axial resolutions. As the algorithm is formulated into an overdetermined equation, a QC log can be generated and this serves as a disagreement flag to further cross-check logs with different resolution. The QC log also improves the efficiency in the sonic processing workflow because it enables an automated switch to a better-quality log when detecting noise in the conventionally labeled logs.

We begin with field and synthetic examples to explain receiver aperture and acquisition frequency effects on sonic log resolution and reliability. These observations motivated us to develop a deconvolution workflow, which is given in the following section. Then we use a 2D finite-difference modeling code to generate synthetic logs to evaluate the proposed method in terms of accuracy and robustness. Finally, we apply the algorithm to field data for geomechanical analysis to demonstrate the values of high-resolution logs to the mechanical earth model (MEM) (Plumb et al., 2000; Berard and Prioul, 2016).

SONIC LOGS AT DIFFERENT RESOLUTIONS

The STC (Kimball and Marzetta, 1984) and dispersive STC (DSTC) (Kimball, 1998) techniques are commonly used to extract compressional and shear slownesses from monopole and dipole waveforms, respectively. These methods are coherence-based methods, meaning that slownesses are estimated from peak coherence between wave trains recorded across an array of receivers. Figure 2 shows a field example of the STC processing results from a sonic logging tool with 13 receivers in a laminated formation. The STC method is applied to sets of waveforms, each made up of a different number of subarray receivers, i.e., 13, 8, 5, and 3. We observe a slowness tendency, where the processing using fewer receiver subarrays gives higher layer contrast for both compressional (labeled as DTSC) and shear (labeled as DTSH) slownesses. This aperture effect represents an apparent axial resolution of the tool.

For instance, a 5-receiver subarray for a logging tool with interreceiver spacing of 0.5 ft yields an apparent axial resolution of 2 ft.

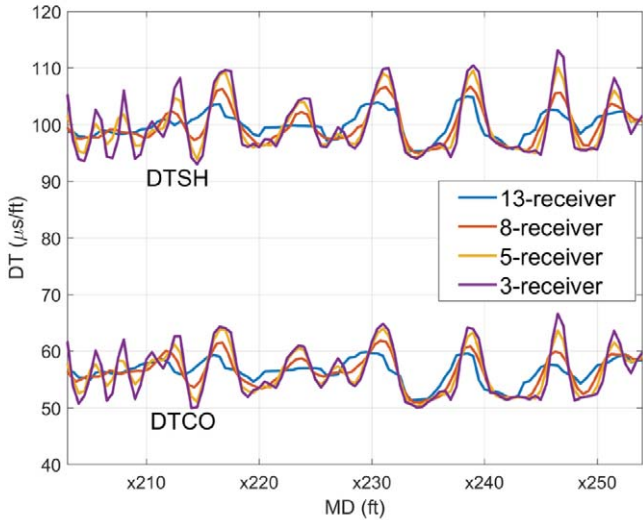


Fig. 2—Sonic field logs processed using different numbers of subarray receivers. A slowness resolution tendency can be observed associated with thin layers.

However, the apparent axial resolution based on the number of receivers and interreceiver spacing does not reflect the resolution that the logging tool is capable of delivering. This issue can be caused by various reasons. They have been studied widely (Zhang et al., 2000; Huang et al., 2015; Zeroug et al., 2016; Zeroug et al., 2018; Walker et al., 2019).

One reason is on the complexity in both the modal structure and signal frequency bandwidth that play a role in defining sonic spatial and slowness resolutions. Generally, for a sonic logging tool that operates at the frequency range of 1 to 15 kHz, the shear slowness from a monopole transmitter is extracted in the relatively high-frequency band, e.g., 8 to 15 kHz, whereas the shear slowness from a dipole transmitter is extracted from the low-frequency asymptote, e.g., at 1 to 2 kHz, of the formation primary flexural dispersion mode. Consequently, in a laminated interval, there is a frequency effect that might cause spatial resolution differences between the monopole shear slowness and the dipole shear slowness.

A field interpretation example is shown in Fig. 3. In Fig. 3, Track 1 displays the gamma-ray log, which confirms the presence of layering; Track 2 plots the compressional slowness from the 3-receiver processing of the monopole waveform; Track 3 overlays the monopole shear (shown in blue) and the dipole shear (shown in red), both of which are processed with the same 3-receiver subarray. We can see that

the monopole shear shows a better axial resolution (spatially and in slowness contrast) than the dipole shear and has better correlation to the compressional slowness, especially from X175 to X215 ft. Note that there is also a difference in depth of investigation between these two measurements. However, a detailed analysis on the radial profile (Zeroug et al., 2018) shows that such an effect is not the dominant factor here.

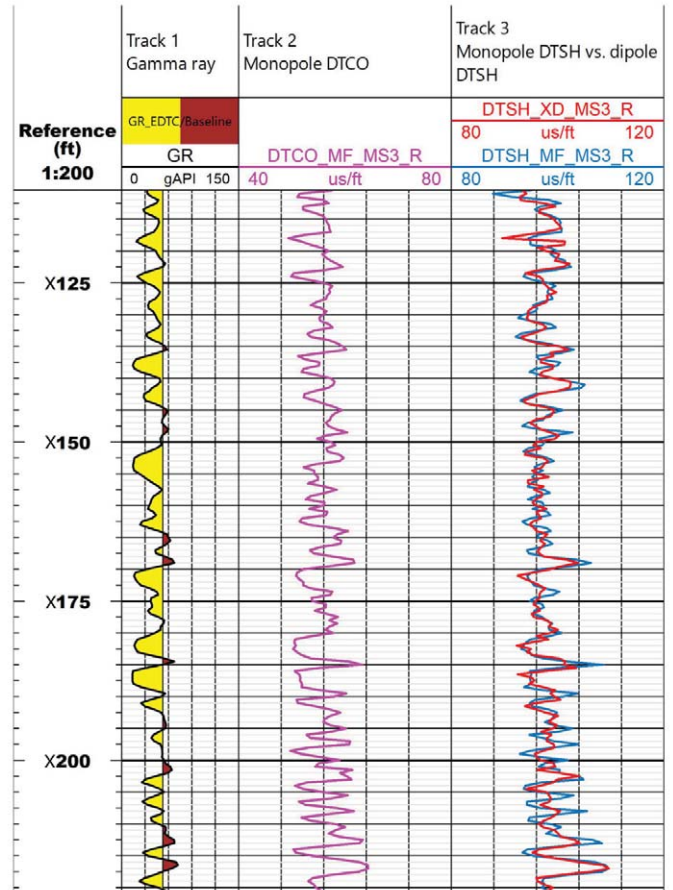


Fig. 3—Field data comparison between monopole shear and dipole shear of a thinly laminated formation. Track 1 plots the gamma-ray log. Track 2 plots the compressional slowness. Track 3 overlays the shear slownesses processed using monopole waveform and dipole waveform in blue and red, respectively. Note, the differing resolution of the monopole and flexural shear.

Such an observation can be reproduced by numerical modeling. For example, in Fig. 4, we simulate the response of the monopole and dipole waveform to a 1-ft thick layer using a 2D finite-difference modeling code (Randall et al., 1991). The output monopole shear and dipole shear are shown in green and orange circles, respectively (Fig. 4), whereas the true input shear log is shown as the solid purple line. We can see that, like the field data, the monopole shear can resolve a slightly better layer slowness contrast

than the dipole shear. The synthetic logs are processed using 5-receiver nondispersive STC with a frequency filter band of 6 to 16 kHz for the monopole waveform, and a filter band of 2 to 3 kHz for the dipole waveform. Note that in the modeling, the transmitter is located below receivers, as in the case shown in Fig. 1. In this modeling configuration, we observe that the output logs are depth shifted with respect to the thin layer. This is caused by the reflection and refraction of the propagating borehole waves. Consequently, in Fig. 4, the synthetic logs are depth matched to the thin layer using a peak-to-peak method. For field data, the depth matching could be done automatically with a traditional correlation-based method or a machine-learning-based method (Zimmermann et al., 2018) to get depth-consistent sonic logs with respect to other petrophysical logs.

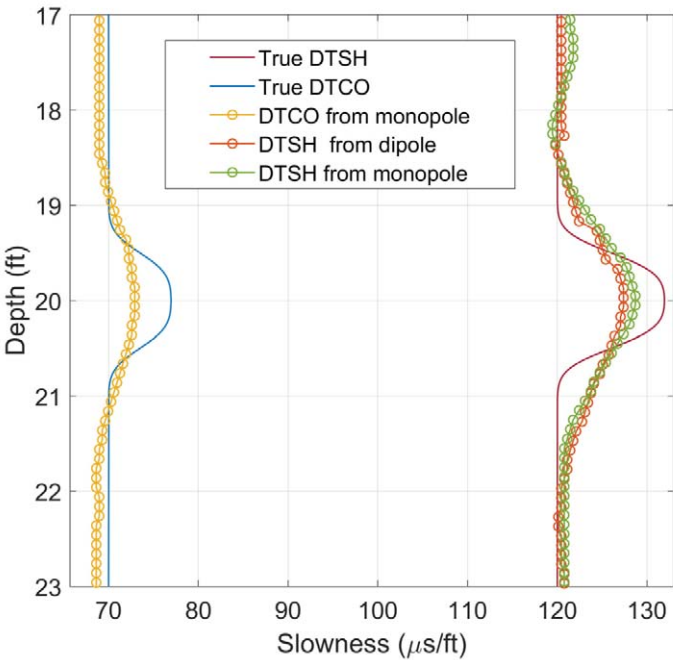


Fig. 4—Synthetic modeling comparison between monopole shear and dipole shear of a 1-ft layered formation. Note, the slight excursion in DTSH from monopole in the shallow depths (between 17 and 18 ft) is caused by the waveform reflection effect in the modeling, where the thin layer is located between the transmitter and the receiver array.

Based on the above comparisons along different receiver apertures and between transmitter frequency ranges, one can conclude that the high-frequency monopole waveform processed with a minimal number of receivers in the subarray is preferred in resolving thin layers. Although this is true in theory, we have found in practice that such an interpretation

poses problems in slowness reliability, because coherence peak position and its labeling with the minimum receiver aperture processing tends to present a robustness challenge to an algorithm and requires a tedious manual relabeling task.

Figure 5 illustrates an example of such a case. In Fig. 5, Track 1 displays the gamma-ray log; Track 2 shows the borehole shapes; Tracks 3, 4, and 5 display the STC slowness projections using 7-, 5-, and 3-receiver subarray processing, respectively, where the black dots represent the coherence peaks. We notice that 3-receiver processing can yield larger coherence values than 5- and 7-receiver processing; however, based on an error bar analysis (Kimball and Scheibner, 1998), a higher coherence does not represent smaller slowness variation. In fact, we notice that with 3-receiver subarray processing, the coherence peaks become very noisy and peak labeling becomes challenging.

Consequently, we believe that the variation of estimated slowness with receiver aperture observed within a layer provides qualitative yet valuable information on laminated formation evaluation. We believe this enables us to confidently distinguish a real layer from an artifact that might be caused by a noisy downhole logging condition. Inspired by this observation, we will, in the next section, present a mathematical formulation to quantify this effect and thereby invert for a high-quality high-resolution sonic log.

AN INVERSION ALGORITHM FOR HIGHER-RESOLUTION HIGH-QUALITY SONIC LOGS

The first step of the algorithm is to calculate multiple slowness estimates from different sets of receiver subarrays. It is well known that the average slowness measured by a N -receiver logging tool can be written as a convolution (Heliot et al., 2005) in the form of

$$s_{\text{measured}}(z) = \int_{-L/2}^{L/2} F_N(l)s(z-l)dl, \tag{1}$$

where $F_N(l)$ denotes the axial transformation function, or the response function, of a sonic logging tool with N receivers, $s(l)$ represents the true slowness profile, L is the tool receiver aperture length, and l is the length coordinate defined from to $-L/2$ to $L/2$.

It is important to note that F_N is model dependent, i.e., it depends on layer contrast, waveform frequency and processing method. Here, under the assumption of a simple propagation mode where layer reflection is ignored, using a

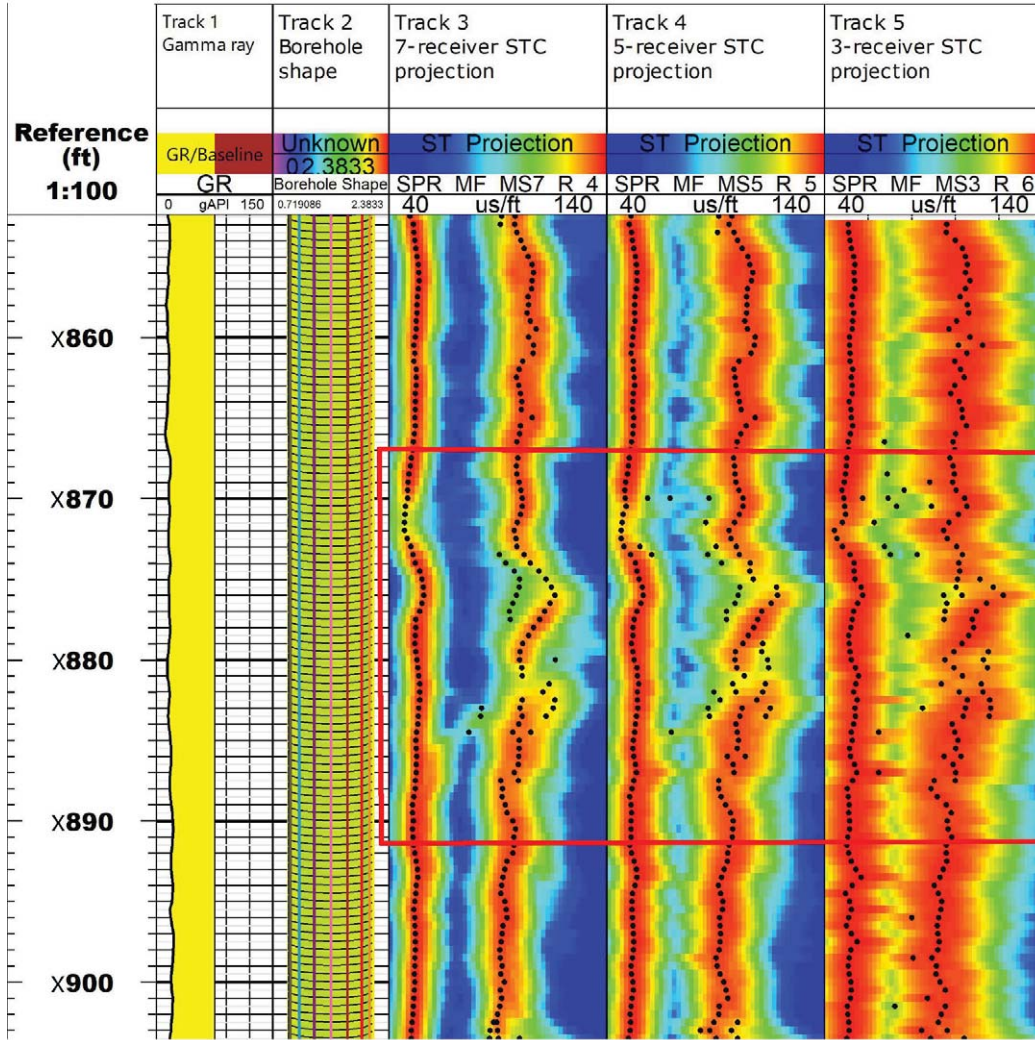


Fig. 5—Example of STC projections and peaks processed using different number of subarray receivers. Track 1 plots the gamma-ray log; Track 2 shows the borehole shapes; Tracks 3 to 5 display the STC projections using 7-, 5-, and 3-receiver subarray processing, respectively, where black dots represent slowness peaks. The scattered distribution of dots inside the red rectangle is believed to be caused by noise in the acquired waveforms.

perturbation approach (Huang et al., 2015), we can obtain (see Appendix 1 for detail)

$$F_N(l) = \frac{L^2(3N^2+1)-12l^2(N-1)^2}{2L^3N(1+N)} \quad (2)$$

Interpolating $s(l)$ using a P^{th} -order Lagrange polynomial shape function and N consecutive slowness values s_k ($k=1,2,\dots,N$) as

$$s(l) = \sum_{k=1}^N P_{Nk}(l)s_k, \quad (3)$$

where P_{Nk} is defined by

$$P_{Nk}(l) = \prod_{j=1(j \neq k)}^N \frac{l-l_j}{l_k-l_j}, \quad (4)$$

we can get

$$s_{\text{measured}} = \sum_{k=1}^N g_{Nk} s_k, \quad (5)$$

where the coefficients g_{Nk} can be evaluated explicitly as

$$g_{Nk} = \int_{-L/2}^{L/2} F_N(l) P_{Nk}(l) dl. \quad (6)$$

Second, based on the formulation to calculate the average slowness, we can derive a linear inversion algorithm that combines sonic logs processed at different apparent resolutions to invert for the high-resolution sonic log.

We define the high-resolution sonic log at each measurement depth as a vector

$$\mathbf{S} = \begin{bmatrix} s_1 \\ s_2 \\ \vdots \\ s_q \end{bmatrix}, \quad (7)$$

where q is the number of measured depths, and $s_1, s_2, \dots,$ and s_q are the slowness values at each depth.

The sonic logs measured by a sonic tool using N -receiver subarray can be written as

$$\mathbf{D}_N = \begin{bmatrix} d_1 \\ d_2 \\ \vdots \\ d_q \end{bmatrix},$$

where d_1, d_2, \dots, d_q are the measured slownesses.

We can therefore write the convolutional relationship between \mathbf{S} and \mathbf{D}_N in matrix form as

$$\mathbf{G}_N \mathbf{S} = \mathbf{D}_N, \quad (8)$$

where the transformation function, \mathbf{G}_N , is an N -by- N matrix defined as

$$\mathbf{G}_N = \begin{bmatrix} g_{N1} & g_{N2} & \dots & g_{NN} & 0 & \dots & 0 \\ 0 & g_{N1} & g_{N2} & \dots & g_{NN} & \dots & 0 \\ \vdots & \vdots & g_{N1} & g_{N2} & \dots & g_{NN} & \vdots \\ \vdots & \vdots & \ddots & \ddots & \ddots & \ddots & \vdots \\ 0 & 0 & \dots & g_{N1} & g_{N2} & \dots & g_{NN} \end{bmatrix} \quad (9)$$

and g_{Nk} ($k=1,2,\dots,N$) is given by Eq. 6.

Mathematically, \mathbf{S} can be found by inverting \mathbf{G}_N . However, because the transformation matrix is ill-conditioned when $N > 3$ (a synthetic example is shown in the next section), we propose to construct an overdetermined linear equation using multiple-resolution logs, denoted as $\mathbf{D}_{N1}, \mathbf{D}_{N2}, \dots, \mathbf{D}_{Np}$. The linear equation can be written as

$$\mathbf{G} \mathbf{S} = \mathbf{D}, \quad (10)$$

Where

$$\mathbf{G} = \begin{bmatrix} \mathbf{G}_{N1} \\ \mathbf{G}_{N2} \\ \vdots \\ \mathbf{G}_{Np} \end{bmatrix}, \quad (11)$$

and

$$\mathbf{D} = \begin{bmatrix} \mathbf{D}_{N1} \\ \mathbf{D}_{N2} \\ \vdots \\ \mathbf{D}_{Np} \end{bmatrix}. \quad (12)$$

A linear inversion can be done to solve for the high-resolution sonic log, \mathbf{S} ,

$$\mathbf{S} = \mathbf{G}^+ \mathbf{D}, \quad (13)$$

where \mathbf{G}^+ denotes the Moore-Penrose pseudoinverse (Weisstein) of the matrix \mathbf{G} .

In the inversion algorithm defined by Eq. 13, we use the input sonic logs that have the same measurement depth. Assuming a sonic logging tool with 13 receivers, sonic logs processed with 13, 11, 9, 7, 5, and 3 receivers share the same measured depth at receiver number 7, which is set as the middle receiver of the subarray. Other input sonic logs can be used in the inversion with proper interpolation.

Finally, a QC log can be obtained simply by calculating a mismatch between measured and modeled logs of each receiver set N as,

$$\mathbf{Y}_N = \mathbf{D}_N - \mathbf{G}_N \mathbf{S}. \quad (14)$$

The QC log can be used to check the correlation between input logs, as will be seen in a field data example in the paper.

SYNTHETIC DATA VALIDATION AND SENSITIVITY ANALYSIS

In this section, we carry out an inversion test using synthetic logs and a sensitivity analysis toward the input uncertainties from logging noise.

We first present our inversion evaluation using synthetic logs. The synthetic logs are generated by a 2D finite-difference time-domain (FDTD) modeling code (Randall et al., 1991). In the forward modeling, the sonic logging tool is placed inside a vertical fluid-filled borehole and is moving upward to cross synthetic horizontal thin layers of 1 to 2 ft in thickness. In order to test our depth-by-depth inversion algorithm, we define the synthetic thin layers as smooth curves instead of blocky logs, based on the fact that the depth sampling rate is usually every 0.5 ft in real logging conditions. Consequently, the curve is defined by polynomial interpolation of slowness values at measured depths. The tool has 13 receivers with an interreceiver spacing of 0.5 ft.

In Figure 6, the synthetic profile of compressional slowness is shown as a black curve whereas the synthetic FDTD logs processed using different number of receiver

subarray (13, 11, 9, 7, 5, and 3 receivers) STC are labeled with different colors. The deconvolved high-resolution log is overlaid as the purple curve. We can see that generally the deconvolved high-resolution log (purple) better approximates the true log (black) than all input logs, and the approximation improves with increase in the layer thickness.

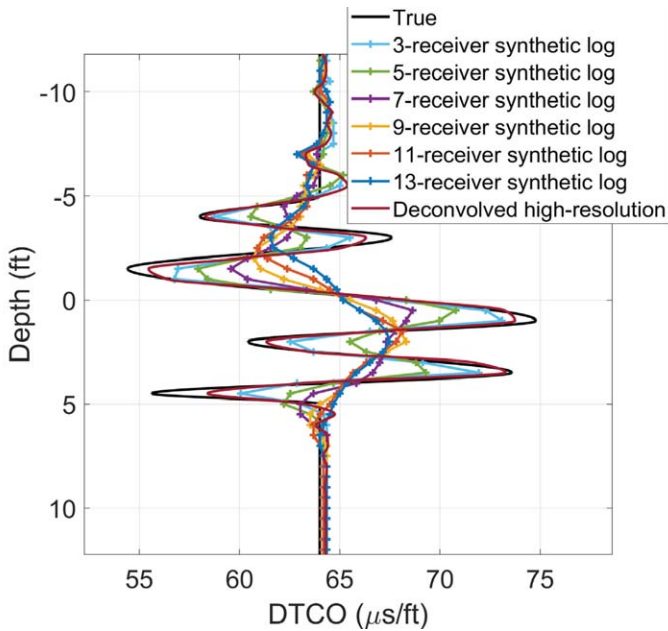


Fig. 6—Multiresolution joint deconvolution result for synthetic finite-difference logs processed using 13, 11, 9, 7, 5, and 3 subarray receivers. The deconvolved high-resolution log, in purple, approaches the closest the true log, in black.

Next, we conduct numerical experiments to test the effect on an inversion using a single-resolution log, i.e., a log that is processed using a fixed number of subarray receivers. Figures 7a, 7b, and 7c, show the inversion result using a single-resolution log with 13-receiver, 5-receiver, and 3-receiver log, respectively. We can see that when $N > 3$, the single-resolution-based inversion becomes numerically unstable. Additionally, the 3-receiver single-resolution inversion shows slightly worse result (at depths around -1 ft and -4 ft) as compared to the multiresolution-based inversion, as shown in Fig. 6.

To test the robustness of the inversion algorithm, we further conduct two numerical experiments by adding random Gaussian noise to the input logs to simulate slowness variations due to downhole logging noise. Figure 8 shows the test result in a case where we only use the 3-receiver log as the input, and where a random Gaussian noise with standard deviation of $0.3 \mu\text{s}/\text{ft}$, i.e., $\pm 1 \mu\text{s}/\text{ft}$ from the mean value in the 99.9% confidence interval, is added to the 3-receiver log, as shown in Fig. 8a. The inversion result is shown in Fig. 8b as overlaid plots with the width representing uncertainty, which shows approximately the same uncertainty as the input 3-receiver log.

Next, we test the sensitivity of the multiresolution joint inversion. Because logs from shorter subarray receiver apertures manifest larger uncertainties, whereas logs with larger apertures have smaller uncertainties but lower contrast, in Fig. 9, we only add the above noise standard deviation to the 3-receiver log maintaining other inputs, including 13-, 11-, 9-, 7-, and 5-receiver logs, as noise-free. The resulting deconvolved high-resolution logs are shown Fig. 9b as overlaid plots with the width representing uncertainty. It features much smaller uncertainty as compared to the single-resolution inversion result in Fig. 8b.

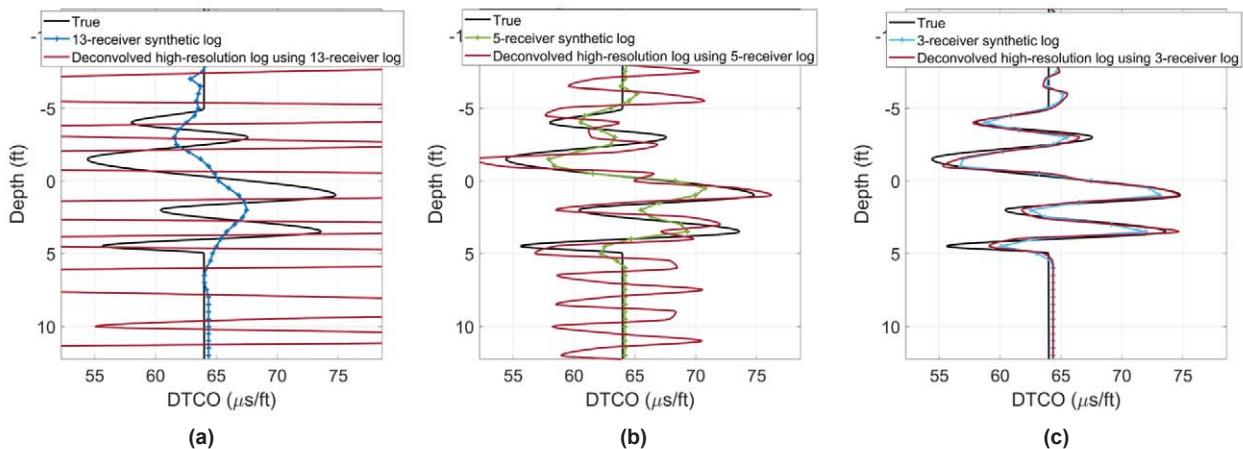


Fig. 7—Deconvolved high-resolution log for a single-resolution synthetic log processed using (a) 13 subarray receivers; (b) 5 subarray receivers; (c) 3 subarray receivers.

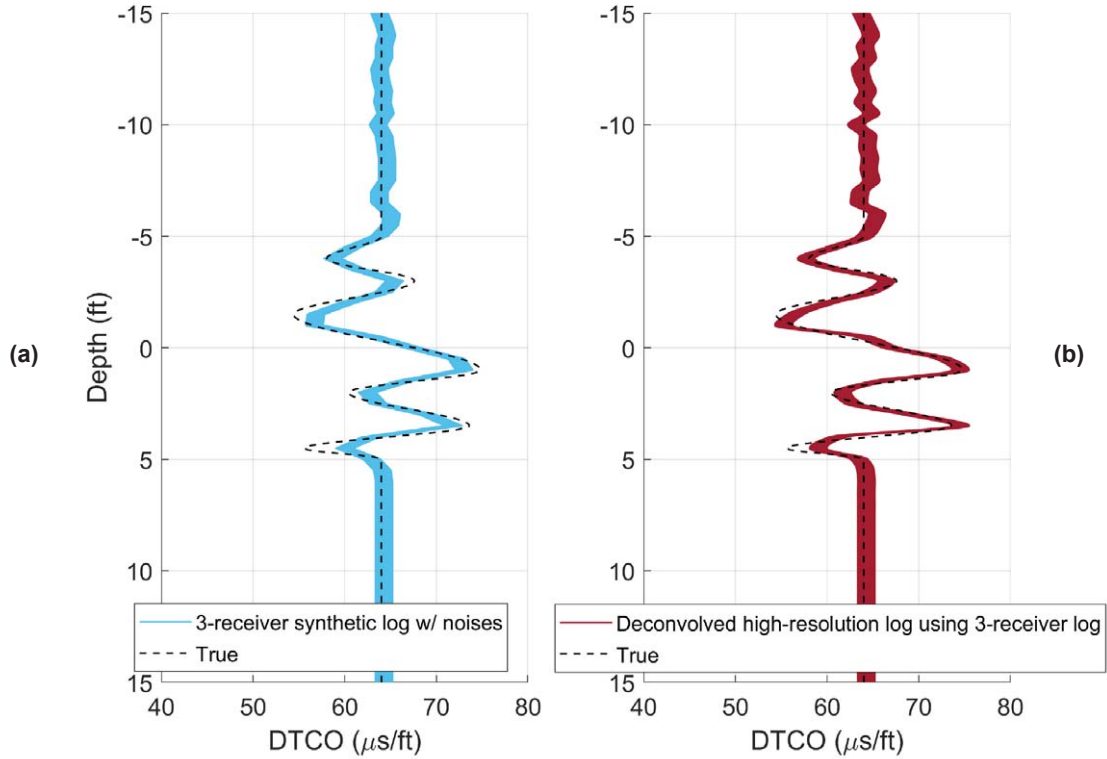


Fig. 8—(a) Synthetic finite-difference log processed using 3-receiver subarray after the addition of 1,000 realizations of random Gaussian noise with a standard deviation of 0.3 $\mu\text{s}/\text{ft}$; (b) the overlaid plots of deconvolved high-resolution sonic logs using the 3-receiver log, with the Gaussian random noise added.

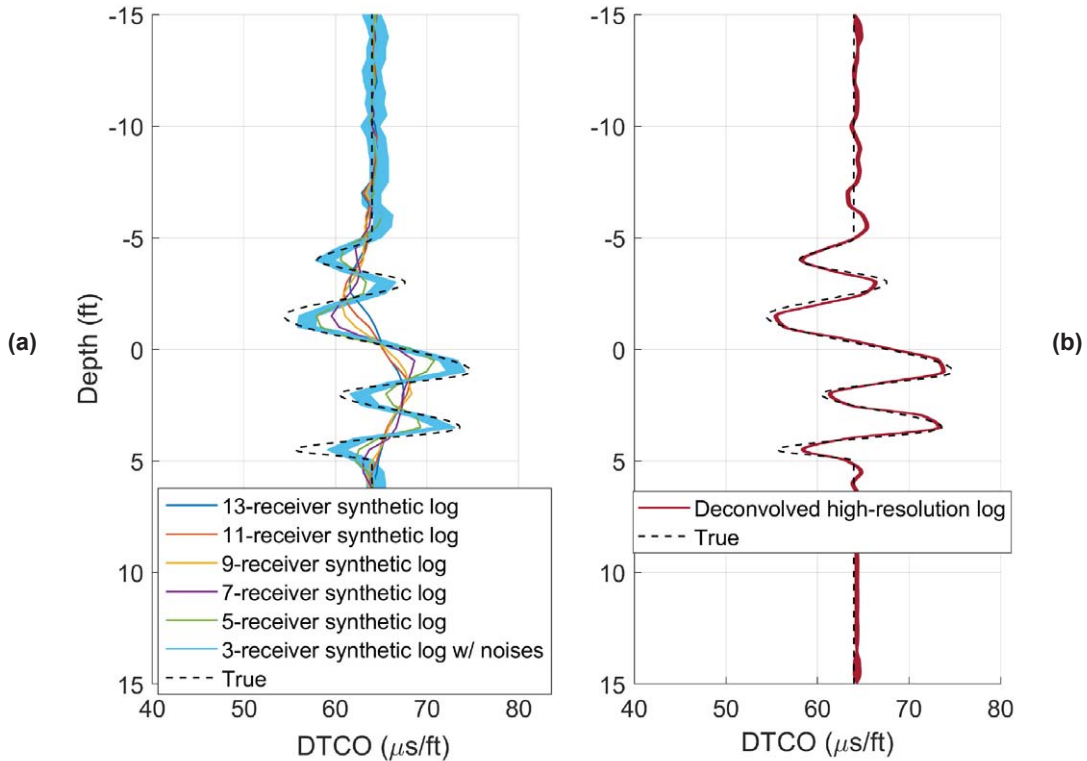


Fig. 9—(a) Synthetic finite-difference log processed with 3, 5, 7, 9, 11 and 13 receivers; (b) the overlaid deconvolved high-resolution sonic logs using inputs from (a). Note that only the 3-receiver log input is given a Gaussian random noise (with a standard deviation of 0.3 $\mu\text{s}/\text{ft}$) and is overlaid with 1,000 random realizations.

The previous two sensitivity tests demonstrate that the algorithm using multiresolution logs yields a high-resolution log that can be well-constrained by all available inputs.

APPLICATIONS TO FIELD DATA

In this section, we apply the proposed workflow to an openhole vertical pilot well traversing a thinly laminated rock formation. Two types of acoustic tools were logged in this well: a conventional sonic logging tool and an ultrasonic tool. The ultrasonic tool is configured with a pitch-catch modality, which employs a transmitter and two receivers spaced 100 mm from each other. The distance between transmitter to near-receiver is 250 mm. The transducers are aligned at angles to enhance coupling to the rock compressional and shear waves, respectively. The tool was logged twice to acquire data for the two wave types with a 1.5-in. axial sampling rate and a 10° azimuthal sampling rate. A direct measure of the slowness across the two receivers is calculated from the transit times of the early-arriving events, estimated with a zero-break detection algorithm. The tool operates in the range of 50 to 600 kHz with an approximately effective probing wavelength ranging from several millimeters to several centimeters (roughly 0.5 to 3 in.), therefore achieving higher spatial resolving capability than the sonic measurement (Zeroug et al., 2018).

Figure 10 plots the standard 2-ft resolution sonic compressional log in black and the deconvolved high-resolution compressional log in magenta (Track 2), and the 2-ft resolution shear log in black and high-resolution shear log in orange (Track 3). The ultrasonic compressional and shear logs, shown in green and cyan, are overlaid in Tracks 2 and 3, respectively, for comparison with sonic measurements. We observe that the slowness contrast from the deconvolved high-resolution sonic log yields much higher spatial resolution than the standard 2-ft resolution. Further, we see that its values fall within the corresponding ultrasonic log—a reasonable outcome reflecting the frequency difference (a factor of 20) between the sonic and ultrasonic logging devices but also confirming that our sonic deconvolution approach is reliable. Note that in Fig. 10, the slightly faster ultrasonic shear log reading is associated with the measurement mechanism, i.e., the pseudo-Rayleigh surface wave, relied upon to extract a shear slowness (Zeroug and Lei, 2017); it is not germane to the discussion in this article.

Figure 11 shows an illustrative example of how the QC log can help us to detect noise in the input logs. In Figure 11, Track 1 plots the gamma-ray log; Track 2 overlays the monopole shear logs, using 7-, 5-, and 3-receiver subarrays. These three shear logs are inputs to the inversion for our

high-resolution shear log, which is shown as the green curve in Track 5. The QC log generated using Eq. 14 is displayed as an area fill in Track 3, with a smaller value representing a better correlation. We observe that this QC log shows large values at an interval between X860 to X900 ft, meaning that it successfully detects the disagreement tendencies among different resolution logs shown in Track 2. Taking advantage of this QC log, we automatically switch to a more reliable log in such an interval. For example, in this case, the dipole shear log shown in Track 4 is used to replace the deconvolved high-resolution log (green curve in Track 5) when the QC log shows a residual value of more than 2% relative to the standard-resolution log, and the final constructed log is shown in the orange curve in Track 5. The last track plots the compressional slowness and we

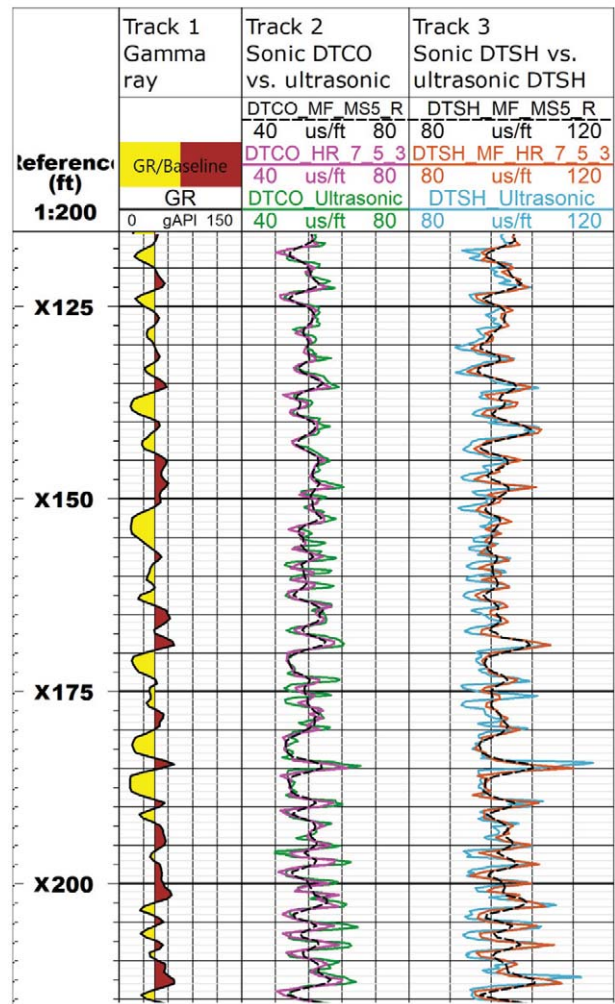


Fig. 10—Comparison of high-resolution sonic logs with ultrasonic logs. Track 1, gamma ray; Track 2, compressional logs from standard 2-ft resolution sonic (black), high-resolution sonic (magenta) and ultrasonic (green); Track 3, shear logs from standard 2-ft resolution sonic (black), high-resolution sonic (orange) and ultrasonic (cyan).

can see the finished high-resolution shear log shows good correlation with the compressional log. Note that the high-resolution compressional log at this interval actually shows good quality based on its QC log (not plotted in Fig. 11).

Figure 12 compares the compressional velocity/shear velocity ratio (VPVS) vs. compressional slowness (DTCO) crossplots using different resolution logs: (a) using the conventional 2-ft monopole compressional and shear, and (b) using the high-resolution monopole compressional and the final high-resolution shear. Colors overlaid on dots represent values of the gamma-ray log. The histogram figures shown above and right of the crossplot represent normalized

distributions of DTCO and VPVS, respectively; the dotted rectangles are placed to help with a visual comparison on the distribution of DTCO/VPVS ratio. We observe that the high-resolution log estimation yields higher ranges in both slowness and VPVS ratio. We believe this should translate into more accurate and representative correlations for the use of sonic data in petrophysical analysis. We also observe that the conventional low-resolution processing in (a), pointed with the black box, there is a coalescence that is not showing a physically meaningful trend line. Such a coalescence is not present in the better resolvable rock slowness in (b). These plots highlight that the high-resolution log estimation

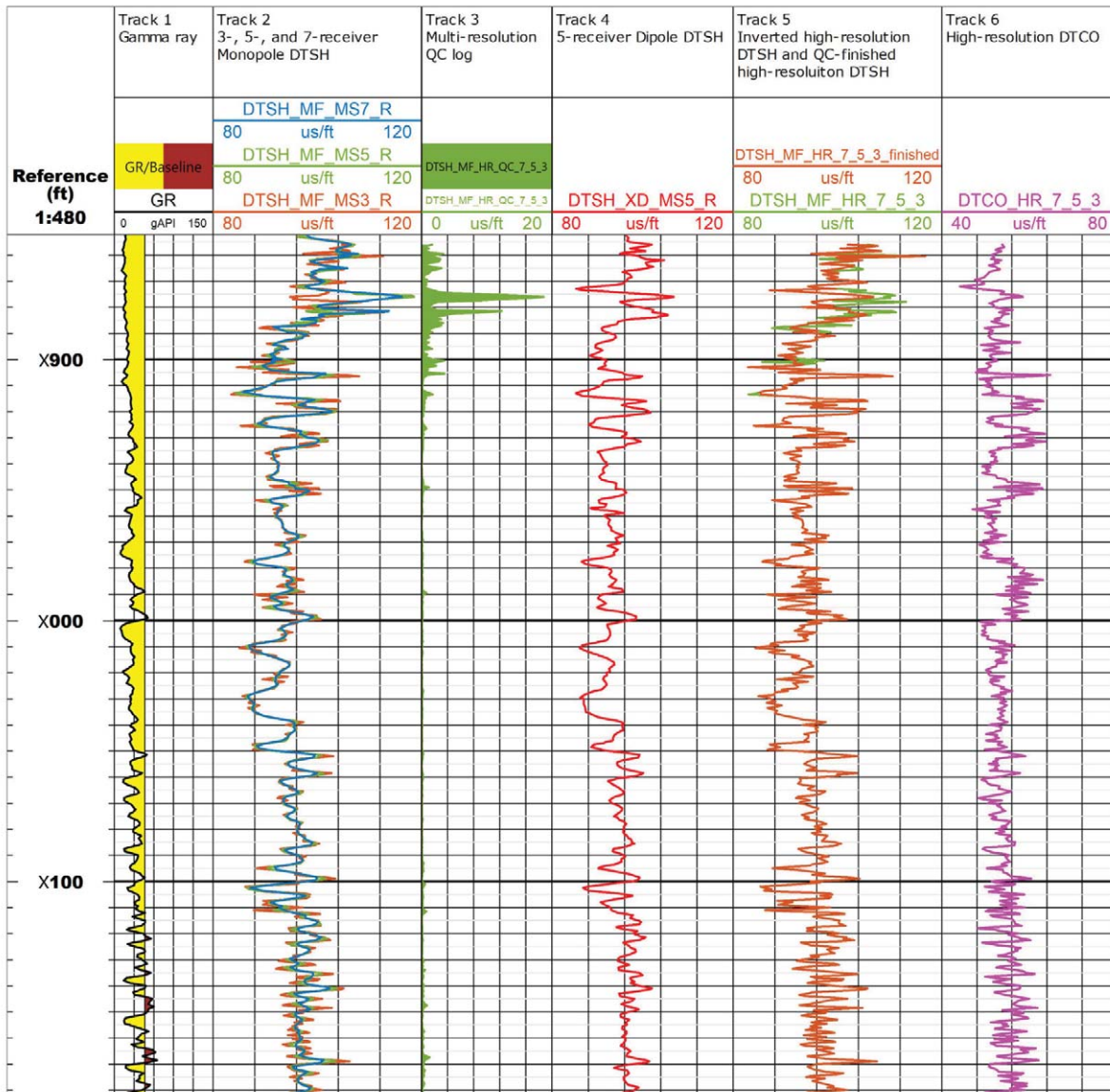


Fig. 11—An illustrative example on the use of the QC log to automatically switch to a more reliable sonic shear log. Track 1, gamma ray; Track 2, monopole shear logs processed using 7, 5, and 3 receivers are shown in blue, green and orange, respectively; Track 3, QC log to check the correlation between monopole shear logs displayed in Track 2; Track 4, a more reliable 2-ft dipole shear log; Track 5, the deconvolved high-resolution shear log (green) and the QC-finished high-resolution shear log (orange); Track 6, the deconvolved high-resolution compressional log.

better honors the layered rock heterogeneities by reducing the averaging effect associated with the conventional low-resolution slowness estimation.

Finally, to illustrate the effect on the MEM using the high-resolution logs, we choose an interval to compare Young’s modulus (YME), Poisson’s ratio (PR) and the minimum horizontal stress built from either the conventional 2-ft resolution logs or the high-resolution logs within an isotropic (vertical-only) assumption for the stress estimation.

In Figure 13, Track 2 compares the static Young’s modulus using conventional 2-ft resolution logs (blue) and the high-resolution logs (orange). The static Young’s modulus is converted from the dynamic modulus using an unpublished core-based correlation method. Similarly, Track 3 compares the static Poisson’s ratio using the conventional 2-ft resolution logs (blue) and the high-resolution logs (orange), where the static Poisson’s ratio is taken the same as the dynamic Poisson’s ratio. Track 4 compares the 2-ft resolution minimum horizontal stress (blue) and the high-resolution minimum horizontal stress (orange), which are computed using the poroelastic horizontal strain equation (Thiercelin and Plumb, 1994), where we assume the horizontal strain terms are neglected. In these plots, we observe that for both elastic moduli and horizontal stress, the high-resolution MEM shows markedly larger amplitude contrast than the conventional MEM. Larger variations in MEM can help to improve the accuracy in core-log integration, where the scale of core samples is usually smaller than the mechanical properties derived from sonic logs (Qiu et al., 2005). In addition, a higher-resolution MEM can capture more closely the thinly laminated mechanical properties and thereby can be applied in the downstream completion job design and sanding prediction models for thinly laminated reservoirs (Abbas et al., 2018). Note that here we build the MEM just to compare between high-resolution and 2-ft resolution logs. The effect of anisotropy on the MEM is not included. Such an effect requires a high-resolution horizontal shear slowness, which cannot be obtained from traditional low-frequency Stoneley processing. A more complete and well-calibrated high-resolution geomechanical case study is deferred to a future study.

CONCLUSIONS

We have demonstrated through field-data examples that formation thin lamination can challenge the conventional, receiver-array and multishort subarray estimation and interpretation workflow due to the averaging effect inherent to the conventional workflow. We have proposed a new method to reliably resolve a better lamination contrast

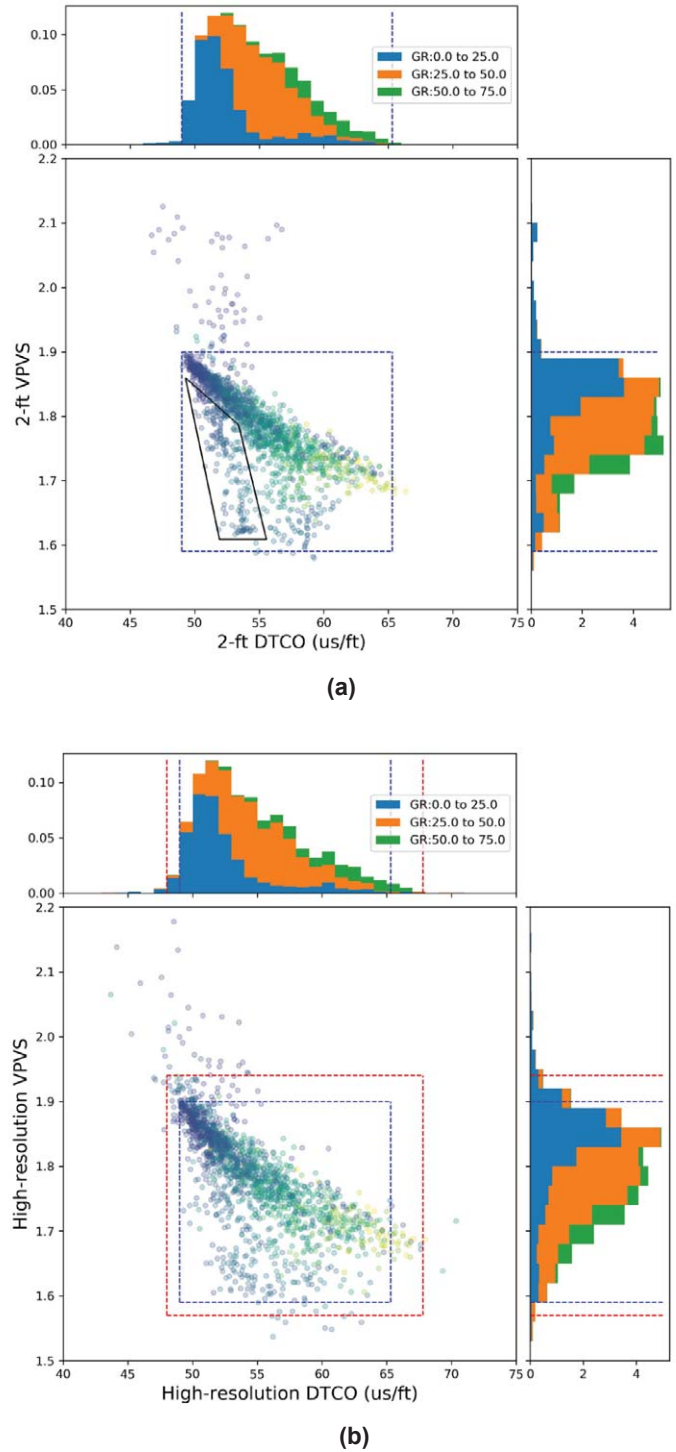


Fig. 12—A comparison of VPVS vs. DTCO plots using different resolutions, with (a) using the 2-ft resolution monopole compressional and shear slownesses, and (b) using the monopole high-resolution compressional and the final high-resolution shear. Colors overlaid on dots represent values of the gamma-ray log. The histogram figures shown above and right to the crossplot represent normalized distributions of DTCO and VPVS, respectively. The dashed rectangles and lines are used to help with a visual comparison between the distributions in (a) and (b).

using a multiresolution approach. We argue that this method yields a sonic log with an optimal apparent resolution that is better in spatial and slowness contrast resolution than that, for instance, estimated from the conventional 1-ft single resolution subarray method with additionally more robustness to noise. We have validated the proposed method using synthetic logs. We have also formulated a QC log to cross-check the input sonic logs. The QC log can help in selecting the best shear log between the monopole shear and the dipole shear, although the best shear selection will also depend on the targeted petrophysics or geomechanics applications.

The algorithm has been applied to field data to obtain a high-resolution sonic log that is consistent with an even higher resolution ultrasonic log from an ultrasonic imaging tool logged in the same well. Our preliminary application to a geomechanical study shows that a high-quality high-resolution sonic log can help to better support operational decisions, such as landing laterals or staging stimulation intervals to avoid weak or strong interfaces.

Finally, it is important to point out that the proposed method remains limited by the physical constraints in the operating frequency range of a sonic logging device (below 20 kHz). For instance, this method will not be able to resolve inch-scale lamination. Such a scale can only be detected by use of a higher-frequency ultrasonic device, which can resolve the rock heterogeneity and layering anisotropy often encountered in unconventional reservoirs (Prioul et al., 2017; Zeroug and Lei, 2017). Sonic measurement from compressional and shear headwaves can probe deep into the formation and is not largely affected by near-wellbore rock property variation in the radial direction, whereas ultrasonic measurements have their own limitations, such as shallow reading of the near-wellbore that can be affected by logging conditions or their inability to yield reliable shear logs in medium to slow formations. Consequently, we believe that a multiscale interpretation that combines sonic and ultrasonic measurements would be an optimal choice to fully characterize a thinly laminated reservoir.

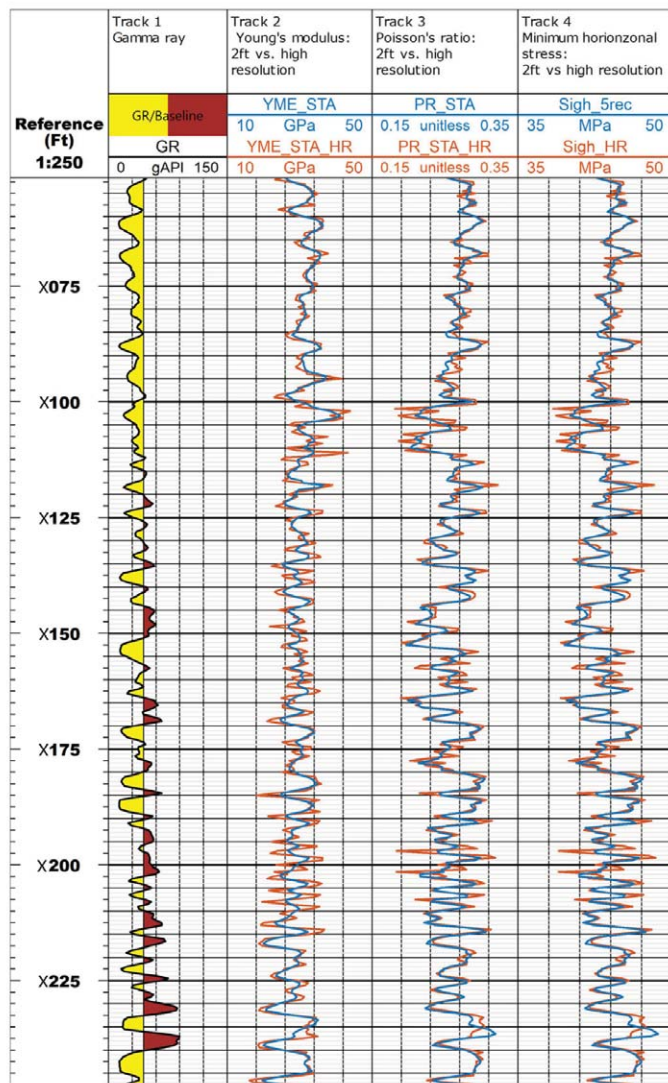


Fig. 13—An illustrative example of building MEM using either conventional 2-ft resolution sonic logs or the deconvolved high-quality high-resolution sonic logs. Track 1, gamma ray; Track 2, static Young's modulus from 2-ft sonic (blue) and high-resolution sonic logs (orange); Track 3, static Poisson's ratio logs from 2-ft sonic logs (blue) and high-resolution sonic logs (orange); Track 4, minimum horizontal stresses from 2-ft sonic logs (blue) and high-resolution sonic logs (orange).

ACKNOWLEDGMENTS

We acknowledge Takeshi Endo for valuable discussions, and all reviewers for their comments and suggestions.

NOMENCLATURE

Abbreviations

- DSTC = dispersive slowness-time-coherence
- DTCO = compressional slowness, $\mu\text{s}/\text{ft}$
- DTSH = shear slowness, $\mu\text{s}/\text{ft}$
- FDTD = finite-difference time domain
- GR = gamma ray
- HR = high-resolution
- MEM = mechanical earth model
- MD = measured depth
- PR = Poisson's ratio
- QC = quality control
- STC = slowness-time-coherence
- VPVS = compressional velocity/shear velocity ratio
- YME = Young's modulus, GPa

Symbols

- σ_{h} = minimum horizontal stress, MPa
 D_N = N-receiver measured sonic log
 G_N = N-receiver convolution matrix
 $F_N(l)$ = N-receiver tool transformation function
 l = length coordinate defined within receiver aperture
 P_{Nk} = Lagrange interpolation function
 S = high-resolution sonic log

REFERENCES

- Abbas, A. K., Al-Hamad, N., and Alsaba, M., 2018, Enhancing Rock Mechanical Properties Estimation for Thin Beds Using Microresistivity Borehole Imaging Tool, Paper SPE-193143 presented at the Abu Dhabi International Petroleum Exhibition & Conference, Abu Dhabi, UAE, 12–15 November. DOI: 10.2118/193143-MS.
- Bérard, T., and R. Prioul, 2016, Mechanical Earth Model: The Defining Series. <https://www.slb.com/-/media/files/oilfield-review/defining-mem.ashx>. Accessed October 30, 2019.
- Heliot, D., Tabanou, J., and Goswami, J., 2005, System and Method for Analyzing a Thin Bed Formation, U.S. Patent 6,963,803, granted November 8, 2005.
- Hsu, K., and Chang, S.K., 1987, Multiple-Shot Processing of Array Sonic Waveforms, *Geophysics*, **52**(10), 1376–1390. DOI: 10.1190/1.442250.
- Huang, S., Matuszyk, P.J., and Torres-Verdín, C., 2015, Spatial Sensitivity Functions for Rapid Numerical Simulation of Borehole Sonic Measurements in Vertical Wells, *Geophysics*, **80**(5), D459–D480, DOI: 10.1190/geo2014-0587.1.
- Huang, S., and Torres-Verdín, C., 2016, Inversion-Based Interpretation of Borehole Sonic Measurements Using Semianalytical Spatial Sensitivity Functions, *Geophysics*, **81**, D111–D124, doi: 10.1190/geo2015-0335.1.
- Khadhraoui, B., Kiswa, S., and Nguyen, H.M.T., 2018, A New Algorithm for High-Depth-Resolution Slowness Estimate on Sonic-Array Waveforms, Paper PPPP, *Transactions, SPWLA 59th Annual Logging Symposium*, London, UK, 2–6 June.
- Kimball, C.V., 1998, Shear Slowness Measurement by Dispersive Processing of the Borehole Flexural Mode, *Geophysics*, **63**(2), 337–344. DOI: 10.1190/1.1444333.
- Kimball, C.V., and Marzetta, T.L., 1984, Semblance Processing of Borehole Acoustic Array Data, *Geophysics*, **49**(3), 274–281. DOI: 10.1190/1.1441659.
- Kimball, C.V., and Scheibner, D.J., 1998, Error Bars for Sonic Slowness Measurements, *Geophysics*, **63**(2), 345–353. DOI: 10.1190/1.1444334.
- Plumb, R., Edwards, S., Pidcock, G., Lee, D., and Stacey, B., 2000, The Mechanical Earth Model Concept and Its Application to High-Risk Well Construction Projects, Paper SPE-59128 presented at the IADC/SPE Drilling Conference, New Orleans, Louisiana, USA, 23–25 February. DOI: 10.2118/59128-MS.
- Prioul, R., Johnson, D., and D'Angelo, R., 2017, Downhole Elastic Anisotropy Measurements, US Patent 9,625,599, granted April 18, 2017.
- Qiu, K., Marsden, R., Solovyov, Y., Safdar, M., Chardac, O., and Shatwan, M., 2005, Downscaling Geomechanics Data for Thin-Beds Using Petrophysical Techniques, Paper SPE-93605 presented at the SPE Middle East Oil and Gas Show and Conference, Bahrain, 12–15 March. DOI: 10.2118/93605-MS.
- Randall, C.J., Scheibner, D.J., and Wu, P.T., 1991, Multipole Borehole Acoustic Waveforms: Synthetic Logs With Beds and Borehole Washouts, *Geophysics*, **56**(11), 1757–1769. DOI: 10.1190/1.1442988.
- Sun, X., Ayadiuno, C., and Li, W., 2019, A Statistical Prony Method for Shear Slowness Estimation from Dipole Measurements, *SEG Technical Program Expanded Abstracts*, 859–863. DOI: 10.1190/segam2019-3216002.1.
- Sunaga, S., Yoneshima, S., Endo, T., and Kinoshita, T., 2007, High Resolution Dispersion Analysis of Array Sonic Waveforms, Paper Q, *Proceedings, Japan Formation Evaluation Society 13th Formation Evaluation Symposium*, Chiba, Japan, 27–28 September.
- Tang, X.M., and Patterson, D., 2001, Detecting Thin Gas Beds in Formations Using Stoneley Wave Reflection and High-Resolution Slowness Measurements, Paper OO, *Transactions, SPWLA 42nd Annual Logging Symposium*, Houston, Texas, USA, 17–20 June.
- Tang, X.M., Reiter, E.C., and Burns, D.R., 1995, A Dispersive-Wave Processing Technique for Estimating Formation Shear Velocity from Dipole and Stoneley Waveforms, *Geophysics*, **60**(1), 19–28, DOI: 10.1190/1.1443747.
- Thiercelin, M.J., and Plumb, R.A., 1994, A Core-Based Prediction of Lithologic Stress Contrasts in East Texas Formations, *SPE Formation Evaluation*, **9**(4), 251–258, DOI: 10.2118/21847-PA.
- Valero, H.P., Hsu, K., and Brie, A., 2000, Multiple-Shot Processing in Slowness and Time Domain of Array Sonic Waveforms, *Technical Program Expanded Abstracts*, 1687–1690. DOI: 10.1190/1.1815743.
- Walker, K., Sun, Q., and Wang, R., 2019, Wavelength-Based Axial Resolution Limitations of Flexural Wave Dispersion Sonic Logging, Paper OOO, *Transactions, SPWLA 60th Annual Logging Symposium*, The Woodlands, Texas, USA, 17–19 June.
- Wang, R., Hornby, B., Chang, C., Sun, B., and Walker, K., 2018, Enhanced-Resolution Dipole Sonic Logging Data Processing, *SEG Technical Program Expanded Abstracts*, 679–683. DOI: 10.1190/segam2018-2995738.1
- Weisstein, E.W., Moore-Penrose Matrix Inverse, From MathWorld -- A Wolfram Web Resource. <http://mathworld.wolfram.com/Moore-PenroseMatrixInverse.html>. Accessed October 30, 2019.
- Weng, X., Chuprakov, D., Kresse, O., Prioul, R., and Wang, H., 2018, Hydraulic Fracture-Height Containment by Permeable Weak Bedding Interfaces, *Geophysics*, **83**(3), MR137–MR152. DOI: 10.1190/geo2017-0048.1.
- Xu, W., Prioul, R., Berard, T., Weng, X., and Kresse, O., 2019, Barriers to Hydraulic Fracture Height Growth: A New Model for Sliding Interfaces, Paper SPE-194327 presented at the SPE Hydraulic Fracturing Technology Conference and Exhibition,

Woodlands, Texas, USA, 5–7 February. DOI:10.2118/194327-MS.

Zeroug, S., and Lei, T., 2017, Subsonic Anisotropy Effects in a Shale Formation Revealed With Pseudo-Rayleigh Surface Waves, *SEG Technical Program Expanded Abstracts*, 870–874. DOI: 10.1190/segam2017-17674643.1.

Zeroug, S., Sinha, B.K., Lei, T., and Jeffers, J., 2016, Rock Mechanical Behavior at the Inch Scale in a Thinly Laminated Unconventional Formation, Paper URTEC-2457496 presented at the Unconventional Resources Technology Conference, San Antonio, Texas, 1–3 August. DOI: 10.15530/URTEC-2016-2457496.

Zeroug, S., Sinha, B.K., Lei, T., and Jeffers, J., 2018, Rock Heterogeneity at the Centimeter Scale, Proxies for Interfacial Weakness and Rock Strength-Stress Interplay from Downhole Ultrasonic Measurements: *Geophysics*, **83**(3), D83–D95. DOI: 10.1190/geo2017-0049.1.

Zhang, T., Tang, X.M., and Patterson, D., 2000, Evaluation of Laminated Thin Beds in Formations Using High-Resolution Acoustic Slowness Logs, Paper XX, *Transactions, SPWLA 41st Annual Logging Symposium*, Dallas, Texas, USA, 4–7 June.

Zimmermann, T., Liang, L., and Zeroug, S., 2018, Machine Learning-Based Automatic Well-Log Depth Matching, *Petrophysics*, **59**(6), 863–872. DOI: 10.30632/PJV59N6-2018a10.

APPENDIX 1: DERIVATION OF THE TRANSFORMATION FUNCTION

Assuming the transformation function is symmetric, we can write $F_N(z)$ as a quadratic function

$$F_N(l) = a_1 l^2 + a_2 l + a_3, \quad (\text{A1.1})$$

where N denotes the number of receivers; l is the length coordinate defined from $-L/2$ to $L/2$; and L denotes the tool aperture.

From $\int_{-L/2}^{L/2} F_N(l) dl = 1$, we can get

$$a_3 = \frac{12 - a_1 L^3}{12L}. \quad (\text{A1.2})$$

Considering the symmetry distribution along $l = 0$ (i.e., $F(l) = F(-l)$), we can see $a_2 = 0$. The last coefficient, a_1 , is addressed using the approach proposed by Huang et al. (2015). In Huang et al. (2015), the wave spectrum is assumed to have a phase delay across the receiver array. Consequently, considering a case where a constant perturbation of Δs is located between receiver $m - 1$ and m ($m = 1, 2, \dots, N - 1$), we can write the arrival time at each receiver as

$$[0, s_r, 2 s_r, \dots, n s_r, (n + 1) s_r + \Delta s, N s_r + \Delta s] \Delta z. \quad (\text{A1.3})$$

An analytical expression for the average slowness is obtained by least square regression as given by (Eq. 10 in Huang et al.),

$$\bar{s} = s_r + \frac{6m(N-m)}{N(N^2-1)} \Delta s, \quad (\text{A1.4})$$

On the other hand, with a constant perturbation of Δs located between receiver $m - 1$ and m , from Eq. (1), we can write the average slowness as

$$\bar{s} = s_r + \int_{\frac{(m-1)L}{N-1}}^{\frac{mL}{N-1}} \frac{L}{2} F_N(l) \Delta s dl. \quad (\text{A1.5})$$

Evaluation of the integration in Eq. A1.5 yields expression as

$$\bar{s} = s_r + \frac{6(N-1)^2 + a_1 L^3 (6m^2 + N - 6mN + N^2)}{6(N-1)^3} \Delta s. \quad (\text{A1.6})$$

Consequently, by comparing Eqs. A1.4 and A1.6, we can derive a_1 as

$$a_1 = -\frac{6(N-1)^2}{L^3 N(1+N)}. \quad (\text{A1.7})$$

Substituting the expressions of a_1 , a_2 , and a_3 into Eq. A1.1, we can get

$$F_N(l) = \frac{L^2(3N^2+1) - 12l^2(N-1)^2}{2L^3 N(1+N)}. \quad (\text{A1.8})$$

ABOUT THE AUTHORS



Ting Lei is a senior research scientist in the Geomechanics program in Schlumberger-Doll Research, USA. Ting joined Schlumberger Beijing Geoscience Center in China as an interpretation engineer in 2006. In 2009, he moved to Schlumberger-Doll Research, USA. Since then, Ting has worked on numerical forward modeling for complex acoustic problems and developed several inversion algorithms using borehole sonic data. Ting received his Ph.D degree in Engineering Mechanics from Tsinghua University in 2006.



Smaine Zeroug is currently the research director of the applied mathematics and data analytics department at Schlumberger-Doll Research, Cambridge, Massachusetts. He received his MS and PhD degrees from New York University Polytechnic School of Engineering in Electrophysics. He's been with Schlumberger for 26 years in various positions in

R&E, marketing, and operations. His research interests lie in the area of acoustics for geophysical applications. More details are available in LinkedIn, ResearchGate and Google Scholar.



Sandip Bose is a Principal Research Scientist and Program Manager in the Applied Mathematics and Data Analytics department at Schlumberger-Doll Research Center in Cambridge, Massachusetts. He has over 20 years of experience in borehole acoustics and has worked on the development of numerous

novel processing techniques for sonic and ultrasonic data for formation evaluation as well as well integrity applications. He graduated with a BTech from the Indian Institute of Technology, Kanpur and a PhD from Cornell University (1995) both in electrical engineering. His current research interests are primarily in signal processing as well as analytics and machine-learning techniques wherein he leads a research program. He is a member of the IEEE and the Society of Exploration Geophysicists.



Romain Prioul is a Scientific Advisor and Program Manager at Schlumberger-Doll Research, Cambridge, Massachusetts. He received a PhD in 2000 in geophysics from Institut de Physique du Globe de Paris, France. From 2000 to 2005, he was research scientist at Schlumberger Cambridge Research,

UK, and, at Schlumberger-Doll Research, Ridgefield, Connecticut, and Cambridge, Massachusetts, USA. He became research Program Manager in 2007 and is currently managing a team of researchers focused on geomechanics applications. Romain is a member of SPWLA, SPE, SEG, EAGE and ARMA. More details are available on LinkedIn, ResearchGate and Google Scholar.



Adam Donald is a Scientific Advisor and Technical Director for Geomechanics & Acoustics at Schlumberger Wireline Headquarters, based in Bucharest, Romania. Adam received BAsC in Geological Engineering from University of Waterloo, Canada and a BAsC in Mining Engineering from Dalhousie

University, Canada. He has been with Schlumberger for 21 years in various roles with technology development and interpretation of borehole acoustics data for applications in formation evaluation, geophysics and geomechanics. He is an active publishing member of SPWLA, SPE and SEG.

New 4.75-in. Ultrasonic LWD Technology Provides High-Resolution Caliper and Imaging in Oil-Based and Water-Based Muds¹

Peng Li², Jonathan Lee², Richard Coates², Jing Jin², and Siong Ming Wong²

ABSTRACT

Imaging technologies from azimuthal logging-while-drilling (LWD) tools provide valuable insight into borehole conditions and address multiple drilling and formation evaluation applications, such as wellbore stability assessment and fracture and bedding plane analysis. Although high-resolution images are widely available for water-based mud (WBM) applications, such as from azimuthally focused resistivity tools, their availability in oil-based mud (OBM) applications is limited.

This paper presents a 4.75-in. LWD ultrasonic imaging tool that provides high-resolution borehole caliper and reflection amplitude images, independent of the mud type

used. Analysis of datasets collected by the tool, in OBM with varying mud weights and under multiple drilling conditions, demonstrate the suitability of the imaging technology in boreholes ranging from 5.75- to 6.75-in. diameter. We present log data and analysis from the field tests that illustrate the quality of both the caliper and the reflection amplitude measurement provided by the tool.

The comparison of these datasets with wireline measurements demonstrates the potential for these LWD ultrasonic logs to be the primary imaging solution in applications where the deployment of wireline technologies is either too risky or costly to be considered.

INTRODUCTION

The deliverables from ultrasonic LWD tools can be used to address a wide range of drilling and formation evaluation challenges in both WBM and OBM. For example, caliper measurements are used for calculation of average borehole size to help calculate cement volumes, as a borehole quality indicator for packer placement, and for environmental corrections for other LWD sensors. Borehole ellipse and azimuthal sector images are used for geomechanics analysis, and high-resolution borehole images for the identification of faults and fractures. Reflection amplitude uses include formation porosity estimation and detailed analysis of faults and fractures, and geological and lithological analyses of bedding planes, laminations, and determination of stratigraphic dips.

Borehole imaging technologies based on electrical measurements have been available for conductive WBM on wireline since the late 1980s (Ekstrom et al., 1987) and early 1990s (Davies et al., 1994). Analogous tools were introduced for LWD a decade later (Li et al., 2005; Bittar et al., 2009).

Options for imaging in nonconductive OBM were more

limited, although tools to produce ultrasonic measurements have been available on wireline from the late 1990s (Hayman, et al., 1998), and LWD azimuthal density image tools were introduced in the early 2000s (Ballay et al., 2001). The resolution of density images is largely limited to the spacing between the source and the detectors, and, to some extent, the spacing between the detectors. This is typically several inches, and therefore, the images are not considered high resolution. Although LWD ultrasonic caliper tools, used primarily for compensating other measurements, were introduced in the early 2000s (Labat, et al., 2002), until recently, ultrasonic LWD tools capable of generating high-resolution borehole caliper and reflection amplitude images have not been available.

In this paper, we describe an LWD ultrasonic imaging tool capable of generating these images in both conductive WBM, and nonconductive OBM. The tool layout and principles of operation are described, followed by an overview of the laboratory testing conducted during tool development, and finally results from a number of field trials are presented and discussed.

Manuscript received by the Editor July 23, 2019; revised manuscript received October 22, 2019; manuscript accepted October 23, 2019.

¹Originally presented at the SPWLA 60th Annual Logging Symposium, The Woodlands, Texas, USA, June 17–19, 2019, Paper T.

²Halliburton, 3000 N. Sam Houston Pkwy E., Houston, TX 77032-3219; Peng.li@halliburton.com; Jonathan.Lee@halliburton.com; Richard.coates@halliburton.com; Wong.SiongMing@halliburton.com; Halliburton, 315 Jalan Ahmad Ibrahim, Singapore, 639940; Jing.Jin@halliburton.com

TOOL LAYOUT AND OPERATION

The sensor section of the tool is shown in Fig. 1. It is composed of four transducers positioned at 90° increments around the tool body at the same axial location. Every transducer acts both as a transmitter and as a receiver. Each transducer only detects and records the echo of the pulse it generates, and not the echo of pulses emitted by other transducers. This mode of use is sometimes denoted “pulse-echo”. During the firing stage, all four transducers (acting as transmitters) are excited simultaneously. After a short mute time, all four transducers are activated in parallel (acting as receivers) to acquire four individual inputs. Four azimuthally distributed transducers are used to compensate for tool motion and eccentricity. The tool is equipped with a high-speed digital signal processor (DSP) that analyzes the four channel raw waveforms, performs ringing removal and then echo detection. The tool can perform 500 firings per transducer every second, from which it can acquire and process 2,000 echoes per second. These elements are described in more detail below.

Each transducer is composed of a single circular diced wafer of piezoelectric material, which is diced from the top surface to about 80% of the thickness (see Fig. 1b). The top surfaces of all columns are connected electrically via conductive epoxy, while the bottom surface acts as the other electrode for the driving voltage to be applied to. This special dicing feature has the benefit of providing high power, together with the wide bandwidth of the piezoelectric composite. The design also retains the robustness of a piezo wafer with a complete bottom surface, and facilitates epoxy bonding of the bottom surface onto the backing material, which serves to attenuate the ultrasounds emitting backwards.

The single-wafer transducer design was chosen in preference to other possible designs because it provides stronger driving forces and greater sensitivities. Other

designs, including a ring transducer with multiple concentric piezo rings allowing a dynamic focusing capability (Morys et al., 2011) were considered, but the diced wafer proved preferable due to its higher power with wider bandwidth, which converts to smaller ring-down noise. A strong signal with low ring-down is especially important for the tool to handle logging in heavy mud.

The ultrasonic source pulse is generated by applying voltage on the piezo transducer, and the ultrasonic pulse travels through the borehole fluids, with part of the wave reflected from the borehole wall. By analyzing the traveltime of the pulse wave from transmitting to the echo being received, the transducer standoff, and therefore borehole radius, can be derived given the fluid sound speed. Analysis of the amplitude of the echo signal enables the reflection amplitude of the borehole surface to be derived. The continuous firing of the pulse signal and receiving of the echo while rotating enables radius and reflection amplitude images to be obtained as functions of azimuth and measured depth.

The pulse-echo transmit-receive operation begins with the transducer acting as a transmitter, where electrical energy is applied to the transducer, and through the piezoelectric effect of the wafer, the electrical energy is converted into acoustic energy. Then, operating as a receiver, the wafer senses the reflected ultrasonic echo and converts the associated pressure wave back into electrical voltages that are ultimately digitized. This is our signal of interest, and the one referred to when we discuss signal/noise ratio (SNR) below. The digitized voltages also consist of those generated by ambient acoustic noise, electrical noise from the tool and others in the bottomhole assembly (BHA), and of residual ringing of the transducer caused by the firing pulse. Ambient acoustic noise in the borehole environment decays rapidly with frequency (Joyce et al., 2001), and electronic noise can be minimized by best-practice circuit design. However, the residual ringing of the transducer must be mitigated with special care.

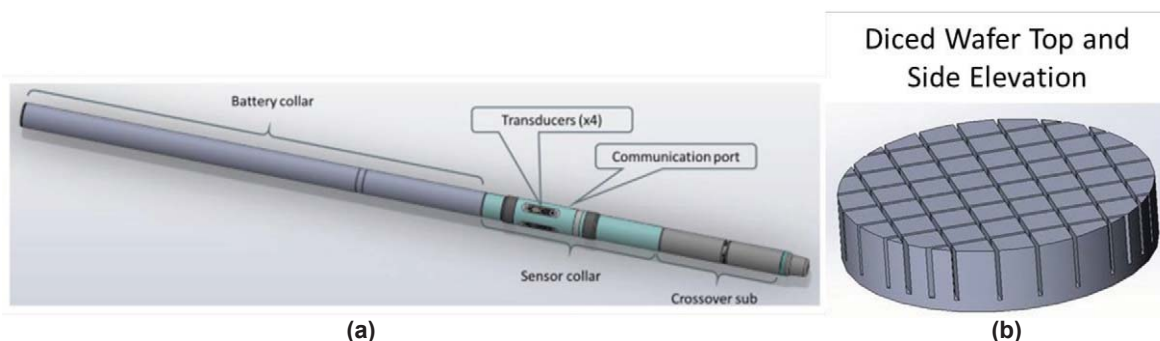


Fig. 1—(a) 4.75-in. ultrasonic imaging tool layout, featuring a sensor section composed of four ultrasonic transducers and a communication port. Stabilizers are recommended on either the battery collar, or the crossover sub or both. (b) A schematic of the diced piezoelectric wafer.

Simply increasing the drive voltage will generate a stronger emitted signal but will also induce higher amplitude ringing. Thus, the resulting SNR may not improve. However, the unique wafer construction of the transducer is designed to achieve both strong transmitting power, high sensitivity, and ensure rapid ringing reduction after firing. Adding a backing material behind the transducer further attenuates residual ringing significantly. Even these steps may not completely solve the problem, particularly in OBM. These muds can attenuate the ultrasonic energy by more than 20 dB/in., i.e., an order of magnitude/inch reduction in signal level in heavy-muds (> 14 lbm/gal). In these circumstances small amplitude echoes can still be buried under transducer ringing noise making them difficult to detect and interpret.

We define the ultrasonic transducer SNR as the peak amplitude of the echo divided by the amplitude of the transducer ringing at the echo detection time. The echo amplitude and detection time are calculated from the recorded waveforms automatically using a proprietary method. Each raw waveform measurement is decomposed in both the time and frequency domains, and then the echo is extracted through a matching filter, to obtain the associated traveltimes and amplitude. Both the amplitude and time vary with the standoff of the tool from the borehole wall, and the transducer ringing decays as a function of time. Hence, the SNR also varies with echo arrival time, or equivalently with

standoff. A group of echo-signal measurements with varying standoffs is shown in Fig. 2, illustrating the decay of echo amplitude with standoff. The amplitude of the transducer ringing does not vary with standoff, hence its amplitude at a point in the waveform can be estimated from recordings corresponding to very large standoffs and very late echo times.

The resulting SNR for varying standoff is demonstrated in Fig. 3. The SNR can be seen to degrade as the standoff increases, although the transducer still achieves more than 10 dB SNR over a large standoff range. In our experience, with a SNR above 10 dB, the echo can be reliably extracted automatically.

The transmitter beam pattern was evaluated by placing the transducer in a fixed location and recording it firing with a calibrated hydrophone moved in a three-dimensional (3D) grid pattern in front of the transducer. The amplitude of recording was extracted as indicative of the acoustic pressure at each point. The displays in Figs. 4a and 4b show two orthogonal slices through this 3D volume crossing in front of the center of the transducer. The images show a well-collimated beam transmission pattern out to at least 2-in. standoff.

Similarly, Figs. 4c and 4d show the sensitivity of the transducer operating in reception mode. These were generated using a calibrated source fired on a 3D grid in

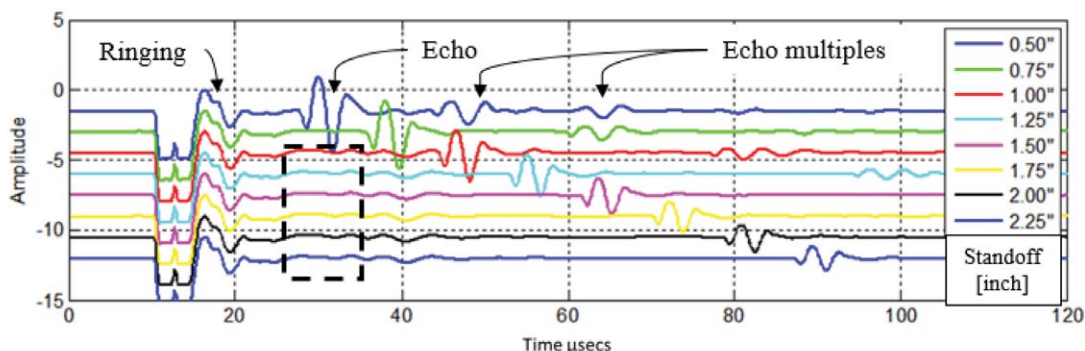


Fig. 2—Transducer echo measurement with different standoff showing a stable echo and consistent ringing. The ringing amplitude for any time can be estimated from waveforms corresponding to large standoffs, e.g., the dashed box contains only ringing for standoffs greater than 0.75-in.

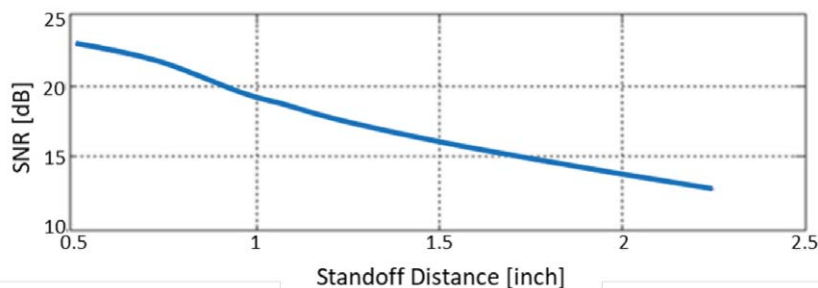


Fig. 3—Transducer SNR response with varying standoff. The SNR remains above 10 dB beyond 2-in. standoff.

front of the transducer. The images show orthogonal slices that cross in front of the center of the transducer. Again, we see a well-collimated response. The collimated nature of the transducer emission and reception patterns are important in producing high-resolution images over a range of standoffs.

The electronics of the tool are composed of three

subsystems that are illustrated in Fig. 5. These are the digitization subsystem, the multiple ultrasonic-transceiver subsystem, and the directional subsystem. The combined electronics system generates the borehole shape and reflection amplitude measurements.

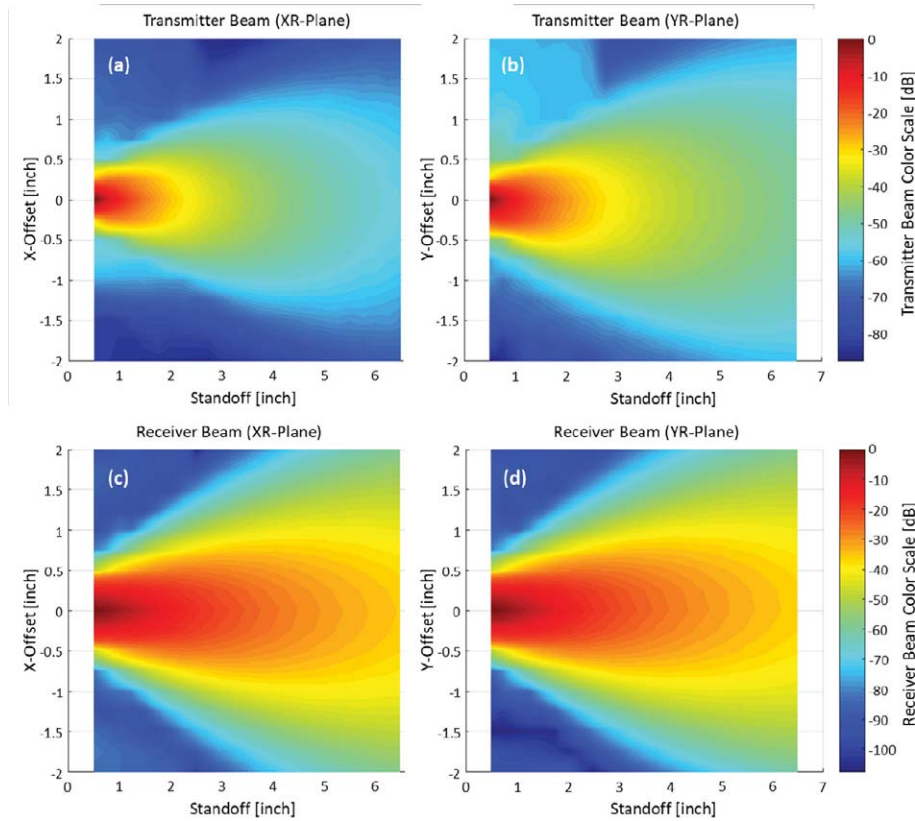


Fig. 4—Transmitter (a) and (b), and receiver (c) and (d) beam pattern in water. The transmitter and receiver beam images are independently normalized to their respective maximum values. The images illustrate that the transducer has a well-collimated response within a 2-in. distance (standoff) for both transmission and reception functions.

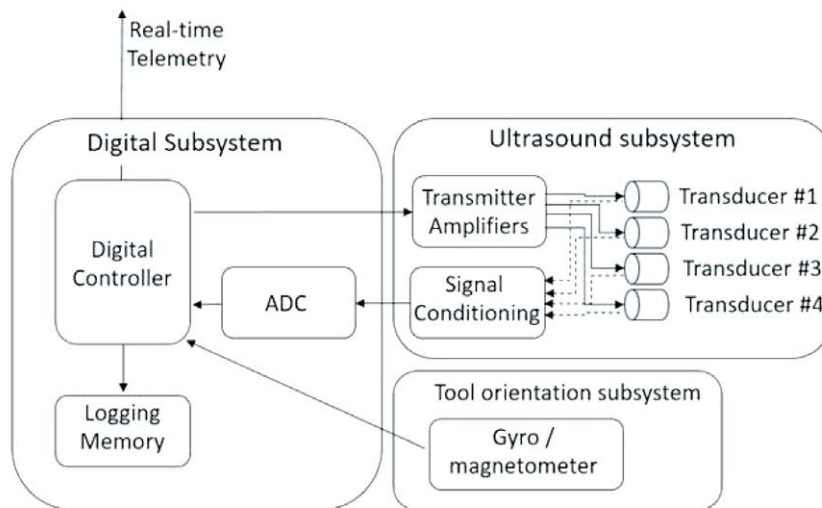


Fig. 5—Block diagram detailing the electronic subsystems.

The ultrasonic-transceiver subsystem is composed of the transmitter amplifier, the analog signal conditioning circuit, and the four ultrasonic transducers. The transmitter amplifier amplifies the firing pulse and applies the high-voltage pulse on the transducer. In order to address the changing attenuation rates of different OBM types and densities, an adjustable power supply is included in the transmitter amplifier so that a different firing voltage can be used for different mud weights. A transmitter/receiver interface circuit is designed to protect the receiver from high-voltage firing signals during the transmitting phase, and also to block the transmitter from loading on receiving paths during the receiving phase. The signal conditioning circuit takes the received charge signals generated from the transducer and amplifies them to a level that is compatible with the analog-to-digital converter (ADC). Appropriate filtering is also included in the signal conditioning circuit to remove nonrelevant switching noises from other parts of the system.

The digital subsystem mainly includes the DSP, the memory components, and the ADCs. The DSP acts as the central control, communication, and processing unit generating the firing reference signals and controlling the transmitter amplifier to enable the firing. In addition, it synchronizes the ADCs to acquire the reflected echoes at the correct echo reflection time. These echoes are processed inside the DSP to generate the transducer standoffs and reflection amplitude values. Gyros and magnetometers are used to acquire the tool-face information during tool rotation. The gyro provides accurate rotational information, and the result is compensated with the magnetometer measurements to remove biasing errors. The tool face is synchronized with the firing pulse to achieve azimuthal standoff and amplitude measurements. The digital processor combines all measurements and processed results together to save into the memory and for transmission to surface.

The accuracy of a conventional wireline mechanical caliper can be affected by both the limited number of arms and borehole spiraling conditions. LWD ultrasonic caliper measurements have the advantage of full-borehole coverage while the sensor is rotating in the drillstring, and therefore, the potential to provide more accurate measurements. However, a number of challenges can affect the accuracy of LWD ultrasonic caliper measurements.

First, the ultrasonic measurement generates a standoff measurement, which represents the distance between the face of the transducer wafer to the borehole wall, and therefore, is not a direct measurement of borehole diameter. The standoff at multiple orientations together with the tool

size are needed to produce a diameter measurement. To minimize the radial motion (eccentering) of the tool we use an undergauge stabilizer, which is a short metal sleeve that is secured over the BHA having an outside diameter (OD) equal to, or a little smaller than the bit size. Consequently, the undergauge stabilizer is slightly smaller than the borehole (hence its name) and serves to minimize, but not eliminate the amount of eccentering the tool experiences.

Second, if the transducer is in too close proximity to the borehole wall, the reflected echo will be hidden beneath the highest amplitude transducer ringing described earlier. To avoid this, and mechanical damage caused by transducers impacting the borehole wall, all four transducers are recessed slightly from the tool's outer diameter. This helps guarantee the minimum standoff required by a pulse-echo measurement and alleviate transducer wear and damage problems.

A final step is real-time ringing removal. This is facilitated by the large amount of memory incorporated in the downhole electronics to store the raw waveform measurement. The transducer ringing components of the waveforms are identified and extracted from the raw waveforms in real time using a proprietary algorithm that identifies invariant portions of the waveforms over an ensemble of multiple firings and subtracts them from adjacent waveforms. Note the ringing may vary with the temperature and pressure experienced by the transducer. To minimize this effect, the estimation of transducer ringing is updated periodically during the drilling run.

Figure 6 illustrates the effect of the implemented ringing removal. Figure 6a shows raw waveforms for a full rotation of the tool plotted as a two-dimensional (2D) azimuthal image. The horizontal axis is the azimuthal angle of the acquired waveform, and the vertical axis indicates the traveltime in microseconds. The amplitude of the waveform is illustrated with a variable density grayscale, with brightness and darkness indicating larger and smaller values, respectively. The heavy black and white stripes in the lower part of Fig. 6a indicate the transducer ringing. The wavelets with variable arrival times in the middle of the displays are the echoes. The varying reflection times result from tool motion and the deviation of the borehole cross-section from circularity. Note the ringing and echo possess similar frequency content, and the ringing component extends to 60 μsec . Figure 6b shows the same 2D azimuthal image with the ringing removed. This figure only shows the effect of ringing removal; the ringing itself is typically estimated from a much larger ensemble of data. After removal of the ringing it is much easier to extract the echo signal.

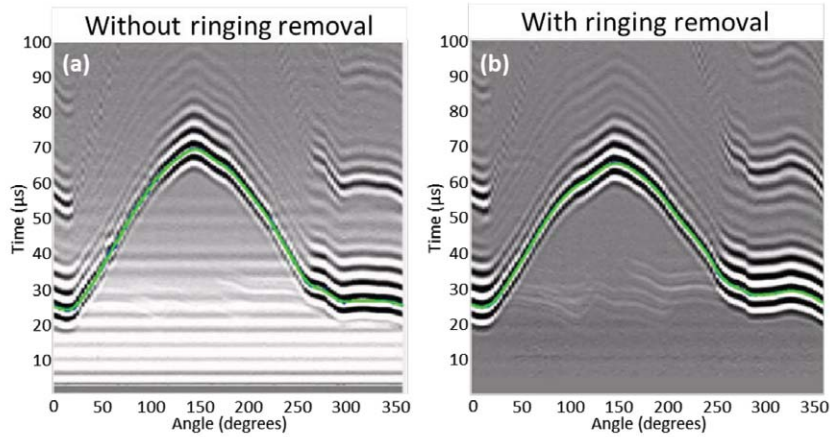


Fig. 6—Transducer ringing removal shown using a variable density display. (a) Raw waveform data from one transducer for one complete rotation of the tool, and (b) the data after transducer ring removal.

In a nonstabilized or poorly-stabilized configuration, tool-body movement during the caliper measurement can be detrimental to the standoff, and corresponding calculated borehole diameter. This is illustrated in Fig. 7a where a 4.75-in. tool is depicted in a 7-in. borehole with enlargement. The center of the tool body is following a circular motion (the motion trajectory shown in red) during the tool rotation. In

this example, the circular motion is off-center with respect to the borehole center, and the tool traverses the trajectory shown in red at the same rate as the tool rotates. As a result, the transducer sees a reduced standoff throughout a full rotation and the generated caliper result (in green) shows the effect of the motion on the caliper measurement (Fig. 7b).

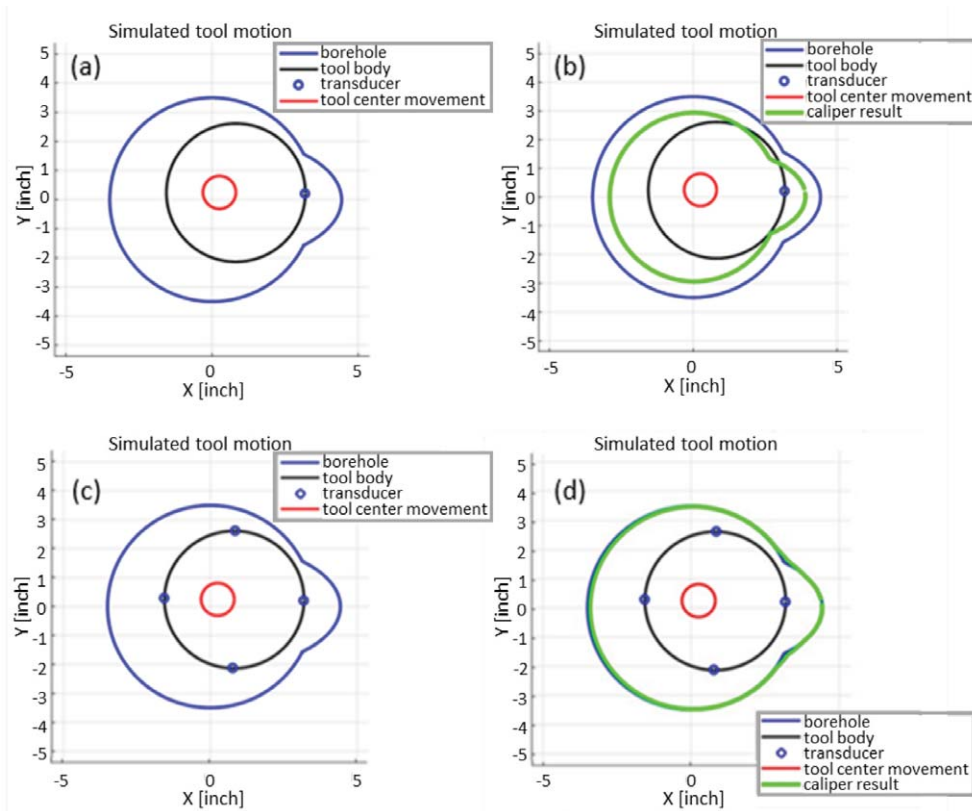


Fig. 7—Schematic representation of the use of multiple azimuthally distributed transducers for tool-motion correction. In this example (a) shows a single transducer (blue dot) mounted on the circumference of a tool (black) whose center traverses a path shown in red as the tool (and transducer) rotates through 360°. (b) Without compensating for tool motion, the inverted borehole shape (green) is systematically smaller than the true borehole (blue). (c) Adding additional transducers distributed azimuthally allows for (d) a more accurate inversion of the borehole shape (green) shown.

The four identical transducers, distributed circumferentially at 90° intervals, allow us to compensate for the tool motion, shown in Figs. 7c and 7d. The motion-correction algorithm relies on the fact that at any given moment standoffs are measured on opposing sides of the borehole and along orthogonal axes. Thus, if the tool is displaced to one side (as in Fig. 7), it is manifest in the raw data as a decreased standoff for one transducer and a corresponding increased standoff for the transducer on the opposite side of the tool. The algorithm uses the fact that the tool measures echo times (borehole standoff) in four orthogonal angles as it rotates. It begins by calculating an approximate borehole shape from these measurements and the associated recorded rotation angles. The tool motion is then calculated by minimizing the difference between measured and modeled echo times by adjusting the assumed tool location for each firing using a least-squared cost function. A refined borehole shape can then be calculated. This removes the requirement for an assumed borehole shape, e.g., circular or elliptical, which is a feature of some borehole-shape algorithms.

The speed of sound in mud is an input into the borehole diameter and shape calculation. The mud speed is known to depend upon mud composition, temperature, and pressure. We use two steps to determine the appropriate speed. First, a casing calibration is performed where the ratio of the known internal casing diameter to the measured echo time is used to calculate the speed of sound in the mud. Second, an environmental correction to that speed is applied, based on temperature and pressure changes to account for varying downhole conditions.

A big challenge in obtaining a continuous high-resolution image is the downhole system's computational power and memory space. High-resolution images require an uninterrupted, rapid firing rate and high-density data throughput on the downhole electrical system. With a limitation on downhole memory size, the downhole computer may not have the capacity to save all the raw waveforms for surface post-processing when long drilling or logging runs are anticipated. To overcome this challenge, the downhole computer processes all the raw waveforms in real time and saves the traveltime and reflection amplitude results.

LABORATORY DETECTION AND RESOLUTION QUANTIFICATION

The detection and resolution capabilities of the transducers are important system characteristics. Detection refers to the smallest size and magnitude of an isolated feature that can be seen. Resolution refers to the smallest

distance between adjacent features that allows them to be discriminated. To investigate these transducer characteristics the 2D scanning system, shown in Fig. 8, was constructed in the laboratory to evaluate the transducer's ability to generate images from various features.

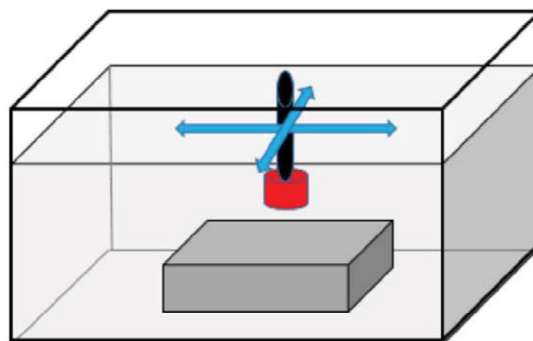


Fig. 8—A schematic representation of the transducer imaging scanning system used for the initial laboratory testing setup. The transducer (red) can scan in a horizontal plane using two orthogonal stepper motors above the target, all immersed in fluid. The height of the transducer above the target may also be adjusted.

A target sample was placed at the bottom of a fluid-filled tank. The transducer was mounted on a slider frame driven by two stepper motors operating in orthogonal directions. This enabled motion in the horizontal plane above the sample. A data acquisition system controls the motor drivers to drive the stepper motors, controls the driving circuit to generate a firing pulse, and interfaces with the preamplifier and signal conditioning circuit to acquire the echo after the firing pulse. A number of tests were conducted on samples designed to evaluate the transducer's ability to identify individual features (detection) and its ability to distinguish the separation between two closely spaced features (resolution).

The first test was designed to study detection. The target was an acrylic block drilled with holes of different diameter and depth. Each hole was sufficiently separated from the others so as not to interfere with each other. The size and pattern of the holes drilled in the acrylic sample are shown in Fig. 9a.

The raw amplitude image created from the transducer moving over the sample at a standoff of 0.5 in. is shown in Fig. 9b, and demonstrates that under the test conditions the transducer detects all the holes, including the two with 0.1-in. diameters and depths of 0.1 and 0.2 in. Note, that while all the holes were detected there is no simple relationship between the amplitude of the ultrasonic image and the diameter and depth of the holes.

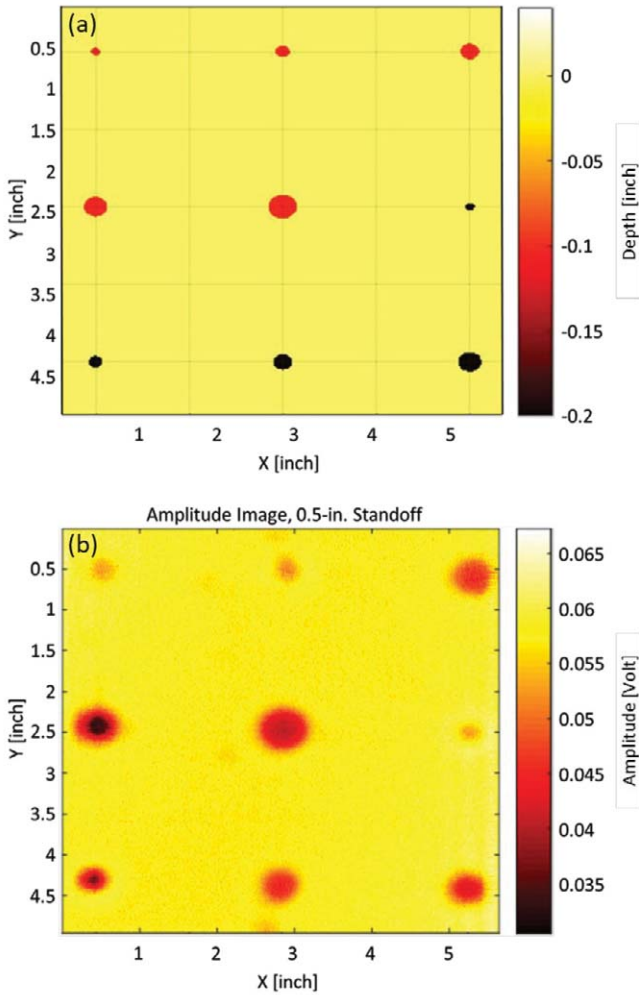


Fig. 9—(a) Schematic of the acrylic test sample, and (b) ultrasonic image used to evaluate feature detection. The targets were holes of varying diameter (0.1, 0.2, 0.25, 0.5 in) and depth (0.1 and 0.2 in).

The second test was conducted to assess the ability of the transducer to distinguish two closely situated features as separate objects (resolution). Again, an acrylic block was used with parallel slots engraved in the surface with varying distance between them, as illustrated in Fig. 10a. Four pairs of thin cuts of 0.1-in. width and 0.1-in. depth were engraved closely together, with distances of 0.1, 0.2, 0.3, and 0.4 in. between each pair. Each pair was separated sufficiently to ensure there was no interference between pairs.

The 2D scanning equipment and procedure used were the same as for the first test. The raw image results are shown in Fig. 10b. The image shows that under the test conditions (in water, with a standoff of 0.5 in.), the transducer resolved a separation between the 0.1-in. wide cuts when the separation between members of the pair was ≥ 0.3 in., but not when the

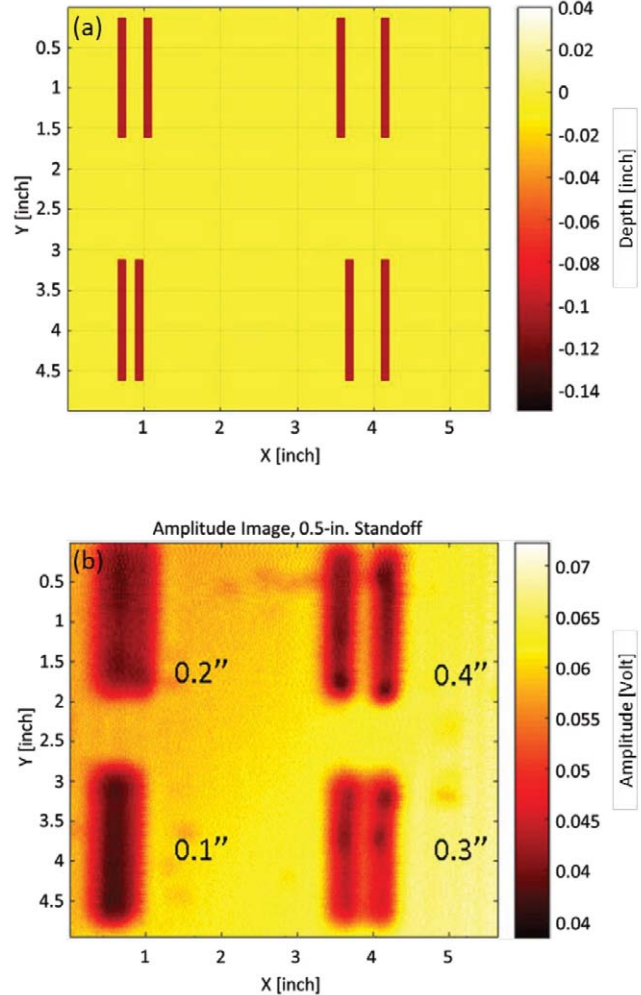


Fig. 10—(a) The schematic of grooves of 0.1-in. depth and 0.1-in width engraved in pairs in the surface of an acrylic block. The grooves were 0.1, 0.2, 0.3 and 0.4 in. apart. Each pair was sufficiently separated from the next that there was no acoustic interference. (b) The ultrasonic image result from scanning the transducer in a 2D plane above the target with a standoff of 0.5 in.

separation was ≤ 0.2 in.

A third test was conducted to simulate the transducer response to fluid-filled fractures. A cement brick broken through its complete thickness was used to mimic a fracture. The two halves of the brick were positioned at varying separations from one another to simulate different fracture widths, as illustrated in Fig. 11. The test was performed in water with a 2-in. standoff. The dashed green boxes in the upper row shows the approximate area covered in the middle and lower images. The gradient in the travelt ime image reflects slight misalignment between the scanner plane and the brick surface.

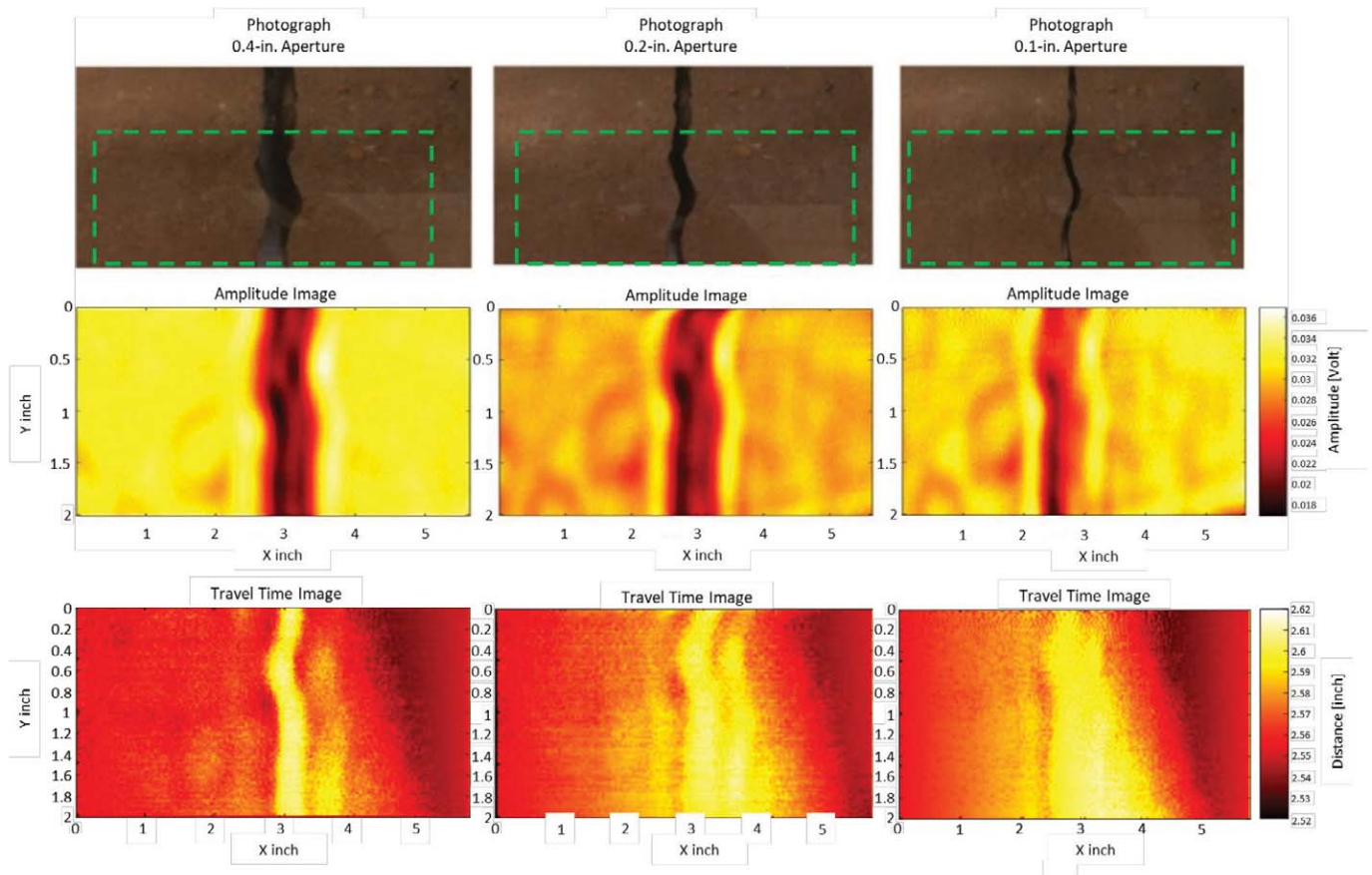


Fig. 11—Cement-block fracture imaging with a 2-in. standoff. The upper row shows photographs of the cement block with varying fracture apertures; the middle row shows the reflection amplitude image; and the lower row shows the standoff image obtained from echo times.

The raw amplitude image clearly detects all the fractures, including the 0.1-in. aperture fracture. Note the standoff image is less sensitive, with the 0.4-in. aperture fracture detectable, the 0.2-in. fracture marginal, and the 0.1-in. fracture almost undetectable. Although the fracture with a 0.1-in. aperture is clearly seen in the 2-in. standoff image, it is more clearly resolved when the experiment was repeated in water with a standoff of 0.5 in. (Fig. 12). The dashed green box in the upper image shows the approximate area covered in the lower images, and again the gradient in the traveltime image reflects slight misalignment between the scanner plane and the brick surface.

Both Figs. 11 and 12 show that the transducer standoff image obtained from the echo traveltimes is less sensitive to small fractures than the amplitude image. This can be explained with reference to Fig. 4, where we see that a signal integrates contributions from a finite area of the target

illuminated by the beam. Thus, the echo time is controlled by the earlier portions of the signal reflected from either side of the fracture but within the beam illumination, while the amplitude is more affected by destructive interference between the reflections from inside and outside the fracture. Therefore, traveltime, and hence, the standoff image, is less sensitive than the amplitude image to small features on the borehole surface. Conversely, the borehole rugosity has a greater impact on the echo amplitudes when the surface roughness is comparable to the ultrasonic wavelength.

Having verified transducer performance under the limited test conditions offered by the 2D setup, a 3D rotating apparatus was constructed to evaluate the transducer's azimuthal measurements. In order to simulate downhole conditions as closely as possible, the 3D system setup included four transducers and the downhole electronics as part of the hardware, as illustrated in Fig. 13.

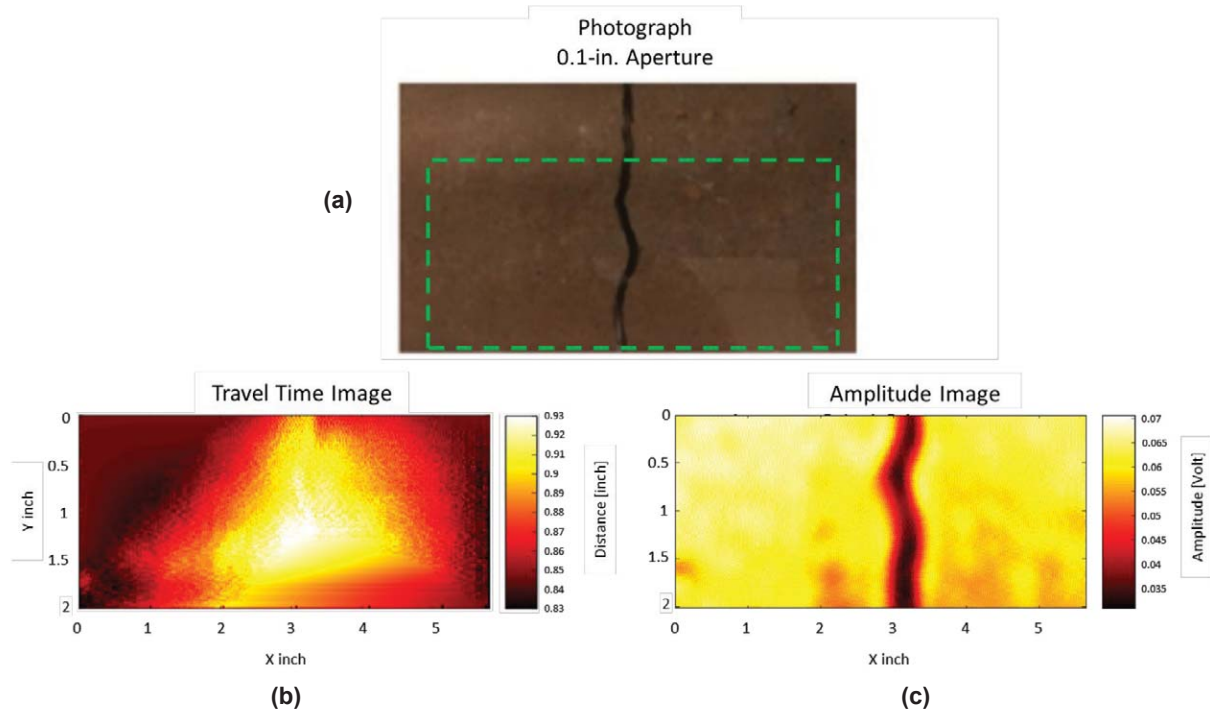


Fig. 12—Cement block fracture imaging with 0.5-in. standoff. (a) A photograph of the cement block with 0.1-in. fracture aperture. The lower row shows the standoff image determined from (b) the echo times, and (c) the reflection amplitude image.

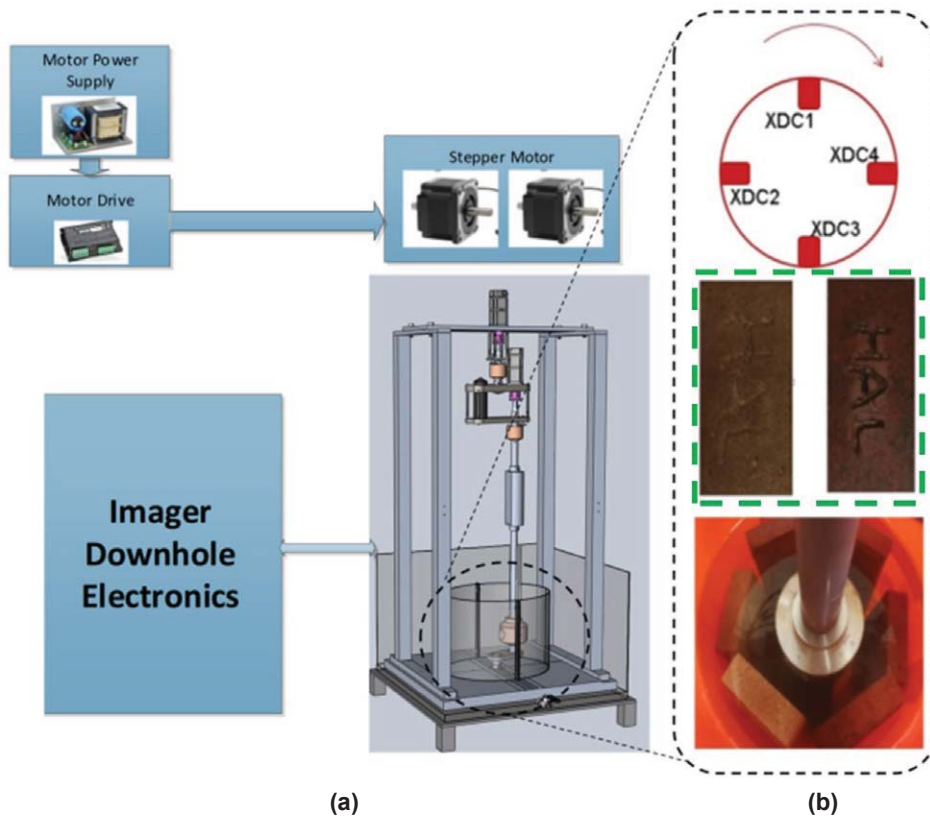


Fig. 13—The 3D rotating laboratory equipment for system-level verification. This setup tested the transducers integrated with the downhole electronics. Figure 13b shows an enlargement of a cross section of the transducer assembly (top); two of the target blocks in the dashed-green box, hand-engraved with the letters “HAL” (middle) and a photograph of the test assembly from above (bottom).

In the 3D setup, two-axial rotational movements are controlled by two stepper motors, and the z -axis motion is controlled by a linear driver. The four transducers were mounted on a head that could be immersed in the drilling fluid containers. In the same way that the combined tool would operate downhole, the setup was directly controlled by the downhole electronics, with synchronized firings and directional measurements being obtained. The test samples used were six concrete bricks, two of which had the letters “HAL” hand-engraved on them.

Figure 14 shows the reflection amplitude images from the rotating test, conducted in water for the individual transducers without compensating for the azimuthal position of the transducers. Thus, each image is rotated by 90° from its adjacent image, reflecting the fact the transducers were located at 90° increments around the assembly. Note that towards the edge of the bricks, specular reflection is not detected by the transmitter.

The laboratory testing described, and further testing discussed by Li et al. (2019), verified the potential for the combined four-transducer configuration to provide caliper measurements and generate traveltimes and reflection

amplitude images in both WBM and OBM. The transducers were incorporated into two 4.75-in. collars, and prepared for field trials.

FIELD TEST COMPARISON WITH WIRELINE TECHNOLOGIES, DIFFERENT LOGGING PARAMETERS AND MUD WEIGHTS

A field test of the tool was conducted at a test rig in Cameron, Texas, USA. For the first trial run, one tool with a 0.25-in. undergauge stabilizer was placed within a BHA comprising a 6.25-in. bit, a 4.75-in. mud motor, a 4.75-in. pressure-while-drilling (PWD) sub, a measurement-while-drilling (MWD) tool, and gamma-ray sensors. The well plan involved logging through a 9.625-in. casing shoe set at 1,290 ft measured depth (MD) and 12.25-in. rathole to 1,380 ft MD and drilling a new borehole while building from vertical with a $10^\circ/100$ ft dogleg to an inclination of 45° . This allowed evaluation of images in both vertical and deviated sections. The first section was drilled using 9.5-lbm/gal OBM. The logged section allowed for assessment of sensor performance within a number of different formations,

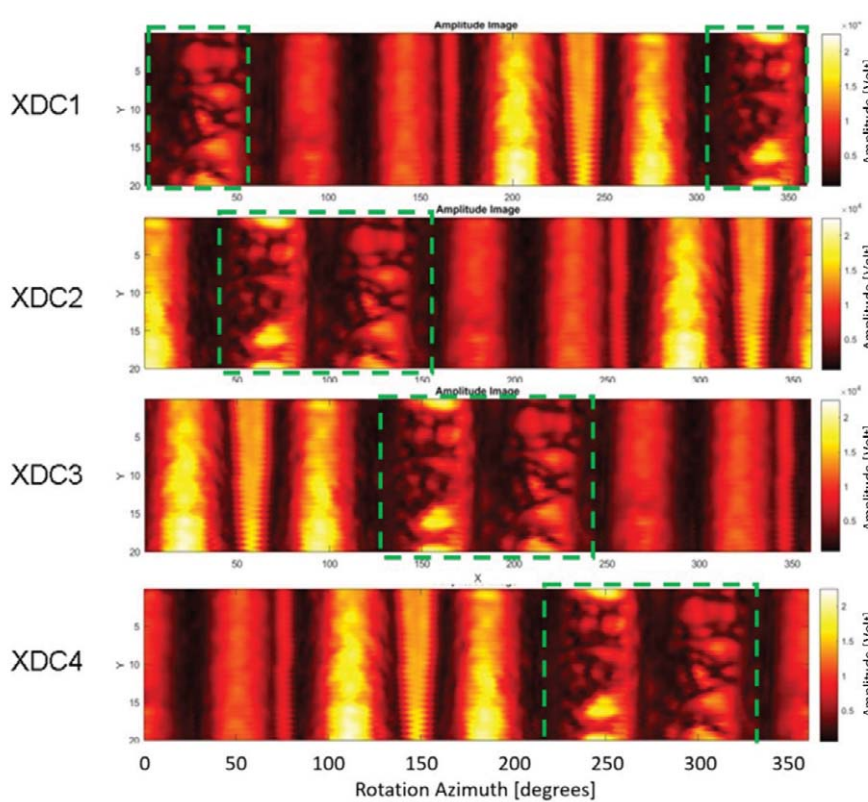


Fig. 14—Reflection amplitude image of the six target bricks for one complete rotation of the 3D rotating apparatus. Each row corresponds to data from a single transducer. Note the dark vertical stripes are the gaps between the bricks where no reflection was detected. The dashed-green boxes highlight the location of the two bricks containing the hand-engraved letters “HAL”.

as shown in Fig. 15. Average drilling rate of penetration (ROP) was 60 ft/hr, with string rotation maintained at 40 rev/min (RPM).

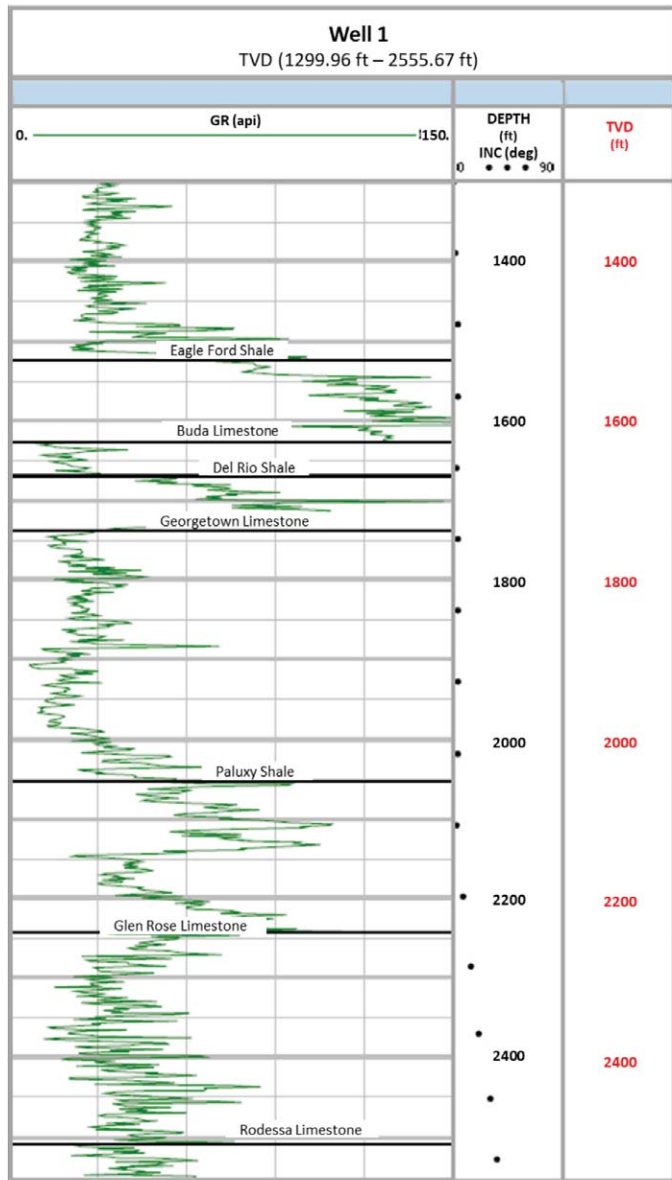


Fig. 15—The well inclination and major formation tops (based upon offset vertical well gamma-ray log correlation) for Well 1. The formation above the Eagle Ford Shale is the Austin Chalk. The vertical and deviated sections of the well are shown.

After landing the well at 45° at 2,669 ft MD, and having acquired 1,289 ft of while-drilling data, the drilling assembly was pulled out of hole, and two wireline runs were

performed to collect high-resolution ultrasonic imaging and pipe-conveyed 6-arm multifinger caliper data. Both datasets were evaluated to identify zones of interest over which a series of wipe runs was performed using the 4.75-in. ultrasonic imaging tool.

Comparison of LWD caliper with the average caliper (obtained from the mean value from each arm) and maximum caliper (obtained from the maximum value of 180° separated pairs of arms) from the multifinger caliper tool showed excellent correlation throughout the drilled section (Fig. 16). The caliper data from both LWD and wireline show that the borehole is slightly overgauge for the majority of the drilling run. Separation between the LWD caliper and the wireline caliper in deviated sections is attributed to the wireline tool not being perfectly centralized within the borehole (Li et al., 2019).

The wireline data also identified a zone of interest between 1,360 and 1,420 ft MD, interpreted as fractures within the Austin Chalk formation. The log example shown in Fig. 17 compares the ultrasonic imaging data from the wireline run with the corresponding reflection amplitude and radius data from the LWD drilling run over a short section of the zone of interest. In general, the images show agreement, with the reflection amplitude images showing more detail than the caliper images, and the LWD images showing a little more detail than the wireline images. The interpreted fractures, highlighted in the green box on the LWD amplitude image, are most prominent on the amplitude images, but are also visible on the radius images. However, there is one significant difference; a vertical feature to the left of center of both the wireline caliper, and more clearly, the wireline amplitude images. This corresponds to a gouge or scratch in the borehole wall of at least 20-ft length, which we believe was caused by the wireline itself or one of the centralizers required for the wireline ultrasonic tool. Obviously, this feature is not present on the LWD data, which were recorded as the borehole was drilled.

Figure 18 shows a further comparison of the wireline and the LWD images in the Eagle Ford Shale and Buda Limestone formations. Again, both sets of images have much in common, this time illustrating borehole characteristic of drilling with a bent mud motor. The amplitude images show more contrast than the caliper images with the LWD caliper images showing more details than the wireline. As in the previous image, a wireline gouge can be seen in the top-right corner of the wireline amplitude image.

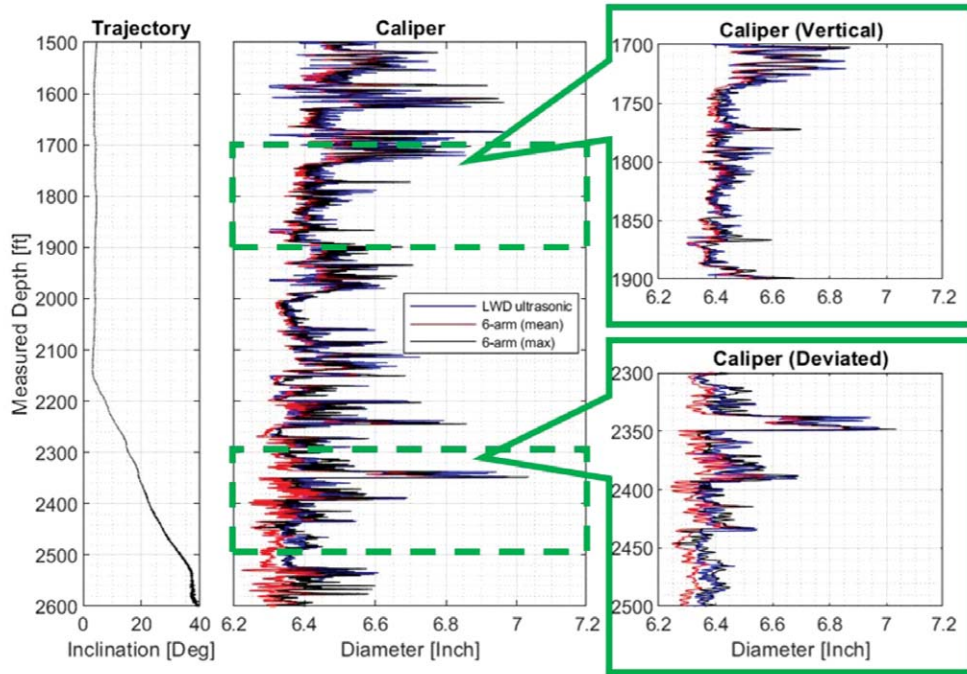


Fig. 16—Comparison of LWD caliper and wireline 6-arm caliper data. The left track shows the well trajectory. The center track shows the LWD ultrasonic caliper data (blue), the 6-arm wireline average caliper (red) and maximum caliper (black). The right track shows details of the caliper in the near-vertical (top) and deviated (bottom) well sections.

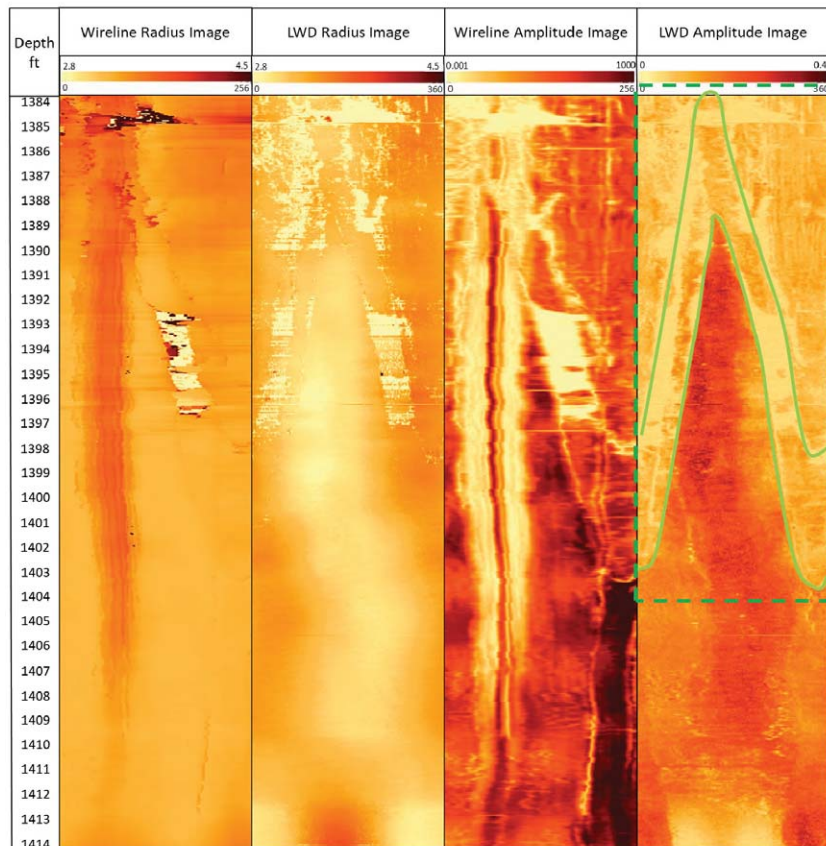


Fig. 17—Log section comparing wireline data with LWD over a short section within the Austin Chalk formation. Track 2, wireline radius image; Track 3, LWD radius image; Track 4, wireline reflection amplitude image; Track 5, LWD reflection amplitude image. The radius images are on the same color scale, but the amplitude images have been independently scaled. Two fractures are shown in green in Track 5.

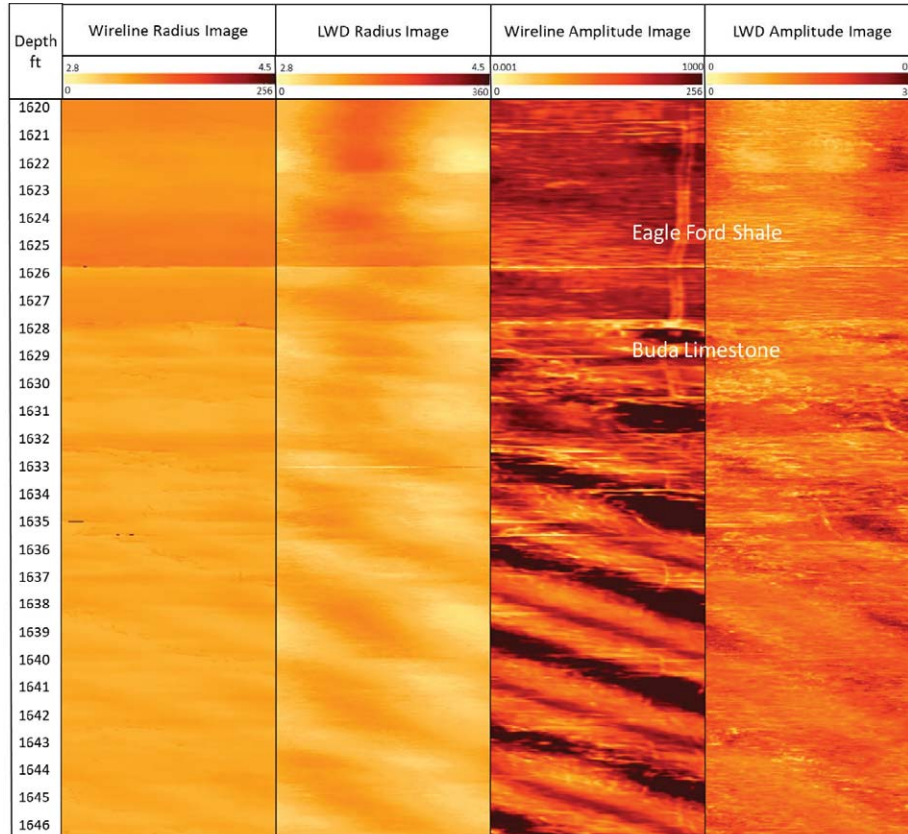


Fig. 18—Log section comparing radius and reflection amplitude images from wireline data with LWD within the Eagle Ford Shale and Buda Limestone formations. Borehole spiraling is observed in each of the images. The radius images are on the same color scale, but the amplitude images have been independently scaled.

The fractures within the Austin Chalk formation were then logged multiple times in wipe mode by the LWD tool within the BHA while tripping in hole (denoted as TI) with varying logging speeds and drillstring RPM with 9.5-lbm/gal OBM. The use of different combinations of ROP and RPM during the wipe runs allows us to evaluate the influence of each on image quality. The relevance of logging speed and drillstring rotation to image quality is illustrated schematically in Fig. 19. Rapid rotation and slow penetration

have the potential to produce finer axial resolution than slower rotation and faster penetration. Thus, the ratio ROP/RPM is the critical parameter.

Table 1 shows the parameters for each logging pass. Note, that from these passes the highest data density (measured in total samples/ft) is obtained with the slowest logging speed (the tool fires at a constant 500 samples/transducer/sec), in this case 30 ft/hr. However, the best axial resolution is expected from a logging speed of 59 ft/hr and 160 RPM due to the resulting low ROP/RPM ratio.

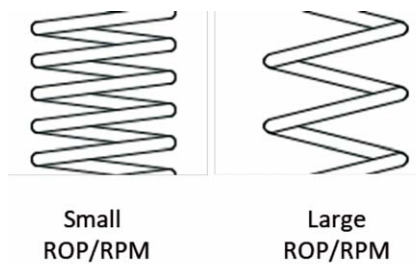


Fig. 19—Schematic illustration of the effect of varying the ratio ROP/RPM on potential axial resolution of images for a single transducer. For slow penetration and rapid rotation, the transducer moves only a small distance axially during each rotation. For rapid penetration or slow rotation, the transducer moves a long distance axially for each rotation.

Table 1—Logging Conditions for Wipe Passes Between 1,370 and 1,450 ft While Tripping in Hole (TI) With 9.5-lbm/gal OBM

Section	ROP (ft/hr)	RPM	Mud Weight (lbm/gal)	ROP/RPM
T11	30	40	9.5	0.15
T12	53	40	9.5	0.27
T13	59	80	9.5	0.15
T14	59	160	9.5	0.07
T15	88	80	9.5	0.22
T16	176	80	9.5	0.44
T17	352	80	9.5	0.88
T18	733	80	9.5	1.83

Figure 20 illustrates the high-resolution reflection amplitude (a) and radius (b) images from the eight wipe passes. Despite the wide range of logging speed and RPM combinations, the notable fracture features observed around 1,390 ft are clearly visible for each wipe pass. The images in

Fig. 20 confirm the predictions shown in Table 1. The near-vertical feature below the fractures, believed to be a gouge mark from the wireline tools, appears progressively less prominent from left to right, suggesting the feature is being eroded by each wipe pass.

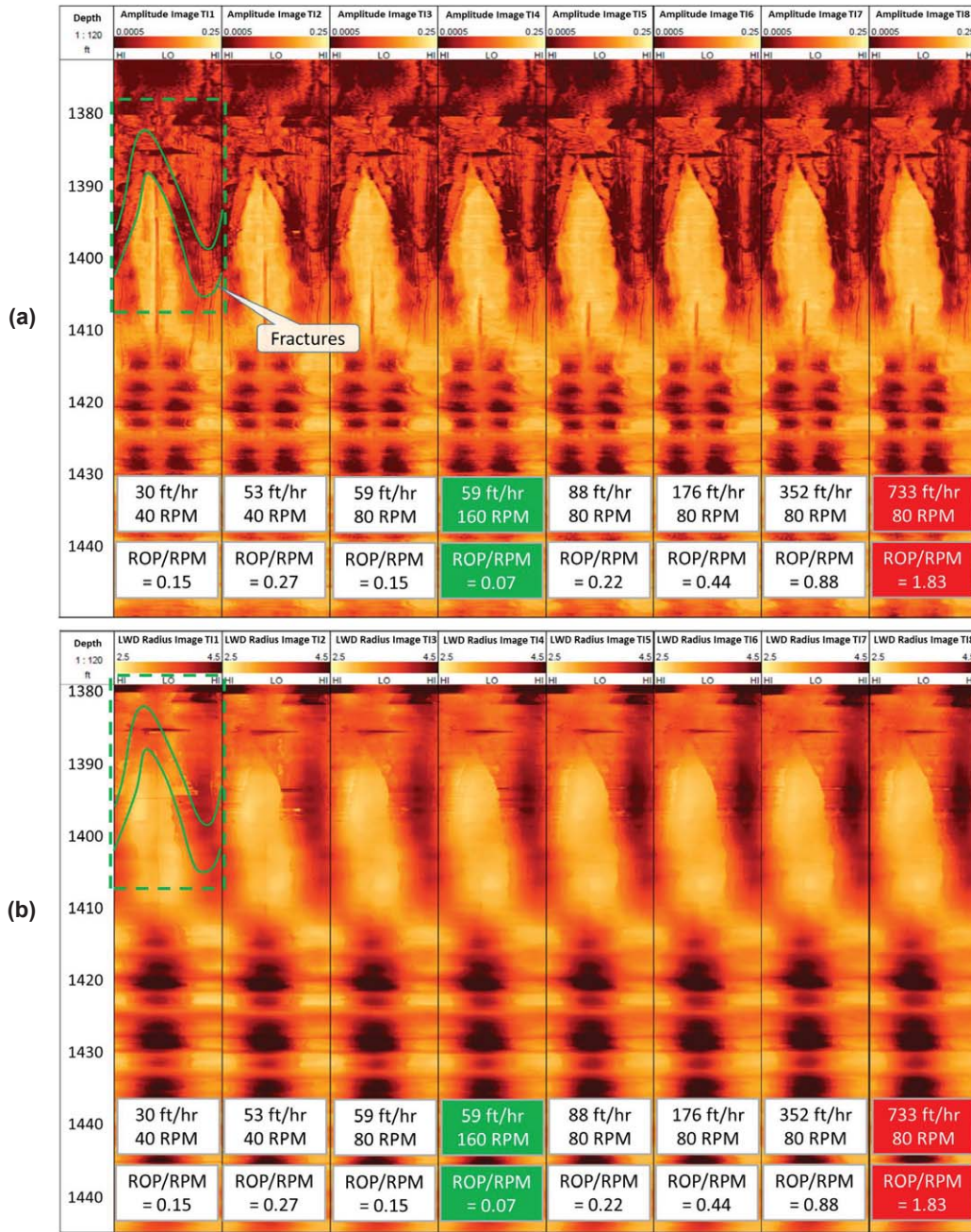


Fig. 20—Reflection amplitude images (a) and radius images (b) from the wipe passes between 1,370 and 1,450 ft while tripping in hole with 9.5-lbm/gal OBM. The logging speed and string rotation, and the ratio of penetration to rotation rate (ROP/RPM) are listed for each example with the lowest and highest, corresponding to the best and worst axial resolution, highlighted in green and red, respectively. The approximate locations of the fractures are shown by the green lines in the top-left panel.

Having completed the wipe passes with 9.5-lbm/gal OBM mud, the well was then displaced to 11.5-lbm/gal OBM and a sequence of wipe runs over the same section of interest was performed while tripping out of hole (denoted as TO) in order to evaluate the impact of different mud weights on the images. The logging conditions for the trip-out wipe passes are shown in **Table 2**.

In Fig. 21, the reflection amplitude (a) and radius (b) image wipe pass plots with 11.5-lbm/gal mud weight again show the highest data density plots occur when the logging speed is slowest (TO1), with a logging speed of 30 ft/hr and string rotation of 40 RPM, and the smallest axial resolution seen during the TO10 pass with a logging speed of 59 ft/hr and 160 RPM string rotation. The fractures within the Austin Chalk are identifiable on all of the reflection amplitude and radius images.

Table 2—Logging Conditions for Wipe Passes Between 1,370 and 1,450 ft While Tripping Out of Hole (TO) With 11.5-lbm/gal OBM

Section	ROP (ft/hr)	RPM	Mud Weight (lbm/gal)	ROP/RPM
TO1	30	40	11.5	0.15
TO2	59	40	11.5	0.30
TO3	59	80	11.5	0.15
TO4	88	80	11.5	0.22
TO5	176	80	11.5	0.44
TO6	352	80	11.5	0.88
TO7	733	80	11.5	1.83
TO8	176	160	11.5	0.22
TO9	88	160	11.5	0.11
TO10	59	160	11.5	0.07

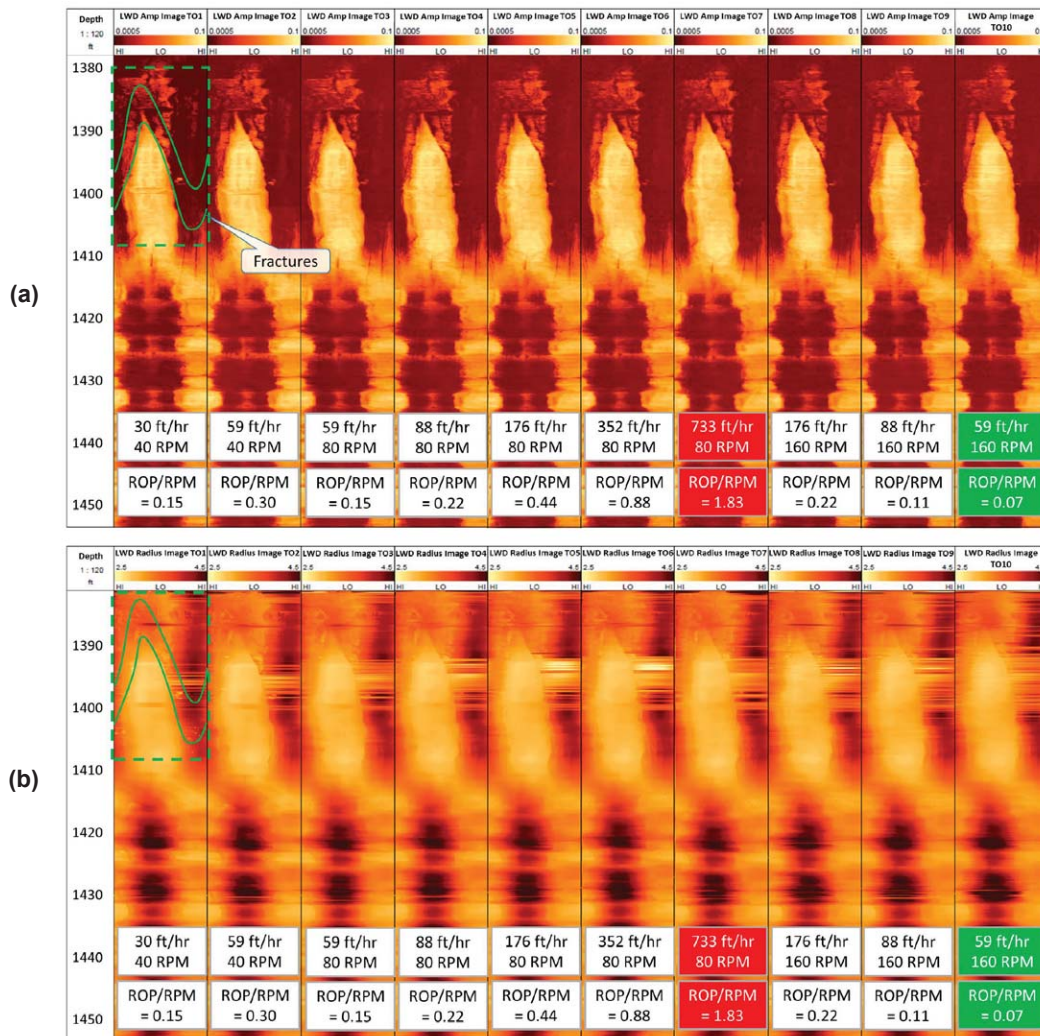


Fig. 21—Reflection amplitude images (a) and radius images (b) from the wipe passes between 1,370 and 1,450 ft while tripping out of hole with 11.5-lbm/gal OBM. The logging speed and string rotation, and the ratio of penetration to rotation rate (ROP/RPM) are listed for each example with the lowest and highest, corresponding to the best and worst axial resolution, highlighted in green and red, respectively. The approximate locations of the fractures are shown by the green lines in the top-left panel.

The drilling data from the 4.75-in. ultrasonic imaging tool showed excellent correlation with both the caliper measurements from the wireline multifinger caliper, and the radius and reflection amplitude images from the wireline high-resolution OBM imaging tool. The impact of logging speed and string rotation variations on LWD image quality was assessed and highlighted how the ROP/RPM ratio determines the axial resolution of the images. Assessment of image quality in different mud weights was made, with high-resolution images obtained in both 9.5- and 11.5-lbm/gal OBM.

FIELD TEST TO DETERMINE IMPORTANCE OF STABILIZATION IN VERTICAL WELL

For the second trial run, a 6.125-in. vertical well was drilled with 9.5-lbm/gal OBM off the same primary wellbore used for Well 1 (open hole drilled from below the same 9.625-in. casing shoe). The main objective of the run was to evaluate the impact of decentralization of the tool in a vertical well on the quality of the images. Two 4.75-in. tools were included in the BHA, one tool with a 0.125-in. undergauge stabilizer, i.e., with OD of 6 in., and the second tool without any stabilization. The vertical well also allowed for assessment of both borehole caliper and image quality through a wide range of formations, as shown in Fig. 22, which highlights the major formations through which the tools were logged.

The 256-sector reflection amplitude images shown in Fig. 23 are from a section of the Austin Chalk formation. In Fig. 23a the image on the left is from the nonstabilized tool, and shows significant “blurring” compared to the image on the right from the stabilized tool. The images from both tools clearly show striations believed to be caused by a section of the mud motor, shown in Fig. 23b. The dark areas on the nonstabilized tool image from 1,428 to 1,444 ft and from 1,452 to 1469 ft, indicate that there was greater standoff, resulting from eccentricity. For reference, each of the circular features on the kickpad is 0.605 in. in diameter.

The vertical well field trial illustrated the importance of stabilizing the 4.75-in. ultrasonic imaging tool in order to minimize the impact of decentralization on the image quality in OBM. High-resolution radius and reflection amplitude images were collected through multiple formations, allowing future assessment of fractures and bedding features in shale, limestone, and sandstone formations.

FIELD TEST TO EVALUATE IMAGES IN HIGH-ANGLE WELL

A third trial well was drilled with 9.5-lbm/gal OBM, building from vertical to horizontal in order to assess both caliper measurements and image quality in a high-angle wellbore. As with Well 2, the wellbore was drilled from below the same 9.625-in. casing shoe as Well 1. The hole was drilled with a mud motor, and a fully stabilized tool was run with 0.125-in. undergauge stabilizers placed directly above and below the tool to minimize decentralization and its potential impact on image quality.

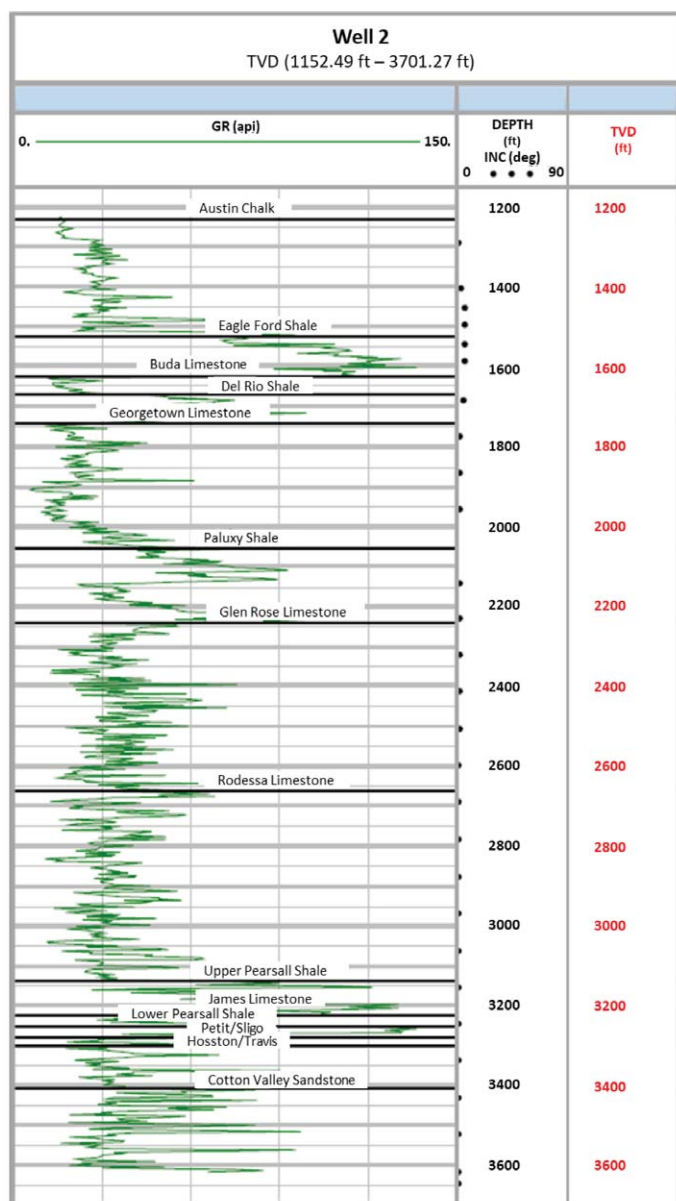


Fig. 22—Well 2 inclination and major formation tops based upon offset vertical well gamma-ray correlation.

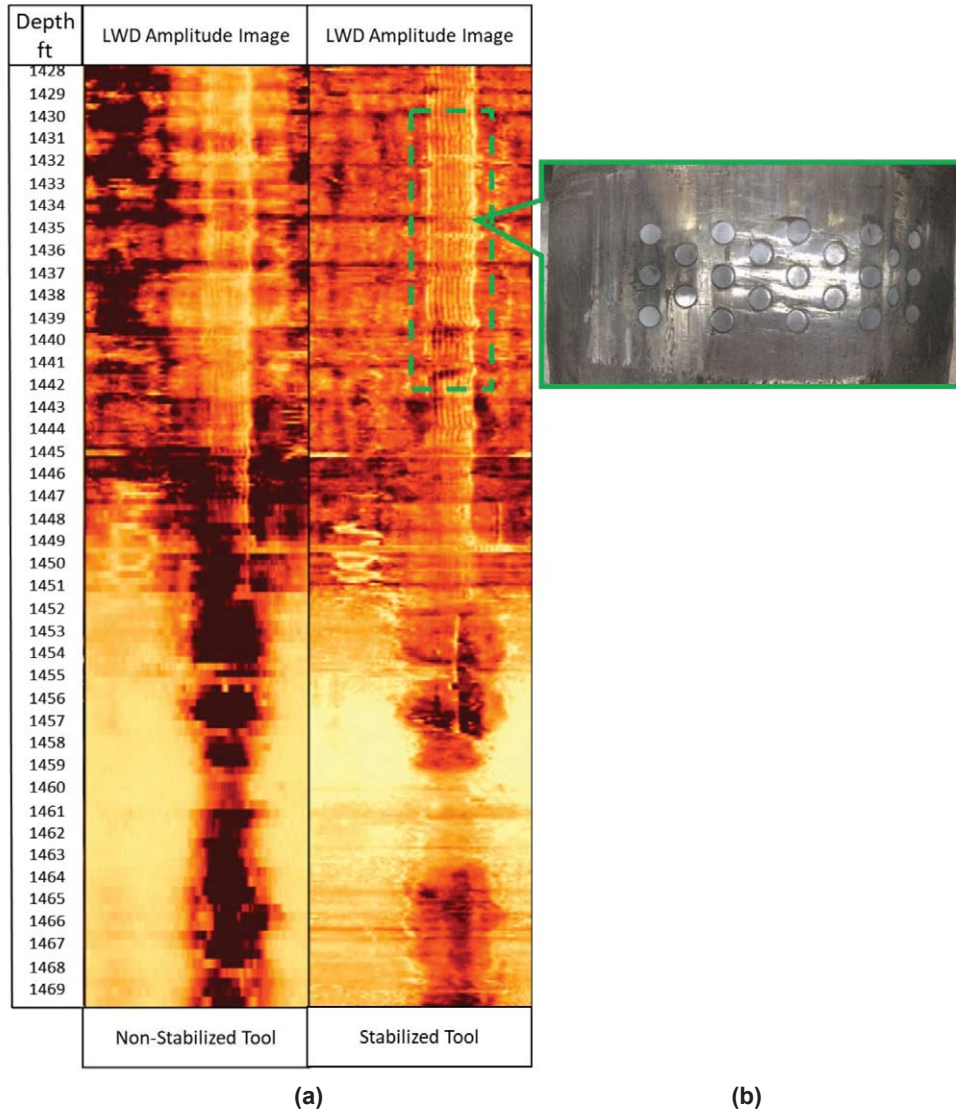


Fig. 23—(a) A comparison of the amplitude images from nonstabilized tool (left) that shows “blurring” and the stabilized tool (right) that shows higher resolution. The vertical striations on the images, highlighted within the dashed-green box, are attributed to gouges made by the kickpad of the mud motor (b).

The fractures observed within the Austin Chalk formation on Well 1 and 2 were again identified on both the high-resolution, 540-sector radius and reflection amplitude images, shown in Fig. 24. The log section also identifies a zone of borehole washout from 1,420 to 1,432 ft, as illustrated by the average borehole size plot (Tracks 4 and 5) and the 3D borehole profiles (Tracks 6 and 7). The reflection amplitude image also shows the same striations believed to be caused by a section of the mud motor that were observed

over the same section in Well 2.

A high-angle section (approximately 80° inclination) of the log within the Rodessa Limestone formation is shown in Fig. 25. Thin laminations, with dip and strike corresponding to the bedding, are clearly visible on the reflection amplitude image, despite the presence of eccentricity and associated large standoff, represented by the dark shading on the radius image.

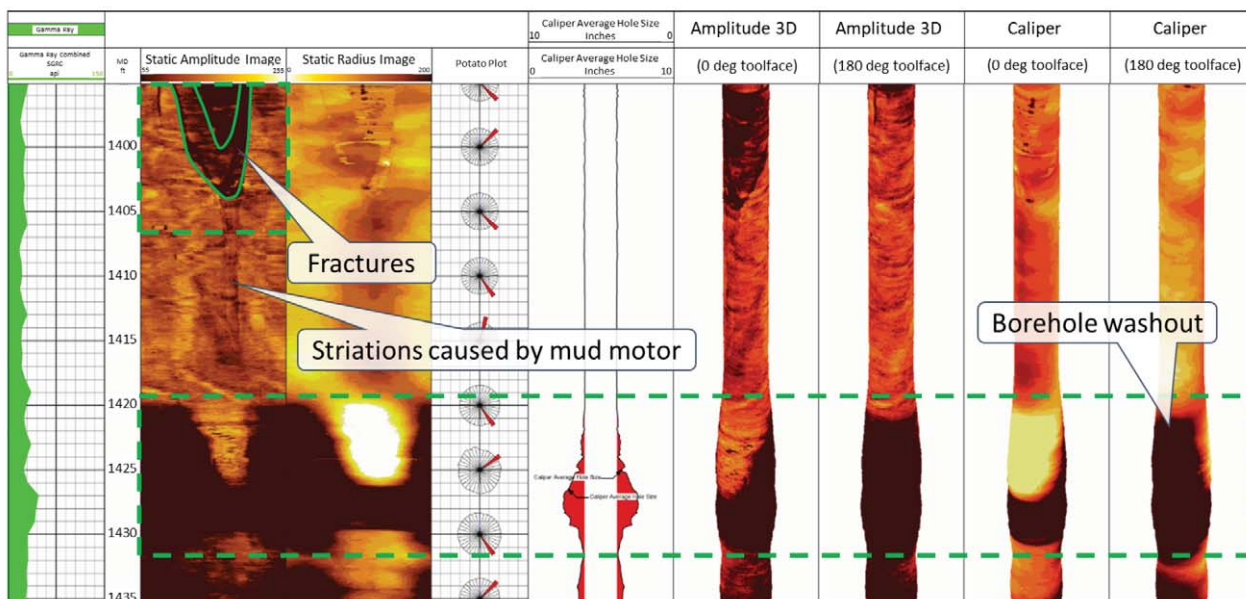


Fig. 24—Log section: Track 1, gamma ray; Track 2, reflection amplitude and radius images; Track 3, potato plots; Track 4, average caliper. Tracks 5 to 8, 3D borehole profile plots across a fracture and borehole washout zone within the Austin Chalk formation.

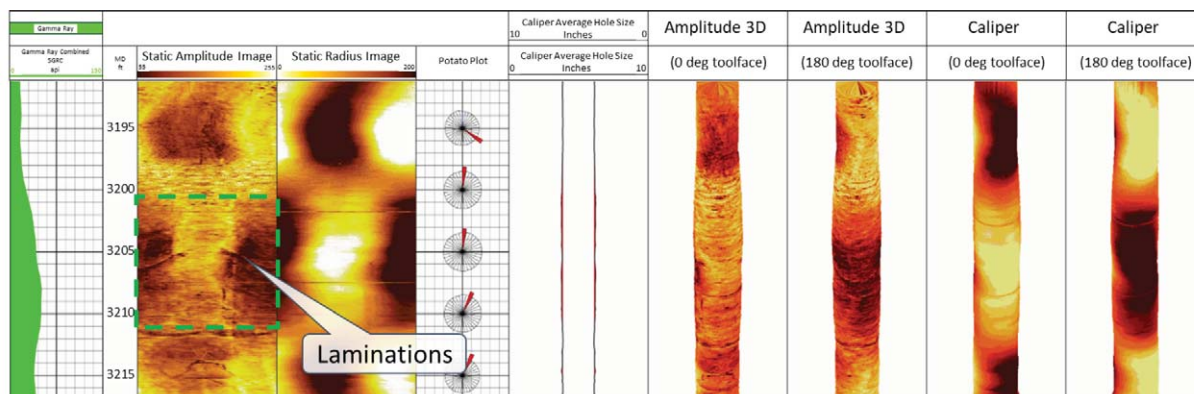


Fig. 25—Log section showing: Track 1, gamma ray; Track 2, reflection amplitude and radius images; Track 3, potato plots; Track 4, average caliper; Tracks 5 to 8, 3D borehole profile plots within an 80° inclination section of the Rodessa Limestone formation.

Bedding features are also visible on the reflection amplitude image taken from a section where the borehole inclination was 87° (Fig. 26). The dark features on both the reflection amplitude and radius images between 3,754 and 3,757 ft are caused by the kickpad on the mud motor at the start of a slide section to drop angle.

The wellbore enabled assessment of both borehole caliper and images in vertical, build, and near-horizontal borehole sections using OBM. The borehole caliper, radius images, and 3D borehole profile plots created from the traveltime measurements identified zones of borehole enlargement, and the high-resolution reflection amplitude images identified fractures and bedding features within multiple formations.

CONCLUSIONS

This paper presents a 4.75-in. LWD ultrasonic imaging tool with four transducers arranged at uniform azimuthal spacings. We demonstrate how the tool’s hardware design and advanced algorithms can compensate for the systematic errors introduced into the caliper and reflection amplitude images by tool center motion. We describe the laboratory testing performed on the transducers using both 2D and 3D apparatus, and measure the potential detection and resolution capabilities of the tool.

Three field tests demonstrate the impact of poor stabilization on both caliper and reflection amplitude

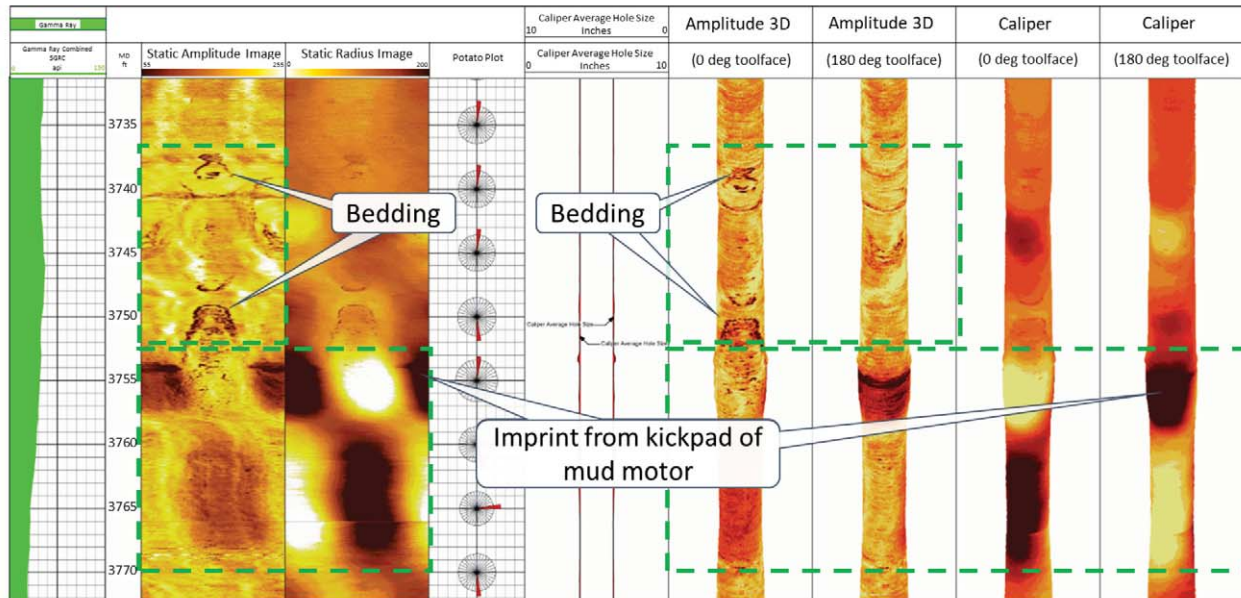


Fig. 26—Log section showing: Track 1, gamma ray; Track 2, reflection amplitude and radius images; Track 3, potato plots; Track 4, average caliper; Tracks 5 to 8, 3D borehole profile plots within a near-horizontal section of the Rodessa Limestone. The section highlighted inside the dashed green boxes represents a slide section to drop inclination where tool marks related to the kickpad of the mud motor are observed at 3,754 ft on the top of the borehole on the amplitude image. The start of the slide sections corresponds to a slight increase in borehole diameter.

images that leads to a recommendation that this tool should be centralized within the borehole using stabilizers with outside diameters that are 0.125-in. smaller than the nominal borehole size, i.e., 0.125-in. undergauge. Comparison of images acquired at different logging and drillstring rotation speeds shows that the resolution of the radius and reflection amplitude images were comparable over a wide range of conditions, although some improvements were seen at low values of the ratio of ROP to RPM, consistent with theory.

The three field tests also demonstrate that the tool is able to produce high-resolution images in both vertical and horizontal borehole sections. From these images we are able to identify fractures, bedding features, and drilling-induced features in multiple formations. The excellent correlation of these results with those from analogous wireline ultrasonic imaging and 6-arm caliper technologies highlights the potential for the 4.75-in. LWD ultrasonic imaging tool to be the primary logging solution in wellbores where the use of wireline may be either risky or costly.

ACKNOWLEDGEMENTS

The authors would like to thank Halliburton for supporting the technologies and publications, and Mohamed Hany for his help in processing the data and preparing the log examples.

REFERENCES

- Ballay, G., Hussein, A-A., Amos, S., and Dennis, B., 2001, In the Driver's Seat With LWD Azimuthal Density Images, Paper SPE-77282 presented at the SPE/IADC Middle East Drilling Technology Conference, Bahrain, 22–24 October. DOI: 10.2118/72282-MS.
- Bittar, M., Klein, J., Beste, R., Hu, G., Wu, M., Pitcher, J., Golla, C., Althoff, G., Sitka, M., Minosyan, V. and Paulk, M., 2009, A New Azimuthal Deep-Reading Tool for Geosteering and Advanced Formation Evaluation, Paper SPE-109971, *SPE Reservoir Evaluation & Engineering*, **12**(2), 270–279. DOI: 10.2118/109971-PA.
- Davies, D.H., Faivre, O., Gounot, M-T., Seeman, B., Trouiller, J-C., Benimell, D., Ferreira, A., Pittman, D.J., Randrianavony, M., Smits, J.W., Anderson, B.I., and Lovell, J., 1994, Azimuthal Resistivity Imaging: A New-Generation Laterolog, Paper SPE-24676, *SPE Formation Evaluation*, **9**(3), 165–174. DOI: 10.2118/24676-PA.
- Ekstrom, M.P., Dahan, C.A., Chen, M.Y., Lloyd, P.M., and Rossi, D.J., 1987, Formation Imaging With Microelectrical Scanning Arrays, *The Log Analyst*, **28**(3), 294–306.
- Hayman, A.J., Parent, P., Cheung, P., Verges, P., 1998, Improved Borehole Imaging by Ultrasonics, Paper SPE-28849, *SPE Production & Operation*, **13**(1), 5–14. DOI: 10.2118/28440-PA.
- Joyce, B., Patterson, D., Leggett, J., and Dubinsky, V., 2001, Introduction of a New Omni-Directional Acoustic System

for Improved Real-Time LWD Sonic Logging—Tool Design and Field Test Results, Paper SS, *Transactions, SPWLA 42nd Annual Logging Symposium*, Houston, Texas, USA, 17–20 June.

Labat, C., Brady, S., Everett, M., Ellis, D., Doghmi, M., Tomlinson, J., and Shehab, G., 2002, 3D Azimuthal LWD Caliper, Paper SPE-77526 presented at the SPE Annual Technical Conference and Exhibition, San Antonio, Texas, USA, 29 September–2 October. DOI: 10.2118/77526-MS.

Li, P., Lee, J., Taher, A., Coates, R., and Marlow, R., 2019, New 4 $\frac{3}{4}$ -in. High-Resolution Ultrasonic Borehole Imaging for Unconventional Reservoir Evaluation. Paper URTEC-2019-322, Unconventional Resources Technology Conference, 22–24 July. DOI: 10.15530/urtec-2019-322.

Li, Q., Omeragic, D., Chou, L., Yang, L., Lau, T., Liu, C., Dworak, R., Dreuilhault, V., and Ye, H., 2005, New Directional Electromagnetic Tool for Proactive Geosteering and Accurate Formation Evaluation While Drilling, Paper UU, *Transactions, SPWLA 46th Annual Logging Symposium*, New Orleans, Louisiana, USA, 26–29 June.

Morys, M., Chemali, R., Goodman, G., Smollinger, G., Schaecher, B., and Maki, V., 2011, Field Testing of an Advanced LWD Imager for Oil-Based Mud Applications, *Petrophysics*, **52**(2), 84–95.

ABOUT THE AUTHORS



Peng Li is Senior R&D Advisor at Halliburton Sperry Drilling. He holds a BSc in the School of Automation Science and MSc in Electrical Engineering from Beihang University, and a PhD degree in Control from the University of Houston. He has worked on a variety of downhole logging technologies including ultrasound

borehole imaging and casing evaluation, electromagnetic-based casing-corrosion detection, and nuclear magnetic resonance logging. His research interests include control and signal processing, embedded systems and instrumentation, motor control and power electronics, and wireless sensor network and high-speed digital communications.



Jonathan Lee is Product Manager for Acoustic and Magnetic Resonance at Halliburton Sperry Drilling. He began his career as a mudlogger in the North Sea with Exlog, before moving to various MWD/LWD field positions. He has since held various product management and business development positions

in Houston with Baker Hughes, GE, and TGT Oil & Gas Services. He holds a BSc in geology from the University of Wales, Cardiff, and is a member of SPE and SPWLA.



Richard Coates is currently Chief R&D Advisor at Halliburton Sperry Drilling. Prior to joining Halliburton, he spent most of his career with Schlumberger working on sonic and seismic topics in a variety of technical and management roles, culminating as a Scientific Advisor.

Prior to joining Schlumberger, he was a Post-Doctoral Fellow at the Earth Resources Lab., MIT. He holds a MA in Natural Sciences (Physics) and a PhD in Geophysics from the University of Cambridge, and is a member of the EAGE, SEG and SPWLA. He is an Associate Editor of the SPWLA journal *Petrophysics* and Associate Editor of the SEG journal *Geophysics*.



Jing Jin is a Scientific Advisor at Halliburton Sperry Drilling, working on the development of ultrasonic transducers for LWD technologies. Prior to joining Halliburton, he was Head of Department at Microfine, focused on the R&D of piezoelectric transducers. He then joined Halliburton as principle mechanical

engineer, working on the development of piezoelectric transducers for both wireline and LWD sensors. He has 20 published papers and five patents awarded. He holds a BE in Civil Engineering and a MSc in Structural Engineering from Shanghai Jiaotong University, and a PhD in Civil Engineering from the National University of Singapore.



Siong (Hans) Ming Wong is a Senior Technical Advisor in the Global Technical Services group at Halliburton Sperry Drilling, providing technical assistance across multiple MWD/LWD technologies. He began his career with Halliburton in 2003 as a MWD/LWD field engineer, before moving to Service

Quality and QA Engineer roles. He holds a BEng Hons Degree in Petroleum Engineering from the University of Malaysia and serves as 2019–2020 Secretary of the Houston SPWLA Chapter.

Deducing Electrical Permittivity of Formations From LWD Resistivity Measurements¹

Stein Ottar Stalheim²

ABSTRACT

The electrical permittivity (ϵ) of rock has been measured and applied in petrophysical evaluation for decades. With the new-generation tools the popularity and application of ϵ has increased in the past years. One of the advances of the new-generation tools is measurement of ϵ at multiple frequencies (f), also known as dispersive permittivity ($\epsilon(f)$). Drawbacks with these tools are that they respond to the invaded zone and the data must be acquired on wireline and therefore is not always accessible.

Logging-while-drilling (LWD) propagation resistivity records the phase shift and attenuation between two receivers and responds differently to electromagnetic rock properties (resistivity, permittivity and permeability). The characteristic of the phase shift and the amplitude decay can therefore, under given conditions, be used to extract both electrical permittivity and resistivity from the measurements.

The purpose with this paper is to show that electrical permittivity and its dispersion can be extracted from

LWD resistivities. The work is motivated by the fact that information about ϵ and $\epsilon(f)$ is hidden in the LWD resistivities, so why not extract it and use it? The permittivity can be used in the petrophysical evaluation, it is acquired in real time and can be used to identify bypassed zones, as geological marker and for geosteering. The LWD resistivity accuracy will also be improved by replacing the empirical-based assumption about ϵ with the more correct value on ϵ in the LWD processing. This improvement in accuracy of LWD resistivity will be significant in rocks with large permittivity, e.g., organic-rich source rocks.

This paper applies classical electromagnetic theory and shows how to extract permittivity from LWD resistivity. Examples are illustrated based on results from different LWD tools. The examples show that LWD permittivity and its dispersion fit very well with data from commercial wireline tools. Limitations of the presented techniques and further application of LWD permittivity and dispersion will be discussed.

INTRODUCTION

This paper unveils that information about electrical permittivity is hidden in LWD resistivity measurements that can be extracted and used.

Electromagnetic properties of a formation determine its response to an electromagnetic (EM) field. Electromagnetic properties are electrical conductivity (σ), magnetic permeability ($\mu \cdot \mu_0$) and electrical permittivity ($\epsilon \cdot \epsilon_0$). σ , μ , μ_0 , ϵ , and ϵ_0 will be explained. Electrical conductivity, σ (inverse of resistivity) is the measure of a formation's ability to conduct electric current. σ is heavily related to the amount of saline water (free charges) in a formation and is a key input for calculation of formation water saturation, e.g., by use of Archie's equation. Relative magnetic permeability,

μ , is the measure of the magnetization of a formation and μ_0 is free-space magnetic permeability. Since magnetic materials are rarely found in oil and gas reservoirs, μ is usually assumed to be unity and independent of formation properties (Jackson and Hagiwara, 1998; Shen, 2002). Relative electrical permittivity, ϵ , is the measure of the electrical polarizability of a formation and is the prominent characteristic of dielectric substance. ϵ_0 is free-space electrical permittivity. Due to strong polarization of water-molecules compared with other substances in a formation, ϵ is strongly related to amount of water in the formation and can be used to calculate formation water saturation, e.g., by use of the CRIM that will be explained later. This paper focus on electrical permittivity.

Electrical permittivity of rocks has been measured and

Manuscript received by the Editor July 3, 2019; revised manuscript received October 17, 2019; manuscript accepted October 23, 2019.

¹Originally presented at the SPWLA 60th Annual Logging Symposium, The Woodlands, Texas, USA June 17–19, Paper VVVV.

²Equinor, Sandslivegen 90, 5254 Sandli. Norway; stos@equinor.com

applied in petrophysical evaluation for decades (Rabinovich and Liu, 2015). Permittivity measurements and interpretation were introduced in the 1980s but were not widely recognized due to measurement limitations and moderate accuracy. With the new-generation dielectric tools, presented by Hizem et al. (2008), the popularity and applications of ϵ have increased in the past few years. One of the revolutionary advances of the new-generation tools is the measurement of ϵ at multiple frequencies (f) from MHz to GHz, also known as dispersive permittivity ($\epsilon(f)$). There are many published papers that show applications of such data, such as pore-fluid analysis including water saturation calculation, matrix analysis, like Archie m , and shaly sand evaluation including clay volume calculations (Seleznev et al., 2006; Hizem et al., 2008; Josh et al., 2009; Wang and Poppitt, 2013). The limitation of the dielectric tools is that they respond to the invaded zone (a few centimeters into the formation), and the data must be acquired on wireline and therefore are not always accessible.

Over the past several decades there have been papers showing algorithms that extract permittivity from conventional logging tools, such as wireline induction resistivity (Wang and Poppitt, 2013) and logging-while-drilling (LWD) resistivity tools (Jackson and Hagiwara, 1998; Wu et al., 1999, Haugland, 2001; Anderson et al., 2007). The goal of these algorithms is to increase the accuracy of the processed resistivity. Only one paper that shows use of permittivity extracted from LWD resistivity is found (Wang and Poppitt, 2013). Wang and Poppitt (2013)

present dielectric-dispersion data extracted from wireline induction resistivity and LWD resistivity and show that the data match very well with dielectric-dispersion data from a multifrequency wireline dielectric tool. The dielectric processing from the induction and LWD resistivity was performed by both Schlumberger and Halliburton. The strength with these approaches is that the processed ϵ normally represents noninvaded formation.

This paper will focus on LWD resistivity. LWD resistivity tools record the phase shift and amplitude decay between two receivers. The tools have multiple sets of receivers and operate at two or three frequencies. For each frequency and for each transmitter-to-receiver spacing (TRS), a set with phase resistivity (R_p) and amplitude resistivity (R_a) is generated (Bittar et al. 1993). R_p and R_a are independent measurements. The characteristics of R_p and R_a depend on the electromagnetic properties of the medium, which, in practice, are resistivity and permittivity when μ is unity. Resistivity and permittivity can therefore, in principle, be simultaneously inverted from phase and amplitude measurements, although this is not common practice when generating LWD resistivity.

When generating LWD resistivity it is common practice to assume a small impact of electrical permittivity, and empirically derived resistivity-dependent permittivity is used in the processing (Anderson et al., 2007; Wang and Poppitt, 2013). Figure 1 shows the models applied by different service providers.

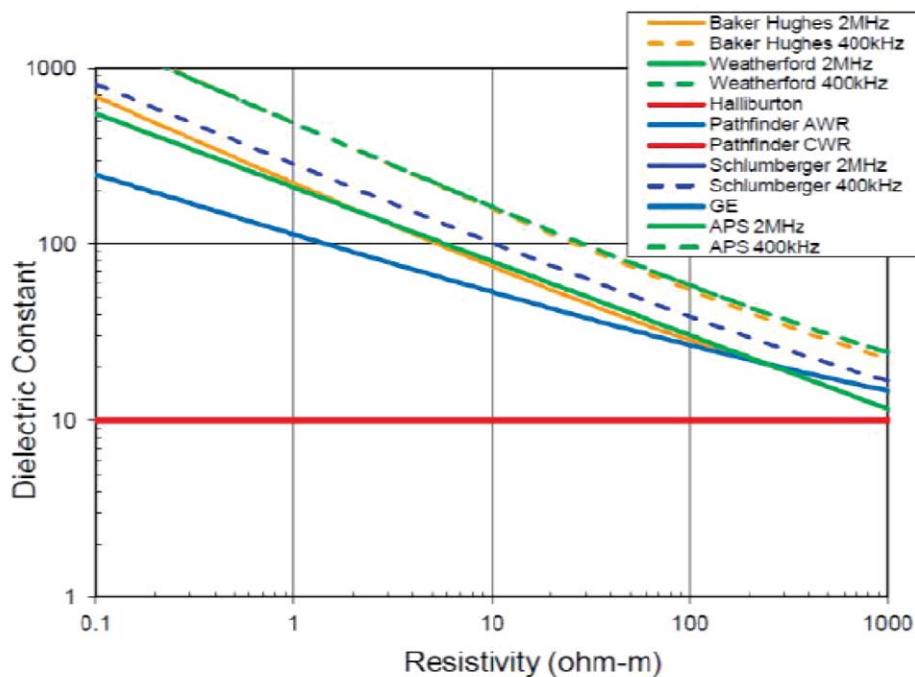


Fig. 1—Dielectric assumptions used by several service providers (Wang and Poppitt, 2013).

If the assumption given by Fig. 1 does not represent the permittivity of rock being measured, it introduces systematic error in generated R_p and R_a (Rodney and Wisler, 1986; Bittar et al., 1993; Wu et al., 1999; Shen, 2002; Anderson et al., 2007). This is known as the dielectric effect. The error is most pronounced in high-resistivity zones, and R_a is more sensitive to ϵ compared with R_p (Bittar et al., 1993; Wu et al., 1999; Anderson et al. 2007). It is shown that the error can be significant with R_a above 10 Ω -m and with R_p above 100 Ω -m (Clark et al., 1988; Wu et al., 1999; Shen, 2002.). Aiming to reduce the dielectric effect on R_p and R_a , a couple of algorithms that simultaneously invert out both resistivity and permittivity have been developed. Jackson and Hagiwara (1998) present an algorithm that simultaneously corrects for both dielectric and anisotropic effects on resistivity. Wu et al. (1999) present a crossplot of computed phase shifts and amplitude decays for a homogeneous medium with different dielectric constants and resistivity values (look-up table). Haugland (2001) presents an algorithm for the Halliburton Pathfinder tool and Anderson et al. (2007) presented an algorithm for the Schlumberger ARC tool. All presented algorithms use raw measurements of phase shift and attenuation as inputs to an inversion process together with detailed knowledge about the complexity of tool physics (tool and antenna geometry, tool calibration, environment correction, borehole correction, skin correction, correction for geometrical scattering) (Clark et al., 1988 and 1990). Lacking this information, the presented algorithms are difficult for the customer of LWD resistivity data to use.

In contrast to the work by Jackson and Hagiwara (1998), Wu et al. (1999), Haugland (2001) and Anderson et al. (2007) this paper proposes an alternative and simpler approach based on classical electromagnetic theory. The LWD amplitude and phase measurements are assumed to be of high accuracy, and that most of the processing algorithms that are in use are based on industry standards, except for the choice of electrical permittivity. The processed answer products of R_p and R_a are assumed to be of high quality. This was also concluded by Shen (2002) who compares various LWD codes from different LWD vendors. The relation between R_p , R_a and the LWD amplitude and phase measurements is described by the electromagnetic-wave properties. For electromagnetic plane waves all corresponding wave properties can be derived from the wavenumber. For an isotropic formation (electromagnetic properties are scalar) the wavenumber, \hat{k} is

$$\hat{k}^2 = \omega^2 \mu \mu_0 \epsilon \epsilon_0 \left[1 + i \frac{\sigma}{\omega \epsilon \epsilon_0} \right] = (k_r + ik_i)^2 \tag{1}$$

The hat, $\hat{\cdot}$, represents a complex number, ω is angular frequency, i is the pure imaginary number $\sqrt{-1}$, and k_r and k_i are the real and imaginary part of \hat{k} , respectively. An expression for σ and ϵ is found by decomposing \hat{k} (Eq. 1) into its real and imaginary parts

$$k_r^2 - k_i^2 = \omega^2 \mu \mu_0 \epsilon \epsilon_0 \tag{2}$$

$$2k_r k_i = \omega \mu \mu_0 \sigma \tag{3}$$

and solved with respect to σ and ϵ ,

$$\sigma = \frac{2k_i k_r}{\omega \mu \mu_0} \tag{4}$$

$$\epsilon = \left(\frac{c}{\omega} \right)^2 \left(\frac{k_r^2 - k_i^2}{\mu} \right) \tag{5}$$

where c is speed of light in vacuum. For a nonmagnetic formation $\mu = 1$ and σ (Eq. 4) and ϵ (Eq. 5) can be calculated if k_r and k_i are known. Eqs. 4 and 5 are also shown by Ellis and Singer (2008), but how to obtain k_r and k_i from LWD resistivity is not mentioned, and not seen presented by others. The main discussion of this paper is related to derivation of k_r and k_i from LWD resistivity measurements and application of Eq. 5.

This paper includes the mathematics that shows how to extract electrical permittivity from LWD resistivity and contain examples that illustrate results from data from different LWD vendors. The examples show that LWD permittivity and its dispersion fit very well with data from commercial wireline tools. Limitations of current techniques and further application of LWD permittivity and dispersion are discussed.

DEDUCING DISPERSIVE PERMITTIVITY FROM LWD RESISTIVITY MEASUREMENTS

The equations presented are applications of classical electromagnetic theory and mathematics (Maxwell, 1873; Apostol, 1969; Chew, 1990; Reitz et al., 1993; Kong, 2000; Feynman, 2010; Choy, 2016).

The presented method to calculate k_r and k_i is based on a plane-wave model for the electrical field (E) given by

$$\begin{aligned} \bar{E}(z, t) &= x' \bar{E}_x(z, t) = \text{Re} \{ x' E_o e^{k_r z + ik_i z} e^{-i\omega t} \} \\ &= x' E_o e^{-k_i z} \cos(k_r z - \omega t) \end{aligned} \tag{6}$$

where z is distance from the source, t is time, and E_0 is electrical field strength at $z = t = 0$. \hat{x} is the direction of the E-field and is perpendicular to direction of the wave propagation. Equation 6 describes a wave that propagates in the direction of k_r and with amplitude decreasing most rapidly in direction of k_i . k_r describes the phase behavior and k_i describes the amplitude behavior to the E-field. k_i represents the energy loss.

The general solutions for k_r and k_i are found by solving Eqs. 2 and 3 with respect to k_r and k_i (Kong, 2000).

$$k_r = \frac{\omega}{c} \sqrt{\mu\epsilon} \left[\frac{1}{2} \left(\sqrt{1 + \left(\frac{\sigma}{\omega\epsilon\epsilon_0} \right)^2} + 1 \right) \right]^{1/2} \tag{7}$$

$$k_i = \frac{\omega}{c} \sqrt{\mu\epsilon} \left[\frac{1}{2} \left(\sqrt{1 + \left(\frac{\sigma}{\omega\epsilon\epsilon_0} \right)^2} - 1 \right) \right]^{1/2} \tag{8}$$

Since R_p is processed from phase shift it is linked to k_r , while R_a is processed from amplitude decay and is linked to k_i . k_r and k_i which represent LWD measurements, are calculated on $\sigma_p = 1/R_p$ for conductivity in Eq. 7 and $\sigma_a = 1/R_a$ for conductivity in Eq. 8. ϵ is given by Fig. 1 and is further named as ϵ_{LWD} . The final equations are found by inserting $k_r(R_p, \epsilon_{LWD})$ (Eq. 7) and $k_i(R_a, \epsilon_{LWD})$ (Eq. 8) into Eqs. 4 and 5

$$\sigma = \omega\epsilon_0\epsilon_{LWD} \left[(A_p + 1)^{1/2} (A_a - 1)^{1/2} \right] \tag{9}$$

$$\epsilon = \frac{1}{2} \epsilon_{LWD} \left[2 + A_p - A_a \right] \tag{10}$$

where

$$A_p = \sqrt{1 + \left(\frac{1}{\omega R_p \epsilon_0 \epsilon_{LWD}} \right)^2} \tag{11}$$

$$A_a = \sqrt{1 + \left(\frac{1}{\omega R_a \epsilon_0 \epsilon_{LWD}} \right)^2} \tag{12}$$

Equations 9 and 10 are basic analytical equations where the inputs are R_p and R_a , and ϵ_{LWD} . In further applications of Eqs. 9 and 10, σ and ϵ are indexed as σ_k^f and ϵ_k^f . The meaning of index k is that σ and ϵ are calculated with the wavenumber by use of Eq. 9 or Eq. 10. Index f illustrates for which

frequency σ and ϵ are calculated; e.g., ϵ_k^{2MHz} is permittivity calculated by use of Eq. 10 and frequency 2 MHz.

Physical Zones to be Considered

Equations 9 and 10 are based on a plane-wave model (Eq. 6) in an isotropic medium (Eq. 1), and physical zones for where these conditions are fulfilled will be considered.

Eq. 6 is an example on plane wave and will, in practice, be valid where the receiver is at sufficiently large distance from the transmitter and sufficiently large distance from free charges. Equation 1 and following equations are based on electromagnetic properties as scalar and therefore valid only for isotropic media.

Since the E-field behaves differently depending on the distance from the source, the E-field is classified into regions as a fraction of the wavelength, λ . Equation 6 shows that λ is

$$\lambda = \frac{2\pi}{k_r} \tag{13}$$

where k_r is given by Eq. 7. Elementary considerations, such as examination of the E-field of a dipole radiator, show that there are three zones to be considered (Choy, 2016). The near-field static zone, where the TRS is small compared with λ , the transition zone, where TRS $\sim \lambda$ and the radiation zone, where TRS $\gg \lambda$. There is no clear cutoff between these regions; the cutoff will, in practice, depend on the physical size of the antenna (Balanis, 2016). In cases with antenna equal to or shorter than one-half wavelength of the radiation they emit, it is common to classify the physical zones as illustrated in Fig. 2 (Balanis, 2016). This classification is assumed to be a good approximation for LWD frequencies and is further used in this work. This assumption will be discussed at the end of the paper.

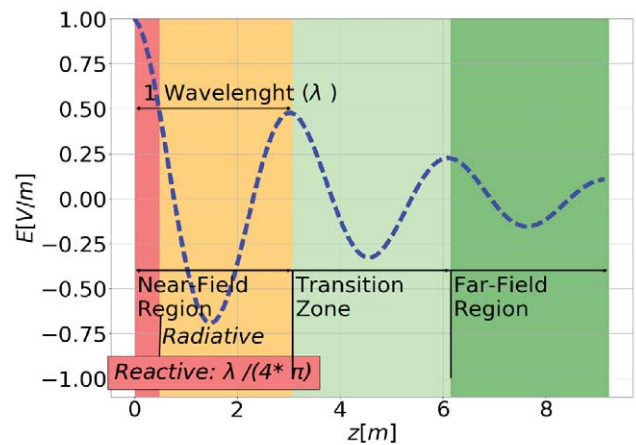


Fig. 2—Physical zones to be considered as fraction of the wavelength.

In the reactive part of near-field zone close to the transmitter, the EM-field is heavily influenced by the transmitter and the plane-wave model shown by Eq. 6 is not valid. It will therefore be a minimum TRS for where a plane-wave approximation is valid. The presented approach is therefore expected to fail with LWD measurements within the reactive part of the near field where $TRS < \lambda/4\pi$. The reactive part of near field is illustrated by red color in Fig. 2 and in subsequent examples.

The radiative part of the near field can be approximated as quasistatic and pertains to low frequency for which the applied EM field varies slowly with time (Choy, 2016). The characteristic feature here is that the wavelength, λ , is large compared with the dimension/volume (TRS) of the rock that is being measured. Equations 9 and 10 are expected to be valid with LWD measurements in the radiative part of the near field where $\lambda/4\pi < TRS < \lambda$. The radiative part of the near field is illustrated by orange color in Fig. 2 and in subsequent examples.

The transition zone is complex since there is no clear cutoff between the near field and the far field. In the transition zone the EM field can behave like the radiative part of the near field, like the far field or something in between. The transition zone is illustrated by light green color in Fig. 2 and in subsequent examples.

In the far-field zone where $\lambda \ll TRS$ the EM radiation will dominate, and the E-field will be more sensitive to absorption and scattering. The far field is illustrated by green color in Fig. 2 and in subsequent examples.

In anisotropic formations, reflection and refraction are expected if the angle of incidence (θ_i) does not exceed the critical angle of total reflection (θ_c) (Chew, 1990; Reitz et al., 1993). The principle is illustrated by Fig. 3. In such situations, the refracted k_r and k_i will have different directions. This is explained by the phase-match principle and Snell's law (Reitz et al., 1993). From the phase-match principle, k_i will always be perpendicular to the conducting surface, while Snell's law states that k_r is refracted by a real refraction angle θ_2 (deduction of the real refraction angle is shown by Reitz et al. (1993).

For LWD measurements in the radiative zones where $\lambda/4\pi < TRS$, Eqs. 9 and 10 are expected to:

- Be valid in isotropic formations
- Be valid if the angle of incidence θ_i is larger than the critical angle for total reflection, θ_c , $\theta_i > \theta_c$
- Fail in anisotropic formation where the angle of incidence θ_i is less than the critical angle for total reflection, θ_c , $\theta_i < \theta_c$
- Fail when the E-field cross into a new formation with large electrical contrast.

Note that θ_c is given by the contrast in electromagnetic properties and can be quite large.

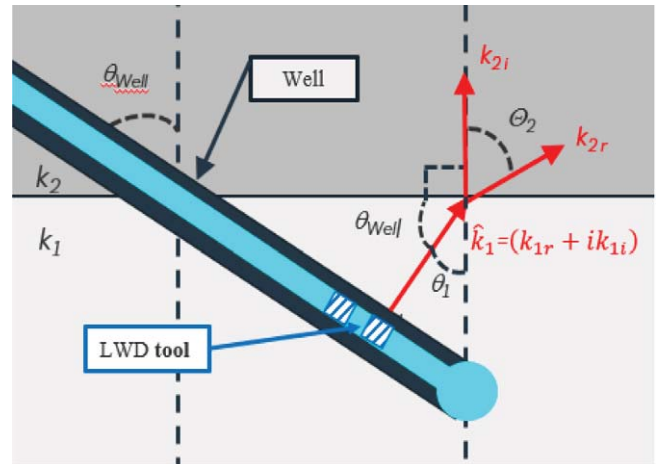


Fig. 3—Refraction of the wavenumber (\hat{k}_1) when the angle of incidence, θ_i , is less than the critical angle for total reflection, θ_c .

WATER SATURATION CALCULATION AND USE OF THE CRIM

The complex refraction index model (CRIM) is the weighted sum of the wavenumber to the elements in the formation, Eq. 14,

$$\hat{k} = \hat{k}_w \phi S_w + \hat{k}_m (1 - \phi) + \hat{k}_{hc} \phi (1 - S_w), \quad (14)$$

and is used to calculate the amount of water (S_w) in formations. ϕ is porosity and subscripts w , m and hc are water, matrix, and hydrocarbon, respectively. It is the high-frequency approximation of the CRIM that is commonly used when calculating S_w (Seleznev et al., 2006; Hizem et al., 2008). With the high-frequency approximation, the wavenumbers in Eq. 14 are replaced by permittivity.

The CRIM does not account for interfacial polarization and is therefore, in principle, not valid at LWD frequencies. Interfacial polarization is also known as the Maxwell-Wagner polarization and is related to the presence of charges that is concentrated at the surface of the rock when an electrical field is applied. Interfacial polarization is one of three main physical phenomena contributing to permittivity and is well described by Hizem et al. (2008). The effect of interfacial polarization disappears at frequencies exceeding 10^8 Hz (Seleznev et al., 2006). Since the LWD frequencies are far below 10^8 Hz the interfacial polarization will contribute to electrical permittivity, and thus affect the wavenumber (Eq. 1). This is also mentioned by Seleznev et al. (2006) who presented a model that accounts for interfacial polarization. They applied the Maxwell-Garnett approximation and the

high-frequency approximation of the CRIM using only permittivity.

The above discussion illustrates that the CRIM can be used even at LWD frequencies by applying the imaginary part of the wavenumber, assuming the contribution of interfacial polarization can be added to Eq. 14 as a new element. The new element is the wavenumber associated with interfacial polarization, k_p , weighted by V_p . V_p is volume water associated with interfacial polarization at the surface of the mineral grains. The proposed modified CRIM is

$$\hat{k} = \hat{k}_w \phi S_w + \hat{k}_m (1 - \phi) + \hat{k}_{hc} \phi (1 - S_w) + \hat{k}_p V_p \quad (15)$$

Subscript p is interfacial polarization.

Equation 15 is then split into its real part and its imaginary part

$$k_r = k_{wr} \phi S_w + k_{mr} (1 - \phi) + k_{hcr} \phi (1 - S_w) + k_{pr} V_p \quad (16)$$

$$k_i = k_{wi} \phi S_w + k_{mi} (1 - \phi) + k_{hci} \phi (1 - S_w) + k_{pi} V_p \quad (17)$$

Since the conductivity of mineral grains and the hydrocarbon is zero, the values of k_{mi} and k_{hci} are zero (Eq. 8). k_{pr} and k_{pi} can be calculated by use of Eqs. 7 and 8 if the electrical properties associated with interfacial polarization (ϵ_p , σ_p) are known. It is commonly accepted that ϵ_p is large (Hizem et al., 2008) as compared to σ_p . σ_p is assumed to be small since the charges concentrated at the surface of the rock are not free to move. With large value on ϵ_p and low value on σ_p , the part $\sigma_p / (\omega \cdot \epsilon_p \cdot \epsilon_o)$ in Eqs. 7 and 8 is expected to be very small and k_{pr} and k_{pi} can be approximated as:

$$k_{pr} \approx \omega \sqrt{\mu_p \epsilon_p} \quad (18)$$

$$k_{pi} \approx 0 \quad (19)$$

Inserting Eq. 19, $k_{mi} = k_{hci} = 0$ into Eq. 17, and solving for S_w gives

$$S_w = \frac{k_i}{k_{wi} \phi}, \quad (20)$$

where k_i (Eq. 8) is calculated by R_a and ϵ_{LWD} , and ϕ can be calculated by use of a porosity log. The value of k_{wi} can be calculated by Eq. 8 if the electrical properties to the formation water (σ_w , ϵ_w) are known, by in-situ calibration in a zone where the pore space is 100% filled with water, ($k_{wi} = k_i / \phi$), or extract it from the dispersion $k_r(f)$ and $k_i(f)$.

TEST OF PRESENTED THEORY

The presented theory was tested by use of LWD resistivity data generated in synthetic models and by LWD resistivity data acquired in wells. The results are illustrated through the five examples below where the purpose is to show that:

- Example 1: ϵ_k^f (Eq. 10) and R_k^f (Eq. 9) calculated from LWD resistivity data that are generated from synthetic models, fit the models.
- Example 2: ϵ_k^f (Eq. 10) calculated from LWD resistivity data acquired in vertical wells fit wireline permittivity measurements.
- Example 3: k_r (Eq. 7) and ϵ_k^f (Eq. 10) exhibit low values in deviated wells and can be corrected by Snell's law.
- Example 4: R_k^f (Eq. 9) calculated from LWD resistivity data can be used as formation resistivity when LWD resistivity is largely influenced by dielectric effect.
- Example 5: water saturation calculated by Eq. 20 matches results given by conventional methods.

Example 1—Test of ϵ_k^f and R_k^f on Synthetic Models

The purpose with this example is to show that ϵ_k^f (Eq. 10) and R_k^f (Eq. 9) calculated from LWD resistivity data that are generated from synthetic models, match with the theoretical models. The synthetic models are shown in Fig. 4 and the results are shown in Fig. 5. Figure 5 shows the models and the LWD resistivity responses, as calculated by the models, ϵ_k^f and R_k^f . The LWD resistivity responses to the models are generated by applying the University of Texas at Austin, 3D UTAPWeLS software (1-D UT code and EcoScope).

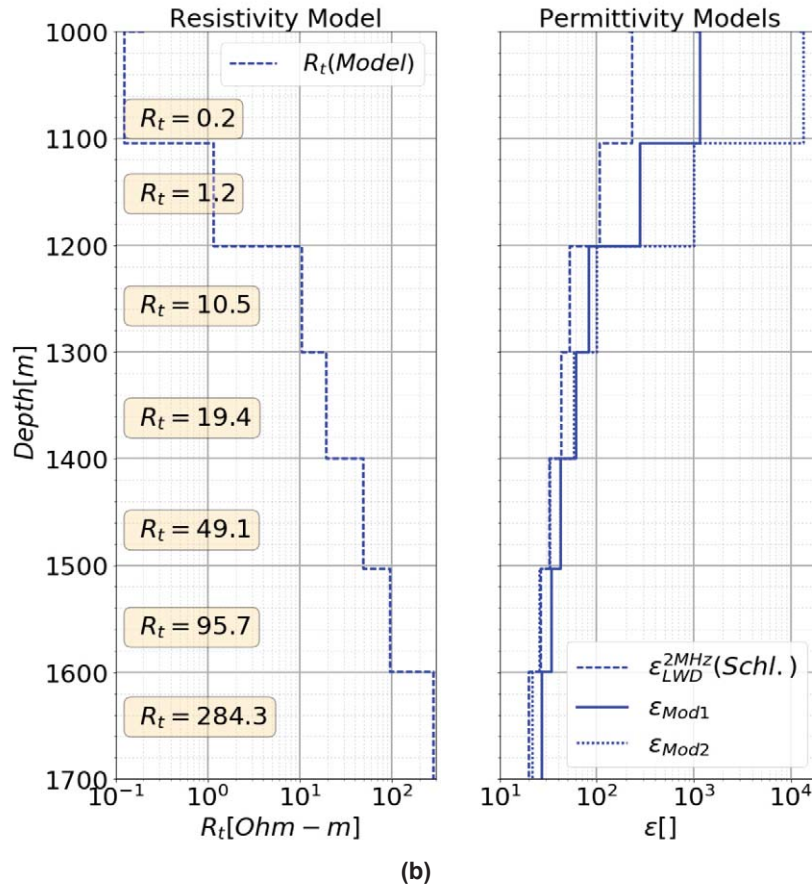
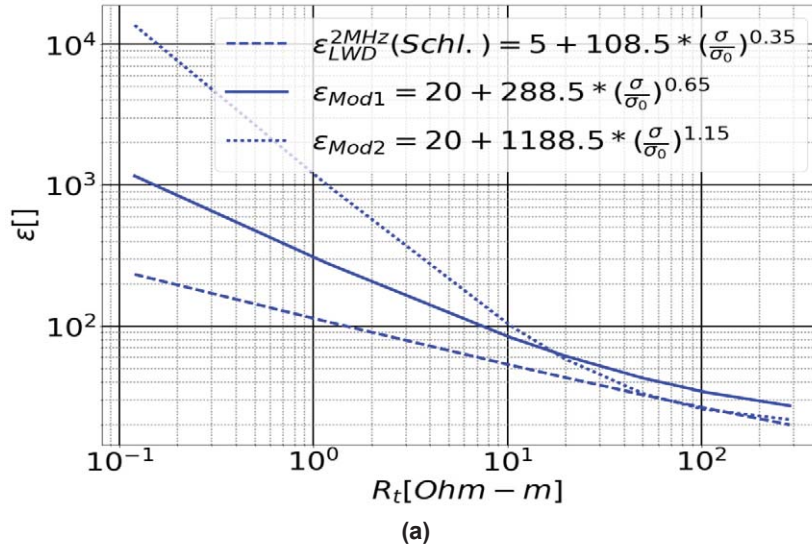


Fig. 4—(a) The dielectric models tested. (b) Synthetic resistivity and permittivity models that are used to generate LWD resistivity responses.

Figure 5 illustrates the following points

- ϵ_k^f and R_k^f match the resistivity and permittivity models at depths less than 1,400 m.
- At depths 1,400 to 1,500 m where $R_t = 49 \Omega\text{-m}$, ϵ_k^f and R_k^f start to deviate from the models.
- At depths > 1500 m where $R_t > 95 \Omega\text{-m}$, the LWD amplitude resistivity (A40H) is unreliable. (A40H is 20,000 $\Omega\text{-m}$ in the interval 1,500 to 1,600 m and shows too low value in the interval 1,600 to 1,700 m.)

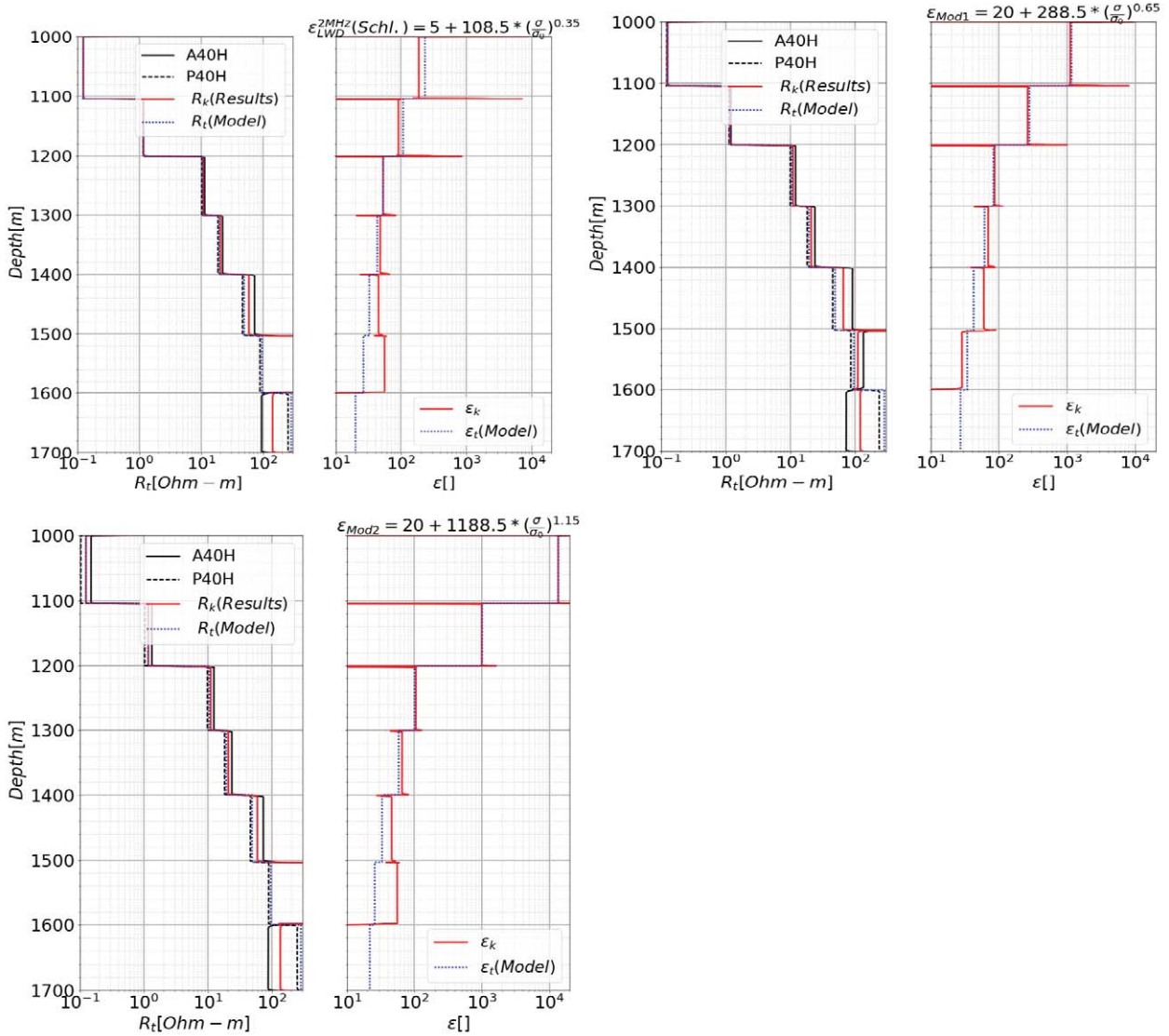


Fig. 5— ϵ_k^f (Eq. 10) and R_k^f (Eq. 9) calculated on LWD resistivity responses generated on synthetic models. (A40H= R_a^{2MHz} , P40H= R_p^{2MHz} . In the interval 1,500 to 1,600 m, A40H is 20,000 Ω -m).

Example 2—Comparing ϵ_k^f With ϵ_{ADT}^f

The purpose with this example is to show that LWD permittivity and its dispersion fit well with permittivity data from commercial wireline tools. To illustrate that the presented method returns reasonable values independent of LWD vendor, examples using both Halliburton and Schlumberger LWD resistivity tools are presented. To minimize the impact of anisotropy and refraction, the examples are in vertical wells. Both wells are drilled with oil-based mud.

The formation presented in Fig. 6 is a shale above a heterolithic hydrocarbon-filled reservoir. The shale resistivity is approximately 2 Ω -m and the reservoir resistivity ranges from 2 to 10 Ω -m. The LWD data were acquired by a Halliburton tool that operates at three frequencies 125 kHz, 500 kHz and 2 MHz. The wireline data were acquired by Schlumberger’s ADT tool. This tool operates at four frequencies 20 MHz, 80 MHz, 400 MHz, and 1 GHz. ϵ_{LWD} is taken from Fig. 1 and is equal to 10 for all frequencies. σ_k^f is calculated using Eq. 9 and ϵ_k^f is calculated using Eq. 10.

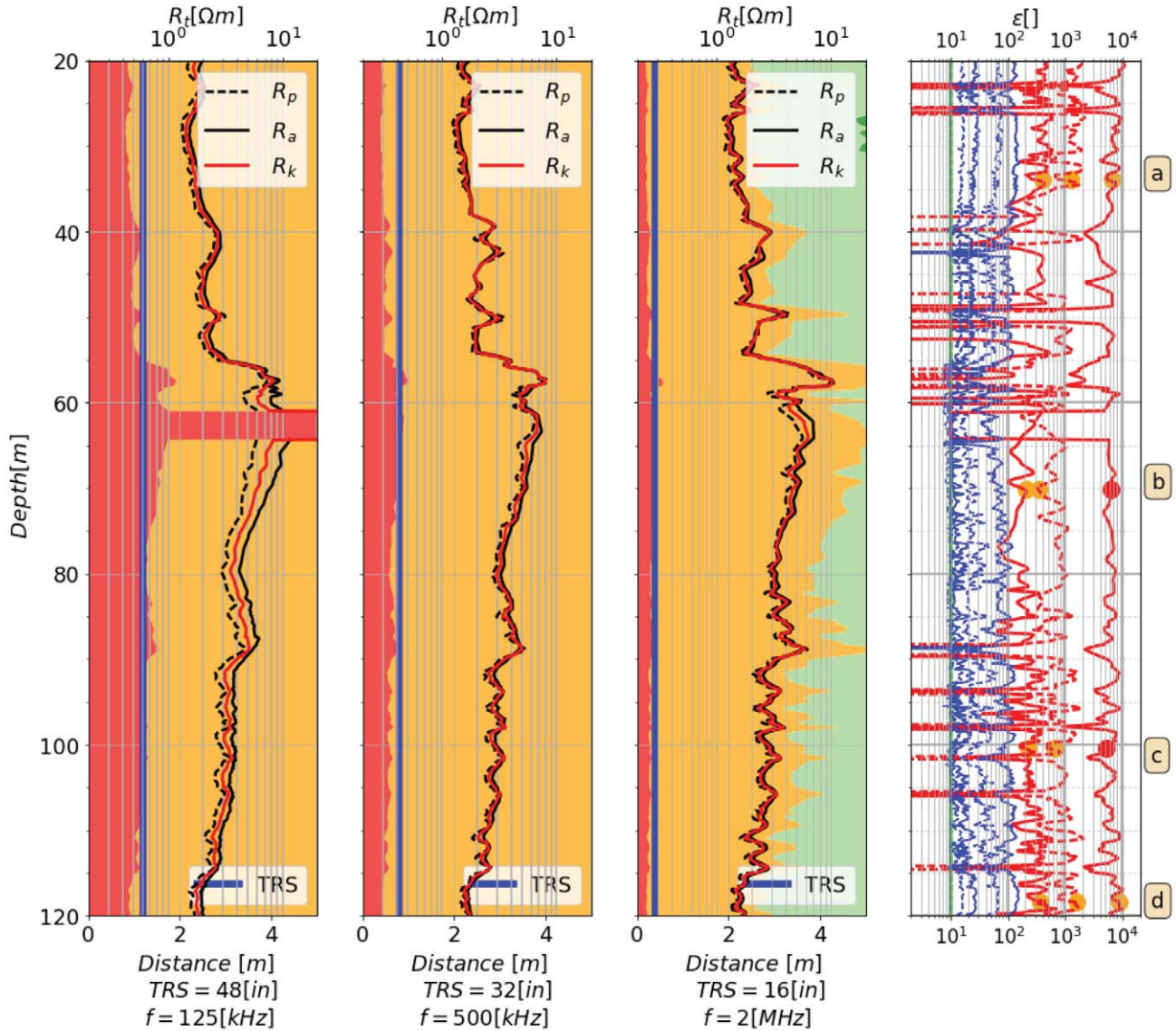


Fig. 6a— ϵ_k^f (Eq. 10) and R_k^f (Eq. 9) calculated for LWD resistivity data acquired by Halliburton in a vertical well. Tracks 1, 2 and 3 show the physical zones, TRS and the resistivities. Track 4 shows ϵ_k^f (red curves), ϵ_{ADT}^f (blue curves) and ϵ_{LWD} (green curves). The color-filled circles show sample intervals that are presented in Fig. 6b.

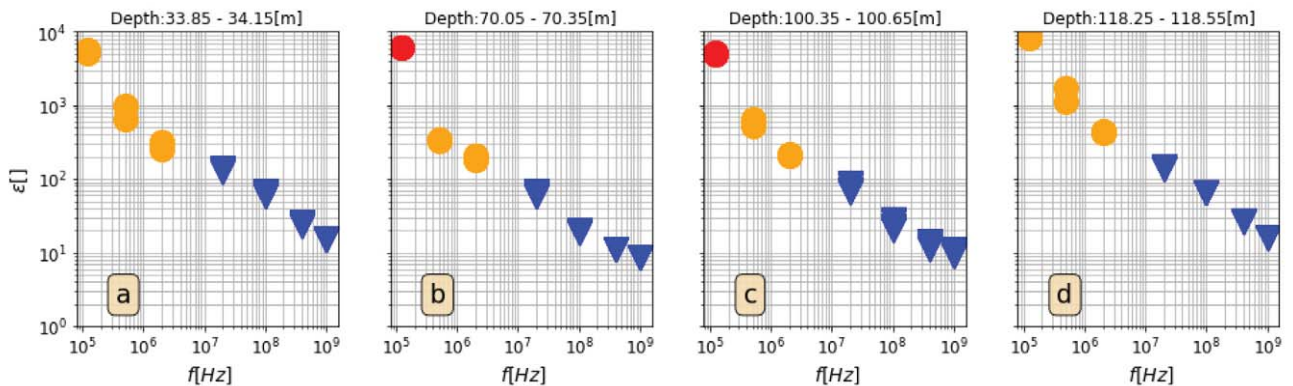


Fig. 6b—Electrical permittivity measured by Schlumberger’s wireline tool (blue triangles) and permittivity extracted from LWD resistivity measurements (color-filled circles) at the sample points a, b, c, and d shown in Fig. 6a.

Figure 6a shows resistivity, physical zones to be considered (as defined by Fig. 2) and electrical permittivity. Tracks 1, 2 and 3 illustrate the same layout but for different frequencies. The black curve is LWD R_a , the black dotted curve is LWD R_p and the red curve is the resistivity ($1/\sigma$) calculated by use of Eq. 9. The resistivity is presented on a log scale from 0.2 to 20 Ω -m. The lower x-axis shows the distance from the transmitter at scale 0 to 5 m, where the blue line is TRS and the background colors are the physical zones as classified in Fig. 2. The boundary between orange and light green zone shows one λ (only seen in Track 3). Figure 6a shows mainly orange color behind the TRS, which means the LWD measurements are mainly in the radiative part of the near field. Track 4 shows electrical permittivity presented on a log scale from 2 to 20,000. The red curves are ϵ_k^f and the blue curves are ϵ_{ADT}^f . The green curve shows ϵ_{LWD}^f . The curve at far left is permittivity at highest frequency, ϵ_{ADT}^{1GHz} , while the curve at far right is permittivity at lowest frequency, ϵ_k^{125kHz} . The color-filled circles mark the depth of the intervals that are used and presented in Fig. 6b.

Figure 6b presents permittivity from LWD and wireline measurements for the sample points illustrated in Fig. 6a. The color code indicates the physical zone of the measurements. The length of each sample interval is 0.3 m and incorporates two LWD data points and five to six wireline data points.

Figures 6a and 6b illustrate the following points

- The LWD measurements are mainly acquired at the border between the reactive (red zone) and radiative part (orange zone) of the near-field zone.
- ϵ_k^f show continuous curves for all three frequencies except for a few small intervals where ϵ_k^f is negative.
- The intervals where ϵ_k^f is negative occur where resistivity and wireline permittivity show large electrical contrast.
- The measurements at lowest frequency, ϵ_k^{125kHz} (red curve at far right in Track 4), are less influenced by electrical contrasts when it is compared with ϵ_k^{400kHz} and ϵ_k^{2MHz} .
- The broadband dispersion plots (Fig. 6b) show that the level of ϵ_k^f fits well with ϵ_{ADT}^f dispersion for measurements in the radiative part of the near field (orange zone).
- The permittivity values that are measured in the reactive part of the near field (red zone) seem to be slightly high when compared with the dispersion trend given by the other measurements.

The formation presented in Fig. 7 is a shale above a homogeneous hydrocarbon-filled reservoir, with a water zone at the base. The shale resistivity is approximately 2 Ω -m, the hydrocarbon-filled reservoir resistivity ranges from 100 to 200 Ω -m and the water-filled formation resistivity is approximately 1 Ω -m. The LWD data were acquired by a Schlumberger tool that operates at the frequencies 400 kHz and 2 MHz. ϵ_{LWD} is taken from Anderson et al. (2007).

Figure 7 has the same layout as Fig. 6. The conductivity scale σ_0 is equal to 1. σ_k^f is given by Eq. 9 and ϵ_k^f is given by Eq. 10. The plotted log-scale resistivity is from 0.1 to 1,000 Ω -m, TRS is 40 in. and permittivity is plotted logarithmically, 2 to 5,000. The green dotted line is ϵ_{LWD}^{2MHz} (Eq. 21) and solid green line is ϵ_{LWD}^{400kHz} (Eq. 22):

$$\epsilon_{LWD}^{2MHz} = 5 + 108.5 \left(\frac{\sigma}{\sigma_0} \right)^{0.35} \quad (21)$$

$$\epsilon_{LWD}^{400kHz} = 5 + 280 \left(\frac{\sigma}{\sigma_0} \right)^{0.46} \quad (22)$$

Figure 7 illustrates the following points

- The LWD measurements are acquired in the reactive near field (red zone) and in the radiative part of the near-field zone (orange zone).
- R_a^{400kHz} (the black curve in Track 1) fails in the reactive part of the near field and the calculated value ϵ_k^f is not correct. (P1 in Fig. 7b).
- For LWD measurements in the reactive part of the near field (red zone), ϵ_k^f is a continuous curve but with a too large value when compared to the dispersion trend (P2 and P3 in Fig. 7b).
- ϵ_k^f fluctuates between negatives and positives values for LWD measurements in the radiative-field zone (orange zone), and ϵ_k^f shows reasonable values when positive. The negative values occur where LWD resistivity and wireline permittivity show large electrical contrast.
- The broadband dispersion plots (Fig. 7b) show that the level of ϵ_k^f dispersion matches well with ϵ_{ADT}^f dispersion in the radiative zone (orange zone). Note that the point P4 is measured very close to the radiative zone and should therefore represent a reliable value.

Example 3— ϵ_k^f in Deviated Well

The purpose of this example is to show that the values of k_p , and thus the calculated ϵ_k^f (Eq. 5) values, are too low in deviated wells, and that they can be corrected by use of Snell's law.

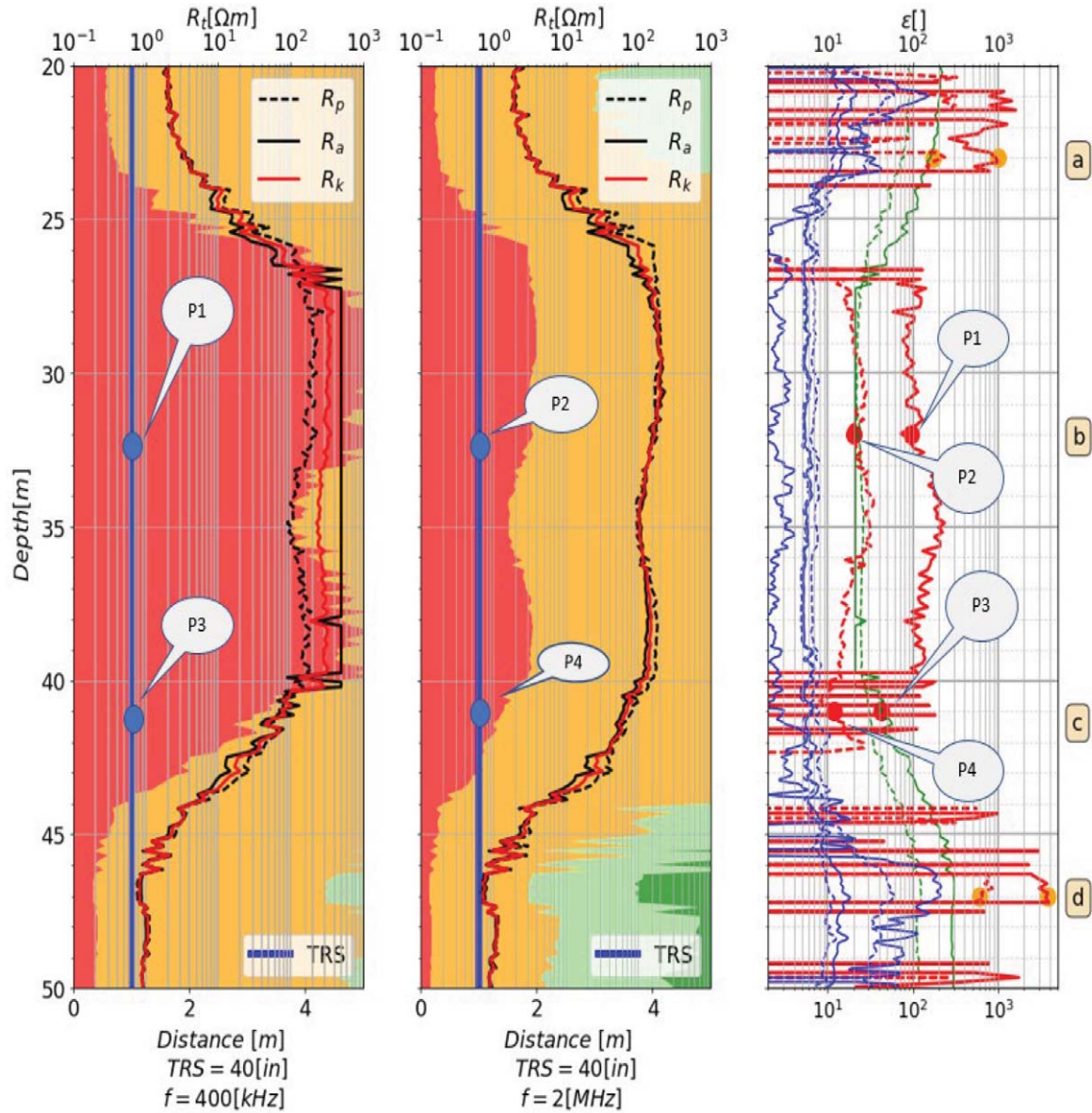


Fig. 7a— ϵ_k^f (Eq. 10) and R_k^f (Eq. 9) calculated on LWD resistivity data acquired by Schlumberger in a vertical well. Tracks 1 and 2 show the physical zones, TRS and the resistivities. Track 3 shows ϵ_k^f (red curves), ϵ_{ADT}^f (blue curves) and ϵ_{LWD} (green curves). The color-filled circles show sample intervals that are presented in Fig. 7b.

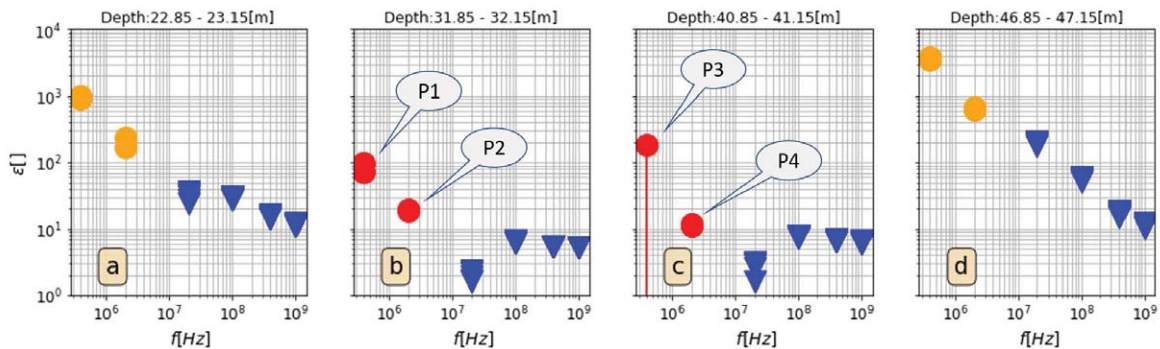


Fig. 7b—Electrical permittivity measured by Schlumberger’s wireline tool (blue triangles) and permittivity extracted from LWD resistivity measurements (color-filled circles) at the sample points a, b, c and d shown in Fig. 7a.

The well presented in Fig. 8 penetrates a heterolithic hydrocarbon-filled reservoir with a shale above and below. The shale resistivity is approximately 0.6 Ω-m and the reservoir resistivity ranges from 5 to 10 Ω-m. The well was drilled with oil-based mud and with an inclination of 30°. The LWD resistivity was acquired by a Schlumberger tool and ϵ_{LWD} is given by Eqs. 21 and 22.

Figure 8 has the same layout as Fig. 6, but with two tracks showing permittivity. The first permittivity track shows LWD permittivity calculated without any correction for refraction. The second permittivity track shows LWD permittivity that is corrected for refraction by applying Snell's law on k_r (Fig. 3). Details about how to correct for refraction are not covered in this paper. The resistivity is plotted on a log scale from 0.2 to 20 Ω-m and permittivity on a log scale from 2 to 20,000.

Figure 8 illustrates the following points

- Several intervals with negative values appear when ϵ_k^f is not corrected for refraction. In the intervals where ϵ_k^f is positive, the permittivity values are too low when compared to ϵ_{ADT}^f . The latter is illustrated by stars in Fig. 8b.
- Fewer intervals with negative values appear when ϵ_k^f is corrected for refraction and the permittivity values fit well with ϵ_{ADT}^f measurements. The latter is illustrated by color-filled circles in Fig. 8b.

Example 4 – R_k^f as true formation resistivity

The purpose with this example is to show that R_k^f (Eq. 9) calculated on LWD resistivity data can be used as formation resistivity when LWD resistivity is influenced by the dielectric effect.

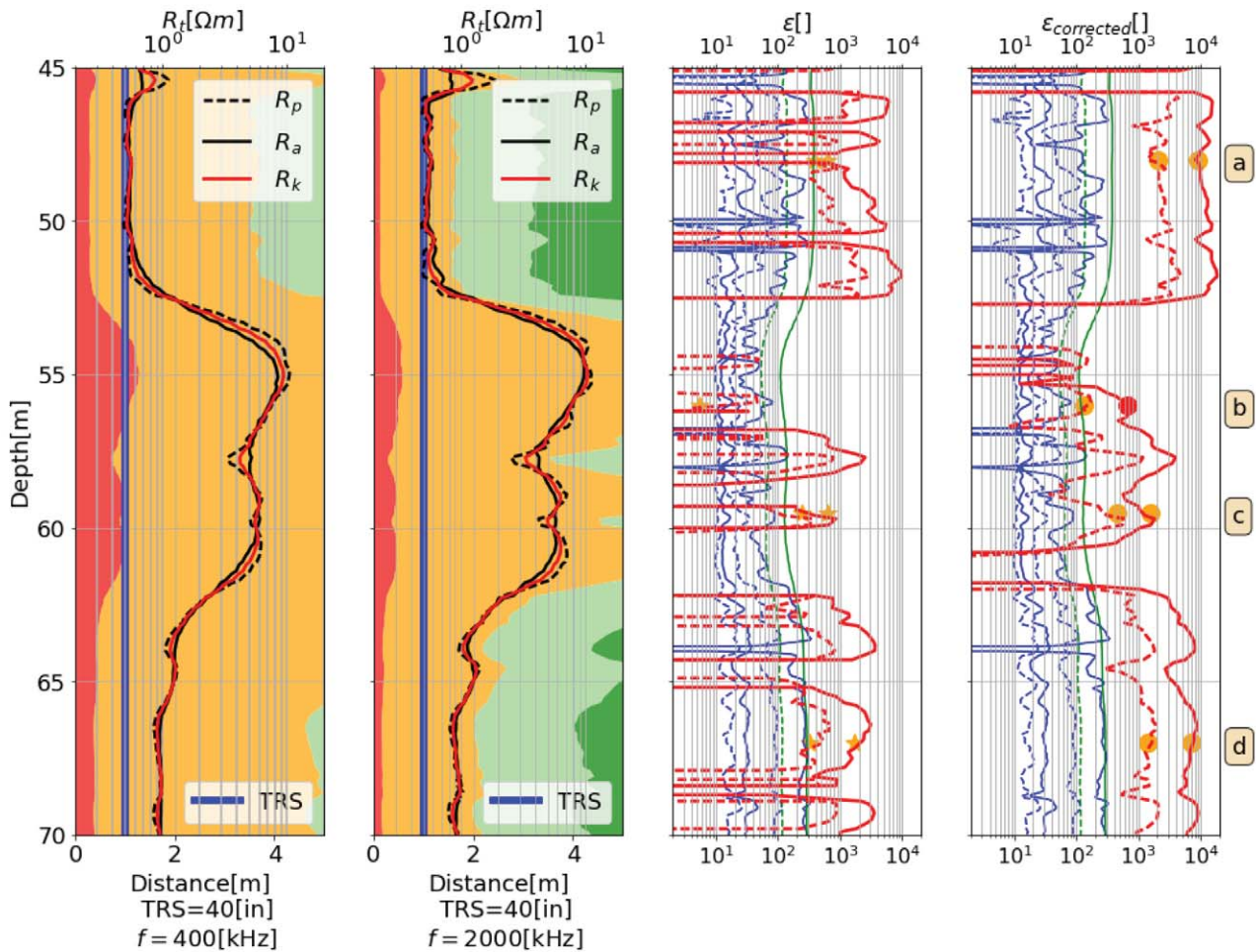


Fig. 8a— ϵ_k^f (Eq. 10) and R_k^f (Eq. 9) calculated on LWD resistivity data acquired by Schlumberger in a 30° deviated well. Tracks 1 and 2 show the physical zones, TRS and the resistivities. Tracks 3 and 4 show ϵ_k^f (red curves), ϵ_{ADT}^f (blue curves) and ϵ_{LWD} (green curves). In track 3, ϵ_k^f is not corrected for refraction while ϵ_k^f in track 4 is corrected for refraction. The color-filled circles show sample intervals that are presented by Fig. 8b.

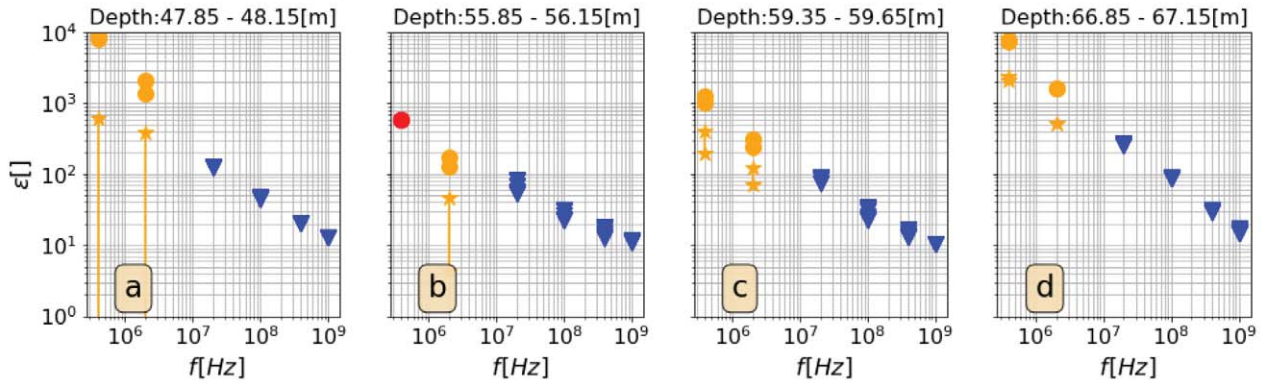


Fig. 8b—Electrical permittivity measured by Schlumberger’s wireline tool (blue triangles) and permittivity extracted from LWD resistivity measurements (color-filled circles and stars) at the sample points a, b, c and d shown by Figure 8a. The color-filled circles and stars are permittivity corrected and not corrected for refraction, respectively.

Figure 9 shows LWD and wireline resistivity data acquired by Schlumberger, calculated ϵ_k^f (Eq. 10) and R_k^f (Eq. 9). The well was drilled with oil-based mud through a clastic formation. The goal was to find formation resistivity from the large spread in LWD resistivity responses illustrated in Track 1.

Only the 2-MHz LWD resistivity curves were used since the 400-kHz amplitude data were not reliable (they were clipped when they exceeded approximately 50 Ω -m).

Figure 9 illustrates the following points

- The large range in LWD resistivity responses.
- LWD amplitude resistivities have higher values when compared to phase resistivities.
- LWD amplitude resistivities show a large range in values. Measurements with short TRS show higher values when compared with longer TRS.
- At 200 Ω -m, the amplitude resistivity curves are being “clipped”.
- LWD phase resistivities show small range.
- R_k^f (Eq. 9) fits very well with resistivity from wireline (R_l) (the red and blue curves in Track 2).
- ϵ_k^f (Eq. 10) shows far higher values compared to ϵ_{LWD} (the red and green curves in Track 3).

Example 5—Water Saturation Calculated Using k_i

The purpose of this example is to demonstrate that water saturation calculated by Eq. 20, $S_w(k_i)$, matches with water saturation calculated by conventional methods, namely, Archie’s equation, $S_w(\text{Archie})$, water saturation delivered by Schlumberger wireline services, $S_w(\text{ADT})$, and water saturation calculated by use of nuclear magnetic resonance (NMR), $S_w(\text{NMR})$. $S_w(\text{NMR})$ is the relation between bound fluid to the total porosity (BFV/TCMR). $S_w(k_i)$ is given by

Eq. 20, where k_i is shown in Track 2 (Eq. 8) and density-derived porosity is shown in Track 4. k_{wi} is 12.5 and found by calibration. k_{wi} is the subject for a future paper and will not be further discussed.

Application of Eq. 20 on the wells presented in Figs. 6 and 7 is shown in Figs. 10 and 11. Track 1 is the 2-MHz phase and amplitude resistivity. Track 2 is the wavenumber calculated by Eqs. 7 and 8. Track 3 shows calculated water saturations and Track 4 shows porosity obtained from different sources.

SUMMARY

Based on classic electromagnetic theory, this paper demonstrates how electrical permittivity and its dispersion can be extracted from LWD resistivities R_p and R_a . The approach given in Eqs. 9 and 10 is valid for plane waves in isotropic formations. An explanation for using plane waves and isotropic approximation is explained by Maxwell’s equations of electrodynamics presented in Appendix 1.

To identify where a plane wave and an isotropic formation approximation can be considered, the LWD resistivity measurements are classified into regions as a fraction of the wavelength, λ . This is due the fact that the E-field behaves differently depending on distance from the source. The different physical zones for the E-field are classified in Fig. 2 and are a good approximation for LWD resistivity measurements in reservoir formations. This classification assumes that the LWD antenna is equal to or shorter than one-half the wavelength of the emitted radiation. For these examples the shortest wavelength was 2.2 m and was expected to be far larger than the dimension of the LWD antenna.

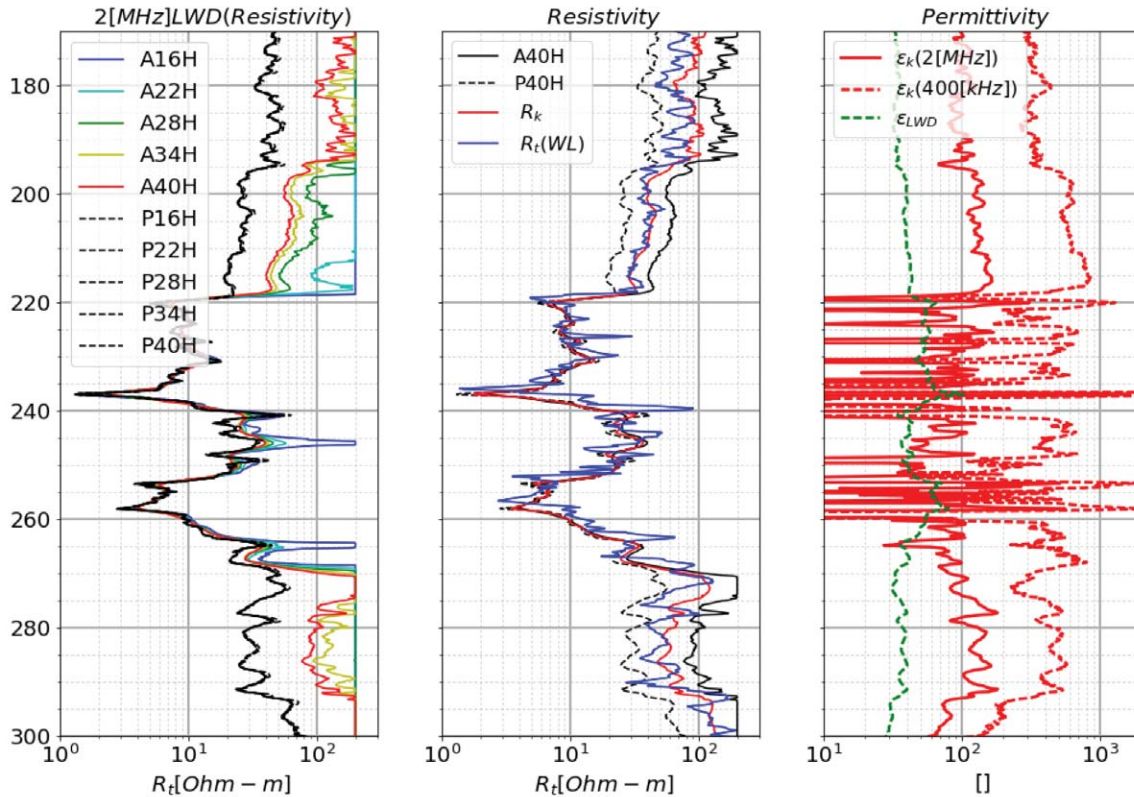


Fig. 9— ε'_k (Eq. 10), R_k^f (Eq. 9), LWD and wireline resistivity. All data were acquired by Schlumberger. Track 1 shows 2-MHz LWD resistivity curves. (Curve mnemonics: A = amplitude, P = phase, H = 2 MHz, and the numbers are TRS (inches). Track 2 shows LWD resistivity curves A40H = $R_a^{2[\text{MHz}]}$ and P40H = $R_p^{2[\text{MHz}]}$, R_k^f (Eq. 9), and R_t acquired by wireline. The last track shows ε'_k (Eq. 10) and ε_{LWD} (Eq. 21).

For the physical zones shown in Fig. 2, it was assumed that a plane wave and an isotropic approximation were met by LWD measurements where $\lambda/4\pi < \text{TRS} < \lambda$. This is the radiative part of the near-field zone for which Eqs. 9 and 10 are expected to validate. A plane-wave approximation is met where the E-field is not influenced by any sources that generate the field. The E-field sources are antennas and free charges (internal sources). With $\lambda/4\pi < \text{TRS}$, the receiver is expected to be at a sufficient distance from the transmitter such that the E-field is not influenced by the antenna. Where the wavelength of the E-field is large compared to the dimension of the rock sample given by TRS ($\text{TRS} < \lambda$), the measurements are expected to approach the quasistatic zone of the E-field. Within this zone, the E-field can be approximated to be static and the impact of internal sources can be neglected since $\nabla \cdot E = 0$ (Kong, 2000; Choy, 2016). A plane-wave solution is therefore expected to be met where $\lambda/4\pi < \text{TRS} < \lambda$. A solution will also be met for $\lambda < \text{TRS}$ if there are no internal sources. Isotropic approximation is met where the electromagnetic properties can be treated as scalars. This is most likely fulfilled in zones where the wavelength becomes large compared to the dimension of the sample given by TRS ($\text{TRS} < \lambda$) since the E-field will

be dominated by diffusion and less sensitive for scattering. This explanation supports the results presented by Stroud et al. (1986): “If the wavelength and attenuation scale lengths of the applied electric field are much greater than the dimensions of largest grains and pores in the composite, the scattering of electromagnetic radiation is negligible.”

If $\text{TRS} < \lambda/4\pi$, the LWD resistivity measurements are expected to be influenced by the transmitter, and so a plane-wave model (Eq. 6) is not valid. For this reactive part of the near field, Eqs. 9 and 10 are expected to fail. To extract both ε and σ from this zone, a full solution of Eq. A1.1 is required (see Appendix 1).

In cases where $\lambda/4\pi < \text{TRS}$, the measurements will approach the radiative part of the field and become sensitive for absorption and scattering. As the wavelength becomes small compared to the dimensions of the sample given by TRS, the E-field will be more wave-dominated and sensitive to anisotropy and electrical contrasts. Classical electromagnetic theory has shown that if the angle of incidence is less than the critical angle of total reflection, k_r and k_i will be refracted if there are electrical contrasts in the media. Due to the phase-match principle and Snell’s law (Reitz et al., 1993), k_r and k_i will be refracted in different

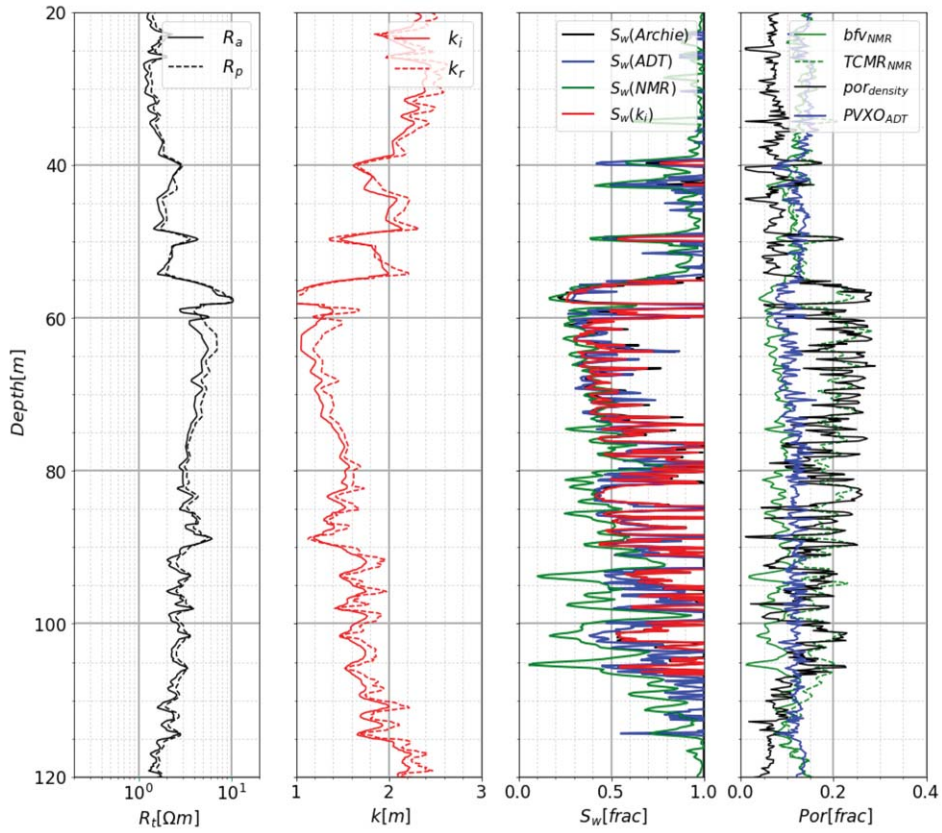


Fig. 10—Water saturation calculated by Eq. 20 compared with conventional methods in the well presented in Fig. 6 (TRS = 48 in.).

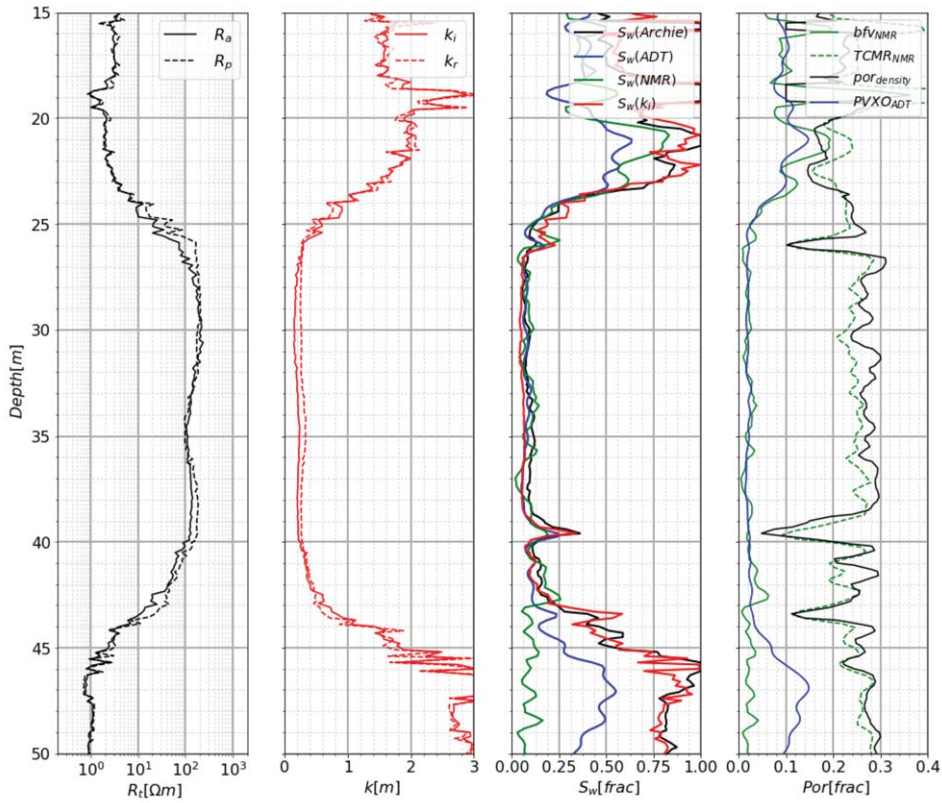


Fig. 11—Water saturation calculated by Eq. 20 compared with conventional methods in the well presented in Fig. 7 (TRS = 40 in.).

directions and, hence, k_r and k_i will sense different electrical properties (Fig. 3). k_i will be perpendicular to the layers with electrical contrast while k_r is refracted by a real refraction angle θ . In such cases, Eqs. 9 and 10 will not be valid. k_i can be larger than k_r and then will ϵ_k^f be negative (Eq. 5). If the formation is isotropic such that there are no electrical contrasts to refract the wave, or if the angle of incidence is larger than the critical angle of total reflection, k_r and k_i will have the same direction and sense the same electrical properties. In such cases k_r will always be larger than k_i (Eqs. 7 and 8) and Eqs. 9 and 10 will be valid.

This explanation supports the results presented by Rabinovich and Liu (2015), who performed a modeling study on sensitivity of dielectric tool responses to dielectric anisotropy. Two homogeneous formation models were studied. One isotropic formation with $\epsilon_v = 8$ and one anisotropic formation with $\epsilon_v = 5$, $R_t = 5 \Omega\text{-m}$ and $\epsilon_h = 8$ in both formations. Rabinovich and Liu (2015) applied TRS of 3.1 and 4.7 in. in their modeling study. One of their conclusions was "... Dielectric tool responses have nearly no sensitivity to σ_v and ϵ_v , when the tool trajectory is perpendicular to the bed boundary or when the relative dip is low." Index v is vertical, and h is horizontal. Rabinovich and Liu (2015) conclude that anisotropy only is observed above a certain frequency level (below a certain wavelength, see Eqs. 7 and 13). This agrees with the results presented in this paper of how sensitivity for anisotropy occurs first in the radiative part of the field for which $\lambda/4\pi < \text{TRS}$.

Figure 12 shows one of the results presented by Rabinovich and Liu (2015) compared to the results from this paper. The upper part of Fig. 12 shows the phase difference in isotropic and dielectric anisotropic formation modeled by Rabinovich and Liu (2015). The figure shows that the sensitivity to anisotropy begins slightly at 20 MHz. The lower part of Fig. 12 shows $\lambda/4\pi$ (calculated by Eqs. 7 and 13) as a function of frequency using the same data as Rabinovich and Liu (2015). The two black lines show TRS used in the modeling study by Rabinovich and Liu (2015). Where TRS exceeds $\lambda/4\pi$, the measurements are approaching the radiative part of the E-field and thus begin to be sensitive for anisotropy. Figure 12 shows that the 4.7-in. transmitter exceeds $\lambda/4\pi$ and approaches the radiative zone for $f \approx 20$ MHz, and at $f \approx 40$ MHz for the 3.1-in. transmitter. This is at the same level as shown by Rabinovich and Liu (2015).

In the presented examples, applications of the described theory on LWD resistivity data generated on synthetic models and acquired in wells were demonstrated. The examples show that dispersive permittivity can, under given conditions, be extracted from LWD resistivity measurements without advanced inversion techniques.

The electrical permittivity ϵ_k^f was calculated by Eq.

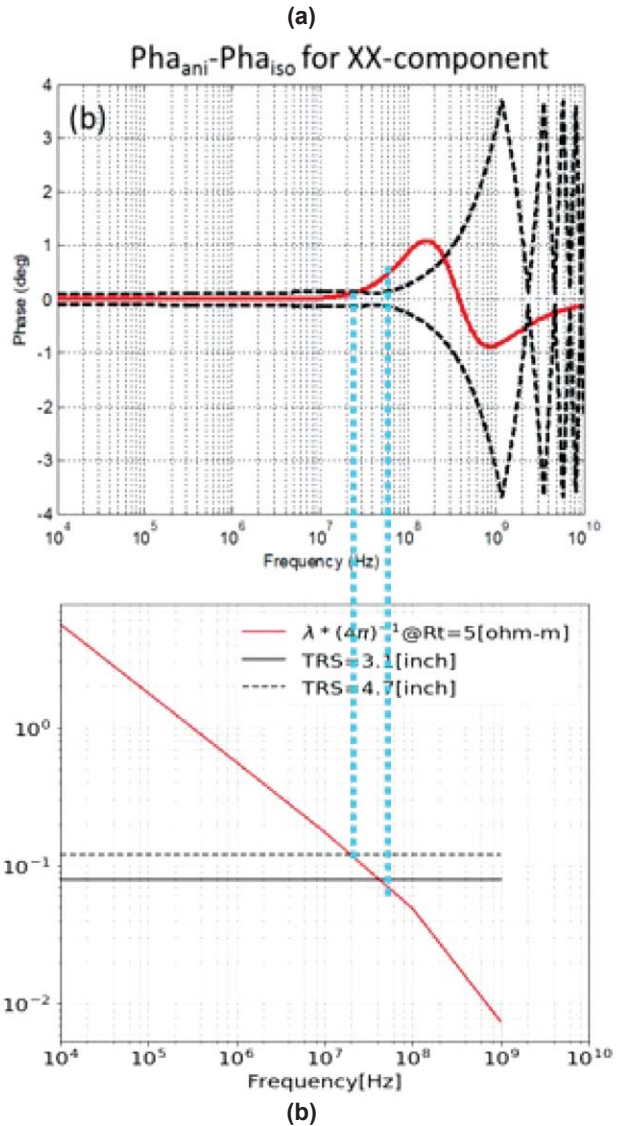


Fig. 12—(a) Results presented by Rabinovich and Liu (2015). Change of phase difference between isotropic and dielectric anisotropic formation responds (red curve) as a function of frequency. The black curve is the noise level used in the experiments. (b) $\lambda/4\pi$ calculated by Eqs. 7 and 13 (red curve) and TRS (black lines) as function of frequency.

10 and physical zones for the LWD measurements were classified as a fraction of the wavelength (see Fig. 2). The wavelength was calculated by Eqs. 7 and 13. The following criteria were used as a quality check (QC) when ϵ_k^f was compared with ϵ_{ADT}^f

- Only LWD resistivity data acquired in intervals where Eq. 10 is valid were used to test the presented theory where $\lambda/4\pi < \text{TRS} < \lambda$.
- The log signature of ϵ_k^f should, within expected log resolution, fit with the signature of ϵ_{ADT}^f
- The level of ϵ_k^f should match the wireline permittivity

- dispersion, ε_{ADT}^f .
- the data points incorporated in the 0.3-m sample intervals shown in Figs. 6b, 7b and 8b, should show minor spread.

In Example 1, ε_k^f and R_k^f were calculated on LWD resistivity data generated in three synthetic models. Figure 5 shows that ε_k^f and R_k^f agree well with the resistivity and permittivity models for resistivities $< 49 \Omega\text{-m}$. For resistivities $> 49 \Omega\text{-m}$ there was some mismatch between ε_k^f , R_k^f and the electrical properties to the models. This is believed to be caused by inaccurate values of the generated amplitude resistivity (A40H). It is well known that the accuracy of R_p and R_a will decrease with increased formation resistivity and/or permittivity. R_a is more sensitive to changes in the electrical properties compared with R_p . These dynamics are well described in the literature by Wu et al. (1999) and Anderson et al. (2007), but is also shown by Eqs. 7 and 8. Equation 8 shows that k_p , that defines the amplitude (Eq. 6), will decrease with the value of resistivity and/or permittivity. At a certain resistivity and permittivity level, k_i is reduced to a level where the amplitude decay approaches the signal/noise ratio and the amplitude resistivity will become inaccurate.

In Example 2, ε_k^f was compared with ε_{ADT}^f in a two vertical wells. Figs. 6 and 7 show LWD data acquired by Halliburton and Schlumberger, respectively. In relation to the quality control, both Figs. 6 and 7 show ε_k^f that fits well with ε_{ADT}^f in the radiated part of the near field (orange zone). Figures 6 and 7 show shorter intervals where ε_k^f has negative values. The negative values occur when $k_i > k_r$ (see Eq. 5) in intervals where LWD resistivity and wireline permittivity show large electrical contrast. In the reactive part of the near-field zone (red zone) the value of ε_k^f is slightly too high when compared with ε_{ADT}^f . There are no measurements in the transition and far-field zone (green zones).

The third example is shown by Figure 8 and illustrates that in deviated wells the calculated permittivity is too low when compared to ε_{ADT}^f . This is believed to be a result of a too low a value of k_r caused by refraction (Fig. 3). By Snell's law, k_r was corrected for refraction, and ε_k^f was shown to agree with ε_{ADT}^f .

The example illustrated by Fig. 9 shows that R_k^f (Eq. 9) calculated on LWD resistivity data can be used as formation resistivity when LWD resistivity is influenced by the dielectric effect. The large range in LWD resistivity responses was identified to be a result of the dielectric effect since

- The characteristic of the LWD multispaceing phase and amplitude resistivities show a typical pattern

for dielectric effect (amplitude resistivities $>$ phase resistivities, a large range in amplitude resistivities and small range in phase resistivities) (Wu et al., 1999),

- The high value on ε_k^f (Eq. 10) supports the assumption about the dielectric effect.

R_k^f (Eq. 9) fits very well with the wireline resistivity, which is commonly accepted to be the resistivity closest to true formation resistivity.

The last example (Figs. 10 and 11) shows that water saturation calculated by Eq. 20 fits very well with water saturation calculated by conventional methods. The conventional methods are water saturation calculated by use of Archie's equation, dielectric and NMR measurements. The benefits of Eq. 20 are:

- The water saturation can be calculated from only LWD resistivity and porosity.
- The impact of interfacial polarization can be disregarded since it is the imaginary part of the wavenumber that is used.
- It is valid even with large dip or well inclination since k_i is not sensitive to refraction.

The motivation of Jackson and Hagiwara (1998), Wu et al. (1999), Haugland (2001) and Anderson et al. (2007) was to extract permittivity from LWD resistivity measurements with the aim to reduce the dielectric effect and error on the processed R_p and R_a . The dielectric effect is most pronounced in high-resistivity zones where $R_a > 10 \Omega\text{-m}$ and $R_p > 100 \Omega\text{-m}$ (Anderson et al., 2007), and it is believed that the algorithms were developed for high-resistivity use. High-resistivity zones are zones for which the LWD measurements approach the reactive part of the near field, and where the presented approach (Eqs. 9 and 10) will not be valid. The disadvantages of earlier presented algorithms are that there was no description of their limitations and for which physical zones these algorithms will work. For example, the algorithm presented by Anderson et al. (2007) is based on the wavenumber on the form given by Eq. 1, which explicitly mean it is valid for isotropic formations. It is assumed this algorithm will be sensitive to anisotropy and that it may fail when the measurements enter the radiative part of the E-field. In formations with lower resistivity, where the EM measurements approaches the radiative part of the E-field ($\lambda/4\pi < \text{TRS}$), the results of this paper are valid and are comparable with the approach used in previously presented algorithms.

There are petrophysical scenarios that can affect the accuracy of the presented approach. One example is the accuracy of R_p and R_a that is briefly discussed in Example 1 with the synthetic cases. Invasion of mud filtrate is another example that can affect the R_p and R_a and the presented approach. It is generally accepted that R_p is more sensitive to the invaded zone compared with R_a (Wu et al., 1999). Invasion of mud filtrate will therefore have a larger impact on k_r than on k_i . Conductive mud will increase the value of k_r (Eq. 7), ϵ (Eq. 5) and σ (Eq. 4), and the opposite for resistive mud. The petrophysical scenarios that give the characteristics of R_p and R_a should therefore be classified, e.g., as was shown in Example 4. Wu et al. (1999) give an overview of the logic for differentiating among these effects and this topic not discussed further in this paper.

Petrophysical scenarios that affect the accuracy of the resistivity should be identified and quantified and be an

integral part of the calculations (Stalheim, 2016). Although this is not covered in this paper, algorithms that use first-order error propagation (Stalheim, 2016) as integral part of k_r (Eq. 7), k_i (Eq. 8), ϵ (Eq. 5), σ (Eq. 4) and S_w (Eq. 20) have been developed. Figure 13 shows one example that illustrates how error in amplitude resistivity propagates through the chains of calculations. Figure 13 shows that the main source to error in S_w (Track 4) is error in k_{wi} (Track 5).

This paper shows how wavenumber (k_r and k_i), electrical permittivity (ϵ_k^f), electrical resistivity (R_k^f) and its dispersion can be extracted from LWD R_p and R_a . k_r and k_i have not been presented in the petrophysical literature before. It was shown that water saturation can be calculated by use of k_i (Eq. 20), and that k_r and k_i can be used to calculate electrical resistivity R_k^f (Eq. 4) and electrical permittivity ϵ_k^f (Eq. 5). The presented theory has many benefits when comparing with conventional log measurements, e.g., ϵ_{ADT}^f , and has many applications:

$$\Delta R_a = 0.1 * R_a, \Delta k_{wi} = 0.2 * k_{wi}$$

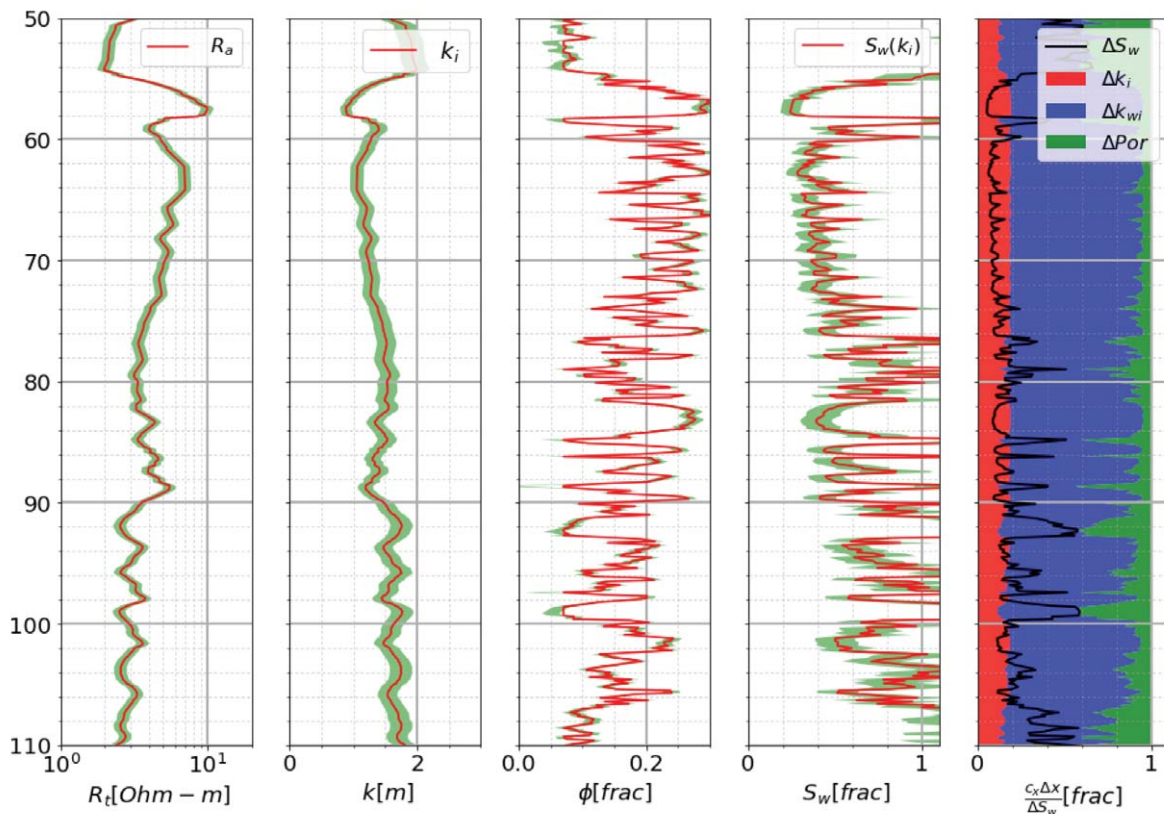


Fig. 13—Calculated water saturation (Eq. 20) with error and error propagation of the well presented in Fig. 10. The green color behind the red log-curves show the calculated error band. The last track presents the fraction of each input error on the total error in S_w (Track 4). (Details of this type of plot are described in Stalheim, 2016.)

1. The most important advantage is that LWD resistivity has been acquired in nearly all drilled wells and that ε_k^f can be extracted from LWD resistivity measurements without additional cost. ε_{ADT}^f are data that are acquired by wireline tools and are often not accessible due to technical and/or economic reasons.
2. Due to lower frequency, larger TRS and shorter time between formation drilling and measurement, LWD resistivity is far less affected by invasion of drilling mud when compared with high-frequency, short TRS dielectric wireline measurements. The values of ε_k^f are therefore more representative for noninvaded formations, which is the target for petrophysical evaluation.
3. Since ε_k^f and the wavenumber are acquired in real time during drilling, they can be used proactively to identify bypassed zones (Eq. 20) or as geological markers, e.g., organic-rich source rocks. This information is useful for geosteering purposes.
4. For organic-rich source rocks or formations where the electrical permittivity is extremely high, 10 to 50,000 (Anderson et al., 2007), the error in processed LWD resistivity R_a and R_p can be large due to the dielectric effect (Fig. 9). In such cases, the formation resistivity can be calculated by use of k_r and k_i with Eq. 9. Equation 9 provides the resistivity that is not influenced by dielectric effects and will be more accurate in comparison to LWD R_a and R_p .
5. Since LWD resistivity and dielectric wireline measurements operate at far different frequencies, they have different sensitivities to polarization mechanisms. These mechanisms are electronic polarization, molecular orientation and interfacial polarization, as described by Hizem et al. (2008). LWD dispersion permittivity ε_k^f is more sensitive to interfacial polarization and salinity to the formation water compared with ε_{ADT}^f (Hizem et al., 2008). This behavior has the potential to be used to extract information about electrical properties of formation water, which is a key parameter in water saturation calculations from electrical logs.
6. It is also believed that use of $\varepsilon_k^f(f)$ has the same potential as $\varepsilon_{ADT}^f(f)$ and can be used to extract information about V_{SHP} , CEC, and Archie m , (Hizem et al., 2008; Josh et al., 2009). $\varepsilon_k^f(f)$ can also be used together with $\varepsilon_{ADT}^f(f)$ as presented by Wang and Poppitt (2013), and shown in Figs. 6b, 7b, and 8b to increase the bandwidth of dielectric dispersion.

The classification of physical zones presented in this paper can also be of help when it comes to optimizing electromagnetic tool configurations. It was shown that the optimal zone for measurements is in the radiative part of the near field where $\lambda/4\pi < \text{TRS} < \lambda$. Since the value of λ (Eqs. 7 and 13) is dynamic and is a function of the frequency and the electromagnetic properties of the formation, an optimal electromagnetic tool should have the capability to tune the frequency and/or TRS to beat the radiative near-field zone, $\lambda/4\pi < \text{TRS} < \lambda$.

CONCLUSIONS

This paper shows that the electrical permittivity and its dispersion can, under given conditions, be extracted from LWD phase and attenuation resistivity without requiring advanced inversion algorithms.

The presented approach relates to a plane wave and isotropic formation approximation. The contention of the presented approximations is that the distance between the LWD transmitter and receiver is far enough that the received signal is not influenced by the transmitter, but not too far to exceed the quasistatic area. The classification of the physical zones, as illustrated in Fig. 2, shows good agreement with LWD resistivity measurements.

The model has been verified on LWD resistivity data generated in synthetic models and on LWD resistivity data acquired in wells. Testing of the synthetic data shows that the presented approach matches the synthetic models very well when the resistivity is $< 49 \Omega\text{-m}$. Testing of LWD resistivity data acquired in wells show that:

- If $\text{TRS} < \lambda/4\pi$, the electrical permittivity from LWD fails or shows a too high value when compared with wireline permittivity. This was expected, since this is into the reactive part of the near field and a plane-wave model is not valid.
- If $\lambda/4\pi < \text{TRS} < \lambda$, the electrical permittivity from LWD shows intervals where it fits very well with the dispersive permittivity from commercial dielectric wireline tools, and shorter intervals where it fails. It fails in intervals where the E-field crosses into a new formation with large electrical contrast.

There are no examples of measurements in the transition and far-field zone for where $\lambda < \text{TRS}$.

The optimal physical zone for electromagnetic measurements was shown to be $\lambda/4\pi < \text{TRS} < \lambda$. This can be used to optimize electromagnetic tool configuration with

respect on TRS and frequency.

The CRIM can be used at LWD frequencies by applying the imaginary part of the wavenumber. The CRIM was used and found to agree with water saturation calculated from conventional methods, such as the Archie equation, dielectric and NMR measurements. The presented model has the potential to calculate water saturation from LWD resistivity and porosity only.

It is believed that $k_r(f)$, $k_i(f)$, $\epsilon(f)$ and R_k extracted from LWD resistivity have a huge potential and will add new information with large value for petrophysical evaluations in the future.

ACKNOWLEDGMENTS

The author thanks management of Equinor and partners for permission to publish this paper. It should be noted that conclusions presented in this paper represent the author's personal viewpoints. The author would also like to thank the SPWLA Symposium steering committee for the opportunity to publish this work. Comments, constructive criticism and suggestions which have been greatly appreciated where made by Steffen Stalheim and my colleagues in Equinor Per Atle Olsen, Alistair Stuart Chandler, Arthur Bale and Niall Fleming. The author would also like to thank the anonymous reviewers for their valuable inputs to the paper.

NOMENCLATURE

Abbreviations

- ADT = Schlumberger's dielectric wireline tool
- BFV = bound-fluid volume (from NMR)
- CEC = cation exchange capacity
- CRIM = complex refraction index model
- EM = electromagnetic
- FOEP = first order error propagation
- LWD = logging while drilling
- NMR = nuclear magnetic resonance
- TCMR = total porosity from NMR
- TRS = transmitter to receiver spacing
- PVXO = water-filled pore volume from ADT

Symbols

- A_a = substitute to Eqs. 9 and 10
- A_p = substitute to Eqs. 9 and 10
- B = magnetic flux density
- E = electrical field strength
- E_o = electrical field strength at $z = t = 0$
- c = speed of light in vacuum, 3×10^8 m/s
- f = frequency
- i = imaginary number ($\sqrt{-1}$)

- k = complex wavenumber
- k_i = imaginary part of k
- k_r = real part of k
- m = cementation exponent
- M = magnetic current density
- r = position in space
- R_a = LWD amplitude resistivity
- R_p = LWD phase resistivity
- R_t = apparent resistivity
- S_w = Water saturation
- t = time
- V_p = Volume of polarized water
- z = Cartesian coordinate
- ϵ = relative electrical permittivity
- ϵ_0 = free-space electrical permittivity, 8.85×10^{-12} Farad/m
- ϵ_{LWD} = relative electrical permittivity used by service vendor in LWD resistivity processing.
- θ_1 = angle of incidence
- θ_c = critical angle for total reflection
- θ_2 = real angle of refraction
- λ = wavelength
- μ = relative magnetic permeability
- μ_0 = the free-space magnetic permeability, $4\pi \times 10^{-7}$ Henry/m
- ρ = free charge density
- σ = electrical conductivity
- ϕ = porosity
- ω = angular frequency
- ∇ = Del operator

REFERENCES

- Anderson, B.I., Barber, T.D., Luling, M.G., Rasmus, J., Sen, P.N., Tabanou, J.R., and Haugland, M., 2007, Observations of Large Dielectric Effects on LWD Propagation-Resistivity Logs, Paper BB, *Transactions, SPWLA 48th Annual Logging Symposium*, Austin, Texas, USA, 3–6 June.
- Apostol, T.M., 1969, *Calculus Volume 2: Multi-Variable Calculus and Linear Algebra, With Applications to Differential Equations and Probability*, 2nd edition, John Wiley & Sons. ISBN: 978-0471000075.
- Balanis, C.A., 2016, *Antenna Theory; Analysis and Design*, 4th edition. John Wiley & Sons. ISBN: 978-1118642061.
- Bittar, M.S. 1993, A True Multiple Depth of Investigation Electromagnetic Wave Resistivity Sensor: Theory, Experiment, and Prototype Field Test Results, Paper SPE-22705, *SPE Formation Evaluation*, **8**(3), 171–176. DOI: 10.2118/22705-PA.
- Chew, W.C., 1990, *Wave and Fields in Inhomogeneous Media*, Kluwer Academic Publishers. ISBN: 978-0442238162
- Choy, T.C., 2016, *Effective Medium Theory*, 2nd edition, Oxford

- Science Publications. ISBN: 978-0198705093.
- Clark, B., Allen, D.F., Best, D.L., Bonner, S.D., Jundt, J., Luling, M.G., and Ross, M.O., 1990, Electromagnetic Propagation Logging While Drilling: Theory and Experiment, Paper SPE-18117, *SPE Formation Evaluation*, **5**(3), 263–271. DOI: 10.2118/18117-PA.
- Clark, B., Luling, M.G., Jundt, J., Ross, M., and Best, D., 1988, A Dual Depth Resistivity Measurement for FEWD, Paper A, *Transactions, SPWLA 29th Annual Logging Symposium*, San Antonio, Texas, USA, 5–8 June.
- Ellis, D.V., and Singer, J.M., 2008, *Well Logging for Earth Scientists*, 2nd edition, Springer. ISBN: 978-1402037382.
- Feynman, R., Sands, M., and Leighton, R.B., 2010, *The Feynman Lectures on Physics, Volume 2: Mainly Electromagnetism and Matter*, The New Millennium Edition. Basic Books. ISBN: 978-0465024940.
- Haugland, S.M. 2001, New Discovery With Important Implications for LWD Propagation Resistivity Processing and Interpretation, Paper LL, *Transactions, SPWLA 42th Annual Logging Symposium*, Houston, Texas, USA, 17–20 June.
- Hizem, M., Budan, H., Deville, B., Ollivier, F., Mosse, L., and Matthieu, S., 2008, Dielectric Dispersion: A New Wireline Petrophysical Measurements, Paper SPE-116130 presented at the SPE Annual Technical Conference and Exhibition, Denver, Colorado, USA, 21–24 September. DOI: 10.2118/116130-MS.
- Jackson, C., and Hagiwara, T., 1998, A New Simultaneous Anisotropy and Dielectric Correction Algorithm for LWD Resistivity Measurements, Paper W, *Transactions, SPWLA 39th Annual Logging Symposium*, Keystone, Colorado, USA, 26–29 May.
- Josh, M., Clennell, B., and Siggins, A., 2009, Practical Broadband Dielectric Measurement of Geological Samples, Paper DD, *Transactions, SPWLA 50th Annual Logging Symposium*, The Woodlands, Texas, USA, 21–24 June.
- Kong, J.A., 2000, *Electromagnetic Wave Theory*, EMW Publishing Cambridge, Massachusetts, USA. ISBN: 0966814398, 978-0966814392.
- Maxwell, J.C., 1873, *A Treatise on Electricity and Magnetism*, v. 1 and v. 2, Oxford at the Clarendon Press.
- Rabinovich, M., and Liu, S., 2015, Challenges of Measuring Dielectric Anisotropy With High-Frequency Dielectric Logging Tools, Paper JJ, *Transactions, SPWLA 56th Annual Logging Symposium*, Long Beach, California, USA, 18–22 July.
- Reitz, J.R., Milford, F.J., and Christy, R.W., 1993, *Foundations of Electromagnetic Theory*, 4th Edition. Addison Wesley Publishing Company. ISBN: 0201526247, 978-0201526240.
- Rodney, P.F., and Wisler, M.M., 1986, Electromagnetic Wave Resistivity MWD Tool, Paper SPE-12167, *SPE Drilling Engineering*, **1**(5), 337–346. DOI: 10.2118/12167-PA.
- Seleznev, N., Habashy, T., Boyd, A., and Hizem, M., 2006, Formation Properties Derived From a Multi-Frequency Dielectric Measurement, Paper VVV, *Transactions, SPWLA 47th Annual Logging Symposium*, Veracruz, Mexico, 4–7 June.
- Shen, L.C., 2002, Comparison of Modeling Codes for Resistivity and MWD Instruments: Part 2, 1-D Thin Beds, *Petrophysics*, **43**(1), 20–25..
- Stalheim, S.O., 2016, On Error Calculation and Use of First-Order Error Propagation as Integral Part of Petrophysical Calculation, *Petrophysics*, **57**(5), 465–478.
- Stroud D., Milton, G., and De, B., 1986, Analytical Model for the Dielectric Response of Brine-Saturated Rocks, *Physical Review B*, **34**(8), 5145–5153. DOI: 10.1103/PhysRevB.34.5145.
- Wang, H., and Poppitt, A., 2013, The Broadband Electromagnetic Dispersion Logging Data in a Gas Shale Formation: A Case Study, Paper AAA, *Transactions, SPWLA 54th Annual Logging Symposium*, New Orleans, Louisiana, USA, 22–26.
- Wu, P., Lovell, J.R., Clark, B., Bonner, S.D., and Tabanou, J.R., 1999, Dielectric-Independent 2-MHz Propagation Resistivity, Paper SPE-56448 presented at the SPE Annual Technical Conference and Exhibition, Houston, Texas, USA, 3–6 October. DOI: 10.2118/56448-MS.

APPENDIX 1: THE UNDERLYING EXPLANATION FOR USING A PLANE WAVE AND ISOTROPIC APPROXIMATION

The underlying explanation for using a plane wave and isotropic approximation is explained by the full set of Maxwell's equations of electrodynamics. Maxwell's equations, the wave equation and solutions are classical electromagnetic theory and well described in the literature (Maxwell, 1873; Apostol, 1969; Chew, 1990; Reitz et al., 1993; Kong, 2000; Feynman et al., 2010; Choy, 2016). The general time-harmonic -wave equation deduced from Maxwell's equation is the vector-wave equation

$$\begin{aligned} \nabla \times \bar{\mu}^{-1} \cdot \nabla \times \bar{E}(r) - \omega^2 \bar{\epsilon} \cdot \bar{E}(r) = \\ i\omega \bar{\sigma} \bar{E}(r) - \nabla \times \bar{\mu}^{-1} \cdot \bar{M}(r) \end{aligned} \quad (\text{A1.1})$$

M is fictitious magnetic current density, r is position in space and ∇ is the Del operator. Equation A1.1 is general and governing the solutions of an E-field in an inhomogeneous, anisotropic medium. Inhomogeneous medium is in relation to Gauss' law ($\nabla \cdot E = \rho(r)$) a medium for where the free charge density $\rho(r) \neq 0$. The internal free charge density, $\rho(r)$, that causes variation in the E-field, represents an internal source. The internal source $\nabla \cdot E$ is implicitly included in Eq. A1.1 by the identity $\nabla \times \nabla \times E = \nabla \cdot E - \nabla^2 E$. The second source to the E-field is given by Faraday's law and is the time-varying magnetic-flux density, B , and the magnetic current, $\frac{\partial B(r)}{\partial t} + M(r)$. Governing the solutions of the E-field by use of Eq. A1.1 are quite complicated. Eq. A1.1 is a nonhomogeneous wave equation and detailed knowledge about the complexity of the measurement physics and rand conditions is needed. If the receiver is at sufficiently great distance from the

transmitter, such that $M(r) \approx 0$, the source parts can be removed, and Eq. A1.1 is reduced to

$$\nabla \times \bar{\mu}^{-1} \cdot \nabla \times \bar{E}(r) - \omega^2 \bar{\epsilon} \cdot \bar{E}(r) - i\omega \bar{\sigma} \bar{E}(r) = 0 \quad (\text{A1.2})$$

Equation A1.2 has plane-wave solutions but they are complicated to find since electromagnetic properties are vectors that do not commute with the Del operator. This can be solved. One solution is shown by Chew (1990). Chew applies a tensor with wavenumbers that describe the wavenumber in the different directions. Equation A1.2 will then be sets of linear equations where the solutions correspond to an eigenvalue, eigenvector problem. In this work, a simpler approach was applied. It was assumed to be no internal free charge, such that $\nabla \cdot E \approx 0$, and the formation was assumed to be isotropic, such that the vectors $(\bar{\epsilon}, \bar{\sigma}, \bar{\mu})$ could be replaced with scalars (ϵ, σ, μ) . This assumption was expected to be fulfilled in the radiative part of the near field when quasistatic approximation can be used. By apply $\nabla \cdot E \approx 0$ with the identity $\nabla \times \nabla \times E = \nabla \cdot E - \nabla^2 E$, the first part of Eq. A1 is reduced to $-(\bar{\mu}^{-1}) \cdot \nabla^2 E$, and with electromagnetic properties as scalars (ϵ, σ, μ) it will commute with the Del operator. Eq. A1.1 is then reduced to

$$(\nabla^2 + \hat{k}^2) \cdot \bar{E} = 0 \quad (\text{A1.3})$$

which is the Helmholtz equation. \hat{k} is given by Eq. 1. Helmholtz equation describes the electrical field in space and time where a plane-wave model, as given by Eq. 6, is one solution. Equation A1.3 is valid for a source-free and isotropic medium and can be used where the receiver is at sufficiently great distance from the transmitter, $M(r) = 0$, for where $\nabla \cdot E = 0$, and electromagnetic properties are scalars. The strength with a plane-wave model is that all wave types can be expanded from plane-wave solution as given by Eq. 6 (Chew, 1990; Reitz et al., 1993). This will of course never be a perfect solution of Maxwell's equations, but can in some cases be very close to the exact solution. This paper shows that this approximation can be used under specific conditions that were discussed in the paper.

ABOUT THE AUTHOR



Stein Ottar Stalheim is specialist in petrophysics with Equinor, Norway. Stein Ottar joined Equinor (former Statoil) in 1993. His main interest is EM physics, multivariate analysis and scientific computing. The primary role to Stein Ottar in Equinor is related to Geoelectrical modeling, dynamic petrophysics and well integrity. Stein Ottar received his MSc and PhD degree in physics from the University in Bergen.

Crushed-Rock Analysis Workflow Based on Advanced Fluid Characterization for Improved Interpretation of Core Data¹

Anton Nikitin², Melanie Durand³, Adam McMullen³, Aidan Blount³, Brian Driskill³, and Amie Hows²

ABSTRACT

Sustained E&P activity levels and slim margins on highly valued Permian Basin acreage drive operators to leverage information as much as possible and in ways not seen in the recent past. Data accuracy, especially in this fast-paced, competitive environment, is strongly desired. Core analyses provide subsurface static calibration, but the thick stratigraphic section comprised largely of sublog scale facies, challenges a cost-effective approach to collect sufficient calibration data.

Saturation determination is a key petrophysical deliverable that has multiple uses, including landing zone assessment. Calibration of saturation models may originate in several ways: proprietary or joint venture core, industry consortia databases, data trades with other operators, government databases, or publications. Internal and external reviews of subsurface model inputs have repeatedly shown that Permian Basin saturations, in particular, have a wide distribution and large uncertainty. Accurately measuring core fluid saturations in tight rock continues to pose significant challenges originating from the currently accepted laboratory methods, assumptions used to interpret those data and more broadly, due to increased relative uncertainty associated with tight, low-porosity formations.

For example, crushing core samples, which enhances fluid extraction in tight rocks, causes systematic fluid losses in the case of core samples of liquid-rich mudstone formations, which are not typically quantified. Instead, as-received air-filled porosity is commonly assumed to represent hydrocarbons that were forced from core during acquisition/retrieval due to gas expansion. Additionally, fluid extraction from commercially available retorting systems have widely variable fluid collection efficiencies (<100%) resulting in significant inconsistencies between the weight of collected fluids and sample weight loss during retorting

experiments. The Dean-Stark technique removes not only water and oil, but an unknown volume of solvent-extractable organic matter, and it only allows for direct quantification of the extracted water volume. Finally, fluid and solid losses during handling in the laboratory are unassessed in current commercial laboratory procedures. The reconciliation of fluid volumes with fluid and sample-weight data delivered by either of the two techniques, i.e., retort or Dean-Stark, requires numerous assumptions about pore fluid properties, which are typically not verified through direct measurements. We demonstrate that such assumptions can lead to extreme uncertainty in estimates of water saturation.

To address such critical uncertainties, a new retort-based core analysis workflow using improved core characterization and fluid-extraction techniques was developed. In one advancement, this workflow employs NMR measurements systematically performed on all as-received and crushed samples to quantify fluid losses during crushing. This approach also uses a specially developed fluid collection apparatus with close to 100% fluid collection efficiency. In addition to these advances in measurements, the workflow is optimized to avoid fluid losses during sample handling and includes repeated grain density and geochemical measurements at different stages for quality control (QC). As a result, the new workflow reduces the uncertainties in acquired data and better addresses the assumptions, i.e., parameter corrections for fluid losses, in interpreting measured data into core total porosity and core fluid saturations. The workflow is demonstrated for a set of Delaware Basin Wolfcamp A formation samples and the results suggest that previous crushed-rock core analysis protocols underestimate water saturation by at least 30% or ~15 saturation units (s.u.) for this liquid-rich mudstone formation.

INTRODUCTION

In the Permian Basin, water cuts typically range from 60 to 80% (Scanlon et al., 2017). Water lifting, handling, and

disposal adds to project costs so having an accurate water saturation model that aligns with water production trends facilitates both economic decisions and field development planning. Petrophysicists seek to predict areas and intervals

Manuscript received by the Editor July 23, 2019; revised manuscript received October 25, 2019; manuscript accepted October 27, 2019.

¹Originally presented at the SPWLA 60th Annual Logging Symposium, The Woodlands, Texas, USA, June 17–19, 2019, Paper AAAA.

²Shell International Exploration and Production Inc., 3333 Highway 6 South, P.O. Box 4685, Houston, TX 77251-7171, USA; Anton.Nikitin@shell.com; amie.hows@shell.com

³Shell Exploration and Production Company, Woodcreek, 150 N. Dairy Ashford, Houston TX 77079; Melanie.durand@shell.com; Adam.McMullen@shell.com; Aidan.Blount@shell.com; Brian.Driskill@shell.com;

that will maximize hydrocarbon production or at least help to adequately allocate funds needed for planned water disposal. Yet, after looking at multiple datasets of crushed-rock analysis, there is evident misalignment of observed water production and available water saturation values derived from the results of core analysis.

In a basin as large as the Permian, where capital is scrutinized, opportunities to collect and analyze core are limited. Petrophysicists often rely on public data and trades with other operators to fill existing data gaps. So how is it possible to make sense of all the available core data that has been acquired over the past few decades, using different acquisition techniques; over thousands of feet of distinctly different formations; and has been analyzed by multiple vendors, using different analysis techniques and assumptions? More importantly, which datasets have higher confidence and how can the uncertainties be reduced?

Over the last few years, the team has tried to address these questions, first, by comparing analysis procedures, and second, by comparing acquisition techniques. In 2017, the team reported the comparisons of retort and Dean-Stark/

Gas Research Institute (GRI) procedures for saturation measurements acquired on Permian samples. The report compared both retort and GRI techniques by two different vendors. The results indicate that Dean-Stark porosity trends higher than the retort from both vendors. The possible reasons reported are (1) bitumen extraction during Dean-Stark, (2) the bucketing of the “missing weight,” and (3) not recovering all oil during the retort process (Blount et al., 2017).

In 2018, the team presented findings comparing three different core-acquisition techniques (1) conventional core, (2) rotary sidewall cores (RSWC), and (3) pressurized rotary sidewall cores (PRSWC). The experiment was designed to minimize fluid loss with each technique to better estimate in-situ saturations. The data showed that PRSWC samples have lower air-filled porosity than the other acquisition methods, possibly allowing more direct measurement of the in-situ saturations (Blount et al., 2019). However, the three core-acquisition methods show a wide range in saturation estimation, leading toward further investigation of the “missing weight” assumptions, as displayed in Fig. 1.

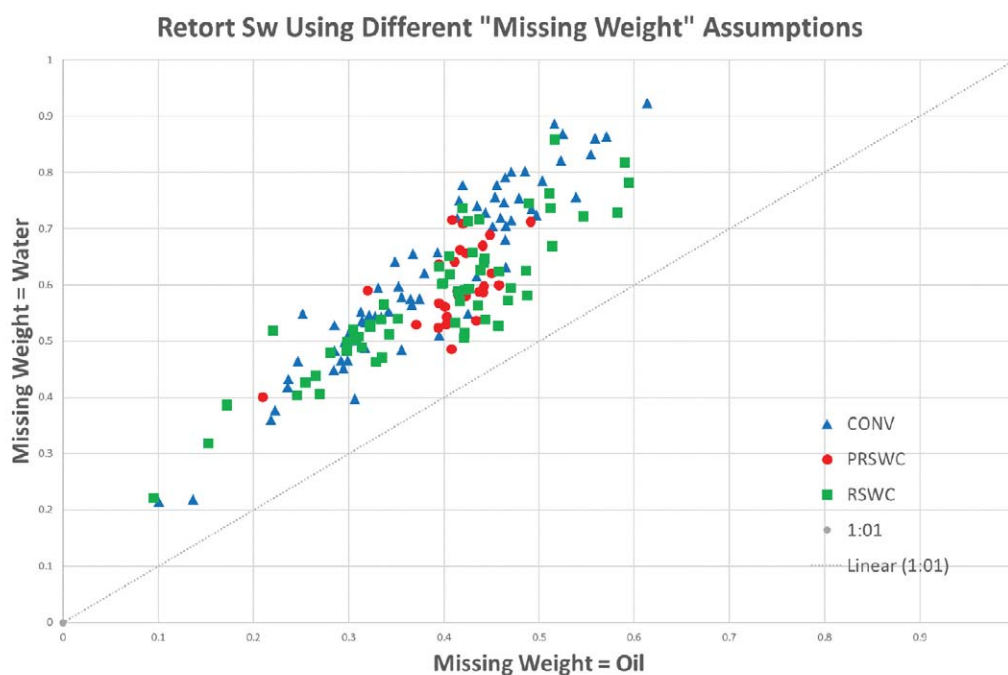


Fig. 1—Example of water saturation uncertainties using different “missing fluid” assumptions. Retort procedures were executed on samples acquired using three different core-acquisition methods: conventional core (CONV), rotary sidewall cores (RSWC), and pressurized rotary sidewall cores (PRSWC). The crossplot compares the calculated S_w assuming all weight of the missing fluid is assigned to hydrocarbon (HC) (horizontal axes) to S_w calculated from the same data when all weight of missing fluid is assigned to water (vertical axes). Deviation from the 1:1 line highlights the uncertainty with the “missing weight” assumptions.

To address these uncertainties, which are critical for formation evaluation of the Permian Basin, a new core analysis workflow with improved core characterization and fluid-extraction techniques was developed. The methodology and fluid saturation measurements acquired on Wolfcamp A formation samples using this workflow are presented in this paper. The workflow results address the following challenges of crushed-rock analysis (1) fluid loss during crushing, (2) extraction of fluids, and (3) quantification of total porosity.

OVERVIEW OF MEASUREMENT TECHNIQUES

The main objective of any Gas Research Institute (GRI)-type (Luffel et al., 1991) crushed-rock core analysis workflow is to deliver data for volumetric composition reconstruction of as-received (AR) samples in tight, submicrodarcy permeability rocks. The volumetric model illustrated in Fig. 2 assumes that AR core samples from organic-rich mudstone (ORM) formations consist of the following components: the matrix, including minerals and immovable organic matter (TOC_{imm}); the pore space occupied by residual oil (BVO), free water (BVW_{free}), clay and capillary-bound water (BVW_{cb}) and the air (Φ_{air}) which previously filled a part of the pore space occupied by hydrocarbon fluid in situ.

Immovable organic matter (OM) consists of bitumen or extractable organic matter (EOM), which can be removed from the core sample using chlorinated solvents along with kerogen and pyrobitumen, or solid organic matter (SOM), which remain within the core sample even after chemical extraction. Both EOM and SOM do not flow under the

conditions present in the reservoir. As a result, they are assumed to be a part of the matrix, as shown in Fig. 2.

Sample Crushing

Fluids occupying pore space are extracted from the core sample for volume quantification. In the case of liquid-rich mudstone formations, core samples have very low permeability and thus, both thermal and chemical extraction is very time-consuming and often unreliable if performed at the whole-plug scale. To make such extraction more feasible, the surface/volume ratio of the core sample is increased through sample crushing. Such crushing also causes the opening of additional pore space to the atmosphere and as a result, water and hydrocarbon (HC) fluid occupying this pore space, in the case of liquid-rich mudstone samples, is lost through evaporation prior to extraction.

Fluid-Extraction Techniques

The original GRI workflow proposed by Luffel et al. (1991) uses the Dean-Stark method to extract and quantify water. In this case, a crushed-rock sample is placed inside of the Dean-Stark apparatus where its surface is exposed to toluene liquid. Toluene interacts with the sample, penetrates the pore system, slowly substitutes for the water and dissolves oil and EOM. Water replaced by the toluene is collected in the Dean-Stark apparatus and can be quantified, as it is not soluble in toluene.

In the case of tight rocks, capillary force-driven penetration of toluene into the crushed-rock fragments is very slow and may not reach all small pores occupied by

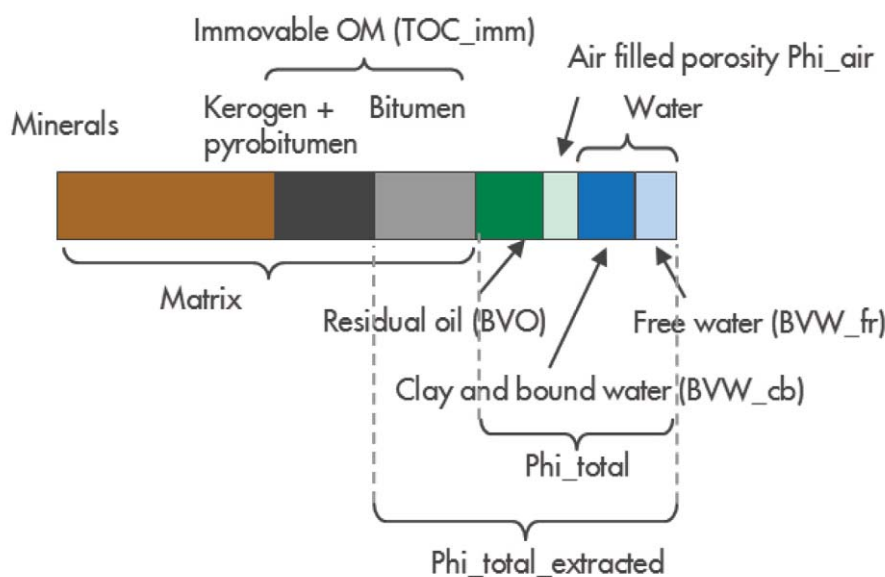


Fig. 2—Volumetric composition of organic-rich mudstone (ORM) core sample.

the water during the time period of the extraction treatment. As a result, not all water present in the AR sample may be removed. Additionally, toluene removes part of EOM through dissolution. Dean-Stark extraction is followed by sample cleaning using Soxhlet extraction, which removes even more EOM. EOM removal by sample treatment with chemical solvents creates additional porosity likely not present in the rock sample in situ. Additionally, after extraction, the crushed sample is dried in a vacuum oven to remove toluene and other chemicals from the pore space. Such drying may also remove the nonextracted water. Therefore, it is not possible to control the efficiency of water extraction using the Dean-Stark method.

Retort analysis is an attractive, alternative extraction technique for tight rocks as it presents the possibility of separating out the saturation of the effective pore space from the total porosity. However, this technique comes with its own challenges.

The main challenge of any retorting apparatus is fluid-collection efficiency. Indeed, retorting apparatuses currently used for core analysis have sample chambers directly connected with the atmosphere (so-called open-retorting systems). Such design allows fluids released from the sample at different temperature steps of the retorting experiment to be separated and collected more efficiently. The open design, however, suffers from only partial collection of extracted water and light HC because of the inefficiency of the condenser. Condenser efficiency depends not only on its design but also on the absolute rate of fluid release by the sample during retorting. Additionally, heavier HC components may not be collected because they condense in solid form inside of the condenser tube and do not reach the fluid collection cylinder. Collection efficiency of the same retorting apparatus can vary from sample to sample. Comparing the sample-weight change resulting from fluid extraction during a retorting experiment with the weight of the collected fluid may only partly address the issue of variable collection efficiency because, a priori, there exists an unknown ratio between collection efficiency of water, light HC and heavier HC.

If the maximum temperature used for thermal extraction of fluids in a retorting apparatus does not exceed 300°C, the thought is that only free water, clay and capillary-bound water, and residual oil should be removed from the ORM rock sample. The temperature is too low to cause cracking of heavier HC into lighter HC. Therefore, this technique does not lead to the formation of the additional organic-hosted porosity, which would not be present in the formation in situ.

Quantifying Total Porosity

Currently, depending on the selected implementation of

GRI workflow (e.g., Handwerger et al., 2011; Weatherford Laboratories, 2012; CoreLab, 2017), total porosity is calculated either through the summation of fluids (Eq. 1) or from the comparison of a sample's bulk volume (V_{bulk}) and its matrix grain volume (V_{grain}) (Eq. 2).

$$\Phi_{tot\ ver1} = \Phi_{air} + BVO + BVW \quad (1)$$

$$\Phi_{tot\ ver2} = (V_{bulk} - V_{grain})/V_{bulk} \quad (2)$$

Both approaches are affected by measurement uncertainties. For $\Phi_{tot\ ver1}$ both the uncertainties in extracted oil and water volumes and the uncertainty of Φ_{air} defined by the AR grain-volume measurement are relevant. The uncertainty of $\Phi_{tot\ ver2}$ is primarily controlled by the uncertainty in matrix grain volume. While the measurement of matrix grain volume (which does not include movable fluid) is quite reliable, its accuracy is predicated on the preservation of crushed-sample matrix material, the loss of which is the main source of uncertainty in $\Phi_{tot\ ver2}$. The crushed-sample grain volume after fluid extraction must be compared with the bulk volume of the same sample before crushing in the $\Phi_{tot\ ver2}$ calculation. Any untracked solid losses of crushed material during fluid extraction results in the underestimation of V_{grain} relative to V_{bulk} leading to a significant overestimation of total porosity. However, total porosity values for $\Phi_{tot\ ver1}$ and $\Phi_{tot\ ver2}$ should be comparable within the range of the uncertainties of the measurements used to quantify them.

NEW METHODOLOGY: GRI+

To overcome challenges associated with the GRI workflow highlighted above, a new workflow, called GRI+, was developed. It is outlined in Fig. 3. At Step 1, the NMR T_2 measurement is performed on a plug of AR core sample. This is used to quantify the fluids occupying the pore space/unit mass of the sample. At Step 2, bulk density is determined by measuring the sample volume either using plug length and diameter (if it has a cylindrical shape) or through the measurement of sample weight change due to its immersion into fluorinert (if it has an irregular shape). At Step 3, the sample is crushed, and fines are removed through sieving using a 300-mesh sieve. Between 60 and 80 grams of crushed material are then split and loaded into two universal sample holders, shown in Fig. 4 (Step 5), after an aliquot is taken for LECO TOC and RockEval measurements of the AR sample (Step 4).

One subsample is placed into a universal sample holder and is used for the open-retorting experiment where

maximum temperature does not exceed 300°C. This allows quantification of the ratio between free water and clay and capillary-bound water in the sample (Step 8a). Another subsample is used for the measurement of AR grain volume and grain density (Step 6) and for the NMR T_2 measurement of the crushed sample (Step 7), providing information about fluid concentration in the crushed sample compatible with the information about fluid concentration in the AR plug sample obtained at Step 1. The same subsample is used for the closed-system retorting experiment at 300°C, providing values of total water and residual oil present in the sample (Step 8b). The subsample used for the open-retorting experiment provides sample aliquots for post-retorting

LECO TOC and RockEval measurements (performed at Step 11) and for other measurements, such as X-ray fluorescence (XRF) and X-ray diffractions (XRD), which are used for interpreting mineral matrix composition. The closed-retorting subsample is then used to measure sample grain volume and grain density (Step 9). The same subsample is cleaned using Soxhlet extraction (Step 12). After cleaning and post-cleaning drying are finished, this subsample is again used to measure sample grain volume and grain density with removed EOM (Step 13); it also provides an aliquot for LECO TOC and RockEval measurements performed for the sample in the cleaned, extracted state.

The universal sample holder (Fig. 4) used for retorting

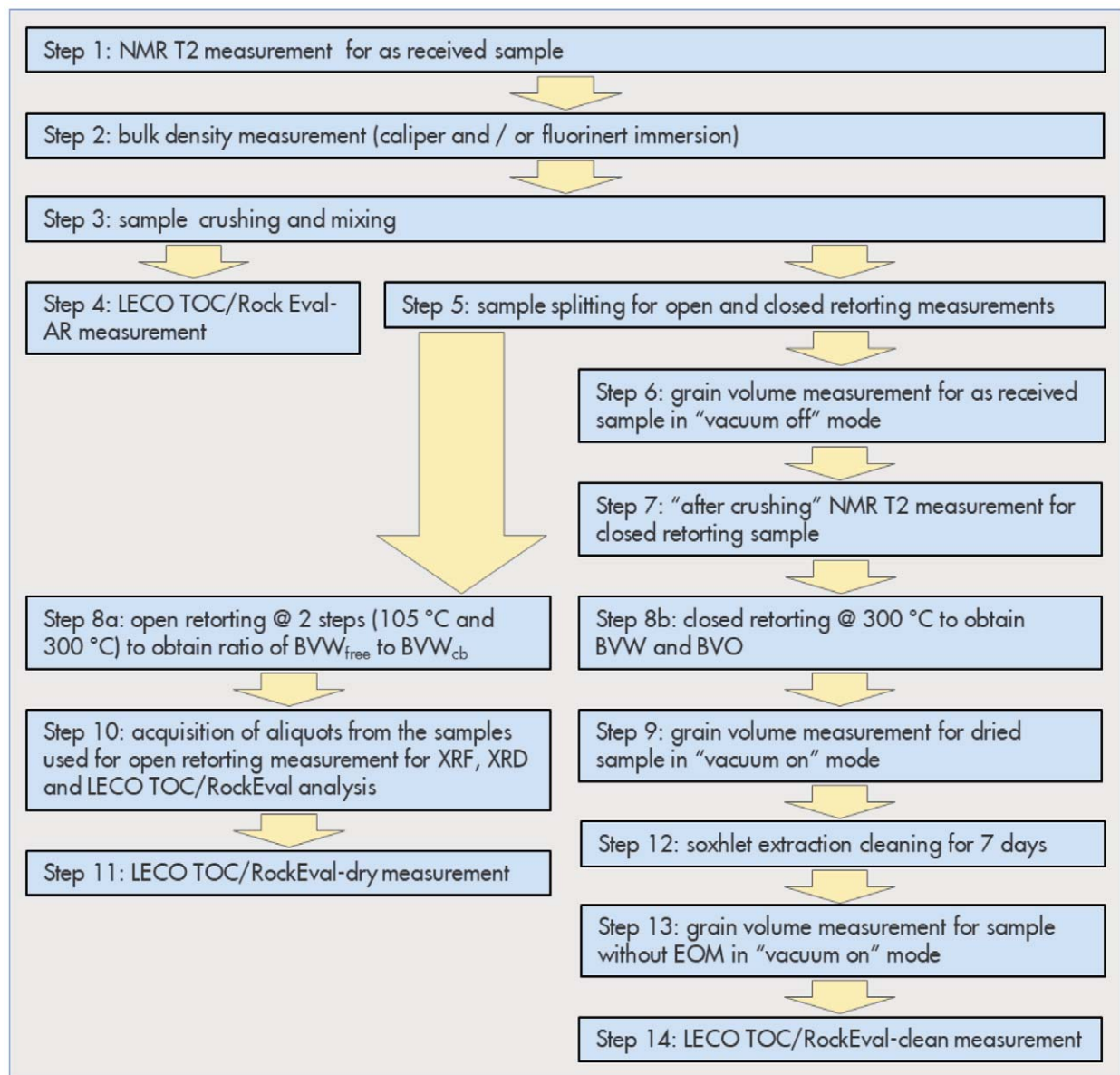


Fig. 3—Scheme illustrating the GRI+ crushed-rock core analysis workflow.

experiments is fully compatible with all measurements and sample treatments employed by the GRI+ workflow, including NMR measurements, grain-volume/density measurements, and Soxhlet extraction. As a result, crushed material is not removed from the sample holder unless a sample aliquot is taken. The use of a universal sample holder ensures the conservation of the crushed-sample material during all steps of the GRI+ workflow. This design, which uses special caps on the sample holder to seal crushed material inside, guarantees that the sample weight is a very good indicator of fluid losses during sample handling.

Two NMR T_2 measurements are performed as a part of the GRI+ workflow: at Step 1 for the AR core sample and at Step 7 for the subsample of the crushed material inside of the universal sample holder destined for the closed-retorting experiment. The main goal of these two NMR T_2 measurements is to estimate fluid loss both in the AR sample and caused by sample crushing. This goal can be

achieved only if both NMR T_2 measurements are properly calibrated in cubic centimeters of water units so quantitative comparison can be performed. In many cases, particularly in the case of RSWC samples, AR plug samples have uneven shapes and their average lengths are quite different from the lengths of crushed samples inside universal sample holders. NMR sensors in off-the-shelf NMR relaxometers have a significant nonuniform response function along their axes, as observed during in-house experiments. As a result, using such NMR relaxometers for NMR T_2 measurements performed at Step 1 and Step 7 of the GRI+ workflow can result in calibration-related uncertainties exceeding the levels required to quantify fluid losses caused by sample crushing. To overcome this problem, Ecotek Inc. developed and built a special NMR sensor that has a response function along its axis with enhanced uniformity (see Fig. 5). This NMR sensor enables the GRI+ workflow to account for the lost fluid caused by sample crushing.

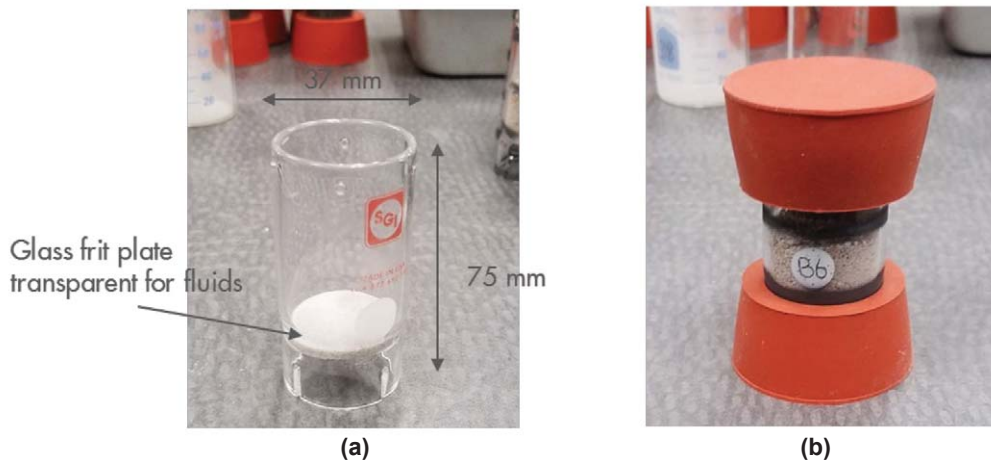


Fig. 4—Empty universal sample holder (a) and full universal sample holder covered with sealing caps (b).

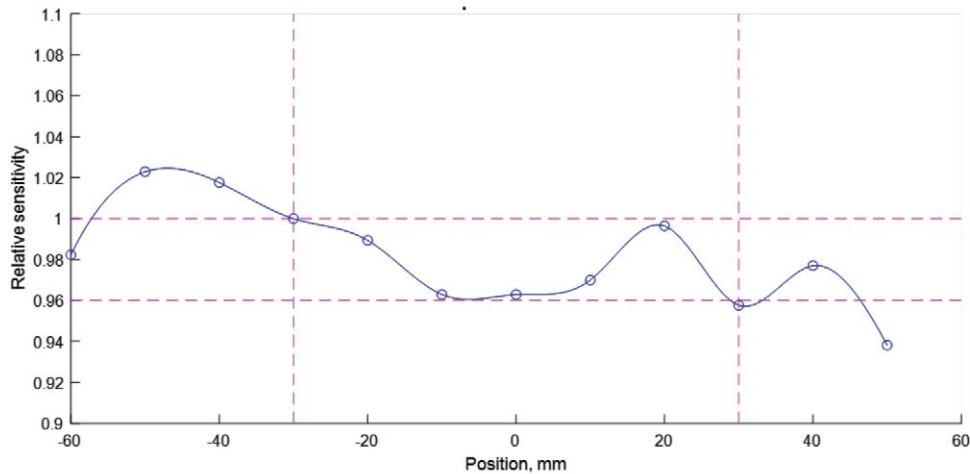


Fig. 5—Variation of the axial sensitivity of the NMR sensor developed by Ecotek Inc. that is used to quantify fluid losses during core sample crushing.

At Step 5, two subsamples of crushed material are loaded into the universal sample holders. One subsample is used for the open-retorting experiment (Step 8a), which delivers the ratio of free water to clay and capillary-bound water, and another one is used for the closed-retorting experiment (Step 8b), which delivers total volumes of extracted water and oil. The open- and closed-retorting apparatuses used for these experiments, specifically designed for the GRI+ workflow, are illustrated in Fig. 6.

Particularly, the open-retorting apparatus is equipped with a computer-controlled heater, a computer-controlled gas valve and a camera to record pictures of the fluid collection cylinder in parallel with sample heating. The gas valve enables injection of small volumes of nitrogen into the sample chamber during sample heating. This retorting apparatus allows custom implementation of any temperature program for retorting experiments, and the camera allows monitoring of fluid collection (see Fig. 7).

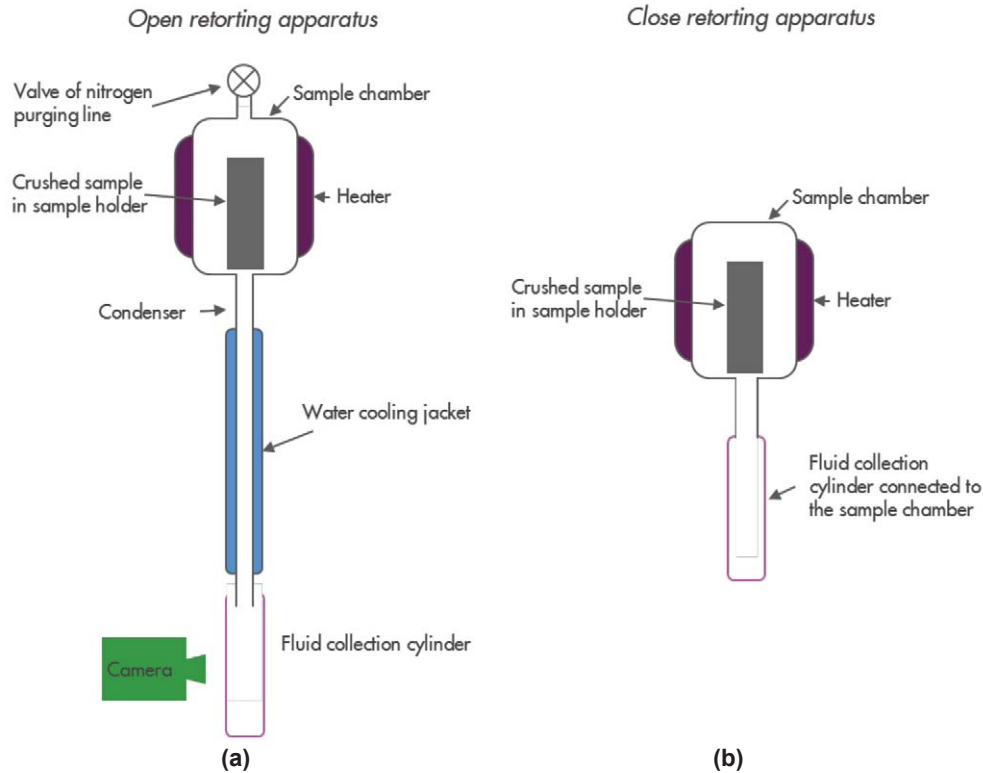


Fig. 6—Design illustration of the open-retorting apparatus (a) and closed-retorting system apparatus (b).

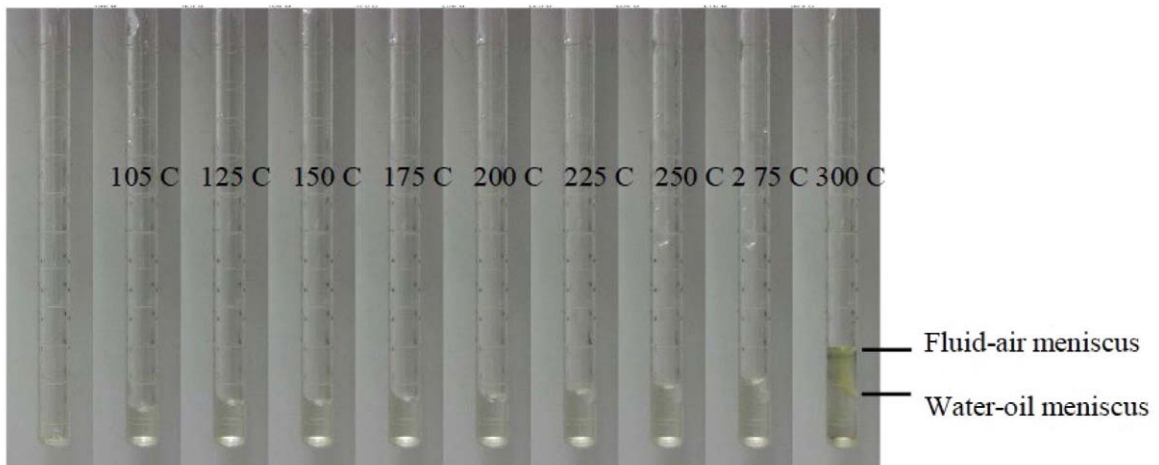


Fig. 7—Pictures of the fluid collection cylinders acquired at different stages of the open-retorting experiment.

Periodic nitrogen injection creates elevated gas pressure in the sample chamber. This eliminates fluid hold-up in the condenser of the retorting system. Fluid released by the sample at a specific temperature is condensed and collected in the fluid collection cylinder almost simultaneously with its release. The pictures of the fluid collection cylinder are taken not only at the end of each temperature step of the retorting experiment but every 30 seconds during the entire open-retorting experiment. Collected images are processed using a proprietary algorithm and the evolution of the fluid level during the retorting experiment is derived in the form of a color map (see Fig. 8). Such maps allow the derivation of more accurate volume values for oil and water collected at different steps of the open-retorting experiment.

The closed-retorting apparatus uses a design where the fluid-collection cylinder is hermetically connected to the sample chamber. In the case of the design shown in Fig. 6, even when the sample chamber is at 300°C, most of the fluid-collection cylinder is at ambient temperature because of the low thermal conductivity of glass. The limitation of this design is that it does not allow for the accurate quantification

of fluids released by the sample during different temperature steps. The main reason for this is the very slow formation of large fluid droplets, which are required before the fluids can reach the bottom of the cylinder and be quantified. However, this design does allow for the collection of virtually all fluid released by the sample including most of the heavier HC components not quantified by the open-retorting apparatus, which are condensed at the walls of the fluid collection cylinder. After the closed-retorting experiment is finished, the fluid-collection cylinder is disconnected from the sample chamber to quantify the mass of collected fluid. Comparison can then be made with the sample mass loss during the same retorting experiment.

CASE STUDY: WOLFCAMP A

Six pairs of twin samples of Permian Wolfcamp A formation were used to test the GRI+ workflow. Twin samples allow repeatability assessment of different measurements employed by the GRI+ workflow.

Figure 9 shows the comparison of the total NMR signal

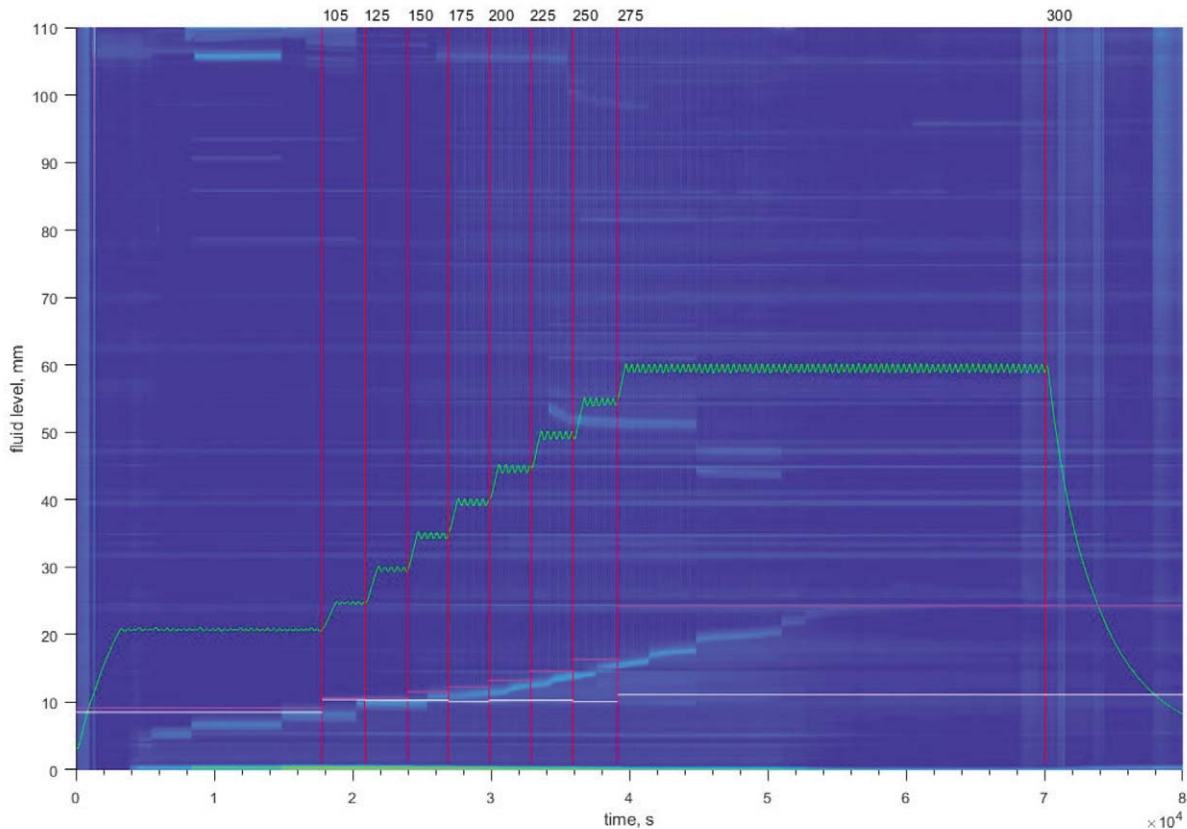


Fig. 8—An example of the fluid-level evolution map generated from the pictures of the fluid-collection cylinder acquired during the open-retorting experiment; the green line indicates the temperature evolution during the open-retorting experiment; vertical red lines mark the ends of different temperature stages; horizontal magenta lines mark the locations of the fluid-air meniscus at the end of each temperature stage; horizontal white lines mark the locations of the oil-water meniscus at the end of each temperature stage.

acquired for AR plug and crushed samples used in this study. The comparison indicates that crushing causes the decrease of total fluid concentration by $\sim 14\%$ for the samples from the Wolfcamp A formation. It also shows that sample sieving does not impact fluid loss, as data points acquired for samples that were crushed but not sieved are occupying the same trend line as data points acquired for samples that were crushed and sieved.

The analysis of the results of decomposition of acquired NMR T_2 distributions suggest that mainly water is lost during crushing (Nikitin et al., 2017). Indeed, the comparison of the intensities of NMR T_2 -distribution components corresponding to HC associated with immovable OM (Peak 1) and corresponding to water present in the samples (Peaks 2 and 3) before and after crushing (Fig. 10) indicates that Peak 1 is barely changed by the sample crushing. At the same time the decrease of the intensity of Peaks 2 and 3 caused by the crushing process is comparable with the decrease of the total intensity of the NMR T_2 distribution. This indicates that, at least in the case of Wolfcamp A formation core samples, it is

mainly water that is lost during sample crushing and not HC fluid, as has been assumed by vendors providing crushed-rock core analysis services (Weatherford Laboratories, 2012; CoreLab, 2017).

Figure 11 compares the results of the closed- and open-retorting experiments performed on six sets of twin pairs. A typical value of the fluid-collection efficiency (defined as the ratio of the mass of collected fluid to the sample mass loss) for the closed-retorting experiment is $\sim 98\%$, and for the open-retorting experiment is $\sim 90\%$. If the data points corresponding to a closed-retorting experiment that failed due to poor sealing of the sample chamber are excluded from analysis (filled points in Fig. 11), the average measurement of extracted fluid volumes from core samples during either open or closed-retorting experiments is $\sim 5\%$.

The comparison of the total volumes of water collected in open and closed-retorting experiments (Fig. 12) show that on average, the open-retorting apparatus collects ~ 8 to 10% less water than the closed-retorting apparatus.

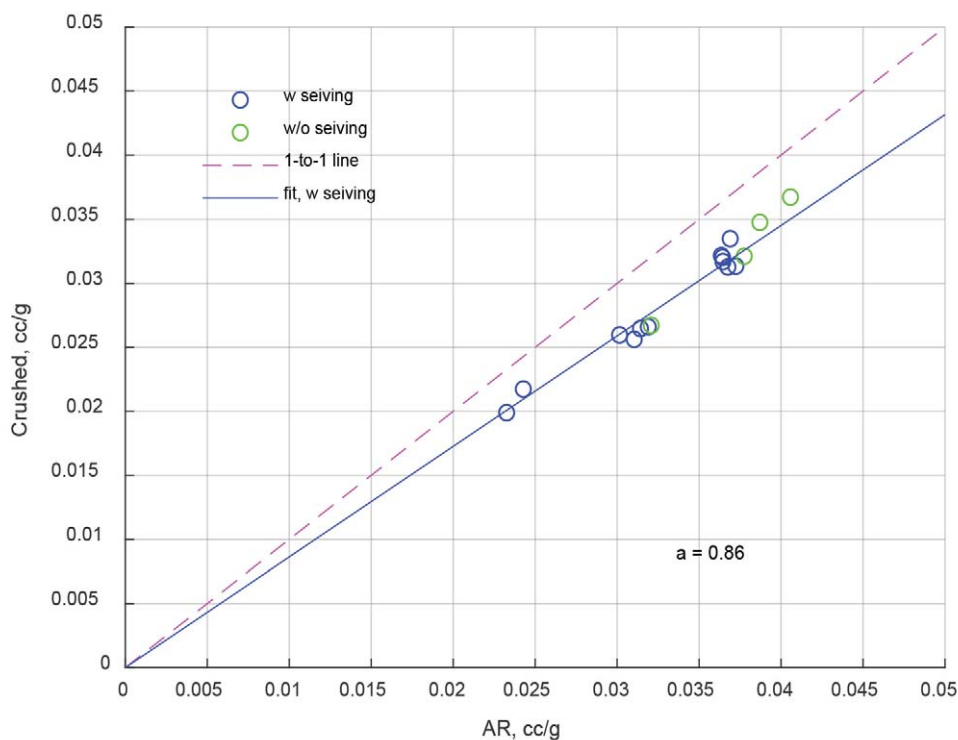


Fig. 9—Dependence of the NMR signal in water volume per mass of the crushed core material on the NMR signal in water volume per mass of the AR core material for the same samples; green points represent crushed samples without sieving; blue points represent sieved samples (as recommended in GRI+ workflow).

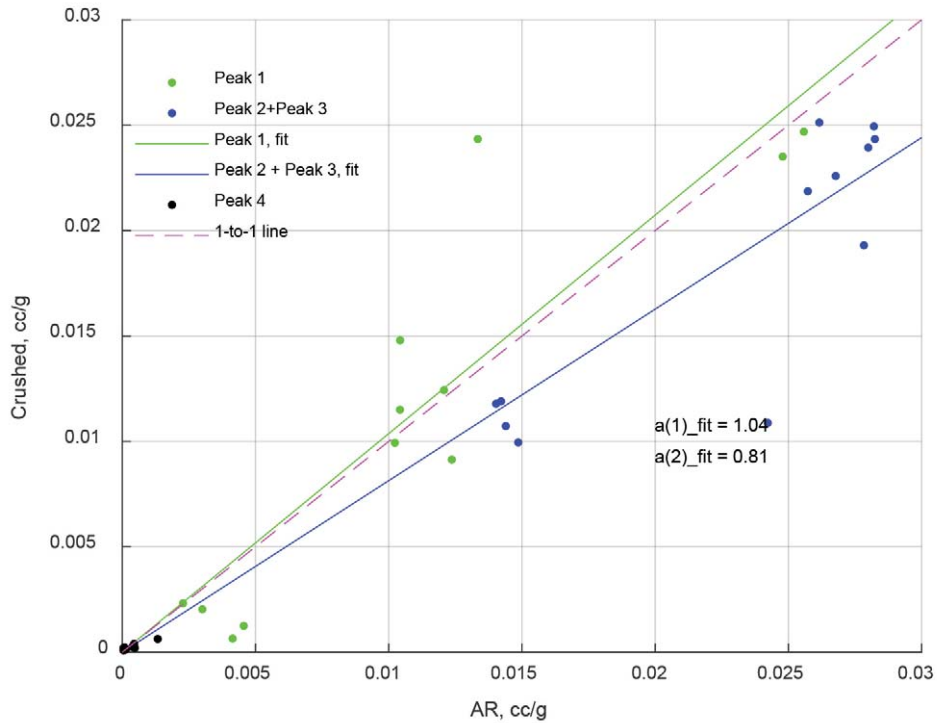


Fig. 10—Intensities of NMR T_2 -distribution components for plug samples versus crushed samples; here Peak 1 corresponds to HC associated with immovable OM, Peaks 2 and 3 are due to water and Peak 4 is due to oil in matrix pores (Nikitin et al., 2017).

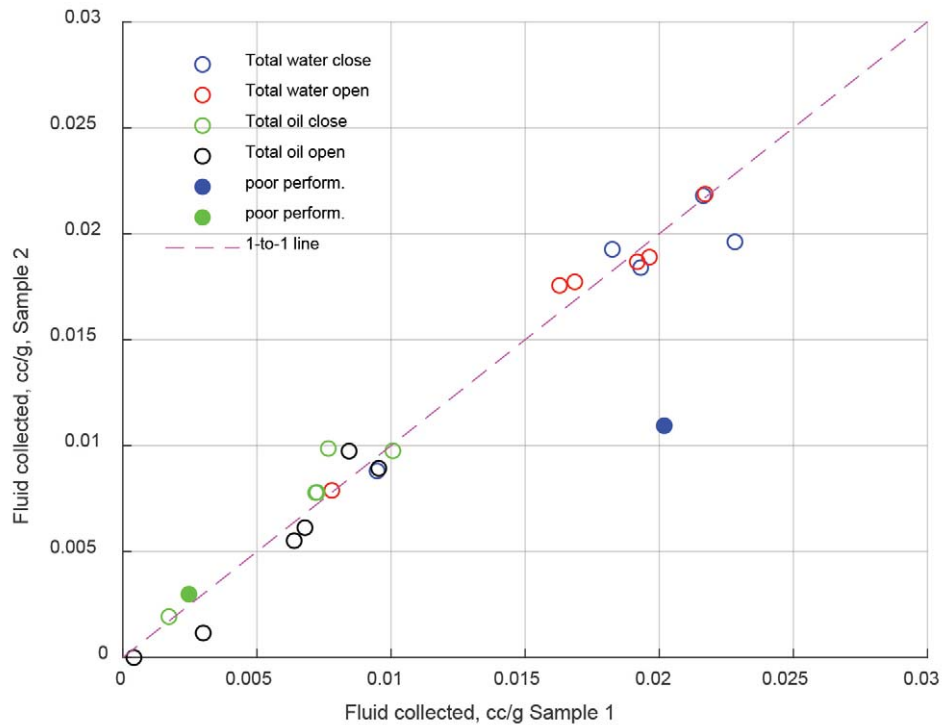


Fig. 11—Comparison of the fluid volumes collected in open- and closed-retorting experiments for samples from twin pairs; filled data points correspond to the closed-retorting experiment with very low collection efficiency caused by a failed seal in the closed-retorting apparatus.

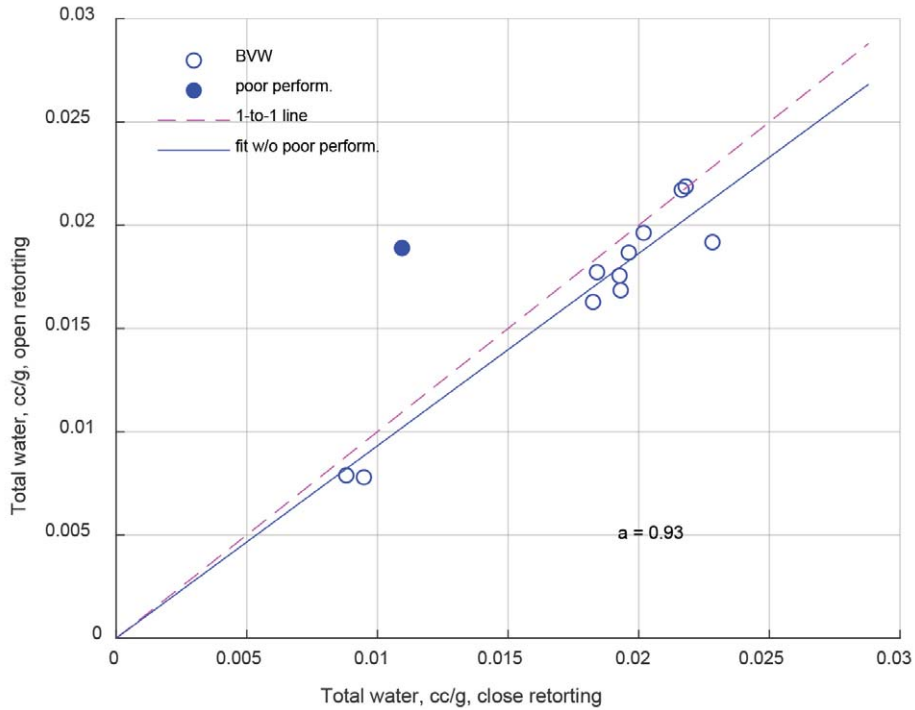


Fig. 12—Comparison of volumes of water collected in open-retorting experiment and volumes of water collected in closed-retorting experiment for the same samples; the filled data point corresponds to the closed-retorting experiment with very low collection efficiency caused by the failed seal of the closed-retorting apparatus.

For the grain-volume measurements at different steps of the GRI+ workflow, the PDP-300 porosimeter by Metarock Laboratories with custom modifications is used. Figure 13 compares the results of grain-volume measurements on twin

plugs for samples before (AR) and after (dry) extraction in the closed-retorting experiments (Steps 6 and 9, respectively). Here grain volumes are converted into total porosity units.

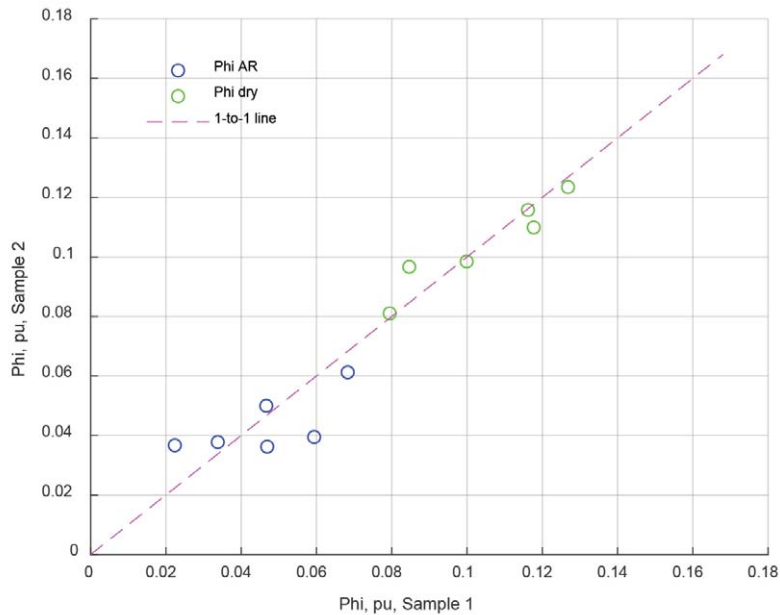


Fig. 13—Comparison of results of grain-volume measurements in porosity units for samples from twin pairs; blue circles correspond to AR crushed samples; green circles correspond to post-retorting crushed samples.

This comparison in Fig. 13 indicates that grain-volume measurements performed for post-retorting or dried samples have an average uncertainty of ~5% that is ~3 times better than the average uncertainty of grain volume measurements performed for AR samples (~18 %). The reason for such difference is different modes of porosimeter operation. In the case of AR samples, the lost fluid from the samples should be minimized during grain-volume measurements, and thus the porosimeter must be operated in “vacuum off” mode when air present in the sample chamber is not removed during the grain-volume measurement. As a result, helium gas from the reference volume mixes with the air from the sample chamber. The formed gas mixture has a temperature that could be substantially different from the temperature at which the calibration of the porosimeter is valid. This increases the uncertainty of the volume measurement for AR samples. Post-retorting or dried samples do not contain any fluid to preserve, thus the porosimeter can be operated in “vacuum on” mode when air from the sample chamber is removed by the vacuum pump before helium gas is released

from the reference volume. In this case, both the sample chamber and reference volume are filled with pure helium gas at the end of the grain-volume measurement, providing lower measurement uncertainty.

As mentioned above, the range of uncertainties for $\Phi_{\text{tot ver1}}$ and $\Phi_{\text{tot ver2}}$, derived from fluid summation and comparison of bulk and grain volumes respectively, should be comparable. However, previous datasets from other crushed-rock core analysis workflows saw an average of ~20% difference in porosity calculations, ~1.5 p.u. Figure 14 demonstrates that better agreement is achieved using the GRI+ workflow. Data points in this plot follow the 1:1 trendline with approximately 1% average uncertainty, indicating a very high degree of consistency of both raw data and their interpretation. In this case, the BVW value used in (Eq. 1) to calculate $\Phi_{\text{tot ver1}}$ was corrected for the efficiency of the water collection from each closed-retorting experiment. BVW was calculated as BVW/α_{ret} where the typical value of α_{ret} was equal to 0.98 as was discussed above.

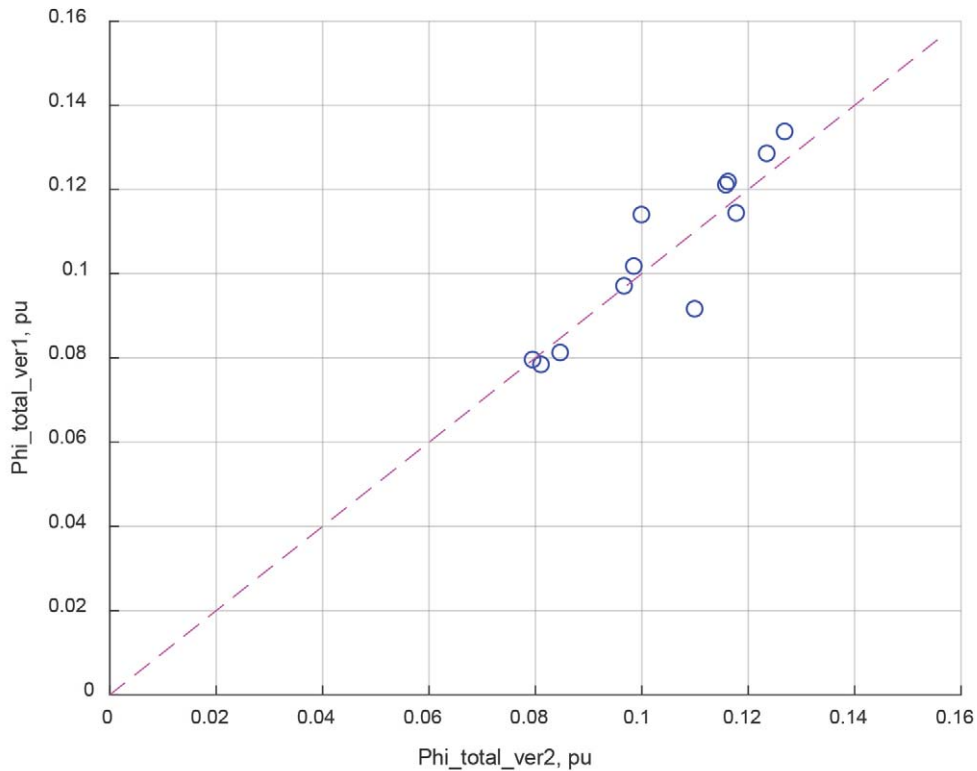


Fig. 14—Comparison of total porosity values derived from fluid summation and from the comparison of bulk volume and dry grain-density volume.

DISCUSSION: SATURATION ESTIMATION

As previously highlighted (Blount et al., 2017), the interpretation of data collected from crushed-rock core analysis (CR) workflows using thermal methods of fluid extraction assumes that the fluid not collected in the retorting experiment is mainly light HC. Also, volumes of extracted fluids are not corrected to account for the losses that occur during sample crushing and handling. As a result, water saturation is calculated according to Eq. 3:

$$Sw_{CR} = \frac{BVW}{BVW+BVO/\alpha_{ret} + Phi_{air}} \tag{3}$$

where BVW is the volume of water extracted from the sample during open retorting divided by the bulk volume of the sample used in the open-retorting experiment (in p.u.), BVO is the volume of oil extracted from the sample during open retorting divided by the bulk volume of sample used in the open-retorting experiment (in p.u.), α_{ret} is the open-retorting apparatus efficiency, which is equal to the ratio of the extracted fluid mass and sample weight loss, and Φ_{air} is the total porosity for the AR sample or air-filled porosity.

In the case of the GRI+ workflow, water saturation is calculated using Eq. 4:

$$Sw_{GRI+} = \frac{BVW/(\alpha_{ret}*\beta_{crush})}{(V_{bulk}-V_{grain})/V_{bulk}} \tag{4}$$

where BVW is the volume of water extracted from the sample during closed retorting divided by the bulk volume of the sample used in the closed-retorting experiment (in p.u.), α_{ret} is the closed-retorting apparatus efficiency which is equal to the ratio of the extracted fluid mass and sample weight loss, β_{crush} is the fluid preservation during crushing derived from NMR measurements for the AR and crushed sample, V_{grain} is the dry grain volume of the sample used in the closed-retorting experiment (in cm³), and V_{bulk} is the bulk volume of the sample used in the closed-retorting experiment.

Data acquired for the 12 samples from the Wolfcamp A formation were used to calculate Sw_{CR} according to Eq. 3 using BVW and BVO from the open-retorting experiments and Sw_{GRI+} according to Eq. 4 using BVW from the closed-retorting experiments. The comparison of Sw_{GRI+} and Sw_{CR} is shown in Fig. 15. On average, Sw_{GRI+} values are ~32% (or ~15 s.u.) higher than values of Sw_{CR} . However, typical commercial retorting systems have much lower fluid collection efficiency than the open-retorting system employed by the GRI+ workflow. Therefore, Sw_{CR} may be even lower than what was calculated in this study.

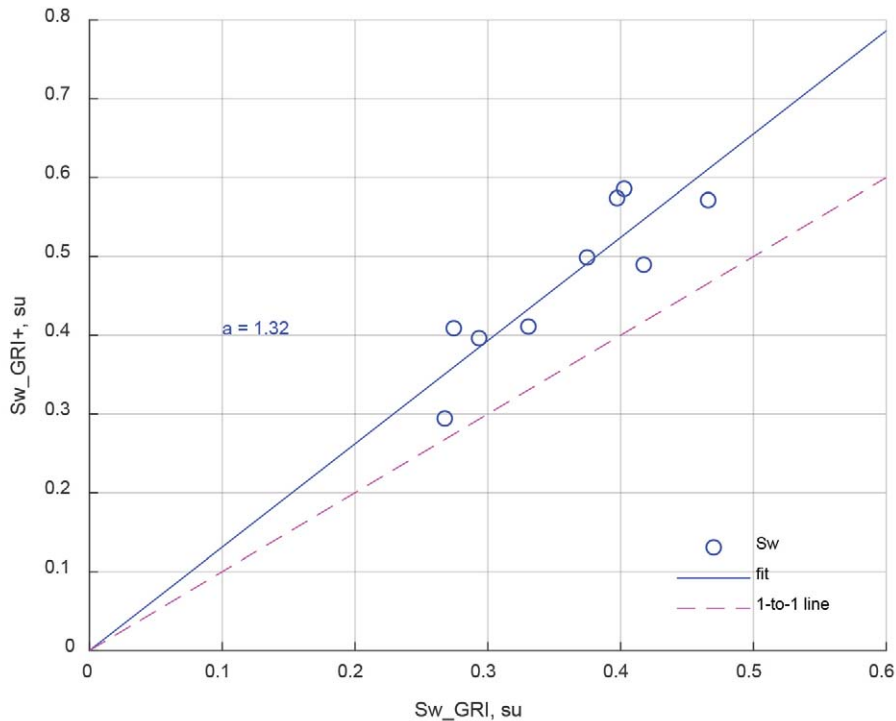


Fig. 15—Comparison of water saturation derived from acquired data according to (Eq. 3) with water saturation derived from the same data according to (Eq. 4).

CONCLUSIONS

The GRI+ workflow presented in this paper employs several measurement innovations that overcome the challenges faced by other crushed-rock core analysis workflows. Three key innovations are (1) a universal sample holder for crushed core material, (2) an NMR relaxometer sensor with increased axial uniformity of the response function, and (3) improved open and closed-retorting apparatus designs.

The universal sample holder limits losses of the solid material from the crushed core sample during the multiple measurement steps of the GRI+ workflow. As a result, reliable total porosity values can be derived from the comparison of sample bulk volume and grain volume measured for the dried sample. The NMR relaxometer sensor with increased axial uniformity of the response function, enables quantification of the different fluids (HC and water) lost from the AR plug samples during crushing. Closed- and open-retorting apparatuses improve volume measurements of different types of water and light HC present in the crushed core sample to a high degree of accuracy using only 60 to 80 grams of core material.

The data quality and information acquired using the GRI+ workflow are significantly improved as a result of these innovations, providing the analyst the ability to reduce and address uncertainty and systematic biases from core analysis results. For example, in the case of the Wolfcamp A formation, results from the GRI+ workflow reduce uncertainty in the porosity estimation, which can be introduced simply by choice of calculation methodology (Eq. 1 versus Eq. 2) for standard workflows. Even more importantly, the results suggest that previous crushed-rock core analysis leads to considerably biased water saturation estimations, such that we expect these methods may underestimate S_w by at least 30% or ~15 s.u. While the case study was limited to six depths of Wolfcamp A core from a single well, the results provide better alignment of S_w and the water cuts observed from production in the corresponding area.

Our next steps include analysis of multiple lithologies, formations, and maturities, as well as using these learnings to investigate correcting legacy core data to improve saturation modeling and our ability to predict water production. We recommend an industry-wide consortium to further improve and enhance GRI+ workflows and to help establish a new industry standard for the routine measurement of fluid saturations in tight, low-permeability rocks.

ACKNOWLEDGEMENTS

The authors thank the management of Shell's Permian Asset for permission to present these findings.

NOMENCLATURE

Abbreviations

AS	= as received
BVW	= bulk volume water, p.u.
BVW _{cb}	= capillary-bound water, p.u.
BVW _{free}	= bulk volume free water, p.u.
BVO	= bulk volume oil, p.u.
CONV	= conventional core
CR	= crushed-rock analysis
EOM	= extractable organic matter
GRI	= Gas Research Institute
HC	= hydrocarbon
OM	= organic matter
ORM	= organic-rich mudstone
Phi _{air}	= air-filled porosity, p.u.
Phi _{tot ver1}	= total porosity calculated using summation of fluids
Phi _{tot ver2}	= total porosity calculated using bulk and grain volumes
PRSWC	= pressurized rotary sidewall cores
p.u.	= porosity units
QC	= quality control
RSWC	= rotary sidewall core
SOM	= solid organic matter
s.u.	= saturation units
TOC	= total organic carbon
TOC _{imm}	= immovable organic matter, wt%
XRF	= X-ray fluorescence
XRD	= X-ray diffraction

Symbols

α_{ret}	= collection efficiency of the retorting system equal to the ratio of the weight of the collected fluid and sample weight loss
β_{crush}	= fluid preservation coefficient during crushing derived from NMR measurements for the as-received and crushed samples
S_w	= water saturation, s.u.
S_{wCR}	= water saturation from crushed-rock analysis (open retorting)
S_{wGRI+}	= water saturation from GRI+ workflow
T_2	= NMR transverse relaxation time
V_{bulk}	= bulk volume, g/cm ³
V_{grain}	= marix grain volume, g/cm ³

REFERENCES

- Blount, A., Croft, T., Driskill, B., and Tepper, B., 2017, Lessons Learned in Permian Core Analysis: Comparison Between Retort, GRI, and Routine Methodologies, *Petrophysics*, **58**(5), 517–527.
- Blount, A., McMullen, A., Durand, M., Croft, T., and Driskill, B., 2019, Maintaining and Reconstructing In-Situ Saturations: A Comparison Between Whole Core, Sidewall Core, and Pressurized Sidewall Core in the Permian Basin, *Petrophysics*, **60**(1), 50–60. CoreLab, 2017, <http://www.corelab.com/ps/gri-analysis>
- Handwerker, D.A., Keller, J., and Vaughn, K., 2011, Improved Petrophysical Core Measurements on Tight Shale Reservoirs Using Retort and Crushed Samples, Paper SPE-147456 presented at the SPE Annual Technical Conference and Exhibition, Denver, Colorado, USA, 30 October–2 November. DOI: 10.2118/147456-MS.
- Luffel, D.L., and Guidry, F.K., 1992, New Core Analysis Methods for Measuring Reservoir Rock Properties of Devonian Shale, Paper SPE-20571, *Journal of Petroleum Technology*, **44**(11), 1184–1190. DOI: 10.2118/20571-PA.
- Nikitin, A., Dolan, S., Reiderman, A., Grover, R., and Blount, A., 2017, The Application of the Combination of NMR Logging and NMR Measurements at RSWC Samples at the Well Site to Identify Producing Oil in Tight Rocks, Paper P, *Transactions, SPWLA 58th Annual Logging Symposium*,
- Scanlon, B.R., Reedy R.C., Male, F., and Walsh, M., 2017, Water Issues Related to Transitioning From Conventional to Unconventional Oil Production in the Permian Basin, *Environmental Science and Technology*, **51**(18), 10903–10912. DOI: 10.1021/acs.est.7b02185.
- Weatherford Laboratories, 2012, Source rock properties protocol description.

ABOUT THE AUTHORS

Anton Nikitin is a Research and Development Petrophysicist at Shell Technology Center, Houston (USA), where he works on fundamental petrophysics of unconventional reservoirs and new subsurface data acquisition technologies. Prior to joining Shell, he spent four years with Baker Hughes developing wireline and LWD formation evaluation tools. He graduated from Stanford University in 2008 with a PhD in applied physics.

Melanie Durand is a Petrophysicist on Shell's Permian Asset. After joining Shell in 2012, Melanie has worked on projects in Brazil, Argentina, and Colombia before transitioning to the Permian Basin. Melanie has a deep breadth of operational experience in both wireline and core acquisition. She has a BS in Mathematics from the University of Louisiana at Lafayette.

Adam McMullen is a Petrophysicist on Shell's Permian Asset. He joined Shell in 2017 after completing his MS in Petroleum Engineering at the University of Texas at Austin and BS in Mechanical Engineering at Rice University. His research focused on laboratory core analysis, and his experience therein was greatly beneficial for this work.

Aidan Blount is an Opportunity Advisor and Petrophysicist with Shell. He joined the company in 2013 after graduating from The University of Texas at Austin with a BS in Petroleum Engineering. Since joining Shell, Aidan worked on several basins as part of a regional exploration team before joining the Permian Asset in 2015. Aidan received the *Best Paper* award for the 2017 SPWLA Symposium. He is also an SPWLA Distinguished Lecturer, 2017–2018 and 2018–2019.

Brian Driskill is Petrophysics Advisor and Exploration Geology Advisor for Shell's Permian Asset. He has 30 years of experience in petrophysics, geophysical modeling, and geology in onshore and offshore domestic and international projects. He has worked in Shell's Unconventionals business since 2010.

Amie Hows is a Research Petrophysicist and Manager of the Petrology and Rock Properties Technology team at Shell Technology Center, Houston (USA). She has a PhD in Geomechanics from Stanford University and joined Shell in 2007.

Regular Submissions

NMR Evaluation of Light-Hydrocarbon Composition, Pore Size, and Tortuosity in Organic-Rich Chalks

Zeliang Chen¹, Philip M. Singer¹, Xinglin Wang¹, Harold J. Vinegar², Scott V. Nguyen³, and George J. Hirasaki¹

ABSTRACT

In this paper, we use core-log integration to estimate the hydrocarbon composition, pore size, and tortuosity in an organic-rich chalk formation.

Our core analysis consists of pressure saturation of the as-received reservoir core plugs followed by in-situ NMR T_1 - T_2 and D - T_2 measurements. The saturating fluids include water and light hydrocarbons, including methane, ethane, propane, *n*-butane, *n*-pentane, and *n*-decane.

The laboratory-measured T_2 distributions of the hydrocarbon-saturated cores are converted to the downhole T_{2app} (T_2 apparent) log by simulating the effects of diffusion in the magnetic-field gradient of the NMR logging tool. The simulated T_{2app} log is compared to the actual log to estimate the qualitative downhole hydrocarbon composition by minimizing the least-squares error.

The simulated downhole T_1/T_{2app} based on the laboratory-measured T_1/T_2 illustrates contrasts between saturating fluids and, therefore, can be used for qualitative fluid typing. We also find that methane and natural gas liquids (NGLs) can be well distinguished from water and heavier hydrocarbons by applying T_{2app} and T_1/T_{2app} 2D cutoffs.

The laboratory-measured restricted diffusivity indicates that the saturating methane can be distinguished from liquid-state hydrocarbons by its higher diffusivity. In addition, the laboratory-measured restricted diffusivities of different light hydrocarbons are fitted to the Padé approximation to estimate the mean pore size, heterogeneity length scale, and tortuosity of the light-hydrocarbon filled porosity.

INTRODUCTION

The recent advances in horizontal drilling and hydraulic fracturing make gas (i.e., methane) and natural gas liquids (NGLs) production from tight reservoirs possible and economical. As a result, the fast-paced growth in the global gas and NGLs production stimulates research interests in this area. NMR was used as a valuable tool for data acquisition because of the versatile and nondestructive natures (Hürlimann et al., 2009; Kausik et al., 2011; Wang et al., 2014; Sigal, 2015; Fleury and Romero-Sarmiento, 2016; Valori et al., 2017; Tinni et al., 2018; Thern et al., 2018). NMR logging and laboratory NMR core analysis continue to contribute significantly to formation evaluation.

NMR measurements on methane-saturated tight rocks are valuable but challenging due to the lower hydrogen index (HI) compared to other liquid-state hydrocarbons. Several recent NMR studies on methane-saturated rock demonstrate the capability of standard low-field NMR (2.3 MHz) benchtop relaxometers and logging tools to capture the signal from methane at achievable pressures. Kausik et

al. (2011) investigates the dynamics of methane in kerogen and report the T_2 and diffusivity of methane are greatly reduced in shale, while the HI is increased, compared to the bulk state. Valori et al. (2017) develop a new methodology to estimate the permeability of gas-bearing shale using NMR-measured methane-saturated T_2 . The research by Tinni et al. (2018) illustrates the effect of methane adsorption on gas production through laboratory NMR measurements.

NMR T_1/T_2 ratio has been proposed as a promising technique for fluid typing and composition estimation early on (Kausik et al., 2016; Singer et al., 2016; Singer et al., 2017a; Singer et al., 2018a; Chen et al., 2017). The research on this technique has recently been extended to gas and NGLs. Thern et al. (2018) studied the responses of methane and propane in activated carbon and shale. They found that hydrocarbon (e.g., propane) is dissolved in kerogen within the shale and tends to yield higher T_1/T_2 , which agrees with previous findings (Yang et al., 2012; Kausik et al., 2016; Singer et al., 2016; Chen et al., 2017). Thern et al. (2018) suggest hydrocarbons in nanoscale pores can be separated from hydrocarbons in intergranular pores by either the T_2

Manuscript received by the Editor June 7, 2019; revised manuscript received August 30, 2019; manuscript accepted September 5, 2019.

¹Department of Chemical and Biomolecular Engineering, Rice University, 6100 Main St., Houston, TX 77005, USA; zlc814@gmail.com; ps41@rice.edu; xw51@rice.edu; gjh@rice.edu

²Vinegar Technologies LLC, 4613 Laurel Street, Bellaire, TX 77401, USA; harold@vinegartech.com

³Braket Technologies, 2400 Homedale Cir, Austin, TX 78704, USA; scott@brakettech.com

cutoff or T_1/T_2 cutoff. The research conducted by Fleury and Romero-Sarmiento (2016) using higher frequency (23 MHz) NMR also suggests exploiting T_1/T_2 for methane identification.

Besides T_1/T_2 , diffusivity (D) measurement by NMR is widely implemented for composition estimation. Hürlimann et al. (2009) confirm that $D-T_2$ measurements contain detailed information about the composition of hydrocarbons. It is demonstrated that methane can be identified by high diffusivity values, even when dissolved in crude oil or kerogen (Hürlimann et al., 2009; Kausik et al., 2011).

The first topic of our research is the evaluation of hydrocarbon composition (i.e., methane and NGLs composition) by T_2 , T_1/T_2 , or D contrast. The differential composition is a critical input to formation evaluation because of the difference in economic value between methane, the NGLs (i.e., ethane, propane, butane, and pentane), and pentane plus. The differential composition is also important in terms of the completion strategy to take advantage of value difference. Note that ethane, propane, and butane are also known as condensates. Methane is a gas generally used for heating and electricity, with a relatively low value in the United States. However, propane, butane, and pentane (a component of natural gasoline) sell for approximately the same price as crude oil. Ethane is also highly prized due to its use as a petrochemical feedstock in ethylene manufacturing. Therefore, the prior knowledge of methane and NGLs composition contributes to reservoir valuation estimates. Our research proposes a new method of determining the volumetric composition and saturation of methane and NGLs in a petroleum reservoir using NMR logging integrated with NMR core analysis.

The second topic of our research is the evaluation of the mean pore size, heterogeneity length scale, and tortuosity of the light-hydrocarbon-filled porosity using NMR restricted diffusion measurements. The mean pore size, heterogeneity length scale, and tortuosity are closely related to the permeability, which determines the producibility of a formation. Thereby, these three petrophysical properties play critical roles in reservoir engineering. Our research proposes a new method of determining the mean pore size, as well as the tortuosity and the heterogeneity length scale, in a petroleum reservoir using NMR core analysis.

This article is organized as follows. The NMR specifications and experimental details, including petrophysical properties of cores and laboratory core saturation procedure, are presented in the Experimental Details section. This is followed by the three types of NMR measurements associated with the analysis, which are divided into individual sections for T_2 , T_1/T_2 , and D . The section for T_2 includes simulations of downhole T_2 logs (namely T_{2app})

and a core-log calibration showcases how to estimate the composition. The section for T_1/T_2 incorporates simulations of downhole-measured T_1/T_{2app} and shows how T_1/T_{2app} can be used for fluid typing and composition estimation. The section for D shows how the Padé approximation is used to interpret the restricted diffusivity and estimate the mean pore size, etc. The Conclusions section summarizes the findings.

EXPERIMENTAL DETAILS

Petrophysical Properties

The core samples used in this work are from the late Cretaceous upper Ghareb formation in the Golan Heights basin in Israel. The Maastrichtian age was one of marine upwelling, high surface productivity, and intermittent bottom water anoxia. This led to a matrix that consists of microcrystalline calcite (micrite) intermixed with high concentrations of organic matter. The upper Ghareb formation in this basin consists of organic-rich bituminous foraminiferal chalks.

These organic-rich chalks are tight rocks with a horizontal permeability (Klinkenberg corrected) of 0.017 mD. The TOC (total organic carbon) of the organic-rich chalks is ~10 wt% (or ~20 vol%), and the kerogenous matter is early-stage mature Type II-S kerogen.

Figure 1 shows an SEM photograph highlighting the calcite matrix and organic matter (OM). The macropore size shown in Fig. 1 is about a few microns, which agrees with the pore size estimated by the Padé approximation shown in the following section.

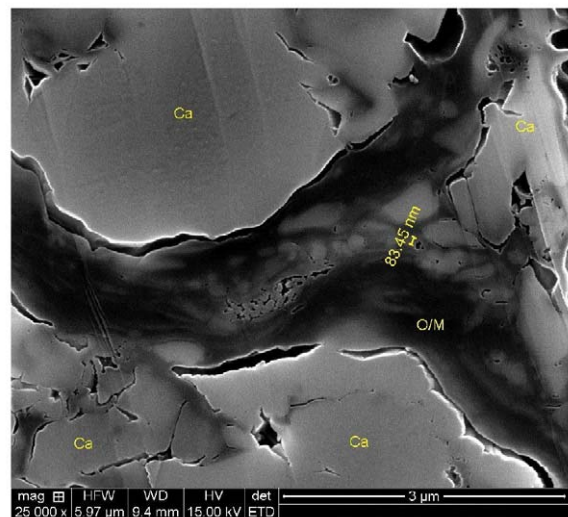


Fig. 1—SEM photograph of a core from the upper Ghareb formation. Note that the pore size illustrated in this figure is comparable to the pore size estimated by the Padé approximation shown in the following section.

Figure 2, performed by Weatherford Laboratories, illustrates a secondary electron image (Fig. 2a) and a backscatter electron imaging (Fig. 2b). The SEI photograph emphasizes fine-scale surface features including micropores. The BEI photograph displays grayscale variations in backscatter coefficient (minerals like calcite with a high atomic number appear white, while matter with relatively low atomic number such as organic matter appears dark grey). Figure 2c illustrates an energy-dispersive (EDS) spectral map of the same field of view seen in the SEI and BEI photographs. A color phase key is shown in Fig. 2d together with the volumetric abundance of various phases by EDS.

Table 1 shows the mineral composition by XRD. The major mineral component is calcite, with secondary amounts of quartz and apatite. There are very small amounts of clay

and pyrite.

The well was drilled with water-based mud. All downhole operations in the reservoir zone were underbalanced to prevent invasion and flushing.

The Baker Hughes MREX logging tool was logged in PoroPerm+Light Oil mode with a $T_{wait} = 16$ seconds. The logging was performed with the slowest logging speed of 0.6 m/min. The vertical resolution was 0.6 m.

Table 2 shows a summary of laboratory core analysis performed at Ben-Gurion University Center for Petroleum and Environmental Science including Rock Eval TOC and T_{max} , Coreval nitrogen gas porosity, bitumen-filled porosity (by extraction), and total porosity (sum of Coreval porosity and bitumen-filled porosity), and horizontal permeability (Klinkenberg-corrected).

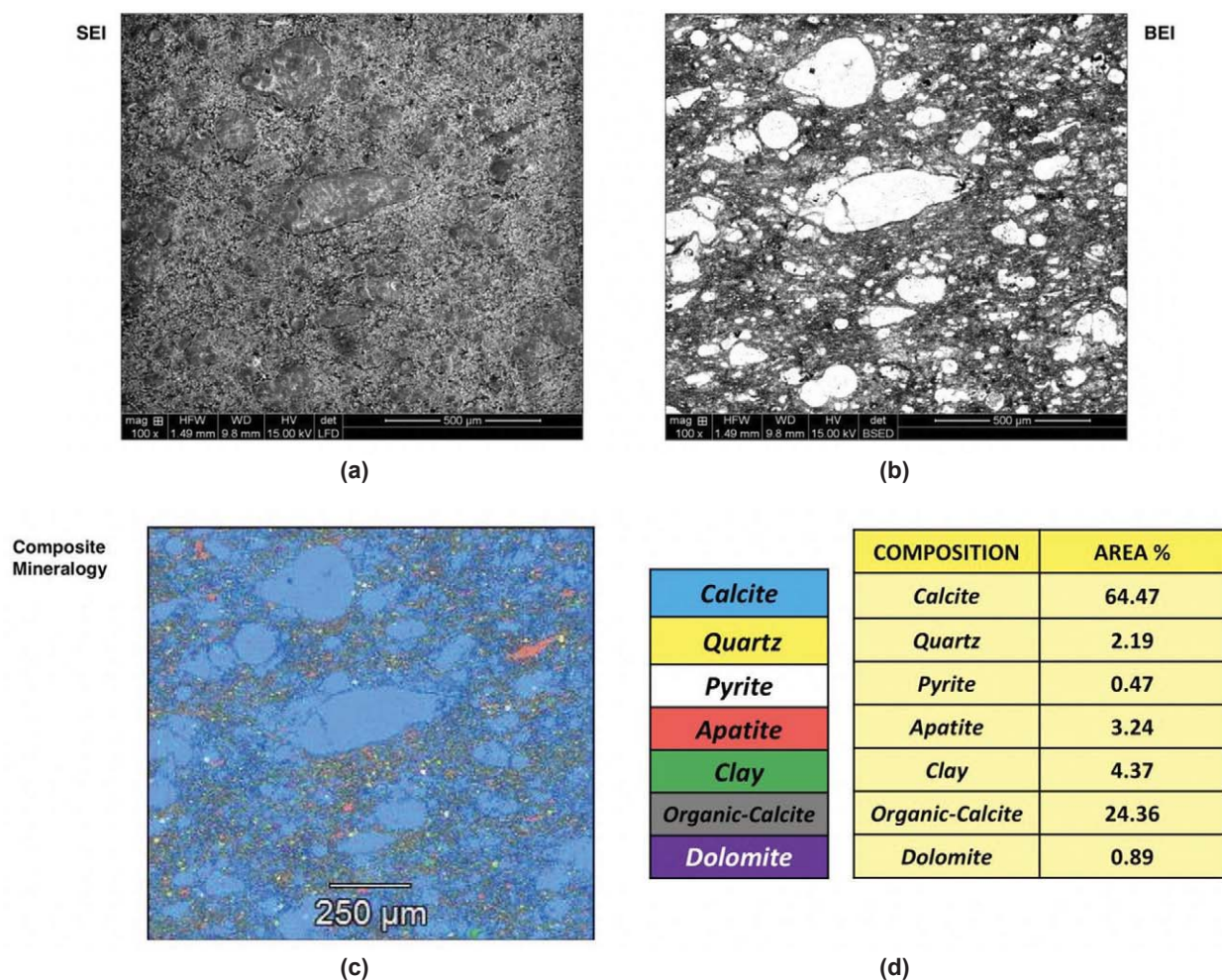


Fig. 2—Photomicrographs of a polished thin section of a foraminiferal chalk from the upper Ghareb formation, including (a) a secondary electron image (SEI), (b) a backscatter electron imaging (BEI), (c) an energy dispersive spectroscopy (EDS) spectral map of the same field of view illustrated in the SEI and BEI photographs, and (d) a color-phase key with the volumetric abundance of various phases (bottom right table). Petrophysically, the cores consist of water-wet micritic calcite that leads to water-wet micropores and intergranular macropores containing kerogen, bitumen, light hydrocarbons, and small quantities of connate water. The macropores are mixed-wet since the kerogen is prone to be oil-wet.

Table 1—Mineralogy by XRD

Mineral	Volume (%)
Calcite	88
Quartz	1.6
Apatite	6.4
Clay	3
Pyrite	1
Dolomite	Trace

Table 2: Summary of Core Analysis of the Core Samples

Property	Value
Rock Eval TOC (wt %)	9.8
T_{\max} (°C)	424
Total porosity (p.u.)	29.2
Bitumen-filled porosity (p.u.)	3.6
Coreval nitrogen-porosity (p.u.)	25.7
Horizontal permeability (Klinkenberg-corrected) (mD)	0.017

NMR Measurements

An Oxford Instruments GeoSpec2 rock-core analyzer with a resonance frequency of $\omega/2\pi = 2.3$ MHz for ^1H (similar to downhole NMR logging tools) was used to acquire the NMR data. The measurements were conducted in an Oxford Instruments overburden core holder at either laboratory or reservoir conditions, which are discussed in the following subsection. The 2D T_1 - T_2 data are acquired using 32 log-spaced points on an inversion-recovery curve ranging from 0.2 to 20,000 ms (typically). Each point on the inversion-recovery curve is followed by a series of CPMG echoes with an echo spacing of $T_E = 0.2$ ms. The 2D D - T_2 data were acquired using a unipolar stimulated-echo sequence (Mitchell et al., 2014) with 32 pulsed-field trapezoidal gradient steps ranging from zero to a maximum strength of $g_y = 43$ G/cm, a gradient encoding time of $\delta = 9$ ms, a diffusion evolution time of $\Delta = 14.7$ ms, and a dead time of $T_d = 25$ ms. The 2D correlation maps were processed using the fast inverse Laplace transform (analogous to Venkataramanan et al., 2002) with 120 (480 for higher resolution only for T_1/T_2 and $T_1/T_{2\text{app}}$ analysis) log-spaced bins for T_1 , T_2 and D . The units of the y -axis on the relaxation time distributions are in “p.u./div”, which means porosity units per x -axis bin-size. In the case of T_2 distribution, the bin size is “div = $\Delta \log_{10} T_2 = (\log_{10} T_{2,i+1} - \log_{10} T_{2,i})$ ”, which is independent of index “ i ” because of the log-spaced bin selection. This unit of the y -axis is also known as bin porosity.

Core Plugs and Fluid Saturations

The well is a vertical well where a conventional (3.25-in. diameter \times 30-ft long) vertical core was taken. At the wellsite, the core was removed from the barrel, sealed in plastic wrap and aluminum foil, and dip-coated in low-melting paraffin to prevent evaporation. In the laboratory, plugs were cut through the core perpendicular to the axis of the core. Therefore, the core plugs are horizontal. We selected the 48-mm section in the center of each core plug to minimize evaporation and invasion. We used air mist during the core plugging to minimize evaporation or invasion of cutting fluid. The 48-mm core plugs were then stored in glass vials until NMR measurements were made.

The core-plug dimensions, 25-mm diameter \times 48-mm long, makes them compatible with the Oxford Instrument NMR overburden core holder. A series of “twin” Cores 1 to 6, originating near the same depth of the formation, were selected for laboratory core analysis. The spatial variation of the “twin” cores is about 0.2 m. It is assumed that these cores are the same in terms of pore geometries and physical properties. These cores were not cleaned before NMR measurements. The pore space of the “as-received” core samples consists of bitumen, connate water (with unknown composition), and air, as detected by the laboratory NMR core-analyzer (shown in the following section). The deuteration result (shown in Appendix 1) suggests that the “as-received” cores have no residual hydrocarbon saturation. The cores were then saturated with either water (i.e., brine with 8,000 ppm of NaCl), methane, ethane, propane, n -butane, n -pentane or n -decane for in-situ NMR measurements. Note that n -butane, n -pentane, and n -decane are hereafter shortened to butane, pentane, and decane, respectively.

The apparatus diagram for in-situ saturation is shown in Fig. 3. The core samples are placed within the NMR overburden core holder for pressure saturation. A syringe pump is used to inject fluids while a hydraulic hand pump is used to maintain the confining pressure. All pressure saturations are conducted by injecting fluids at constant inlet-pressure with the outlet which is closed and connected to a pressure transducer. All of the laboratory NMR measurements are performed at a temperature of 30°C. The targeted pore pressure (1,200 psia) is adjusted such that the density of ethane at laboratory conditions would be the same as that at reservoir temperature and pressure (68°C and 2,755 psia). The pressurization to the targeted pore pressure takes two steps. The cores are initially pressurized from 14.7 psia (ambient pressure) to 500 psia, and then from 500 to

1,200 psia. The step-wise pressurization is meant to limit the pressure gradient and effective stress (a.k.a. net pressure, namely the net stress between overburden stress and pore pressure) to avoid irreversible change in the cores. The effective stress is kept constant at 1,000 psi during the NMR measurements.

Table 3—Core Number, Saturating Fluid, Temperature, Pore Pressure, and Confining Pressure for NMR Measurements on “Twin” Cores

Core	Fluid	Label	T (°C)	P _{pore} (psia)	P _{confining} (psia)
1	Propane	C3	30	1,200	2,200
	D ₂ O	D2O	30	1,200	2,200
	Methane (D ₂ O)	C1(D2O)	30	1,200	2,200
2	Methane	C1	30	1,200	2,200
	Ethane	C2	30	1,200	2,200
3	H ₂ O	H2O	30	1,200	2,200
4	Pentane	C5	30	1,200	2,200
5	Decane	C10	30	1,200	2,200
6	Butane	C4	30	1,200	2,200

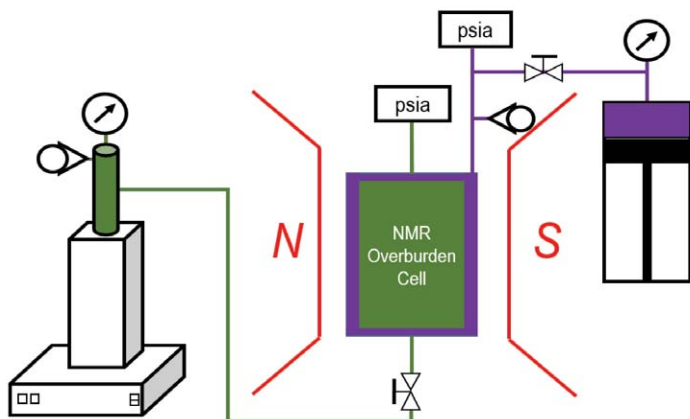


Fig. 3—Schematic of the saturation apparatus for in-situ NMR measurements.

The details of saturations and measurements are tabulated as Table 3. These series of “twin” cores are used in parallel for different saturating fluids because the saturation alters the cores. More specifically, some connate water is mobilized and expelled during pressurization and depressurization of light hydrocarbons, as shown in Appendix 2. The NMR results on the as-received cores reveal similar NMR responses (shown in the next section for T_2), except for Core 4. Core 4 has slightly less connate water saturation, but similar total porosity, as indicated by the T_2 measurements (as shown

below). Therefore, no distinction is made between these as-received “twin” cores. The order of saturation listed in Table 3 for Cores 1 and 2 follows the order of actual experiments. After each fluid saturation on Cores 1 and 2, the cores were depressurized and taken out of the overburden cell to remove excess fluid for the next step. The deuterated Core 1 (denoted as “D₂O”) was prepared by immersing the core into fresh D₂O brine twice. Each deuteration step lasted for one week at ambient conditions. It should be noted that the “C1(D₂O)” is done by injecting methane into Core 1, which has been deuterated after propane saturation. The purpose of “C1(D₂O)” is to study the NMR responses of pure methane without the interference from connate water so that the T_2 , T_1/T_2 , and diffusivity of the methane can be readily observed.

The bulk properties of water and hydrocarbons at both laboratory conditions (30°C, 1,200 psia) and downhole conditions (68°C, 2,755 psia) are estimated and summarized in Table 4. The details of the procedure use in computing the bulk fluid properties are provided in Appendix 4.

Table 4—Bulk Properties of Fluids on Both Laboratory and Reservoir Conditions

Fluid	30°C, 1,200 psia (Laboratory)				68°C, 2,755 psia (Reservoir)			
	Density (g/cm ³)	HI	(cP)	Diffusivity (μm ² /ms)	Density (g/cm ³)	HI	Viscosity (cP)	Diffusivity (μm ² /ms)
Water (H ₂ O)	1.00	1.00	0.797	2.3	0.99	1.00	0.420	5.6
Methane (C1)	0.06	0.13	0.013	250.0	0.12	0.27	0.018	125.0
Ethane (C2)	0.36	0.65	0.047	30.1	0.35	0.64	0.046	34.5
Propane (C3)	0.50	0.83	0.106	13.4	0.48	0.80	0.092	17.4
Butane (C4)	0.58	0.90	0.168	8.5	0.56	0.88	0.141	11.3
Pentane (C5)	0.63	0.94	0.232	6.1	0.61	0.92	0.200	8.0
Decane (C10)	0.73	1.02	0.869	1.6	0.71	1.00	0.616	2.6

COMPOSITION ESTIMATION BY T_2

This section presents T_2 laboratory measurements on as-received and saturated cores. Note that the T_2 distributions are projected from 2D T_1 - T_2 correlation maps. This section also shows how the laboratory T_2 is used to calibrate the log to estimate the light-hydrocarbon composition.

Figure 4 shows the detection range of the NMR T_2 measurements. The matrix of the rock, which mostly consists of calcite and kerogen, is in the solid phase. Therefore, the matrix is not detectable by the low-field NMR relaxometer. As for fluids, the as-received reservoir cores preserve bitumen and connate water. The bitumen is partially visible in NMR measurements depending on the viscosity. The connate water in either micro- or macropores is detectable. When the cores are saturated with light hydrocarbons, the light hydrocarbons can dissolve in kerogen and bitumen (i.e., with short T_2), or stay in the macropores (i.e., with long T_2).

The entire T_2 distributions can be divided into three regions by T_2 cutoffs, as shown in Fig. 4 (also shown in

Fig. 5). The three regions are identified as (A) bitumen and/or dissolved light-hydrocarbon region, which may contain light hydrocarbons dissolved in both bitumen and kerogen, as inferred from its high T_1/T_2 ratio revealed by the T_1 - T_2 measurements (shown in the following section for T_1/T_2); (B) micropore region that has connate water, inferred from the fact that its signal intensity is decreased to almost zero by deuteration (i.e., exchange with D_2O , a.k.a. heavy water, shown in Appendix 1); (C) macropore region that contains saturating light hydrocarbons and a small amount of connate water, where most of the connate water signal can be eliminated by deuteration (also shown in Appendix 1). Note that fluids in Regions A and C can be in the same spatial region.

T_2 Distributions of As-Received Cores

Figure 5 shows the T_2 distributions of six as-received cores close to the same depth. It should be noted that the reported “NMR porosity” of the as-received cores in Fig. 5 and following plots is NMR liquid-filled porosity, while the “NMR porosity” of the saturated cores is the NMR total

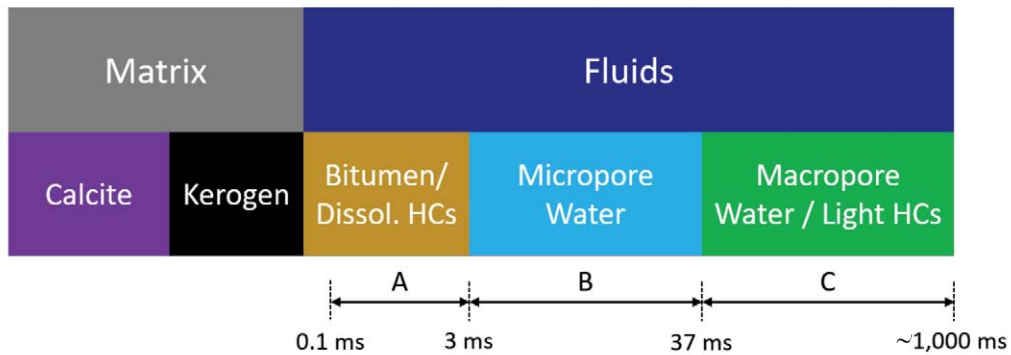


Fig. 4—Schematic of the detection range of the low-field (2.3 MHz) NMR T_2 measurements.

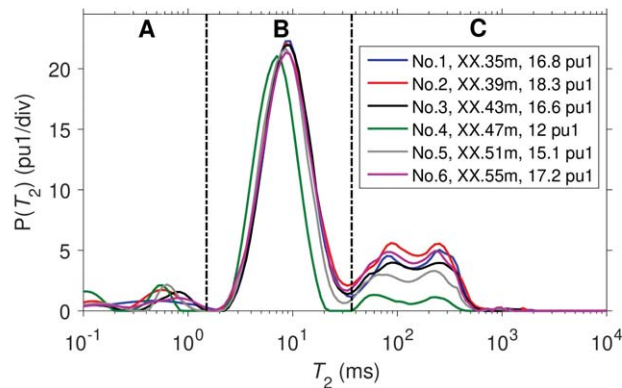


Fig. 5— T_2 distributions of the as-received cores from near the same depth. Dashed lines divide the T_2 distributions into three regions: (A) the leftmost region is the bitumen and/or dissolved hydrocarbon region; (B) the middle region is the connate-water region; (C) the rightmost region is the light-hydrocarbon region (with small amounts of connate water). The legend indicates core number, concealed core depth, and NMR porosity. “pu1” refers to porosity units assuming HI = 1.

porosity. The reported porosity assumes that all the detected fluids have a hydrogen index of unity, i.e., $HI = 1$, which is the same as water. As such, the porosity values are listed in units of pu1, which is short for porosity units (p.u.) assuming $HI = 1$. The reported NMR liquid-filled porosity or NMR total porosity follows a relationship with the actual porosities as such

$$\begin{aligned} \phi_l(\text{pu}) &= \frac{\phi_l(\text{pu1})}{HI}, \\ \phi(\text{pu}) &= \frac{\phi(\text{pu1})}{HI}, \end{aligned} \tag{1}$$

where $\phi_l(\text{pu})$ and $\phi(\text{pu})$ are the actual liquid-filled and total porosity respectively, while $\phi_l(\text{pu1})$ and $\phi(\text{pu1})$ are the reported NMR liquid-filled porosity and NMR total porosity assuming $HI = 1$, respectively. It should be noted that a large fraction of the bitumen signal, with short T_2 due to its high viscosity, is not detectable by the low-field NMR relaxometer in this study. Therefore, the total porosity (i.e., NMR total porosity) reported in this study does not include

the invisible portion of bitumen.

Figure 5 indicates that the cores near the same depth share very similar T_2 distributions, except that Core 4 has less connate water in Regions B and C, which also leads to a T_2 shift in Region B. The loss of connate water in Core 4 may be due to the evaporation during core plugging.

T_2 Distributions of Saturated Cores

Saturating the as-received cores in the laboratory is critical to study the NMR responses of different fluids (see Table 3 for saturation details). In this study, we use the water and hydrocarbons respectively to saturate the core under the laboratory conditions. The T_2 distribution acquired on the 100% water-saturated core provides the total NMR porosity. Figure 6a presents the T_2 distribution of Core 3 before and after water saturation. It is clear that there is around 8.1 p.u. of water introduced by water saturation. The fully water-saturated Core 3 suggests a total NMR porosity of ~ 25 p.u. for all of the six “twin” cores.

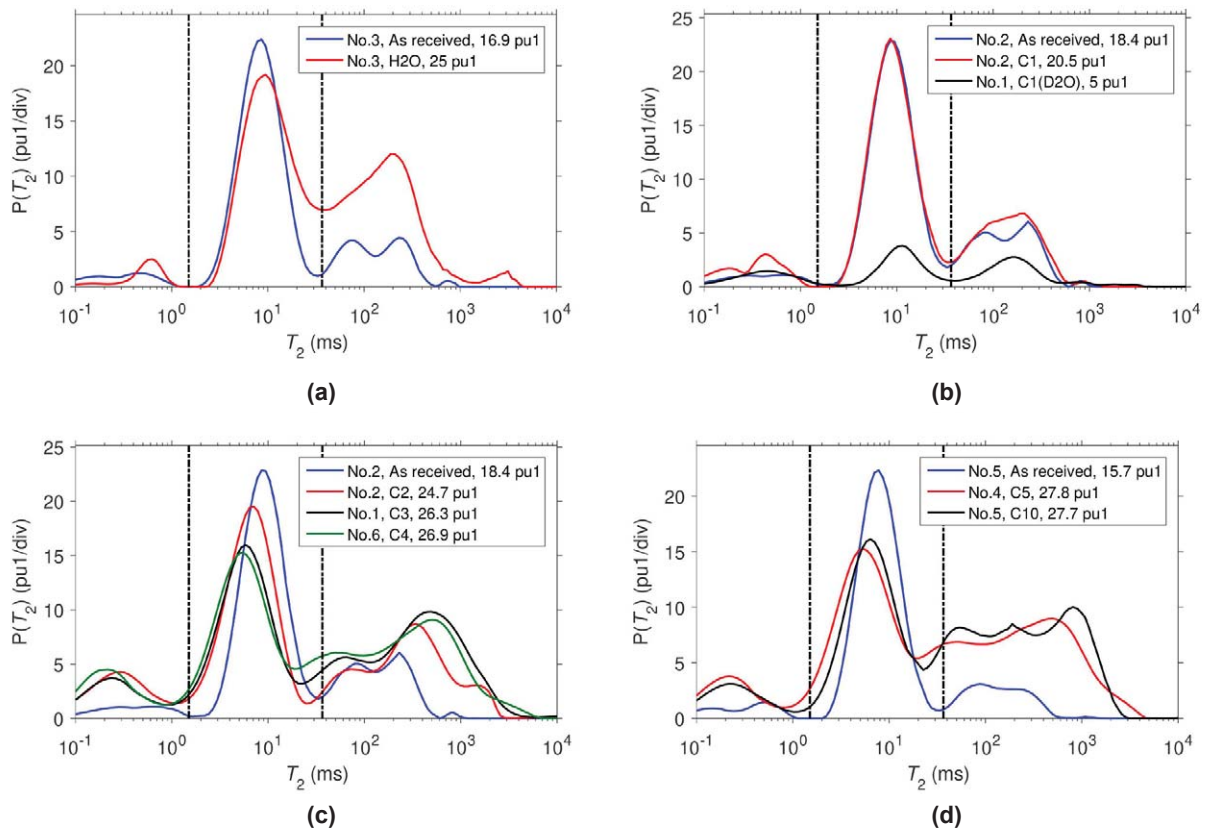


Fig. 6— T_2 distributions of as-received and fully-saturated cores. Dashed lines divide the T_2 distributions into three regions, the same as in Fig. 5. Subfigures (a), (b), (c), and (d) show different combinations of data, each labeled in the legend according to core number, saturating fluid, and NMR porosity. “pu1” refers to porosity units assuming $HI = 1$.

Figures 6b, 6c, and 6d provide T_2 distributions of hydrocarbons in the cores. The measurements illustrate different NMR porosity, especially in Region C, which is due to the differences in HI between the hydrocarbons. Under laboratory conditions, methane is supercritical and yields a low HI of 0.13, while ethane, propane, butane, pentane, and decane are all liquids and yield a much higher HI (see Table 4). It should be noted that since the HI of methane at reservoir conditions is twice that at laboratory conditions (also see Table 4), the simulated downhole T_2 response (shown below) should be compensated.

The total NMR porosity of water-saturated core in Region A is slightly lower than that of pentane- and decane-saturated cores, even though water, pentane, and decane share similar HI (see Table 4). This is interpreted as the dissolution of alkanes into either bitumen or kerogen, as suggested by the increase in signal intensity of Region A after pentane and decane saturation (see Fig. 6d).

In addition to the NMR porosity, there are other noticeable changes in T_2 distributions of the saturated cores. For the water-saturated Core 3, a slight increase in T_2 of connate water in Region B is observed. This is because the connate water in micropores in the micritic calcite (Region B) is weakly diffusive-coupled with the water in the macropores that are between the large grains of kerogen and calcite (Region C). The diffusive coupling is weak because some bitumen clogging up the pore throats limits the water exchange.

It is also observable that the T_2 of connate water (Region B) is shifted to shorter values after saturation with longer alkanes, but not after methane. This indicates the connate water is mobilized by a gas-liquid drive of liquid hydrocarbons. The trend of T_2 shifting agrees with the mobility ratios of alkanes with respect to water (e.g., alkanes with longer carbon-chain length yield higher viscosities, which are closer to the viscosity of water). This also explains why the connate-water loss in cores after experiments increases with alkane carbon-number (see Appendix 2). Note that even though the T_2 of Region B for connate water is shifted, the NMR porosity for this region is nearly unchanged for all the cases (except for “C1(D2O)”). This is because the invaded hydrocarbons occupy the pore space originally for the expelled connate water. The invaded hydrocarbons have longer T_2 than connate water because the micritic calcite pores associated with Region B are water-wet, such that hydrocarbons are relaxed by the water film coating the pore surface, and therefore have longer relaxation times compared to the connate water.

Since low-HI methane (“C1”) only contributes a small amount of signal in Region C, indicated by Fig. 6b, deuteration is useful when the methane response is analyzed.

The T_2 of pure methane (“C1(D2O)”) in Region C is the same as methane in the saturated core (“C1”), confirming that the extra signal seen on “C1” is not an artifact. It should be noted that the signal in Region B of “C1(D2O)” is due to water contamination because this part of the signal does not disappear after desaturation of methane, and also can be deuterated from the desaturated core. The source of contamination may be from the moisture and remaining droplets of water (< 0.5 mL) in the tubing and valves of the apparatus.

The T_2 response of ethane and longer alkanes in Region C is separated into several peaks. The wettability may account for the distinct peaks. The pores for Region C are in-between the grains of kerogen and calcite. Therefore, the pores associated with Region C are likely to be mix-wet. The longest T_2 of decane in Region C is close to its bulk T_2 (about 3 seconds for deoxygenated decane). This may be because of a thin water film coating some surface of the mixed-wet pores, such that decane does not directly contact the pore walls. In such cases, the surface relaxation of decane is provided by the decane-water interface instead of the decane-solid interface. It can be expected that the surface relativity of the decane-water interface is much smaller compared to the decane-solid interface. On the other hand, decane in contact with the kerogen solid surface may yield a shorter T_2 that is distinct from the bulk T_2 . The same interpretation applies to other alkanes that have distinct peaks in Region C.

T_{2app} Distributions and Composition Estimation

Due to magnetic-field gradients, NMR logging tools measure the “apparent” T_2 relaxation, defined as T_{2app} and given by

$$\frac{1}{T_{2app}} = \frac{1}{T_2} + \frac{1}{T_{2D}} \quad (2)$$

T_2 is the transverse relaxation time without applied magnetic-field gradients, as reported in the previous subsections. T_{2D} is the additional term due to fluid diffusion in an applied magnetic-field gradient generated by the logging tool as such:

$$\frac{1}{T_{2D}} = \frac{\gamma^2 G^2 T_E^2 D}{12} \quad (3)$$

$\gamma/2\pi = 42.58$ MHz/T is the gyromagnetic ratio of the proton. The NMR logging tool involved in this study has an echo spacing T_E of 0.4 ms. G is the magnetic-field gradient applied by the NMR logging tool. The NMR logging tool provides six shells of equal volume with G values of 17.0, 22.0, 23.4,

27.4, 32.7 and 38.7 G/cm, respectively. D represents the diffusivity of hydrocarbons, where the restricted diffusivities under logging conditions (derived in the following diffusivity section using Padé fit) are used. This is because the diffusion lengths of fluids, especially that of methane, are close to the pore diameter, which means the fluids experience restriction from the limited pore space. Note that in the cases where the restriction is negligible (i.e., the pore diameter is much greater than the diffusion length), bulk diffusivity of fluids can be used to calculate the magnetic-field gradient effect, which leads to simpler implementation.

For a better core-log comparison, the extra T_{2D} term is added to the laboratory-measured T_2 distributions. In addition, the first echo (at 0.2 ms) of the time-domain raw data for the laboratory measurements is dropped to match the first echo time of the logging tool. Besides, the simulated T_{2app} is rescaled by the HI of fluids (see Table 4), which means the bin porosity in the T_{2app} distribution of methane is boosted by a factor of two because of the difference in HI under reservoir and laboratory conditions (see Table 4).

As for longer alkanes and water, the effect of rescaling is insignificant because those fluids share similar HI at both conditions.

Figure 7 presents the T_{2app} distribution from the downhole log and the T_{2app} distributions from the as-received (i.e., with connate-water saturated) and hydrocarbon-saturated cores simulated based on the laboratory measurements. Note that for simulated T_{2app} distributions, only Region C is shown because Region B is less informative due to the T_2 shift. The log data acquired at the closest depth where the as-received plugs were cored are used for comparison. It should be noted that the vertical resolution of the log is about 0.6 m, which is comparable to the spatial variation of the “twin” cores.

Introducing the T_{2D} term to laboratory-measured T_2 has no impact on Regions A and B where T_2 is much shorter than T_{2D} . However, introducing the T_{2D} term leads to shorter relaxation time T_2 in Region C, with narrower and higher peaks. It is found that methane has shorter T_{2app} and lower HI than the log, while longer alkanes have longer T_{2app} and higher HI (or comparable HI in the case of ethane) than the

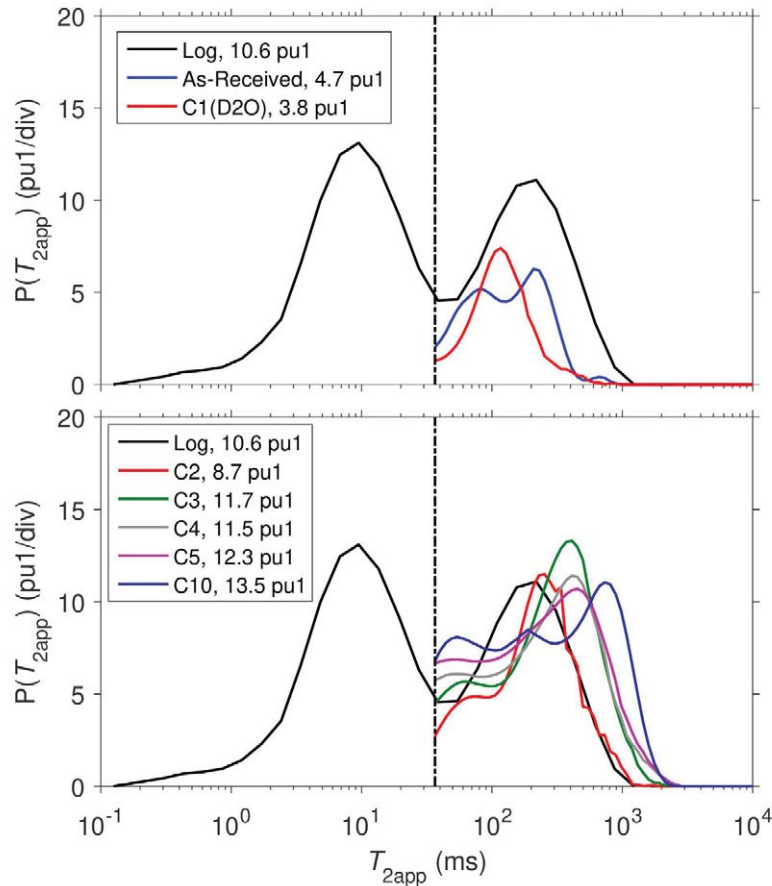


Fig. 7—Comparison of incremental T_{2app} distribution from the downhole log and simulated T_{2app} distribution (Region C only) based on laboratory-measured data. Note that the two subplots share the same log data. Also, note that the simulated T_{2app} distribution has the HI difference under different conditions compensated. The dashed vertical lines separate Region C from the other two regions. The legend indicates measurement name and the NMR porosity of Region C. “pu1” refers to porosity units assuming HI = 1.

log; therefore a combination of the hydrocarbons is expected to match with the log.

To determine the composition of light hydrocarbons in the reservoir, the T_{2app} distributions of light hydrocarbons in the core are numerically “mixed” in data post-processing by averaging their T_{2app} distributions according to different volume fractions. This analysis assumes that hydrocarbons yield the same T_{2app} distribution in the mixture as they would in single component form (i.e., the T_{2app} distributions are linearly additive). It is also assumed that, in the ethane- and higher alkane-saturated core, the signal of Region C is from hydrocarbons with a negligible amount of connate water (i.e., only thin water films coating the water-wet portions of pores but not contributing to the signal intensity). This is suggested by the measurements shown in Appendix 2 on desaturated cores, of which the T_2 distributions provide nearly zero signal in Region C, except for methane. In the case of methane, “C1(D2O)” is used instead of “C1” for “numerical mixing” because “C1(D2O)” is measured after the propane experiment where the connate water in Region C was expelled by propane (see Appendix 2). Hence, “C1(D2O)” presents the T_{2app} distribution when methane occupies the entire pore space of Region C.

The “numerical mixing” of T_{2app} makes use of the T_{2app} of the “As-Received” (i.e., the “as-received” Core 2) as the baseline to represent the connate water in the reservoir. It is assumed that there is no residual hydrocarbon saturation in Region C in the “As-Received” as suggested by the deuteration result (see Appendix 1). The T_{2app} ’s of hydrocarbons are added to the “As-Received” after being multiplied by the total hydrocarbon saturation of Region C and the volume fraction (i.e., composition) of individual hydrocarbon (see Appendix 3 for the workflow). The total light-hydrocarbon saturation in Region C is about 65% since the connate-water saturation is 4.7/13.5 p.u. \approx 35%. Note that the NMR porosity of the fully decane-saturated (instead of water-saturated) core is adopted for the above saturation calculation because the water in macropores (Region C) is diffusively coupled to water in micropores (Region B), which leads to shorter T_{2app} and less NMR porosity for Region C. A grid (i.e., brute-force) search algorithm is implemented to determine the optimal volume fraction of hydrocarbons that minimizes the discrepancy (i.e., mean squared error) between “numerically mixed” T_{2app} distribution and the log for Region C where $T_{2app} \geq 36.6$ ms. Note that the T_{2app} of Region B is shifted due to loss of connate water, and is therefore not of interest.

The optimal volumetric fractions of hydrocarbons obtained by the grid search are listed in the legend of Fig. 8. It is obvious that butane, pentane, and decane do not contribute to the optimal “mix”. Methane contributes

around 27%, while ethane and propane contribute about the same amounts, around 36% to the “mix”. The HI of the “mix” is about 0.58 providing the estimated composition. By converting the volumetric fraction to the porosity unit, one can derive that the total fluid-filled porosity of the three hydrocarbons is 8.8 p.u. Methane, ethane, and propane occupy approximately 2.4, 3.2, 3.2 p.u, respectively. This approach can be used to generate a qualitative estimate of the composition of light hydrocarbons in the reservoir.

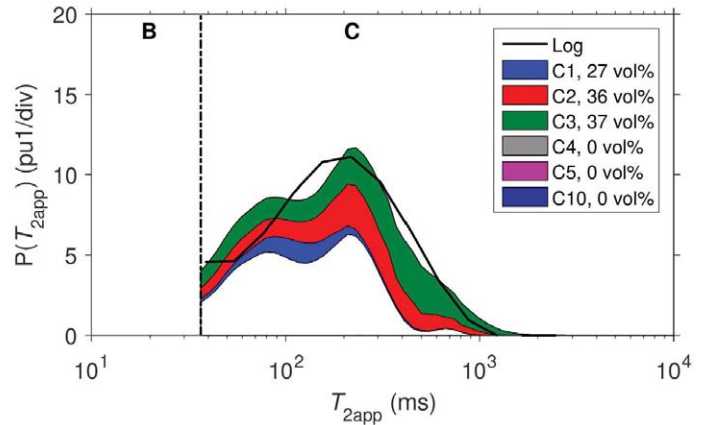


Fig. 8—Comparison of incremental T_{2app} distributions from the downhole log and artificially “mixed” hydrocarbons saturated core (Region C only). The T_{2app} distributions of hydrocarbons in the “mix” are broken down to single components with a color scheme to visualize the composition. The total colored area denotes the light-hydrocarbon-filled porosity. The outline of the green area denotes the final T_{2app} distributions of the “mix”. The white area under the blue area is associated with connate water. The optimal volumetric fraction of the “mix” is illustrated in the legend. The dashed vertical line indicates the T_{2app} above the Region C cutoff is considered when searching for an optimal volumetric fraction. The “pu1” means NMR porosity shown in plots is assuming HI = 1.

FLUID TYPING BY T_1/T_2 AND T_1/T_{2app}

This section presents T_1 - T_2 measurements conducted in the laboratory on as-received and saturated cores. The contrasts in simulated T_1/T_{2app} and T_{2app} are discussed in detail and proposed as techniques for fluid typing and saturation estimation.

Laboratory-Measured T_1/T_2

The laboratory-measured 2D T_1 - T_2 correlation map can be transformed into a T_1/T_2 vs. T_2 correlation map. Figure 9 shows the T_1/T_2 vs. T_2 correlation maps of connate water and saturating fluids in the cores. It is found that the signal in Region A has $T_1/T_2 \approx 10$ for both as-received and saturated states, indicating that the signal comes from viscous bitumen and/or hydrocarbons dissolved in kerogen (Singer et al., 2016, 2017a, 2018a; Chen et al., 2017). Furthermore, the

signal intensity in Region A increases after hydrocarbon saturation, but not after water saturation. This results from lowering the viscosity of the bitumen after mixing with the saturating hydrocarbons, which leads to longer T_2 and thereby more detectable signal (Yang et al., 2012; Singer et al., 2017a, 2018a), as well as more signal from the saturating hydrocarbons dissolved in the kerogen grains (Singer et al., 2016; Chen et al., 2017).

As for Region B and C, Fig. 9a indicates that saturating water has the same T_1/T_2 as connate water. The “C1” shown in Fig. 9b overlays with the “as-received” 2D correlation map, which results from the low HI of methane. However, the pure methane signal, shown in black in Figs. 9c and 9d, also suggests that the saturating liquid-state hydrocarbons tend to yield broader T_1/T_2 distributions and higher T_1/T_2 ratios than connate water.

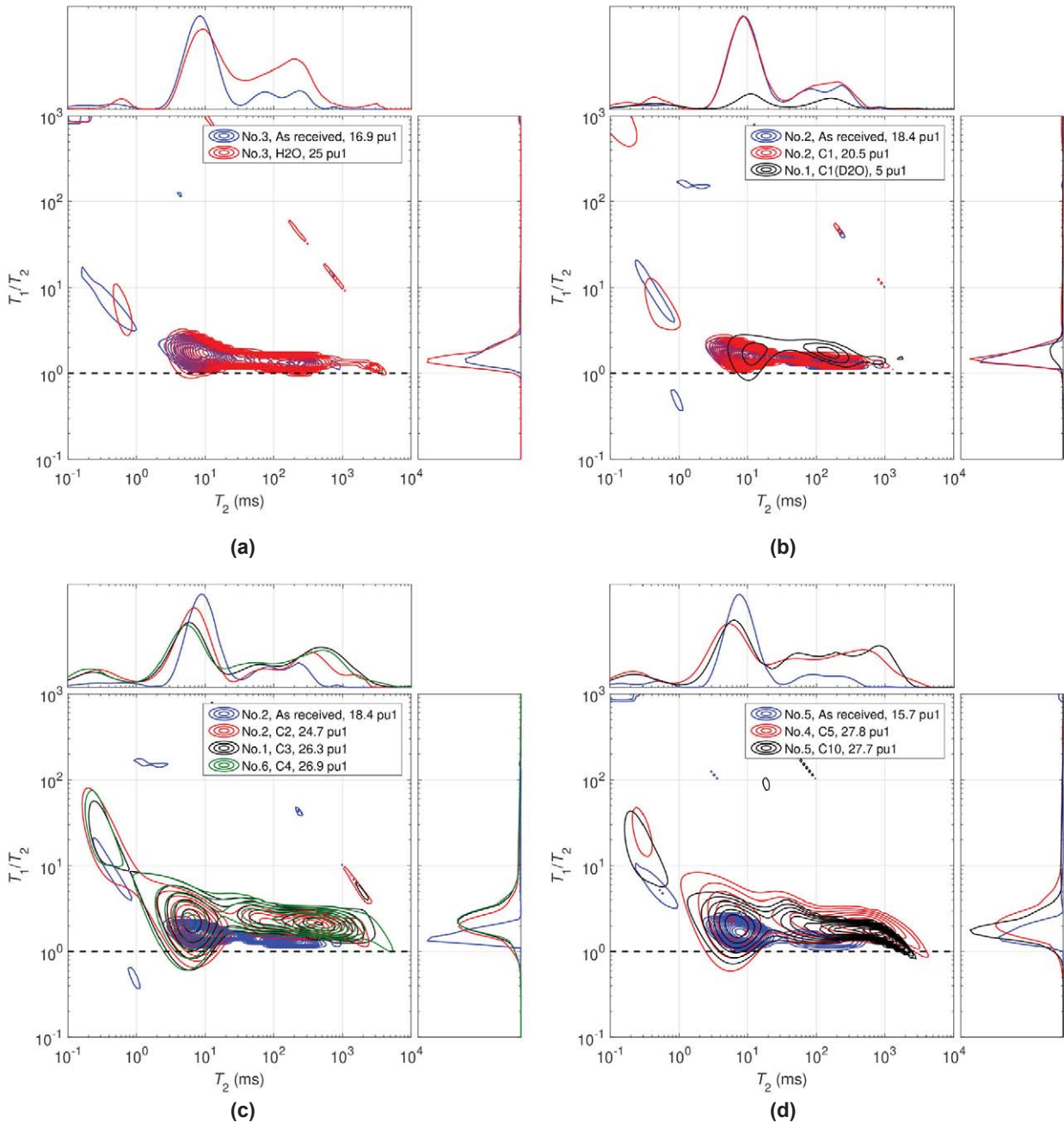


Fig 9—2D correlation maps of as-received and fully-saturated cores, with T_1/T_2 ratio on the y-axis, T_2 on the x-axis and porosity perpendicular to the page. For each subplot, the top subplot is the projected T_2 distribution. The right subplot is the projected T_1/T_2 ratio distribution. Subfigures (a), (b), (c), and (d) show different combinations of data, each labeled in the legend according to core number, saturating fluid, and NMR porosity. “pu1” refers to porosity units assuming HI = 1. The dashed horizontal line is the $T_1/T_2 = 1$ line.

The T_1/T_2 ratio at the peak of Region B and C in Fig. 9 is plotted in Fig. 10. The reason for choosing the peak values instead of the commonly chosen log-mean values is that the peak values are subject to less interference from the connate water, especially in Region C (Fig. 10c). For Region A (Fig. 10a), the log-mean value for T_1/T_2 is chosen instead, given that the peak value has large amounts of scattering, plus Region A is most likely bitumen (see Appendix 6) with no connate water.

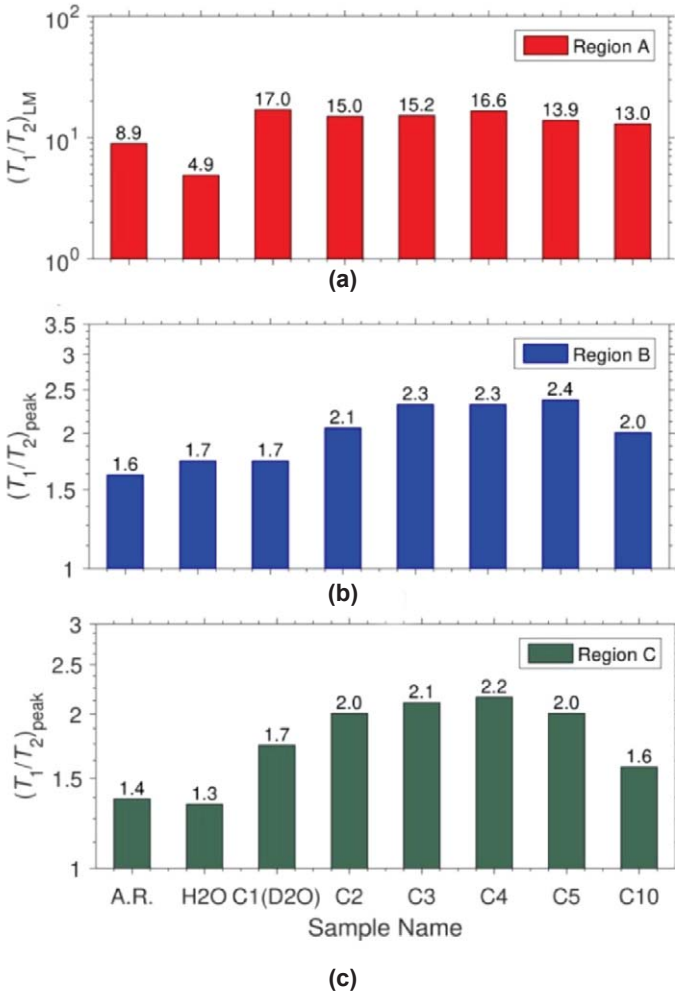


Fig. 10—Comparison of T_1/T_2 log-mean values in Region A, (a) and T_1/T_2 peak values in Region B (b) and Region C (c). The x-axis indicates connate water (i.e., as-received) or saturating fluids.

The signal in Region B is dominated by connate water in micritic pores, except for the case (“C1(D2O)”) where the core is deuterated beforehand. The T_1/T_2 ratios in Region B (Fig 10b) are roughly 2. The scattering is due to the small amount of invasion of hydrocarbons into Region B (see Appendix 2), which leads to more complexity and

less interest. Region C (Fig. 10c) is mostly affected by the injecting fluids, since saturating hydrocarbons mainly exist in macropores. It is found that methane in the as-received core yields the same T_1/T_2 as water as a result of low HI. By contrast, methane in the deuterated core generates much higher T_1/T_2 . It is readily observed that the light hydrocarbons in Region C (Fig. 10c) have higher T_1/T_2 than water. It is also found that the T_1/T_2 of light hydrocarbons in Region C peaks at butane. However, the mechanism that results in the peak should be further investigated, potentially by molecular dynamics (MD) simulation.

Simulated Downhole-Measured T_1/T_{2app}

The 2D T_1/T_{2app} vs. T_{2app} correlation maps (not shown) are simulated by introducing the effect of the magnetic-field gradient similar to the simulation of T_{2app} distributions. As a result, the T_1/T_{2app} acquired by logging tools is reproduced from the laboratory measurements. The projected 1D T_1/T_{2app} distributions of the signal in Region C are isolated and plotted in Fig. 11. This plot also indicates that hydrocarbons provide broader T_1/T_{2app} distributions compared to water.

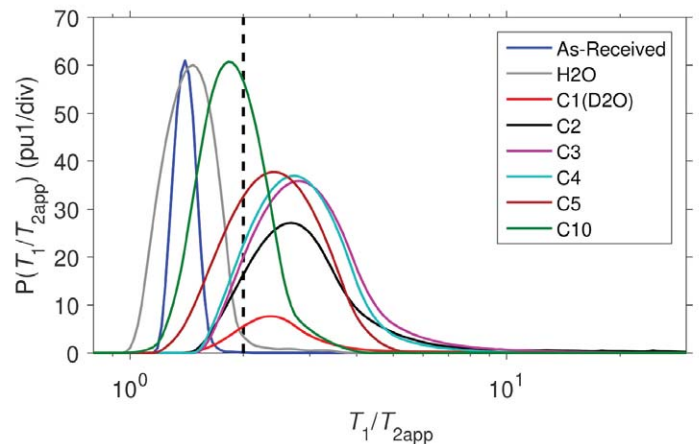


Fig. 11—Projected 1D T_1/T_{2app} distributions of the signals in Region C from 2D T_1/T_{2app} - T_{2app} correlation maps. The legend indicates the states of cores, including saturating fluid. The vertical dashed line is the proposed T_1/T_{2app} cutoff separating lighter hydrocarbons from water and decane in Region C.

It should be noted that unlike the numerical mixing of T_{2app} , the connate-water signal is not compensated during the simulation. The peak values of Region C on the simulated 2D plots are used as the representative T_1/T_{2app} for saturating fluids and are presented in Fig. 12. It is obvious that the T_1/T_{2app} provides amplified contrast compared to T_1/T_2 (shown Fig. 10c). This finding suggests the downhole logs have a better chance of separating fluids with different diffusivity by T_1/T_{2app} contrast.

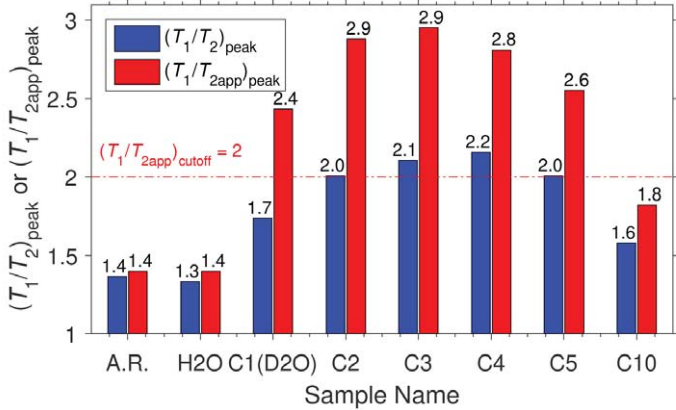


Fig. 12— T_1/T_2 and $T_1/T_{2\text{app}}$ at the peak of Region C on the 2D maps for the as-received state and different fluid saturations. Blue is for T_1/T_2 and red is for $T_1/T_{2\text{app}}$ simulated using the logging tool magnetic-field gradients. The horizontal dashed line is the proposed $T_1/T_{2\text{app}}$ cutoff separating lighter hydrocarbons from water and decane in Region C.

It is readily observed that the methane and NGLs (i.e., ethane, propane, butane, and pentane) yield higher values of $T_1/T_{2\text{app}}$ due to higher diffusivities in contrast to water and decane. Hence, a $T_1/T_{2\text{app}}$ cutoff, denoted by the dashed lines

in Fig. 11 and 12, around 2 can be applied to distinguish methane and NGLs from other fluids, such as water and decane, in the downhole logs.

In addition to $T_1/T_{2\text{app}}$ cutoff, $T_{2\text{app}}$ can provide additional information for fluid typing. The peak values on the simulated $T_1/T_{2\text{app}}$ vs. $T_{2\text{app}}$ correlation maps are plotted in Fig. 13. Figure 13 shows four cutoffs to separate the entire plot to several regions. Methane and NGLs have $T_{2\text{app}}$ in between 37 ms (i.e., the cutoff for Region C) and 500 ms, and $T_1/T_{2\text{app}} > 2$. Instead, decane has $T_{2\text{app}}$ longer than 500 ms and $T_1/T_{2\text{app}} < 2$. As for the water in both micro- and macropores, the $T_1/T_{2\text{app}}$ is < 1.7 .

Besides the connate water and light hydrocarbons, the responses of crude oils in macropores (i.e., Region C) are simulated and plotted in Fig. 13. The bulk T_1 and T_2 of crude oils are estimated using the regression relationship between relaxation times and viscosity over temperature (μ/T) built on Hirasaki group crude oil database (see Fig. A5.1 in Appendix 5). Fig. 13, five viscosities of crude oils, log-spaced between 2 and 1,000 cP, at the reservoir temperature are selected. The surface relaxation terms (namely $T_{1\text{S}}$ and $T_{2\text{S}}$) and the diffusion term (namely $T_{2\text{D}}$) of decane (i.e.,

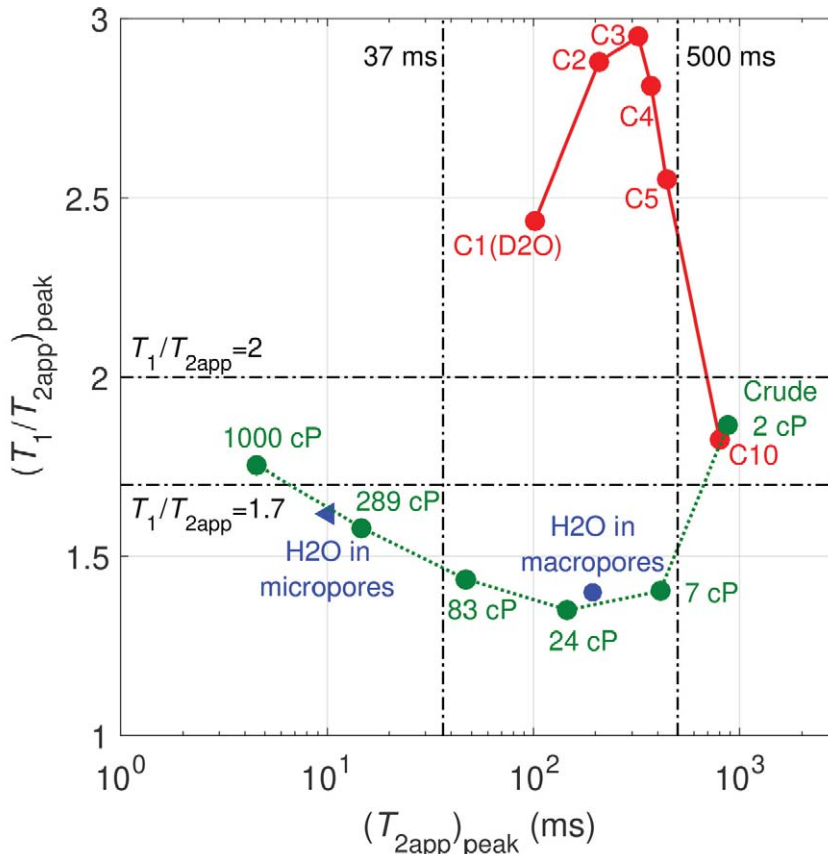


Fig. 13— $T_1/T_{2\text{app}}$ vs. $T_{2\text{app}}$ of connate water at the peak of Region B (blue triangle) and saturating fluids at the peak of Region C (blue dot for macropore water, red dots for light hydrocarbons, and green dots for crude oils). The horizontal and vertical dashed lines are cutoffs for fluid typing. Note that the responses of crude oils are simulated.

“C10”) are added to the bulk relaxation terms to simulate the NMR responses of crude oils in the macropores at reservoir conditions.

The green curve in Fig. 13 indicates that crude oils with $\mu < 1,000$ cP have $T_1/T_{2app} < 2$, while T_2 ranges from about 1,000 to 4 ms. As for more viscous crude oils, a decrease in T_2 and an increase in T_1/T_{2app} can be expected. Therefore, Fig. 13 suggests a qualitative approach to identifying NGLs. By applying T_{2app} cutoffs (i.e., $37 \text{ ms} < T_2 < 500 \text{ ms}$) and a T_1/T_{2app} cutoff (i.e., $T_1/T_{2app} > 2$), one can separate methane and NGLs from water, decane, and crude oils.

RESTRICTED DIFFUSION AND PORE SIZE

This section presents D - T_2 measurements conducted in the laboratory on as-received and saturated cores. The diffusivities of light hydrocarbons are fitted to the Padé approximation to estimate the mean pore size, the heterogeneity length scale, and the tortuosity of the light hydrocarbon-filled porosity.

D - T_2 Measurements

Figure 14 shows the measurements of restricted diffusion on the cores at different states. Generally, the 2D D - T_2 measurements are challenging due to the commonly short T_2 of tight rocks. For the unipolar stimulated-echo sequence (Mitchell et al., 2014) adopted here, the dead time $T_d = 25$ ms required to encode diffusion also acts as a dead time for the T_2 measurement, which results in loss of signal below $T_2 < 7$ ms (signal intensity attenuated to $\leq 5\%$, indicated by the dashed vertical line in Fig. 14). The dead time, T_d , is composed of two parts as:

$$T_d = \Delta + \tau_{se}, \quad (4)$$

where Δ is the diffusion evolution time (a.k.a. observation time), and τ_{se} is the spin-echo time that consists of the gradient encoding time, δ , and dead times. As mentioned in the Experimental Details section, $\Delta = 14.7$ ms and $\tau_{se} = 10.3$ ms during the laboratory measurements. In this research, the T_2 from Regions A and B are mostly < 7 ms where the diffusion measurement is limited, even though a small portion of Region B can be seen. However, the signal from Region C can be measured without significant loss. Hence, the restricted diffusivity at the peak of Region C was picked for later analysis (see the following subsection).

The first thing to note from Fig. 14 is that the measured diffusivities are all less than bulk values due to the restriction in the porous medium. Note that the bulk diffusivity of

methane is around $250 \mu\text{m}^2/\text{ms}$, which is out of range of the y -axis in the 2D correlation map. Pure methane (“C1(D2O)”) in Fig. 14b generates a small peak with higher diffusivity which cannot be observed while the connate-water signal is present. It is also found that decane (“C10”) follows the alkane correlation line proposed by Lo et al. (2002).

Figure 15 shows the projected 1D diffusivity (D) distributions of the signals in Region C. The diffusivity distributions are isolated from the 2D correlation maps (see Fig. 14). The top subplot of Fig. 15 shows the restricted diffusivities of connate water in the cores. The signal of “C1” is dominated by the water signal due to the low HI of methane. The bottom subplot shows the restricted diffusivity of light hydrocarbons. This plot demonstrates a clear trend of the increase in the restricted diffusivity as the carbon number decreases.

Interpretation of Restricted Diffusion

The restriction of diffusion of fluid molecules results from the constraint from pore walls. The restricted diffusion implicitly contains the pore-size and tortuosity information about the porous medium. Therefore, the analysis of the measured restricted diffusivity can extract valuable information for formation evaluation.

Figure 16 provides laboratory-measured restricted diffusivity at the peak of Region C on the 2D maps (Fig. 16a), bulk diffusivity under laboratory conditions, as shown in Table 4 (Fig. 16b) and in the normalized restricted diffusivity (Fig. 16c). The normalized restricted diffusivity is computed by dividing the restricted diffusivity (Fig. 16a) by the bulk diffusivity (Fig. 16b). The normalized restricted diffusivity characterizes the degree of restriction experienced by fluid molecules during the diffusion evolution time. Water and decane share similar bulk diffusivity, therefore almost the same amount of restriction (i.e., the same normalized restricted diffusivity). Instead, methane and NGLs have much higher bulk diffusivities, and therefore more restriction (i.e., lower values of normalized restricted diffusivity compared with water or decane). Furthermore, the restriction experienced by hydrocarbons becomes less as the carbon number increases (e.g., as bulk diffusivity decreases). The measured restricted diffusivity of methane suggests that a cutoff of $3 \mu\text{m}^2/\text{ms}$ (indicated by the horizontal dashed line in Fig. 16a) can be implemented to qualitatively separate the methane, which is the only supercritical hydrocarbon, from the other liquids in the laboratory diffusion measurements. Note that the extremely small value of the normalized restricted diffusivity indicates methane is highly restricted and approaching the tortuosity limit.

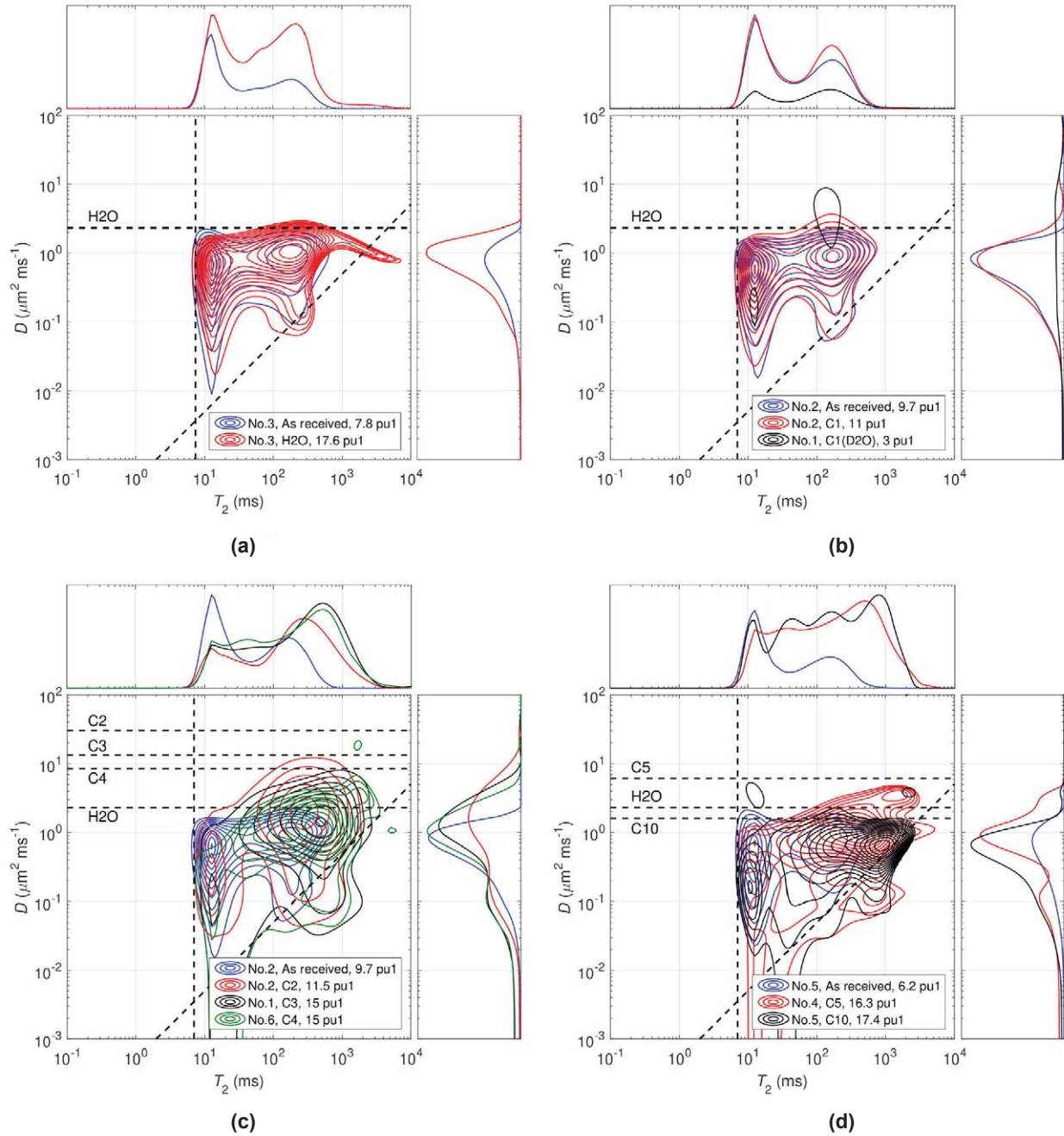


Fig. 14—2D correlation maps of as-received and saturated cores, with D (diffusivity) on the y -axis, T_2 on the x -axis and porosity perpendicular to the page. For each subplot, the top subplot is the projected T_2 distribution. The right subplot is the projected D distribution. Dashed black horizontal lines are the bulk diffusivity of the fluids (labeled next to the lines) in laboratory conditions except for methane (which is out of range of the y -axis), dashed black diagonal line is the alkane correlation line (Lo et al., 2002), dashed black vertical line is to indicate the limitation from dead time ($T_2=25$ ms) inherent in the diffusion-encoding pulse sequence. Subfigures (a), (b), (c), and (d) show different combinations of data, each labeled in the legend according to core number, saturating fluid, and NMR porosity. “pu1” refers to porosity units assuming HI = 1.

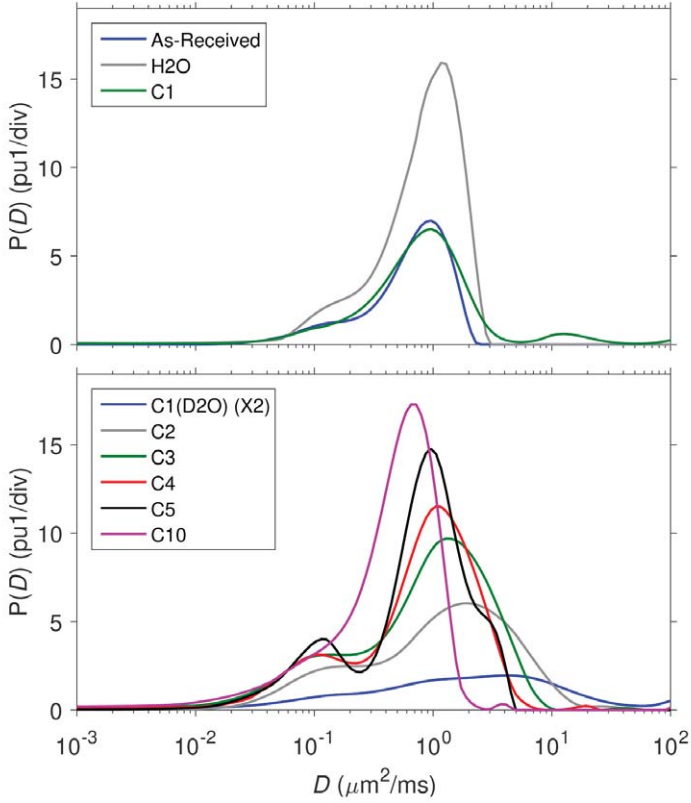


Fig. 15—Projected 1D diffusivity (D) distributions of the signals in Region C from 2D D - T_2 correlation maps. The legend indicates the states of cores, including saturating fluid. Note that the amplitude of “C1(D2O)” is boosted by a factor of 2 for a better comparison.

In Fig. 17, the normalized restricted diffusivity of different hydrocarbons are plotted against diffusion length L_D calculated by Eq. 5:

$$L_D = \sqrt{D_0 \Delta}, \quad (5)$$

where D_0 is the bulk diffusivity on laboratory conditions and $\Delta = 14.7$ ms is the diffusion evolution time. Based on Padé approximation, Hürlimann et al. (1994) suggest that the normalized restricted diffusivity D/D_0 follows a relationship with diffusion length L_D as in Eq. 6:

$$\frac{D}{D_0} = 1 - \left(1 - \frac{1}{\tau}\right) \frac{\frac{4}{9\sqrt{\pi V}} L_D + \left(1 - \frac{1}{\tau}\right) \frac{L_D^2}{L_M^2}}{\frac{4}{9\sqrt{\pi V}} L_D + \left(1 - \frac{1}{\tau}\right) \frac{L_D^2}{L_M^2} + \left(1 - \frac{1}{\tau}\right)}, \quad (6)$$

where S is the pore surface area and V is the pore volume, and $S/V \approx 3/r_p$, where r_p stands for the pore radius of the hydrocarbon-filled space in Region C, assuming spherical pores. τ is the tortuosity of the hydrocarbon-filled space in

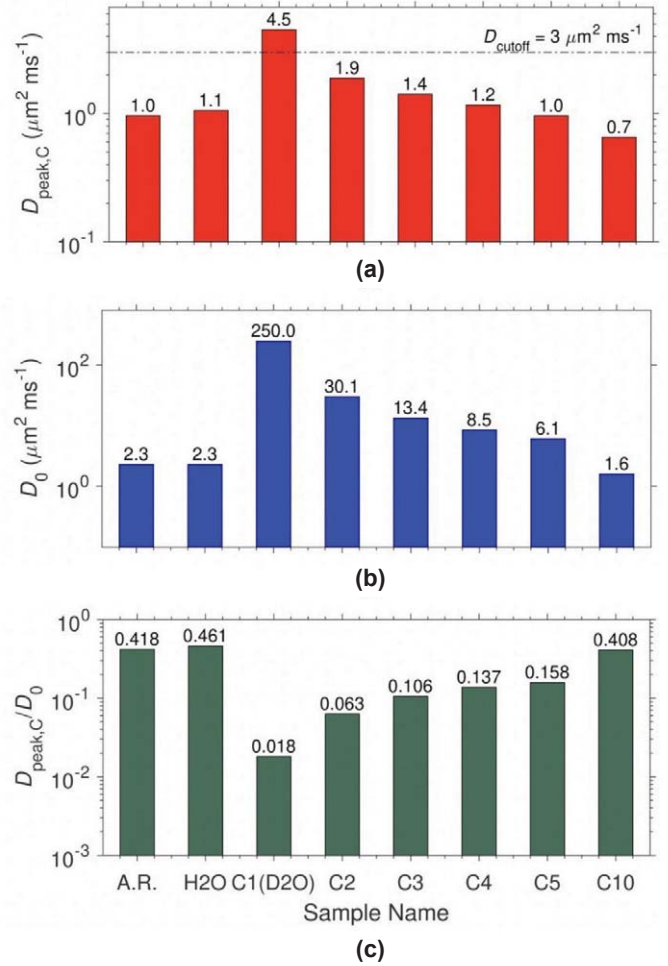


Fig. 16—Comparison of restricted diffusivity (a), bulk diffusivity in laboratory conditions (b) and normalized restricted diffusivity of fluids at the peak of Region C under laboratory conditions (c). The y-axis shows diffusivity; the x-axis indicates connate water (as-received) or saturating fluids; and the horizontal dashed line in (a) is the proposed diffusivity D cutoff separating methane from the liquids in Region C.

Region C, and can be expressed by Eq. 7 (Hürlimann et al., 1994):

$$\tau = \frac{D_0}{D_\infty}, \quad (7)$$

where D_∞ is the diffusivity at the tortuosity limit and L_M is the macroscopic heterogeneity length scale. It should be noted that in the model suggested by Latour et al. (1993), L_M is expressed by $(D_0 \theta)^{1/2}$, where θ is the fitting parameter for a fluid. However, since there are different fluids with various D_0 involved in this work, the L_M is used as the fitting parameter as a whole, which means θ changes to accommodate different fluids.

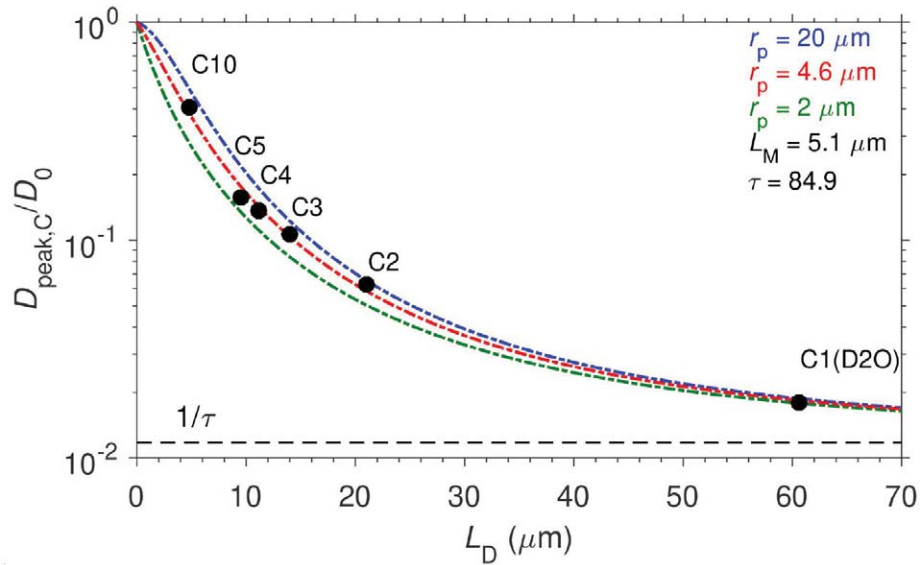


Fig. 17— Normalized restricted diffusivity plotted against diffusion length L_D . The label indicates the source of each data point. Red dashed line is the model fit by Eq. 6 (Hürlimann et al., 1994). The optimal three free-fitting parameters (r_p , L_M and τ) are listed in the top-right corner. Note that the blue and green dashed lines are generated by tuning the mean pore-radius r_p , while keeping the other two parameters the same as red, to visualize the sensitivity of the fit to the mean pore size. Also, note that the normalized restricted diffusivity of water is not included in the model fitting.

Note that the data of saturating water are not plotted in Fig. 17 because the water in macropores is diffusively coupled with the connate water in micropores, which affects the normalized restricted diffusivity.

According to the above model, there is a total of three free parameters: r_p , τ , and L_M . A least-squares fit based on this model is applied to the \log_{10} -transformed restricted diffusivity and shown in Fig. 17. The final fit is presented in Fig. 17 with $r_p = 4.6 \mu\text{m}$, $L_M = 5.1 \mu\text{m}$ and $\tau = 84.9$ as the optimized parameters. The pore size estimated here is comparable to the pore size illustrated by the SEM image (see Fig. 1). Another two curves are plotted by changing r_p to $20 \mu\text{m}$ and $2 \mu\text{m}$, along with the final fit to demonstrate the sensitivity of this model to different pore size. The sensitivity analysis suggests this approach can be applied to estimate the pore size $r_p \leq 5 \mu\text{m}$ with relatively high resolution.

It should be noted that the original model proposed by Hürlimann et al. (1994) is for the case of 100% saturation and 100% wetting. Minh et al. (2015) suggest the equation should be changed accordingly if the investigated case is not 100% saturation nor 100% wetting. In this research, only the hydrocarbon-filled porosity (Region C) is considered, thereby, the original model by Hürlimann et al. (1994) is still adopted in the present case.

The macroscopic heterogeneity length scale L_M is $5.1 \mu\text{m}$, which is close to the pore radius of $4.6 \mu\text{m}$. To our knowledge, there is no existing theory to interpret the L_M . Empirically the L_M should scale with pore size, as suggested by Latour et al. (1993) and Hürlimann et al. (1994). More investigation into the physical meaning of L_M is required.

According to the above Padé fit acquired in the laboratory conditions, one can estimate the restricted diffusivities experienced by fluids during downhole logging by extrapolating the Padé fit to the downhole diffusion length L_D (shown in Fig. 18). To achieve this, the bulk diffusivity D_0 in laboratory conditions in Eq. 5 is replaced by the bulk diffusivity in the reservoir conditions (as illustrated in Fig. 19a). Meanwhile, the diffusion evolution time in Eq. 5 is changed to echo spacing $T_E = 0.4 \text{ ms}$ for the logging tool instead of $\Delta = 14.7 \text{ ms}$ for the laboratory core analyzer.

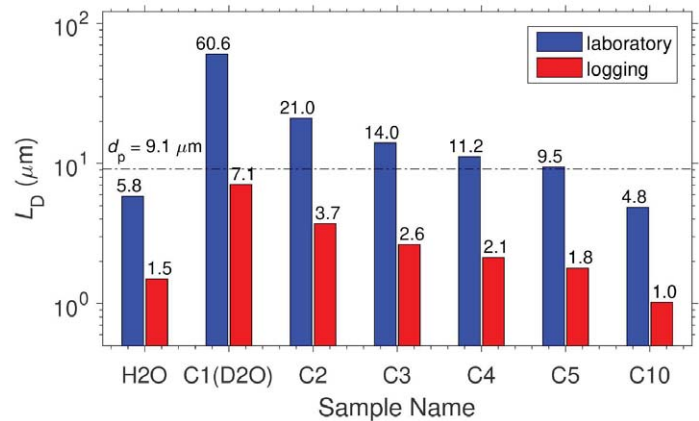


Fig. 18— Comparison of diffusion length of saturating fluids during D - T_2 laboratory measurements (blue), and during T_{2app} measurements under logging conditions (red). The dashed horizontal line indicates the diameter of the pore space associated with Region C estimated by the Padé fit as shown in Fig. 17.

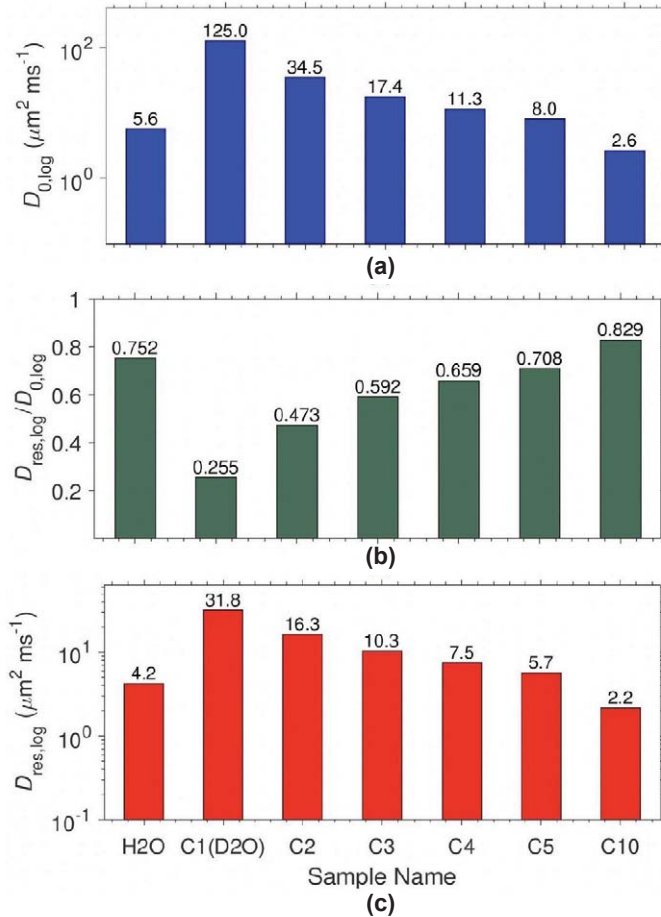


Fig. 19—Bar chart of diffusivities during $T_{2,\text{app}}$ measurements under logging conditions. (a) Is the plot of the estimated bulk diffusivity of fluids in the reservoir as listed in Table 4. (b) Is the plot of the extrapolated normalized restricted diffusivity based on the diffusion length L_D on logging conditions. (c) Is a plot of the restricted diffusivity. For each subplot, the y-axis shows diffusivity and the x-axis indicates fluid types.

The diffusion lengths on logging conditions are plotted in Fig. 18 along with those at laboratory conditions for comparison. The pore diameter estimated by the Padé fit is also plotted as the dashed line. Note that the diffusion length of methane at logging conditions is close to the pore diameter, such that methane experiences restriction provided by the limited pore space in porous media. The restriction is decreased as the diffusion length decreases. The restriction for fluids other than methane is less significant, as suggested by the Padé fit. However, the restriction is still not negligible. This is the reason why the restricted diffusivity is applied in Eq. 3 in place of the bulk diffusivity.

The Fig. 19b illustrates the normalized restricted diffusivity obtained by extrapolating the Padé fit to the diffusion length at logging conditions. These values confirm that the diffusion of all fluids is restricted, to different extents. For example, methane is greatly restricted with a normalized

restricted diffusivity of only 26%. The calculated restricted diffusivities are presented in Fig. 19c. The restricted diffusivities are implemented in the previous $T_{2,\text{app}}$ core-log calibration and $T_1/T_{2,\text{app}}$ subsections to simulate the NMR responses from the logging tool for composition estimation.

The pore radius, derived by the Padé fit assuming spherical pores, was then used to estimate the surface relaxivities, ρ_1 and ρ_2 , of fluids in macropores (Region C) under laboratory conditions by Eq. 8:

$$\rho_1 = \frac{v}{ST_{1S}} = \frac{r_p}{3T_{1S}}, \quad (8)$$

$$\rho_2 = \frac{v}{ST_{2S}} = \frac{r_p}{3T_{2S}},$$

where T_{1S} and T_{2S} are the surface relaxation components of T_1 and T_2 , respectively. For water, methane, ethane, propane, and butane, T_{1S} and T_{2S} are approximated by T_1 and T_2 at the peak of Region C where contributions from the bulk relaxation terms, T_{1B} and T_{2B} , are negligible. While for pentane and decane, the contributions from the bulk relaxation terms (i.e., $T_{1B} = T_{2B} = 3,754$ ms for pentane and $T_{1B} = T_{2B} = 1,350$ ms for decane by measurements with dissolved oxygen) are not negligible and thereby subtracted. The results are plotted in Fig. 20. It is obvious that methane, including both “C1” and “C1(D2O)”, undergoes higher surface relaxivities than the other liquid-state hydrocarbons. The longer alkanes experience lower surface relaxivities provided by the water-oil interface due to the mixed wettability. It is remarkable that the surface relaxivity for T_1 of decane is nearly zero, which means T_1 is dominated by bulk relaxation. The surface relaxivities for water are close to methane. The high surface relaxivities of water in the macropores may be due to two reasons (1) diffusive coupling exists between water in macro- and micropores, and (2) water is relaxed by the pore surface instead of a liquid-liquid interface, unlike hydrocarbons.

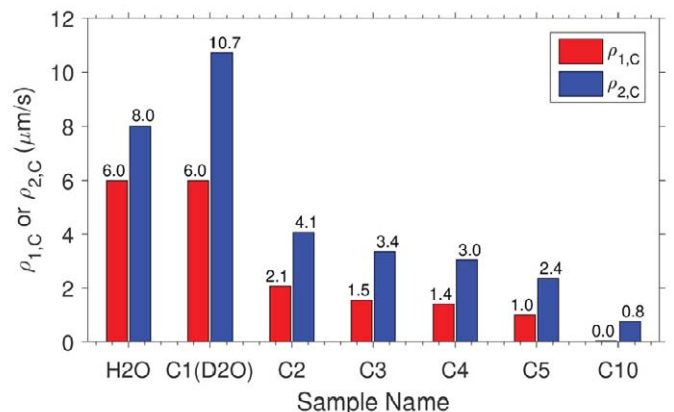


Fig. 20—Comparison of surface relaxivities experienced by fluids in macropores (Region C). The surface relaxivity of T_1 is plotted in red while the surface relaxivity of T_2 is plotted in blue.

CONCLUSIONS

In this work, tight rocks (~ 0.01 mD) from an organic-rich chalk reservoir were saturated with various fluids, including water, methane, NGLs (ethane, propane, butane, and pentane) and decane. The laboratory NMR measurements provided T_2 , T_1/T_2 , and D for qualitative composition estimation, fluid typing and mean pore-size calculation.

The laboratory-measured T_2 distributions were transformed to downhole-measured T_{2app} distributions by simulating the magnetic-field gradient effect from the logging tools. The “numerically mixed” T_{2app} distribution successfully reproduces the downhole T_{2app} distribution from NMR logs, thereby yielding the qualitative downhole hydrocarbon composition. The core-log calibration indicates that methane, ethane, and propane are the main components in the reservoir, while butane and longer alkanes have negligible contributions.

The laboratory-measured T_1/T_2 ratio and simulated downhole-measured T_1/T_{2app} ratio both demonstrate a contrast between saturating fluids. The magnetic-field gradient generated by logging tools amplifies the contrast in T_1/T_{2app} such that T_1/T_{2app} can in principle be exploited as a qualitative fluid-typing technique. It is found that methane and NGLs yields $T_1/T_{2app} > 2$. As such, a $T_1/T_{2app} = 2$ cutoff for downhole logs is proposed to distinguish methane and NGLs from heavier hydrocarbons and water. T_{2app} cutoffs can also be used in addition to T_1/T_{2app} cutoffs on the 2D T_1/T_{2app} vs. T_{2app} map for more robust fluid typing.

The laboratory-measured restricted diffusivity suggests that methane has higher diffusivity than all other liquids. The Padé approximation is used to fit the restricted diffusivity as a function of diffusion length of the saturating hydrocarbons, all the way from C1 (with the highest degree of restriction) to C10 (with the lowest degree of restriction). According to the Padé fit, the mean pore radius of the hydrocarbon-filled porosity is estimated to be $r_p \approx 4.6$ μm . The heterogeneity length scale $L_M \approx 5.1$ μm and the tortuosity $\tau \approx 84.9$ of the light-hydrocarbon-filled porosity are also estimated from the Padé fit.

ACKNOWLEDGMENTS

The authors thank Vinegar Technologies, LLC and Afek Oil & Gas for sponsoring this research. The authors thank Dr. Yoav Rosenberg for the core measurements at Ben-Gurion University and Dr. Yuval Bartov for providing the core. The authors thank Maura Puerto for experimental advisory. The authors thank Dr. Kelly McCann, Abby Vinegar, Brandon Fleet, Dr. Qian Zhang for their contributions to the crude oil database. The authors thank Dr. Pengfei Dong, Dr. Guoqing

Jian, and Leilei Zhang for their support in building the core-saturation system.

NOMENCLATURE

Abbreviations

BEI	=	backscatter electron imaging
EDS	=	energy-dispersive spectrometry
^1H	=	hydrogen nucleus (proton)
HI	=	hydrogen index
MD	=	molecular dynamics
MSE	=	mean squared error
NMR	=	nuclear magnetic resonance
NGLs	=	natural gas liquids
p.u.	=	porosity units
pu1	=	porosity units assuming HI = 1
pu/div	=	porosity units per division
pu1/div	=	porosity units per division assuming HI = 1
SEI	=	secondary electron image
SEM	=	scanning electron microscopy
TOC	=	total organic carbon

Symbols

D	=	diffusivity of fluids
D_0	=	bulk diffusivity of fluids
D_∞	=	diffusivity at the tortuosity limit
G	=	magnetic-field gradient
L_D	=	diffusion length
L_M	=	macroscopic heterogeneity length scale
r_p	=	pore radius
S	=	pore surface area
S/V	=	surface area to pore-volume ratio
T	=	temperature
T_d	=	dead time
T_E	=	interecho spacing of T_2 measurement
T_1	=	longitudinal relaxation time
T_{1S}	=	surface component of T_1
T_2	=	transverse relaxation time
T_{2app}	=	simulated downhole T_2
T_{2S}	=	surface component of T_2
T_{1B}	=	bulk component of T_1
T_{2B}	=	bulk component of T_2
T_{2D}	=	diffusion component of T_2
$(T_1/T_2)_{\text{peak}}$	=	T_1/T_2 ratio at the peak of 2D maps
$(T_1/T_{2app})_{\text{peak}}$	=	T_1/T_{2app} ratio at the peak of 2D maps
V	=	pore volume
δ	=	gradient encoding time
Δ	=	diffusion evolution time
μ	=	viscosity
ρ_1	=	surface relaxivity for T_1

- ρ_2 = surface relaxivity for T_2
 ϕ = total porosity
 ϕ_1 = liquid-filled porosity
 τ = tortuosity
 τ_{se} = spin echo time
 ω = NMR resonance (i.e. Larmor) frequency

REFERENCES

- Chen, Z., Singer, P.M., Jun, K., Vargas, F.P., and Hirasaki, G.J., 2017, Effects of Bitumen Extraction on the 2D NMR Response of Saturated Kerogen Isolates., *Petrophysics*, **58**(5), 470–484.
- Fleury, M., and Romero-Sarmiento, M., 2016, Characterization of Shales Using T_1 - T_2 NMR Maps, *Journal of Petroleum Science and Engineering*, **137**, 55–62. DOI: 10.1016/j.petrol.2015.11.006.
- Gerritsma, C.J., and Trappeniers, N.J., 1971, Proton Spin-Lattice Relaxation and Self-Diffusion in Methanes: I. Spin-Echo Spectrometer and Preparation of the Methane Samples, *Physica*, **51**(3), 365–380. DOI: 10.1016/0031-8914(71)900467-4.
- Hürlimann, M.D., Freed, D.E., Zielinski, L.J., Song, Y.Q., Leu, G., Straley, C., Minh, C.C., and Boyd, A., 2009, Hydrocarbon Composition from NMR Diffusion and Relaxation Data, *Petrophysics*, **50**(2), 116–129.
- Hürlimann, M.D., Helmer, K.G., Latour, L.L., and Sotak, C.H., 1994, Restricted Diffusion in Sedimentary Rocks. Determination of Surface-Area-to-Volume Ratio and Surface Relaxivity, *Journal of Magnetic Resonance, Series A*, **111**(2), 169–178. DOI: 10.1016/jmra.1994.1243.
- Kausik, R., Fellah, K., Rylander, E., Singer, P.M., Lewis, R.E., and Sinclair, S.M., 2016, NMR Relaxometry in Shale and Implications for Logging, *Petrophysics*, **57**(4), 339–350.
- Kausik, R., Minh, C.C., Zielinski, L., Vissapragada, B., Akkurt, R., Song, Y., Liu, C., Jones, S., and Blair, E., 2011, Characterization of Gas Dynamics in Kerogen Nanopores by NMR, Paper SPE-147198 presented at the SPE Annual Technical Conference and Exhibition, Denver, Colorado, USA, 30 October–2 November. DOI: 10.2118/147198-MS.
- Krynicky, K., Green, C.D., and Sawyer, D.W., 1978, Pressure and Temperature Dependence of Self-Diffusion in Water, *Faraday Discussions of the Chemical Society*, **66**, 199–208. DOI: 10.1029/DC9786600199.
- Latour, L.L., Mitra, P.P., Kleinberg, R.L., and Sotak, C.H., 1993, Time-Dependent Diffusion Coefficient of Fluids in Porous Media as a Probe of Surface-to-Volume Ratio, *Journal of Magnetic Resonance, Series A* **101**(3), 342–346. DOI: 10.1006/jmra.1993.1056.
- Lo, S.-W., Hirasaki, G.J., House, W.V., and Kobayashi, R., 2002, Mixing Rules and Correlations of NMR Relaxation Time with Viscosity, Diffusivity, and Gas/Oil Ratio of Methane/Hydrocarbon Mixtures, Paper SPE-77264, *SPE Journal*, **7**(1), 24–34.
- Minh, C.C., Crary, S., Singer, P.M., Valori, A., Bachman, N., Hursan, G.G., Ma, S.M., Belowi, A., and Kraishan, G., 2015, Determination of Wettability from Magnetic Resonance Relaxation and Diffusion Measurements on Fresh-State Cores, Paper III, *Transactions.SPWLA 56th Annual Logging Symposium*, Long Beach, California, USA, 18–22 July.
- Mitchell, J., Gladden, L.F., Chandrasekera, T.C., and Fordham, E.J., 2014, Low-Field Permanent Magnets for Industrial Process and Quality Control, *Progress in Nuclear Magnetic Resonance Spectroscopy*, **76**, 1–60. DOI: 10.1016/j.pnmrs.2013.09.001.
- Singer, P.M., Asthagiri, D., Chapman, W.G., and Hirasaki, G.J., 2017b, Molecular Dynamics Simulations of NMR Relaxation and Diffusion of Bulk Hydrocarbons and Water, *Journal of Magnetic Resonance*, **277**, 15–24. DOI: 10.1016/j.jmr.2017.02.001.
- Singer, P.M., Asthagiri, D., Chapman, W.G., and Hirasaki, G.J., 2018b, NMR Spin-Rotation Relaxation and Diffusion of Methane, *The Journal of Chemical Physics*, **148**, 204504. DOI: 10.1063/1.5027097.
- Singer, P.M., Asthagiri, D., Chen, Z., Valiya Parambathu, A., Hirasaki, G.J., and Chapman, W.G., 2018c, Role of Internal Motions and Molecular Geometry on the NMR Relaxation of Hydrocarbons, *Journal of Chemical Physics*, **148**, 164507. DOI: 10.1063/1.5023240.
- Singer, P.M., Chen, Z., Alemany, L.B., Hirasaki, G.J., Zhu, K., Xie, Z.H., and Vo, T.D., 2017a, NMR Relaxation of Polymer-Alkane Mixes, a Model System for Crude Oils, Paper XX, *Transactions, SPWLA 58th Annual Logging Symposium*, Oklahoma City, Oklahoma, USA, 17–21.
- Singer, P.M., Chen, Z., Alemany, L.B., Hirasaki, G.J., Zhu, K., Xie, Z.H., and Vo, T.D., 2018a, Interpretation of NMR Relaxation in Bitumen and Organic Shale Using Polymer-Heptane Mixes, *Energy & Fuels*, **32**(2), 1534–1549. DOI: 10.1021/acs.energyfuels.7b03603.
- Singer, P.M., Chen, Z., and Hirasaki, G.J., 2016, Fluid Typing and Pore Size in Organic Shale Using 2D NMR in Saturated Kerogen, *Petrophysics*, **57**(6), 604–619.
- Sigal, R.F., 2015, Pore-Size Distributions for Organic-Shale-Reservoir Rocks from Nuclear-Magnetic-Resonance Spectra Combined With Adsorption Measurements, Paper SPE-174546, *SPE Journal*, **20**(4), 824–830. DOI: 10.2118/174546-PA.
- Thern, H., Horch, C., Stallmach, F., Li, B., Mezzatesta, A., Zhang, H., and Arro, R., 2018, Low-field NMR Laboratory Measurements of Hydrocarbons Confined in Organic Nanoporous Media at Various Pressures, *Microporous and Mesoporous Materials*, **269**, 21–25. DOI: 10.1016/j.micromeso.2017.11.047.
- Tinni, A., Sondergeld, C., and Rai, C., 2018, New Perspectives on the Effects of Gas Adsorption on Storage and Production of Natural Gas from Shale Formations, *Petrophysics*, **59**(1), 99–104.
- Valori, A., Van den Berg, S., Ali, F., and Abdallah, W., 2017, Permeability Estimation from NMR Time Dependent Methane Saturation Monitoring in Shales, *Energy & Fuels*, **31**(6), 5913–5925. DOI: 10.1021/acs.energyfuels.7b00433.
- Venkataramanan, L., Song, Y., and Hürlimann, M.D., 2002, Solving Fredholm Integrals of the First Kind with Tensor Product Structure in 2 and 2.5 Dimensions, *IEEE Transaction on Signal*

Processing, **50**(5), 1017–1026. DOI: 10.1109/78.995059.

Wang, H.J., Mutina, A., and Kausik, R., 2014, High-Field Nuclear Magnetic Resonance Observation of Gas Shale Fracturing by Methane Gas, *Energy & Fuels*, **28**(6), 3638–3644. DOI: 10.1021/ef5002937.

Yang, Z., Hirasaki, G.J., Appel, M., and Reed, D.A., 2012, Viscosity Evaluation for NMR Well Logging of Live Heavy Oils, *Petrophysics* **53**(1), 22–37.

APPENDIX 1: DEUTERATION OF CONNATE WATER

It has been mentioned in previous sections that the signals in Regions B and C in the as-received cores originate from connate water. This is confirmed by the result of deuteration illustrated in Fig. A1.1, which focuses on the measurements on Core 1. The “As-received” is measured in the as-received state. The “C3, Desat” is the state after desaturation of propane following the NMR measurements. The NMR porosity dropping by ~ 7 pu1 from “As-received” to “C3, Desat” indicates that propane saturation and desaturation removes connate water, which is discussed in detail in Appendix 2. The “Deuterated” state measured after “C3, Desat” is prepared by immersing Core 1 in D_2O brine. The “Deuterated” state shows nearly zero signal, which confirms that the signal in Regions B and C are both from connate water.

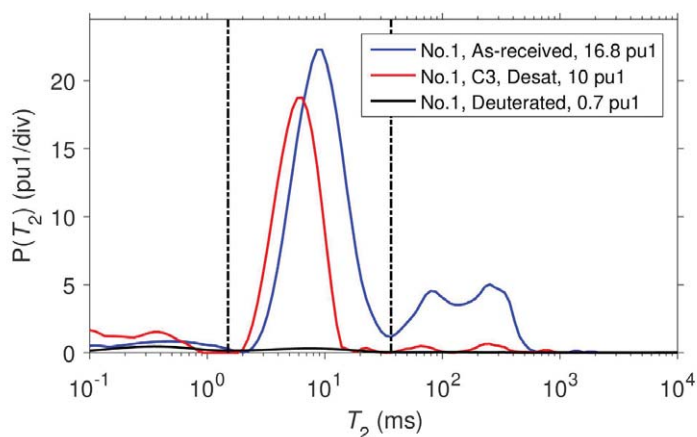


Fig. A1.1— T_2 distributions of Core 1 at three different states. The “As-received” is measured at the as-received state. The “C3, Desat” state is measured after propane desaturation. The “Deuterated” measured after “C3, Desat” is deuterated by D_2O . Dashed lines divide the T_2 distributions into three regions, as in Fig. 5. The legend indicates the core number, the state, and the NMR porosity. “pu1” refers to porosity units assuming HI = 1.

APPENDIX 2: EXPULSION OF CONNATE WATER

The loss of connate water and the shift of T_2 are results of connate water mobilization and expulsion by the hydrocarbon saturation and desaturation, which is confirmed by the expelled water collected after desaturation of hydrocarbons. Figure A2.1 also clearly indicates the occurrence of water expulsion. The comparison between T_2 distributions of the as-received and desaturated cores was shown in Fig. A2.1. It is known that these “twin” Cores 1 to 6 share similar T_2 distributions as indicated by Fig. 5. Therefore only the as-received Core 2 is plotted as the baseline.

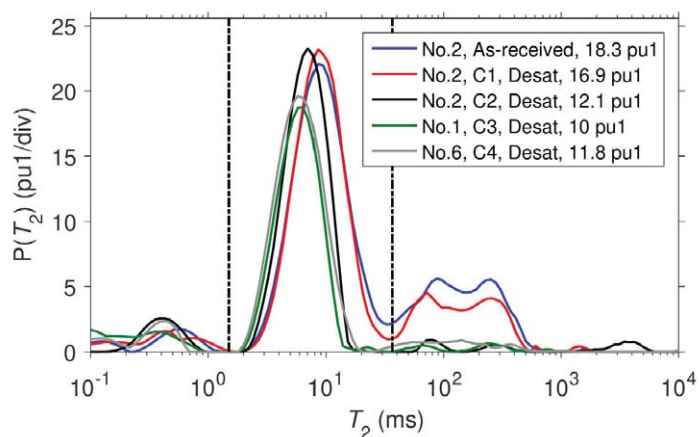


Fig. A2.1— T_2 distributions of as-received and desaturated cores. The “As-received” is measured at the as-received state. The “Desat” states are measured after the desaturation of hydrocarbons. Dashed lines divide the T_2 distributions into three regions, as in Fig. 5. The legend indicates the core number, the state, and the NMR porosity. “pu1” refers to porosity units assuming HI = 1.

Figure A2.1 indicates the connate water is removed after hydrocarbon desaturation. As noticed, methane barely removes the connate water from the core. The amount of connate water expelled by hydrocarbons increases with the carbon-chain length. The connate water in Region C is nearly zero after desaturation of ethane, propane, and butane. The trend of the amount of water expulsion can be explained by the difference in mobility ratios of hydrocarbons, as proposed in the section on T_2 distributions. Meanwhile, the shift of T_2 in Region B can be explained by Eq. 8. In the current case, S stays constant while V is reduced as a result of less connate water. This shift of T_2 after desaturation agrees with the T_2 shift observed in Fig. 6 in saturated cores.

Figure A2.2 presents additional clear evidence of connate water expulsion. Figures A2.2a and A2.2b are the 2D profile- T_2 correlation maps of water-saturated Core 3 and decane-saturated Core 5. The T_2 profiles are measured by applying the frequency-encoded CPMG pulse sequence with an echo spacing $T_E = 2$ ms. The resolution of the profiles is 1.5 mm along the core plug axis. Note the T_2 distributions are homogeneous along the axial direction in the water-saturated core. In contrast, heterogeneity is found in the decane-saturated core, where the inlet has less fluid in Region B at the expense of more fluids in Region C. This is interpreted as connate water in micropores being displaced by decane near the inlet. The connate-water expulsion results from the high pressure gradient during the early stage of pressurization or depressurization. In the case of methane, ethane, propane, and decane, the fluids are injected at a constant pressure of 500 psia to the cores with ambient pore pressure for the first stage, which leads to a large pressure gradient in the inlet. As for butane and pentane, the injection is done by gradually increasing the injecting pressure to avoid the pressure-surge problem. However, water expulsion is still observed (see Fig. A2.2).

Based on the measurements on the desaturated cores shown in Fig. A2.1, the fluid saturations in Region C are visualized in Fig. A2.3. As indicated in Table 3, the hydrocarbon saturation of ethane and higher carbon-number alkanes (i.e., “C2” to “C10”) is conducted on the as-received

cores, where the connate water in Region C is expelled by the alkanes during saturation. The C2 to C10 alkanes occupy nearly the entire pore space of Region C, except for a water-film coating the pore surface.

However, in the case of methane saturation on the as-received core (i.e., “C1”), the connate water is not removed, such that the methane only partially occupies the pore space of Region C, and the NMR measurement on “C1” has interference from the water signal. The “C1(D2O)” is conducted on the C3-desaturated core, where the connate water has already been expelled by the saturation and desaturation of propane, furthermore, the remaining water film in the core is deuterated. Under these conditions, the methane takes up the entire pore space, similar to the NGLs and decane. Therefore, the NMR distributions in Region C for “C1(D2O)” and “C2” to “C10” are dominated by pure alkanes. This is the reason why “C1(D2O)” is used in the saturation estimation instead of “C1”.

APPENDIX 3: SATURATION ESTIMATION WORKFLOW

Fig. A3.1 illustrates the workflow for the hydrocarbon-saturation estimation, the results of which are presented in Figs. 7 and 8. This estimation is based on the comparison between the simulated T_{2app} distributions from laboratory measurements and the downhole logged T_{2app} distribution.

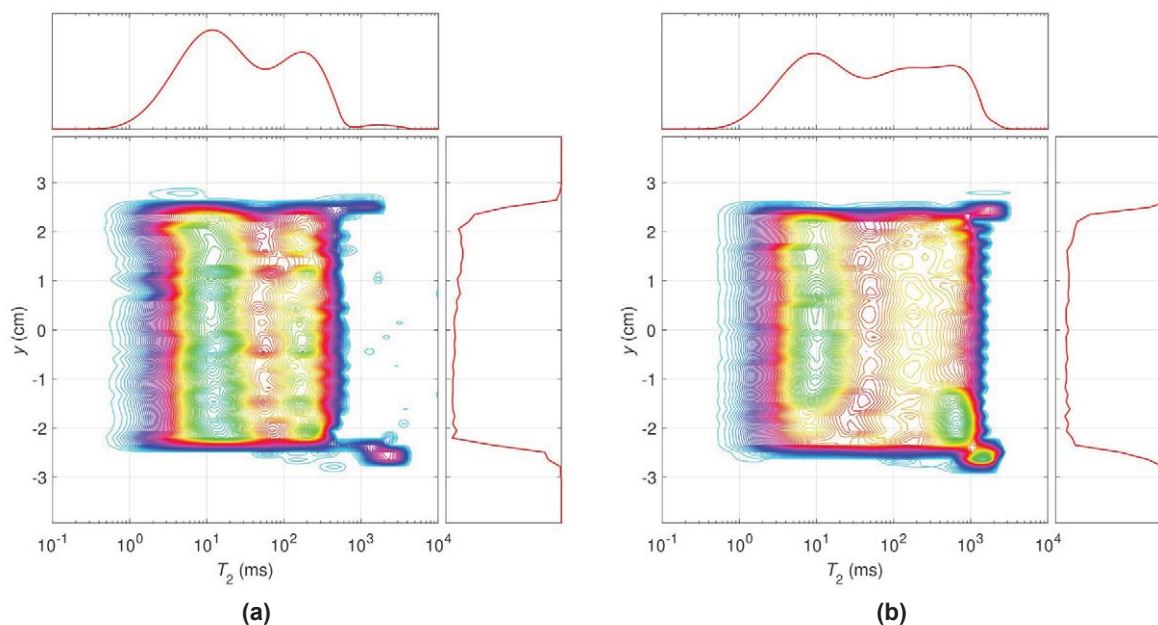


Fig. A2.2—2D correlation maps of (a) water- and (b) decane-saturated Cores 3 and 5, respectively, with y (position in the axial direction) on the y -axis, T_2 on the x -axis and porosity perpendicular to the page. The top subplot is the projected T_2 distribution. The right subplot is the projected porosity profile.

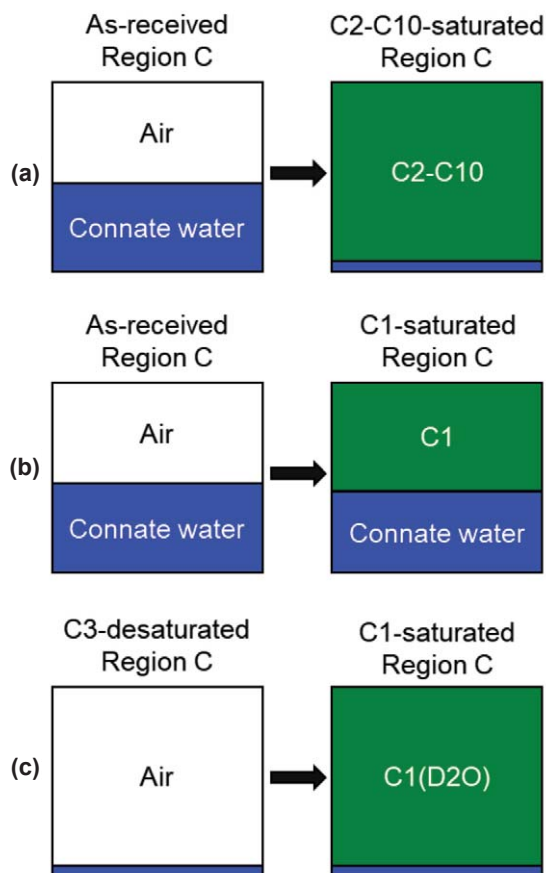


Fig. A2.3—A visualization of fluid saturation in the pore space of Region C before and after each hydrocarbon-saturation: (a) for NGLs and “C10”; (b) for “C1”; and (c) for “C1(D2O)”. Note that the residual water of the “C3-desaturated” in subplot (C) is deuterated.

As mentioned in the previous section, the laboratory-measured T_2 distributions were converted to the T_{2app} distributions by considering the effect of magnetic gradients from the logging tool. It should be noted that the restricted diffusivities in the downhole conditions used in the simulation of T_{2app} distributions are different from the laboratory-measured restricted diffusivities, due to the difference in diffusion length (see Eq. 5). Therefore, the downhole restricted diffusivity is calculated by extrapolating the Padé approximation to the diffusion length for the logging tool. Also note that during the simulation of T_{2app} distributions from T_2 distributions, the difference in HI of each fluid between laboratory and downhole conditions (see Table 4) are corrected by rescaling the T_{2app} distribution.

As shown in Fig. A3.1, the numerically mixed T_{2app} distribution from laboratory measurements is compared to the T_{2app} logging data. The difference in the T_{2app} distribution between the laboratory “mix” and the log is quantified by the

mean squared error (i.e., MSE). The optimal volume fraction of each hydrocarbon is estimated by minimizing the MSE using a grid-search algorithm.

APPENDIX 4: BULK FLUID PROPERTIES

The bulk properties of water and hydrocarbons at both laboratory conditions (30°C, 1,200 psia) and downhole conditions (68°C, 2,755 psia) are shown in Table 4. This appendix shows the details on how the bulk properties are estimated.

The density and viscosity of fluids are inferred from the NIST REFPROP (<https://www.nist.gov/srd/refprop>) database with temperature and pressure as the inputs. The hydrogen indexes (HI) of fluids other than water are calculated by comparing the proton densities with that of water at the same temperature and pressure. Note that only methane shows significant differences in density and HI under different conditions. Also, note that methane under both conditions is a supercritical fluid instead of a gas.

The diffusivity of water measured at 25°C and ambient pressure is used for the laboratory conditions. For the reservoir conditions, Krynicki et al. (1978) measure the diffusivity of water at 70.05°C and at around 1,470 and 4,410 psia, respectively, which are similar to the reservoir conditions in this work. These two measurements at different pressures both yield diffusivities around $5.6 \mu\text{m}^2/\text{ms}$ which is adopted here as the bulk diffusivity of water at reservoir conditions.

The diffusivity of ethane, propane, butane, pentane, and decane are estimated by substituting the temperature and viscosity into Eq. A4.1, which is an empirical correlation proposed by Lo et al. (2002):

$$D_0 = 4.69 \times 10^{-3} \frac{T}{\mu} \quad (\text{A4.1})$$

where D_0 is bulk diffusivity with a unit of $\mu\text{m}^2/\text{ms}$, T is temperature with a unit of K and μ is viscosity in cP.

The diffusivity of methane is obtained differently. It is inferred from the experimental data published by Gerritsma and Trappeniers (1971), who measured the bulk diffusivity of methane as a function of bulk density and temperature. The original data (Gerritsma and Trappeniers, 1971) are reorganized and plotted in Fig. A4.1. The measured bulk diffusivities in different phases are clustered and plotted against the predicted viscosity/temperature (μ/T). The predicted μ/T is inferred from REFPROP based on the bulk density and temperature. In Fig. A4.1, the data points of methane vapor (black) overlay with those of supercritical

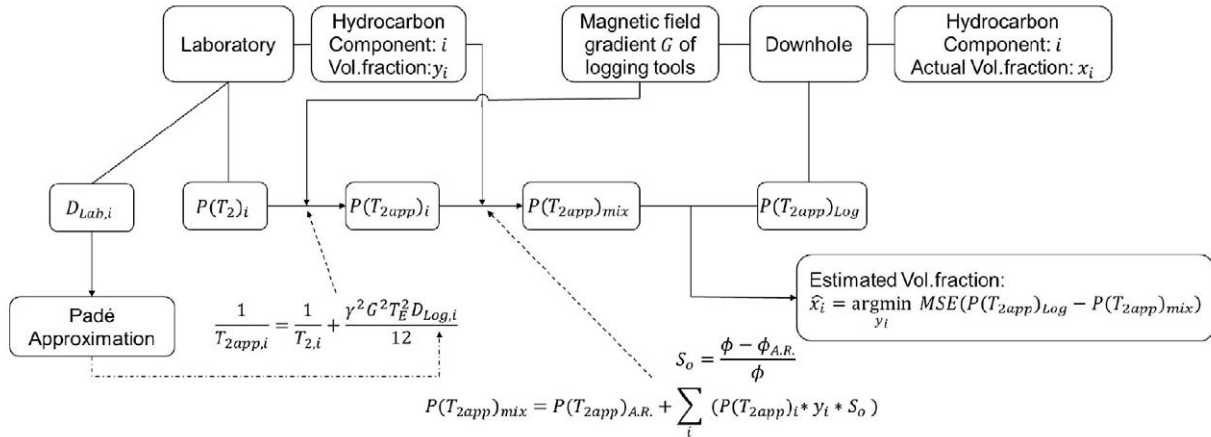


Fig. A3.1—The workflow for the hydrocarbon-saturation estimation based on the T_{2app} distributions simulated using laboratory-measured T_2 distributions and the Padé approximation.

methane (red). It is obvious that the bulk diffusivity of the methane vapor and some of the supercritical methane do not follow the Stokes-Einstein equation, which predicts that D vs. μ/T is a straight line on a log-log plot, similar to Eq. A4.1. Therefore, the μ/T of methane, under both laboratory and reservoir conditions, is used to estimate the bulk diffusivity (shown as the two vertical dashed lines in Fig. A4.1). The μ/T of methane under laboratory conditions suggests a bulk diffusivity $\sim 250 \mu\text{m}^2/\text{ms}$, while methane under downhole conditions yields a bulk diffusivity $\sim 125 \mu\text{m}^2/\text{ms}$. Note that it is expected that ethane is the predominant fluid in the

reservoir. Therefore, the laboratory condition (i.e., the pore pressure) is selected such that the density of ethane at the laboratory condition matches with its density at the reservoir condition. The mismatch in the methane diffusivity between the laboratory and reservoir conditions is a compromise of a better match in the ethane density.

It should be noted that molecular dynamics (MD) simulation serves as a more fundamental approach to estimate the bulk diffusivity, as well as NMR T_1 and T_2 relaxation times, of water and alkanes (including methane). It has been demonstrated that the MD simulation yields T_1 , T_2 and diffusivity predictions in excellent agreements with experimental results (Singer et al., 2017b, 2018b, 2018c).

APPENDIX 5: BULK CRUDE OILS

In Fig. 13, the responses of crude oils are simulated and plotted. The bulk relaxation times of crude oils are computed based on the Hirasaki group crude oil database (contributed by Kelly McCann, Abby Vinegar, Brandon Fleet, Qian Zhang), of which the detailed information is tabulated in Table A5.1.

Figure A5.1 shows the T_1 and T_2 peak values of bulk crude oils and a few hydrocarbons. According to Table A5.1, the log-mean values are systematically lower than the peak values. The reason for using the peak values instead of the log-mean values for analysis is because, in this study, the representative T_1 and T_2 of Region C are picked at the peak of 2D maps. Therefore, using the peak value yields a more comparable result.

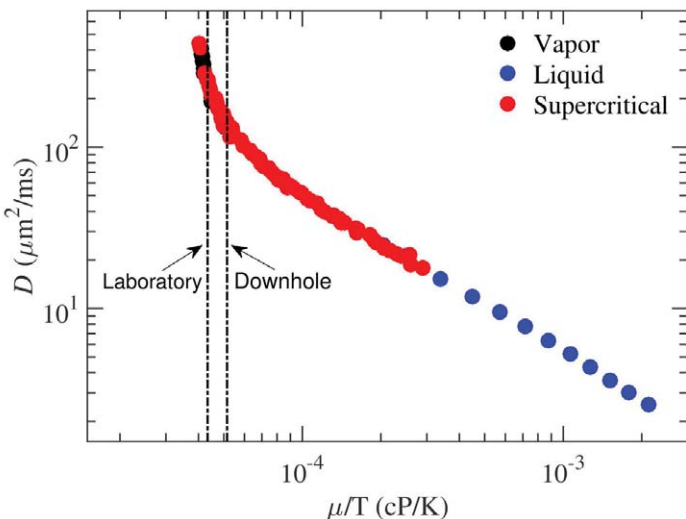


Fig. A4.1—Bulk diffusivity D vs. viscosity/temperature μ/T of methane in different phases (Gerritsma and Trappeniers, 1971). The μ/T of methane under laboratory and downhole conditions is labeled by the vertical dashed lines.

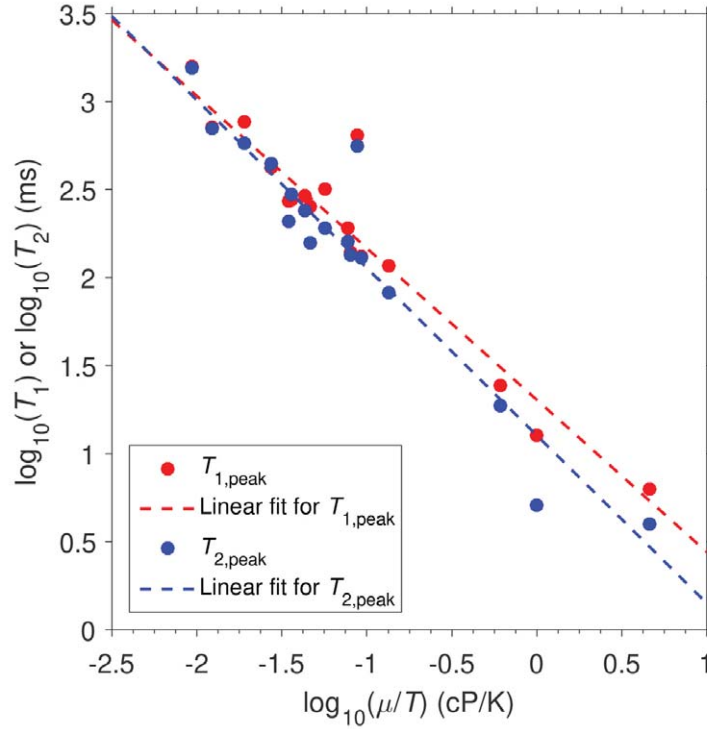


Fig. A5.1— T_1 and T_2 peak values of crude oils and other hydrocarbons versus viscosity over absolute temperature (μ/T). Dashed lines are the linear fittings for T_1 and T_2 , respectively. The raw data are from Hirasaki group crude oil database and tabulated in Table A5.1. Note that only the data with available viscosity are plotted.

Table A5.1—Data for Crude Oils and Hydrocarbons Measured by the Hirasaki Group

Sample	Asphaltene Content (%)	Density at 30 C (g/cm ³)	Viscosity at 30 C (cP)	HI	H:C Ratio at 30°C	T_2 Log Mean (ms)	T_1 Log Mean (ms)	T_2 Peak (ms)	T_1 Peak (ms)	T_1/T_2 Peak Ratio
M14	12.50	---	---	0.648	---	0.5	4.7	0.5	1.4	2.80
SNS	---	0.843	26.50	0.955	1.73	243.7	336.7	560.8	648.1	1.16
Diluted Bitumen	---	0.886	14.00	0.980	1.68	30.8	83.5	158.3	251.9	1.59
M13	9.00	0.938	302.00	0.847	1.34	2.8	9.8	5.1	12.7	2.49
SM	---	0.849	---	0.953	1.71	92.2	121.2	221.2	249.0	1.13
SMP69	---	0.870	13.10	0.954	1.67	118.3	131.3	241.3	291.7	1.21
SMP	3.10	0.940	184.00	0.902	1.43	7.2	11.0	18.7	24.3	1.30
SMT	2.30	0.890	40.60	0.924	1.57	30.9	49.5	81.5	116.9	1.43
SMY	5.50	0.881	23.40	0.951	1.64	43.7	79.7	160.0	191.7	1.20
SMID	7.50	0.869	10.50	0.893	1.55	70.1	144.4	210.0	272.3	1.30
NB	0.30	0.841	8.28	0.984	1.80	230.6	246.6	444.1	422.7	0.95
M11	0.20	0.831	3.70	0.942	1.73	438.7	452.1	706.0	720.1	1.02
M2	0.50	0.831	5.78	0.954	1.76	413.6	364.5	577.2	765.9	1.33
M4	6.81	0.959	1400.00	0.851	1.31	2.1	6.9	4.0	6.3	1.58
M1	0.71	0.901	28.40	0.949	1.59	62.3	64.8	129.1	132.4	1.03
SWCQ	1.60	0.902	24.40	0.967	1.62	64.8	85.1	135.5	139.9	1.03
M10	8.54	0.879	17.20	0.957	1.65	45.3	101.4	192.4	320.0	1.66
1-Methylnaphthalene	0.00	1.016	2.82	0.621	0.87	1549.1	1499.0	1543.1	1574.3	1.02
Squalene	0.00	0.852	11.00	0.911	1.62	262.6	268.6	299.1	277.5	0.93
Toluene	0.00	0.857	0.82	0.672	1.15	2329.7	2241.5	2494.6	2478.0	0.99

Including asphaltene content, density, viscosity, hydrogen index (HI), hydrogen to carbon ratio, and T_1 and T_2 values. Note that the measurements are conducted at 30°C. Contributed by Kelly McCann, Abby Vinegar, Brandon Fleet, and Qian Zhang.

Along with the raw data, two linear fittings (on the log scale) are generated, as shown in Fig. A5.1. The two fittings illustrate the relationship between either T_1 or T_2 and the viscosity over the absolute temperature. The viscosity over the absolute temperature is a combined parameter, and thereby the regression relationship obtained at laboratory conditions can be generalized to the reservoir conditions. In other words, for a given viscosity of crude oil at reservoir temperature, the corresponding T_1 and T_2 values can be inferred.

APPENDIX 6: POROSITY PARTITIONING

The porosity partitioning between Regions A, B, and C is shown in Fig. A6.1. We find that the as-received NMR porosity in Region A ($T_2 < 3$ ms) is ~ 1 pu1, has a large $T_1/T_2 \sim 10$ (see Fig. 10), and could therefore be bitumen (Chen et al., 2017). The NMR porosity in Region A increases to ~ 3 pu1 after saturating with C2 to C10, and maintains a large $T_1/T_2 \sim 15$.

The most likely explanation for the increase in NMR porosity in Region A after hydrocarbon saturation is that some saturating hydrocarbons dissolve in the bitumen, thereby decreasing the viscosity of the bitumen, and thereby increasing the bitumen T_2 to within the detection limit (i.e., T_2 becomes comparable to T_E). The ~ 3 pu1 in Region A corresponds roughly to the 3.6 p.u. of bitumen by extraction (Table 4), which adds credibility to this interpretation.

Further evidence of this interpretation comes from independent T_2 measurements at elevated temperatures carried out at Ben-Gurion University (on cores from similar depths). Increasing temperature results in a comparable increase in porosity in Region A, which can be explained by an increase in bitumen signal due to a decrease in bitumen viscosity.

In addition to the above interpretation, a portion of the increase in NMR porosity in Region A after hydrocarbon saturation could originate from the saturating hydrocarbons dissolved in the bitumen and/or kerogen, which have been shown to have short T_2 and large T_1/T_2 (Chen et al., 2017).

We note that the saturating fluids interact with the kerogen surface, which contributes to the “apparent” surface relaxivity of the pore fluid in Region C (Chen et al., 2017). The separation of the signal between the pore fluid in Region C and the dissolved fluid in the bitumen and/or kerogen depends on the degree of diffusive coupling between the two fluids. In the case of weak diffusive coupling, the two fluids have distinct T_2 values (dissolved fluid in Region A, and pore-fluid in Region C). In the case of strong diffusive coupling, the two fluids have only one (merged) peak located in Region C.

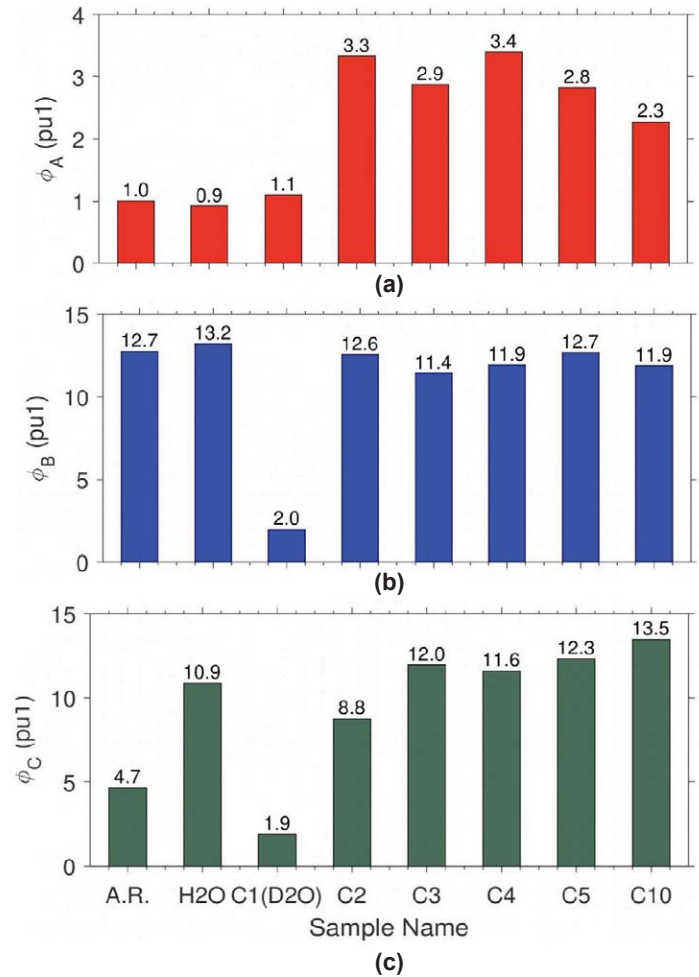


Fig. A6.1—NMR porosity partitioning between Regions A, B, and C. Subfigures (a), (b), and (c) correspond to porosity in Regions A, B, C, respectively. “pu1” refers to porosity units assuming HI = 1.

ABOUT THE AUTHORS



Zeliang Chen is a research assistant in the Hirasaki research group at Rice University in Houston, Texas. His research focuses on laboratory core analysis and numerical simulation for unconventional formation evaluation. He received his PhD in applied physics at Rice University in Houston, Texas, and BSc in Applied Physics at the University of Science and Technology of China (USTC) in Hefei, China.



Philip M. Singer is a research scientist in the Hirasaki research group at Rice University in Houston, Texas, focused on NMR core and fluid analysis. Previously, he worked at Schlumberger for 10 years, as laboratory supervisor of the NMR core analysis department at the Schlumberger Reservoir Laboratories in Houston Texas, and as senior research scientist at Schlumberger-Doll Research in Cambridge, Massachusetts, and Schlumberger Dhahran Carbonate Research Centre in Saudi Arabia. He holds a MSc in Physics from the University of Oxford, and a PhD in Physics from the Massachusetts Institute of Technology.



Xinglin Wang is a Chemical and Biomolecular Engineering PhD candidate in the Hirasaki research group at Rice University in Houston, Texas. He focuses on NMR core analysis for unconventional formation evaluation. He received his bachelors degree in Chemical Engineering in Qiushi Honor College at Tianjin University in Tianjin, China.



Harold J. Vinegar is president of Vinegar Technologies, LLC in Houston, Texas. He spent 32 years at Shell's research laboratories in Houston, Texas, working on novel E&P technologies before retiring as Chief Scientist of Royal Dutch Shell in October 2008. Harold served as President and VP Technology of the Society of Core Analysts. He received the Distinguished Technical Achievement Award of the SPWLA (1992) and the SPWLA Gold Medal for Lifetime Technical Achievement (2009). In 2003, he was inducted into the National Academy of Engineering. After retiring from Shell, Harold and his family lived 8 years in Israel where he was Chief Scientist of Israel Energy Initiatives and Afek Oil & Gas, as well as Professor of Petroleum Geoscience at Ben-Gurion University of the Negev.



Scott V. Nguyen is CEO of 17TeraWatts and Founder of Braket Technologies. Previously, he was Vice President of Technology for Genie Oil and Gas and Senior Petrophysicist for Shell E&P. He is the holder of 17 US patents and 16 peer-reviewed publications. He

received his MS and PhD from Harvard University.



George J. Hirasaki is the A.J. Hartsook Professor Emeritus in Chemical Engineering at Rice University in Houston Texas. Before his 24-year faculty position at Rice University, he was a research engineer for 26 years with Shell Development and Shell Oil Company in Houston, Texas. His research work broadly encompasses the area of enhanced oil recovery processes, wettability in petroleum systems, NMR core and fluid analysis, and gas hydrates. Among his numerous scientific awards and accomplishments, he has been a member of the National Academy of Engineers for 26 years, and was recently awarded the 2016 OTC Heritage Award and the 2016 SPE Lucas Gold Medal.

Influence of Magnetic Susceptibility Contrast on NMR Studies—Experimental Analysis From Siliciclastic Reservoirs

Partha Sarathi Sarkar¹, Soma Chatterjee¹, Mohan Lal¹, Manoj Kumar¹, and P.P. Deo¹

ABSTRACT

Nuclear magnetic resonance (NMR) experiments are performed on the nuclei of atoms by exposing these nuclei to magnetic field. NMR measurement is lithology-independent as the only source of the measured signal is from the pore fluids. As the pore fluids interact with rock surfaces, the rock matrix influences the fluid response and complicate the data interpretation. In this regard, two phenomena, namely internal gradients and restricted diffusion, come into the picture. In porous media, contrast in the magnetic susceptibility of rock grains and pore fluids might lead to significant magnetic-field inhomogeneities. The internal gradients resulting from these local field heterogeneities can cause further reduction in T_2 relaxation times as well as the T_2 cutoff. Under specific conditions, more precisely, in a free-diffusion regime, internal magnetic-field gradients can be calculated from the increase in the transverse relaxation rate of pore fluids with increasing interecho time.

A comprehensive NMR study was carried out on two distinct formations/pays from two different basins located in the eastern and western parts of India, namely, low-resistivity, low-contrast (LRLC) pay of the Tipam formation (Charali field, Assam and Assam Arakan basin) and the

Chhatral pay of the Cambay shale formation (Gamij field, Cambay basin). The influence of magnetically susceptible material on NMR T_2 relaxation and hence, on T_2 cutoffs, has been analyzed.

We studied echo-spacing dependence on the diffusion component of transverse relaxation and could observe different asymptotic relaxation regimes. In the present study, T_1/T_2 2D laboratory data have also been acquired and T_1/T_2 ratios have been studied alongside the echo-spacing dependence of T_2 relaxation. In two presented case studies, although we have contrasting permeability ranges (poor in one set/field to moderate/high in other), we obtained perceptibly low T_2 cutoff values (compared to a default 33-ms T_2 cutoff) for both cases.

Our study shows the presence of an internal field gradient, which in turn indicates a magnetic susceptibility contrast between pore-filling fluids and rock matrix. The presence of paramagnetic minerals is one of the factors in lowering the T_2 cutoff values that has also been reported in mineralogical studies. The observed range of T_1/T_2 ratios indicates the presence of varying size, susceptibility, concentration and distribution of magnetically susceptible sites as well as different orders of grain sizes.

INTRODUCTION

Nuclear magnetic resonance (NMR) is recognized as a powerful tool for reservoir characterization. The porosity and pore-size information from NMR measurements can be used to estimate both the permeability and the potentially producible porosity. As pore fluids interact with rock surfaces, the rock matrix influences the fluid response and complicates the data interpretation. In this regard, two phenomena, namely internal gradients and restricted diffusion, come into play. If the applied magnetic field is not homogeneous, NMR measurements become very sensitive to the molecular diffusion of the pore fluid. In

porous media, a contrast in magnetic susceptibility of rock grains and pore fluids might lead to significant magnetic field inhomogeneities i.e., internal magnetic-field gradients. These internal field gradients in rocks have a significant effect on NMR transverse relaxation time (T_2) distribution. It can cause further reduction in T_2 relaxation times as well as the T_2 cutoff. These field gradients are primarily due to the presence of paramagnetic ions, such as iron, nickel or manganese (Kleinberg et al., 1994). If the T_2 changes with echo spacings in a homogeneous applied magnetic field, the most probable factor is the phenomenon of diffusion under internal gradients. In general, clean sand has a T_1/T_2 ratio between 1 and 2. If paramagnetic materials, such as iron,

Manuscript received by the Editor March 27, 2019; revised manuscript received July 29, 2019; manuscript accepted July 31, 2019.

¹ONGC Ltd., Makarpura Main Road, Vadodara; Gujarat, India, Pin-390009; sarkar_ps@ongc.co.in; chatterjee_soma@ongc.co.in; lal1234_mohan@ongc.co.in; kumar_manoj3@ongc.co.in; deo_pritiprasad@ongc.co.in

are present, the T_1/T_2 ratio in most cases increases above that of clean sand (depending on the relaxation regimes). This increase of the T_1/T_2 ratio is due to diffusion in internal gradients.

A strong dependence of transverse relaxation on echo spacing has been reported in different studies on fluid-saturated porous media (Hürlimann, 1998; Appel et al., 1999; Dunn et al., 2001; Zhang et al., 1998, 2001, 2003; Fantazzini and Brown, 2005). But, this dependence is not always quadratic, as inferred by the classical expression (Carr and Purcell, 1954). Hence, the principles that govern the relaxation characteristics of sedimentary rocks must be understood properly for an accurate interpretation of NMR measurements.

In the present study, an attempt has been made to understand the additional transverse relaxation, i.e., diffusion contribution to T_2 relaxation, caused by the loss of phase coherence between nuclear spins due to diffusion in magnetic-field inhomogeneities, and also to estimate the maximum prevailing internal gradient.

In laboratory conditions, measurements are carried out in a homogeneous static magnetic field. Internal magnetic-field gradients can be calculated from the increase of the transverse relaxation rate of pore fluids with increasing interecho time. The increase of transverse relaxation rate and the squared interecho time are linearly related for the case of unrestricted molecular diffusion of the pore fluid. Deviations from this linear relationship can be observed in the restricted-diffusion regime.

We present results of laboratory NMR experiments on two sets of core samples taken from fields of Assam Arakan Basin and Cambay Basin, India. This study will be of significant importance for the interpretation of wireline NMR log data, which will help in better understanding the reservoir and lead to realistic reservoir characterization. For these samples, we found significant internal magnetic-field gradients that exceed those applied by wireline tools or standard rock-core NMR analyzers.

Concept of T_2 Relaxation

T_2 relaxation time is also known as transverse, or spin-spin, relaxation time. The time constant of the transverse magnetization decay is called the transverse relaxation time, T_2 . For fluids filling rock pores, there are three independent relaxation mechanisms namely bulk, surface and diffusion relaxation. All these relaxations work in parallel. Hence T_2 can be represented as

$$\frac{1}{T_2} = \frac{1}{T_{2B}} + \rho_2 \frac{S}{V} + \frac{1}{12} (TE \cdot \gamma \cdot G)^2 D, \quad (1)$$

where ρ denotes the surface relaxivity, S/V the surface/volume ratio of the pore structure, TE is the echo spacing, γ is the nuclear gyromagnetic ratio, G is the gradient of the magnetic field, and D is the diffusivity of the fluid.

A CPMG sequence (Carr-Purcell-Meiboom-Gill) is used to measure T_2 . This pulse sequence eliminates effects due to local variations in the magnetic field. Therefore, the signal decay is due to interactions with neighboring spins and surfaces. The CPMG sequence eliminates dephasing effects due to magnet inhomogeneities and, therefore, measures the true T_2 of the sample. In a porous rock system, there will be a continuous range of pore sizes, rather than several discrete sizes. This means that the CPMG echo-train comprises of a continuous range of relaxation times. Each pore-size has a distinctive T_2 value. The echo-train corresponding to one particular pore-size will have a characteristic T_2 value and signal amplitude proportional to the amount of fluid contained in pores of that size. For a pore system with a continuous range of pore sizes, each pore size has a corresponding T_2 value and signal amplitude. The resulting echo-train therefore consists of a continuous distribution of T_2 values each with different signal amplitudes.

Influence of Magnetically Susceptible Constituents—Concept of Internal Gradient

If the applied magnetic field is inhomogeneous and possesses a gradient over length scales that are comparable with the dephasing length of the spins, i.e., the typical displacement length of fluid molecules before they dephase during the time of the NMR experiment, the measurements become sensitive to the molecular diffusion of the pore fluid. NMR data interpretation requires knowledge of the gradient in which the pore fluids reside. Generally, this gradient is the one applied by the wireline tool or laboratory spectrometer and thus, it is known. However, in porous media, if magnetic susceptibility differences exist between the solid phase and the fluid filling the pore space it would lead to significant magnetic-field inhomogeneities, causing internal magnetic-field gradients. It is commonly assumed that these field gradients are primarily caused by paramagnetic ions, such as iron, nickel or manganese, which are frequently found in clays (Kleinberg et al., 1994).

Again, following the concept of diffusion under the influence of confinement within a fractal structure, such as in a porous medium, the diffusion of the pore fluids, in terms of molecular mean-squared displacement during the diffusion time, depends on the fractal dimension of confinement/propagation and may, in turn, be classified into unrestricted, or “free” diffusion and restricted diffusion (Avenir, 1989).

Echo-Spacing Dependence on T_2 Relaxation and T_1/T_2 Ratio

Several studies with fluid-saturated porous media have reported a strong dependence of the transverse relaxation on the echo spacing (e.g., Brown and Fantazzini, 1993; Hurlimann, 1998; Appel et al., 1999; Fantazzini and Brown, 2005). However, the dependence is not always quadratic, as predicted by the expression for unrestricted diffusion in a constant gradient (Carr and Purcell, 1954).

To obtain a deeper insight of NMR T_2 relaxation phenomenon in sedimentary rocks, echo-spacing dependence and T_1/T_2 ratio are the two relaxation characteristics that bear the maximum significance. The diffusion component of transverse relaxation in porous media under constant gradient (unrestricted and restricted diffusion) as well as in inhomogeneous field gradients or with internal gradients (by influence of magnetically susceptible constituents) thus, needs to be discussed in brief. In later sections, the effects seen on field samples in the study areas will be elaborated upon.

INFLUENCE OF MAGNETIC-FIELD INHOMOGENEITIES IN POROUS MEDIA

In porous media, field inhomogeneities are often induced due to differences in magnetic susceptibility of pore fluids and paramagnetic minerals on pore surfaces. Diffusion of fluid molecules in such inhomogeneous fields leads to additional relaxation of transverse magnetization (i.e., $T_{2,D}$ component) due to dephasing.

DeSwiet and Sen (1994) and Hurlimann (1998) described three length scales that characterize the diffusion contribution to T_2 relaxation:

- Pore structural length, $L_s (= V/S)$.
- Diffusion length, L_d , $L_d = \sqrt{D \cdot \tau}$, where D is the diffusivity of the fluid and τ is the half echo spacing ($\tau = TE/2$) for CPMG pulse sequences.
- Dephasing length, L_g , defined as the distance over which the spins have to diffuse in order to dephase by 1 radian given as $L_g = \sqrt{D/\gamma G}$ where γ is the proton gyromagnetic ratio.

Depending on the smallest length scale, diffusion-induced relaxation can be characterized into three asymptotic relaxation regimes of motionally averaging, free diffusion and localization, as introduced by Hurlimann (1998).

ASYMPTOTIC REGIMES OF DIFFUSION COMPONENT TO T_2 RELAXATION:

Diffusion-induced relaxation in inhomogeneous fields can be characterized by three regimes of free diffusion, localization and motionally averaging depending on the shortest characteristic length scale, as described below:

Free-Diffusion Regime

The free-diffusion regime arises when the diffusion length (L_d) is much smaller compared to the dephasing length and the pore length. It mostly arises for small echo spacings such that the spins do not experience the restriction effects in the time for echo formation. In the presence of paramagnetic bodies attributing to internal field gradients, the $T_{2,D}$ relaxation rate shows similar quadratic dependence on echo spacing as is given by the classical expression derived by Carr and Purcell (1954) and Neuman (1974) for unrestricted diffusion in a constant gradient:

$$\frac{1}{T_{2,D}} = \frac{1}{12} (TE \cdot \gamma \cdot G)^2 D \quad (2)$$

Localization Regime

In this relaxation regime, dephasing length (L_g) is the smallest characteristic length. It applies to large enough pores so that the diffusing spins dephase to an extent such that they do not contribute to the total magnetization during the measurement time. Physically, the localization-relaxation regime arises in presence of strong magnetic susceptibility contrast such that $\Delta\omega \cdot \tau > 1$.

Motionally Averaging Regime

If the pore structural length (L_s) is the smallest in comparison to the diffusion length (L_d) and the dephasing length (L_g), we observe the motionally averaging regime of relaxation. In this regime, fast-diffusing protons motionally average the inhomogeneities in magnetic field. Thus, the spins typically diffuse several times the pore size during the measurement and any magnetic-field inhomogeneities are averaged by their motion. Thus, the relaxation rate is independent of the echo spacing and shows a quadratic dependence on field inhomogeneity ($\Delta\omega$) in the motionally averaging regime. Also, in this regime, the $T_{2,D}$ component of relaxation increases with the size and susceptibility of the paramagnetic particle.

Overall, the relaxation rates show quadratic dependence on echo spacing in the free-diffusion regime and less than linear (sublinear or quasilinear) dependence in the

localization regime. A change in slope is therefore observed as the systems transition from the free-diffusion to the localization regime. In case of the motionally averaging regime, it is independent of echo spacing.

For the case of paramagnetic relaxation in sedimentary rocks, the characteristic time scales depend not only on the size and susceptibility of paramagnetic particles but also on the concentration of the particles and the size of silica grains.

T_1/T_2 RATIO

Kleinberg et al. (1994) [studied the low-field (2 MHz) NMR response of several sandstones and found that the T_1/T_2 ratio varied over a large range from 1 to 2.6. On average, sandstones have a T_1/T_2 ratio of 1.6, whereas clean silica has a ratio of about 1.3. In porous media, field inhomogeneities are often induced due to differences in magnetic susceptibility of pore fluids and paramagnetic minerals on pore surfaces. The presence of paramagnetic minerals of various sizes and susceptibilities on the pore surfaces of sandstones can result in a range of T_1/T_2 ratio as well as cause it to vary with echo spacing, depending on the diffusion regime of T_2 relaxation.

The experimental results from previous work (Anand and Hirasaki, 2007) theoretically explains the wide range of the T_1/T_2 ratio in sandstones, including the case with no echo-spacing dependence of the T_2 relaxation (Kleinberg et al., 1994) which actually corresponds to that of the motionally averaging regime.

In the present study, T_1/T_2 2D laboratory data have been acquired and T_1/T_2 ratios have been studied alongside the echo-spacing dependence of T_2 relaxation.

CASE STUDY FROM TWO PETROLIFEROUS BASINS OF INDIA

A comprehensive NMR study carried out on two distinct

formations/pay from two different basins from the eastern and western parts of India, specifically, low-resistivity, low contrast (LRLC) pay of the Tipam formation (Charali field, Assam and Assam Arakan basin) and the Chhatral pay of the Cambay shale formation (Gamij field, Cambay basin). The influence of magnetically susceptible material on NMR T_2 relaxation and hence, on the T_2 cutoff have been studied. Observations on a few sample from wells Charali X, Y, and Z and Gamij X, Y, and Z discussed in in subsequent sections. Details of plugs and their petrophysical parameters are presented in Table 1.

Tipam Formation, Charali Field

Charali Field is a satellite field in north Assam Shelf of Assam and Assam-Arakan (A and AA) Basin of India and is producing significant amount of oil and gas. The Charali structure can be described as an anticlinal fault closure developed on a predominantly NNE–SSW trending fault, termed the Charali Western Bounding Fault that extends from the north of Changmaigaon field and northward up to the Rudrasagar Field.

In this part of the region, the Miocene Tipam formation offers examples of low- to moderate-resistivity and low-contrast (LRLC) sandstones and at times reverse contrast reservoirs. Typical log motifs are presented in Fig. 1. Such LRLC reservoirs have always been a challenge to log analysts for identification of probable hydrocarbon-bearing zones and the realistic computation of water saturation of the reservoirs. Thick sands of Tipam Group of Mio-Pliocene age were deposited in a fluvial system where accommodation has a tectonic control forming a composite system of low-accommodation system tracts (LAST) and high-accommodation system tracts (HAST), which define a single sequence.

Table 1—Petrophysical Study Results

Charali Field				Gamij Field			
Plug	Helium Porosity (p.u.)	Gas Permeability (mD)	Grain Density (g/cm ³)	Plug	Helium Porosity (p.u.)	Gas Permeability (mD)	Grain Density (g/cm ³)
CH-1	21.80	291.47	2.54	GM-10	32.14	0.31	2.97
CH-2	22.00	414.18	2.50	GM-12	33.45	0.45	3.03
CH3A	22.80	41.45	2.59	GM-13	13.94	0.08	3.21
CH-9B	21.10	193.79	2.59	GM-14	32.98	0.90	2.86
CH-11	22.40	1,063.30	2.49	GM-16	27.59	0.90	2.78
CH-12	21.50	110.86	2.63	GM-15	33.00	0.13	2.78
CH-13A	20.80	122.04	2.58	GM-8	19.80	0.13	2.94
CH-14A	23.80	2,169.27	2.42	GM-18	6.76	0.01	3.57

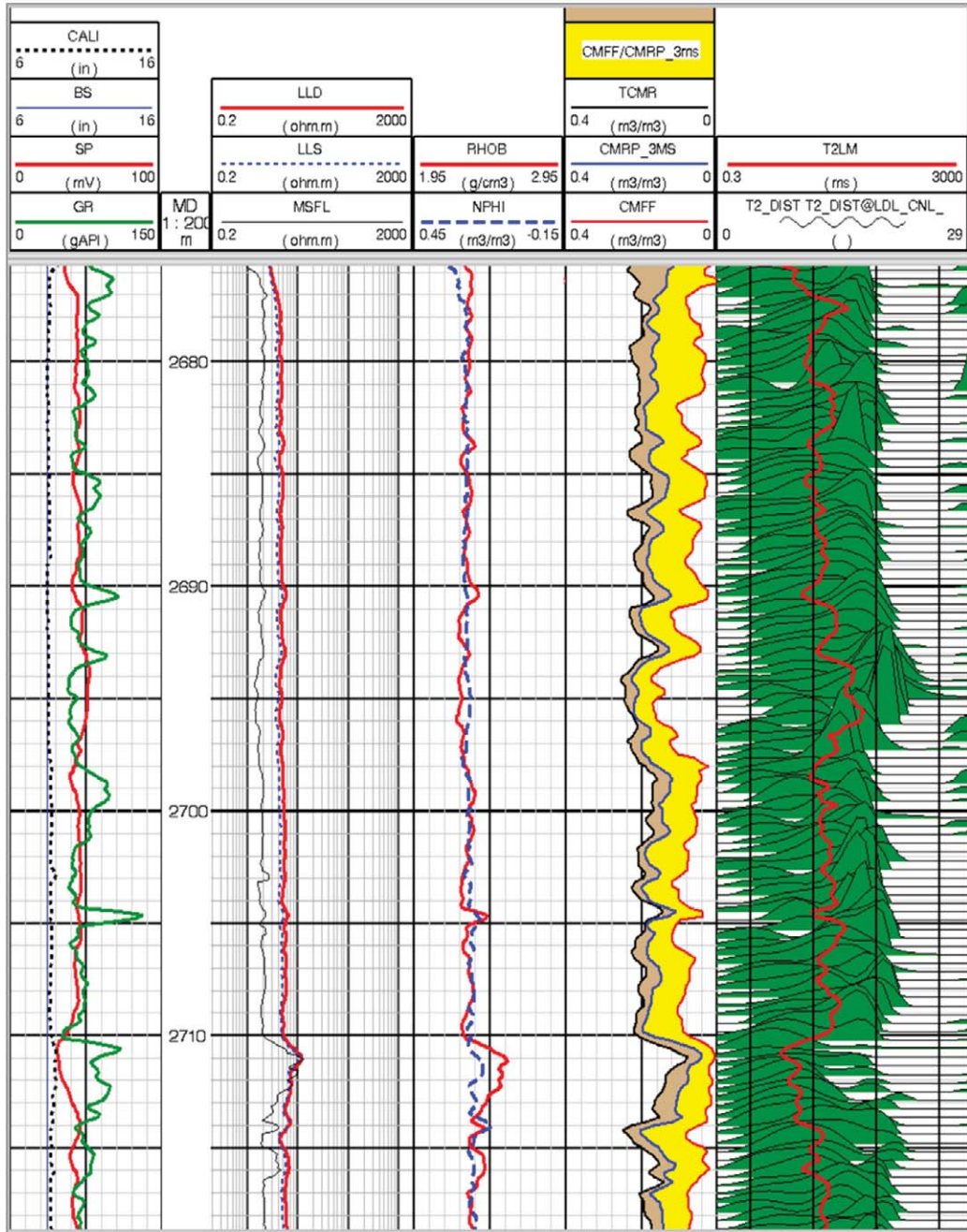


Fig. 1—Typical well-log motif for the Tipam formation in the Charali field. Track 1, SP, GR, caliper, bit size; Track 2, resistivity logs; Track 3, density and neutron logs; Track 4, CMR porosity logs (CMFF is computed using the default 33-ms T_2 cutoff), and Track 5, NMR T_2 distribution.

The lithology of the Tipam formation in this field reported from core studies consists of fine- to medium-grained sandstone. The presence of authigenic clay minerals, pore-filled kaolinite and grain-coating smectite are reported in core studies. These clay minerals are dispersed, due to diagenesis, which resulted in pore filling and coating of grain surfaces that leads to generation of microporosity in the formation.

Results of the X-ray diffractions (XRD) study show that quartz is the main framework grain type, constituting up to 80% of the total rock with an average abundance of 75%. Studies of the magnetic minerals in cores from the Charali field reveal that the percentage of magnetic minerals in sample plugs varies from 10.54 to 19%. The EDS energy spectra has recorded the presence of up to 19 wt% iron (Fe) (Fig. 2). Compositionally, the XRD mineralogical analysis

has marked the presence of siderite, ilmenite and chamosite (along with mica, ankerite and actinolite in a few of them) in most of the samples, which are all paramagnetic in nature with varying degrees of magnetic susceptibility.

Porosity and permeability determined on cores of the Charali field is good. Permeability measured on cores is of the order of 300 to 400 mD and at places reaches 900 to 1,000 mD showing low capillary-bound water.

Chhatral Pay, Gamij Field

Gamij field is situated near the rising eastern margin of Ahmedabad-Mehsana block of the Cambay basin, western onshore India.

The palynological studies of the Cambay Shale in the Gamij field indicate subtidal to inner neritic conditions of deposition during the Early Eocene, whereas the micropaleontological studies suggest a fluctuating environment. Chhatral pay is developed within Younger Cambay Shale (end of the Early Eocene deposition) and

is a heterogeneous clastic reservoir which consists of fine-grained sandstone and siltstone along with interbedded shales. These reservoirs have good porosity but very low permeability, low production rates and low water cuts during production. A typical log motif is presented in Fig. 3. Though the total thickness of Chhatral pay is generally large, it has poor reservoir characteristics, as indicated by cores, logs and production data.

Due to the dominant microporosity, the formation contains high amounts of bound/capillary water. Complex mineralogical assemblages have been reported in XRD studies. The sandstones are dominantly quartz-wacke where detrital grains include quartz, minor feldspar and clasts of claystone. Mixed-type clays are mainly kaolinite and chloritic (chamosite and chlorite). Secondary/minor mineral occurrences include siderite, muscovite/biotite, hematite, ilmenite, augite, magnesite, pyrite, goethite, and dolomite (as indicated by the sample XRD data shown in Table 2).

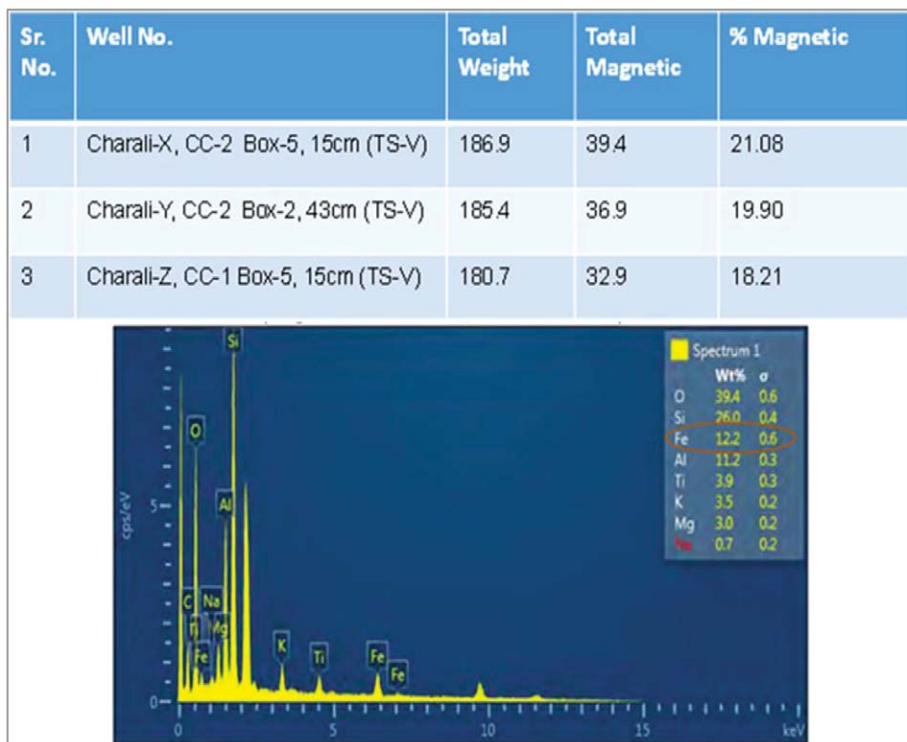


Fig. 2—Charali field sample XRD data.

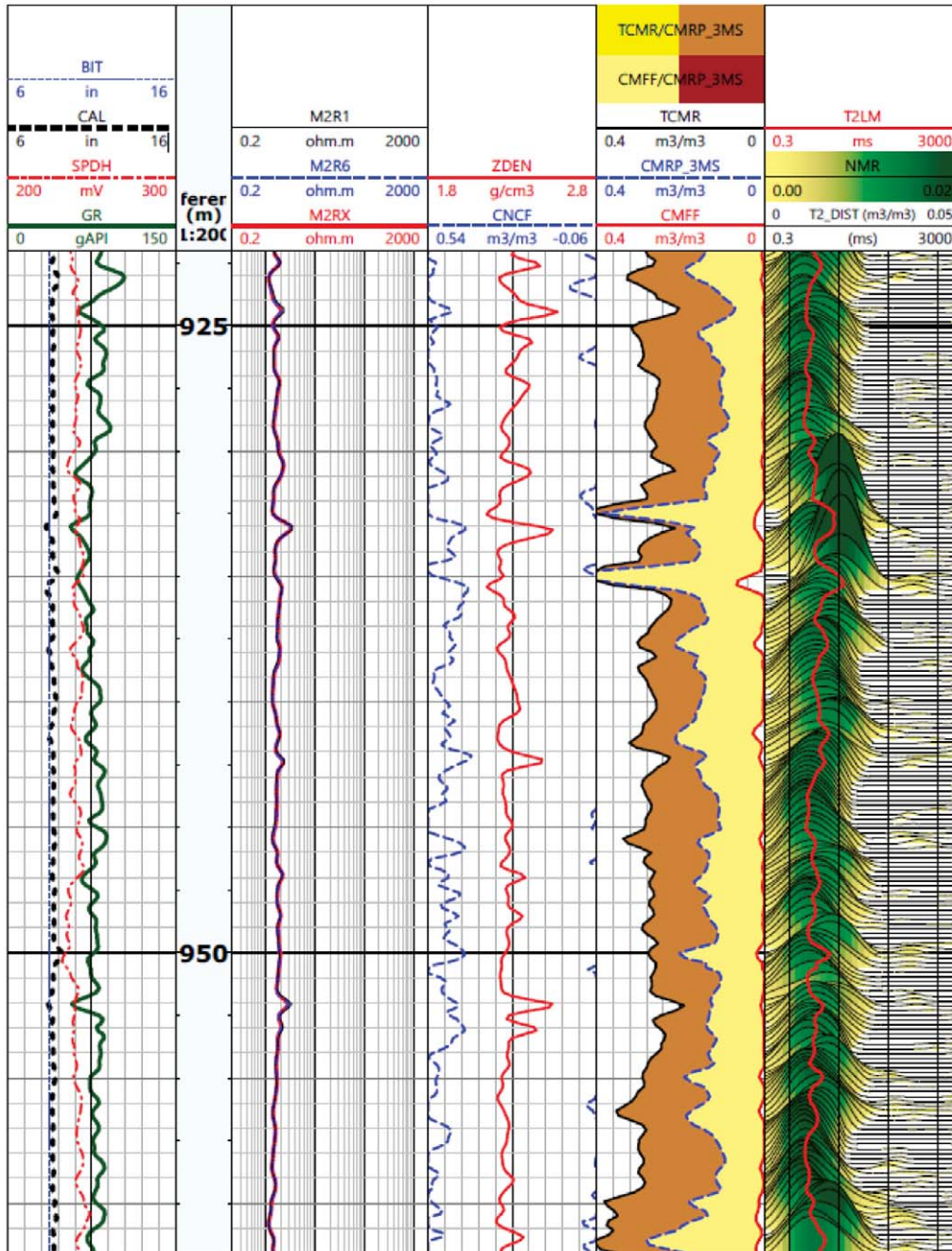


Fig. 3—Typical log motif for the Chhatral pay in the Gamij field Track 1.; SP, GR, caliper, bit size; Track 2, resistivity logs; Track 3, density and neutron logs; Track 4, CMR porosity logs (CMFF is computed using the default 33-ms T₂ cutoff), and Track 5, NMR T₂ distribution.

Table 2—XRD Mineral Data (wt%) of the Gamij Field

Plug	Quartz	Siderite	Chamo	Pyrite	Kaolonite	Chlorite	Smectite	Mag	Dolomite	Calcite	Others
GM-18	11.77	70.5	7.04	1.77	---	5.11	---	---	---	1.69	1.33
GM-14	89.73	---	1.88	---	2.05	0.43	---	3.79	---	---	2.08
GM-13	57.76	8.05	31.67	---	0.57	1.23	0.49	---	---	---	---
GM-10	84.56	2.78	5.88	---	---	3.81	---	---	1.17	---	1.77

EXPERIMENTAL NMR ANALYSIS

Experimental NMR analysis was performed using a 2-MHz low-field Geospec 2/75 NMR spectrometer by M/S Oxford Instrument. The spectrometer operates at a magnet strength of ~550 Gauss. Prior to the NMR measurements, the samples were saturated with brine (formation water salinity). All measurements were performed at room temperature and normal atmospheric pressure. The core plugs were wrapped with NMR-silent material using a tested procedure to avoid any loss of saturation during the experiment.

NMR Measurements at $S_w = 1$

NMR T_2 relaxation times were measured for all brine saturated samples using variable echo spacing, TE, that ranged from 100 μ s to 10 ms. To better characterize the plugs, additional measurements of the fully water-saturated conditions were performed including T_1 relaxation, diffusion distribution, T_1 - T_2 correlations, and 1D porosity profile.

T_1 - T_2 2D mapping is performed by an inversion recovery sequence followed by a CPMG. D - T_2 is performed with a stimulated echo followed by a CPMG sequence. One-dimensional (1D) profiles (porosity distribution along the axis of the plug) are acquired using a frequency encoding

technique. This consists of acquiring an NMR echo in the presence of a magnetic-field gradient. Performing a Fourier transform on the time-domain data leads directly to the profile in the space domain. Pulse-sequence schematics for transverse relaxation (T_2), longitudinal relaxation (T_1), T_1 - T_2 mapping, and diffusivity measurement are shown in Figs. 4a, 4b, 4c and 4d, respectively.

NMR Measurements on Samples at $S_w = S_{wir}$

The samples were desaturated using a centrifuge up to S_{wir} . NMR T_2 measurements and a 1D porosity profile were carried out on all desaturated samples. T_2 cutoff analysis was carried for all samples.

DISCUSSION AND ANALYSIS OF NMR DATA MEASURED ON PLUGS AT $S_w = 1$

Observations on T_2 Measurements Measured With Varying TE

The measured T_2 relaxation spectrums at different echo spacing (100 μ s to 10 ms) were studied without applying any external gradient. For both the sets of sample plugs, shifts in relaxation peaks with increasing interecho spacing were observed (Figs. 5 to 8).

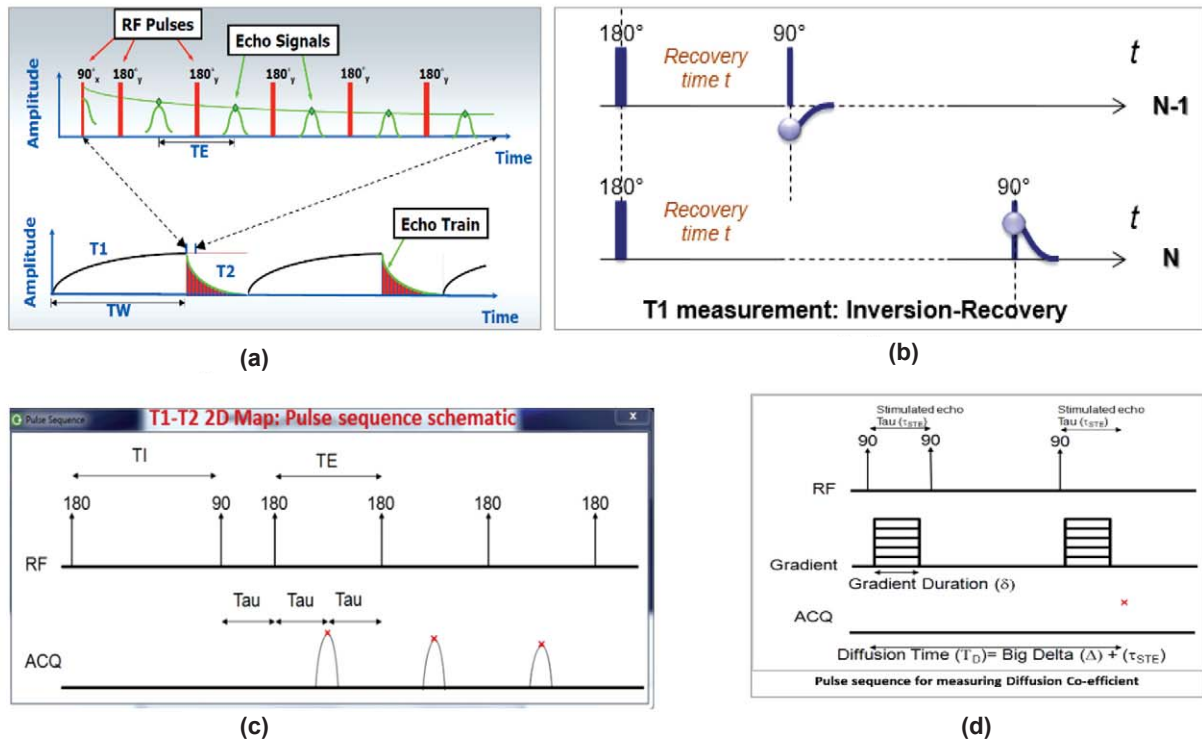


Fig. 4—Schematics of a basic pulse sequence. (a) CPMG pulse sequence, (b) pulse sequence of inversion recovery method for T_1 measurement, (c) pulse sequence for T_1 - T_2 correlation map, and (d) pulse sequence for measuring diffusion coefficient.

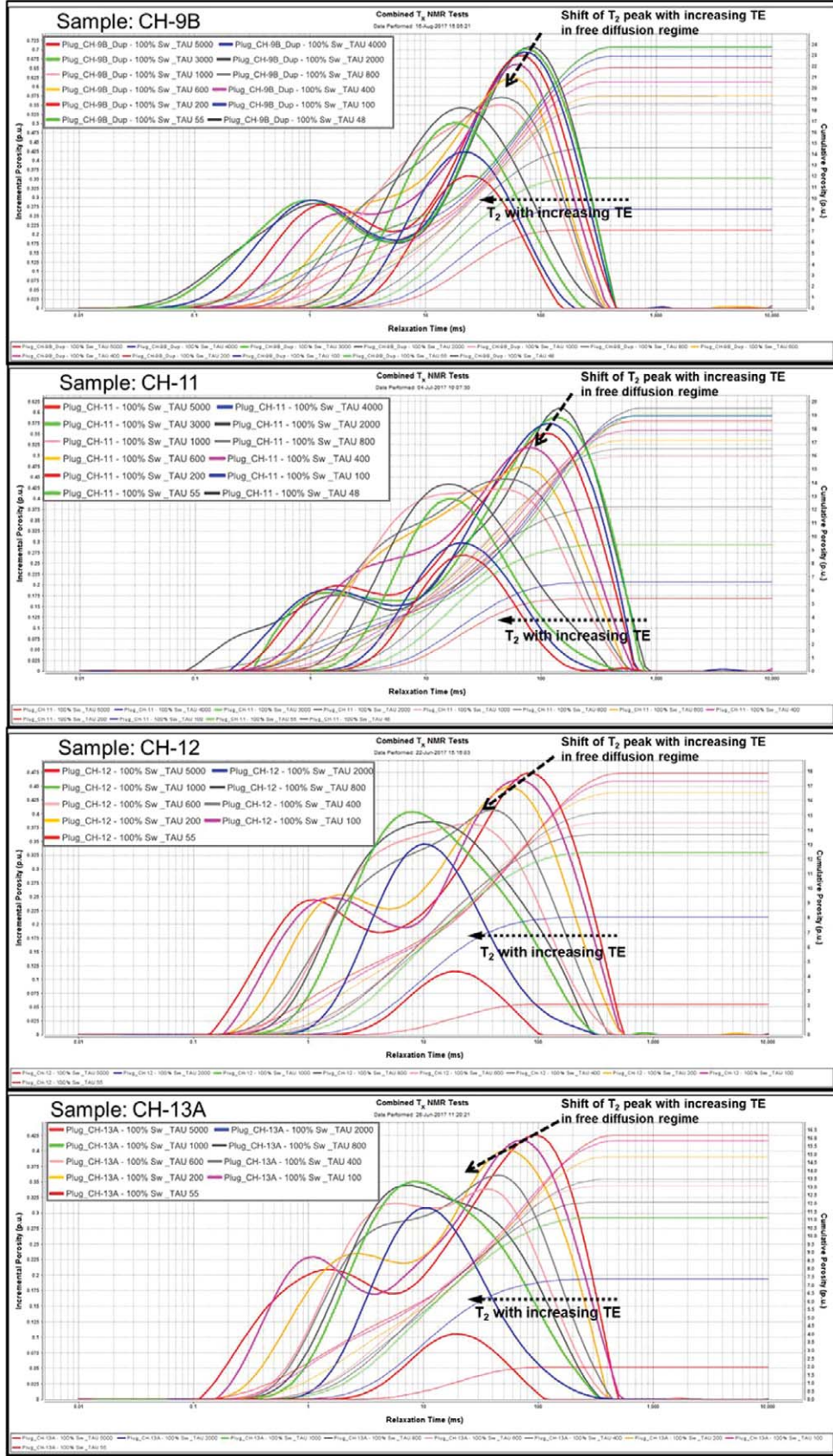


Fig. 5—T₂ measured on samples CH-9B, CH-11, CH-12, and CH-13A from the Charali field with TE (2τ) ranging from 100 μs to 10 ms.

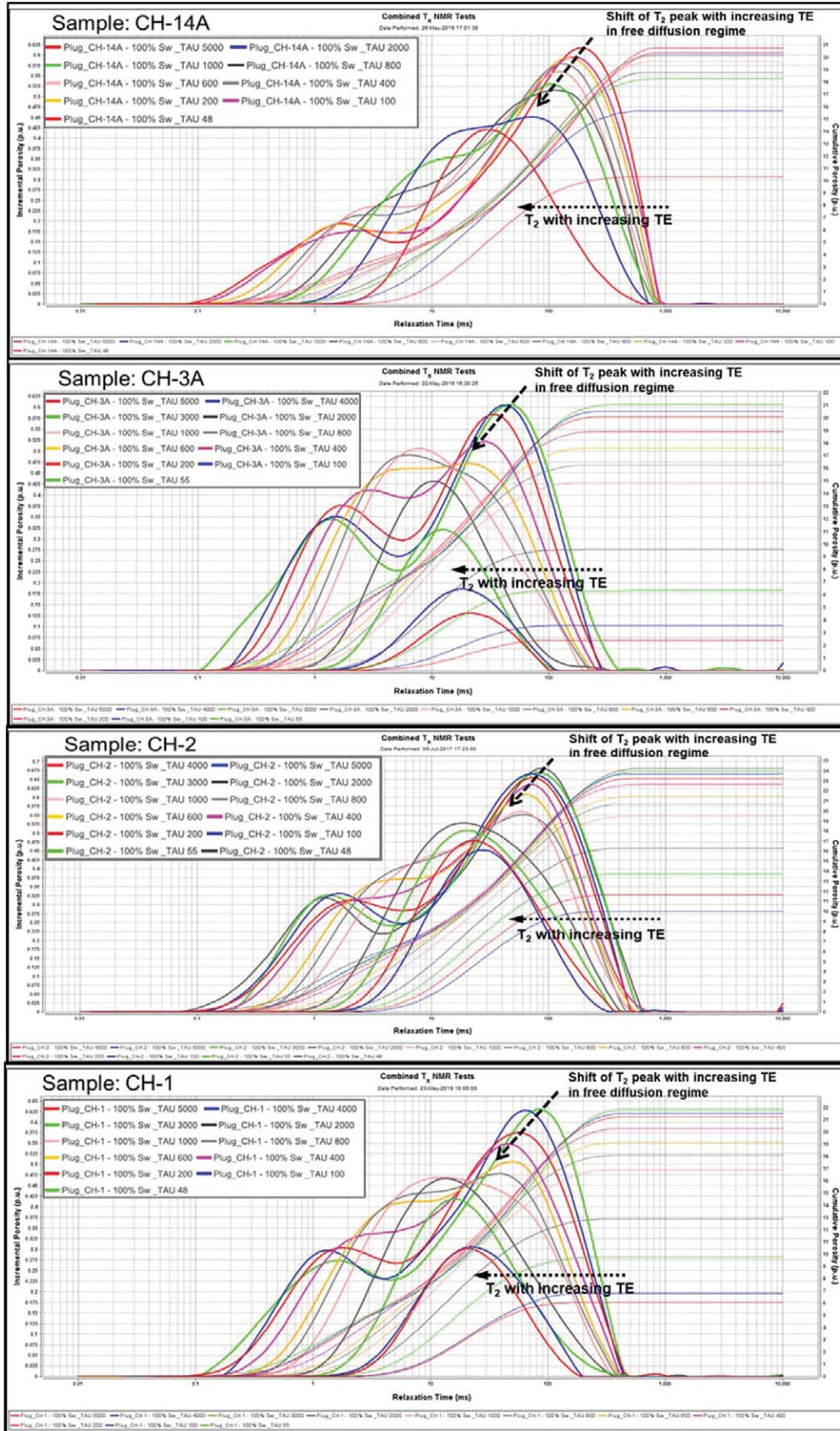


Fig. 6— T_2 measured on samples CH-1, CH-2, CH-3A, and CH-14A from the Charali field with TE (2τ) ranging from 100 μ s to 10 ms.

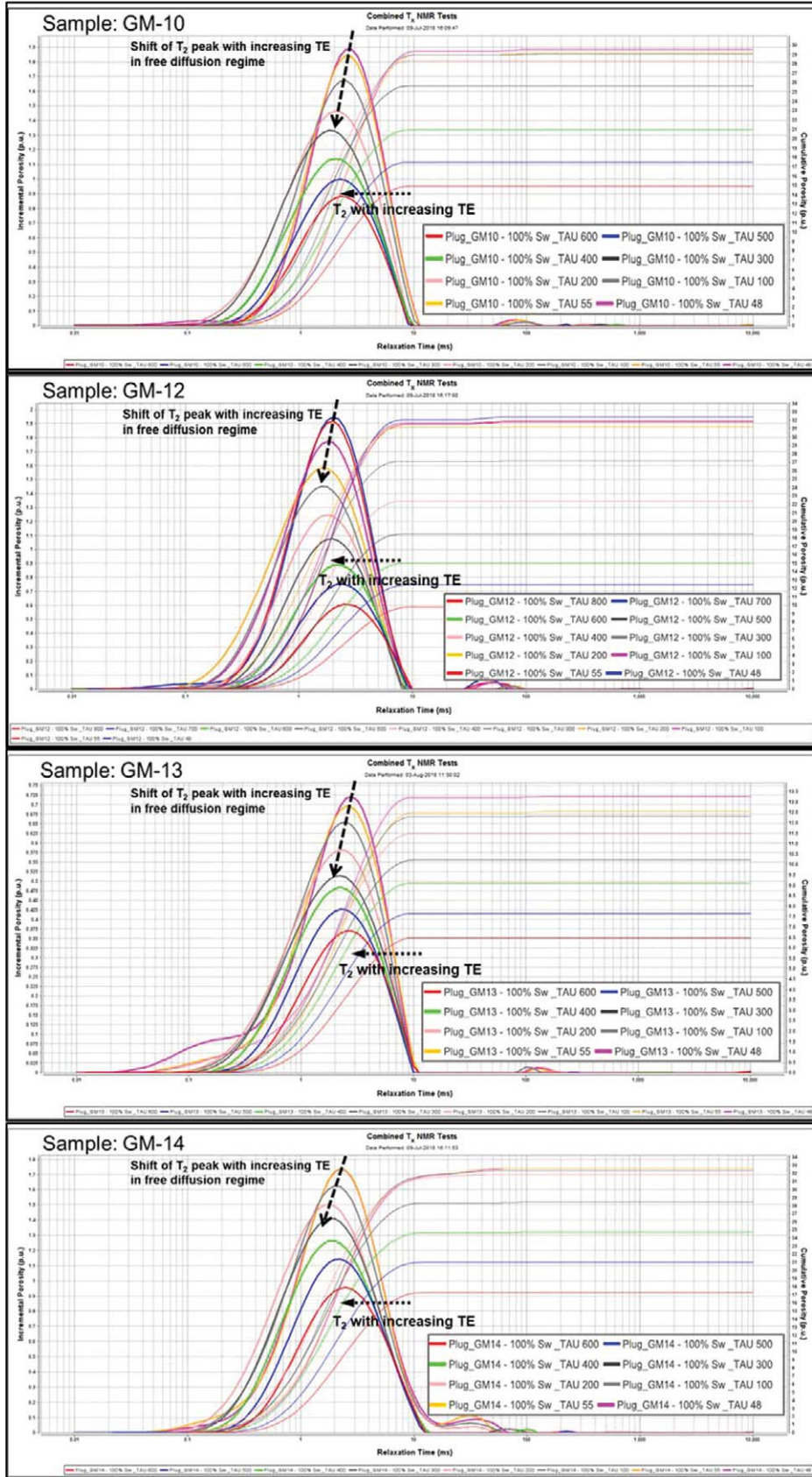


Fig. 7— T_2 measured on samples GM-10, GM-12, GM-14, and GM-14 from the Gamij field with TE (2τ) ranging from 100 μ s to 2 ms.

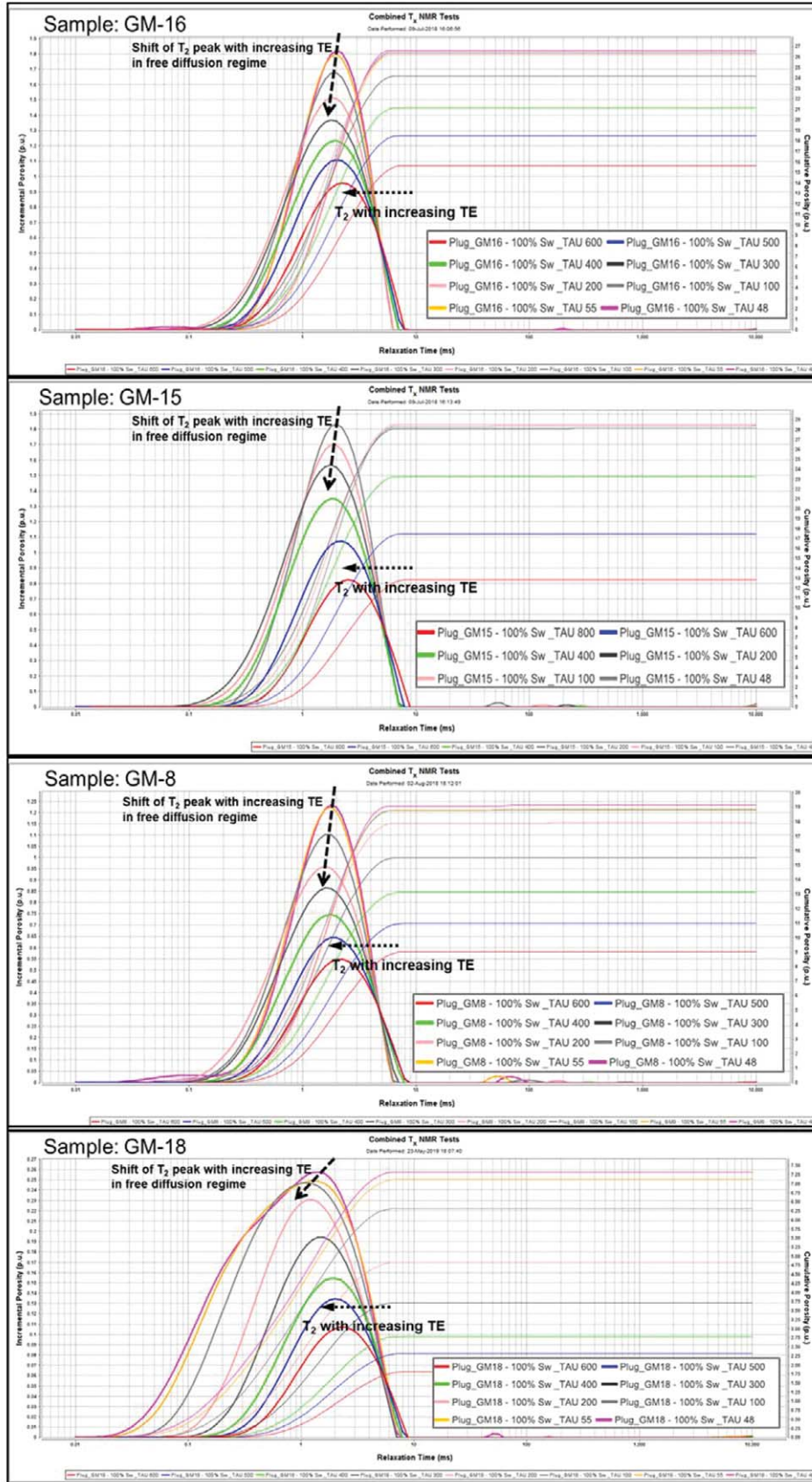


Fig. 8—T₂ measured on samples GM-16, GM-15, GM-8, and GM-18 from the Gamij field with TE (2τ) ranging from 100 μs to 2 ms.

An attempt has been made to better understand the relationship of T_2 relaxation rate and echo-spacing dependence and, in turn, the diffusion component of T_2 relaxation and also to estimate the upper limit of the internal field gradients (if present). For each interecho spacing, the shift of the position of the T_2 relaxation peak relative to its position at the shortest measured TE was plotted as function of the difference between the squared respective interecho spacing and the squared shortest measured TE. Since only the contribution due to diffusion depends on TE (Eq. 2), plotting the experimental data in this way separates the relaxation due to diffusion from the bulk and surface relaxations and thereby presents the data in different asymptotic regimes of $T_{2,D}$ relaxation. Equation 2 can be rewritten in terms of G (field gradient) as

$$G = \sqrt{\frac{\frac{1}{T_{2,A}} - \frac{1}{T_{2,i}}}{(TE_A^2 - TE_i^2) * \frac{1}{12} D \gamma^2}} \tag{3}$$

where $T_{2,A}$ is the T2 relaxation peak at the shortest measured echo-spacing i.e. TE_A ; and $T_{2,i}$ is position of i^{th} relaxation peak at i^{th} echo-spacing TE_i .

Another set of T_2 response with varying TE was measured on Berea sandstone samples (Fig. 9a) to confirm whether any inhomogeneities of the magnetic background field are present. As in the cleaned Berea sandstone, no significant internal magnetic-field gradients are expected at low resonance frequency, any shift in the peak positions to shorter relaxation times with increasing interecho spacing

would be due to diffusion within gradients of the external background field, B_0 . Similar experiments were carried out on Hazad pay (Cambay Basin, India) samples (Fig. 9b) which are mostly sandstone and devoid of any paramagnetic materials (as seen on XRD). In both cases, no perceptible shift in T_2 peak to the shorter relaxation times was observed.

In line with the theory described in a previous section, the following observations can be made over the measured data to estimate an upper limit of the internal field gradients from the experimental data:

1. Among the three asymptotic relaxation regimes, within the free-diffusion regime, the $T_{2,D}$ relaxation rate is given by the classical expression derived by Carr and Purcell (1954) (Eq. 2) for unrestricted or free diffusion in a constant gradient and holds for porous media with magnetically susceptible constituents posing internal gradients.

Depending on characteristic length-scale interrelations, relaxation can be classified in three regimes, namely, free-diffusion regime, localization regime, and motionally averaging regime, as previously mentioned. Figure 10 presents one of the sample plots showing these three relaxation regimes. Initial points (shown in blue color) depict the free-diffusion regime where the relaxation rates show quadratic dependence on echo spacing.

Free diffusion is also characterized by a time-independent diffusion coefficient. In Figs. 11 and 12 the trend line (shown in red) connecting the initial 3 to 4 data points (corresponding to lesser TE values of ~100 to 400 μs) represent the free-diffusion regime.

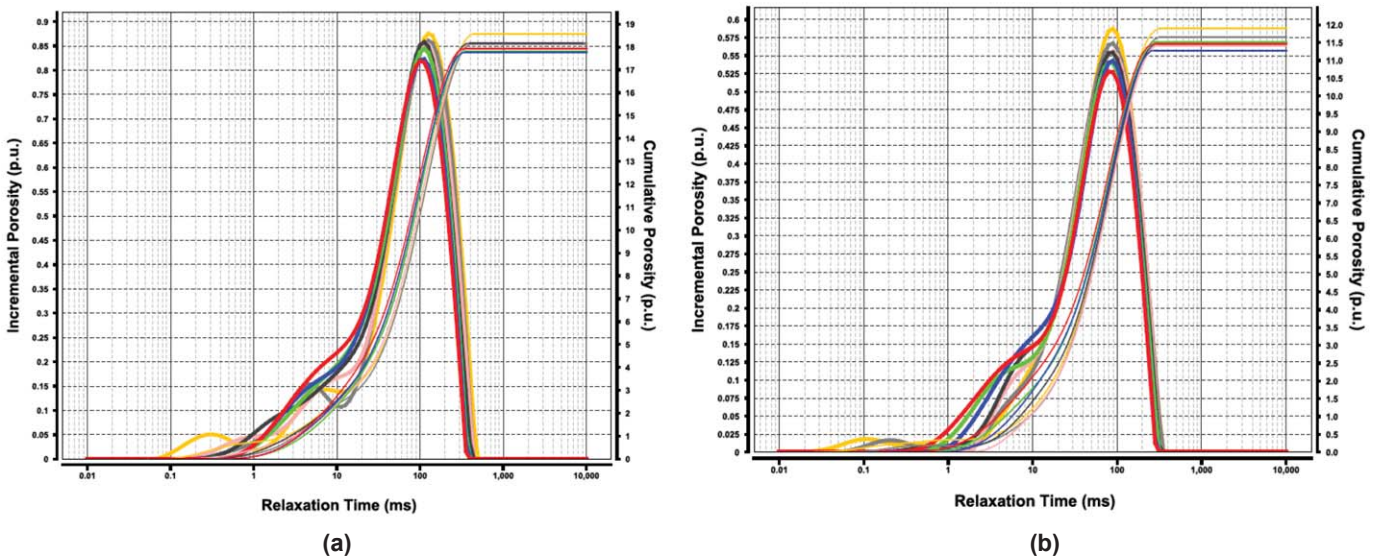


Fig. 9— T_2 response with varying TE on Berea and Hazad sandstone Samples. (a) Berea sandstone example, (b) Hazad sandstone example.

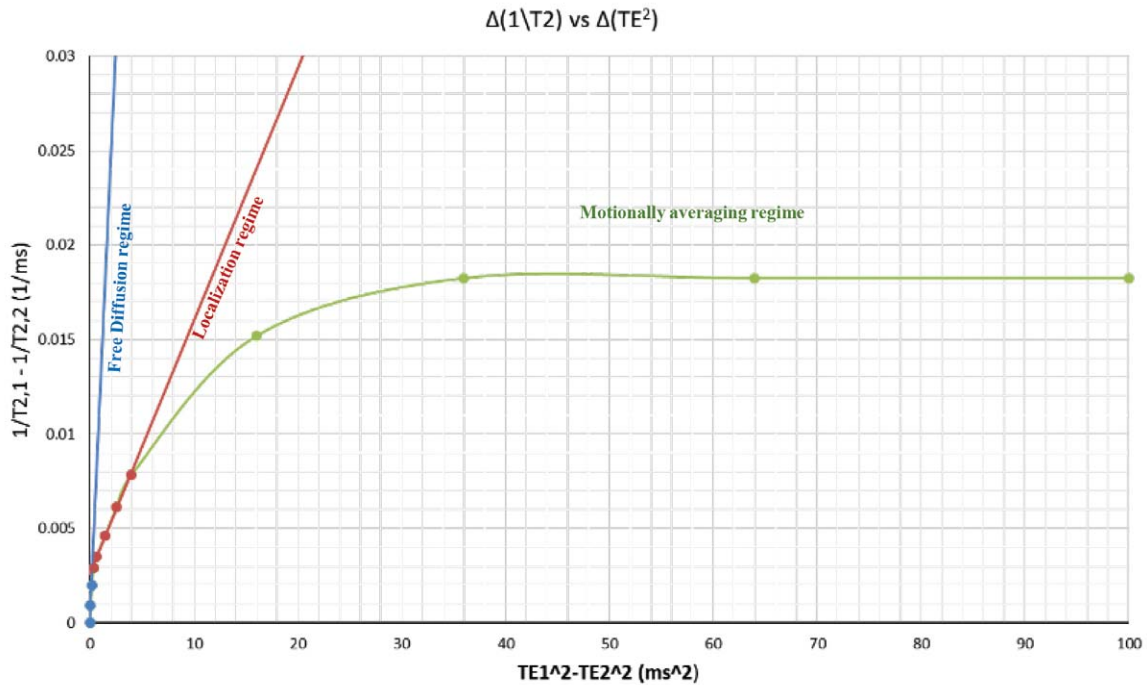


Fig. 10—Sample $\Delta(1/T_2)$ vs. $\Delta(TE^2)$ plot showing different asymptotic regimes.

2. As restricted diffusion starts taking place, the relaxation regime moves off from the free-diffusion regime and relaxation will be in the localization regime. In this regime, the plot of peak shift versus difference of squared interecho spacings will have a smaller and constantly decreasing slope due to the TE dependence of the restricted diffusion coefficient. Hence, the relationship is sublinear or quasilinear and has not been used in any quantitative analysis for the present work. Red points in sample plot (Fig. 10) fall in the localization regime. In Fig. 11, the trend line (shown in blue) connecting the latter data points (corresponding to higher TEs ~400 to 1,600 μ s) represents the localization-diffusion regime. In Fig. 12, this regime is almost absent. That is why we do not see leftward shift of T_2 peak/distribution except for the initial few echo-spacing changes (which are in the free-diffusion regime). The formation being dominantly microporous, we see the free-diffusion regime directly grading in to TE independent regime.
3. Green points in the Fig. 10 represent data points in the motionally averaging regime. This regime is

characterized by fast diffusion of protons such that the inhomogeneities in magnetic field are motionally averaged. When the pore structural length is smallest among the characteristic length scale, the relaxation rate is independent of the echo spacing and shows a quadratic dependence on field inhomogeneity ($\Delta\omega$) in the motionally averaging regime. In Figs 11 and 12 corresponding data points are not shown to enhance the resolution and scale factor.

This diffusion model in principal only estimates an upper limit for the internal field gradient. The coefficient of free diffusion was measured by PFG NMR for brine (the sample diffusion distribution plot presented in Fig. 13). The crossover from free diffusion at short times to restricted diffusion at longer TE was determined from the measured peak shifts as the points at which deviations from the linear relation between the peak shift and the difference of the squared interecho spacing first occurred. A change in slope is observed as the systems transitions from the free-diffusion regime to the localization regime.

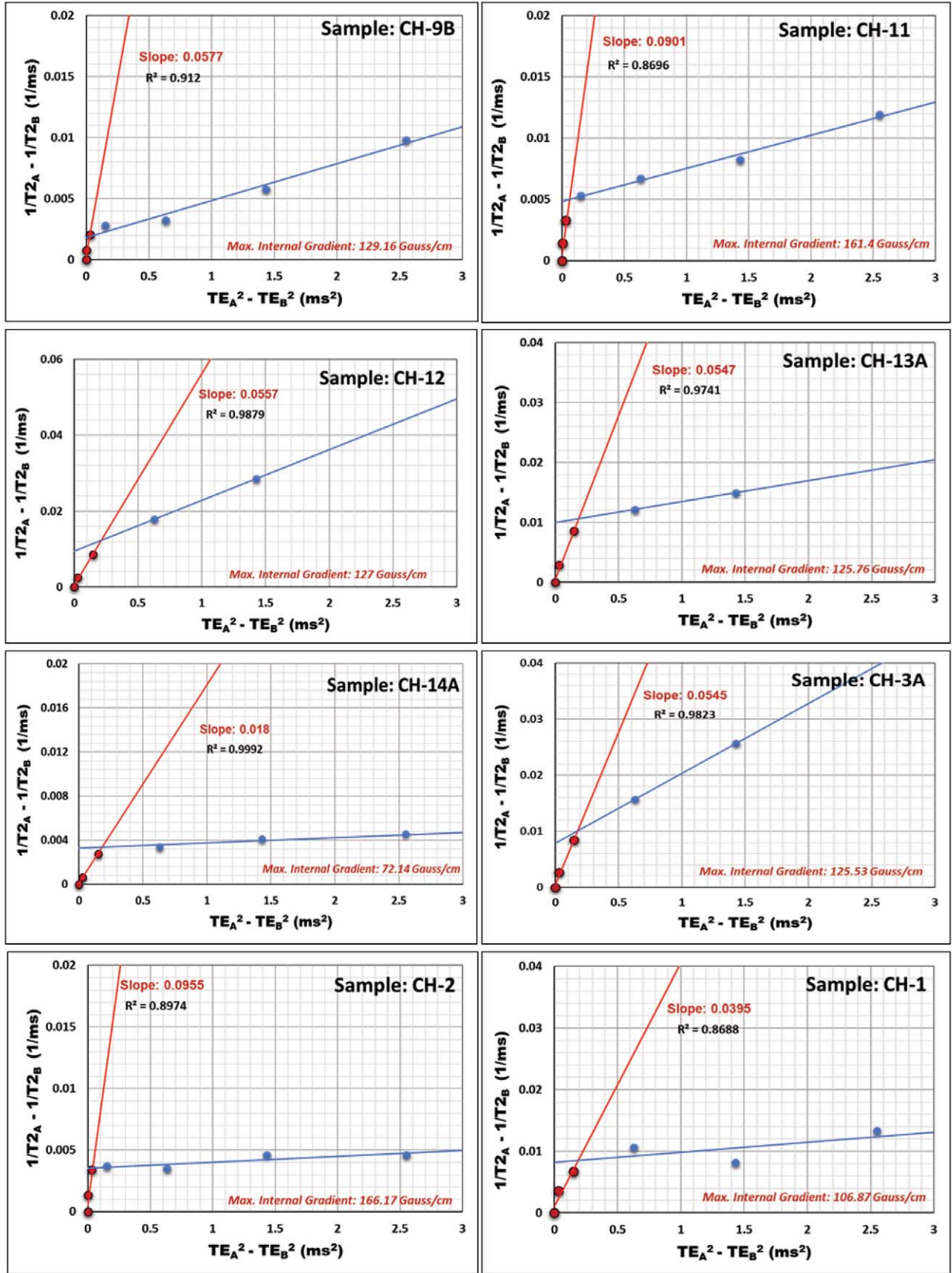


Fig. 11— $\Delta(1/T_2)$ vs. $\Delta(TE^2)$ plots for samples from the Charali field.

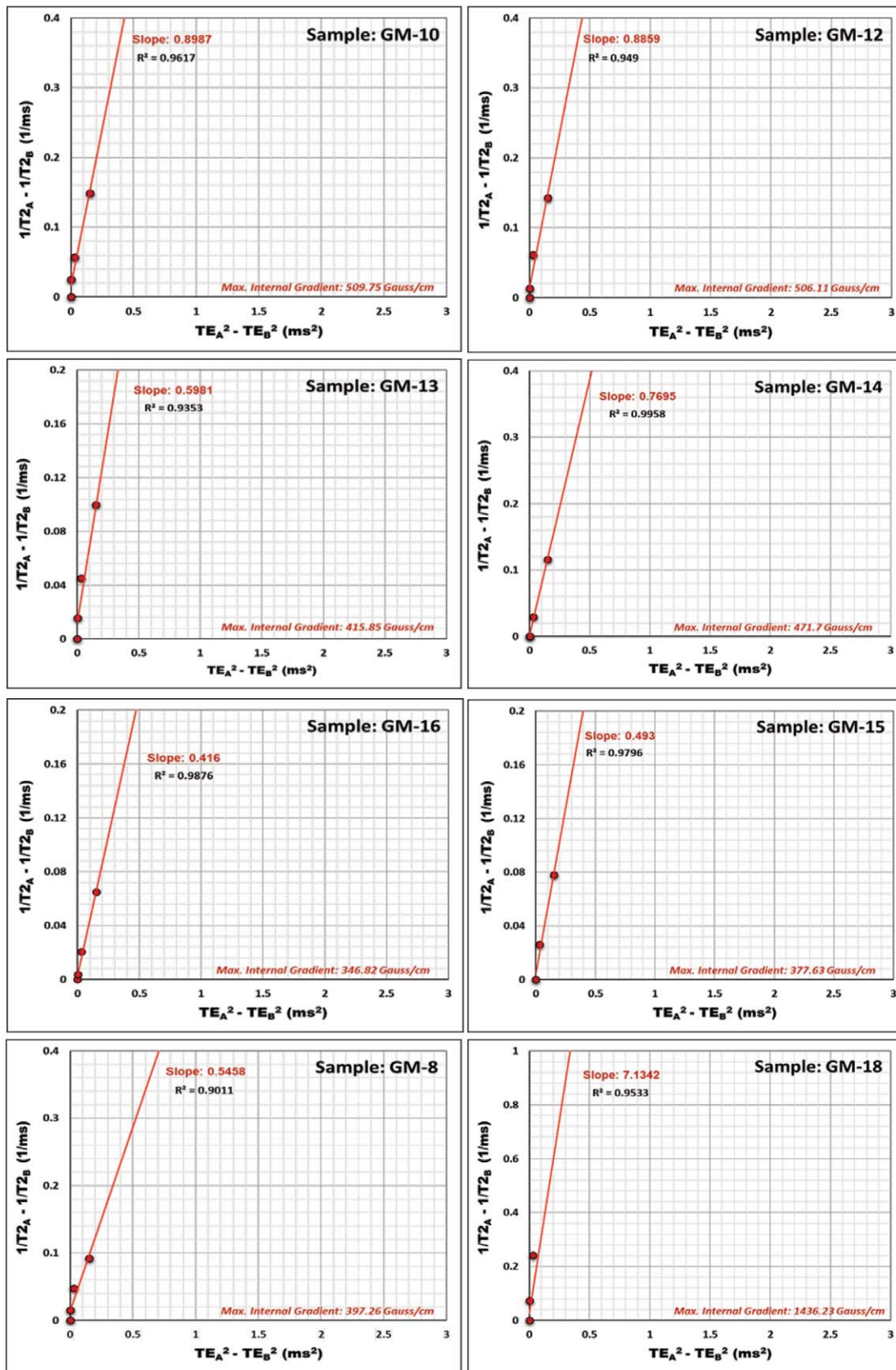


Fig. 12— $\Delta(1/T_2)$ vs. $\Delta(TE^2)$ plots for samples from the Gamij field. The formation is dominantly microporous and the localization-diffusion regime is almost absent here. Hence, only data corresponding to the free-diffusion trend have been plotted.

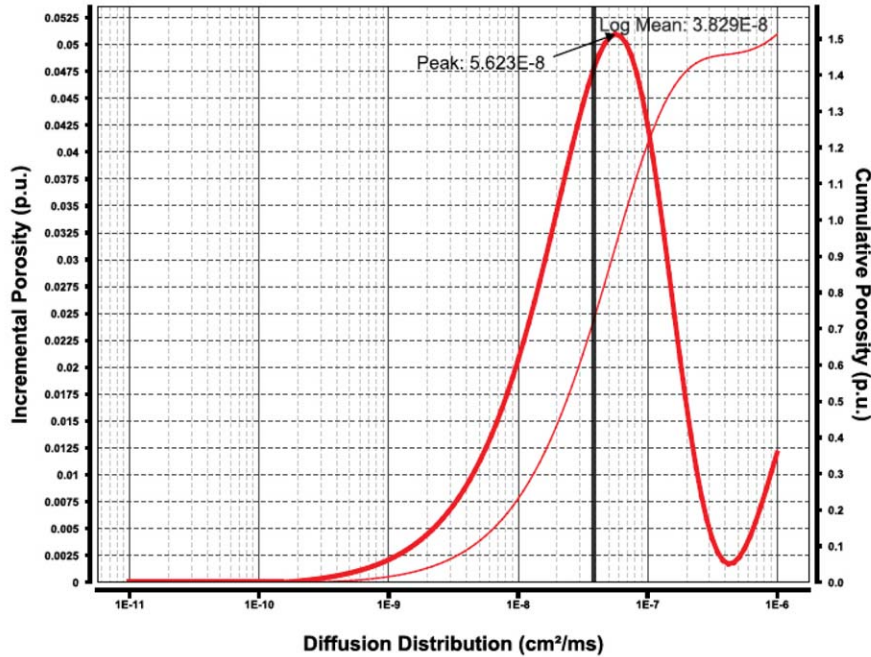


Fig. 13—Diffusion distribution.

Computation of Internal Field Gradient

A plot of $(1/T_{2A} - 1/T_{2i})$ (T_{2A} is T_2 with the minimum echo spacing) vs. $(TE_A^2 - TE_i^2)$ (the difference of the squared interecho spacing; TE_A is the minimum echo spacing) for all the plugs that were prepared (Figs. 11 and 12). The echo spacing varies from 0.1 to 5 ms. For each plug, the first few points fit very well to a straight line, while points at larger τ^2 deviate from it. The magnitude of the internal field gradient can be calculated from the slope of the line fitted to the first few points on plot. The γ value of a proton is 2.675×10^8 / Tesla/s.

In samples from Tipam formation (Charali field, Assam and Assam Arakan basin) the estimated maximum internal gradient is in the range 72 to 166 Gauss/cm (Fig. 11), whereas in samples from the Chhatral pay of the Cambay shale formation (Gamij field, Cambay basin) the estimated maximum internal gradient is mostly in the range of 346 to 510 Gauss/cm (with one sample $\sim 1,436$ Gauss/cm) (Fig. 12).

T_1 - T_2 correlation:

Figures 14 and 15 show the T_1 - T_2 correlation experiment maps. The signal is expected to lie in between the lines for $T_1 = T_2$ and $T_1 = 2T_2$ (diagonal lines on T_1 - T_2 map represents T_1/T_2 ratio values in logarithmic scale) in ideal conditions. Figure 14 presents the T_1 - T_2 maps for the samples from the Tipam formation and Fig. 15 shows the T_1 - T_2 maps for the samples from Chhatral pay. Histograms for the same samples are presented in Figs. 16 and 17.

In Fig. 14, for the samples from Tipam formation, we obtained a broad T_1 - T_2 spectrum, with ratios mostly in the range of 1 to 4, with very high T_1/T_2 values at places (up to 500). It is clearly observed in corresponding histograms (Fig. 16) as well. In Fig. 15, for the Chhatral pay, the T_1 - T_2 maps show a distribution of T_1/T_2 ratio values mostly in the wide range of 1 to 7, along with some higher values as evident in the corresponding histograms (Fig.17). A statistical summary of experimental results is presented in Table 3. All T_2 laboratory measurements are in the presence of zero applied magnetic-field gradient. Thus, the higher T_1/T_2 ratios possibly indicate the presence of additional relaxation ($T_{2,D}$), thereby preferentially reducing T_2 relative to T_1 .

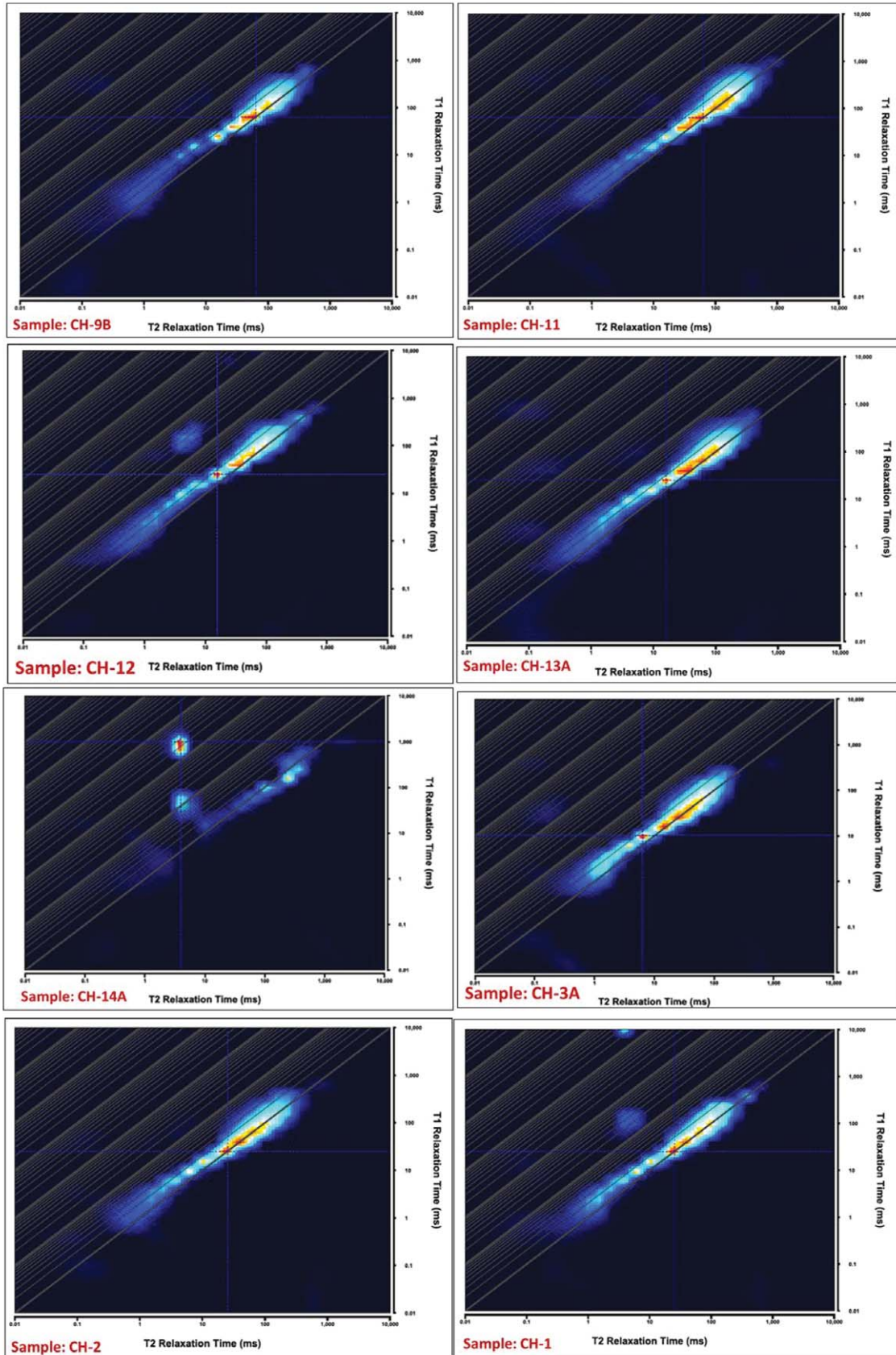


Fig. 14— T_1 - T_2 correlation maps for the Tipam formation of the Charali field.

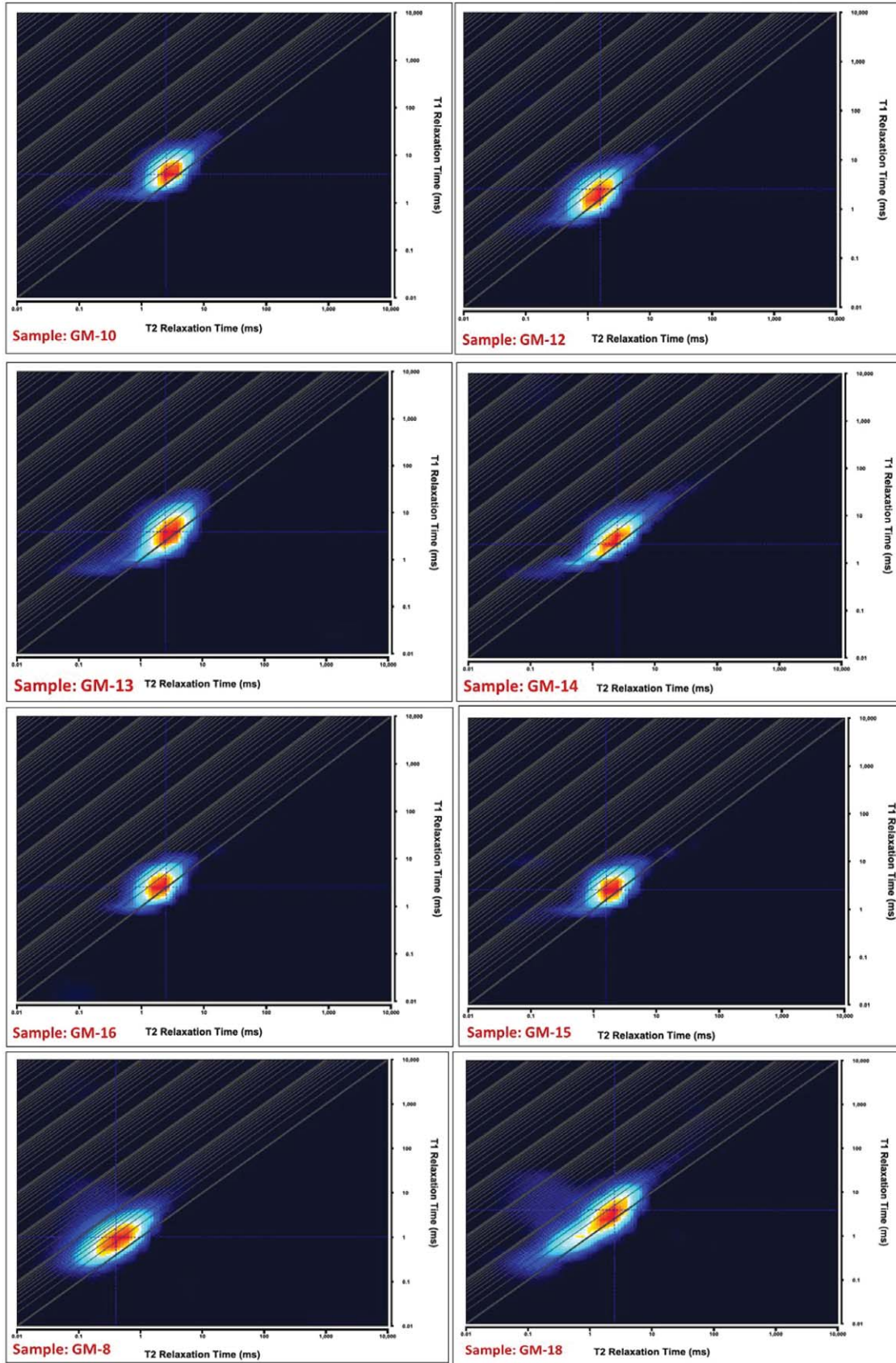


Fig. 15— T_1 - T_2 correlation maps for the Chhatral pay of the Gamij field.

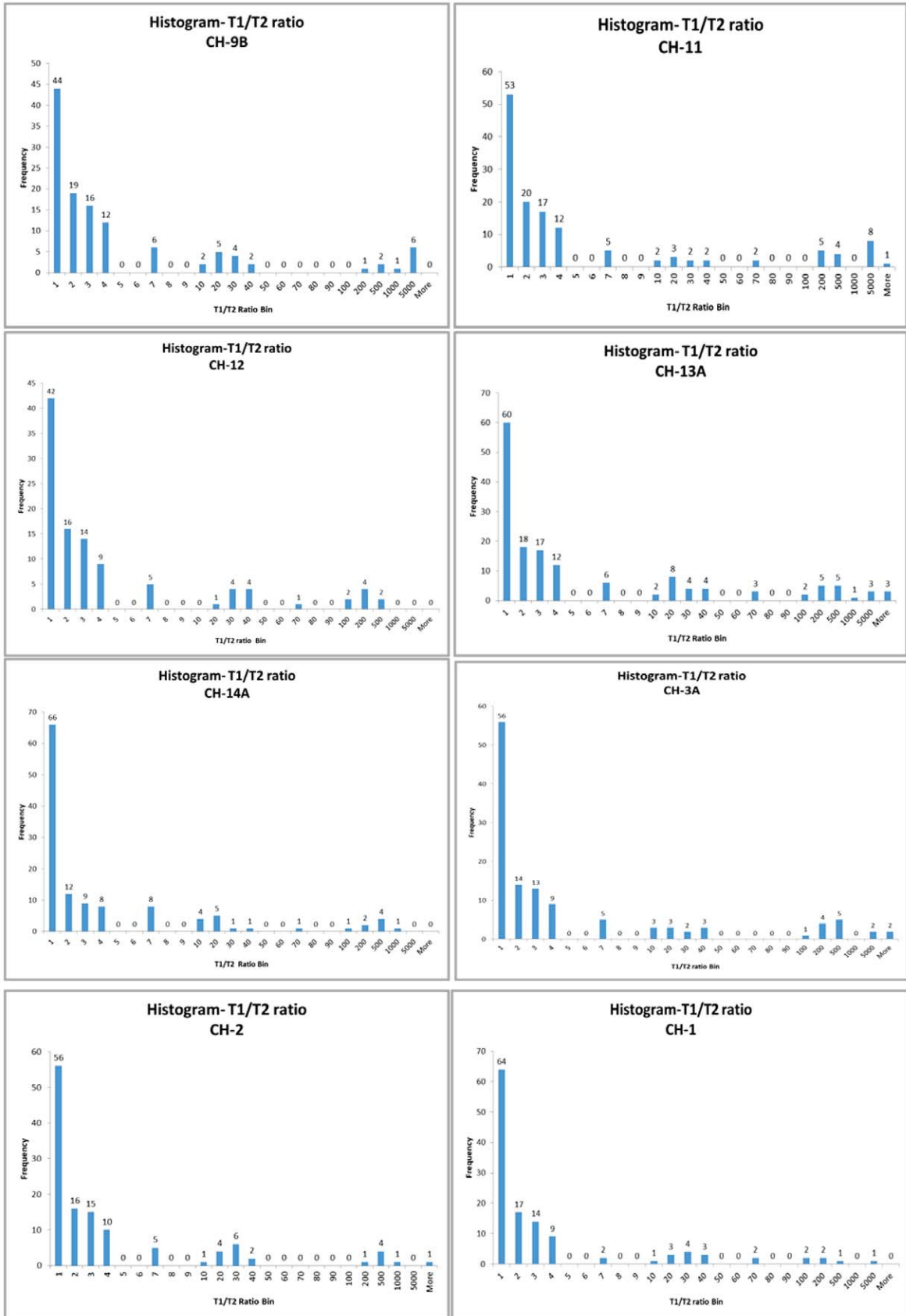


Fig. 16—Histograms of T_1/T_2 ratio for samples from the Tipam formation of the Charali field.

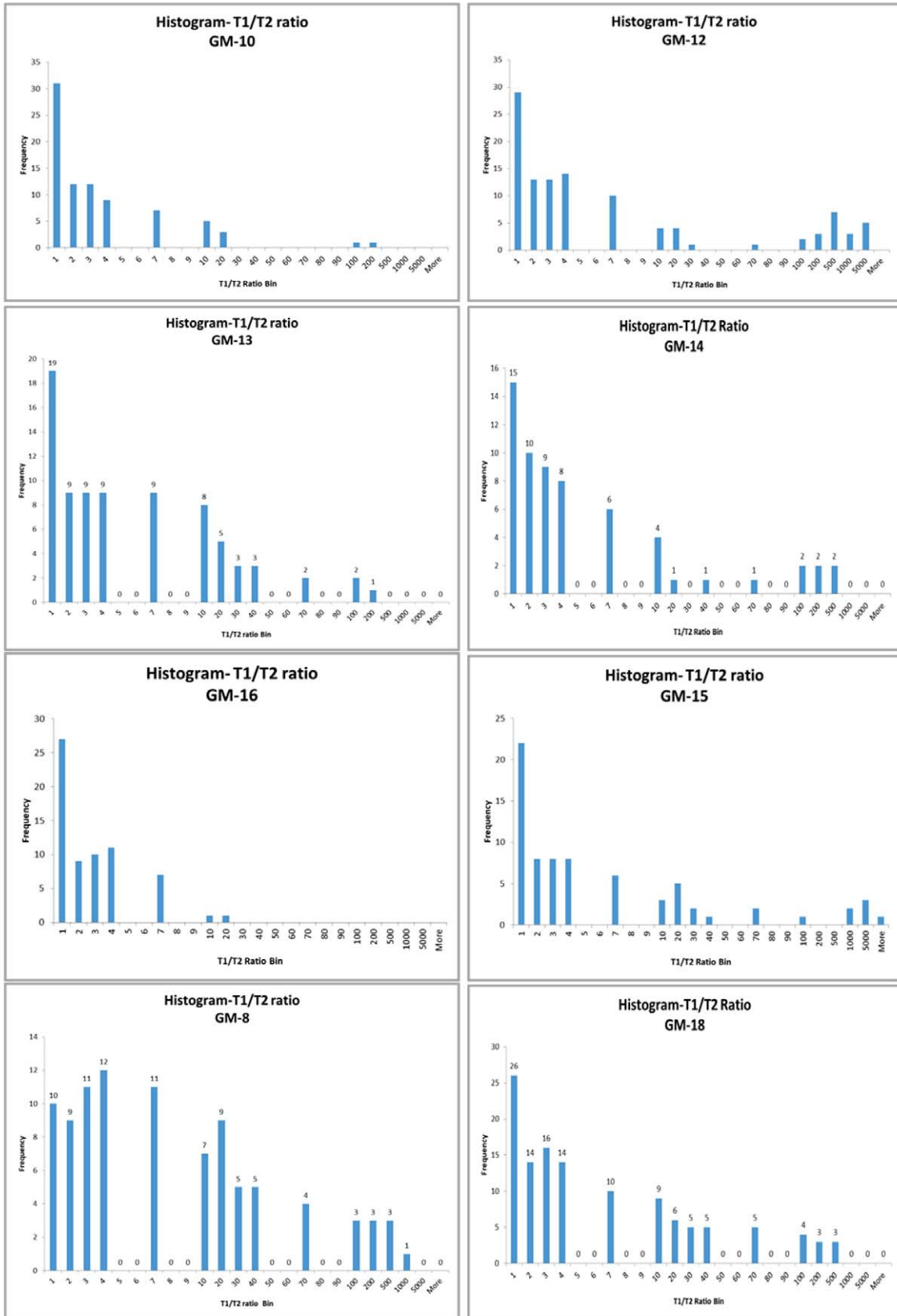


Fig. 17— Histograms of T_1/T_2 ratio for samples from the Chhatral pay of Gamij field.

Table 3—NMR Study Results Summary

Charali Field – Tipam Formation					
Plug	Maximum Internal Gradient (Gauss/cm)	NMR T_2 Cutoff (msec)	T_1/T_2 Ratio		Remarks
			Mode	Arithmetic Mean	
CH-1	106.87	6.12	1.15	43.18	Broad spectrum of T_1/T_2 ratios, mostly in the range of 1 to 4 with very high values (≥ 500) in places.
CH-2	166.17	8.47	1.15	23.17	
CH-3A	125.53	11.90	1.16	20.37	
CH-9B	129.16	7.97	2.51	18.32	
CH-11	161.40	5.79	2.51	38.53	
CH-12	127.00	8.14	2.51	18.18	
CH-13A	125.76	5.76	2.51	9.91	
CH-14A	72.14	6.99	1.15	38.56	

Gamij Field – Chhatral Formation					
Plug	Maximum Internal Gradient (Gauss/cm)	NMR T_2 Cutoff (msec)	T_1/T_2 Ratio		Remarks
			Mode	Arithmetic Mean	
GM-10	509.75	4.03	2.51	6.23	Distribution of T_1/T_2 ratio values mostly in the range of 1 to 7 along with some higher values.
GM-12	506.11	3.21	1.15	35.03	
GM-13	415.55	4.17	2.51	10.72	
GM-14	471.70	5.41	1.15	12.97	
GM-16	346.82	3.44	1.00	2.46	
GM-15	377.63	3.61	1.14	7.17	
GM-8	397.26	3.00	2.51	34.97	
GM-18	1436.23	3.53	2.51	25.97	

An example of T_1/T_2 ratio dependence on echo spacing was shown in Fig. 18. T_1 - T_2 correlation maps of a sample plug acquired at two echo spacings, 100 and 400 μ s, clearly illustrates the scenario.

The T_1/T_2 ratio in the presence of paramagnetic bodies may not always be high. As discussed in an earlier section, the observed range of T_1/T_2 ratios indicates the presence of varying size, susceptibility, concentration and distribution of magnetic susceptible sites as well as different orders of grain sizes. These are the controlling factors for different relaxation regimes as well. The T_1/T_2 ratio range/values and/or its dependence on echo spacing depends on abovementioned factors and prevailing relaxation regimes. As such, the T_1/T_2 ratios do not have a linear relationship with the estimated

maximum internal gradient.

T_2 Cutoffs for Bound Fluid

T_2 cutoffs define the transition point from free to bound fluid. T_2 cutoffs can be calculated from the point where the endpoint brine saturation (cumulative T_2 at S_{wir}) intercepts the saturated-state cumulative T_2 curves. The estimated T_2 cutoff values in the presented core plugs range from 6 to 12 ms for the Tipam formation (Fig. 19) and 3 to 5 ms for the Chhatral pay (Fig. 20). In the plugs from Chhatral pay, a high percentage of siderite along with chamosite is reported and in the case of the LRLC Tipam pay under study, around 18 to 20% of magnetic constituents are reported in XRD studies.

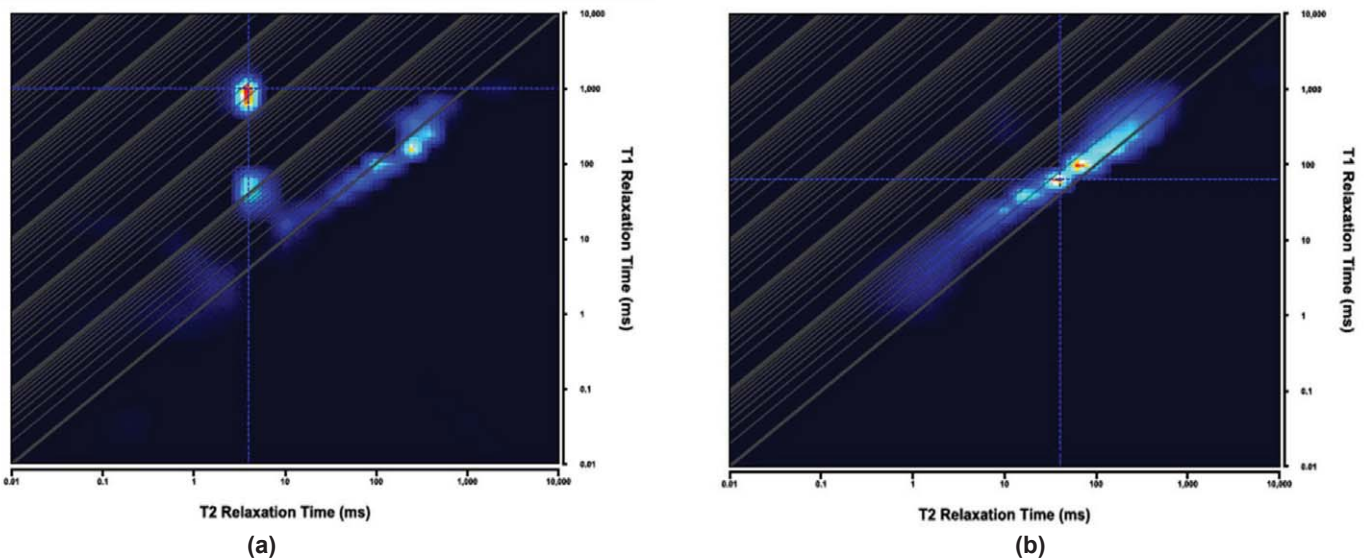


Fig. 18— T_1 - T_2 correlation map of the plug CH-14A using two echo spacing showing the echo spacing dependence on the T_1/T_2 ratio. (a) Acquired with TE = 100 μ s and (b) acquired with TE = 400 μ s.

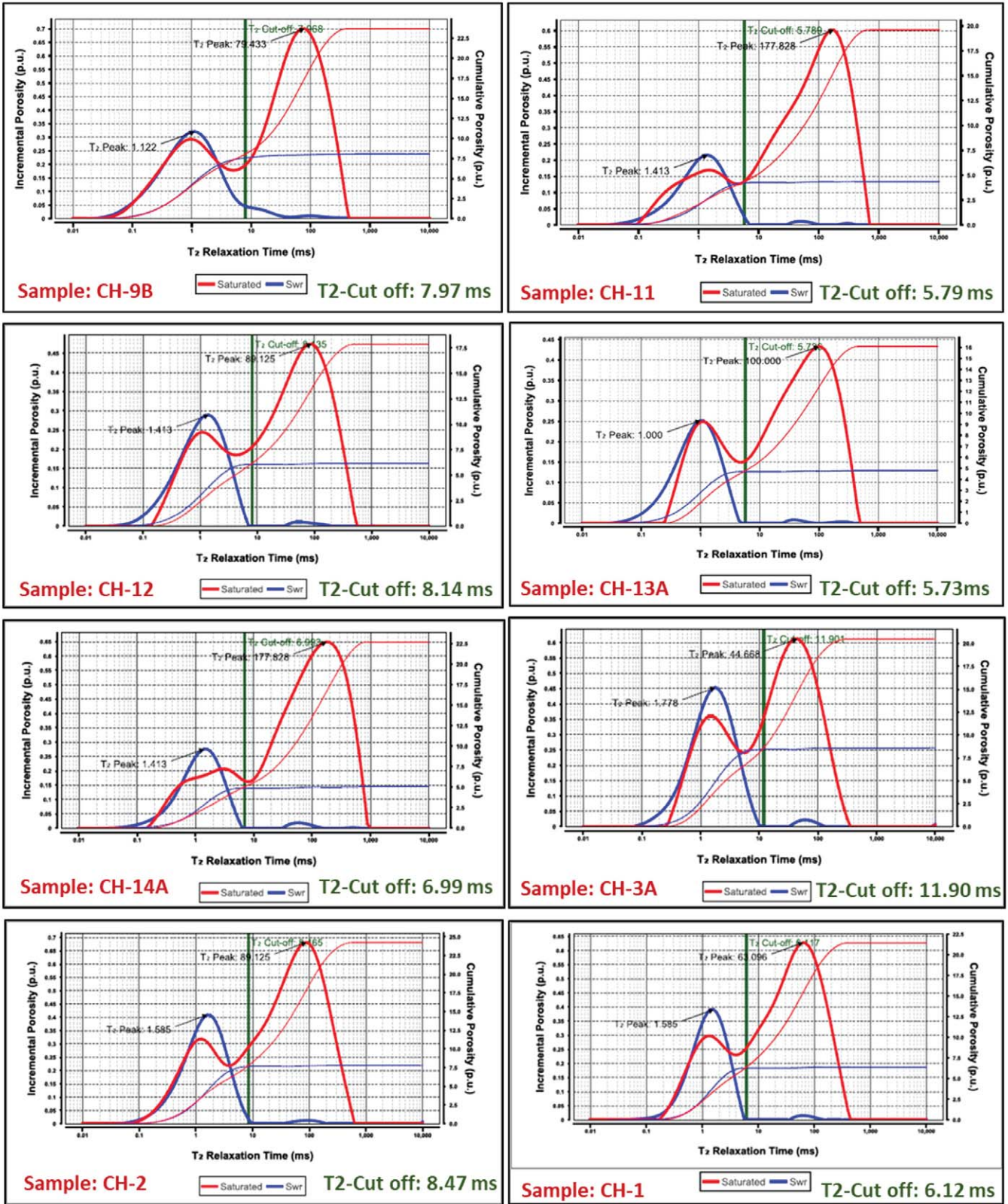


Fig. 19— T_2 cutoffs for the studied core samples from the Charali field.

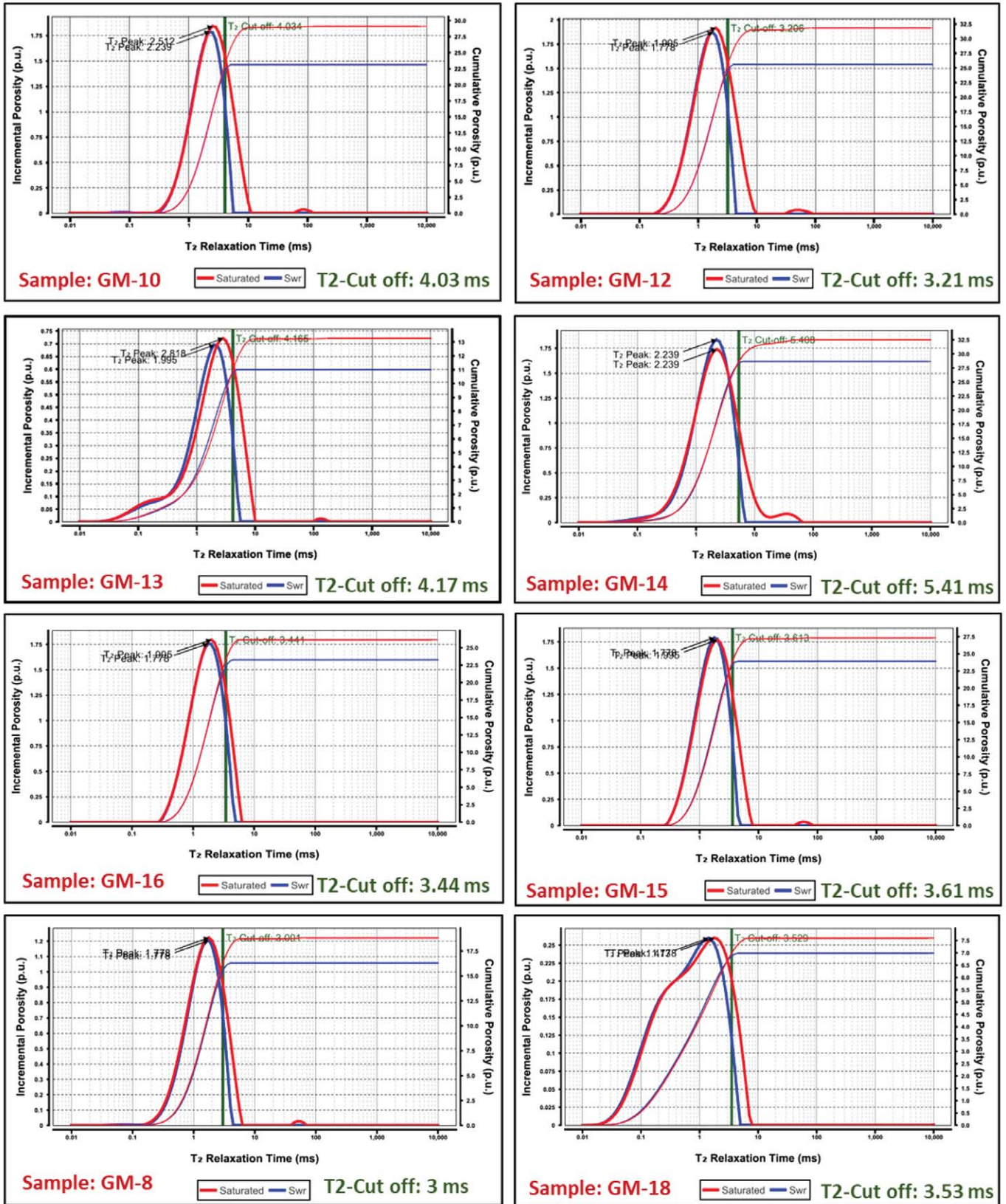


Fig. 20— T_2 cutoffs for the studied core samples from the Gamij field.

CONCLUSIONS

In the presented case studies, although we have two contrasting permeability ranges (poor in one set/field to moderate/high in other), perceptibly low T_2 cutoff values (compared to the default 33 ms T_2 cutoff) have been found experimentally for both the cases. Irreducible saturation from capillary studies carried out on the same samples, corroborates the values derived from the NMR T_2 cutoff study as well.

Our study shows the presence of internal field gradients, which in turn indicates magnetic susceptibility contrast between pore-filling fluids and rock matrix. We studied echo-spacing dependence on the transverse relaxation and could observe different asymptotic relaxation regimes. Crossplots of $(1/T_{2A} - 1/T_{2i})$ vs. $(TE_A^2 - TE_i^2)$ and T_1 - T_2 correlation maps bring out the variations in data distributions/trends (that belongs to different asymptotic relaxation regimes) indicating different controlling factors, such as varying size, susceptibility, concentration and distribution of magnetically susceptible sites as well as different orders of grain sizes acting together.

Internal gradients have been estimated from the data points that lie in the free-diffusion regime. In samples from Tipam formation the estimated maximum internal gradient is in the range of 72 to 166 Gauss/cm, whereas in samples from Chhatral pay of Cambay shale formation the estimated maximum internal gradient is mostly in the range of 346 to 510 Gauss/cm (with internal gradient reaching ~1,436 Gauss/cm in one sample). In both cases, we obtained a wide range of T_1/T_2 ratios. The T_2 cutoff as well as T_1/T_2 ratio do not have a linear relationship with maximum internal gradient and are influenced by different controlling factors as discussed.

The presence of paramagnetic minerals, which has also been reported in mineralogical studies from the same horizon, produce a susceptibility contrast and creates internal field gradients along with enhanced surface relaxivity are the prime factors in reducing the T_2 cutoff values.

Understanding the effect of field inhomogeneities and restricted diffusion on the relaxation of nonwetting fluid is particularly useful for interpretation of 2D NMR measurements, which in turn is useful for fluid identification. As diffusivity components are underestimated due to restricted diffusion, and overestimated in the presence of internal field inhomogeneities, laboratory measurements may be required to support interpretation of wireline NMR data. Knowledge of internal gradients is a key factor in correcting the interpretation of 2D measurements.

NOMENCLATURE:

CPMG	= Carr-Purcell-Meiboom-Gill pulse sequence
D	= diffusion coefficient/diffusivity
G	= gradient of the magnetic field
L_d	= diffusion length
L_g	= dephasing length
L_s	= pore structural length
S/V	= surface to volume ratio
T_1	= longitudinal relaxation time
T_2	= transverse relaxation time
$T_{2,D}$	= diffusion component of T_2 relaxation
$T_{2,A}$	= T_2 with minimum echo spacing
$T_{2,i}$	= T_2 at i th echo spacing
T_{2B}	= bulk fluid relaxation
TE	= echo spacing
TE_A	= minimum echo spacing
TE_i	= i th echo spacing
γ	= nuclear gyromagnetic ratio
ρ	= surface relaxivity
τ	= half of echo spacing
τ_d	= diffusion time
τ_E	= TE/2
τ_ω	= dephasing time
Δ_ω	= spread in Larmor frequencies

ACKNOWLEDGMENTS

The authors are very thankful to ONGC management for allowing to publish the work. The views expressed in the paper are solely the opinions of the authors and not necessarily those of ONGC.

REFERENCES

- Anand, V., and Hirasaki, G.J., 2007, Paramagnetic Relaxation in Sandstones: Distinguishing T_1 and T_2 Dependence on Surface Relaxation, Internal Gradients and Dependence on Echo Spacing, Paper V, *Transactions, SPWLA 48th Annual Logging Symposium*, Austin, Texas, USA, 3–6, June.
- Appel, M., Freeman, J.J., Perkins, R.B., and Hofman, J.P., 1999, Restricted Diffusion and Internal Field Gradient, Paper FF, *Transactions, 40th Annual Logging Symposium*, Oslo, Norway, 30 May–3 June.
- Avenir, D., Editor, 1989, *The Fractal Approach to Heterogeneous Chemistry. Surfaces, Colloids, Polymers*, John Wiley & Sons. ISBN: 0-471-91723-0.
- Brown, R.J.S., and Fantazzini, P., 1993, Conditions for Initial Quasilinear T_2^{-1} Versus τ For Carr-Purcell-Meiboom-Gill NMR With Diffusion and Susceptibility Differences in Porous Media and Tissues, *Physical Review B*, 47(22), 14823–14834. DOI: 10.1103/PhysRevB.47.14823.

- Carr, H.Y., and Purcell, E.M., 1954, Effects of Diffusion on Free Precession in Nuclear Magnetic Resonance Experiments, *Physical Review*, **94**(3), 630–638. DOI: 10.1103/PhysRev.94.630.
- DeSwiet, T.M., and Sen, P., 1994, Decay of Nuclear Magnetization by Bounded Diffusion in a Constant Field Gradient, *Journal of Chemical Physics*, **100**(8), 5597–5604. DOI: 10.1063/1.467127.
- Dunn, K.-J., Appel, M., Freeman, J.J., Gardener, J.S., Hirasaki, G. J., Shafer, J.L., and Zhang, G.Q., 2001, Interpretation of Restricted Diffusion and Internal Field Gradients in Rock Data, Paper AAA, *Transactions, SPWLA 42nd Annual Logging Symposium*, Houston, Texas, USA, 17–20 June.
- Fantazzini, P., and Brown, R.J.S, 2005, Initially Linear Echo-Spacing Dependence of $1/T_2$ Measurements in Many Porous Media With Pore Scale Inhomogeneous Fields, *Journal of Magnetic Resonance*, **177**(2), 228–235. DOI: 10.1016/j.jmr.2005.08.001.
- Hurlimann, M.D., 1998, Effective Gradients in Porous Media Due to Susceptibility Differences, *Journal of Magnetic Resonance*, **131**(2), 232–240. DOI: 10.1016/j.jmre.1998.1364.
- Kleinberg, R.L., Kenyon, W.E., and Mitra, P.P., 1994, Mechanism of NMR Relaxation of Fluids in Rocks, *Journal of Magnetic Resonance, Series A*, **108**(2), 206–214. DOI: 10.1006/jmra.1994.1112.
- Zhang, G.Q., Hirasaki, G.J., and House, W.V., 1998, Diffusion in Internal Field Gradients, Paper 9823 presented at the Society of Core Analysts International Symposium, The Hague, The Netherlands, 14–16 September.
- Zhang, G.Q., Hirasaki, G.J., and House, W.V., 2001, Effect of Internal Field Gradients on NMR Measurements, *Petrophysics*, **42**(1), 37–47.
- Zhang, G.Q., Hirasaki, G.J., and House, W.V., 2003, Internal Field Gradients in Porous Media, *Petrophysics*, **44**(6), 422–434.

ABOUT THE AUTHORS



Partha Sarathi Sarkar holds a postgraduate degree in applied geophysics from Banaras Hindu University (BHU). He joined Oil and Natural Gas Corporation Ltd, (ONGC), India in 2006. He initially worked in logging field operations. Later he has worked in formation evaluation, integrated field studies, and reservoir characterization. Sarkar is currently in the NMR team at Centre for Excellence in Well Logging Technology (CEWELL), ONGC, and is primarily involved in making laboratory measurements and analysis of rocks and fluids.



Soma Chatterjee, a post-graduate in Geophysics from BHU, Varanasi, India, joined ONGC Ltd., India in 1999. With an initial stint of wireline field operations, she has worked in formation evaluation, integrated field studies, reservoir characterization, brownfield studies along with database management, QC and system maintenance, workover planning as petrophysicist for fields in different basins and assets. Ms. Chatterjee is currently working in CEWELL, an R&D institute of ONGC, India and is presently associated with experimental NMR studies.



Mohan Lal holds a postgraduate degree in physics from Rohilkhand University. He had joined Oil and Natural Gas Corporation Ltd (ONGC), India, in 1990. He has more than 25 years of experience in log data acquisition, processing & interpretation and petrophysics laboratory. He has a special interest in generation of various petrophysical parameters in the laboratory for integration with log data for realistic formation evaluation. Currently he is in charge of the laboratory group at the Centre for Excellence in Well Logging Technology (CEWELL), ONGC.



Manoj Kumar is currently working in the Centre for Excellence in Well Logging Technology (CEWELL), an R&D institute of ONGC, the national E&P Company of India. He has two decades of rich experience in wireline data acquisition in different basins and assets of Indian oil fields. For the past 12 years, Mr. Kumar has been working on various domains of integrated petrophysical evaluation pertaining to clastic and carbonate reservoirs of different sedimentary basins of India. At present, he is leading teams involved in geomechanical research and petrophysical and NMR laboratory studies. Mr. Manoj Kumar holds a Master's degree in Physics from University of Delhi and a Post-Graduate Diploma in Management.



P.P. Deo holds a Postgraduate (Physics) degree from Indian Institute of Technology (IIT), Kharagpur and Postgraduate diploma in International Management (PGDIM) from IMI, New Delhi. After graduating from IIT-KGP, he joined Tata Institute of Fundamental Research (TIFR), the prime institute of the Department of Atomic Energy, India. During his stint at TIFR he was associated with numerical simulation of hydrodynamical instability of stellar collapse. He joined Oil and Natural Gas Corporation Ltd (ONGC), India, in 1984. During his 34-year association with ONGC, he has worked extensively on fields with varied depositional settings and geological complexity in various capacities as petrophysicist. His area of expertise and experience in various subdisciplines of petrophysics include petrophysical core studies, map and contract management, log analysis, slick-well analysis and production enhancement, prospect evaluation for release of location, and geocellular modeling. Later, he led the G&G group and laboratories in the premier R&D institute, the Institute of Reservoir Studies, ONGC. Mr. P.P. Deo has published 42 technical papers in various national and international journals. Currently, Mr. Deo is the Head of Institute, Centre for Excellence in Well Logging Technology (CEWELL), an R&D institute of ONGC Ltd., India.

New Robust Model to Estimate Formation Tops in Real Time Using Artificial Neural Networks (ANN)

Salaheldin Elkatatny^{1,2}, Ahmed Al-AbdulJabbar¹, and Ahmed Abdulhamid Mahmoud¹

ABSTRACT

Determination of the formation tops is an important and critical parameter while drilling a hydrocarbon well since it is one of the main factors affecting selection of the casing setting depths and drilling fluid design. During the field exploration and delineation phase and based on the geological data, the formation tops are estimated with low accuracy because of data limitations.

In this study, a potential alternative technique for predicting formation tops is introduced. This technique involves application of artificial neural networks (ANN) and the use of a combination of the drilling mechanical parameters and the rate of penetration (ROP) to provide an accurate prediction of the formation tops. Incorporating the drilling mechanical parameters in this technique is suggested to help in predicting the true increase or decrease in the ROP regardless of the fluctuation on the other drilling parameters.

Field data from two vertical oil wells (Well-A and Well-B) from the Middle East were used in this study. Seventy percent of the data from Well-A (4,436 data points) was used to train the ANN model, which was then tested on the remaining 30% of the data for Well-A (1,900 data points) and validated using the data from Well-B (6,569 data points).

The sensitivity analysis confirmed that using a ANN model that consists of 25 neurons, one hidden layer, and with the Levenberg-Marquardt backpropagation function as the training function, is the optimum for predicting the formation tops with correlation coefficients (R) of 0.94 and 0.98 for the testing and validation data of Well-A and Well-B, respectively. The developed ANN model showed high accuracy in estimating the formation tops for both the testing and validation datasets of Well-A and Well-B, respectively.

INTRODUCTION

Accurate and real-time determination of the formation tops or the lithology of the formation currently being drilled is one of the most essential factors to ensure efficient and safe drilling operations (Al-AbdulJabbar et al., 2018). Knowledge of the formation tops is required when designing the casing program because it is needed to select the proper casing setting depths to ensure efficient zonal isolation, and to effectively design the correct mud weight, which helps to keep the wellbore conditions under control (Bourgoyne et al., 1986; Rabia, 2001; Hossain and Al-Majed, 2015).

Currently, four techniques are used by the drilling engineers in oil fields to determine different reservoir zones or formation tops (a) the rate of penetration (ROP) charts, (b) gamma-ray logs (GR), (c) formation cuttings, and (d) mud logging (Holstein and Warner, 1994; Crain, 2000; Zhu et al., 2018). Although all these techniques help the drillers to delineate the formation tops, each technique has some limitations, such as high cost, relatively low accuracy, or

huge manpower, and most of these measurements have a lag in time or depth that prevents instantaneous estimation of the formation tops, these limitations restrict the applicability and reduce the efficiency of the available techniques for determination of formation tops.

Although the ROP is significantly affected by the lithology, several other factors influence the ROP, e.g., fluctuation of the drilling parameters considerably affects the ROP (Elkatatny, 2018). Therefore, estimation of the lithology change or formation tops based on ROP only is not sufficiently accurate, especially when the other drilling parameters are highly fluctuating. The drill cuttings require time to reach to the surface, this time considerably increases with the increase in the hole depth, which means a delay in predicting the formation currently being drilled (Crain, 2000). Deploying GR logging while drilling (LWD) or mud logging in every section is not economically wise and doesn't provide the required information instantaneously. GR and LWD sensors are installed a distance from the drill bit; thus, the currently indicated formation by these logs is

Manuscript received by Editor April 5, 2019; revised manuscript received July 20, 2019; manuscript accepted July 31, 2019.

¹Department of Petroleum Engineering, King Fahd University of Petroleum & Minerals, Dhahran 31261, Saudi Arabia; elkatatny@kfupm.edu.sa; gr200679600@kfupm.edu.sa; eng.ahmedmahmoud06@gmail.com

²Petroleum Engineering Department, Cairo University, Cairo, Egypt.

*Corresponding Author E-mail: elkatatny@kfupm.edu.sa

not the actual formation being drilled by the drill bit. Also, mud logging has its own lag time, which varies from few minutes to hours, based on the drilling fluid and the depth, since the wellbore needs to be circulated bottoms up in order to get the mud or the cuttings out of the well (Crain, 2000). Today, most use a combination of these techniques to improve the predictability of formation tops depending on section criticality and whether it's deep, shallow or near the reservoir.

Recently, several artificial intelligence (AI) techniques have been applied extensively in different petroleum engineering applications, such as evaluation of unconventional resources (Mahmoud et al., 2017a, 2017b), estimation of the bubblepoint pressure (Alakbari et al., 2016; Elkatatny and Mahmoud 2018), real-time prediction of rheological parameters of the different drilling fluids (Elkatatny et al., 2016a; Elkatatny, 2017), well-log interpretation (Houze and Allain, 1992; Lim et al., 1998; Long et al., 2016), estimation of rock mechanical parameters (Elkatatny et al., 2016b, 2017a), reservoir characterization (Barman et al., 2000; Finlay et al., 2014; Elkatatny and Mahmoud, 2017), optimization of ROP (Amar and Ibrahim, 2012; Amer et al., 2017; Elkatatny 2018), pressure-transient analysis (Aydinoglu et al., 2002; Alajmi and Ertekin, 2007; Almaraghi and El-Banbi, 2015).

Several previous studies aimed to improve the predictability of the lithology through the application of the AI techniques (Rogers et al., 1992; Benaouda et al., 1999; Wang and Zhang, 2008). All these studies used well-log data as inputs to teach the AI models.

Benaouda et al. (1999) predicted the formation lithology in an offshore field using a neural-network classification model with 17 logs: Spectral gamma ray, computed gamma ray, radioactive potassium, thorium, and uranium, deep, medium, and shallow resistivity, bulk density, photoelectric effect, sonic velocity and the oxide contents of calcium, silicon, iron, titanium, potassium, and aluminium. The authors applied their model using data collected from the forearc sedimentary basin of the Izu-Bonin arc south of Japan. Although the results obtained by the authors are acceptable, the model was not able to correctly predict the formations with thickness of < 2 m, this is attributed to the high vertical resolution of the resistivity logs used to develop the model. Another limitation of this model is that at certain depths, the density and photoelectric effect data are not available and the model is developed based on the remaining 15 logs. Density is one of the most important logs affected by the lithology, hence, in the sections where density logs were not considered in developing the model, the model predictability will significantly be decreased.

Wang and Zhang (2008) studied the use of log data to

estimate the lithology using the backpropagation neural network. The authors developed their model based on the sonic transit time and gamma ray logs only. In this study, the model was developed and tested using data collected from Kela-2 gas field, Tarim Basin, in West China. The model was developed to differentiate between two types of formations: mudstone and sandstone.

Recently, Moazzeni and Haffar (2015) evaluated the possibility of using the artificial neural network (ANN) to determine the lithology of the formation. The authors used 13 input parameters to develop their model, these parameters are: drill-bit depth, ROP, torque (T), weight on bit (WOB), bit revolutions/minute (RPM), pump output, pump pressure, bit size, bit type, length of drilled interval for the current bit, lifetime of the current bit, mud weight, and total flow area of bit (TFA). Most of the parameters used as inputs for lithology estimation in this model (e.g., drill-bit depth, bit size, bit type, length of drilled interval for the current bit, lifetime of the current bit, mud weight, and TFA) are not directly affected by the change in the formation type but may be considerably affected by the change in other factors.

In this paper, the ROP and different drilling parameters, such as mud flow rate (Q_m), drillpipe rotation (RPM), standpipe pressure (SPP), torque (T), and weight on bit (WOB) are combined to estimate the formation tops by applying the backpropagation ANN pattern-recognition function (nprtool). With this new technique, detecting formation tops will be faster compared to other methods since no logs need to be processed, and there is no need to wait for the drilled cuttings to reach the surface. This ensures that formations can be picked in real time with high accuracy at a very low cost since real-time data are already available.

DATA COLLECTION AND PREPARATION

In this work, field data of ROP, Q_m , RPM, SPP, T , and WOB were collected in the intermediate borehole section (16 in.) from two oil wells (Well-A and Well-B) in the Middle East and used to develop the ANN model. The data were collected from the borehole interval in the same formations in both wells and consist of 6,336 data points from Well-A and 6,569 data points from Well-B. Both wells are vertical boreholes and a conventional bottomhole assembly (BHA) was used to drill the sections under study. The data were recorded by the surface real-time data transmitter sensor on a footage base and originally contained the information of all the operations (i.e., drilling, tripping, and running the casing) performed on the 16-in. hole section for both wells.

In the first step of this study, only the data recorded during drilling operations (when new footage was made) was captured and the rest of the data were discarded. In the

second step, the data were further smoothed by removing the nonrealistic values, the outliers, and the noise. The efficiency of the moving average technique (MAT) with a span of 2, 3, 4, and 5 and the Savitzky-Golay filter (SGF) in reducing the noise and smoothing the input data was compared. MAT is a widely used indicator in technical analysis that helps to smooth by filtering out the “noise” from random short-term data fluctuations, and SGF is a digital filter that can be applied to a set of digital data points for the purpose of smoothing the data to increase the precision of the data without distorting the signal tendency. This is achieved, in a process known as convolution, by fitting successive subsets of adjacent data points with a low-degree polynomial by the method of linear least squares.

Figure 1 compares the actual data (blue points) with the smoothed data (red curve) for the ROP values of the training dataset (Well-A). The output showed that the use of MAT with a span of 5 (Fig. 1a) is the best to smooth the input data without changing its structure significantly compared to the other techniques (Figs. 1b to 1e). MAT with a span of 5 was then used to smooth all the input parameters of the training

and testing datasets used in this study. Although the SGF was also good in smoothing the input data, as shown in Fig. 1b, it affected the structure of the input data by neglecting many data points, thus, it affected the actual trend of the data. On the other hand, SGF requires long computational time which will delay the prediction when a new formation is reached.

Since the output parameters or the formation tops in this study will be predicted using a classification technique that gives the model outputs as binary numbers (i.e., 0 and 1), the output parameters or formations 1, 2, 3, and 4 will be defined for the model using the binary numeral system. Since every formation must be defined in the model with a unique format, four digits are needed to differentiate between the four formations under study using the binary system. The four digits representing each formation were defined in the model as a row vector of four elements, three of them are “zeros” and one is “1” as explained in Table 1, the position of the element “1” in the row vector is used to differentiate between the formations. The representation of the four formations in the binary system is illustrated by the schematic diagram of Fig. 2.

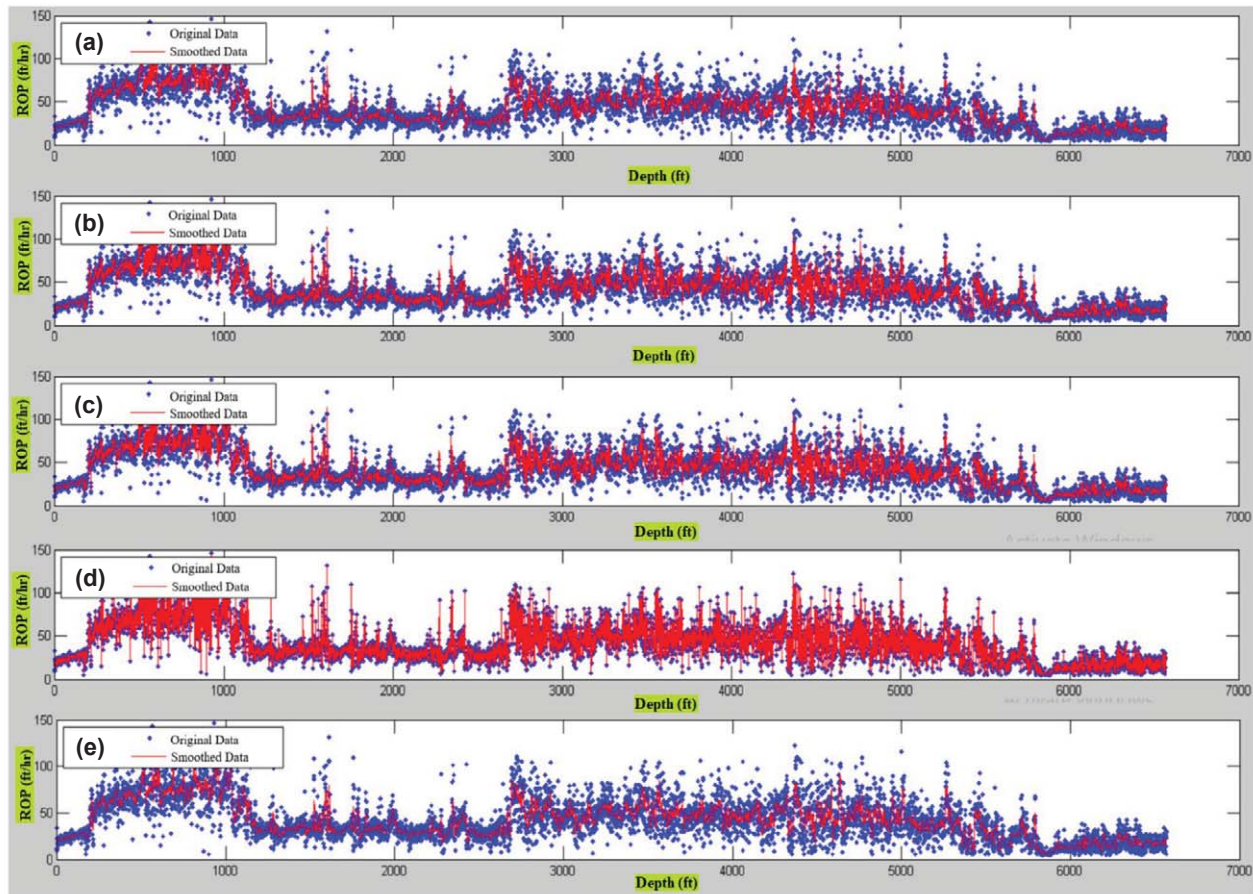


Fig. 1— Comparison of the performance of MAT with spans of (a) 5, (b) 4, (c) 3, (d) 2, and (e) SGF in reducing the noise in the ROP for the training data of Well-A plotted as a function of the formation depth. Blue dots represent the original data and the red curves denote the filter data.

Table 1—Representation of the Formations Under Study in the Binary Numeral System Using a Row Vector of Four Elements

Formation	Formation Representation			
	1 st Element	2 nd Element	3 rd Element	4 th Element
Formation 1	1	0	0	0
Formation 2	0	1	0	0
Formation 3	0	0	1	0
Formation 4	0	0	0	1

DEVELOPING THE ANN MODEL

The ANN model was trained using 70% of the data points collected from Well-A (i.e., 4,435 data points). Six parameters, ROP, Q_m , RPM, SPP, T , and WOB, were considered as inputs to learn the ANN model on predicting the formation tops as an output, the use of the drilling parameters with the ROP is considered to enhance the accuracy of the prediction, especially at depths where the drilling parameters are highly fluctuating, since ROP at these depths is not a function of the formation type only. Figure 3 shows the relative importance of the different input variables in predicting the formation tops: the SPP has a high correlation coefficient of 0.88 with the formation tops; the ROP and the torque have moderate correlation coefficients of -0.61 and -0.44 , respectively, with the formation tops; while the correlation coefficients of Q_m , WOB, and RPM with the

formation tops are only 0.09, 0.04 and 0.01, respectively. Although the correlation coefficients for Q_m , WOB, and RPM are relatively small, including these data with the input dataset improved the formation tops determination considerably.

Figure 4 shows the changes in the input parameters of Well-A as a function of the depth, these are the data used to develop the ANN model. Figure 5 shows the clusters of the data collected from Well-A, the clusters are grouped based on the formations. Table 2 summarizes the statistical parameters of the input parameters of the training dataset. Table 2 shows that the ROP in the teaching data used to develop the model ranges from 5.6 to 114.4 ft/hr, drilling fluid flow rate is between 838.2 and 1109.7 gal/min, RPM ranges from 68.4 to 157.3, SPP is between 1227 and 3102 psi, T ranges from 6.02 to 24.18 klb/ft, and the WOB ranges from 10.0 to 63.4 klb.

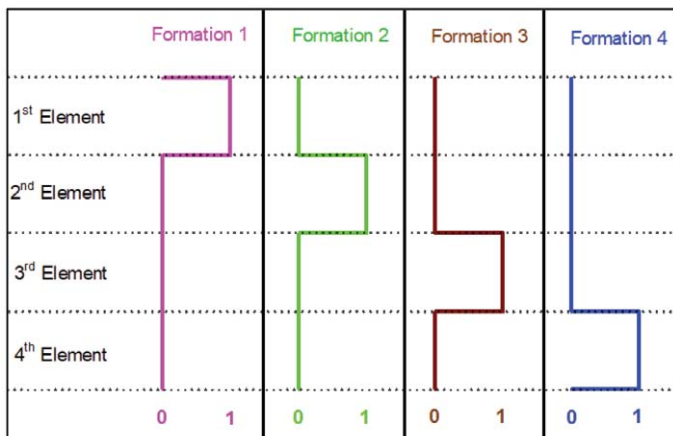


Fig. 2—Schematic illustration of the formation representation in the binary system for the four formations under study.

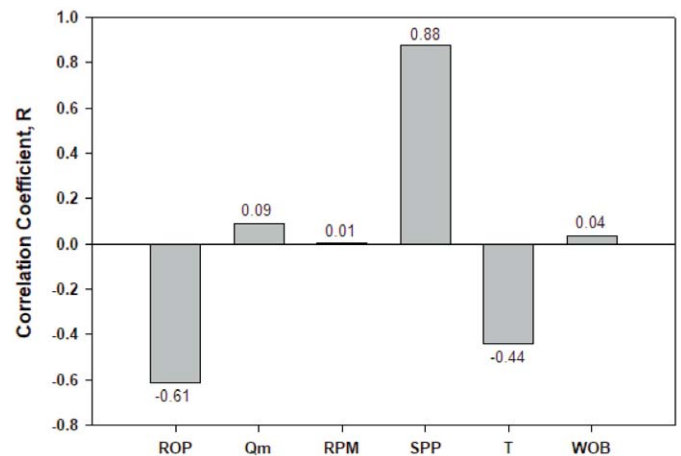


Fig. 3—The relative importance of the parameters used to train the ANN model for formation tops prediction.

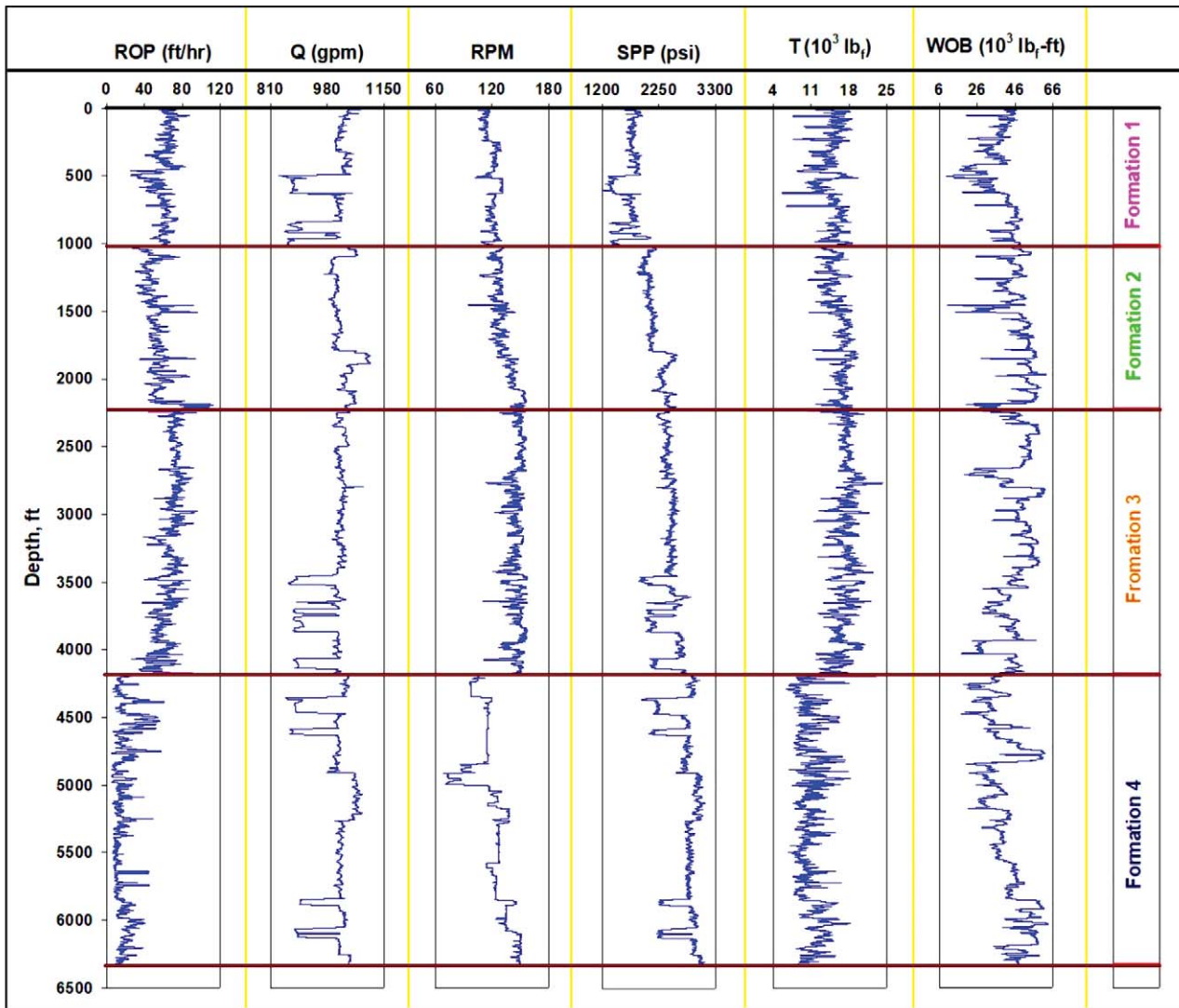


Fig. 4—The six input parameters used to develop the ANN model using the data of Well-A as a function of depth.

Table 2—Statistical Parameters of the Training Dataset (70% of Well-A Data Points)

Statistical Parameter	ROP (ft/hr)	Q _m (gal/min)	RPM	SPP (psi)	Torque (klbf-ft)	WOB (klbf)
Minimum	5.6	838.2	68.4	1,227	6.02	10.0
Maximum	114.4	1,109.7	157.3	3102	24.18	63.4
Mean	46.7	1,006.0	131.4	2383	14.54	43.7
Range	108.9	271.5	88.8	1875	18.16	53.5
Variance	564.1	2,624.3	259.4	17,3630	11.22	92.9
Kurtosis	-0.24	-1.52	-0.63	-0.45	-0.38	-0.40
Skewness	1.85	4.75	3.62	2.43	2.11	2.67

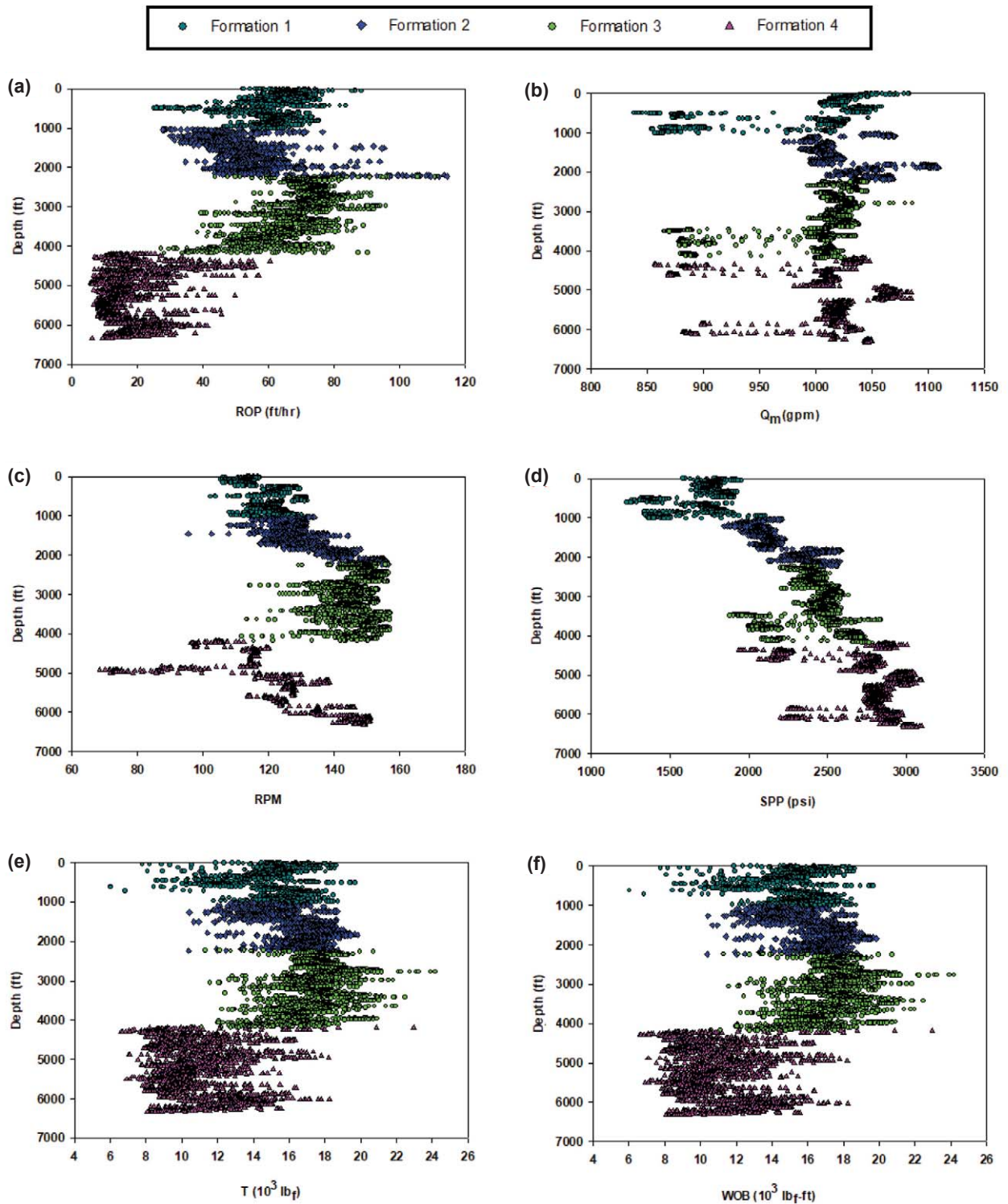


Fig. 5—The clusters of the typical input parameters of (a) ROP, (b) Q_m , (c) RPM, (d) SPP, (e) T , and (f) WOB, for the data collected from Well-A. The clusters are grouped based on the formations.

The input parameters were selected based on the outcomes published in our previous papers Elkatatny (2018) and Elkatatny et al. (2017b) in which the mechanical parameters were found to considerably affect the ROP, thus, they can be bundled with the ROP to mask or remove fluctuations in ROP caused by changes in the parameters. This way the model can truly detect ROP changes due to formation characteristics only and not because of changes in other drilling parameters.

The ANN model was optimized for its different design parameters, including the number of the training layers, the number of the neurons per each training layer, training function, and transferring function. The optimum parameters were selected based on the mean squared error (MSE) and the correlation coefficient (R) between the predicted and actual formation, the model predictability was evaluated for the number of the neurons, ranging from 5 to 25 neurons. The use of 25 neurons showed the lowest MSE of 4.4 and the highest R of 0.989 for the training dataset, as shown in Fig. 6. Nine training functions of trainlm, trainbfg, trainrp, trainlscg, trainlcbg, trainlcbf, trainlcbp, trainloss, and trainlgdx were tested on predicting the formation tops for the training dataset. Trainlm was found to be the best training function for estimating the formation tops with the lowest MSE of 1.6 and the highest R of 0.999, as shown in Fig. 7.

The model was built using nprtool which uses a two-layer feed-forward network with sigmoid output neurons. The six inputs (i.e., ROP, Q_m , RPM, SPP, T , and WOB) were introduced to the model in the input layer. The ANN model with one input layer having the six inputs, a single training layer (hidden layer) having 25 neurons built using Levenberg-Marquardt backpropagation (trainlm) as the

learning function and sigmoid function as a transferring function between the training and output layer, and an output layer with four outputs, was determined to represent the optimum ANN model to classify the four formations under study, as explained in Fig. 8. Table 3 summarizes the design parameters for the developed ANN model for formation tops prediction.

RESULTS AND DISCUSSION

Building the ANN Model

At first, the ANN model was trained by introduced only ROP as an input to predict the correct formation. The results showed that, when ROP is considered as the only input for the ANN model, the actual formation in Well-A was predicted with a very low accuracy, where the MSE for the training data (i.e., 4,436 inputs from Well-A) was 30% and the R is only 0.724, and the MSE and R for the testing 1,900 data points from Well-A were 44% and 0.328, respectively.

In the second step, 4,436 data points of all the six input parameters (ROP, Q_m , RPM, SPP, T , and WOB) were used to teach the ANN model. The predictability of the ANN model was considerably improved in this case, where the MSE was reduced to 4.4, and R is considerably increased to 0.989 for the training data when 25 neurons and trainlm functions are used, as indicated in Fig. 7.

As shown in Fig. 9, for the first formation (Formation 1), 720 depths were predicted correctly, which represent 98.6% of the depths evaluated in this formation, as indicated in Fig. 9b, while 10 of the depths (1.4%) were incorrectly determined as apart of Formation 2. In Formation 2, the ANN model predicted 96.8% of the depths correctly and

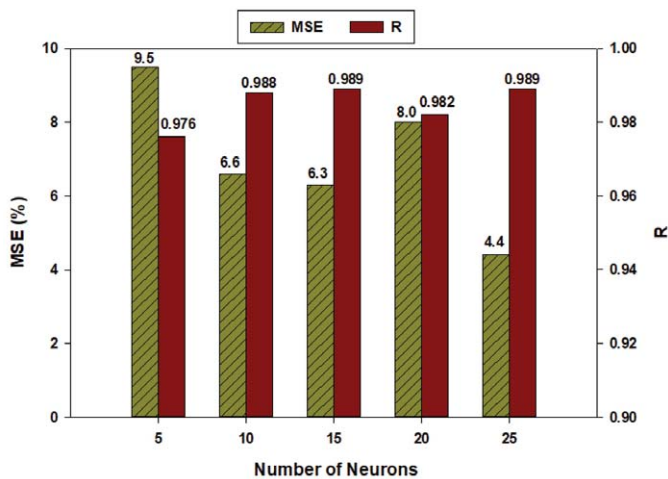


Fig. 6—The effect of the number of neurons on the MSE and R between the actual and predicted formation for the training dataset (4,436 data points).

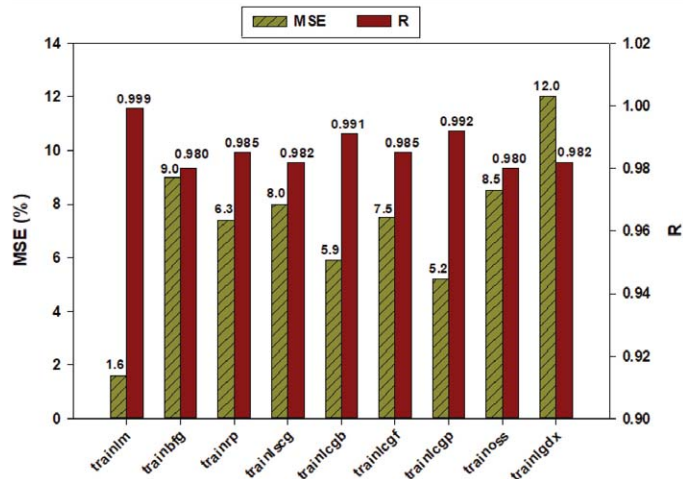


Fig. 7—The effect of the training function on the MSE and R between the actual and the predicted formation for the training dataset (4,436 data points).

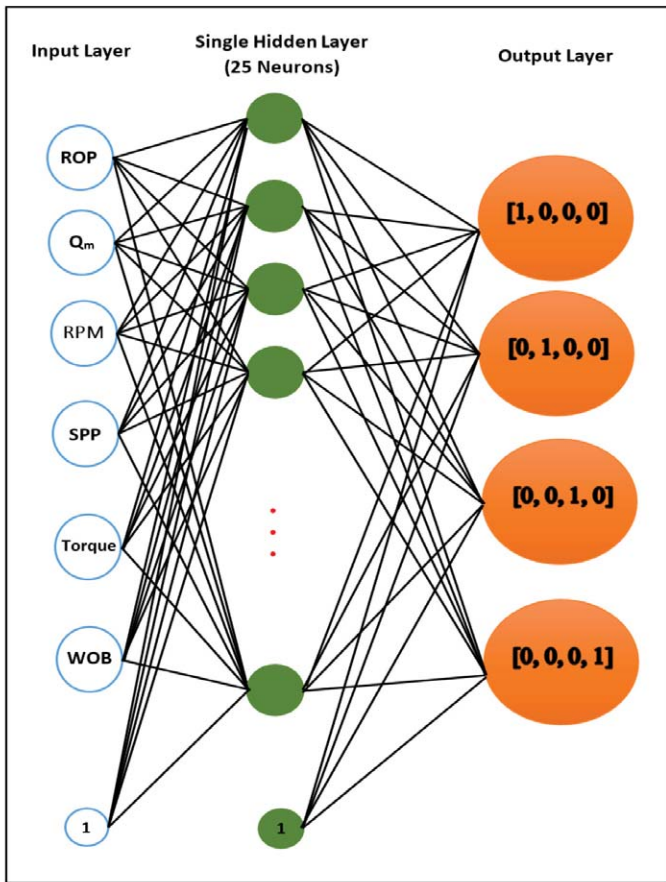


Fig. 8—The structure of the ANN model with a single input layer having six inputs, a single hidden layer with 25 neurons, and an output layer with four outputs.

Table 3—The Optimized ANN Model Design Parameters for Formation Tops Prediction

Parameter	Value
Number of the training layers	Single layer
Number of the neurons/training layer	25
Training function	trainlm
Transferring function	sigmoid

3.2% were predicted to be in Formation 1 (6 depths) and Formation 2 (21 depths); 97.7% of the depths evaluated in Formation 3 were correctly predicted, while 2.3% were not. The ANN model predicted all the depths of Formation 4 correctly.

Testing and Validating the Developed ANN Model

The ANN model was tested using unseen data from Well-A, which is the same well used to train the ANN model at 1,900 depths (Fig. 4), and then tested at 6,569 different depths in Well-B. All these data points are unseen data which

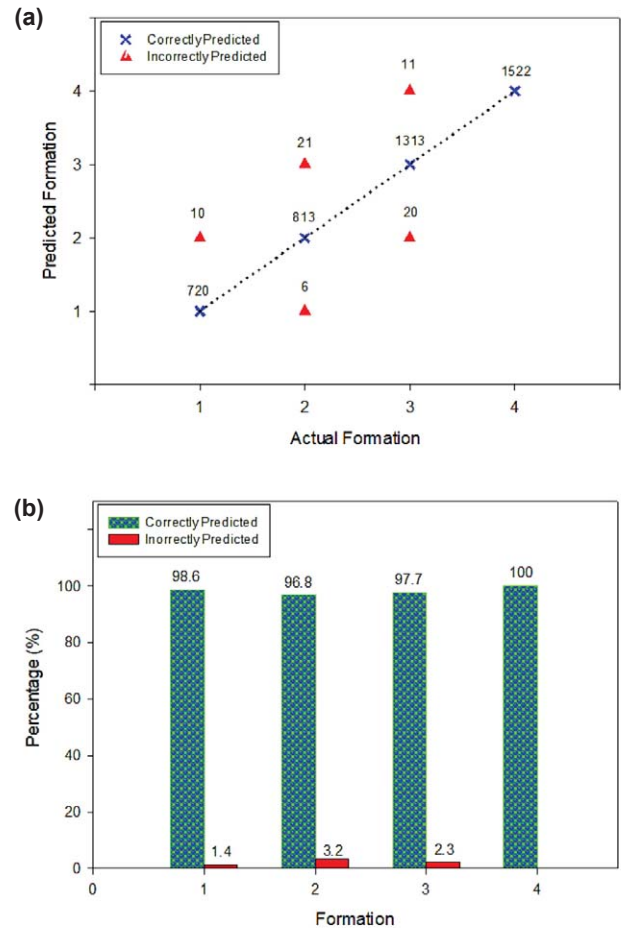


Fig. 9—(a) Crossplot of the number of the actual formation depths predicted correctly and incorrectly, and (b) the percentage of the depths predicted correctly and incorrectly for each formation, for the training data (4,436 depths in Well-A).

were introduced to the ANN model after training to predict the correct formation. In Well-A, the actual formations were predicted with accuracy and R of 98.0% and 0.98, respectively, while in Well-B, the actual formations were predicted with an accuracy of 90.3% and R of 0.94, respectively.

As indicated in Fig. 10 for the testing data of Well-A, for Formation 1, which has 289 data points, the ANN model predicted 282 depths (97.6%) correctly in Formation 1 and 7 depths (2.4%) in Formation 2. For Formation 2, as shown in Fig. 10a, 359 depths were correctly predicted, which represent 96.2% of the depths evaluated in this formation, as shown in Fig. 10b, while 4 and 10 depths were predicted incorrectly in Formations 1 and 3, respectively. In total, 98.5 and 99.8% of the depths of Formations 3 and 4 were correctly determined, as explained in Fig. 10b.

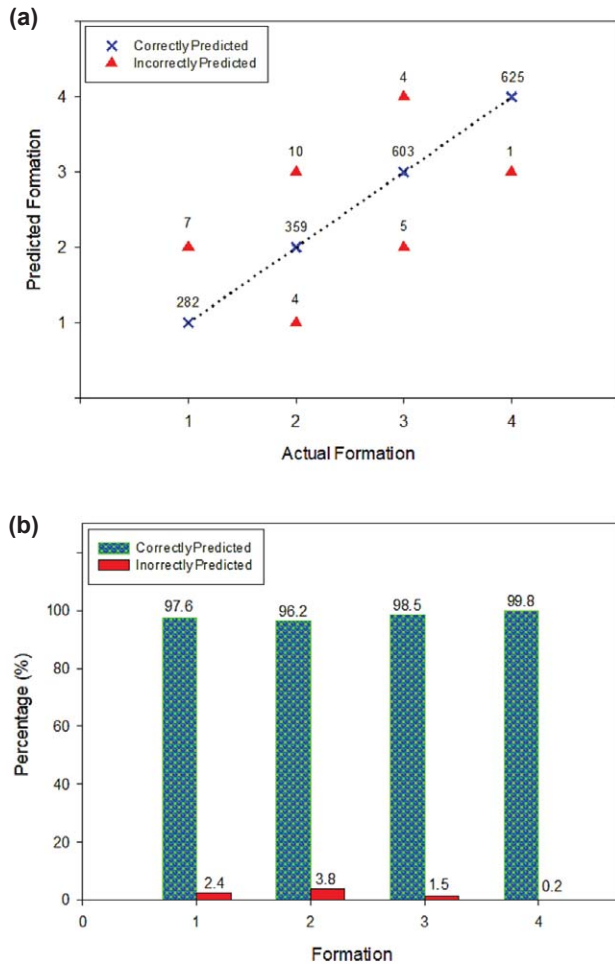


Fig. 10—(a) Crossplot of the number of the actual formation depths predicted correctly and incorrectly, and (b) the percentage of the depths predicted correctly and incorrectly for each formation, for the testing data from Well-A (1,900 depths).

The model is also validated using Well-B data, shown in Fig. 11. As explained in Fig. 12, 78 depths of Formation 1 were predicted mistakenly in Formation 2, while 681 depths were correctly determined. As indicated in Figs. 10b and 12b, 93.9% of Formation 2 depths were correctly determined and 6.1% of the depths were mistakenly determined to belong to Formation 3. Fig. 12a shows that 166 and 143 depths of Formation 3 were predicted in Formations 2 and 4, respectively, and 2,468 (89.0%) were correctly determined. In Formation 4, 1,355 of the depths were correctly predicted while 8 and 164 were incorrectly predicted to belong to Formations 2 and 4, respectively, as shown in Fig. 12a.

Figure 13 compares the actual and predicted formation tops for the testing data of Well-A and validation data of Well-B. As indicated in this figure, the ANN model was able to provide a correct prediction for the formation tops in both wells.

CONCLUSIONS

In this study, a new model for prediction of formation tops is developed based on the application of the backpropagation ANN pattern-recognition function and the use of the rate of penetration, mud flow rate, drillpipe rotation, standpipe pressure, torque, and the weight on bit as input parameters. The ANN model was built and trained on data collected from Well-A and then validated using unseen data collected from Well-B, both wells are in the Middle East. The outcomes show that the use of the ANN model with one training layer having 25 neurons with the use of Levenberg-Marquardt backpropagation training function enabled us to predict the correct formation in Well-A and Well-B with correlation coefficients of 0.98 and 0.94, respectively, and an accuracy of 98.0% in Well-A, which is the well used to train the ANN model, and 90.3% in Well-B, which is a different well not used to train the model. The developed ANN model showed high accuracy in estimating the formation tops for both testing and validation datasets of Well-A and Well-B, respectively.

NOMENCLATURE

Abbreviations

AI	=	artificial intelligence
ANN	=	artificial neural networks
BHA	=	bottomhole assembly
LWD	=	logging while drilling
MSE	=	mean squared error
nprtool	=	network pattern-recognition function
ROP	=	rRate of penetration
RPM	=	revolutions/minute
SPP	=	standpipe pressure
trainlm	=	Levenberg-Marquardt backpropagation function
WOB	=	weight on bit

Symbols

Q_m	=	drilling mud flowrate
R	=	correlation coefficients
T	=	torque

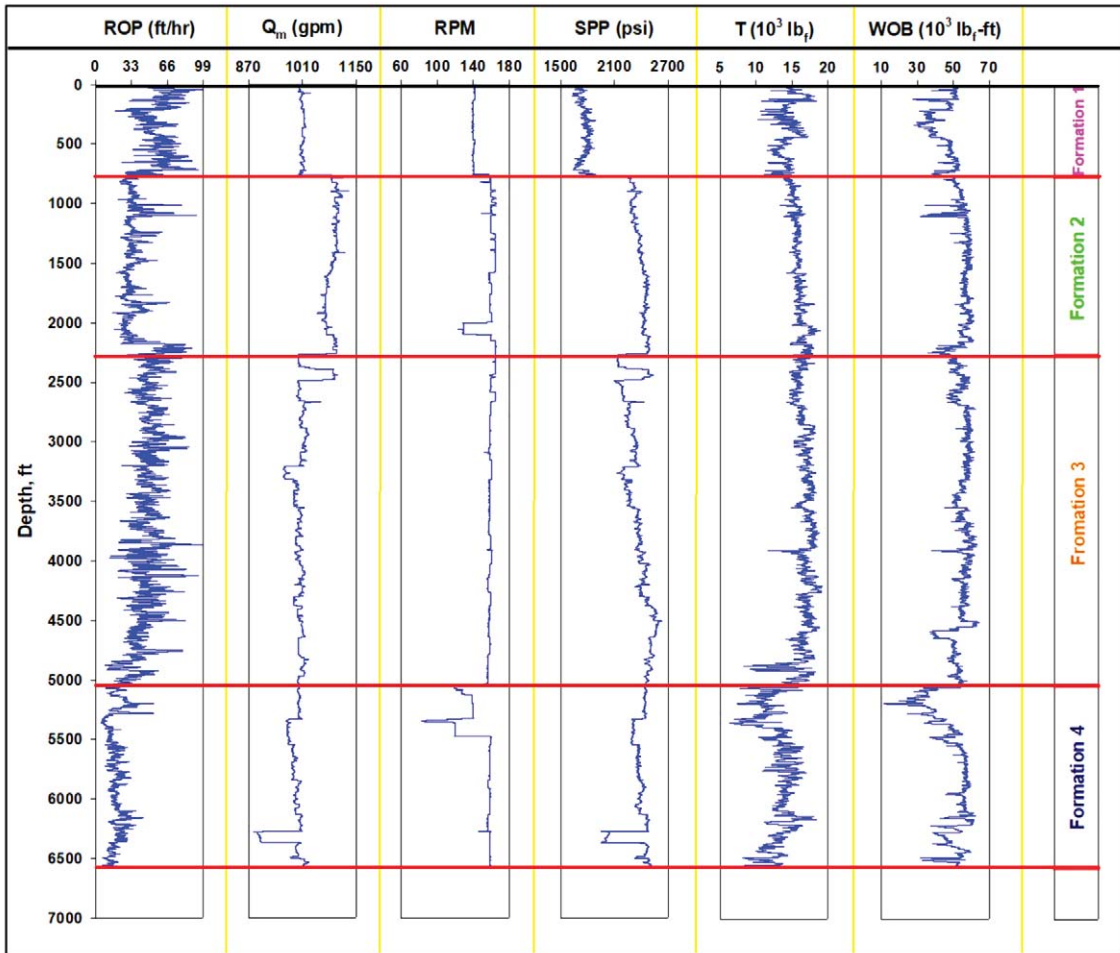


Fig. 11—The input parameters for Well-B as a function of depth, these inputs are unseen data used to test the suggested ANN model.

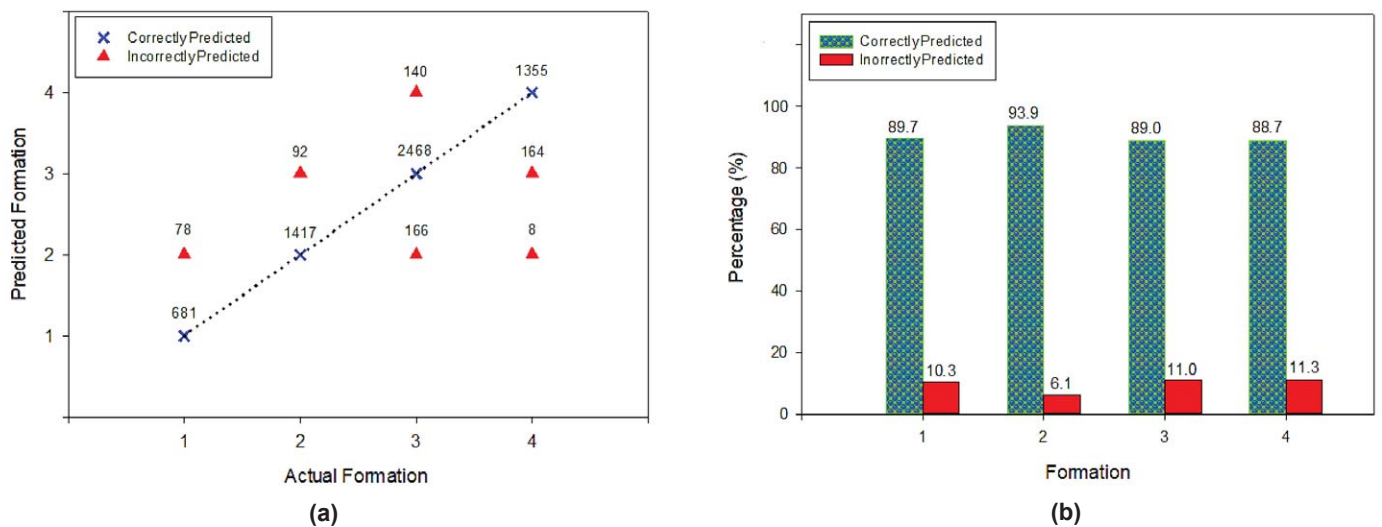


Fig. 12—(a) Crossplot of the number of the actual formation depths predicted correctly and incorrectly, and (b) the percentage of the depths predicted correctly and incorrectly at each formation, for the testing data from Well-B (1,900 depths).

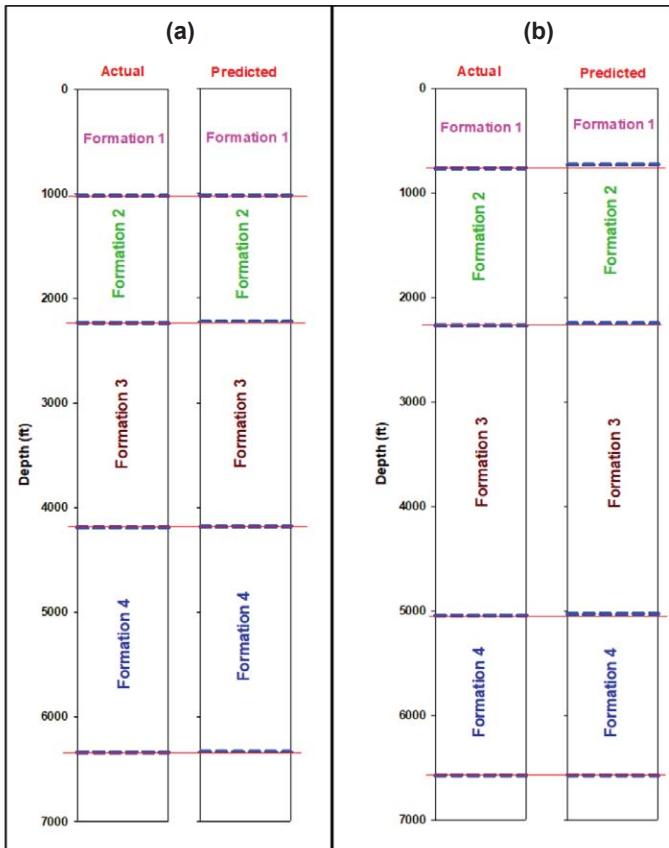


Fig. 13— Comparison of the predictability of the ANN model for the formation tops for (a) the testing data of Well-A, and (b) the validation data of Well-B.

REFERENCES

- Al-AbdulJabbar, A., Elkatatny, S.M., Mahmoud, M., Abdelgawad, K., and Abdulaziz, A., 2018, A Robust Rate of Penetration Model for Carbonate Formation, Paper JERT-18-1278, *Journal of Energy Resources Technology*, **141**(4), 042903, DOI: 10.1115/1.4041840.
- Alajmi, M., and Ertekin, T., 2007, The Development of an Artificial Neural Network as a Pressure Transient Analysis Tool for Applications in Double-Porosity Reservoirs, Paper SPE-108604 presented at the Asia Pacific Oil and Gas Conference and Exhibition, Jakarta, Indonesia, 30 October–1 November. DOI: 10.2118/108604-MS.
- Alakbari, F.S., Elkatatny, S. M., and Baarimah, S.O., 2016, Prediction of Bubble Point Pressure Using Artificial Intelligence AI Techniques, Paper SPE-184208 presented at the SPE Middle East Artificial Lift Conference and Exhibition, Manama, Kingdom of Bahrain, 30 November–1 December. DOI: 10.2118/184208-MS.
- Almaraghi, A.M., and El-Banbi, A.H., 2015, Automatic Reservoir Model Identification Using Artificial Neural Networks in Pressure Transient Analysis, Paper SPE-175850 presented at the SPE North Africa Technical Conference and Exhibition, Cairo, Egypt, 14–16 September. DOI: 10.2118/175850-MS.
- Amar, K., and Ibrahim, A., 2012, Rate of Penetration Prediction and Optimization Using Advances in Artificial Neural Networks, a Comparative Study, *Proceedings of the 4th International Joint Conference on Computational Intelligence*, 647–652. DOI: 10.5220/0004172506470652. <https://pdfs.semanticscholar.org/4b31/9a48df6ff68d6a4deed9b149e9e35c7ba8af.pdf>. Access November 18, 2019.
- Amer, M.M., Dahab, A.S., and El-Sayed, A.-A.H., 2017, An ROP Predictive Model in Nile Delta Area Using Artificial Neural Networks, Paper SPE-187969 presented at the SPE Kingdom of Saudi Arabia Annual Technical Symposium and Exhibition, Dammam, Saudi Arabia, 24–27 April. DOI: 10.2118/187969-MS.
- Aydinoglu, G., Bhat, M., and Ertekin, T., 2002, Characterization of Partially Sealing Faults from Pressure Transient Data: An Artificial Neural Network Approach, Paper SPE-78715 presented at the SPE Eastern Regional Meeting, Lexington, Kentucky, USA, 23–26 October. DOI: 10.2118/78715-MS.
- Barman, I., Ouenes, A., and Wang, M., 2000, Fractured Reservoir Characterization Using Streamline-Based Inverse Modeling and Artificial Intelligence Tools, Paper SPE-63067 presented at the SPE Annual Technical Conference and Exhibition, Dallas, Texas, USA, 1–4 October. DOI: 10.2118/63067-MS.
- Benaouda, D., Wadge, G., Whitmarsh, R.B., Rothwell, R.G., and MacLeod C., 1999, Inferring the Lithology of Borehole Rocks by Applying Neural Network Classifiers to Downhole Logs: An Example From the Ocean Drilling Program, *Geophysical Journal International*, **136**(2), 477–491. DOI: 10.1046/j.1365-246X.1999.00746.x.
- Bourgoyne, A.T., Jr., Millheim, K.K., Chenevert, M.E., and Young, F.S., Jr., 1986, *Applied Drilling Engineering*, SPE Textbook Series **2**. ISBN: 978-1555630010.
- Crain, E.R., 2000, *Petrophysical Handbook*, <https://www.spec2000.net/08-mud.htm>. Accessed November 18, 2019.
- Elkatatny, S.M., 2017, Real Time Prediction of Rheological Parameters of KCl Water-Based Drilling Fluid Using Artificial Neural Networks, *Arabian Journal of Science and Engineering*, **42**(4), 1655–1665. DOI: 10.1007/s13369-016-2409-7.
- Elkatatny, S.M., 2018, New Approach to Optimize the Rate of Penetration Using Artificial Neural Network, *Arabian Journal of Science and Engineering*, **43**(11), 6297–6304. DOI: 10.1007/s13369-017-3022.0.
- Elkatatny, S.M., and Mahmoud, M.A., 2017, Porosity Determination Using Artificial Intelligent Techniques for Carbonate Reservoirs (White Box), Paper ICCDMTA-2017-EDAS-7-1570328361 presented at the International Conference on Computers, Data Management & Technology Applications, Cairo, Egypt, 28–29 January.
- Elkatatny, S.A., and Mahmoud, M.A., 2018, Development of a New Correlation for Bubble Point Pressure in Oil Reservoirs Using Artificial Intelligent Technique, *Arabian Journal of Science and Engineering*, **43**(5), 2491–2500. DOI: 10.1007/

s13369-017-2589-9.

Elkatatny, S.A., Mahmoud, M.A., and Tariq, A., 2017b, Real Time prediction of the Rheological Parameters of NaCl Water-Based Drilling Fluid Using Artificial Neural Networks, Paper SPE-187976 presented at the SPE Kingdom of Saudi Arabia Annual Technical Symposium and Exhibition, Dammam, Saudi Arabia, 24–27 April. DOI: 10.2118/187976-MS.

Elkatatny, S.M., Tariq, Z., and Mahmoud, M.A., 2016a, Real Time Prediction of Drilling Fluid Rheological Properties Using Artificial Neural Networks Visible Mathematical Model (White Box), *Journal of Petroleum Science and Engineering*, **146**, 1202–1210. DOI: 10.1016/j.petrol.2016.08.021.

Elkatatny, S.M., Tariq, Z., Mahmoud, M.A., Abdurraheem Abdelwahab, Z.A., and Woldeamanuel, M., 2017a, An Artificial Intelligent Approach to Predict Static Poisson's Ratio, Paper ARMA-17-771 presented at the 51st US Rock Mechanics/Geomechanics Symposium, San Francisco, California, USA, 25–28 June.

Elkatatny, S.M., Tariq, Z., Mahmoud, M.A., Mohamed I.M., and Abdulazeez, A., 2016b, Application of Artificial Intelligent Techniques to Determine Sonic Time from Well Logs, Paper ARMA-2016-755 presented at the 50th U.S. Rock Mechanics/Geomechanics Symposium, Houston, Texas, USA, 26–29 June.

Finlay, S., Marquez, X., Solling, T., Bounoua, N., and Gagigi, T., 2014, Multi-Scale Carbonate Reservoir Characterization and Artificial Neural Networks Reveals Complexity in the Shuaiba Reservoir, Al Shaheen Field, Paper IPTC-17639 presented at the International Petroleum Technology Conference, Doha, Qatar, 19–22 January. DOI: 10.2523/IPTC-17639-MS.

Holstein, E.D., and Warner, H.R., Jr., 1994, Overview of Water Saturation Determination for the Ivishak (Sadlerochit) Reservoir, Prudhoe Bay Field, Paper SPE-28573 presented at the SPE Annual Technical Conference and Exhibition, New Orleans, Louisiana, USA, 25–28 September. DOI: 10.2118/28573-MS.

Hossain, M., and Al-Majed, A.A., 2015, *Fundamentals of Sustainable Drilling Engineering*, John Wiley & Sons. ISBN: 978-0470878170.

Houze, O.P., and Allain, O.F., 1992, A Hybrid Artificial Intelligence Approach in Well Test Interpretation. Paper SPE-24733 presented at the SPE Annual Technical Conference and Exhibition, Washington, D.C., 4–7 October. DOI: 10.2118/24733-MS.

Lim, J.-S., Kang, J.M., and Kim, J., 1998, Artificial Intelligence Approach for Well-to-Well Log Correlation. Paper SPE-39541 presented at the SPE India Oil Gas Conference and Exhibition, New Delhi, India, 17–19 February. DOI: 10.2118/39541-MS.

Long, W., Chai, D., and Aminzadeh, F., 2016, Pseudo Density Log Generation Using Artificial Neural Network, Paper SPE-180439 presented at the SPE Western Regional Meeting, Anchorage, Alaska, USA, 23–26 May. DOI: 10.2118/180439-MS.

Mahmoud, A.A.A., Elkatatny, S., Mahmoud, M., Abouelresh, M., Abdurraheem, A., and Ali, A., 2017a, Determination of

the Total Organic Carbon (TOC) Based on Conventional Well Logs Using Artificial Neural Network, *International Journal of Coal Geology*, **179**, 72–80. DOI: 10.1016/j.coal.2017.05.012.

Mahmoud, A.A., Elkatatny, S., Abdurraheem, A., Mahmoud, M., Ibrahim, M.O., and Ali, A., 2017b, New Technique to Determine the Total Organic Carbon Based on Well Logs Using Artificial Neural Network (White Box), Paper SPE-188016 presented at the SPE Kingdom Saudi Arabia Annual Technical Symposium and Exhibition held Dammam, Saudi Arabia, 24–27 April. DOI: 10.2118/188016-MS.

Moazzeni A., and Haffar M.A., 2015, Artificial Intelligence for Lithology Identification through Real-Time Drilling Data, *Journal of Earth Science & Climatic Change*, **6**(3), 265. DOI: 10.4172/2157-7617.1000265.

Rabia, H., 2001, *Well Engineering and Construction*, Entrac Consulting, ISBN: 978-0954108701.

Rogers, S.J., Fang, J.H., Karr, C.L., and Stanley, D.A., 1992, Determination of Lithology From Well Logs Using a Neural Network, *AAPG Bulletin*, **76**(5), 731–739.

Wang, K., and Zhang L., 2008, Predicting Formation Lithology From Log Data by Using a Neural Network, *Petroleum Science*, **5**(3), 242–246. DOI: 10.1007/s12182-008-0038-9.

Zhu, L., Li, H., Yang, Z., Li, C., and Ao, Y., 2018, Intelligent Logging Lithological Interpretation with Convolution Neural Networks, *Petrophysics*, **59**(6), 799–810. DOI: 10.30632/PJV59N6-2018a5.

ABOUT THE AUTHORS



Salaheldin Elkatatny is an associate professor at King Fahd University of Petroleum & Minerals. He is an associated professor at Cairo University, on leave. He worked as a senior geomechanical engineer at Advantek International Company for 5 years. He received his PhD in Petroleum Engineering at Texas A&M University, College Station, Texas. He received his BSc and MSc degrees from the Petroleum Engineering at Cairo University, Egypt. He worked with SUCO Oil Company as a drilling engineer for 1 year. His areas of research include drilling fluid optimization, filter-cake removal, formation damage, oilwell cementing, geomechanics, and artificial intelligence.



Ahmed Al-AbdulJabbar is a PhD candidate at King Fahd University of Petroleum & Minerals. He is also working as a drilling engineering supervisor at Saudi Aramco. He joint Aramco in February 2011, and has worked as

drilling engineer in offshore and onshore fields. He received his MSc and BSc from King Fahd University of Petroleum & Minerals.



Ahmed Abdulhamid Mahmoud is a PhD candidate at King Fahd University of Petroleum & Minerals. He is a lecturer at the University of Khartoum, on leave. He worked as a course's coinstructor at Estidama Training Centre for 1 year and worked with PTC as an instructor for the advanced oil production optimization courses for 6 months. He received his MSc in petroleum engineering from King Fahd University of Petroleum & Minerals, Saudi Arabia, and received his BSc in petroleum engineering from the University of Khartoum, Sudan. His areas of research include oil-well cementing, chemical enhanced oil recovery, geomechanics, artificial intelligence, and oil production optimization.

A Comparative Study of Three Supervised Machine-Learning Algorithms for Classifying Carbonate Vuggy Facies in the Kansas Arbuckle Formation

Tianqi Deng¹, Chicheng Xu^{2,*}, Dawn Jobe³, and Rui Xu¹

ABSTRACT

Diagenetic features, such as vugs, fractures and dolomite bodies can have significant impacts on carbonate reservoir quality. Challenges remain in characterizing these diagenetic features from well logs, as they are often mixed with changes in mineral and fluid concentrations. In this paper, a data-driven approach is developed to classify vuggy facies based on core and well logs from a key well penetrating the Arbuckle formation in Kansas. Three supervised machine-learning methods, namely artificial neural networks (ANN), support vector machines (SVM), and random forests (RF), are compared for their accuracy, stability, and computational efficiency. Hyperparameters are tuned using cross-validation and Bayesian optimization. Different feature selection methods and data labeling schemes are also evaluated to optimize the prediction.

Results indicate predicting a binary classification (vuggy/nonvuggy) presents an ~80% accuracy, compared to a ~65% accuracy using a five-class vug-size-based classification label. A direct input of well logs as training features is recommended instead of using derived petrophysical properties. Among the three machine-learning algorithms, ANN outperforms the other two methods for vug/nonvug detection, whereas for vug-size classification, RF is the best algorithm to apply. This work also suggests RF shows the least sensitivity to hyperparameters (i.e., maximum number of splits and minimum leaf sizes) according to the response surfaces constructed via Bayesian optimization. For the dataset used in this study, SVM is the most computationally efficient algorithm.

INTRODUCTION

Formation evaluation is challenging in carbonate reservoirs because of the presence of various diagenetic features, including vugs, fractures, and dolomite bodies. These post-depositional diagenetic overprints can affect the mineralogy, pore connectivity, and pore-size distribution in carbonate rocks, leading to inaccurate assessments of effective porosity, water saturation, and permeability (Lucia 2007; Xu et al., 2012; Xu and Torres-Verdin, 2013; Clerke et al., 2014; Doveton and Watney, 2014). The most accurate method for identifying vugs and fractures is through detailed core and thin-section description. Indirect methods for identifying vugs and fractures include wireline logging measurements and interpretations. Logging measurements, such as nuclear magnetic resonance (NMR), can capture the pore-size distribution and therefore can be used to infer vugs in carbonate formations (Clerke et al., 2014; Doveton and Watney, 2014). Borehole image logs can also be used to directly identify near-borehole vugs and fractures (Luthi and Souhaite, 1990; Newberry et al., 1996). These techniques

require either advanced NMR or borehole image logs, and/or core data, which are not typically available in most wells due to cost constraints. This paper is intended to demonstrate a method that can be applied to wells with only basic well-log suites that include resistivity, sonic, density, and neutron tools.

Challenges remain in using basic well-log datasets to identify vugs and fractures in carbonate reservoirs. Visual interpretations of physical core, thin sections and core photos by experienced geologists are required to characterize vugs and fractures explicitly. This procedure is time-consuming and heavily biased, as it is subject to interpreters' personal experience. Fractures and vugs will also affect resistivity and sonic logs via the Archie cementation factor and bulk acoustic slowness (Ellis and Singer, 2007). Existing correlations and physical models make assumptions on specific and simplified vug and fracture distributions and are therefore, not universally applicable (Brie et al., 1985; Perez-Rosales et al., 2002). Additionally, vugs and fractures can be identified using a grayscale-value cutoff based on borehole resistivity images (Cunningham et al., 2004). This

Manuscript received by the Editor May 17, 2019; revised manuscript received September 9, 2019; manuscript accepted September 15, 2019.

¹ Hildebrand Department of Petroleum and Geosystems Engineering, the University of Texas at Austin; tianqizx@utexas.edu; rui_xu@utexas.edu

² Aramco Services Company: Aramco Research Center – Houston, 16300 Park Row, Houston, TX 77084; Chicheng.Xu@aramcoservices.com

³ T. Dawn Jobe, Geologic Consultant, dawn.job@gmail.com

*Corresponding author: Chicheng.Xu@aramcoservices.com

method is subject to uncertainty regarding the pore-fluid types. Vugs will not appear consistently dark or bright in borehole images depending on the physical properties of the pore-filling fluid.

New data-driven approaches, such as artificial neural networks (ANN), support vector machines (SVM) and random forest (RF) are being developed to identify features of interest in geologic data. Jobe et al., (2018) developed a convolutional neural network (CNN) based method for Dunham texture prediction based on thin-section images. Tang et al. (2011) demonstrated use of a probabilistic neural network to predict carbonate well-log facies based on basic well-log sets with an accuracy of 55 to 70%. Bize-Forest et al. (2018) used well-log derived features, such as rock-fabric number (RFN) and flow zone indicator (FZI) to train and test machine-learning models. Machine learning has also been applied in the areas of lithology identification and geological mapping, and proved to be capable of obtaining reliable predictions (Cracknell and Reading, 2014). Xie et al. (2018) outlined procedures for tuning hyperparameters and make comparisons of cross-validation accuracy for different machine-learning models.

Applications of machine-learning models to classify lithology based on well logs have been widely reported (Tang et al., 2011; Tan et al., 2015; Hall, 2016; Lang et al., 2019; Xu et al., 2019). However, for vug facies identification, there is very limited research work focusing on the comparison of different algorithms and features. In the following sections, a general procedure is presented for applying machine-learning models for the identification of

vuggy intervals from well-log data. The model is prototyped using well logs and core data from a key well penetrating the Arbuckle formation in Kansas. A rigorous comparison is performed with respect to cross-validation accuracy between three common machine-learning algorithms: ANN, SVM, and RF. In addition, sensitivity of the three algorithms to hyperparameters is studied using Bayesian optimization. Using original well logs as machine-learning input features is compared to using log-derived petrophysical properties for classification accuracy. Finally, recommendations and discussion are presented for vug identification using basic well logs.

DATA PREPARATION

Data used in this study were collected from core and wireline logging in the Wellington 1-32 well located in southern Kansas. The formations of interest include the Cambrian-Ordovician Arbuckle Group. Dominant geologic facies include dolomitic mudstones to boundstones, intra-Arbuckle shales and cherts as well as conglomeritic and brecciated limestones and dolostones (Fig. 1) (Franseen et al., 2004). Diagenetic features, such as vugs, fractures, and dolomite bodies, are commonly observed in the Arbuckle group interval (Fig. 2). The Wellington 1-32 well used in this study is an injection well, which penetrates the entire Arbuckle deep saline aquifer. The well was drilled with water-based mud and the effect of hydrocarbon on wireline measurements is considered negligible (Doveton and Watney, 2014).

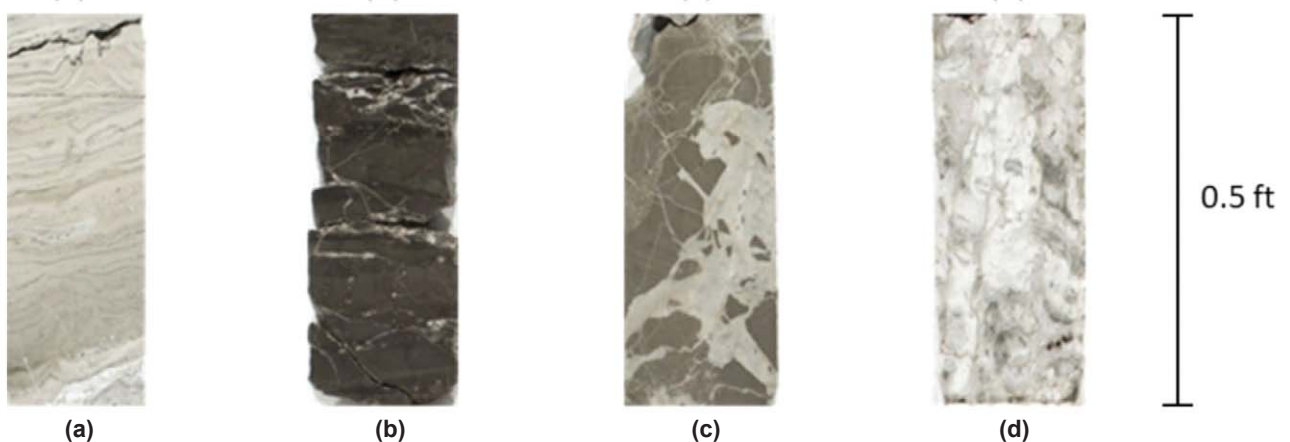


Fig. 1—Dominant facies in the Arbuckle formation in Kansas. (a) to (d) show dolomite, shale, conglomerate and breccia, and chert, respectively.

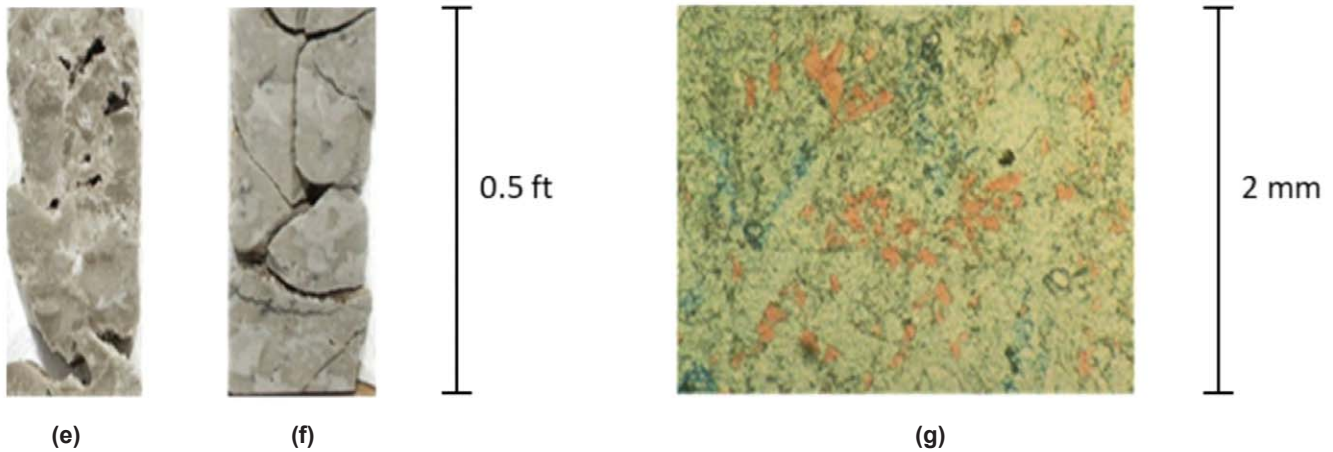


Fig. 2—Diagenetic features in the Arbuckle formation. (e) and (f) show vugs and fractures in the Arbuckle formation, respectively. (g) shows an example of dolomitization in thin section (modified from the Schlumberger Oilfield Glossary).

A total depth interval of more than 1,000 ft is used to develop the machine-learning models presented in this paper. Available well data included caliper (CAL), gamma ray (GR), array induction resistivity (AT), neutron porosity (NPHI), photoelectric factor (PEF), bulk density (RHOB), compressional and shear slowness (DTCO and DTSM), NMR T_2 distribution, core porosity, and a geological description.

To assure the quality of the dataset, the following steps were performed before any well-log interpretation and machine-learning model training. First, depth shift was applied to the acoustic logging dataset and core porosity by setting the bulk density log as the reference and matching peaks and troughs in each log (Fig. 3). Second, the caliper log was checked to make sure no significant borehole problems, such as washouts and mudcake, were present. Next, the data were all normalized by the mean and standard deviation of each log curve before training the machine-learning models. The final input dataset included 1,952 core-log pairs, where 75% were randomly selected as training-validation sets and the remaining 25% were used for testing prediction accuracy.

The selection of input features and output can have a significant impact on the accuracy of machine-learning models. An improvement of 35% accuracy was previously reported by including FZI and dip class in predicting

depositional facies over using only quad-combo logging sets (Bize-Forest et al., 2018). In predicting carbonate facies, using log-derived features, such as rock-fabric number (RFN) and rock quality index (RQI), can also improve the prediction accuracy (Lucia, 2007; Tang et al., 2011).

In this paper, four different input-output combinations are adopted to (1) find the best feature for predicting vuggy facies, and (2) determine the sensitivity of basic logging sets to vug sizes. In the benchmark case, basic log sets are directly used as the input features without log-derived properties to predict vuggy facies based on core description. In the first case, mineralogy and petrophysical properties, such as porosity derived from joint inversion of all the logs, are also used as input features. In the second case, a vug-size-based core classification is used as the training label. Intervals with poor core recovery were assumed to contain super-sized vugs. These intervals correlated well with megaporosity interpreted from NMR T_2 relaxation times (Fig. 4). Megaporosity in this case is defined as the summation of relation times from the 1024- to 2048-ms bins (Doveton and Watney, 2014). Finally, since cores can be biased while sampling and geological description may have a higher vertical resolution than well logs, an NMR-derived vug label (based on a megaporosity cutoff) is compared to core descriptions as the classification labels for machine-learning models (Fig. 4).

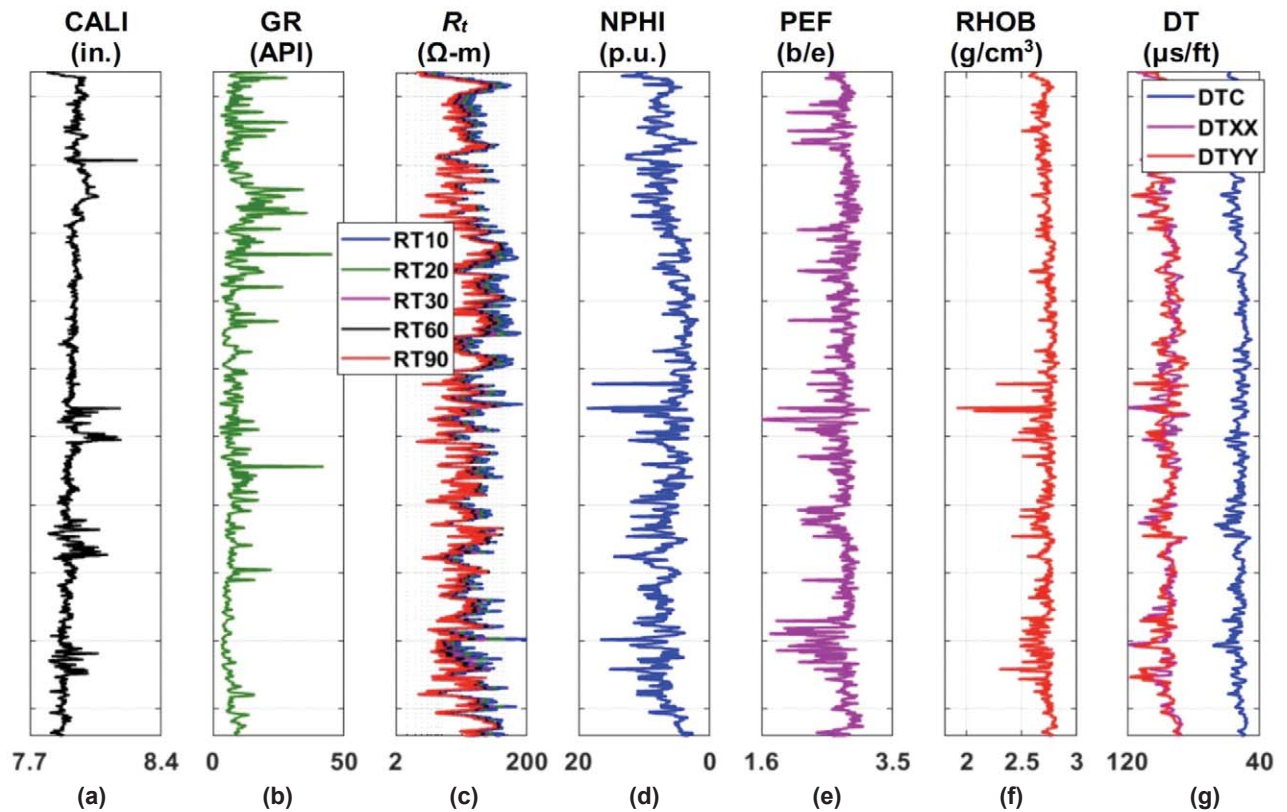


Fig. 3—Input well-log features for vug-facies classification. Tracks (a) to (g) show caliper (CALI), gamma ray (GR), resistivity (R_t), neutron porosity (NPHI), photoelectric factor (PEF), bulk density (RHOB), and acoustic slowness (DT). The total depth interval is approximately 1,000 ft.

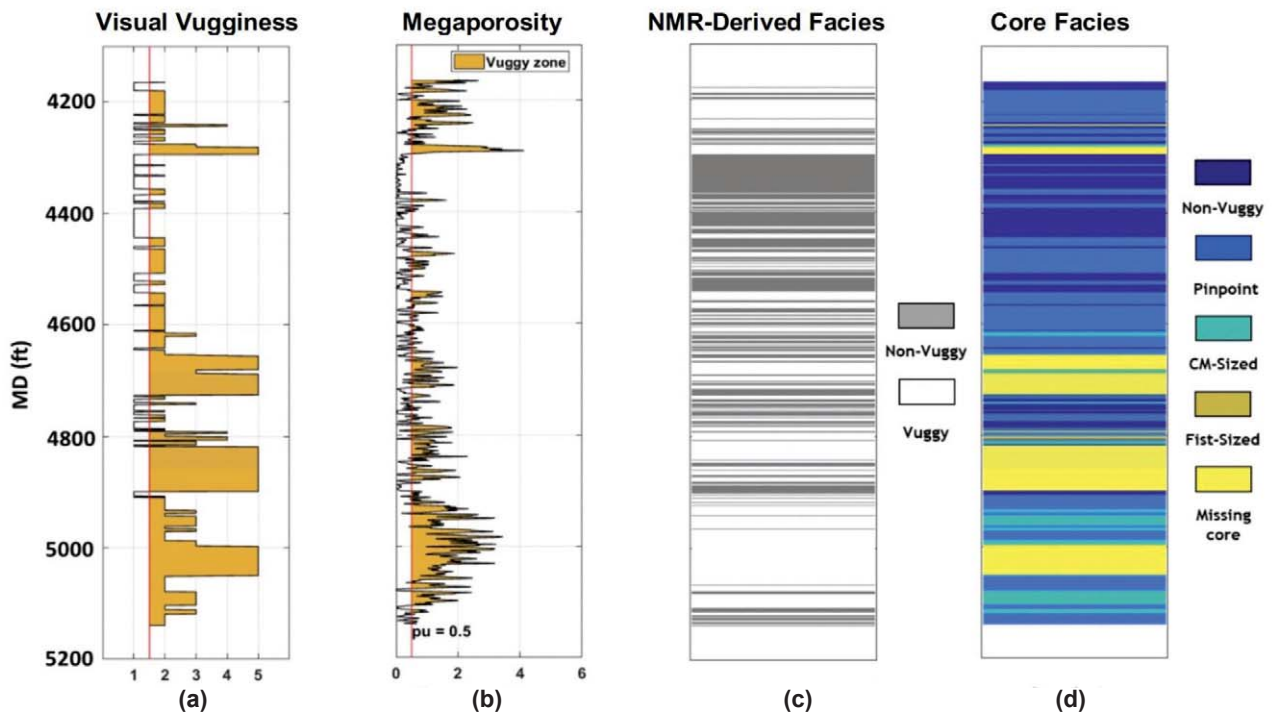


Fig. 4—Reference facies label derived from core description and NMR T_2 cutoff. Tracks (a) and (b) show visual vugginess from core and megaporosity from NMR. Tracks (c) and (d) show NMR-derived facies and core facies. Facies shown as 1 to 5 in Track (a) corresponding to nonvuggy to missing core shown in Track (d). Missing core zones are considered as supersized vugs where cores are unable to be recovered (Doveton and Watney, 2014).

The identification of vugs is more challenging in the presence of hydrocarbon. Using a combination of well logs that are sensitive to both matrix and fluid can potentially remove the fluid effect and improve the classification results. However, NMR logs can no longer be used directly as classification labels since they are affected by both diagenetic features and fluid concentrations.

METHOD

Workflow

Figure 5 summarizes the workflow for predicting vuggy facies using machine-learning models. The first step is rigorous quality control over well logs, core measurements, and geological descriptions. Core geological descriptions (text) are converted to a vug-facies log by extracting the key word “vug” using a commercial script (MATLAB). A cutoff of NMR T_2 porosity is also applied to derive a vug-facies label. A multiminerals analysis is performed by a joint inversion of gamma ray, resistivity, bulk density, neutron porosity, photoelectric factor, and acoustic slowness. Then original logs/interpreted petrophysical properties and vug-facies labels are integrated as training and testing set. K -fold cross-validation (Arlot and Cellisse, 2010) and Bayesian optimization are applied to tune hyperparameters and avoid overfitting. Finally, the prediction accuracy for different models is compared in the testing set.

Multiminerals Analysis

Multiminerals analysis is the most common method of predicting lithology in a mixed-lithology formation by honoring all the well logs through a probabilistic model (Quirein et al., 1986). This method assumes a certain logging response for each endmember component in the formation and the bulk formation property can be approximated by a linear mixing law with respect to volumetric concentrations:

$$\xi_b = \sum \xi_i V_i. \quad (1)$$

In Eq. 1, ξ_b is the bulk property, such as gamma ray and bulk density, ξ_i is the property of a single component i , and V_i is volumetric concentration of component i satisfying $\sum V_i = 1$. Mineral concentrations were estimated through linear inversion using a commercial software package. A synthetic log-derived feature, apparent rock-fabric number (ARFN) based on total porosity, was also included. The RFN is defined by (Lucia, 2007) as:

$$\log_{10} RFN = \frac{3.1107 + 1.8824 \log(\phi_t) + \log(S_{wt})}{3.0634 + 1.4045 \log(\phi_t)}, \quad (2)$$

where ϕ_t is the total porosity and S_{wt} is the total water saturation. The ARFN defines different rock classes based on their permeability-porosity correlation. A larger ARFN suggests that the total porosity is less capable of conducting fluid. This indicates the existence of isolated vuggy porosity that does not contribute to fluid flow.

Machine-Learning Algorithms

There are many cases and discussions on how shallow learning (e.g., neural networks with only a single layer) methods and deep learning (e.g., convolutional neural networks) methods can be applied in petrophysics analysis (Xu et al., 2019). Based on the amount of data available, supervised machine-learning algorithms ANN, SVMs, and RF are implemented as the diagenetic facies classifiers. Hyperparameters of different machine-learning algorithms are tuned by optimizing cross-validation score via Bayesian optimization.

Artificial Neural Network (ANN). ANNs mimic the function of biological neural networks in human brains. They can approximate any continuous function given enough training samples and structural complexity. In

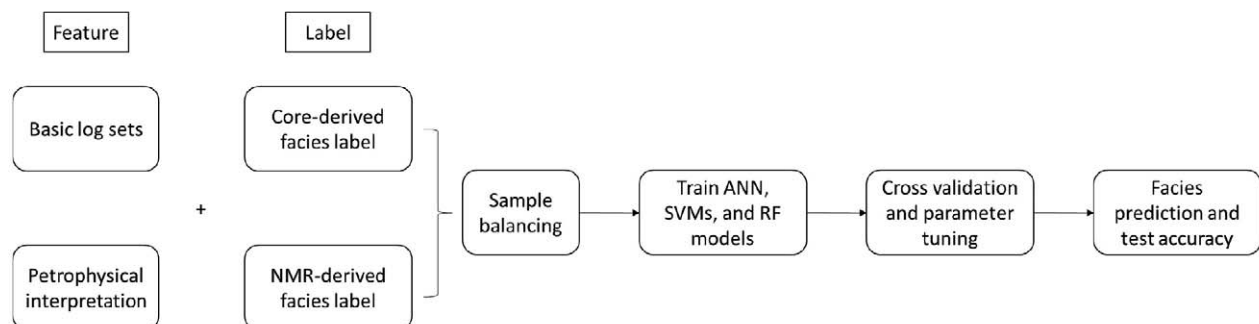


Fig. 5—Workflow chart of vug-facies prediction.

the application to petrophysics, they are widely used to calculate petrophysical properties, generate synthetic logs, and classify rock facies (Saneifar et al., 2015; Li and Misra, 2017; Mahmoud et al., 2017). The fundamental elements in a neural network include layers, neurons and activation functions. The structure of the neural network is simplified by using a feed-forward neural network with one hidden layer. The neurons in two adjacent layers are connected by a weighted linear combination and an activation function to introduce the nonlinearity. The most common choices of activation functions are sigmoid function, ReLU, and TanH. Due to the size of our dataset, the activation function is limited to a sigmoid function for the hidden layer, and a soft-max function for the output layer. However, for deep neural networks, ReLU and TanH functions are preferred because they do not suffer from the vanishing gradient problem (Glorot et al., 2011).

The value y on the hidden layer is calculated by:

$$y = \sigma(\sum \omega_i x_i), \tag{3}$$

where x_i is the input logs, ω_i is the weight corresponding to x_i , and σ is the sigmoid function and defined as:

$$\sigma(x) = \frac{1}{1+e^{-x}}. \tag{4}$$

The cost function and gradient are calculated using back propagation and the weights are optimized with a conjugate gradient solver.

Support Vector Machine (SVM). SVMs are classifiers that define a decision boundary that optimally separates two classes. In linear cases, the decision boundary becomes a hyperplane. The construction of the hyperplane that separates two classes is based on a subset of sample points that is close to the decision boundary (the support vectors). In the linear case, two classes are defined by boundaries: $\mathbf{w} \cdot \mathbf{x} - \mathbf{b} \geq 1$ and $\mathbf{w} \cdot \mathbf{x} - \mathbf{b} \leq -1$. A margin is defined as the distance between these two hyperplanes as: $2/\|\mathbf{w}\|$. The training of SVMs maximizes the margin between training points from two different classes. A box constraint parameter, C is used to control the penalty when training instances are misclassified. For a large value of C , the SVMs will tend to generate a smaller margin at the risk of overfitting. A small value of C will allow more misclassifications at the cost of training accuracy. In the application to petrophysics, Tan et al., (2015) apply SVMs for regression to estimate TOC from wireline logs and compare it to the traditional *AlogR* method.

One advantage of SVMs is that it is easy to apply a kernel trick to map the lower dimension data and linear decision boundaries into a high dimension space to solve nonlinear

classification problems. Some of the most commonly used kernels (Trevor et al., 2003) are:

$$\text{dth-degree Polynomial: } K(\mathbf{x}, \mathbf{x}') = (\mathbf{x}^T \mathbf{x}' + c)^d \tag{5}$$

$$\text{Gaussian/Radial Basis Function (RBF):} \tag{6}$$

$$K(\mathbf{x}, \mathbf{x}') = \exp(-\gamma \|\mathbf{x} - \mathbf{x}'\|^2)$$

To reduce the number of hyperparameters, only Gaussian kernel functions are considered. The kernel is controlled by the kernel scale γ . In diagenetic facies classification, a one vs. one classification is implemented to generate better multiclass classification results because the low number of classes will not significantly increase the computational cost.

Random Forest (RF). Random forest is an ensemble method based on decision-tree models proposed by Breiman (2001). A good explanation of decision-tree models can be found in Bishop (2006). Decision trees divide all samples into different regions using axis-aligned boundaries. Cross-entropy H and the Gini index G , shown in Eqs. 7 and 8, are often used to determine the performance of decision-tree models:

$$H = \sum_{k=1}^K p_k \ln(p_k), \tag{7}$$

$$G = \sum_{k=1}^K p_k (1 - p_k), \tag{8}$$

where p_k is the proportion of data points assigned to class k for a certain region.

RF uses bootstrap aggregating (bagging) to train multiple decision-tree models by randomly sampling from the training set and training the decision tree on each of them separately. The prediction is made by averaging the results obtained from the ensemble.

In this paper, to reduce the computational time for cross-validation, hyperparameters considered in parameter tuning are the maximum number of tree splits, number of features used for splitting, and minimum split sizes.

Parameter Tuning and Imbalanced Sample Set

K -fold cross-validation (Arlot and Cellisse, 2010) is used to tune hyperparameters of machine-learning algorithms. All the samples are separated as either training set or test set. Within the training set, the samples are portioned into k groups. Then $(k - 1)$ groups are randomly selected to be

used for training, whereas the one group of samples left is used to create the cross-validation error function. The cross-validation error function is minimized by changing hyperparameters in each machine-learning algorithm.

For neural networks, the number of units in the hidden layer and the regularization parameter are optimized. For SVMs, the kernel is fixed as radial basis function (Gaussian). The parameter kernel scale γ and box constraint are considered as hyperparameters. For RF, the maximum number of splits, number of features used for each splitting, and minimum split sizes are optimized.

Bayesian optimization was implemented using commercial software package (MATLAB R2018a and Statistics and Machine Learning Toolbox) to obtain the hyperparameter combination with the highest cross-validation score. Bayesian optimization uses a Gaussian Process (GP) as a priori information to build a surrogate model for the objective function with uncertainty. Then an acquisition function (usually expected-improvement) is maximized to decide where to take the next sample:

$$EI = \mathbb{E}_{f|(x_i, y_i)}(\max(0, f' - f(x))), \tag{9}$$

where f' is the current minimum of function f , (x_p, y_i) are observations (Snoek et al., 2012).

One common situation in facies classification is that the dataset can be imbalanced: there is a large difference in the number of samples in the majority class and minority class (Fig. 6). Downsampling and upsampling were invoked to address this problem. They are also compared to an adaptive synthetic sampling approach (ADASYN) based on interpolations from K -nearest neighbors (He et al., 2008).

RESULTS

The variations of gamma ray, resistivity, neutron porosity, bulk density, photoelectric factor and acoustic slowness are shown in Fig. 6. In the first part, a multiminerall analysis was applied to the Arbuckle formation. The resultant mineralogy and porosity were used as features for vuggy facies classification. In the second part, the classification results were assessed using four different feature-label combinations. They include (1) using original well logs to predict NMR-derived facies labels; (2) using original well logs to predict core facies labels, (3) using multiminerall analysis results to predict NMR-derived facies labels, and (4) using multiminerall analysis results to predict core facies labels.

The linear joint inversion results coupled with porosity are shown in Fig. 7. The mineral model consists of illite, quartz, dolomite, chert, and water. The vuggy facies shown

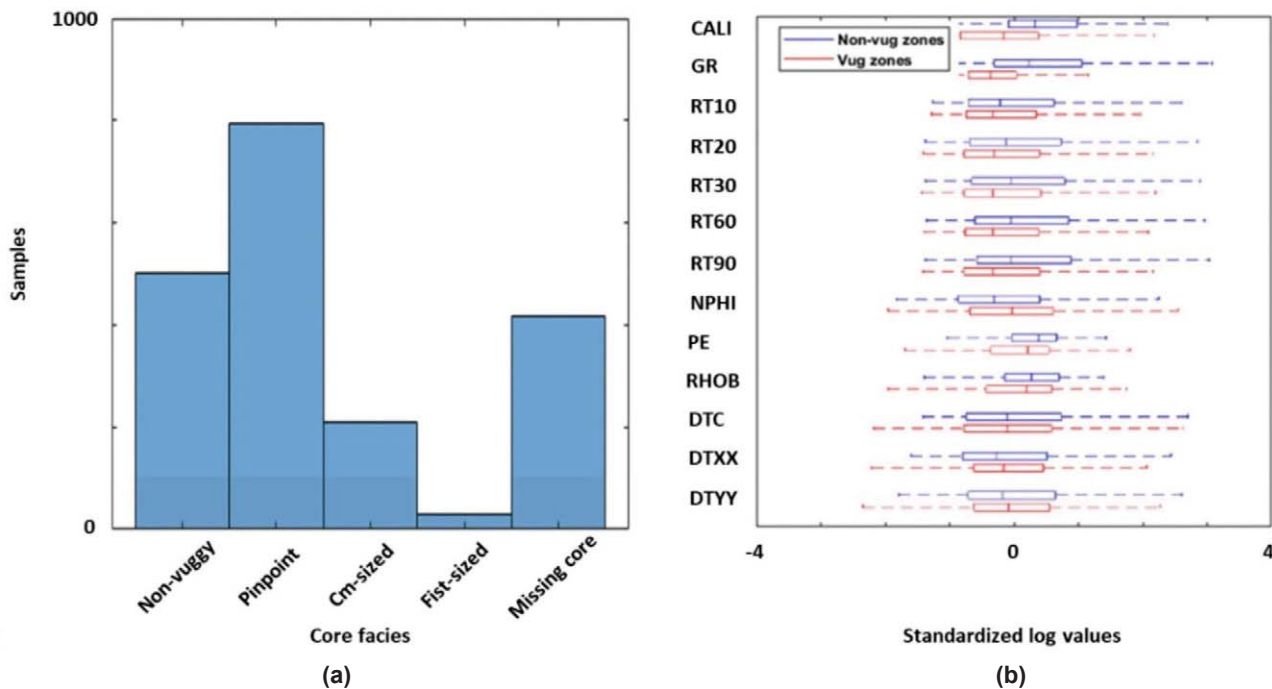


Fig. 6— (a) Shows samples distribution in each facies. (b) Shows a comparison of the standardized values of caliper (CALI), gamma ray (GR), resistivities (RT10, RT20, RT30, RT60, and RT90), neutron porosity (NPHI), photoelectric factor (PE), bulk density (RHOB), compressional and shear acoustic slowness (DTC, DTXX, and DTYY) in vuggy and nonvuggy zones. In (b) the box shows the 25th and 75th percentiles and the dashed line shows 99.3% coverage of the data.

are derived from the NMR megaposity cutoff at 0.5, and core description based on vugs and vug sizes. The last track shows rock-fabric number (RFN). The interpreted results indicate that the lower half of the Arbuckle formation has more vuggy zones than the upper part. In the upper part, the vuggy zone is around 4,250 ft MD. The RFN curve agrees with core- and NMR-derived facies, where a high RFN indicates low permeability for a given porosity because the vugs are not fully connected.

A visual representation of the vuggy facies prediction is shown in Fig. 8. Three algorithms are compared with four different input-output combinations. For all classification

labels, the predictions of NMR-derived label have the best prediction accuracy, around 80% in the testing set. Vug-size predictions are more challenging (around 65% accuracy) because of the uneven distribution in class representation. Vug-size classes such as centimeter-sized and fist-sized vugs have fewer samples available. Using original logs as input gives rise to a higher prediction accuracy than using joint inversion, especially in the case of predicting vug sizes. One possible explanation is that the joint inversion causes a loss of information compared to original well logs and involves a new source of uncertainty when mineral models and mixing laws are assumed.

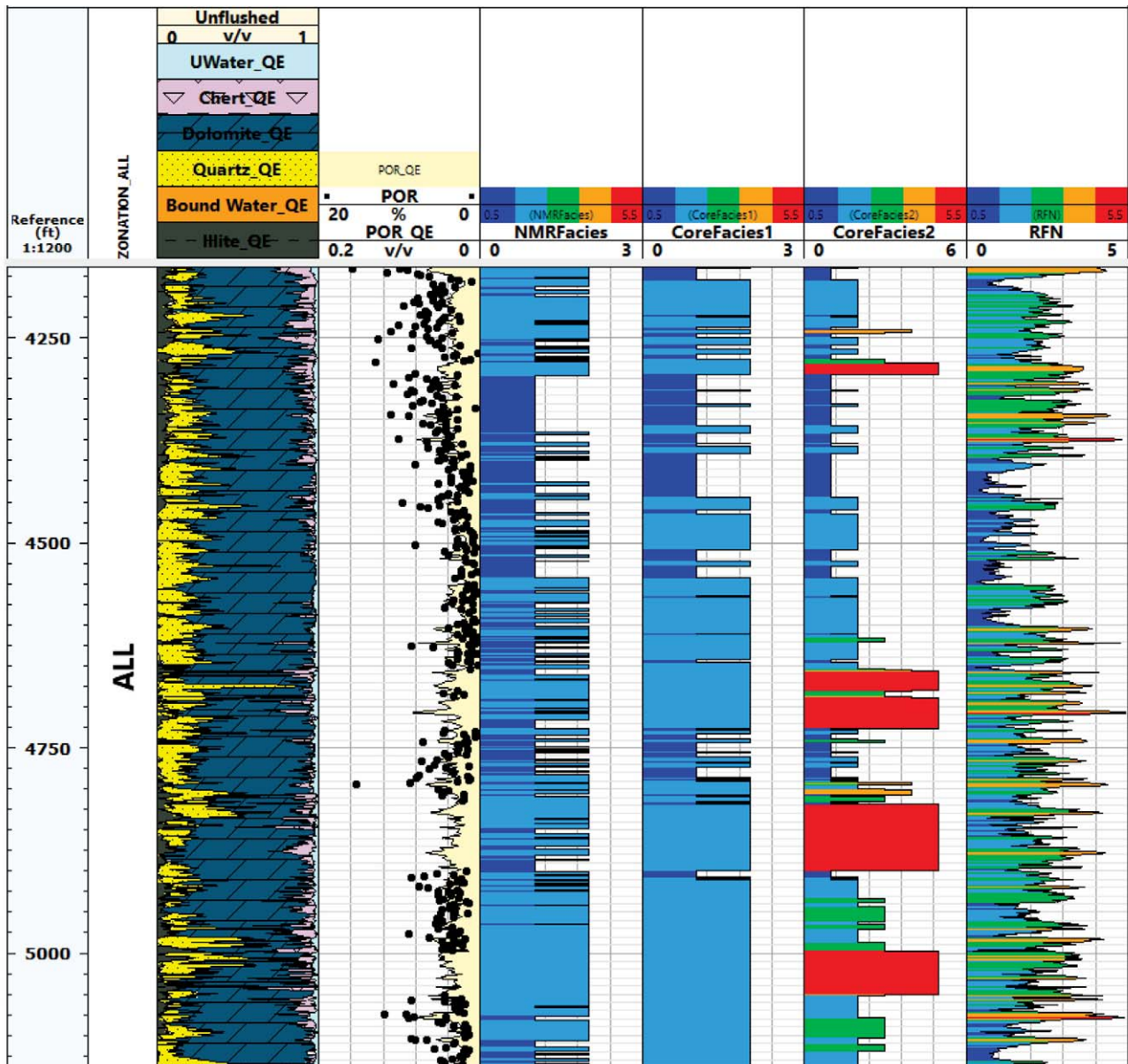


Fig. 7—The mineral composition and porosity calculated by linear joint inversion. The facies, from left to right, are NMR-derived facies, core facies, core facies based on vug size, and RFN. From dark blue to red color labels indicates: no vugs, pinpoint-sized vugs, centimeter-sized vugs, fist-sized vugs, and missing core (caused by supersized vugs).

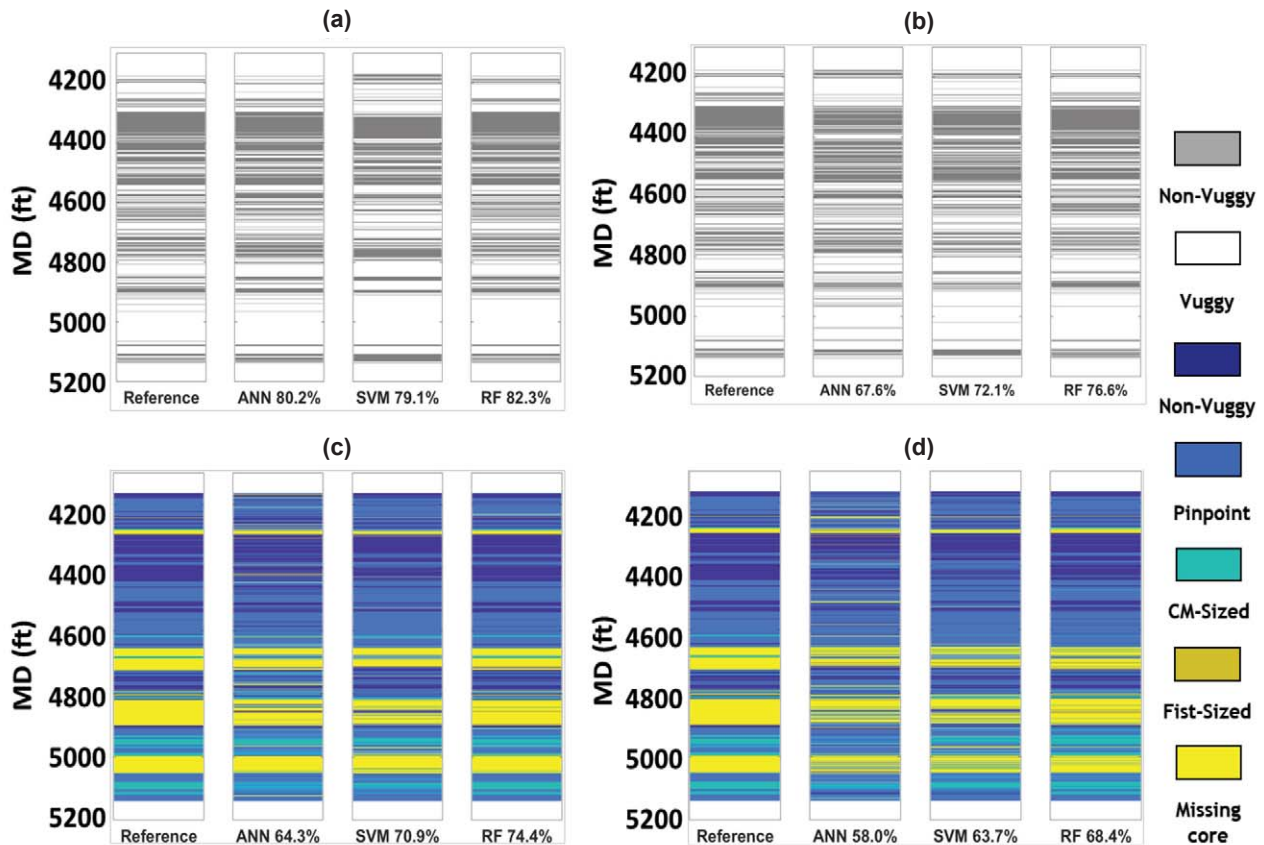


Fig. 8—Visualization of vug facies prediction results. (a) and (b) show 2-class vuggy facies based on NMR-derived labels. (c) and (d) show 5-class vuggy facies from core description. Prediction accuracy is compared using ANN, SVM, and RF. In all four situations, RF shows slightly higher prediction accuracy than the other two algorithms. A higher prediction accuracy is achieved using original well logs as training input compared to using joint inversion results.

Table 1 shows the computational cost of ANN, SVM, and RF for training and prediction in 2-class label and 5-class label respectively. In all cases, SVM is significantly more computationally efficient for classification than ANN and RF. ANN and RF show a similar time required for training and cross-validation. For all algorithms, training a 5-class label model costs slightly more computational time than a 2-class label model.

The response surface for cross-validation score with respect to different hyperparameters is shown in Fig. 9. The cross-validation score in this paper is determined by:

$$score_{CV} = \min(accuracy_i), \tag{10}$$

where i is the index for different classes. To simplify the problem, the hyperparameters were limited to hidden layer size and L2 regularization factor for ANN, kernel scale and box constraint for SVM, and maximum number of tree splits and minimum leaf size for RF. All three algorithms have a similar cross-validation (CV) score minimum, indicating three algorithms have similar cross-validation accuracy given proper parameter tuning. They have different sensitivity to hyperparameters. RF has a relatively stable CV

Table 1—Computational Cost of Training and Testing Each Algorithm

Computational Efficiency						
Algorithm \ Label	ANN (Training)	ANN (Prediction)	SVM (Training)	SVM (Prediction)	RF (Training)	RF (Prediction)
2-class label	50.10	3.77E-04	25.22	0.01	49.32	0.07
5-class label	60.79	4.33E-04	27.10	0.03	54.19	0.06

The results are generated with a Desktop PC 64-bit Intel Core Coffee Lake 6-Core i7-8700k CPU @ 3.70 GHz and 16 GB RAM. The platform is MATLAB R2018a with Parallel Computing Toolbox.

score compared to ANN and SVM. The higher sensitivity in SVM and ANN requires searching in a larger hyperparameter space which can be computationally prohibitive.

The distributions of the cross-validation scores for all computed combinations of hyperparameters of each machine-learning algorithm are shown in Fig. 10 for 2-class and 5-class classifications, respectively. Roughly a normal distribution is observed, which indicates a reasonable selection of the hyperparameter spaces. For both 2-class and 5-class facies labels prediction, ANN results in the highest mean cross-validation score. But the optimal hyperparameters should be chosen based on the maximum cross-validation score and the final prediction performance needs to be evaluated on the hold-out testing samples that are never seen by the algorithms.

Prediction accuracy for the three machine-learning algorithms based on 10 sets of numerical experiments is presented in Fig. 11. In the 2-class situation, ANN shows a higher accuracy for predicting nonvuggy facies than SVM and RF. For the 5-class facies label, in general, RF has the highest prediction accuracy. All algorithms show significantly lower accuracy in predicting centimeter-sized vugs and fist-sized vugs because too few samples are obtained in those zones. One interesting observation is that using original logs as classification input shows higher prediction accuracy than using interpreted mineralogy data. The possible reasons for this are: (a) some useful information is removed through linear multiminereral inversion, and (b) the construction of a multiminereral model involves other uncertainty, such as the endmember property for a single component.

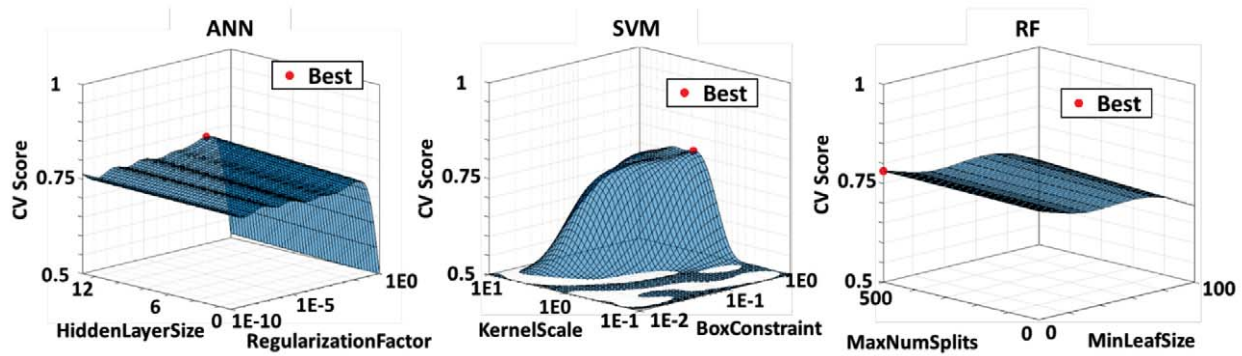


Fig. 9—Response surface of cross-validation score as a function of hyperparameters showing the sensitivity of each algorithm to hyperparameters. The best hyperparameter set is shown in red dots where the highest CV score is taken. SVM shows higher sensitivity to hyperparameters compared to ANN and RF.

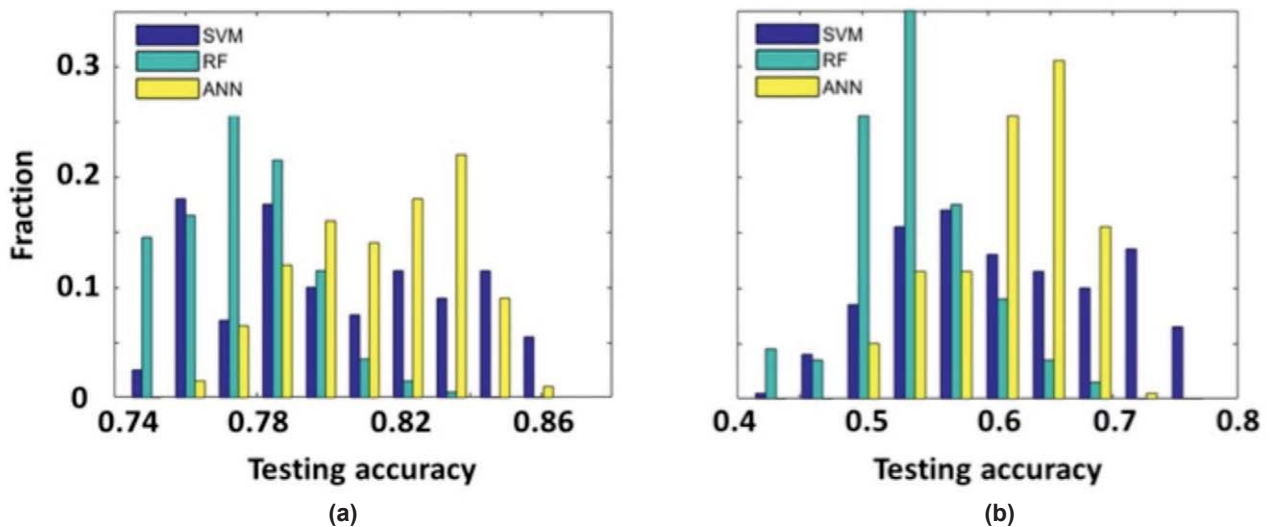


Fig. 10—Histogram of the cross-validation scores. (a) and (b) show prediction accuracy for 2-class and 5-class labels, respectively. Hyperparameters are tuned using Bayesian optimization and the three machine-learning algorithms are compared for prediction accuracy (ANN, SVM, and RF).

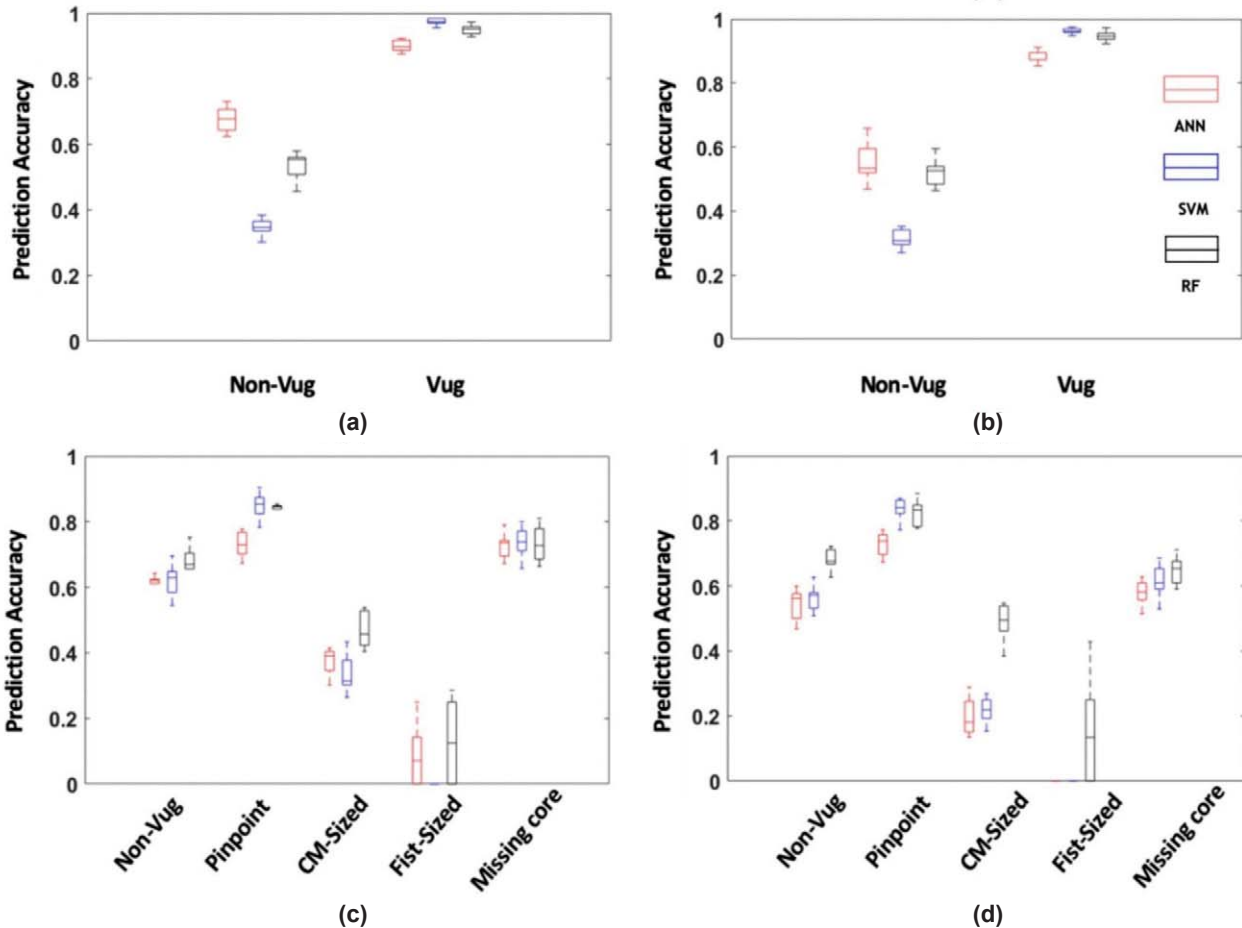


Fig. 11—Prediction accuracy boxplot based on 10 sets of numerical experiments. (a) and (b) show the prediction accuracy for the 2-class NMR-derived facies label. (c) and (d) show the prediction accuracy for 5-class core facies label. (a) and (c) are predicted with original logs whereas (b) and (d) are predicted with linear joint inversion results. The red, blue, and black colors show results from ANN, SVM, and RF, respectively. The box shows the 25th and 75th percentiles and the dashed line shows 99.3% coverage of the data.

DISCUSSION

Comparison of Machine-Learning Algorithms for Vuggy Facies Classification

For a binary vuggy/nonvuggy facies classification, all three algorithms have similar prediction accuracy of approximately 80%. The use of ANN and RF algorithms, is recommended because ANN has a relatively high accuracy for minority class and RF has low sensitivity to hyperparameters and is less computationally expensive to optimize. For the 5-class facies labels, RF outperforms the other two algorithms. SVM is more computationally efficient than ANN and RF for training, while ANN uses less time-consuming predictions. This result is in agreement with other work on the application of ANN, SVM and RF in lithology classification using well-log and remote sensing data (Cracknell and Reading, 2014; Xie et al., 2018). The ANNs are more flexible than other two algorithms: with more hidden layers, ANN can automatically extract features.

However, optimization of ANNs is much more difficult: it is a nonconvex optimization problem and can always have local minimums. The computational cost increases dramatically with the increasing number of hidden layers.

Influence of Feature and Classification Label

This study found that using linear joint inversion results for identifying vuggy facies is unreliable because it leads to loss of information and involves new uncertainty about mineral model and single-component properties. For classification output, identifying vuggy zones using a binary classification is more reliable (80% accuracy) compared to a vug-size-based classification (70% accuracy). In this dataset, the number of samples in each class is not the same. Usually, methods such as upsampling, downsampling, and ADASYN can improve the prediction accuracy for minority classes (Provost, 2000; He et al., 2008). These results show that for the binary classification, ADASYN improves the prediction accuracy for nonvuggy zones from 63.2 to 84.9%. For the

vug-size-based classification, however, ADASYN generates inaccurate synthetic samples and decreases the prediction accuracy because some classes are difficult to distinguish (Fig. 12). The number of training sample sizes also affects the classification accuracy. For the binary vug-facies label, the test accuracy stabilizes after 200 training samples. For the 5-class vug-size-based label, the test accuracy is still increasing after the number of training samples reaches 1,300. Adding new training data can still improve the classification accuracy for the vug-size-based label (Fig. 13).

CONCLUSIONS AND FUTURE WORK

In this work, vuggy facies are predicted using multiple machine-learning methods for both a binary classification and a 5-class vug-size- based classification. The approach

is demonstrated using data from a key well penetrating the Arbuckle formation in Kansas. Three machine-learning algorithms were compared for prediction accuracy, sensitivity to hyperparameters, and computational cost. A comparison was made using original well logs directly as training input and using linear inversion results as input.

The results show that an accuracy of approximately 80% can be achieved using a basic well-log set and machine-learning models for vuggy facies prediction. Prediction using a vug-size classification is more challenging, with a lower accuracy of around 70%. For all three machine-learning algorithms, ANN shows a higher prediction accuracy for vuggy-facies identification while RF is better at predicting vug sizes. The results indicate that the three algorithms all have different levels of sensitivity to hyperparameters. RF displays the least sensitivity to hyperparameters while

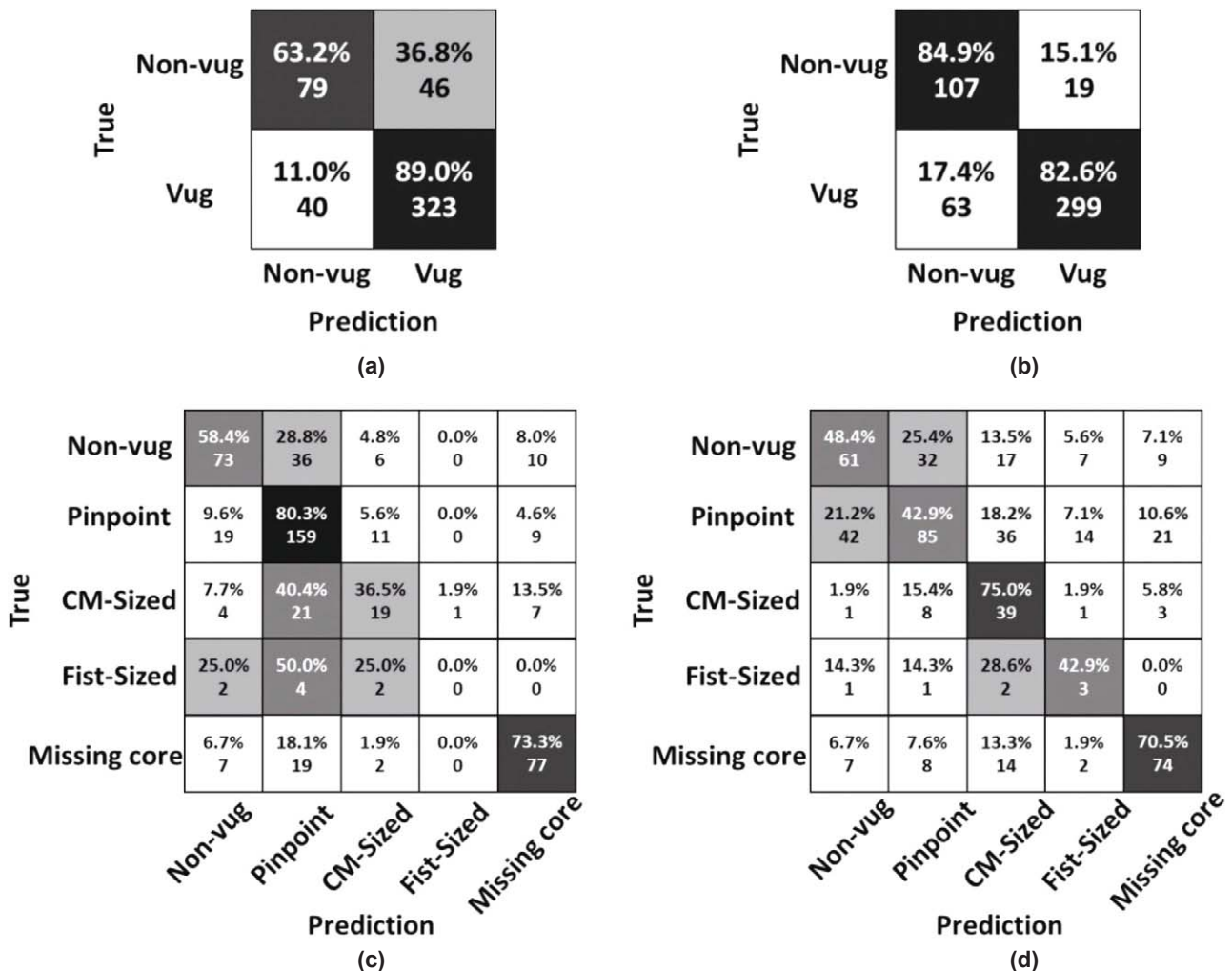


Fig. 12—Comparison of confusion matrices for without ADASYN (a) and (c), and with ADASYN (b) and (d). (a) and (b) are generated with a 2-class label while (c) and (d) are with 5 classes. The accuracy is normalized by the total number of true instances per class. For all cases, the machine-learning model is ANN. ADASYN increases the prediction accuracy for minority classes while decreases the prediction accuracy for majority classes.

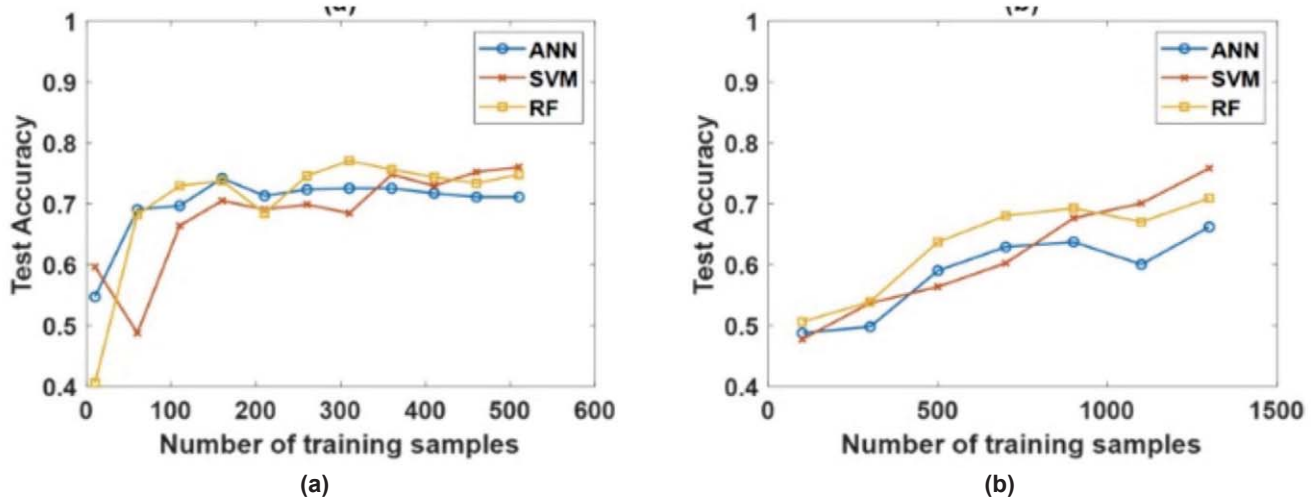


Fig. 13—Comparison of learning curves for ANN, SVMs, and RF. (a) and (b) show the testing accuracy for different training set sizes for NMR-derived vug label (binary) and vug-size based label (5 classes), respectively. For the binary labels, the test accuracy stabilizes after 200 training samples. For the 5-class label, the test accuracy is still increasing after the number of training samples reaches 1,300.

SVMs are the most computationally efficient algorithm. The prediction results from SVMs are not as good as ANN and RF. In a biased dataset where training samples do not cover all classes evenly, it may lead to unsatisfactory prediction accuracy for minority classes. In this dataset, data balancing methods, such as ADASYN, are useful in identifying vug zones. For the vug-size classification, however, ADASYN decreases the classification accuracy because some classes are difficult to distinguish from available features.

Future work for this study includes using deep-learning methods in key wells to classify diagenetic facies based on NMR logs and borehole images and testing the proposed methods in hydrocarbon wells and multiwell scenarios. Moreover, a possible implementation of recurrent neural networks (RNNs) and hidden Markov model (HMM) may improve the prediction accuracy by considering the vertical correlation.

ACKNOWLEDGMENTS

Dr. John Doveton and the Kansas Geological Survey are thanked for providing the dataset to test the algorithms and workflow. A special note of thanks goes to Jiajun Jiang for investigating a method of optimizing hyperparameters in these machine-learning methods. We also appreciate Dr. Weichang Li's constructive feedback on machine-learning algorithm selection and development.

NOMENCLATURE

Abbreviations

ADASYN	=	adaptive synthetic sampling
ANN	=	artificial neural networks
ARFN	=	apparent rock-fabric number
AT	=	array induction resistivity
Bagging	=	bootstrap aggregating
CAL	=	caliper
CNN	=	convolutional neural networks
CV	=	cross validation
DTCO	=	compressional-wave slowness
DTSM	=	shear-wave slowness
EI	=	expected improvement
FZI	=	flow zone indicator
GP	=	Gaussian process
GR	=	gamma ray
HMM	=	hidden Markov model
NMR	=	nuclear magnetic resonance
NPHI	=	neutron porosity
PEF	=	photoelectric factor
RBF	=	radial basis function
RF	=	random forests
RFN	=	rock-fabric number
RHOB	=	bulk density
RNNs	=	recurrent neural networks
RQI	=	rock quality index
SVMs	=	support vector machines
TOC	=	total organic carbon

Symbols

- C = box constraint
- G = Gini index
- H = cross entropy
- $K(x, x')$ = kernel function for calculating inner product of (x, x')
- p_k = proportion of data points assigned to class for a certain region
- S_{wr} = total water saturation
- V_i = volumetric concentration of component i
- σ = activation function
- ϕ_t = total porosity
- γ = scale of Gaussian kernel
- ζ_b = bulk physical property
- ζ_i = physical property of component i
- ω_i = weight of a node

REFERENCES

Arlot, S., and Celisse, A., 2010, A Survey of Cross-Validation Procedures for Model Selection, *Statistics Surveys*, **4**, 40–79. DOI: 10.1214/09-SS054.

Bishop, C.M., 2006, *Pattern Recognition and Machine Learning*, Springer. ISBN: 978-0-387-31073-2

Bize-Forest, N., Lima, L., Baines, V., Boyd, A., Abbots, F., and Barnett, A., 2018, Using Machine-Learning for Depositional Facies Prediction in a Complex Carbonate Reservoir, Paper NNN, *Transactions, SPWLA 59th Annual Logging Symposium*, London, England, UK, 2–6 June.

Breiman, L., 2001, Random Forests, *Machine Learning*, **45**(1), 5–32. DOI: 10.1023/A:1010933404324.

Brie, A., Johnson, D.L., and Nurmi, R.D., 1985, Effect of Spherical Pores on Sonic and Resistivity Measurements, Paper W, *Transactions, SPWLA 26th Annual Logging Symposium*, Dallas, Texas, USA, 17–20 June.

Clerke, E.A., Allen, D.F., Crary, S.C., Srivastava, A., Ramamoorthy, R., Saldungaray, P., Savundararaj, P., Heliot, D., Goswami, J., and Bordakov, G., 2014, Wireline Spectral Porosity Analysis of the Arab Limestone—From Rosetta Stone to CIPHER, Paper D, *Transactions, SPWLA 55th Annual Logging Symposium*, Abu Dhabi, UAE, 18–22, May.

Cracknell, M.J., and Reading, A.M., 2014, Geological Mapping Using Remote Sensing Data: A Comparison of Five Machine Learning Algorithms, Their Response to Variations in the Spatial Distribution of Training Data and the Use of Explicit Spatial Information, *Computers & Geosciences*, **63**, 22–33. DOI: 10.1016/j.cageo.2013.10.008.

Cunningham, K.J., Carlson, J.I., and Hurley, N.F., 2004, New Method for Quantification of Vuggy Porosity From Digital Optical Borehole Images as Applied to the Karstic Pleistocene Limestone of the Biscayne Aquifer, Southeastern Florida, *Journal of Applied Geophysics*, **55**(1–2), 77–90. DOI: 10.1016/j.jappgeo.2003.06.006.

Doveton, J., and Watney, L., 2014, Textural and Pore Size Analysis of Carbonates From Integrated Core and Nuclear Magnetic Resonance Logging: An Arbuckle Study, *Interpretation*, **3**(1), SA77-SA89. DOI: 10.1190/INT-2014-0050.1.

Ellis, D.V., and Singer, J.M., 2007, *Well Logging for Earth Scientists*, 2nd edition, Springer. ISBN: 978-1-40203738-2

Franseen, E.K., Byrnes, A.P., Cansler, J.R., Steinhauft, D.M., and Carr, T., 2004, *The Geology of Kansas: Arbuckle Group*, Kansas Geological Survey, Bulletin 250. <https://journals.ku.edu/mg/article/view/11789/11137>. Accessed November 11, 2019.

Glorot, X., Bordes, A., and Bengio, Y., 2011, Deep Sparse Rectifier Neural Networks, *Proceedings of Machine Learning Research*, **15**, 315–323. <http://proceedings.mlr.press/v15/glorot11a/glorot11a.pdf>. Accessed November 12, 2019.

Hall, B., 2016, Facies Classification Using Machine Learning, *The Leading Edge*, **35**(10), 906–909. DOI: 10.1190/tle35100906.1

He, H., Bai, Y., Garcia, E.A., and Li, S., 2008, ADASYN: Adaptive Synthetic Sampling Approach for Imbalanced Learning, *2008 IEEE International Joint Conference on Neural Networks (IEEE World Congress on Computational Intelligence)*, 1322–1328. DOI: 10.1109/JCNN.2008.4633969. <https://sci2s.ugr.es/keel/pdf/algorithm/congreso/2008-He-ieee.pdf>. Accessed November 12, 2019.

Jobe, T.D., Vital-Brazil, E., and Khaif, M., 2018, Geological Feature Prediction Using Image-Based Machine Learning, *Petrophysics*, **59**(6), 750–760. DOI: 10.30632/PJV59N6-2018a1.

Lang, X., Sengupta, M., Xu, C., Deng, T., and Grana, D., 2019, Log-Facies Classification Using Expectation-Maximization, *SEG Technical Program Expanded Abstracts*, 3161–3165. DOI: 10.1190/segam2019-3214255.1

Li, H., and Misra, S., 2017, Prediction of Subsurface NMR T_2 Distributions in a Shale Petroleum System Using Variational Autoencoder-Based Neural Networks, *IEEE Geoscience and Remote Sensing Letters*, **14**(12), 2395–2397. DOI: 10.1109/LGRS.2017.2766130.

Lucia, F.J., 2007, *Carbonate Reservoir Characterization: An Integrated Approach*, 2nd edition, Springer Science. ISBN: 978-3540727408.

Luthi, S.M., and Souhaite, P., 1990, Fracture Apertures From Electrical Borehole Scans, *Geophysics*, **55**(7), 821–833. DOI: 10.1190/1.1442896.

Mahmoud, A.A.A., Elkatatny, S., Mahmoud, M., Abouelresh, M., Abdulraheem, A., and Ali, A., 2017, Determination of the Total Organic Carbon (TOC) Based on Conventional Well Logs Using Artificial Neural Network, *International Journal of Coal Geology*, **179**, 72–80. DOI: 10.1016/j.coal.2017.05.012.

Newberry, B.M., Grace, L.M., and Stief, D.O., 1996, Analysis of Carbonate Dual Porosity Systems From Borehole Electrical Images, Paper SPE-35158 presented at the Permian Basin Oil and Gas Recovery Conference, Midland, Texas, USA, 27–29 March. DOI: 10.2118/35158-MS.

Perez-Rosales, C., Mercado-Diaz, A., Cruz-Hernandez, J., and Islas-Juarez, R., 2002, Electric Resistivity of Vuggy Fractured Media, Paper SPE-74340 presented at the SPE International Petroleum Conference and Exhibition in Mexico, Villahermosa, Mexico, 10–12 February. DOI: 10.2118/74340-MS.

- Provost, F., 2000, Machine Learning From Imbalanced Data Sets 101 [extended abstract], AAAI Technical Report WS-00-05, **68**, 1–3. <https://www.aaai.org/Papers/Workshops/2000/WS-00-05/WS00-05-001.pdf>. Accessed November 12, 2019.
- Quirein, J., Kimminau, S., LaVigne, J., Singer, J., and Wendel, F., 1986, A Coherent Framework for Developing and Applying Multiple Formation Evaluation Models, Paper DD, *Transactions, SPWLA 27th Annual Logging Symposium*, Houston, Texas, USA, 9–13 June.
- Saneifar, M., Aranibar, A., and Heidari, Z., 2015, Rock Classification in the Haynesville Shale Based on Petrophysical and Elastic Properties Estimated From Well Logs, *Interpretation*, **3**(1), SA65–SA75. DOI: 10.1190/INT-2013-0198.1.
- Snoek, J., Larochelle, H., and Adams, R.P., 2012, Practical Bayesian Optimization of Machine Learning Algorithms, *Advances in Neural Information Processing Systems*, **25**, 2951–2959. <https://arxiv.org/pdf/1206.2944.pdf>. Accessed November 12, 2019.
- Tan, M., Song, X., Yang, X., and Wu, Q., 2015, Support-Vector-Regression Machine Technology for Total Organic Carbon Content Prediction From Wireline Logs in Organic Shale: A Comparative Study, *Journal of Natural Gas Science and Engineering*, **26**, 792–802. DOI: 10.1016/j.jngse.2015.07.008.
- Tang, H., Meddaugh, W.S., and Toomey, N., 2011, Using an Artificial-Neural-Network Method to Predict Carbonate Well Log Facies Successfully, Paper SPE-123988, *SPE Reservoir Evaluation & Engineering*, **14**(1), 35–44. DOI: 10.2118/123988-PA.
- Trevor, H., Tibshirani, R., and Friedman, J.H., 2003, *The Elements of Statistical Learning: Data Mining, Inference, and Prediction*, Springer. ISBN: 978-0387952840.
- Xie, Y., Zhu, C., Zhou, W., Li, Z., Liu, X., and Tu, M., 2018, Evaluation of Machine Learning Methods for Formation Lithology Identification: A Comparison of Tuning Processes and Model Performances, *Journal of Petroleum Science and Engineering*, **160**, 182–193. DOI: 10.1016/j.petrol.2017.10.028.
- Xu, C., Heidari Z., and Torres-Verdín C., 2012, Rock Classification in Carbonate Reservoirs Based on Static and Dynamic Petrophysical Properties Estimated From Conventional Well Logs, Paper SPE-159991 presented at the SPE Annual Technical Conference and Exhibition, San Antonio, Texas, 8–10 October. DOI: 10.2118/159991-MS.
- Xu, C., Misra, S., Srinivasan, P., and Ma, S., 2019, When Petrophysics Meets Big Data: What Can Machine Do? Paper SPE-195068 presented at the SPE Middle East Oil and Gas Show and Conference, Manama, Bahrain, 18–21 March. DOI: 10.2118/195068-MS.
- Xu, C., and Torres-Verdín, C., 2013, Pore System Characterization and Petrophysical Rock Classification Using a Bimodal Gaussian Density Function, *Mathematical Geosciences*, **45**(6), 753–771. DOI: 10.1007/s11004-013-9473-2.

ABOUT THE AUTHORS



Tianqi Deng is a PhD Candidate in the Department of Petroleum and Geosystems Engineering and a Graduate Research Assistant in the Formation Evaluation Consortium Research Program at The University of Texas at Austin. He received his BS degree from China University of Geosciences (Beijing). He worked as an Intern for Aramco Services Company (Houston) and Quantum Reservoir Impact (QRI) as a petrophysicist in the summers of 2018 and 2019, respectively. He is also an officer of The SPWLA Student Chapter at The University of Texas at Austin. His research interests include petrophysics, well-log interpretation, inverse problems and uncertainty quantification, machine learning, and statistical methods.



Chicheng Xu obtained his PhD degree in petroleum engineering from the University of Texas at Austin in 2013. He worked for Schlumberger Beijing Geoscience Center from 2004 to 2009. From 2013 to 2017, he worked as a petrophysicist/rock physicist for BP America and BHP Billiton to support US asset operations and reservoir characterization in deepwater turbidite fields as well as onshore unconventional fields. Chicheng is currently working as a research petrophysicist and project leader in Aramco Houston Research Center. His research focus is on petrophysical reservoir characterization using advanced computational techniques and data analytics for interpretation, classification, and modeling based on multiscale subsurface data integration. Chicheng Xu served on the SPE Reservoir Description and Dynamics committee (2016–2018) and the Formation Evaluation subcommittee of SPE ATCE (2015–2020). He is an associate editor of *Interpretation* (copublished by SEG and AAPG), *SPE Reservoir Evaluation & Engineering*, and *Petrophysics*. He founded and chaired the SPWLA PDDA SIG and was selected to receive the regional Formation Evaluation technical award by the SPE Gulf Coast chapter in 2018.



Dawn Jobe holds both PhD (2013) and MS (2010) degrees in Geology from the Colorado School of Mines. Her geologic expertise spans both carbonate and clastic sedimentary systems. Dawn spent the last 6 years at the Aramco Research Center – Houston where she was a lead developer

for innovative rapid reservoir characterization technology designed to capture and represent rock properties simultaneously over nano- to kilometer scales. Dawn's early career focused on quantification, modeling and prediction of carbonate microporosity, reservoir geometries and enhanced recovery potential. Her findings highlighted significant additional hydrocarbon volumes that had gone previously unrecognized which could be produced from microporous reservoirs thought out the Middle East region. Dawn's broader research interests include multiscale-multispectral rock and sediment characterization, applications of statistical and machine learning approaches for geologic data integration and prediction as well as the use of 3D printed rock proxies in geoscience experiments. She is a member of the American Association of Petroleum Geologists and was recently appointed as the Early Career Councilor to serve on the Society for Sedimentary Geology (SEPM) Board of Directors Executive Council, which provides essential advice on the future directions of sedimentary geology research.



Rui Xu is currently a PhD candidate majoring in Petroleum Engineering at the University of Texas at Austin. His research focuses on integration of machine learning to facilitate well log and core data analysis, and pore scale modeling of thermodynamic and hydrodynamic behavior in unconventional rocks for characterization of petrophysical properties. He worked as a data science/petrophysics intern at Aramco Services Company in Houston, Texas, in 2019. He earned his BS degree from China University of Petroleum Beijing.

Joint Interpretation of Elastic and Electrical Data for Petrophysical Properties of Gas-Hydrate-Bearing Sediments Using Inverse Rock Physics Modeling Method

Haojie Pan¹, Hongbing Li¹, Yan Zhang^{1*}, Jingyi Chen², Shengjuan Cai¹, and Chao Geng³

ABSTRACT

Accurate interpretation of the petrophysical properties of gas-hydrate-bearing sediments, such as porosity, hydrate saturation and clay content, are of great importance for reservoir characterization and resource evaluation. Typically, these parameters are estimated using either elastic properties or electrical properties instead of both. We propose to take advantage of multiple types of measurements and improve the accuracy of prediction by using an inverse rock physics modeling (IRPM) method, which allows us to combine elastic and electrical attributes. First, we generate constraint cubes of 3D elastic and electrical data in the reservoir parameter domain using suitable rock physics models calibrated by 3D elastic-electrical rock physics templates (RPTs). Then, we extract the isosurfaces from the 3D elastic and electrical data constraint cubes with the marching-cubes algorithm.

Finally, we use the iterative least-squares method to find the optimal intersection point of three isosurfaces by minimizing the objective function. To demonstrate the feasibility of this strategy, we apply it to synthetic data and well logs measured at the Ocean Drilling Program (ODP) Hole 1247B drilled on the Hydrate Ridge, South Cascadia Margin. For the synthetic data, the estimated petrophysical properties are consistent with those produced using noise-free initial synthetic model parameters. In addition, our estimated results for real field localities consistently fit with the core data. The smaller root-mean-square errors between inversion results and referenced petrophysical properties for both synthetic case (≤ 0.06) and real field data (≤ 0.061) further confirm that the inverse rock physics modeling method is feasible for estimating petrophysical properties by integrating elastic and electrical properties.

INTRODUCTION

Gas hydrates are naturally occurring ice-like substances that are composed of gas molecules (mainly methane) and water. They are widespread in continental margin sediments and beneath permafrost, where relatively high pressures and low temperatures stabilize the hydrate structure. In recent years, the study of gas hydrates has become an important research topic because of their recognition as a potential energy resource, as a negative controlling element in global climatic change, and as a critical factor affecting sea-floor stability and safety issues (Sloan et al., 1999). Hence, the detection and evaluation of gas-hydrate-bearing sediments are of great significance. Generally, the presence of gas hydrates is associated with increases in the elastic velocities and electrical resistivity of gas-hydrate-bearing sediments (Lee and Waite, 2008). Thus, these two types of information are commonly used to quantitatively estimate the petrophysical properties of hydrate formations. Elastic velocities are generally most sensitive to changes in porosity and lithology. Electrical resistivity, on the other hand, is often

highly dependent on hydrate saturation and its distribution (Gomez and Dvorkin, 2007). By combining these two sets of measurements, we can improve the prediction accuracy and reduce the uncertainty of the interpretation.

Rock physics models comprise many of the same elastic and electrical properties and petrophysical properties (e.g., hydrate saturation, porosity and clay content). Although numerous elastic and electrical rock physics models are capable of modeling hydrate accumulation, the application of these models is limited by the fact that they are site-specific, empirically derived from laboratory measurements, and customized for local geological factors (Liu et al., 2015). Rock physics models generally need to be calibrated using experimental data or well logs from the area under consideration (Avseth et al., 2005; Liu et al., 2015). After calibration, these suitable models can be used to perform forward modeling or inversion of geophysical data.

The estimation of petrophysical properties from geophysical measurements is an inverse problem which is complicated to solve and has nonunique solutions. Thus, robust and flexible methods for estimating reservoir

Manuscript received by the Editor June 7, 2019; revised manuscript received August 21, 2019; manuscript accepted September 24, 2019.

¹ Department of Geophysical Technology, Research Institute of Petroleum Exploration and Development, Xueyuan Road No.20, Haidian District, 100083 Beijing, China; panhj88@petrochina.com.cn; hbingli@petrochina.com.cn; zya@petrochina.com.cn; cai_sj@petrochina.com.cn

² Department of Geosciences, University of Tulsa, 800 South Tucker Drive, Tulsa, OK 74104 USA; jingyi-chen@utulsa.edu

³ Southwest Oil & Gas Field Company, Petrochina, Fuqing Road Section 01 No.3, Chenghua District, 610051 Chengdu, China; 635036093@qq.com

properties are essential for successful quantitative interpretation in reservoir characterization and monitoring settings. Inverse rock physics modeling (IRPM) (Johansen et al., 2004; Moyano et al., 2011) has proved to be a very useful and efficient in predicting rock properties using appropriate rock physics models. Some authors have applied this method to analyze and predict the petrophysical properties from well logs and seismic data. Moyano et al. (2015) proposed an IRPM procedure for the prediction of reservoir properties from seismic data with a spatial constraint. Bredesen (2016) performed quantitative reservoir characterization using IRPM based on the seismic inversion data. Liu et al. (2017) estimated reservoir parameters with a constrained IRPM method using the prestack seismic inversion results. Zheng et al. (2017) predicted the reservoir properties with inverse digital rock physics modeling. However, the correlation between objective function and computation efficiency and speed remains poorly understood. Moreover, little work has been done on the joint interpretation of elastic and electrical properties using the IRPM method.

To investigate the feasibility of incorporating both electrical data and elastic data for the estimation of petrophysical properties, we propose a joint inversion scheme using an IRPM approach. First, we select and calibrate the appropriate elastic and electrical rock physics models based on the core data and well-log interpretations. Then, we construct the 3D constraint cubes of three inputs based on the models. After that, we use the marching-cubes algorithm (Lorenson and Cline, 1987) to extract the isosurfaces for the given measured data at the given sampling point. Finally, we intersect the three isosurfaces to achieve the optimal intersection point, the coordinates of which represent three inverted petrophysical properties: hydrate saturation, porosity and clay content. To test our approach for application in the quantitative characterization of gas-hydrate-bearing sediments, we apply it to both synthetic data and actual field data measured at ODP Hole 1247B (Hydrate Ridge).

ROCK PHYSICS MODELING OF GAS-HYDRATE-BEARING SEDIMENTS

Rock physics models provide a quantitative relationship between petrophysical properties and elastic and electrical properties. Various theoretical and semiempirical models have been proposed for the quantitative delineation of gas hydrate-bearing sediments.

For elastic rock physics models, Lee et al. (1996) proposed weighted equations that weight the Wood (Wood, 1941) and Wyllie (Wyllie et al., 1958) equations; this equation is simple to use but lacks a strictly theoretical basis

and the weighting factor requires well-log or core data to be calibrated and constrained. Dvorkin et al. (1994) and Dvorkin and Nur (1996) proposed a contact-cementation theory (CCT) which is often used to calculate the elastic velocities of hydrate-bearing sediments by supposing hydrate to be either accumulated at grain contacts or evenly enveloped on the grain surface. Helgerud et al. (1999) offered a first-principle-based effective-medium theory (EMT) based on the modified upper or lower Hashin-Shtrikman boundary (Hashin and Shtrikman, 1963) and Hertz-Mindlin contact theory (Mindlin, 1949) by treating gas hydrates either as part of matrix grains or part of pore fluids. Carcione and Tinivella (2000) assumed an idealized arrangement in which sediment, hydrate and pore fluid form three homogeneous, interwoven frameworks, and then developed a three-phase Biot-type equation (TPBE) to calculate the elastic properties of gas-hydrate-bearing sediments. However, it is difficult to derive the sediment and hydrate framework moduli. Lee and Waite (2008) proposed a simplified three-phase equation (STPE) based on the expressions for moduli of sediments and hydrate frameworks proposed by Pride et al. (2004), and for dry framework proposed by Lee (2005). Also, some other anisotropic models for calculating elastic velocities have been proposed. For instance, the layered-medium theory (White et al., 1955) combined with STPE (Lee and Collett, 2009) or EMT (Helgerud et al., 1999) can be used to calculate the velocities of sediments containing fracture-filling hydrate.

For electrical models, Archie's equation (Archie, 1942) is frequently used to calculate the resistivity response. This model, however, is an empirical law that is developed to determine water saturation in clean sands from measurements of resistivity and porosity across a sand-fluid mixture. When clay minerals are present in the sediments, Archie's equation is no longer accurate. This is mainly because the presence of clay minerals significantly lowers resistivity. Thus, it is crucial to account for the effect of clay content on the resistivity when calculating the hydrate saturation. Simandoux (1963) proposed a shaly sand model by introducing another conductivity source arising from shale- (or clay-) bound water. Other models include a shaly sand model proposed by Waxman and Smits (1968) and a dual-water model by Clavier et al. (1984). On the basis of Archie's law and the Simandoux equation, Lee and Collett (2006) established a relationship between the amount of clay conductivity and the Archie constants, and proposed a method of correcting for the clay effect on the estimation of water saturations. Sava and Hardage (2007) applied the modified Archie equation (MAE) to predict the gas-hydrate concentration and the associated uncertainty for well-log data from the Green Canyon area of the Gulf of Mexico.

Ellis (2008) investigated the feasibility of self-consistent approximation (SCA)-differential effective-medium (DEM) model to predict the hydrate saturation by accounting for the effect of clay content. Cook (2010) proposed an anisotropic resistivity model to evaluate the gas-hydrate saturation for fracture-filling hydrate-bearing sediments.

Pan et al. (2019a) diagnosed hydrate morphology with the crossplot of P- and S-wave velocities versus hydrate saturation, and concluded that hydrates mainly occur as pore-filling form in the sediments at the studied site ODP Hole 1247. Hence, we relate elastic properties with petrophysical properties by using the Gassmann equation (Gassmann, 1951) with EMT, and employ the modified Archie equation to obtain the resistivity.

Effective-Medium Theory

Dvorkin et al. (1999) proposed a modified Hashin-Shtrikman-Hertz-Mindlin theory to calculate the elastic moduli of high-porosity ocean-bottom sediments. The main assumption of this model is that the modulus behavior of sediments at critical porosity (0.36 to 0.40) can be characterized by that of a dense random pack of identical elastic granular grains. Then, the modulus of sediments at intermediate porosity can be derived with the modified upper or lower Hashin-Shtrikman bound for the mixture of two endpoints' components: the pure solid phase with zero porosity, and the pure fluid phase with 100% porosity. It means that the model is suitable for both consolidated and unconsolidated sediments. On the basis of this model, Helgerud et al. (1999) further developed an EMT model by accounting for the effects of hydrate formation and partial gas saturation. It starts by computing the effective bulk and shear moduli of the dry rock frame at critical porosity using Hertz-Mindlin contact theory (Mindlin, 1949):

$$K_{HM} = \left[\frac{n_p^2 (1-\phi_c)^2 G_{ma}^2 P}{18\pi^2 (1-\nu_{ma})^2} \right]^{\frac{1}{3}}, \tag{1}$$

$$G_{HM} = \frac{5-4\nu_{ma}}{5(2-\nu_{ma})} \left[\frac{3n_p^2 (1-\phi_c)^2 G_{ma}^2 P}{2\pi^2 (1-\nu_{ma})^2} \right]^{\frac{1}{3}}, \tag{2}$$

where ϕ_c is the critical porosity (0.36 to 0.40); K_{HM} and G_{HM} are the elastic moduli at critical porosity; the coordination number is $n_p = (20 - 34\phi + 14\phi^2)$, ϕ is the porosity; G_{ma} and ν_{ma} are the shear modulus and Poisson's ratio of rock frame, respectively. ν_{ma} is related to G_{ma} and K_{ma} (the bulk modulus of matrix) by $\nu_{ma} = 0.5(K_{ma} - 2/3G_{ma}) / (K_{ma} + 1/3G_{ma})$. K_{ma} and

G_{ma} are calculated from the moduli of m mineral constituents using Hill's average (Hill, 1952):

$$K_{ma} = \frac{1}{2} \left[\sum_{i=1}^m f_i K_i + \left(\sum_{i=1}^m \frac{f_i}{K_i} \right)^{-1} \right], \tag{3}$$

$$G_{ma} = \frac{1}{2} \left[\sum_{i=1}^m f_i G_i + \left(\sum_{i=1}^m \frac{f_i}{G_i} \right)^{-1} \right], \tag{4}$$

Where K_i and G_i are the bulk and shear moduli of the i th mineral constituent, f_i is the volumetric fraction of the i th mineral constituent. The effective pressure P can be calculated as

$$P = (1-\phi)(\rho_s - \rho_f)gh, \tag{5}$$

where ρ_s and ρ_f and are the densities of the solid and fluid phase, respectively; g is the gravity acceleration; h is the depth below the seafloor.

For porosity values ranging between zero and the critical porosity, the bulk modulus and shear modulus of dry rock can be derived by interpolating the grain elastic modulus and the elastic modulus of dry rock at the critical porosity with a modified lower Hashin-Shtrikman (H-S) bound (Dvorkin and Nur, 1996):

$$K_{dry} = \left[\frac{\phi/\phi_c}{K_{HM} + \frac{4}{3}G_{HM}} + \frac{1-\phi/\phi_c}{K_{ma} + \frac{4}{3}G_{HM}} \right]^{-1} - \frac{4}{3}G_{HM}, \tag{6}$$

$$G_{dry} = \left[\frac{\phi/\phi_c}{G_{HM} + z} + \frac{1-\phi/\phi_c}{G_{ma} + z} \right]^{-1} - z, \quad z = \frac{G_{HM}}{6} \left(\frac{9K_{HM} + 8G_{HM}}{K_{HM} + 2G_{HM}} \right). \tag{7}$$

For porosities above the critical porosity, these moduli can be calculated using the modified upper H-S bound:

$$K_{dry} = \left[\frac{(1-\phi)/(1-\phi_c)}{K_{HM} + \frac{4}{3}G_{HM}} + \frac{1-(1-\phi)/(1-\phi_c)}{\frac{4}{3}G_{HM}} \right]^{-1} - \frac{4}{3}G_{HM}, \tag{8}$$

$$G_{dry} = \left[\frac{(1-\phi)/(1-\phi_c)}{G_{HM} + z} + \frac{1-(1-\phi)/(1-\phi_c)}{z} \right]^{-1} - z. \tag{9}$$

The saturated bulk modulus, (K_{sat}) and shear modulus, (G_{sat}) and shear modulus can be calculated using the Gassmann equation (Gassmann et al., 1951) as:

$$K_{sat} = K_{ma} \frac{\phi K_{dry} - (1 + \phi) K_{fl} K_{dry} / K_{ma} + K_{fl}}{(1 - \phi) K_{fl} + \phi K_{ma} - K_{fl} K_{dry} / K_{ma}}, \quad (10)$$

$$G_{sat} = G_{dry}, \quad (11)$$

where K_{dry} is the dry bulk modulus, G_{dry} is the dry shear modulus, and K_{fl} is the modulus of the pore fluid.

Finally, the elastic velocities of the sediments, compressional velocity, V_p , and shear velocity, V_s , can be computed using the following formulas:

$$V_p = \sqrt{\frac{K_{sat} + 4G_{sat}/3}{\rho_b}} \quad \text{and} \quad V_s = \sqrt{\frac{G_{sat}}{\rho_b}}, \quad (12)$$

where ρ_b is the bulk density calculated from the volumetric average of the rock densities,

$\rho_b = (1 - \phi)(1 - V_{sh}) \rho_s + (1 - \phi) V_{sh} \rho_{sh} + \phi S_{gh} \rho_{gh} + \phi (1 - S_{gh}) \rho_w$, where ρ_s , ρ_{sh} , ρ_{gh} , and ρ_w , refer to the densities of sand, clay, hydrate, and water, respectively; S_{gh} and V_{sh} and are, the hydrate saturation and clay content, respectively.

When gas hydrate exists within the pore space without affecting the framework, the bulk modulus of the fluid (K_{fl}) is the Reuss average of the bulk moduli of water (K_w) and hydrate (K_h); and hydrate:

$$K_{fl} = \left[\frac{1 - S_{gh}}{K_w} + \frac{S_{gh}}{K_h} \right]^{-1}. \quad (13)$$

When gas hydrate becomes a component of the dry-sediment frame, the elastic properties of the frame will be altered by reducing the porosity. First, the reduced porosity ϕ_r is defined as

$$\phi_r = \phi(1 - S_{gh}). \quad (14)$$

Then, the elastic moduli of the altered solid phase are recalculated using Hill's (1952) average of the hydrate and mineral components using

$$K_{ma} = \frac{1}{2} \left(f_h K_h + (1 - f_h) K_s + \left[\frac{f_h}{K_h} + \frac{(1 - f_h)}{K_s} \right]^{-1} \right), \quad (15)$$

$$G_{ma} = \frac{1}{2} \left(f_h G_h + (1 - f_h) G_s + \left[\frac{f_h}{G_h} + \frac{(1 - f_h)}{G_s} \right]^{-1} \right), \quad (16)$$

where

$f_h = \frac{\phi_r \phi_r}{1 - \phi_r}$, K_s and G_s are the bulk and shear moduli of the mixture of the mineral constituents, respectively. G_h is the shear modulus of gas hydrates.

Modified Archie Equation

Gas hydrates are electrical insulators, in the same way as hydrocarbons are, and their presence will increase bulk resistivity. Therefore, in principle, we can use the same techniques to estimate hydrate saturation as those used to estimate hydrocarbon saturation in the oil industry. The most common empirical technique is the Archie equation. This equation has been used to analyze resistivity responses of fluid-filled porous rocks for more than six decades in the form (Archie, 1942)

$$R_t = \frac{a R_w}{(1 - S_{gh})^n \phi^m}, \quad (17)$$

where R_t is the resistivity of sediments; a is the tortuosity factor, n is the saturation exponent, m is the cementation exponent. Here, R_w is the formation water resistivity. However, Archie's equation (Archie, 1942) is only suitable for deriving water saturation in clean sands and not applicable to the prediction of the saturation of clay-rich sediments. To overcome this shortcoming, a modified Archie's equation (MAE) (Sava and Hardage, 2007) has been used:

$$\frac{1}{R_t} = \frac{\phi^m (1 - S_{gh})^n}{a R_w (1 - V_{sh})} + \frac{V_{sh} (1 - S_{gh})^{n-1}}{R_{sh}}, \quad (18)$$

where the clay resistivity R_{sh} can be measured in the laboratory. If the core sample is not available, we must use the resistivity data measured across pure-clay intervals from nearby fields or rely on published resistivity measurements for clays in the similar environments. Here, we choose the value of resistivity of clay minerals as 5 Ω -m (Lee, 2011).

INVERSE ROCK PHYSICS MODELING (IRPM) STRATEGY

Due to natural variabilities in rock composition, physical properties, geometrical distributions of constituent, textural complexities, geological conditions (e.g., compaction and cementation), and relationships between elastic and electrical properties and petrophysical properties are usually complex and nonlinear. This makes it practically impossible to find an analytical inverse function to estimate model parameters from acquired measurements (Jensen, 2011) and thereby will cause the ambiguities in estimation and poor stability in the real application. Therefore, a reasonable and efficient approach for transforming the geophysical parameters to petrophysical properties is necessary. The IRPM approach (Johansen et al., 2004, 2013) is a generic method for predicting petrophysical properties, such as porosity, lithology and fluid saturation, from various types

of inputs and rock physics models. It has been demonstrated previously on well-log data (Liu et al., 2017) and seismic-inverted elastic properties (Bredesen et al., 2015).

In this paper, we extend IRPM to use the elastic and electrical properties as inputs for quantitative prediction of petrophysical properties of gas-hydrate-bearing sediments. This method mainly consists of two steps: rock physics modeling and inverse rock physics modeling (Bredesen, 2016). In the first step, we choose and calibrate suitable rock physics models based on the geologic characteristics of the target zone. In the second step, we carry out the orthogonal analysis of input data and take advantage of calibrated elastic and electrical models to generate 3D elastic-electrical constraint cubes for various effective reservoir properties, and then use the marching-cubes algorithm (Lorenson, 1987) to extract the isosurfaces from the cubes. Finally, we use the iterative least-squares algorithm to conduct an exhaustive search to achieve the intersection point by intersecting three isosurfaces of three input datasets with a minimal objective function (J_{min}) (less than given error ϵ). Figure 1 shows the workflow of the IRPM strategy for reservoir parameter prediction. In the following sections, we discuss this strategy in detail.

IRPM can be used to obtain the intersection point by intersecting three isosurfaces calculated from rock physics models in the reservoir parameter domain. The IRPM method involves four steps (1) orthogonal analysis of input data, (2) the generation of 3D rock physics constraint cubes, (3) extraction of isosurfaces, and (4) the search for the intersection point. The bulk and shear moduli and density for the sediment constituents are listed in the Table 1.

Table 1—Basic Parameters for the Sediment Constituents

Material	Bulk Modulus (GPa)	Shear Modulus (GPa)	Density (g/cm ³)
Quartz	36.6	45	2.65
Clay	20.9	6.85	2.58
Gas Hydrate	6.41	2.54	0.91
Water	2.25	0	1.03

The properties of gas hydrates are from Lee and Waite (2008); the others are from Lee and Collett (2009). The bulk and shear moduli of a matrix composed of quartz and clay are computed using Hill's (1952) average equation.

Orthogonal Analysis of Input Data

The best combination of measured properties for obtaining stable solutions largely depends on the local shape of the isosurfaces at the intersection points (Johansen

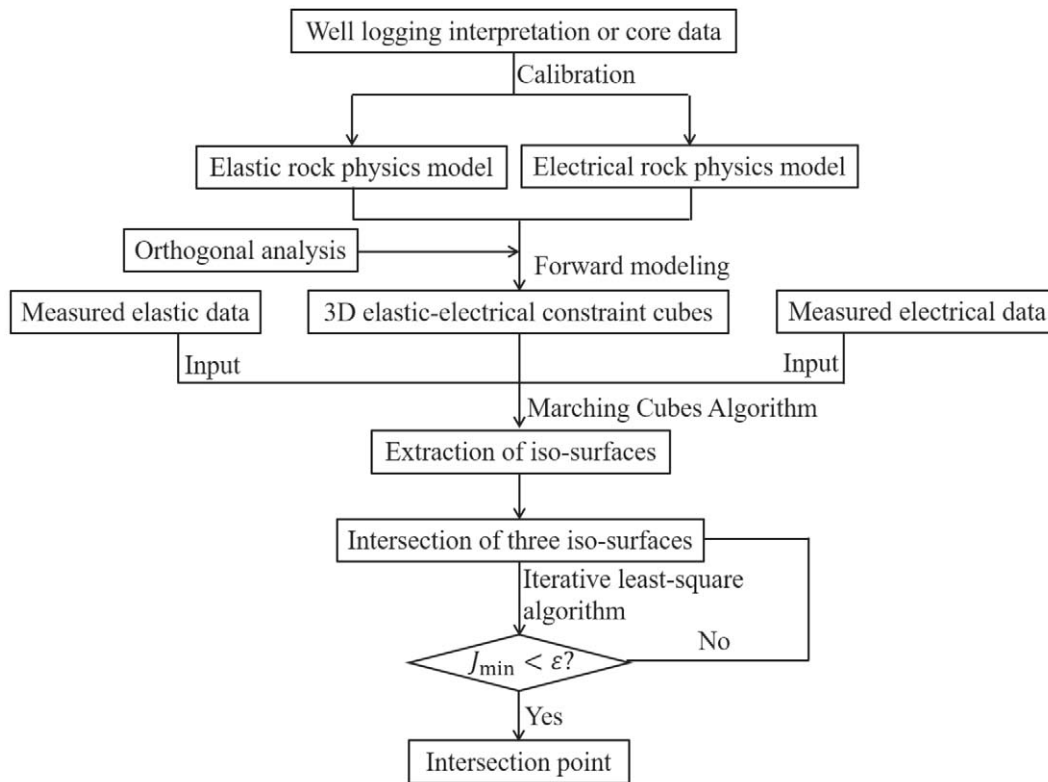


Fig. 1—Workflow for reservoir parameter prediction based on the IRPM method.

et al., 2013; Liu et al., 2016). The main reason is that no intersecting line exists when the two isosurfaces are parallel to each other, while it is possible to get the intersecting line when the isosurfaces are nonparallel, especially for the two perpendicular isosurfaces. Thus, we should use the scalar product of the normal vectors of isosurfaces to perform orthogonal analysis of input data and choose the suitable combination of elastic and electrical properties used for the IRPM. The orthogonal property between two isosurfaces can be expressed as

$$OF_{d_1,d_2} = \left| \nabla S_{d_1}^T \mathbf{g} \cdot \nabla S_{d_2} \right|, \quad (19)$$

Where OF_{d_1,d_2} is the orthogonality factor, d_1 and d_2 represent the two input data parameters.

$$\nabla S_{d_1} = \left(\frac{\partial S_{d_1}}{\partial S_{gh}}, \frac{\partial S_{d_1}}{\partial \phi}, \frac{\partial S_{d_1}}{\partial V_{sh}} \right)^T \text{ and } \nabla S_{d_2} = \left(\frac{\partial S_{d_2}}{\partial S_{gh}}, \frac{\partial S_{d_2}}{\partial \phi}, \frac{\partial S_{d_2}}{\partial V_{sh}} \right)^T$$

denote the normalized gradient vectors of two single-value isosurfaces at the intersection points. Then, we can use a mean orthogonality factor MOF to evaluate the applicability of input data. It can be written as:

$$MOF = \frac{1}{N} \sum_{i,j=1}^N OF_{d_i,d_j}, \quad (20)$$

where OF_{d_1,d_2} represents the orthogonality factor of arbitrary two input data. The indices $i = 1, 2, \dots, N$ and $j = 1, 2, \dots, N$. N is the number of orthogonality factor. If the MOF tends to zero, which indicates that the orthogonality of different isosurfaces at intersection points is strong and helpful to find a unique solution. On the contrary, if the MOF tends to one, the orthogonality of different isosurfaces at intersection points is weak and likely to produce nonunique solutions.

Generation of 3D Rock Physics Constraint Cubes

The IRPM approach is strongly dependent on the rock physics constraints between the effective elastic and electrical properties and the petrophysical properties. On the basis of rock physics modeling, here we adopt the P-wave impedance, Poisson's ratio, and logarithm of resistivity as the input datasets. Meanwhile, the hydrate saturation, porosity, and clay content, related to the x -, y - and z -axes in a 3D coordinate system, act as the expected output datasets. Firstly, the minimum and maximum values of these three petrophysical properties analyzed from core data or well-log interpretations are used to make up the corners of the constraint cubes. For instance, one corner for $(S_{ghmin}, \phi_{min}, V_{shmin})$ coincides with origin position and the corner diagonally to it is defined by $(S_{ghmax}, \phi_{max}, V_{shmax})$. Then, the 3D reservoir parameter domain can be divided into a grid

with $L_m \times L_m \times L_m$ equidistant nodes. Here, L_m is set to be 51. Next, the elastic and electrical properties for each node can be calculated based on the abovementioned elastic and electrical models. Finally, the elastic and electrical properties constraint cubes can be generated, as shown in Fig. 2.

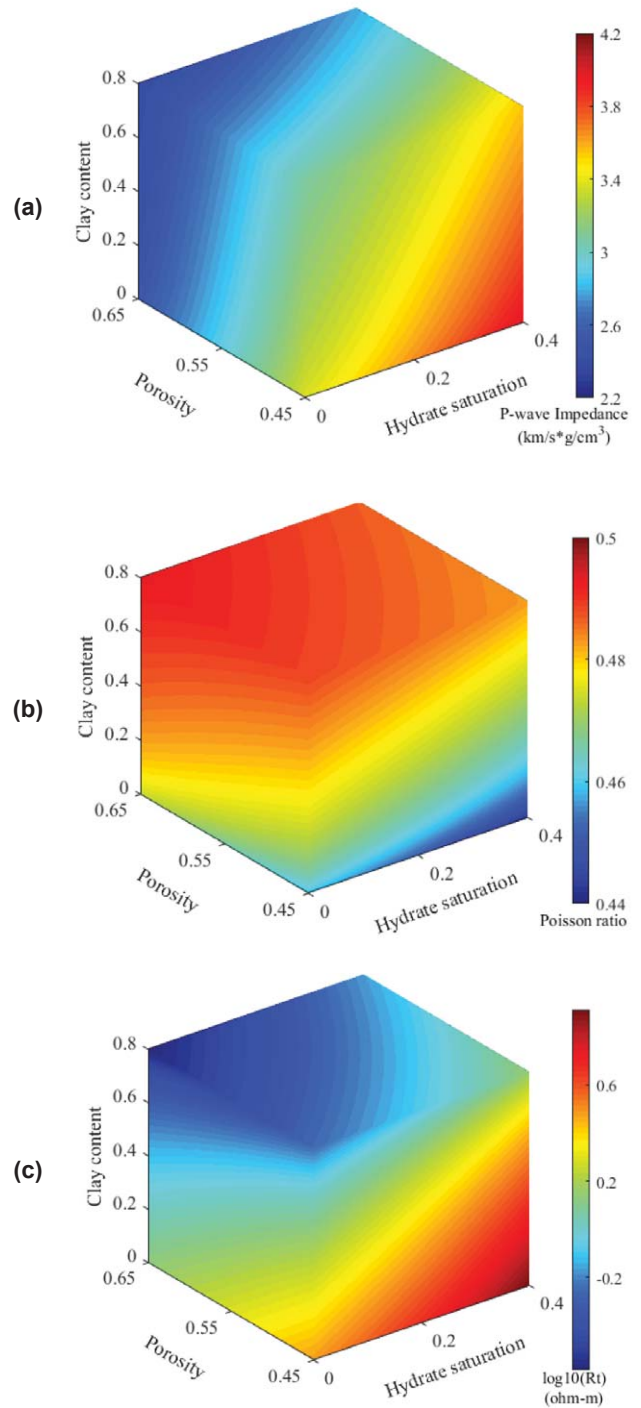


Fig. 2—Three-dimensional constraint cubes for elastic and electrical data in the reservoir parameter domain: (a) P-wave impedance, (b) Poisson's ratio, and (c) logarithm of resistivity. The colors correspond to the data parameter values.

Typically, for a given property d , the discretely sampled constraint cube φ is

$$\begin{aligned} \varphi(S_{gh}, \phi, V_{sh}) = d, \forall S_{gh} \in \{S_{gh\min}, S_{gh\min} + \Delta S_{gh}, S_{gh\min} + 2\Delta S_{gh}, \dots, S_{gh\min} + (L_m - 1)\Delta S_{gh}, S_{gh\max}\} \\ \phi \in \{\phi_{\min}, \phi_{\min} + \Delta\phi, \phi_{\min} + 2\Delta\phi, \dots, \phi_{\min} + (L_m - 1)\Delta\phi, \phi_{\max}\} \\ V_{sh} \in \{V_{sh\min}, V_{sh\min} + \Delta V_{sh}, V_{sh\min} + 2\Delta V_{sh}, \dots, V_{sh\min} + (L_m - 1)\Delta V_{sh}, V_{sh\max}\} \end{aligned} \quad (21)$$

where $\Delta S_{gh} = \frac{S_{gh\max} - S_{gh\min}}{L_m - 1}$, $\Delta\phi = \frac{\phi_{\max} - \phi_{\min}}{L_m - 1}$, $\Delta V_{sh} = \frac{V_{sh\max} - V_{sh\min}}{L_m - 1}$

To improve the prediction accuracy and extract all the reservoir parameter combinations corresponding to a set of fixed data values, we need to perform a resampling of discrete constraints φ . Before resampling, we can retrieve the minimum (φ_{\min}) and maximum (φ_{\max}) values of φ . Linear interpolation can be expressed by

$$\varphi_j(S_{gh}, \phi, V_{sh}) = \varphi_{\min} + (j - 1)\Delta\varphi, \quad (22)$$

where φ_j is the continuous scalar field function; $\Delta\varphi = \frac{\varphi_{\max} - \varphi_{\min}}{L_\varphi - 1}$ and $J = 1, \dots, L_\varphi$. L_φ denotes a predefined number of values of the measured data to be extracted.

Extraction of Isosurfaces

Any given set of petrophysical properties will be equivalent to one specific data parameter value, while a single value corresponds to numerous possible reservoir parameter combinations, which form a surface denoted as the isosurface in the reservoir parameter domain. In other words, all of the points on the isosurface are possible solutions for the given data. For the specific measured data d_{obs} , its single-value isosurface $IS_{d_{obs}}(S_{gh}, \phi, V_{sh})$ can be expressed as:

$$IS_{d_{obs}}(S_{gh}, \phi, V_{sh}) = d_{obs} \quad (23)$$

Generally, the single-value isosurface can be extracted using the marching-cubes algorithm (Lorenson, 1987) or isosurface function in Matlab software. The projection width of the isosurface on the three axes represents the constraint capacity of the elastic-electrical properties on the petrophysical properties, which suggests that the estimation of petrophysical properties will be more accurate when the projection width is much narrower. For example, the isosurfaces in Fig. 3 denote a rock property with a P-wave impedance value $IP = 2.937 \text{ km/s} \cdot \text{g/cm}^3$, Poisson's ratio value $PR = 0.4764$ and the logarithm of resistivity value $\log_{10}(R_t) = 0.2833 \text{ } \Omega\text{-m}$. The constraints placed on porosity by P-wave impedance are stronger than those imposed by the other two parameters. The constraint of resistivity on hydrate saturation is stronger, with a narrower projection width on the x -axis.

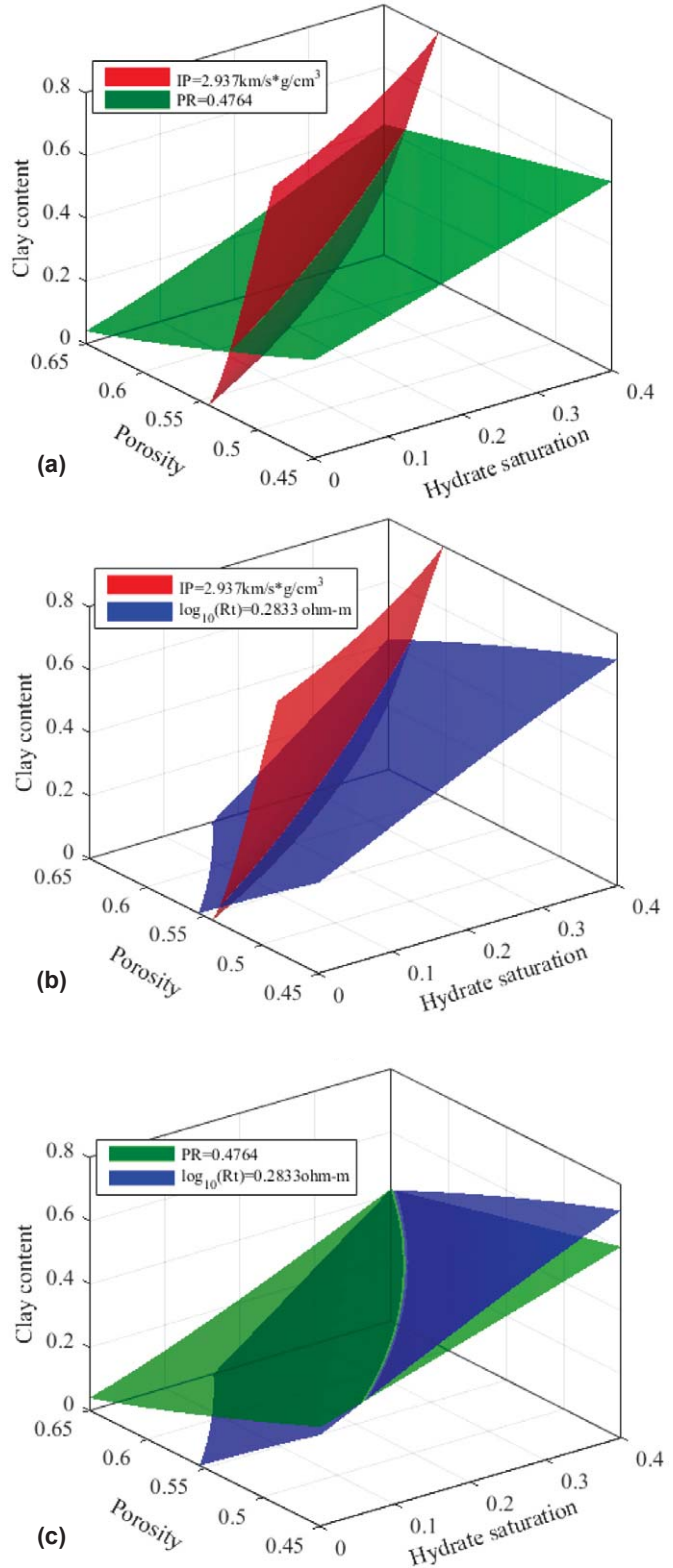


Fig. 3—Intersection of three different isosurfaces. (a) The intersection of P-wave impedance (IP) and Poisson's ratio (PR), (b) the intersection of P-wave impedance and the logarithm of the resistivity $\log_{10}(R_t)$, and (c) the intersection of Poisson's ratio and the logarithm of resistivity.

Search of Intersection Point

Figure 4a shows that the intersection of every two single-value isosurfaces produces an intersection line; three intersection lines will intersect at one stable point (marked by a green circle) (Fig. 4b). To obtain the optimal intersection point, we can perform an exhaustive search with the least-squares algorithm by solving the following equation:

$$IS_{IP}(S_{gh}, \phi, V_{sh}) = IS_{PR}(S_{gh}, \phi, V_{sh}) = IS_{\log_{10}(R_t)}(S_{gh}, \phi, V_{sh}), \quad (24)$$

Where $IS_{IP}(S_{gh}, \phi, V_{sh})$, $IS_{PR}(S_{gh}, \phi, V_{sh})$, and $IS_{\log_{10}(R_t)}(S_{gh}, \phi, V_{sh})$ refer to the single value isosurfaces of the P-wave impedance, Poisson ratio, and logarithm of resistivity, respectively. Through three intersections we can achieve three intersecting isolines, which provide us with all of the combinations of petrophysical properties. Only these isolines are needed to obtain a solution. Hence, the objective function is given by:

$$J_1 = \left\| IS_{IP}(S_{gh}, \phi, V_{sh}) - IS_{PR}(S_{gh}, \phi, V_{sh}) \right\|^2 + \left\| IS_{IP}(S_{gh}, \phi, V_{sh}) - IS_{\log_{10}(R_t)}(S_{gh}, \phi, V_{sh}) \right\|^2, \quad (25)$$

Then, we further reformulate the above misfit function as:

$$J_1 = (S_{gh,IP} - S_{gh,PR})^2 + (\phi_{IP} - \phi_{PR})^2 + (V_{sh,IP} - V_{sh,PR})^2 + (S_{gh,IP} - S_{gh,\log_{10}(R_t)})^2 + (\phi_{IP} - \phi_{\log_{10}(R_t)})^2 + (V_{sh,IP} - V_{sh,\log_{10}(R_t)})^2. \quad (26)$$

where $(S_{gh,IP}, \phi_{IP}, V_{sh,IP})$, $(S_{gh,PR}, \phi_{PR}, V_{sh,PR})$, and $(S_{gh,\log_{10}(R_t)}, \phi_{\log_{10}(R_t)}, V_{sh,\log_{10}(R_t)})$ are the possible point coordinates on the isosurfaces $IS_{IP}(S_{gh}, \phi, V_{sh})$, $IS_{PR}(S_{gh}, \phi, V_{sh})$, and $IS_{\log_{10}(R_t)}(S_{gh}, \phi, V_{sh})$, respectively. By minimizing the above objective function, we can acquire the coordinate of the intersection point (0.368, 0.621 and 0.416), which represents the predicted values for hydrate saturation, porosity and clay content for the given sets of P-wave impedance-Poisson ratio-logarithm of resistivity values (2.937, 0.4764 and 0.2833).

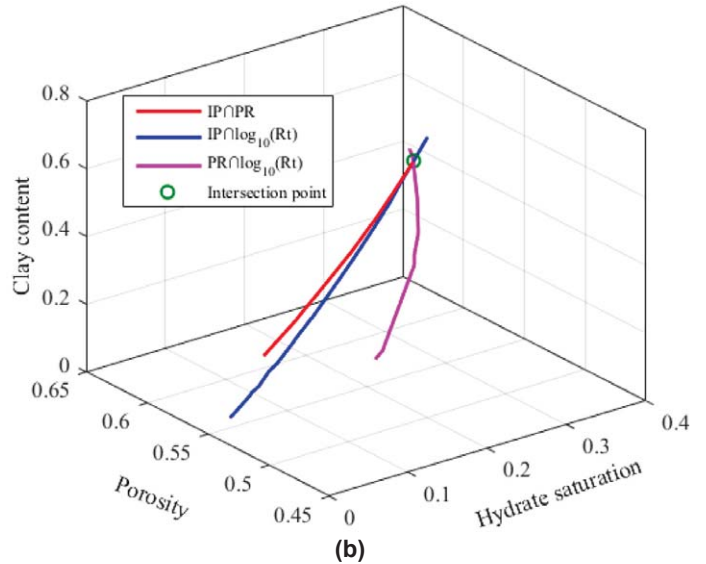
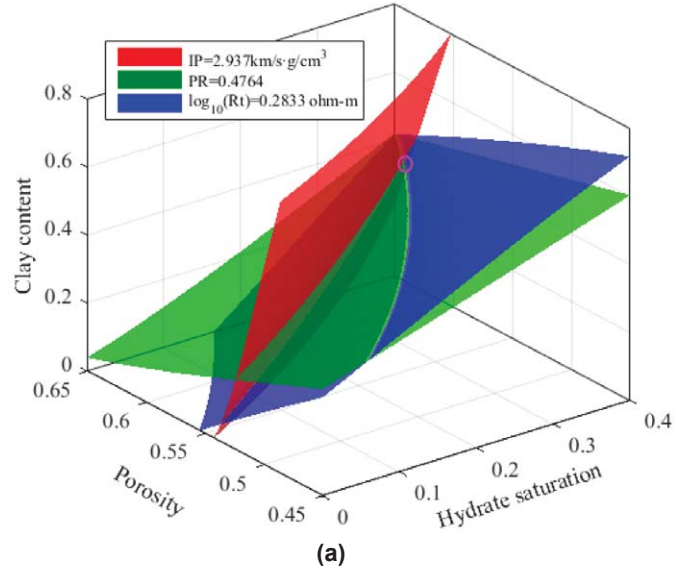


Fig. 4—The intersection of (a) three single-valued isosurfaces, and (b) and the intersection of three intersection lines. The isosurface for P-wave impedance corresponds to 2.937 km/s·g/cm³, while the Poisson's ratio and logarithm of resistivity are 0.4764 and 0.2833 Ω-m, respectively.

APPLICATION

The application section is divided into two parts: first, we validate our method using noise-free synthetic data (Example 1) to investigate its feasibility for the prediction of petrophysical properties. Second, we apply our method to a well-log dataset (Example 2) measured at ODP Hole 1247B in Hydrate Ridge.

Synthetic Example

We start by building an initial model that contains 54 points, and each point corresponds to hydrate saturation (10 to 30%), porosity (0.4 to 0.6) and clay content (10 to 50%) (Fig. 5). This allows us to calculate the synthetic datasets of P- and S-wave velocities and impedances, velocity ratio, density, Poisson's ratio and resistivity using EMT and MAE models. Then, Eqs. 19 and 20 can be used to evaluate the mean orthogonality factors for different input data combinations. Figure 6 reveals that, in this case, the combination of IP , PR , and R_p in general, provides the most stable solutions, while a combination of V_p , V_s , and V_p/V_s provides the least stable solutions. Additionally, combining IP , PR , and R_i is only slightly poorer than using of IP , PR , and R_r . This is mainly because different input information, such as, of IP , PR , and R_p , can effectively keep a strongly nonlinear relationship with petrophysical properties. Finally, we use the synthetic P-wave impedance, Poisson's ratio and logarithm of resistivity as input data for forecasting the petrophysical properties using the IRPM method.

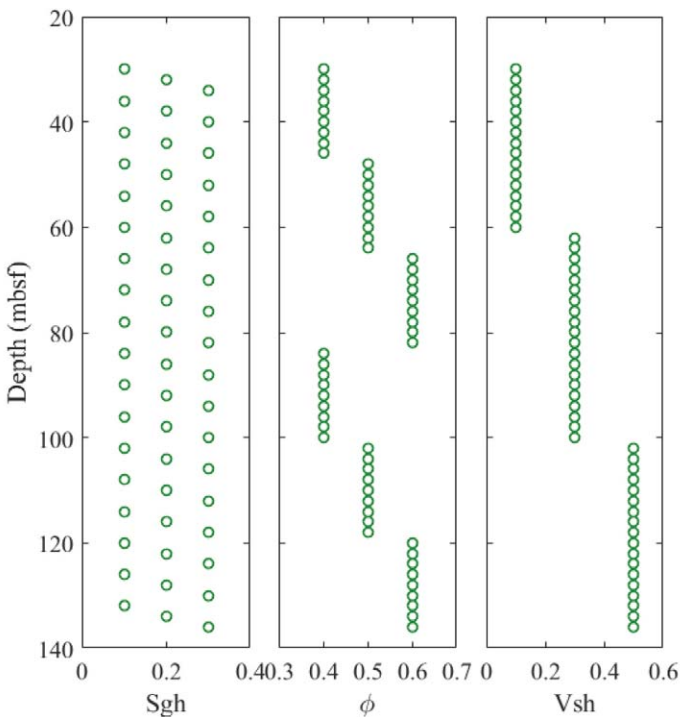


Fig. 5—Synthetic model with variations of hydrate saturation, porosity and clay content. The unit of depth is meters below sea floor (mbsf).

Figure 7 shows the comparison of the IRPM results from the input data with free noise and with $\pm 5\%$ perturbations. To validate the performance of this inversion method, we also calculate the root-mean-square (RMS) errors of inverted petrophysical properties for three sets of input data, as shown

in Fig. 8. It can be found that the estimations predicted from noise-free input data show a fairly good match with the initial model parameters. Moreover, the results from the noisy input data ($\pm 5\%$ change) show that the inverted porosity is much more robust compared with clay content and hydrate saturation. It is predominately due to the fact that the three inputs are highly correlated with porosity and clay content, which makes them constrained with each other for the predictions. Since the hydrate saturation is strongly sensitive to resistivity and insensitive to S-wave velocity, which will cause large error in the prediction when using the noisy P-wave impedance and Poisson's ratio as the input data. Overall, the IRPM method not only allows us to predict the petrophysical properties by integrating the elastic and electrical properties, but also provides us a strategy to evaluate the corresponding uncertainties of the estimation.

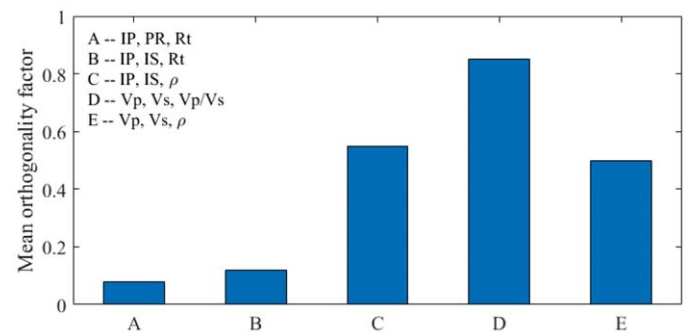


Fig. 6—Comparison of mean orthogonality factors for different input data combinations.

Field Example

To further verify the ability of our proposed method to estimate petrophysical properties, we apply it to the gas-hydrate-bearing sediments at ODP Hole 1247B, Hydrate Ridge (Trehu et al., 2003). For the bottom-simulating reflector (BSR) located at 128 mbsf (Trehu et al., 2006), we choose to focus on the gas-hydrate stability zone extending from 85 to 125 mbsf. We assume that the matrix of the gas-hydrate formation consists of sand and clay, and the pore space is only saturated with gas hydrates and water. For the selected site, ODP Hole 1247, conventional wireline logs and logging-while-drilling logs are available (Shipboard Scientific Party, 2003). For this study, we use the conventional wireline logs from Hole 1247B. The well-logging data in our studied zone mainly include P- and S-wave velocities, density, resistivity and gamma-ray (GR) measurements. To calibrate the rock physics models, we construct 3D logarithmic resistivity-P-wave impedance-Poisson's ratio RPTs and adjust the modeling parameters to harmonize the RPTs with the projected data clouds (Fig. 9). The colored legends in Figs. 9a and 9b represent the hydrate saturation

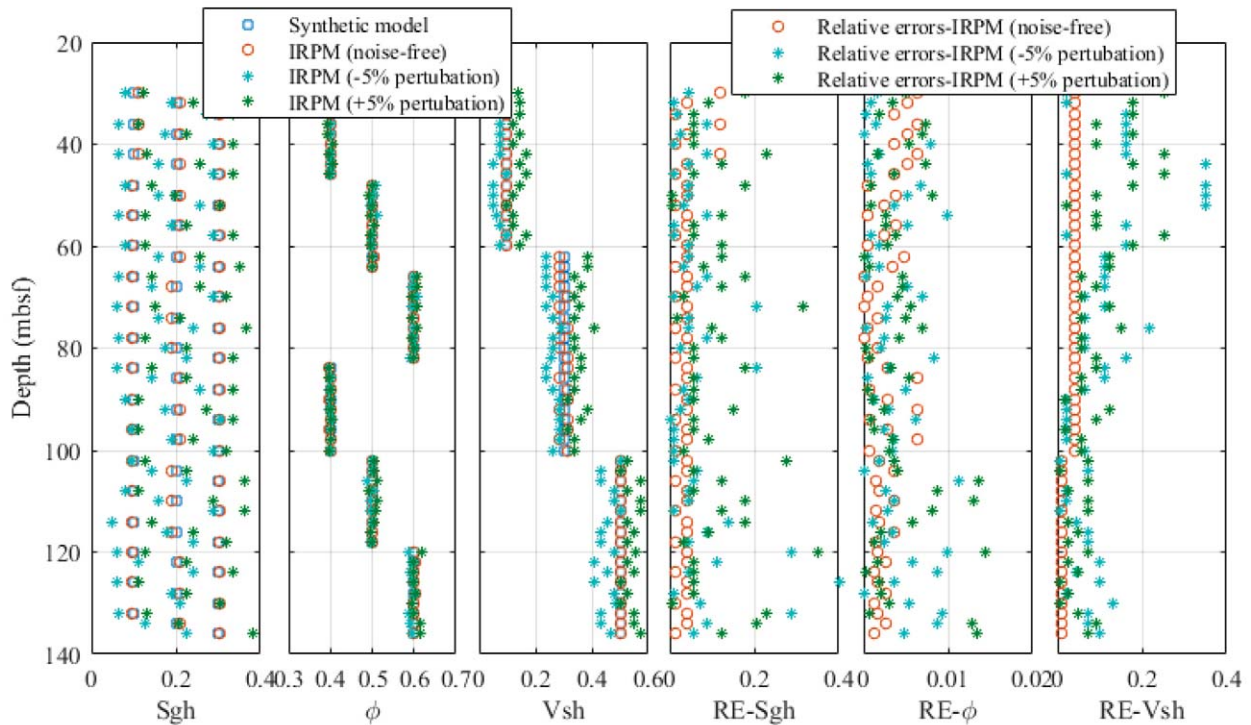


Fig. 7—Reservoir parameter solutions and relative errors (REs) produced from P-wave impedance (IP), Poisson’s ratio (PR), and logarithmic resistivity ($\log_{10}(R_t)$) using IRPM method. The model parameters are symbolized by blue squares and the inverted solutions from noise-free input data are denoted by red circles. The cyan and green stars represent the inverted results with $\pm 5\%$ perturbations in the input data.

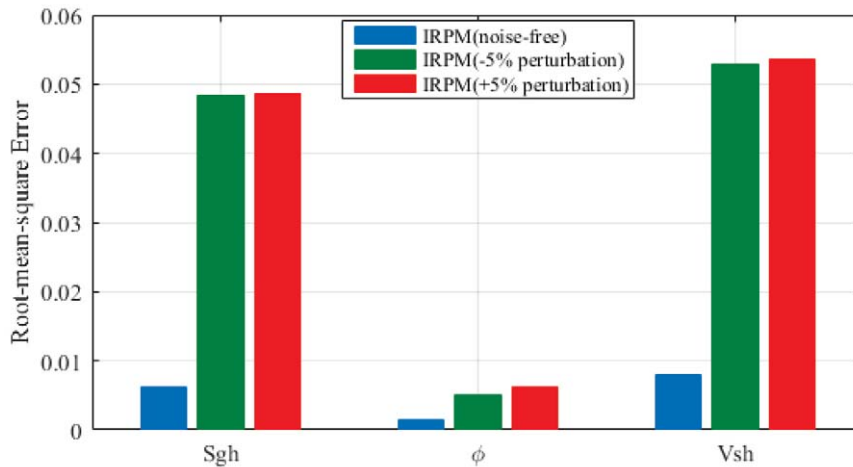


Fig. 8—The RMS deviations for the inverted petrophysical properties with three different sets of input data.

interpreted from resistivity and the porosity derived from density, respectively. By comparing the measured data with the 3D RPTs, we obtain the parameters associated with the two models. For EMT, the critical porosity and coordination number are 0.4 and 4, respectively. For MAE, the tortuosity factor is 1.05, the cementation exponent is 2.4, and the saturation exponent is 1.9386. Here, $0.4 \Omega\text{-m}$ was used for R_w based on a salinity of 35 ppt, a geothermal gradient of $53^\circ\text{C}/$

km and an inferred seafloor temperature of 4.26°C (Shipboard Scientific Party, 2003). Moreover, Fig. 9 indicates that the gas-hydrate saturation ranges from 0 to 40%, the porosity varies between 0.4 and 0.7, and the clay content falls to 30 and 90% for Hole 1247B. We can take advantage of these estimated ranges as the effective boundary conditions of the x -, y -, and z -axes in the reservoir parameter domain for the application of IRPM.

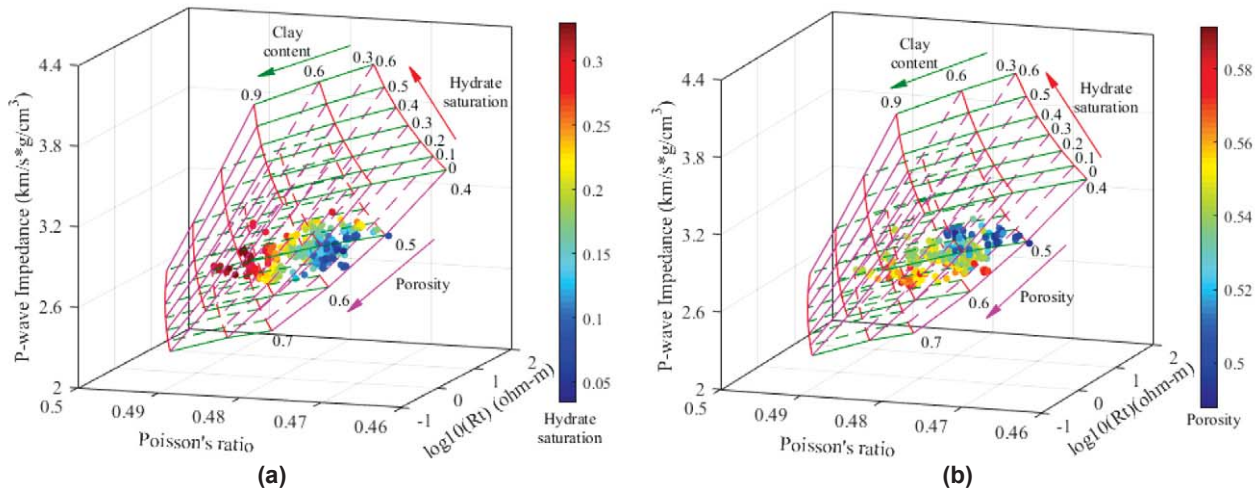


Fig. 9—3D rock physics template of P-wave impedance, Poisson's ratio, logarithm of resistivity ($\log_{10}(R_t)$) versus hydrate saturation, porosity and clay content. The superposed data are well-log data from ODP Hole 1247B. The different colors refer to (a) hydrate saturation, and (b) and porosity interpreted from resistivity and density logs, respectively.

Figure 10 shows the comparison of the elastic and electrical properties computed from the elastic and electrical models with the actual measurements and the inversion results (green lines) of the well-log data and their corresponding references, including core data (blue dots) and other previous interpretations (red lines) (Guerin et al., 2006) of Hole 1247B. The left three panels are the measured and simulated P-wave impedance, Poisson's ratio and logarithm of resistivity, while the right three panels are the predicted hydrate saturation, porosity and clay content and their corresponding references. Here, the reference hydrate saturations are derived from P- and S-wave velocities with CCT or resistivity with Archie's equation, as well as chloride data (yellow dots) (Shipboard Scientific Party, 2003). The hydrate saturation calculated from chloride data using the equation $S_{gh} = 1/\rho_{gh} \cdot (1 - Cl_{pw}/Cl_{sw})$ (Yuan et al., 1996), where Cl_{pw} is the measured chloride concentration and Cl_{sw} is the in situ baseline pore-water chlorinity which can be determined by smoothly fitting the chloride data with a second degree polynomial of depth (Wang et al. 2011). The reference porosities are calculated from density and derived from moisture and density (MAD) samples (Shipboard Scientific Party, 2003). The reference clay values were obtained from X-ray diffraction (XRD) data (Shipboard Scientific Party, 2003) and from GR log data using the standard equation $V_{sh} = (GR_{log} - GR_{min}) / (GR_{max} - GR_{min})$, where GR_{log} is the measured GR log value at any given depth, and GR_{max} and GR_{min} are the maximum and minimum GR log values.

In general, the simulated data match well with the measured data, suggesting that a good convergence between elastic and electrical data. Also, we can further visualize that the analysis results based on core data are largely consistent with our inversion with the exception of a deviation associated with free gas around 110 mbsf; the P-wave velocity and Poisson's ratio decrease, while the resistivity increases. The inverted hydrate saturation falls among the results derived using only elastic properties and only electrical properties. This means that the use of the elastic properties or electrical properties alone is a less effective method for evaluating gas-hydrate saturation. Also, the clay content calculated only from the gamma-ray measurements will result in large errors in the highly unconsolidated marine sediment. Furthermore, to make the comparison more intuitive, we generate the crossplots between inversion results and the corresponding reference values (Fig. 11). In addition, we calculate the correlation coefficients and the RMS errors for each petrophysical properties. Usually, the higher correlation coefficients and lower RMS coefficients represent the smaller difference between the inverted results and the referenced predictions. The correlation coefficients between inverted results and core data at given depths are generally much higher than those predicted from single elastic or electrical properties. Based on the statistical analysis of correlation coefficients and RMS errors, we can conclude that this inversion approach enables us to achieve more accurate petrophysical properties from the elastic and electrical properties.

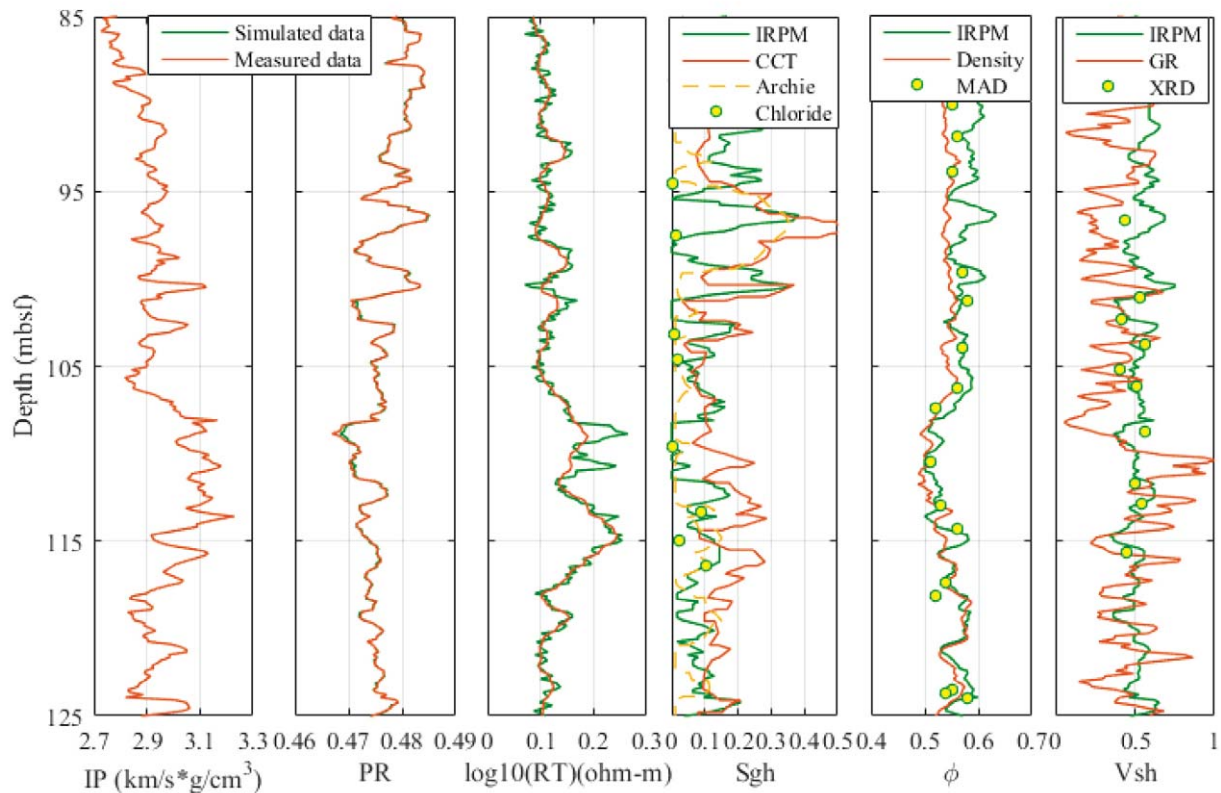


Fig. 10—Inversion results using the IRPM method. From left to right: P-wave impedance (IP), Poisson's ratio (PR), logarithm of resistivity ($\log_{10}(R_t)$), hydrate saturation (S_{gh}), porosity (ϕ) and clay content (V_{sh}) at ODP Hole 1247B. The red and green lines represent measured data and simulated results in left three panels. The inverted results from the RPT1 method are denoted by green lines in the right three panels. Results obtained using previous interpretation results as references are shown for comparison (hydrate saturation calculated from CCT (Guerin et al., 2006) in red line, from Archie's equation (Guerin et al., 2006) in yellow dashed line with electrical resistivity, from chloride data in yellow dots; porosity obtained from density log in red line, and from MAD in yellow dots; clay content computed from gamma ray in red line and from XRD in yellow dots.).

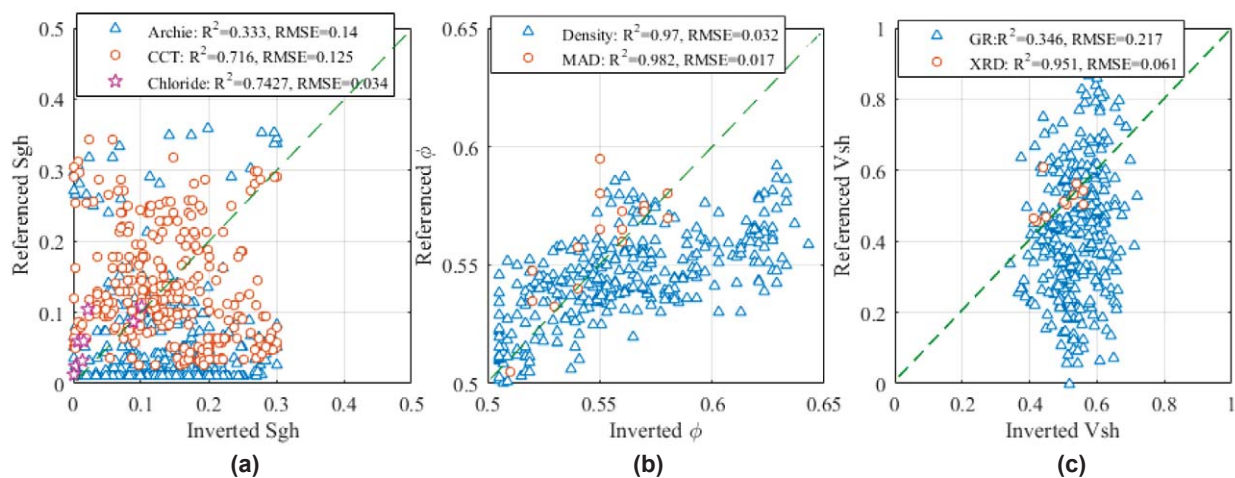


Fig.11—Crossplots between inversion results of petrophysical properties and the corresponding reference values. (a) hydrate saturation (S_{gh}), (b) porosity, and (c) clay content.

DISCUSSION

Recently, two main methods for reservoir characterization using rock physics inversion have been the

focus of much attention: IRPM (Johansen et al., 2013) and 3D RPT inversion (Li et al., 2018; Pan et al., 2019b, 2019c). Although both methods can be used for the simultaneous inversion of petrophysical properties in the 3D spatial

domain, there are several important differences. First, the IRPM method performs the estimation in the reservoir parameter domain, but the 3D RPT inversion is performed in the elastic (-electrical) data domain. Second, the former method exhaustively searches the intersection point of three isosurfaces by using the least-squares algorithm to minimize the objective function of 3D coordinates from different isosurfaces, while the latter method can realize its estimation by using the grid-searching method to look for the minimum distance between the projected data and the adjacent node. Finally, the IRPM method can be impacted by the predefined error, the number of nodes and the sensitivity between input data and petrophysical properties, as well as the established objective function, whereas estimations produced using the RPT inversion are dominated by the presetting minimum interval between two adjacent nodes, the sensitivity between input data and petrophysical properties and the chosen model.

IRPM is used to find the intersection point (best inverse solution) exhaustively from the three isosurfaces (all possible solutions) extracted from the 3D rock physics constraints using the iterative least-squares algorithm. It is noteworthy that, unlike the conventional gradient-based inversion method, IRPM avoids calculating the Jacobian matrix, which requires much more run time and enough storage capacity, especially for the high-dimensional inverse problem. Based on the synthetic example and real application discussed above, it is clear that the IRPM method is effective for the quantitative interpretation of the petrophysical properties of gas-hydrate-bearing sediments. However, the application of the IRPM method may lead to no solution or more than one solution; therefore, the effective introduction of prior information is of great importance for this strategy. Liu et al. (2017) demonstrated that the inverse rock physics modeling can improve the accuracy of the estimations when adding the constraint information in the objective function. To further improve the computation speed and reduce the risk of no solution or multiple solutions, we can also take advantage of the estimations from 3D RPT as constraints for the prediction of petrophysical properties from IRPM. In addition, the extended IRPM method can be developed for the estimation of high-dimensional petrophysical properties with multiple input datasets.

We predict the intersection point of the three isosurfaces by constructing the objective function (Eq. 12). However, the form of the objective function may play a key role in calculating the speed and the stability and accuracy of the solution. Hence, it is necessary to build the appropriate misfit function to quickly search for the stable and accurate intersection point. For example, we not only establish the

function with the intersection of three isolines achieved by intersecting any two of the three isosurfaces, but also build it with the intersection of one isosurface and one isoline, which is obtained from the intersection of the other two isosurfaces. The objective function can be expressed as:

$$J_2 = \left\| IL_{IP,PR} - IS_{\log_{10}(R_t)} \right\|^2, \quad (27)$$

where the isoline $IL_{IP,PR}$ denotes the intersection of isosurfaces IS_{IP} and IS_{PR} . In addition to above two objective functions, we can also establish the objective function as:

$$J_3 = \left\| IL_{IP,PR} - IL_{IP,\log_{10}(R_t)} \right\|^2. \quad (28)$$

where the isoline $IL_{IP,\log_{10}(R_t)}$ signifies the intersection of isosurfaces IS_{IP} and $IS_{\log_{10}(R_t)}$. This function requires us to calculate the arbitrary two isolines from the extracted three isosurfaces, and then obtain the intersection point by intersecting the two isolines.

To investigate the calculation efficiency and accuracy for three different objective functions, we now use the noise-free synthetic log data generated by synthetic models in Fig. 5 to invert the petrophysical properties with the parallel calculation (Intel Core 4 and 16 GB RAM). Then, we compare the inversion results based on different objective functions shown in Fig. 12. Interestingly, the hydrate saturation is more stable than other two parameters with different objective functions, which might be attributed to the high sensitivity of hydrate saturation to resistivity. Moreover, we calculate the RMS errors of inversion results (Fig. 13) and evaluate the computational efficiency (Fig. 14). The results demonstrate that searching the intersection point by directly intersecting three isosurfaces is more time consuming than those by intersecting one isoline and one isosurface or two isolines, but it is more accurate than the other two cases. Even though the computational speed improved a lot for the intersection of two isolines, the accuracies of the results, such as porosity and clay content, are heavily reduced. It is most likely to be caused by the larger cumulative error. For the intersection of one isoline and one isosurface, although the accuracy of inversion results, especially clay content, is less than that from directly intersecting three isosurfaces, the computational speed has been largely improved. Consequently, the objective function for intersecting on isoline and one isosurface will be a good choice for the prediction of petrophysical properties from prestack seismic inversion results, whereas the direct intersection of three isosurfaces is recommended when performing the predictions from well logging measurements.

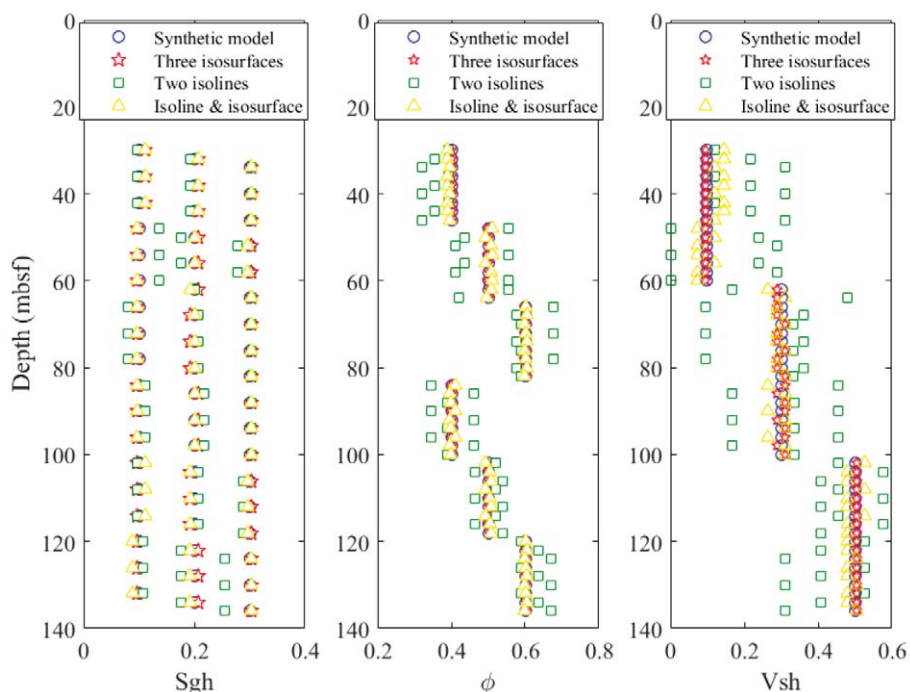


Fig. 12—Comparison between real model parameters and inversion results for three different objective functions.

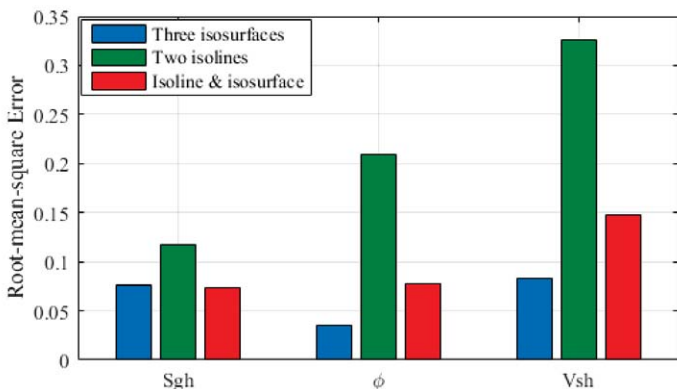


Fig. 13—The RMS errors for the inversion results of petrophysical properties with three different objective functions.

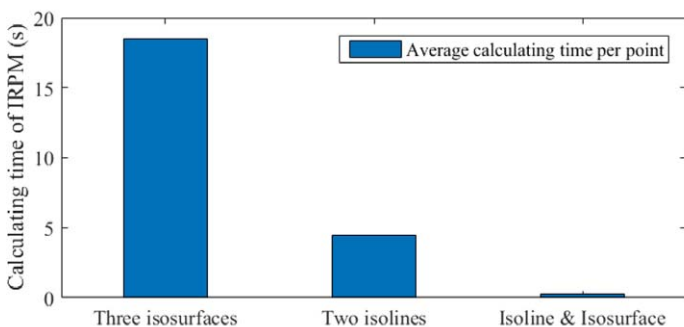


Fig. 14—The average calculation speeds of three different objective functions for performing IRPM with the synthetic logs data.

Seismic data have been widely used for hydrocarbon exploration, but it is not equally reliable for fluid saturation discrimination. We have seen this effect from the comparison between the joint inversion results (e.g., hydrate saturation) and interpretations from elastic properties alone in the field example. By introducing the electrical properties, we have shown that the IRPM predictions of petrophysical properties, especially hydrate saturation, are better constrained than those from elastic properties alone or electrical resistivity alone. Thus, we can extend our approach to the joint inversion of seismic-derived elastic properties and electromagnetic-derived electrical properties in future work.

CONCLUSIONS

In this paper, we have presented a new joint inversion strategy based on the IRPM to invert elastic and electrical data for predicting petrophysical properties in gas-hydrate-bearing sediments. This technique uses suitable elastic and electrical rock physics models to generate the 3D constraint cubes and obtains the intersection point by intersecting the extracted isosurfaces for the given measured elastic and electrical data. A good match between the inversion results and core samples with lower RMS errors (less than 0.061) at ODP Hole 1247B suggests that this approach is feasible to accurately delineate gas-hydrate-bearing sediments by integrating elastic and electrical data.

ACKNOWLEDGEMENTS

This work is supported by the Scientific Research & Technology Development Project of China National Petroleum Corporation (2018D-4305), Basic Research and Strategic Reserve Technology Funds for Affiliated Institutions of China National Petroleum Corporation (2018D-500811) and China Scholarship Council (201805150004). We are grateful to Dr. James Jennings Howard and other three anonymous reviewers for their constructive comments. We would like to acknowledge Research Institute of Petroleum Exploration and Development for the permission to publish this work.

NOMENCLATURE

Abbreviations

BSR = bottom-simulating reflector
 CCT = contact cementation theory
 EMT = effective medium theory
 GR = gamma ray
 IL = intersection line
 IP = P-wave impedance
 IRPM = inverse rock physics modeling
 IS = single-value isosurface
 MAD = moisture and density
 MAE = modified Archie equation
 mbsf = meter below seafloor
 MOF = mean orthogonality factor
 PR = Poisson's ratio
 RAM = random access memory
 RPT = rock physics template
 SCA-DEM = self-consistence approximation-differential equivalent model
 STPE = simplified three-phase equation
 TPBE = three-phase Biot-type equation
 XRD = X-ray diffraction

Symbols

a = tortuosity factor
 Cl_{pw} = measured chloride concentration
 Cl_{sw} = in-situ baseline pore water chlorinity
 $d_{1,2}$ = two input data
 d_{obs} = measured (observed) data
 f_{gh} = volume fraction of gas hydrate in the matrix
 f_i = volume fraction of the i th mineral constituent
 G_{dry} = shear modulus of dry rock
 G_{gh} = shear modulus of gas hydrate
 G_{ma} = shear modulus of matrix
 G_{HM} = effective shear modulus calculated from Hertz-Mindlin theory
 G_i = shear modulus of the i th mineral constituent
 G_s = shear modulus of solid phase

G_{sat} = shear modulus of saturated rock
 $J_{1,2,3}$ = objective functions
 K_{dry} = bulk modulus of dry rock
 K_{fl} = bulk modulus of fluid
 K_{gh} = bulk modulus of gas hydrate
 K_{HM} = effective bulk modulus calculated from Hertz-Mindlin theory
 K_i = bulk modulus of the i th mineral constituent
 K_{ma} = bulk modulus of matrix
 K_s = bulk modulus of solid phase
 K_{sat} = bulk modulus of saturated rock
 K_w = bulk modulus of water
 L_m = number of grids in reservoir domain
 L_φ = number of values of the measured data
 m = cementation exponent
 n = saturation exponent
 $OF_{d1,d2}$ = orthogonality factor for two input data
 P = effective pressure
 R_{sh} = clay resistivity
 R_t = resistivity of sediments
 R_w = formation water resistivity
 S_{gh} = gas-hydrate saturation
 \mathbf{V} = P-wave velocity
 V_p/V_s^p = ratio of P-wave and S-wave velocity
 V_s = S-wave velocity
 V_{sh} = clay content
 ρ_b = bulk density
 ρ_{gh} = density of gas hydrate
 ρ_s = density of sand
 ρ_{sh} = density of clay
 ρ_w = density of water
 ϕ = porosity
 ϕ_c = critical porosity
 ϕ_r = reduced porosity
 φ = discretely sampled constraint cube
 φ_j = continuous scalar field function
 ν_{ma} = Poisson's ratio of matrix
 $\log_{10}(R_t)$ = logarithm of resistivity
 ∇_s^d = normalized gradient vectors of two single-value isosurfaces

REFERENCES

- Archie, G.E., 1942, The Electric Resistivity Log as an Aid in Determining Some Reservoir Characteristics, Paper SPE-942054-G, *Transactions, AIME*, **146**, 54–62. DOI: 10.2118/942054-G.
- Avseth, P.A., Mukerji, T., and Mavko, G., 2005, *Quantitative Seismic Interpretation*, Cambridge University Press. ISBN: 978-0511600074.
- Bredesen, K., Jensen, E.H., Johansen, T.A., and Avseth, P., 2015, *Quantitative Seismic Interpretation Using Inverse Rock*

- Physics Modelling, *Petroleum Geoscience*, **21**(4), 271–284. DOI: 10.1144/petgeo2015-006.
- Bredesen, K., 2016, On Integration of Rock Physics in Quantitative Seismic Interpretation, Unpublished PhD Dissertation, University of Bergen. <http://hdl.handle.net/1956/15679>. Accessed November 22, 2019.
- Carcione, J.M., and Tinivella, U., 2000, Bottom-Simulating Reflectors: Seismic Velocities and AVO Effects, *Geophysics*, **65**(1), 54–67. DOI: 10.1190/1.1444725.
- Clavier, C., Coates, G., and Dumanoir, J., 1984, Theoretical and Experimental Bases for the Dual-Water Model for Interpretation of Shaly Sands, Paper SPE-6859, *SPE Journal*, **24**(2), 153–168. DOI: 10.2118/6859-PA.
- Cook, A.E., 2010, Gas Hydrate-Filled Fracture Reservoirs on Continental Margins, unpublished PhD dissertation, Columbia University. <https://pdfs.semanticscholar.org/d30e/d9829b768c747fe0e36b7b6fa2df1470b7bf.pdf>. Accessed November 22, 2019.
- Dvorkin, J., and Nur, A., 1996, Elasticity of High-Porosity Sandstones: Theory for Two North Sea Data Sets, *Geophysics*, **61**(5), 1363–1370. DOI: 10.1190/1.1444059.
- Dvorkin, J., Nur, A., and Yin, H., 1994, Effective Properties of Cemented Granular Materials, *Mechanics of Materials*, **18**(4), 351–366. DOI: 10.1016/0167-6636(94)90044-2.
- Dvorkin, J., Prasad, M., Sakai, A., and Lavoie, D., 1999, Elasticity of Marine Sediments: Rock Physics Modeling, *Geophysical Research Letters*, **26**(12), 1781–1784. DOI: 10.1029/1999GL900332.
- Ellis, M.H., 2008, Joint Seismic and Electrical Measurements of Gas Hydrates in Continental Margin Sediments, unpublished PhD Dissertation, University of Southampton. <https://eprints.soton.ac.uk/id/eprint/63293>. Access November 22, 2019.
- Gassmann, F., Maggiorini, M., Städler, E., and Winkler, W., 1951, *Verteljahrsschrift Der Naturforschenden Gesellschaft in Zurich, Uber Die Elastizitat Poroser Medien*, **96**, 1–23.
- Gomez, C.T., and Dvorkin J., 2007, Feasibility of Reserve Estimate From Combined Elastic and Resistivity Data, *SEG Technical Program Expanded Abstracts*, 1475–1479. DOI: 10.1190/1.279776.
- Guerin, G., Goldberg, D.S., and Collett, T.S., 2006, Sonic Velocities in an Active Gas Hydrate System, Hydrate Ridge, in Trehu, A.M., Bohrmann, G., Torres, M.E., and Colwell, F.S., Editors, *Proceedings, Ocean Drilling Program Scientific Results*, **204**, 1–38. DOI: 10.2973/odp.proc.sr.204.124.2006.
- Hashin, Z., and Shtrikman, S., 1963, A Variational Approach to the Theory of the Elastic Behaviour of Multiphase Materials, *Journal of The Mechanics and Physics of Solids*, **11**(2), 127–140. DOI: 10.1016/0022-5096(63)90060-7.
- Helgerud, M.B., Dvorkin, J., Nur, A., Sakai, A., and Collett, T., 1999, Elastic-Wave Velocity in Marine Sediments With Gas Hydrates: Effective Medium Modeling, *Geophysical Research Letters*, **26**(13), 2021–2024.
- Hill, R., 1952, The Elastic Behaviour of a Crystalline Aggregate, *Proceedings of the Physical Society, Section A*, **65**(5), 349. DOI: 10.1088/0370-1298/65/5/307.
- Jensen, E.H., 2011, Methods for Improved Prediction of Elastic, Electrical and Reservoir Properties, unpublished PhD dissertation, University of Bergen. <http://hdl.handle.net/1956/5192>. Accessed November 22, 2019.
- Johansen, T.A., Jensen, E.H., Mavko, G., and Dvorkin, J., 2013, Inverse Rock Physics Modeling for Reservoir Quality Prediction, *Geophysics*, **78**(2), M1-M18. DOI: 10.1190/geo2012-0215.1.
- Johansen, T.A., Spikes, K., and Dvorkin, J., 2004, Strategy for Estimation of Lithology and Reservoir Properties From Seismic Velocities and Density, *SEG Technical Program Expanded Abstracts*, 1726–1729. DOI: 10.1190/1.184516.
- Lee, M.W., 2005, *Proposed Moduli of Dry Rock and Their Application to Predicting Elastic Velocities of Sandstones*, US Geological Survey Scientific Investigations Report, 2005-5119. <https://pubs.usgs.gov/sir/2005/5119/pdf/SIR-2005-5119.pdf>. Accessed November 22, 2019.
- Lee, M.W., 2011, *Connectivity Equation and Shaly-Sand Correction for Electrical Resistivity*, US Geological Survey Scientific Investigations Report, 2011-5005. <https://pubs.usgs.gov/sir/2011/5005/downloads/SIR11-5005.pdf>. Accessed November 22, 2019.
- Lee, M.W., and Collett, T.S., 2006, *A Method of Shaly Sand Correction for Estimating Gas Hydrate Saturations Using Downhole Electrical Resistivity Log Data*, US Geological Survey Scientific Investigations Report, 2006-5121. DOI: 10.2122/sir20065121. https://pubs.usgs.gov/sir/2006/5121/pdf/sir5121_508.pdf. Accessed November 22, 2019.
- Lee, M.W., and Collett, T.S., 2009, Gas Hydrate Saturations Estimated From Fractured Reservoir At Site NGHP-01-10, Krishna-Godavari Basin, India, *Journal of Geophysical Research: Solid Earth*, **114**(B07102), 1–13. DOI: 10.1029/2008.JB006237.
- Lee, M.W., Hutchinson, D.R., Collett, T.S., and Dillon, W.P., 1996, Seismic Velocities for Hydrate-Bearing Sediments Using Weighted Equation, *Journal of Geophysical Research: Solid Earth*, **101**(B9), 20347–20358. DOI: 10.1029/96JB01886.
- Lee, M.W., and Waite, W.F., 2008, Estimating Pore-Space Gas Hydrate Saturations From Well Log Acoustic Data, *Geochemistry, Geophysics, Geosystems*, **9**(7), 1–8. DOI: 10.1029/2008GC002081.
- Li, H.B., and Zhang, J.J., 2018, Well Log and Seismic Data Analysis for Complex Pore-Structure Carbonate Reservoir Using 3D Rock Physics Templates, *Journal of Applied Geophysics*, **151**, 175–183. DOI: 10.1016/j.jappgeo.2018.02.017.
- Liu, Q., Dong, N., Ji, Y.X., and Chen, T.S., 2017, Reservoir Parameter Prediction Based on a Constrained Inverse Rock Physics Modeling Method, *SEG Global Meeting Abstracts*, 1225–1228. DOI: 10.1190/IGC2017-311.
- Liu, Q., Yin, X. and Li, C., 2015, Fluid Discrimination Based on Rock Physics Templates, *Journal of Geophysics and Engineering*, **12**(5), 830–838. DOI: 10.1088/1742-2132/12/5/830.
- Liu, Q., Yin, X., and Li, C., 2016, Quantitative Prediction of Reservoir Characteristics Based on Inverse Modeling Theory, *Chinese Journal of Geophysics (In Chinese)*, **59**(9), 3491–

3502. DOI: 10.6038/cjg20160931.
- Lorensen, E., and Cline E., 1987, Marching Cubes: A High-Resolution 3D Surface Construction Algorithm, *Computer Graphics*, **21**(4), 163–169. DOI: 10.1145/37401.37422.
- Mindlin, R.D., 1949, Compliance of Elastic Bodies in Contact, *Journal of Applied Mechanics*, **16**, 259–268.
- Moyano, B., Jensen, E.H., and Johansen, T.A., 2011, Improved Quantitative Calibration of Rock Physics Models, *Petroleum Geoscience*, **17**, 345–354. DOI: 10.1144/1354-079311-028.
- Moyano, B., Jensen, E.H., and Johansen, T.A., 2015, Spatial Constrained Inverse Rock Physics Modelling, *Geophysical Prospecting*, **63**, 183–191. DOI: 10.1111/1365-2478.12178.
- Pan, H.J., Li, H.B., Grana, D., Zhang, Y., Liu, T.Y., and Geng, C., 2019a, Quantitative Characterization of Gas Hydrate Bearing Sediment Using Elastic-Electrical Rock Physics Models, *Marine and Petroleum Geology*, **105**, 273–283. DOI: 10.1016/j.marpetgeo.2019.04.034.
- Pan, H.J., Li, H.B., Zhang, Y., and Cai, S.J., 2019b, 3D Elastic-Electrical Rock Physics Template Inversion for Reservoir Parameters of Gas Hydrate Bearing Sediment, Paper Th_R14_02 presented at the 81st EAGE Conference and Exhibition. DOI: 10.3997/2214-4609.201901639.
- Pan, H.J., Li, H.B., Chen, J.Y., Zhang, Y., Liu, X.B., Cai, S.J., and Cao, C., 2019c, Evaluation of Gas Hydrate Resources Using Hydrate Morphology-Dependent Rock Physics Templates, *Journal of Petroleum Science and Engineering*, **182**, 106268, 1–16. DOI: 10.1016/j.petrol.2019.10628.
- Pride, S.R., Berryman, J.G., and Harris, J.M., 2004, Seismic Attenuation due to Wave-Induced Flow, *Journal of Geophysical Research: Solid Earth*, **109**(B1), 1–19. DOI: 10.1029/2003JB002639.
- Sava, D.C., and Hardage, B.A., 2007, Gas-Hydrate Concentration and Uncertainty Estimation From Electrical-Resistivity Logs: Examples From Green Canyon, Gulf of Mexico, *SEG Technical Program Expanded Abstracts*, 1579–1583. DOI: 10.1190/1.2792797.
- Shipboard Scientific Party, 2003, Leg 204 Summary, in Tréhu, A.M., Bohrmann, G., Rack, F.R., Torres, M.E., et al., *Proceedings of the Ocean Drilling Program, Initial Reports*, **204**, 1–75. http://www-odp.tamu.edu/publications/204_IR/VOLUME/CHAPTERS/IR204_01.PDF. Accessed November 22, 2019.
- Simandoux, P., 1963, Dielectric Measurements in Porous Media and Application to Shaly Formation, *Revue De L' Institut Français Du Pétrole*, **18**, Supplementary Issue, 193–215.
- Sloan, E.D., Brewer, P.G., Paull, C.K., Collett, T.S., Dillon, W.P., Holbrook, W.S., and Kvenvolden, K.A., 1999, Future of Gas Hydrate Research, *Eos, Transactions American Geophysical Union*, **80**(22), 247–249. <https://agupubs.onlinelibrary.wiley.com/doi/pdf/10.1029/99EO00184>. Accessed November 22, 2019.
- Tréhu, A.M., Bohrmann, G., Rack, F.R., Torres, M.E., et al., 2003, *Proceeding of the Ocean Drilling Program, Initial Reports*, **204**. http://www-odp.tamu.edu/publications/204_IR/VOLUME/CHAPTERS/IR204_01.PDF. Accessed November 22, 2019.
- Tréhu, A.M., Torres, M.E., Bohrmann, G., Colwell, F., 2006, Leg 204 Synthesis: Gas Hydrate Distribution and Dynamics in the Central Cascadia Accretionary Complex, in Tréhu, A.M., Torres, M.E., Bohrmann, G., Colwell, F., Editors, *Proceedings of the Ocean Drilling Program, Scientific Results*, **204**, 1–40. DOI: 10.2973/odp.proc.sr.204.101.2006.
- Wang, X., Hutchinson, D.R., Wu, S., Yang, S., and Guo, Y., 2011, Elevated Gas Hydrate Saturation Within Silt and Silty Clay Sediments in the Shenhu Area, South China Sea, *Journal of Geophysical Research: Solid Earth*, **116**(B5), 1–18. DOI: 10.1029/2010JB007944.
- Waxman, M.H., and Smits, L.J.M., 1968, Electrical Conductivities in Oil-Bearing Shaly Sands, Paper SPE-1863-A, *SPE Journal*, **8**(2), 107–122. DOI: 10.2118/1863-A.
- Wood, A.B., 1941, A Textbook of Sound, Bell and Sons, London.
- Wyllie, M.R.J., Gregory, A.R., Gardner, G.H.F., 1958, An Experimental Investigation of Factors Affecting Elastic Wave Velocities in Porous Media, *Geophysics*, **23**(3), 459–493. DOI: 10.1190/1.1438493.
- Yuan, T., Hyndman, R.D., Spence, G.D., and Desmons, B., 1996, Seismic Velocity Increase and Deep-Sea Gas Hydrate Concentration Above a Bottom-Simulating Reflector on the Northern Cascadia Continental Slope, *Journal of Geophysical Research: Solid Earth*, **101**(B6), 13655–13671. DOI: 10.1029/96JB00102.
- Zheng, Y., Yin, X.Y., and Zong, Z.Y., 2017, Estimation of Reservoir Properties With Inverse Digital Rock Physics Modeling Approach, *SEG Technical Program Expanded Abstracts*, 3893–3897–3117. DOI: 10.1190/segam2017-17654833.1.

ABOUT THE AUTHORS

Haojie Pan received his master's degree from Tongji University, and he is now a PhD candidate majoring in Geophysics at the Research Institute of Petroleum Exploration and Development, Petrochina. His research interests include rock physics, well-log interpretation, prestack seismic inversion and CSEM modeling and inversion.

Hongbing Li is a professor in geophysics and currently serves as a senior engineer and expert in seismic interpretation at the Research Institute of Petroleum Exploration and Development, PetroChina. His research interests include seismic rock physics, reservoir characterization and fluid identification.

Yan Zhang received his PhD from the Guangzhou Institute of Geochemistry, Chinese Academy of Sciences in 2007, and he is now a senior expert of geophysics and geology at the Research Institute of Petroleum Exploration and Development, Petrochina. His research interests include seismic reservoir characterization, seismic data processing, seismic imaging and inversion.

Jingyi Chen is Decker Dawson Associate Professor of Geophysics at The University of Tulsa. He is the director of Seismic Anisotropy Group at The University of Tulsa. He received a PhD degree in Solid Geophysics from Institute of Geology and Geophysics, Chinese Academy of Sciences in 2005. His research interests focus on both conventional and unconventional reservoirs including numerical simulation of seismic-wave propagation, seismic imaging and inversion, and reservoir characterization.

Shengjuan Cai is a postgraduate in geophysics at the Research Institute of Petroleum Exploration and Development, PetroChina. She received a BS in Geophysics from the China University of Petroleum (East China) and her research interests include seismic rock physics and quantitative fluid identification.

Chao Geng is a logging engineer in the Southwest Oil & Gas Field Company, Petrochina. He earned his BS degree from Yangtze University in 2012. His research interests include well-log interpretation of shale-gas and tight-gas reservoirs. Additional areas of interest include seismic interpretation.

Review of Micro/Nanofluidic Insights on Fluid Transport Controls in Tight Rocks

Ayaz Mehmani*¹, Shaina Kelly*², and Carlos Torres-Verdín¹

ABSTRACT

Microfluidics and nanofluidics have been used in the oil and gas industry for pore-scale research experiments and as application-specific tools (such as lab-on-a-chip PVT analyzers). The former technology constructs pore and pore-network proxies on compact lab-on-a-chip devices. Such proxies are then used to investigate the impact of specifically tuned geometric and/or material variable(s) on fluid transport via direct observation with microscopy. This paper reviews micro/nanofluidics findings by the authors and other geoscience and general porous-media researchers. Findings are related to the impacts of pore size, surface chemistry (wettability), fluid type and composition, and surface texture (roughness) on fluid transport variables, such as effective viscosity, imbibition, capillary trapping, adsorption, and diffusive processes. For example, the

authors' microfluidic findings include a critical surface roughness value beyond which capillary trapping during drainage increases drastically due to changes in subpore-scale flow regimes. The authors' nanofluidic findings include that the fluid polarity and surface chemistry of a silica nanoconfinement can lead to additional contact-line friction that causes significant deviations from the continuum Washburn equation for imbibition; these effects can potentially be incorporated in the quantitative analysis through an increased effective viscosity. Finally, this review highlights practical approaches for using lab-on-a-chip devices and their associated pore-scale findings as diagnostic tools to augment petrophysical laboratory measurements and guide field-scale pilot operations.

INTRODUCTION

Predicting multiphase flow dynamics in subsurface formations requires understanding fluid behavior at length scales spanning from subpore to field (herein, subpore scale refers to length scales that are pertinent to single pores). The genesis of tight rocks is preceded by a myriad of mechanical and chemical reactions from weathering during sediment deposition, to bioturbation, pressure dissolution at high temperature and pressures, and authigenic clay growth after burial. The resultant morphological and topological complexities of the pore space, as well as nontrivial surface chemistry properties can cause deviations from traditional petrophysical flow models, such as Carman-Kozeny for absolute permeability or Brooks-Corey for relative permeability. Subsequently, such equations can result in non-negligible errors in the assessment of the storage and flow properties of highly diagenetic rocks. For example, Byrnes et al. (2008) showed that although the Carman-Kozeny equation can predict permeability in the same order of magnitude as core measurements, it did not capture permeability variance with porosity; such differences in

permeability were up to an order of magnitude.

Microfluidic and nanofluidic chips (also referred to as lab-on-a-chip devices and sometimes generally as micromodels) are synthetic porous media that can be fabricated in a controlled manner. These lab-on-a-chip devices allow control/characterization of synthetic microscale and nanoscale geometry, which dramatically reduces the variable space when studying unconventional pore-scale behavior. Fluidic devices allow interstitial fluid movements (typically interfaces or tracers) to be visualized directly, which is challenging to accomplish in coreflood experiments, especially in tight rocks. Research at the subpore scale and pore scale (where pore scale refers to an explicit ensemble of multiple pores) attempts to explain and correct discrepancies observed between estimated and measured rock transport properties. This review covers examples where micro/nanofluidics have shown to be promising experimental tools for diagnosing nontrivial pore-scale transport phenomena.

Despite the recent spike in interest for geologic applications of microfluidics (Jacobs, 2019), the field actually originates in the late 19th century in the form of

Manuscript received by the Editor April 6, 2019; revised manuscript received August 15, 2019; manuscript accepted August 23, 2019.

¹The University of Texas at Austin, Hildebrand Department of Petroleum and Geosystems Engineering, 200 E. Dean Keeton, Mail Stop C0300, Austin, TX 78712-1585; mehmani.ayaz@utexas.edu; cverdin@austin.utexas.edu

²ConocoPhillips Company, 925 N Eldridge Pkwy, Houston, TX 77079; Shaina.A.Kelly@conocophillips.com

*Co-first authorship: S.K. and A.M. have contributed equally to this article

Hele-Shaw cells (Hele-Shaw, 1898). Micro/nanofluidics has yielded several notable research contributions within the oil and gas industry. For example, microfluidics has been leveraged to investigate the extent pore-structure features, such as coordination number and pore-throat-size ratios (i.e., pore aspect ratio), impact residual oil saturation (Chatzis et al., 1983). Microfluidics has also made observation of viscous fingering possible (Saffman and Taylor, 1958), highlighting the effects of mobility ratio on breakthrough time and ultimate recovery following various enhanced oil recovery (EOR) methods. Microfluidics has demonstrated the occurrence of snap-off during drainage, elucidating one of the first known pore-scale phenomena contributing to capillary trapping (Roof, 1970), which is currently still a topic of research for pore-scale numerical models (Raeini et al., 2014; Herring et al., 2018). Furthermore, microfluidics has catalyzed the field of multiphase pore-network modeling, a popular reduced-order pore-scale modeling approach (reduced-order numerical models refer to algorithms that capture simplified descriptions of fluid dynamics), through a series of what are now regarded as classic research articles Lenormand and Zarcane (1984, 1985) and Lenormand et al. (1988). The Lenormand et al. (1988) proposal for a parameter space based on two key nondimensional numbers, capillary number $(\nu\mu/\sigma)_{displacing}$ and mobility ratio $(\mu_{displacing}/\mu_{displaced})$, is still used to characterize immiscible flow as stable, capillary or viscous dominated (Joekar-Niasar et al., 2010; Islam et al., 2014; Mehmani et al., 2019a). Due to fabrication challenges, nanofluidics is generally a less studied field in the oil and gas industry. However, the study of fluid flow under nanoconfinement is of considerable interest for the production of unconventional (nanoporous) rocks and recent nanofluidic pursuits have ranged from studying nanoscale wettability effects (Kelly et al., 2018) to probing completions

fluid imbibition in nanopore network proxies (Kelly et al., 2016b; Hasham et al., 2018).

Given the presence of multiple length scales when analyzing fluid flow phenomena in earth sciences, it is challenging to categorize the use of micro/nanofluidics in the spectrum of subpore to field scales. In addition, despite ongoing insights made by using microfluidics, workflows for academic and industrial research and development, geoscience applications are not well-established. Figure 1 shows how micro/nanofluidics can provide information for reservoir simulation grids corresponding to characterized facies. In this article, we review each of the micro/nanofluidics applications shown in Fig. 1; that is, their applied and diagnostic capabilities, derivation of functional relationships, and ability to benchmark numerical models. We conclude with a roadmap for leveraging micro/nanofluidics for applied research efforts in the oil and gas industry.

APPLIED MICROFLUIDICS

Microfluidics requires extremely small fluid volumes for analysis (on the order of μL). This feature renders microfluidic fluid analyzer platforms attractive in the oil and gas industry since they can assist in conserving available crude oil samples that accurately represent in-situ composition. In addition, the time scales associated with microfluidic experiments are shorter than traditional laboratory-scale apparatuses, resulting in faster turnaround times. For example, successful designs for obtaining thermodynamic phase diagrams (PVT analysis) leveraging microfluidics have recently been accomplished (Mostowfi et al., 2012; Fisher et al., 2013). Those microfluidics-based PVT analyzers use a serpentine channel with membrane

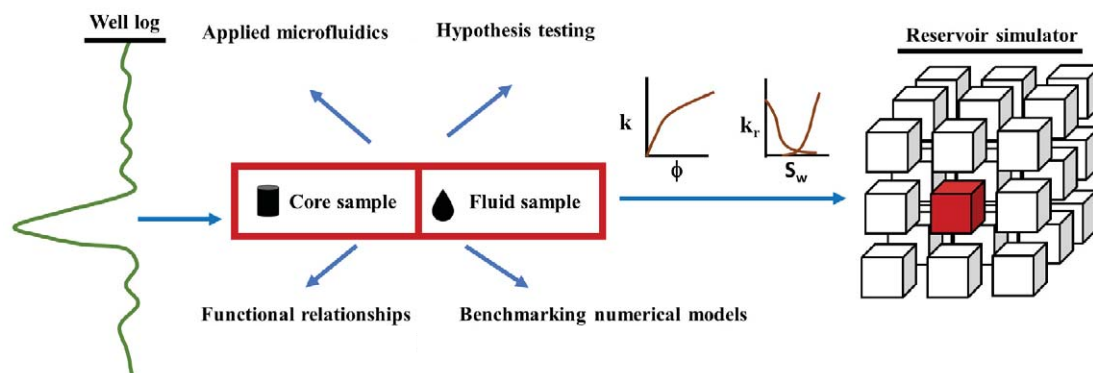


Fig. 1—Micro/nanofluidics can be used to measure reservoir fluid properties (applied microfluidics) on small sample volumes, identify effective production methods (hypothesis testing), establish functional relationships between reservoir quality, chemistry and flow, and benchmark subpore-scale and pore-scale numerical methods. The latter can inform dynamic inputs (such as relative permeability curves) for reservoir simulation gridblocks.

pressure sensors installed along their path. A fluid sample is injected with a constant flow rate, which corresponds to a pressure gradient along the channel. Interstitial visualizations allow gas/oil ratios to be determined directly for each pressure measurement. Turnaround time is reduced from hours to minutes with three orders of magnitude less fluid volume consumed as compared to a traditional PVT cell. In addition, the miniature nature of microfluidics enables temperatures to be changed in minutes instead of the hours typically needed for a traditional PVT analyzer cell. Lab-on-a-chip devices have also shown use in measuring bulk fluid properties, such as bitumen-CO₂ diffusivity (Fadaei et al., 2011), minimum miscibility pressure of CO₂ in oil (Nguyen et al., 2015), asphaltene content (Schneider et al., 2013), and flow-induced polymer degradation (Nghe et al., 2010) in orders of magnitude smaller volumes and shorter time scales as compared to traditional analyses. In addition, microfluidics can provide rapid supplemental first-order information, such as identifying the most impactful solvents for heavy-oil recovery (Lele et al., 2018).

Microfluidic platforms have also been used for the case where limited rock material is available (such as cuttings) or where there is a desire to isolate measurements to a specific subcore-scale lamina. Such works include capturing flow in micromodels composed of 2- to 3-mm thick rock slabs sandwiched between glass plates with gaskets via CT scans (Tomutsa et al., 1990; Sun et al., 2004), microplug cylinders embedded in a lab-on-chip devices (Nguyen et al., 2013), and injecting geologic substances, such as bitumen, into a microfluidic channel for controlled diffusivity measurements (Fadaei et al., 2011).

Given the heightened surface-to-volume ratios of microfluidic conduits, bulk fluid-property measurements become sensitive to the surface chemistry and rugosity of the chip itself. However, using microfluidics as measurement tools for properties related to fluid-rock interactions must be approached with caution. Earth science addresses porous materials that are complex and difficult to replicate in the laboratory (a catalyst that reduces millions of years of mechanical and chemical reactions into days has yet to be discovered). In addition, surface texture is an oftentimes overlooked property in micro/nanofluidics. As ongoing research on using high-resolution microscopy is revealing (Schmatz et al., 2015) that ignoring the unique surface mineralogy and roughness of a formation can lead to erroneous characterization of reservoir wettability hysteresis. Ergo, as opposed to the promising results of microfluidics in measuring bulk fluid properties, microfluidics may be of limited use when used to directly determine the petrophysical properties of rocks (see Fig. 2). Core-based methods, despite

their challenges in operation and longer time scales, should still be considered the gold standard in measuring fluid-rock interaction properties. Meanwhile, microfluidics is an additional tool to probe results.

Finally, the novelty of lab-on-a-chip devices, in contrast to traditional measurement methods, implies a lack of standardized workflows and best practices. Performing microfluidics in production mode therefore requires specialized care and experience for ensuring consistent accuracy and reproducibility (for example, examining and mitigating chip fouling and leakage). Computational fluid dynamics simulations can assist in identifying relevant parameters influencing an observed behavior and therefore make inference-based measurements of fluid-rock interaction properties possible. We note that fabrication of microfluidics is not necessarily cheap (as cleanroom facilities usage is typically needed), can be time consuming (for instance, it takes the authors, on average, two weeks to generate a single glass micromodel), and can sometimes require the usage of extremely hazardous chemicals (such as hydrofluoric acid for etching glass).

Overall, we posit that the state of using lab-on-a-chip devices for measuring bulk fluid and rock transport properties for earth science applications is analogous to the use of such devices in medicine. Specifically, although a rapid blood test may reveal cancer biomarkers in a patient, traditional clinical practice is still required to confirm and elaborate on the presence of the disease in the appropriate physiological context.

DIAGNOSTIC MICROFLUIDICS

Testing Hypotheses

Given the ability to visualize interstitial fluid movements in microfluidic networks, microfluidics is a powerful tool to verify hypotheses related to fluid flow in porous media. This feature is especially helpful in EOR, where a particular chemical mix or flow recovery method is speculated to increase production from a reservoir. For instance, glass micromodels have evidenced that tertiary gasflooding of residual waterflood oil increases because of the formation of thin oil layers between gas and water for a positive spreading coefficient ($\sigma_{wg} > \sigma_{og} + \sigma_{ow}$) and water-wet system (Oren et al., 1992). The importance of oil films in tertiary gasflooding has been further investigated via microfluidics (Dong et al., 1995; Keller et al., 1997) and the presence of oil films was ultimately incorporated into three-phase pore-network models (Piri and Blunt, 2005a, 2005b). The pore-scale efficacy of other EOR operations, such as low-salinity waterflooding (Du et al., 2019), steam-assisted

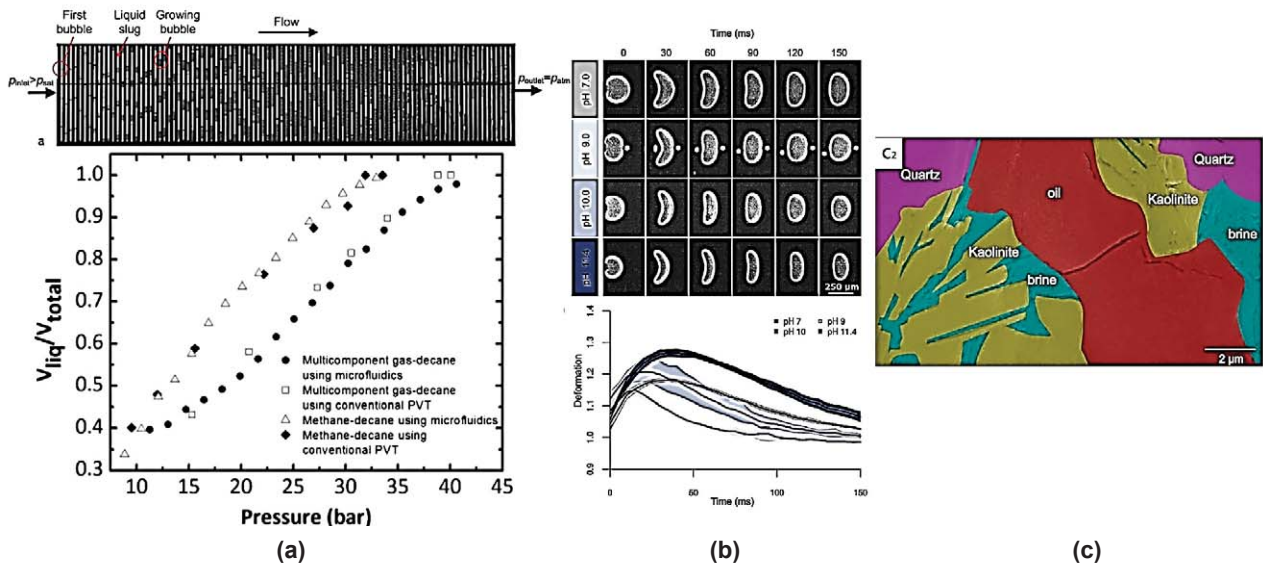


Fig. 2—Microfluidics has been shown capable of rapidly (a) measuring hydrocarbon PVT properties (Mostowfi et al., 2012), and (b) identifying effective solvents for heavy oil recovery (Lele et al., 2018). Extrapolating such applications to determining rock transport properties must be approached with caution given (c) subpore-scale complex fluid behaviors (Schmatz et al., 2015) on account of geometric and surface properties.

gravity drainage (De Haas et al., 2013), water-alternating-gas injection (Dehghan et al., 2012), surfactant/polymer flooding (Mejia et al., 2019b), microbial EOR (Khajepour et al., 2014), and nanoparticle injection (Xu et al., 2016) has been studied with microfluidics. The challenges in testing EOR agents and techniques are similar to those discussed in previously; that is, rocks, in contrast to micromodels, are not simple porous ensembles with ideal smooth surfaces. While microfluidics provides a flexible parameter space, any inferences from microfluidics should be anchored on coreflood experiments as much as possible.

Benchmarks for Processes That are Challenging to Simulate

Direct numerical simulation of fluid interstitial movements at a representative domain size is both nontrivial and computationally costly. The obstacles are especially challenging for unconventional rocks where pore spaces at multiple length scales are in close proximity to each other. Although numerical advances to counter computational challenges have been made, including hybrid (coupling Darcy flow with the Navier-Stokes equation) and multiscale pore-level simulations (Mehmani et al., 2013), the veracity of these simulations needs to be confirmed with experimental data. Microfluidics offers the unique ability to provide

controlled fluid behavior observations for benchmarking numerical methods. In addition, microfluidics experiments can offer a priori rules and conceptual models for reduced-order simulations, such as pore-network models (PNM).

Pore-network models have benefited directly from fluid percolation rules (Lenormand and Zarcone, 1984; Valvatne and Blunt, 2004). Their contribution to reduced-order modeling is still ongoing, as recent fast experiments visualizing drainage interfacial movements have shown that capillary invasion jumps are nonlocal (Armstrong and Berg, 2013). This observation implies that spatial distribution of immiscible phases during drainage is not simply a function of critical capillary pressure thresholds, as assumed in invasion percolation algorithms (Mason and Mellor, 1995), but also a function of local fluid velocities. In addition, conceptual models have been provided through microfluidics experiments, which are a priori qualitative descriptions of complex fluid behaviors, for the spatial distributions of immiscible phases in unsaturated fractured rocks (Wan et al., 1996; Jones et al., 2018). Other predictive numerical methods have benefited from microfluidics experiments as well, including determining solute transport in moderate and high Peclet numbers (Mehmani et al., 2014), spatial distribution of immiscible phases (Niasar et al., 2009) and morphology of unstable flow (Chen et al., 2018).

The advantage of microfluidics for providing controlled environments for benchmarking numerical methods is offset by their typical limitation to two dimensions. However, micromodels can in fact be extended to three dimensions, as was developed by Avraam et al. (1994) through fusing three substrates together, with the middle layer containing drilled “pores” connecting two etched pores/throats. The somewhat ungainly additional step of adding a third layer for bonding is potentially the reason why microfluidics has been primarily limited to only two dimensions. Boundary effects along chip edges are a factor to consider as well. Nonetheless, given that microfluidic devices enable visualization of various local/macroscopic transport properties in controlled environments, they can still serve as first-order benchmarking tools for numerical models; an example of this is the impact of surface roughness on immiscible flow dynamics (Frank et al., 2018; Mehmani et al. 2019a).

Upscaling and Integration

Upscaling pore-scale dynamics in earth science is a major challenge and requires transforming sophisticated pore-scale numerical models into applicable parameters for field-scale reservoir simulations. These reservoir-scale simulators are often limited to a few inputs per rock type (porosity, permeability, capillary pressure, relative permeability, etc.). In contrast to other disciplines, such as those investigating synthetic or biological porous materials, analytical upscaling of porous geomaterials is much more intractable, given the presence of space and time-induced heterogeneity from subpore to field scale. Upscaling exercises for tight rocks are therefore phenomenological (albeit with some physical descriptions formulated via a conceptual model); that is, linkage between emergent nonlinear phenomena and small-scale properties is established following a variety of laboratory and numerical experiments. The shortcoming of this approach is that a single self-consistent model that can also link various nonlinear emergent properties to each other becomes challenging to establish. For example, in unconsolidated grain packs or conventional sandstones, the greatly simplified bundle-of-tubes model has been shown to be reliable (Peters, 2012a). The model’s deviation from experimental data is linked to tortuosity, which can, for all practical purposes, be used as a fitting parameter. However, the model is incapable of linking capillary pressure saturation curves with relative permeability without additional fitting parameters (Peters, 2012b). This discrepancy is because the error of the bundle-of-tubes model is inherent to its conceptualization of a three-dimensional (3D) porous medium; that is, capillary trapping following invasion percolation cannot be replicated by a bundle of parallel tubes. Tight rocks, with complex diagenetic histories and

likely tortuous pore systems, further exacerbate the problem of upscaling, as obtaining robust core data measurements to compare to phenomenological models becomes difficult.

Microfluidics, despite its challenges representing a 3D domain with high fidelity to rock pore texture, can incorporate microscale and macroscale heterogeneity such that relevant fluid-rock interaction properties are identified and a parameter space for upscaling is derived. For example, upscaling the effects of intrinsic wettability changes (a subpore-scale parameter) on oil recovery at the mesoscale, i.e., length scales just above pore scale where continuum assumptions for fluid movements appear valid, has been shown with lab-on-a-chip devices (Zhao et al., 2016). Microfluidics have furthermore proven useful in determining mesoscale heterogeneity effects, such as permeability contrast, on foam-based oil recovery (Conn et al., 2014). Further, Mehmani et al. (2017, 2018) have upscaled the impacts of microfracture connectivity and surface roughness on capillary trapping during imbibition and drainage.

In addition to testing hypotheses and benchmarking, microfluidics enables observation of nonlinear emergent relationships, some of which can be difficult to simulate. Direct fluid movement observations have been used to make quantitative descriptions of interstitial single-phase fluid movements using particle velocimetry (Datta et al., 2013). The authors discovered that the local fluid velocities in a glass-bead pack follow a non-Gaussian distribution, which is intuitively consistent with throat-size and path-length distributions calculated from random grain packs (Bryant et al., 1993; Mason and Mellor, 1995). In other work, the local velocity visualization based on particle imaging velocimetry (PIV) measurements has discovered that nonwetting compressible phases at dead-end pores are not stagnant but impose a shear stress on the trapped wetting phase (Y. Li et al., 2017). Such pore-scale insights contribute directly to planning chemical oil recovery procedures where local fluid velocities alter the efficacy of the displacing agent. For instance, Qi et al. (2017) confirmed the ability of viscoelastic polymers to increase oil recovery (via coreflooding) subsequent to waterflooding. Even though they did not investigate the pore-scale mechanisms responsible for the increase in recovery, it is likely that changes in local velocity impact recovery. PIV can provide quantitative relationships between trapped saturation of oil and the local velocity of the displacing phase.

Viscous fingering is a common occurrence during primary water/gas oil recovery in heavy-oil reservoirs (Doorwar and Mohanty, 2017). Such unstable immiscible displacements are computationally challenging to simulate (Doorwar and Mohanty, 2014). Lab-on-a-chip devices have allowed viscous fingering dendrite morphologies to be

directly visualized and quantified as a function of capillary number (Stokes et al., 1986; Li et al., 2009), gravity effects (Islam et al., 2014) and wettability (Zhao et al., 2016). Such quantitative descriptions can directly link various fluid/rock properties to flow patterns and how effectively displacing agents distribute in the formation. Determining relationships between rock transport properties, such as permeability and capillary pressure, and fluid-rock interaction properties is also possible with microfluidics. Micromodel two-dimensionality has been shown to skew said relationships quantitatively, but qualitatively, lab-on-a-chip devices are capable of providing insightful information (Avraam et al., 1994). For example, micromodels have determined that the nonwetting relative permeability increases with capillary number and flow ratio (q_{nw}/q_w), and in contrast to assumptions made in reduced-order pore-scale modeling (Mason and Mellor, 1995; Valvatne and Blunt, 2004; Bultreys et al., 2015; Mehmani et al., 2019b), is dependent on the movement of trapped ganglia at low capillary numbers (Avraam et al., 1994; Avraam and Payatakes, 1995). Given the relative ease of fabricating microfluidics as compared to nanofluidics, mesoscale experiments can be conducted in representative elementary volumes (although the latter has currently not been subjected to a systematic investigation).

Figure 3 shows a summary of using microfluidics as a diagnostic tool. Because micro/nanofluidics is in two dimensions (2D), it cannot replicate a 3D representative

elementary volume (REV) of an actual rock sample. A representative elementary area (REA) of a micromodel for a particular transport property can be achieved by using a “large enough” system. To our knowledge, a systematic study toward determining REAs in microfluidics for various transport phenomena has not been conducted. The REA can be determined by consecutively increasing the porous domain size and repeating the experiment until a plateau is reached when visualizing the transport property. In our literature survey, the majority of microfluidics were designed either as an idealized pillar ensemble or a homogenous disordered medium. More complex porous systems that resemble diagenetically altered rocks were recently published by the authors (Mejia et al., 2019a), but to our knowledge a systematic study of their domain representativeness is lacking. We therefore recommend (see section on Industry Applications and Best Practices) microfluidics as a diagnostic tool for hypothesis testing or for acquiring first-order approximations that can be subsequently adjusted via history matching.

DIAGNOSTIC NANOFLUIDICS

Testing Hypotheses

In contrast to microfluidics, nanofluidics enables the replication of nanometer-scale influences on fluid behaviors. For example, Hasham et al. (2018) used a nanofluidic chip to

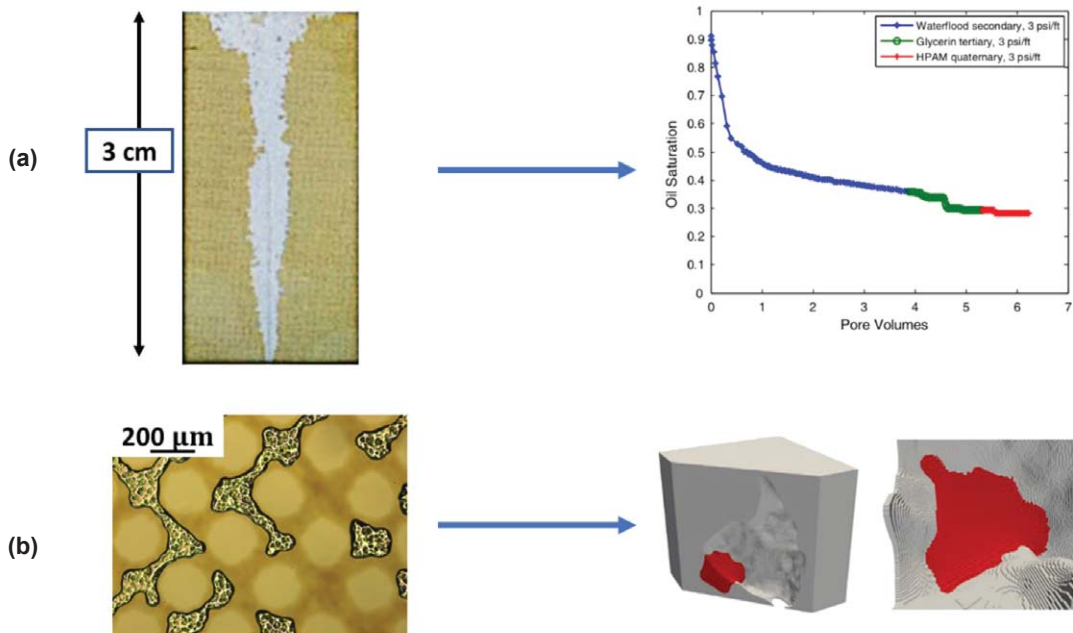


Fig. 3—Diagnostic microfluidics can be used to test hypotheses for identifying EOR methods, benchmark numerical models, and establish upscaled relationships. (a-left) micromodel surfactant flooding (Mejia et al., 2019b) can assist in (a-right) interpreting coreflood recovery plots (Qi et al., 2017) (a-right). (b-left) Flow experiments on rough micromodels can help in benchmarking (Mehmani et al., 2019a) (b-right) direct numerical simulation algorithms (Frank et al., 2018).

compare the infiltration rates of deionized water, potassium chloride solution and slick water and select the fluid type with the highest amount of flowback (amount of recovered fracture fluid following hydraulic fracturing). The nanofluidic chips had depths of 175 nm and micrometer scale widths and two types of grain shapes (circles and squares). Methodologies such as this are foundational in that they enable investigators to visualize interstitial fluid dynamics in a nanoslit pore network, an insight not possible with conventional capillary imbibition experiments on shale plugs (Dehghanpour et al., 2013). Deviations of capillary imbibition experiments on shale core samples from a dimensionless form of Washburn's equation have been attributed to water adsorption and the generation of microfractures (Dehghanpour et al., 2013). Spontaneous imbibition experiments in nanomodels with pore textures similar to those of shale cores used for bulk imbibition can further elucidate such deviations and provide selection criteria for the most desirable fracture fluid. It is important to note that, unlike conventional sandstones, 3D micro-CT visualization of fluid interfaces within pores is currently intractable for many tight rocks (in particular, mudrocks) given their submicrometer pore sizes. Recent promising nano-CT visualization techniques of imbibed shale core samples have been published (Akbarabadi et al., 2017) but are still often resolution-limited and need to be investigated further for the development of facile workflows.

Workflows for nanofluidic fabrication have been adopted to investigate EOR methods, such as huff-and-puff (Zhong et al., 2018) and the efficacy of adding surfactants to fracturing fluids for oil recovery (He et al., 2014, 2015). However, compared to leveraging microfluidics, research on this topic is still in its infancy. An underused approach to studying nanoconfinement effects on fluid transport uses synthetic nanoporous media. For example, Gruener et al. (2012) conducted spontaneous capillary-rise experiments in a disordered nanoporous medium (Vycor glass) with mean pore radii of 4 nm and dimensions of $4.6 \times 4.6 \times 20 \text{ mm}^3$. The authors found an anomalous front broadening behavior that was attributed to elongated pore aspect ratios (~ 5 to 7) but not nanoconfinement effects. The authors had used neutron radiography to visualize the mesoscale fluid movements. In other works, Fogden et al. (2015) tracked the diffusion of a miscible liquid (toluene) in a diiodomethane saturated shale sample with micro-CT. The authors could visualize the front movement and therefore discover nanoporous influences at the mesoscale during production. Given the subpore- to mesoscale heterogeneity of tight rocks, coupling direct nanofluidics visualization with mesoscale imaging is

imperative for upscaling to discern prominent influences on fluid flow and benchmark numerical models effectively.

It is important to note that the majority of geoscience-targeted nanofluidic designs used to study fluid transport have been nanoslits (nanometer scale only in one dimension (1D)), with a few fully nanoscale exceptions such as Kelly, et al. (2016a) and Kelly et al. (2018). This selection appears to be due to fabrication ease, as generating nanometers in two dimensions requires electron-beam lithography, which is time-consuming compared to photolithography (used to fabricate nanoslits; which are micron-scale patterns etched nanoscale in depth). The presence of a second nanometer-scale dimension can enhance surface-liquid molecular forces and give rise to significant deviations from the nanoslit results. For instance, although H. Li et al. (2017) showed that at 10 nm slits, deviations from Lucas-Washburn's equation for spontaneous imbibition are minimal, measurements with nanochannels with nanometer scales in two dimensions deviate significantly from Lucas-Washburn and Young-Laplace's equations (Kelly, et al., 2016a). Figure 4, as will be discussed below in the section Observed Functional and Emergent Relationships also discusses how such nanoscale results are highly dependent on material properties.

Benchmarks for Processes That are Challenging to Simulate

Considerable nontrivial observations on the behavior of fluids in tight rocks have been made by calibrating nanofluidics, molecular dynamics (MD) simulations, and numerical models. For example, analytical equations for gas flow in single nanotubes (Beskok and Karniadakis, 1999; Roy et al., 2003; Javadpour, 2009) are generally derived based on segmentation of flow into regimes separated by their Knudsen number (ratio of mean free molecular path to characteristic channel size). Such equations were then used in single-scale and two-scale pore-network models to observe the sensitivity of apparent permeability to pore size at various pressures and temperatures (Sakhaee-Pour and Bryant, 2012; Mehmani et al., 2013; Ma et al., 2014). However, experimental verification of these models with hydrocarbons at in-situ conditions remains open. Comparison of analytical models, such as the aforementioned example to controlled nanofluidic experiments is especially important, since significant deviations with molecular-level simulations have been shown. Wang, Feng, et al. (2016) showed that slip flow of methane in calcite nanopores is twice slower than the slip flow predicted by Beskok and Karniadakis (1999) indicating the influence of attractive surface forces on

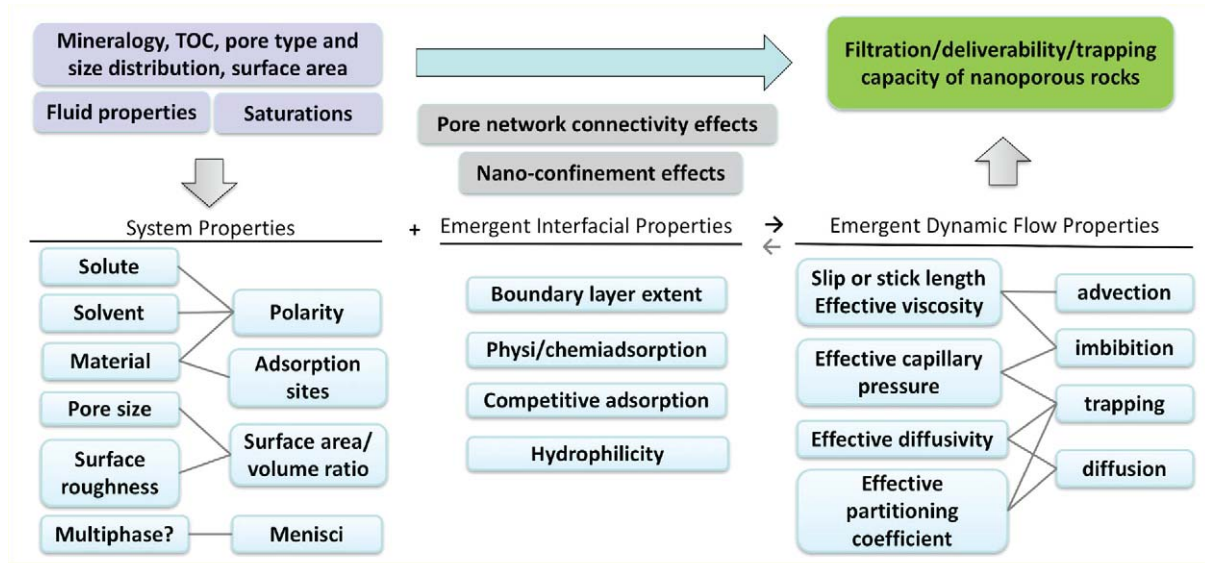


Fig. 4—Roadmap of the variable space that can be probed with nanofluidics to establish functional relationships for determining effective transport variables.

transport. Wang et al. (2017) furthermore utilized molecular dynamics simulations to show that diffusion of supercritical methane is dependent on mineral types and moisture content. Riewchotisakul and Akkutlu (2016) discovered an unexpected contribution of adsorbed layers to fluid permeability for the organic nanopores of Marcellus shale through molecular dynamics simulation.

Nanofluidic devices as standalone tools can identify nontrivial influences of surface chemistry which can then be further investigated with numerical models. For instance, Alfi et al. (2016) showed that contact angles of three different hydrocarbons decrease due to surface forces in 10 nm nanoslits (in other words, fluid affinity to pore walls increases) whereas Martic et al. (2002) have shown dependence of contact angle on fluid velocity in the early stages of imbibition. A reliable molecular level simulator can expand on such data to establish functional relationships between contact angle (both static and dynamic) and slit size, pressure/temperature values and pore-wall mineral types. Two-phase drainage/imbibition experiments have been successfully visualized in 1D nanoslits as well (Wu et al., 2014). Such experiments can validate liquid movements calculated via molecular dynamics simulations. For instance, Wang, Javadpour, et al. (2016b) showed that n-octane molecules in inorganic nanoslit with aperture sizes down to

3.6 nm continue to retain a bulk fluid Hagen-Poiseuille-type velocity profile with a slip boundary condition assumption. On the other hand, in organic nanoslits (with aperture sizes 1.5 to 11.2 nm), molecular dynamics simulations have found a plug-like no-slip velocity profile for octane (Wang, Javadpour, et al., 2016a). Bakli and Chakraborty (2012) proposed a functional relationship between capillary filling of water in nanopores, intrinsic wettability, and surface roughness using molecular dynamics simulations.

Similar to microfluidics, nanofluidics, conceptually, holds the potential to establish upscaled functional relationships that can ultimately be used in reservoir simulation grids as a first-order approximation (with subsequent accuracy gain by history matching). However, as discussed in the following section on Robust Fabrication, fabricating nanochips and performing flow experiments in them is challenging. Unconventional nanofluidics fabrication methods (Kelly et al., 2015; Kelly et al., 2016a) and ultimately reduced-order numerical simulations, such as pore-network models (Mehmani et al., 2013; Mehmani and Prodanović, 2014) can, therefore, be used to expand the domain of investigation into representative scales. Currently, attempts to obtain upscaled constitutive relationships for rock transport properties using nanofluidics (and to a lesser extent microfluidics) are sparse.

Observed Functional and Emergent Relationships

As alluded to in the previous section, various experimental and numerical studies have evidenced that interfacial interactions can govern fluid and solute transport in nanoscale confinements; however, the generation of robust predictive nanoscale transport models that decouple competing phenomena has proven challenging. Liquid imbibition, the capillary pressure-driven flow of a liquid into a gas, provided a spontaneous mechanism for fluid conveyance and observation in the nanochannels. For example, through a series of polar and nonpolar liquid imbibition studies in different sized silica-glass nanochannels, Kelly et al. (2018) show how nanofluidic experiments provide an approach to probe the influence of pore size, surface roughness, hydrophilicity, solvent, solute and resultant interfacial interactions on effective nanoscale transport values including boundary layers/slip lengths, capillary pressure, liquid viscosity, diffusion, and interfacial gas partitioning coefficients. The findings were benchmarked against bulk values and the classic Lucas-Washburn equation for imbibition, which does not consider interfacial fluidity effects. Overall, imbibition efficacy in the hydrophilic channels decreased dramatically below Lucas-Washburn trends with decreases in channel size, increases in liquid polarity, and solute presence. The imbibition anomalies were attributed to physical/chemical adsorption-dependent excessive contact-line friction at interfaces and increased effective viscosity, whereupon the results matched a modified version of the Lucas-Washburn equation.

Meanwhile, nearly frictionless transport of both gases and liquids, including water, within carbon nanotubes (CNT) has been observed with both MD and experimental work. Insights gained from MD simulations include that water confined in CNTs exhibited extremely fast responses to osmotic pressure (Kalra et al., 2003) and that light gas transport in CNTs is at least three orders of magnitude higher than in crystalline zeolite membranes (Skoulidas et al., 2002). Holt et al. (2006) show that experimentally measured fluid permeability actually increases with decrease in CNT size, a finding counterintuitive to Poiseuille-flow predictions. The superfluidity effect is attributed to the hydrophobic and extremely smooth surfaces of graphene (see Fig. 5).

The aforementioned material cases, silica and CNTs, represent endmember in terms of surface polarity and wettability. There is a need to probe and collate results for upscaled terms such as effective viscosity and diffusivity as a function of nanofluidic experimental properties. These variables can be benchmarked against bulk values, analogous molecular dynamics simulations, relevant special core analysis findings, analytical solutions (where available), and continuum theories, the goal being to assess a convergence

of fluidic findings. Figure 4 displays a visual roadmap of the variable space that can be probed with nanofluidics. Figure 6 provides a summary of how to use nanofluidics as a diagnostic tool.

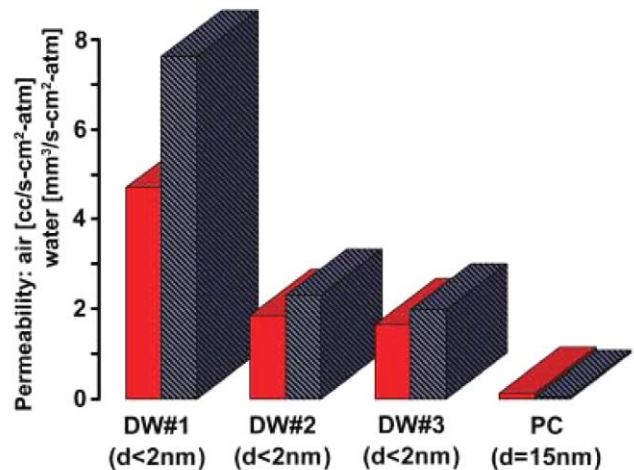


Fig. 5—Diagnostic nanofluidics can reveal anomalous functional relationships, such as the increase in water permeability with decrease in carbon nanochannel size, as presented in the work of Holt et al. (2006) shown in this figure. “Air (red) and water (blue) permeability as measured for three DWNT (double-walled carbon nanotubes) membranes (DW#1, 2, and 3) and a polycarbonate membrane (PC). Despite considerably smaller pore sizes, the permeabilities for all DWNT membranes greatly exceed those of the polycarbonate membrane.”

ROBUST FABRICATION

Fabrication is a roadblock in large-scale and/or routine application of micro/nanofluidic workflows for petrophysical applications. These workflows are not routinely offered by core analysis vendors. Fabricating micromodels appears deceptively simple, yet any in-house fabrication efforts require experienced staff. Given the many ad hoc recipe adjustments that arise due to unpredictable (and sometimes unexplainable) obstacles, such as production discontinuation of a particular photoresist or changes in glass substrate composition, a continuous expertise lineage in a research laboratory is critical. Transferring fabrication steps to other groups must be done in detail and with extensive illustrations. An ideal fabrication recipe should require inexpensive and widely available material, can be transferred in articulable and repeatable steps, and abide by health, safety and environmental (HSE) protocol. The importance of clear dissemination of experimental steps, which given their fabrication nuance, is particularly important for lab-on-a-chip devices, has prompted several peer-reviewed journals, such as *MethodX* and *Journal of Visualized Experiments*, to dedicate documentation space for researchers to share their fabrication methods in sufficient detail.

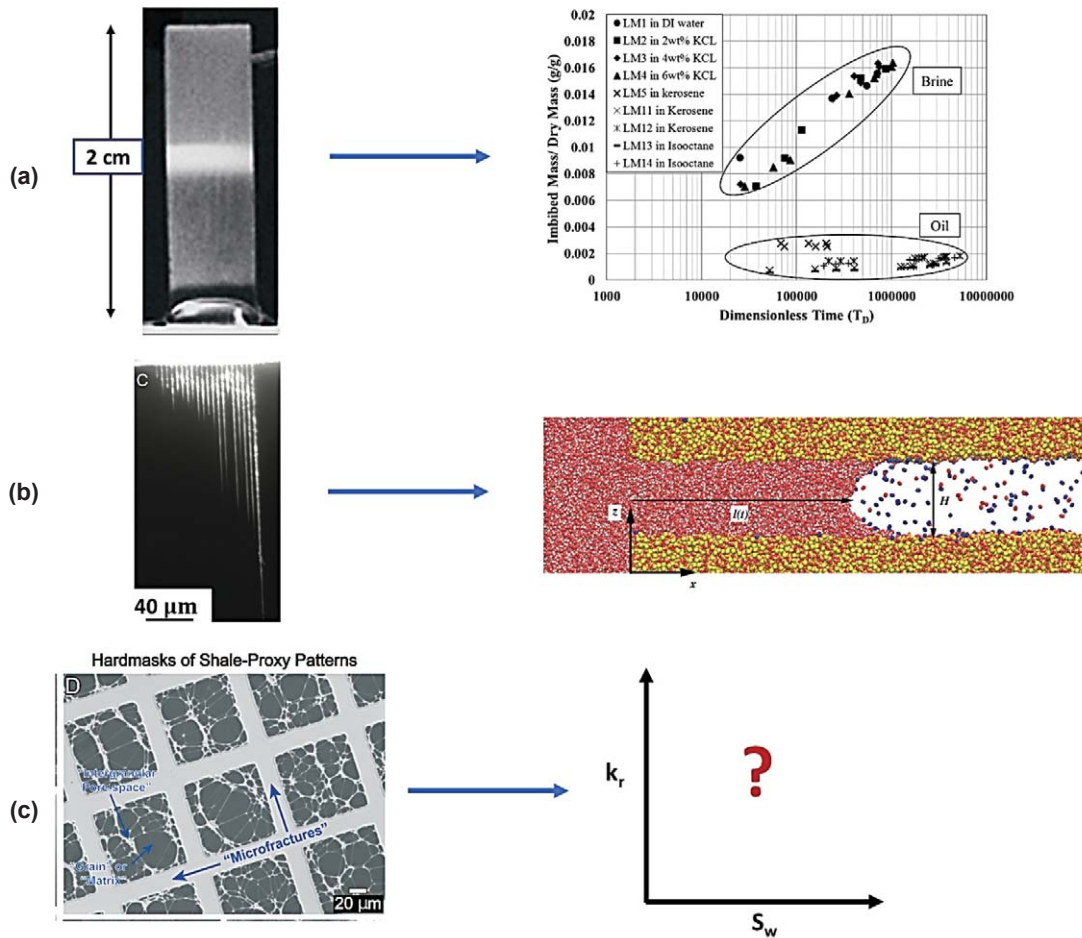


Fig. 6—Diagnostic nanofluidics can be used to (a) test hypotheses related to nanoporous media, and (b) benchmark numerical simulations. The recent development of facile fabrication techniques for multiscale unconventional rocks can be leveraged to establish upscaled constitutive relationships for rocks. Image (a-left) shows an imbibition experiment conducted on a 3D Vycor glass (Gruener et al., 2012). Such experiments can provide a standardized control tool to assist with verifying (a-right) core-scale experiments conducted on shale samples (Dehghanpour et al., 2013). (b-left) imbibition experiments on nanochannels (Kelly, et al., 2016b) can be used to benchmark molecular dynamics simulations (Oyarzua et al., 2015). Recent developments in facile nanofluidics fabrication techniques (c-left) may allow the establishment of upscaled constitutive relationships (Kelly, et al., 2016).

As was discussed previously, micromodels have typically been designed to capture multiphase flow dynamics in simple geometries to identify nontrivial subpore-scale flow behavior and benchmark analytical models.

We discussed in preceding sections that given the complexity of pore-space topology in porous geomaterials, reservoir-on-a-chip designs have been introduced to validate direct numerical simulation algorithms as well as reduced-ordered two-phase flow predictions using pore-network models. However, functionalizing micromodels, that is altering their surface properties to resemble those of reservoir rock materials, is an underexplored area in lab-on-a-chip devices for earth science applications. The majority of the studies on functionalizing micromodels have been directed toward changing surface wettability.

Wettability in microfluidics can be altered by either

changing the substrate material with a particular native wettability (such as glass for water-wet and PDMS for oil-wet media) or administering chemicals post-fabrication. The wettability-alteration method depends on the type of substrate and bonding method used in fabrication. For oil-wet PDMS substrates, oxygen plasma treatment can temporarily generate water-wet surfaces prior to bonding (Bhattacharya et al., 2005). For nonfusion bonding, such as PDMS to glass, the pattern resolution for wettability alteration will depend on the resolution of the hard mask used (Zhou et al., 2010). For glass microfluidics using fusion bonding (heating the substrates to sintering temperature), wettability changes can be implemented after the micromodel is fabricated. This change in wettability can be achieved by coating the porous space with silane (Grate et al., 2013; Mejia et al., 2019b) or aging the micromodel with crude oil (retaining crude oil

inside micromodels for a prolonged period of time) (Song and Kovscek, 2016). Incorporating controlled mixed-wet distributions is difficult but can be achieved to some extent by manipulating the phase distributions of the silane/crude oil based on their viscosity differences with the original phase in place (water for instance) and exploiting the particular geometrical features of the micromodel. Recently, a stop-flow-lithography (injecting oligomer inside a channel and stopping the flow prior to polymerization) (Dendukuri et al., 2007) has been developed to incorporate mixed-wet porous patterns inside glass microchannels by injecting and UV-initiating hydrophilic and oleophilic polymers (Lee et al., 2015). To what extent such wettability alterations can give rise to wettability patterns similar to rocks at reservoir conditions requires additional research.

Etching depth in micro/nanofluidics is dependent on the application. For instance, if a gravity drainage experiment with a reservoir fluid sample is required then the pore size should be on the same order of magnitude as the formation rock. In contrast, if a theory is investigated with idealized fluids (such as mineral oil instead of crude oil), then more flexibility exists with using dimensionless parameters such as capillary number or Bond number. For nanofluidics, H. Li et al. (2017) have shown that if the pore width is in micrometers, then one can ignore nanoconfinement effects perpendicular to the micromodel plane. If both pore width and pore depth are in nanometer scale, then nanoconfinement effects on fluid properties, such as viscosity and capillary pressure, become considerable (Kelly et al., 2018). Overall, the micro/nanofluidics design depends on the particular problem statement and can be simplified accordingly.

As shown in Fig. 7a, functionalizing micromodels may require fabrication recipes that go beyond changing surface wettability. Weathering and deposition of authigenic minerals give rise to surface properties that are highly different from smooth silica/glass/PDMS surfaces with altered wettability. Figure 7b shows a functionalized micromodel in which kaolinite was deposited on glass-silica micromodels; these micromodels were subsequently used to study the effects of clay detachment and migration on oil recovery following low-salinity waterflooding. Figures 7c and 7d show two novel examples of using native calcite minerals/shale rock samples as etching substrates to investigate reactive and two-phase flow dynamics. Applications of functionalized micromodels are highly pertinent to tight rocks given the extensive diagenesis associated with their formation.

There are several options to make nanofluidic platforms more accessible to investigators. For example, CNT membranes used for fluidic studies consist of CNTs embedded within a filler matrix material (an excellent review of CNT nanofluidic platforms is provided by Noy

et al., 2007); these constructs can possibly be tailored to represent mudrock constituents. In addition, self-assembly chemistry instead of lithograph methods can be used to generate large amounts of sublithography scale pores. To probe wettability, options include synthesis of organic-inorganic hybrid materials (Ford et al., 2005; Hoffmann et al., 2006) or simply aging the devices with crude oil or brine. The synthesis of smaller pores (i.e., smaller than attainable with electron-beam lithography methods) within relatively larger nanopores (traditionally easier to fabricate) by means of hydrocarbon deposition has been performed as well (Radenovic et al., 2008). In that method, adsorbed hydrocarbon is polymerized/immobilized by the electron beam.

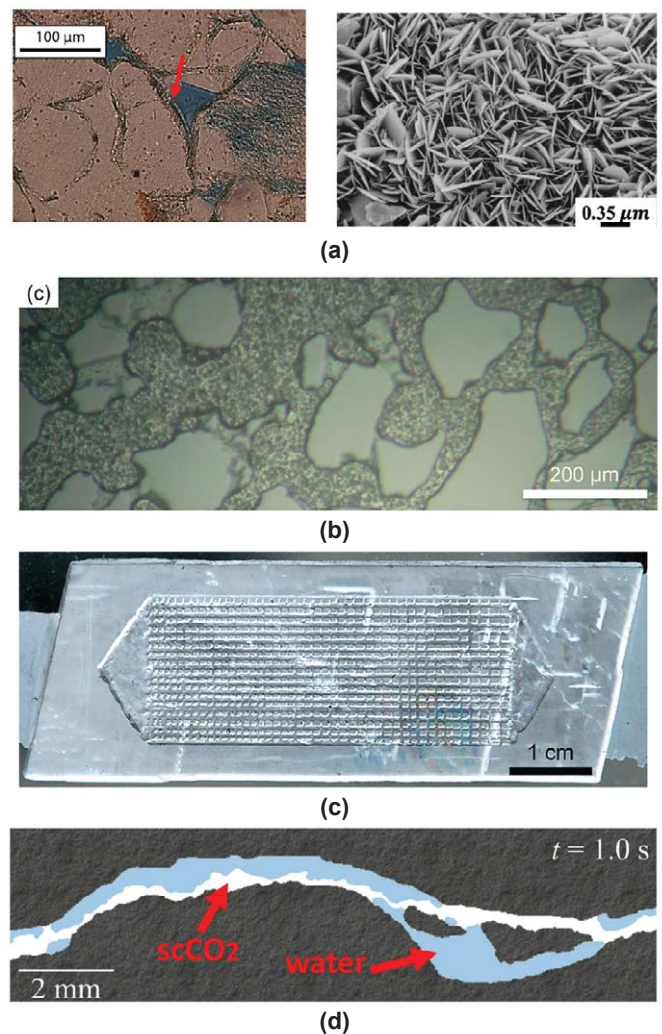


Fig. 7—(a) Polarized plane light (PPL) image of grains coated with chlorite cement (see arrow) (Mehmani et al., 2019b) and scanning electron microscopy (SEM) image of chlorite cement (Ulmer-Scholle et al., 2015). (b) Functionalized micromodels by depositing kaolinite clay on pore walls (Song and Kovscek, 2015). Micromodel fabricated using (c) calcite mineral (Song et al., 2014) and (d) shale (Porter et al., 2015) as the etching substrates.

INDUSTRY APPLICATIONS AND BEST PRACTICES

Repeat experiments are, in general, necessary for establishing uncertainty intervals for an observed flow behavior. Micro/nanofluidic experiments should therefore be subjected to repeated runs. However, the time scales of each fluid flow experiment and fabrication time/cost can render brute force Monte Carlo-like assessments unfeasible. This challenge is also encountered by molecular and pore-scale numerical simulations. Recent data-sharing initiatives by journals, such as the Transparency and Openness guidelines published by *Science* (Nosek et al., 2015) and adopted by the American Geophysical Union, are beneficial for data aggregation and uncertainty quantification.

Regarding industry applications, fluid/core analyses remain the preferred measurement methods and micro/nanofluidics should not be considered as a replacement for core measurements. In the absence of core samples, synthetic cores fabricated based on geological information are a potential future avenue but currently have not been sufficiently explored. For instance, fabrication of 3D representative cores (pseudocores) has been attempted with 3D printing (Head and Vanorio, 2016), but this method is currently limited by printer resolution and challenges with control of pore-surface texture and chemistry. It is very feasible that the 3D printing technology will improve with time. As Head and Vanorio (2016) discuss, CT scans, a basis for pseudocores, started with millimeter resolution until they rapidly reached micrometers and even nanometers in their voxel resolution. Other methods, such as 3D laser engraving

hold promise as well. Finally, 3D media, such as Vycor glass (Gruener and Huber, 2009), can serve as interesting proxies for nanoporous rocks, though their geologic representativeness may not be ideal. We therefore propose that, in the case of limited availability to reservoir fluid and rock samples, micro/nanofluidics can be used to obtain first-order estimations of rock-type-dependent transport properties. Such estimations can subsequently be corrected with history matching. Figure 8 shows the use of micro/nanofluidics in providing fluid and rock transport property measurements when only limited samples are available. The example in Fig. 8 shows the application of microfluidics to determine an approximate residual saturation for a vuggy carbonate sample following waterflooding. The residual saturation provides a starting point for reservoir development and can be adjusted as field data become available.

For core measurements that require impractical time scales, which is typical of two-phase flow properties of tight rocks, micro/nanofluidics can provide a priori rules for alternative investigations with reduced-order numerical methods, such as pore-network models. Micro/nanofluidics should be leveraged when current pore-network model algorithms or, in general, digital rock physics simulation prove inadequate in accuracy. Further, micro/nanofluidics are ideal for quick verification of hypotheses involving the efficacy of EOR methods. Similar to the use of applied micro/nanofluidics, each hypothesis testing effort should be informed with production field data. The use of micro/nanofluidics for rapid hypothesis testing is shown in Fig. 9. A given hypothesis should be first investigated via core

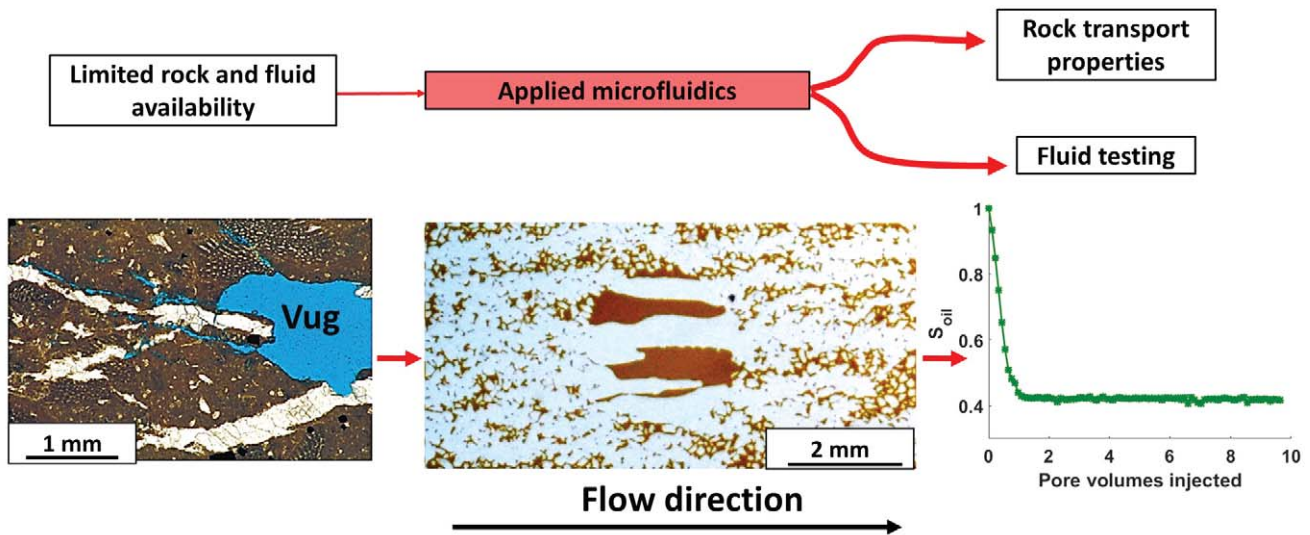


Fig. 8—(Upper) Roadmap for incorporation of micro/nanofluidic studies for obtaining a first-order approximation for a fluid or rock transport property. (Lower) An example application of the roadmap for determining the residual saturation of a vuggy carbonate sample. Petrographic thin section is from Scholle and Ulmer-Scholle (2003) while the microfluidics experiment was investigated in Mejia et al. (2019a).

measurements (high accuracy) and digital rock physics (ability to provide large parameter space for sensitivity analysis). If the hypothesis remains undetermined, micro/nanofluidics can serve as a diagnostic tool to validate the hypothesis. In the case of reservoir quality characterization and access to a robust chip fabrication facility, micro/nanofluidics can be used to perform a rapid sensitivity analysis of the implications of a particular reservoir property. In the example provided in Fig. 9, the hypothesis of whether authigenic cement can enhance oil recovery following gas injection was investigated with microfluidics (Mehmani et al., 2019a). This hypothesis can be difficult to test via coreflooding (given challenges in isolating/decoupling pore-scale variables) or digital rock physics (the high voxel resolution required to capture submicrometer roughness length scales pushes the boundaries of imaging resolution and computational cost). The main advantages and disadvantages of the three methods illustrated in Fig. 9 (micro/nanofluidics, digital rock physics and core measurements) are shown in Table 1. We emphasize that the three methods should be considered as complementing one another and exclusive.

Finally, we recommend that outsourcing micro/nanofluidics work to vendors be done with the agreement to deliver as many measurement details as possible. Otherwise, long-term partnership with an academic institute that

develops expertise in lab-on-a-chip devices and provides workflows for company review is encouraged. Such a long-term approach can additionally assist in developing and updating in-house micro/nanofluidics workflows.

CONCLUSIONS

Based on this review, we recommend lab-on-a-chip devices as tools to augment petrophysical laboratory measurements when the following criteria are met:

- (1) Practicality/Simplicity in Design – Fabrication of the devices is facile and replicable such that many disposable devices are available. Examples of chips of varying complexity were reviewed herein.
- (2) Consistency – One critical variable, such as pore size, material, or fluid composition is tuned at a time to form robust functional relationships, leveraging the critical benefit of controlled fluidic workflows, as contrasted to actual rocks.
- (3) Validation – Anomalous fluidic observations should be complemented with theory and/or molecular dynamics and other direct numerical simulation methods, again leveraging the powerful benefit that the majority of the fluidic geometry and boundary and initial conditions are known.

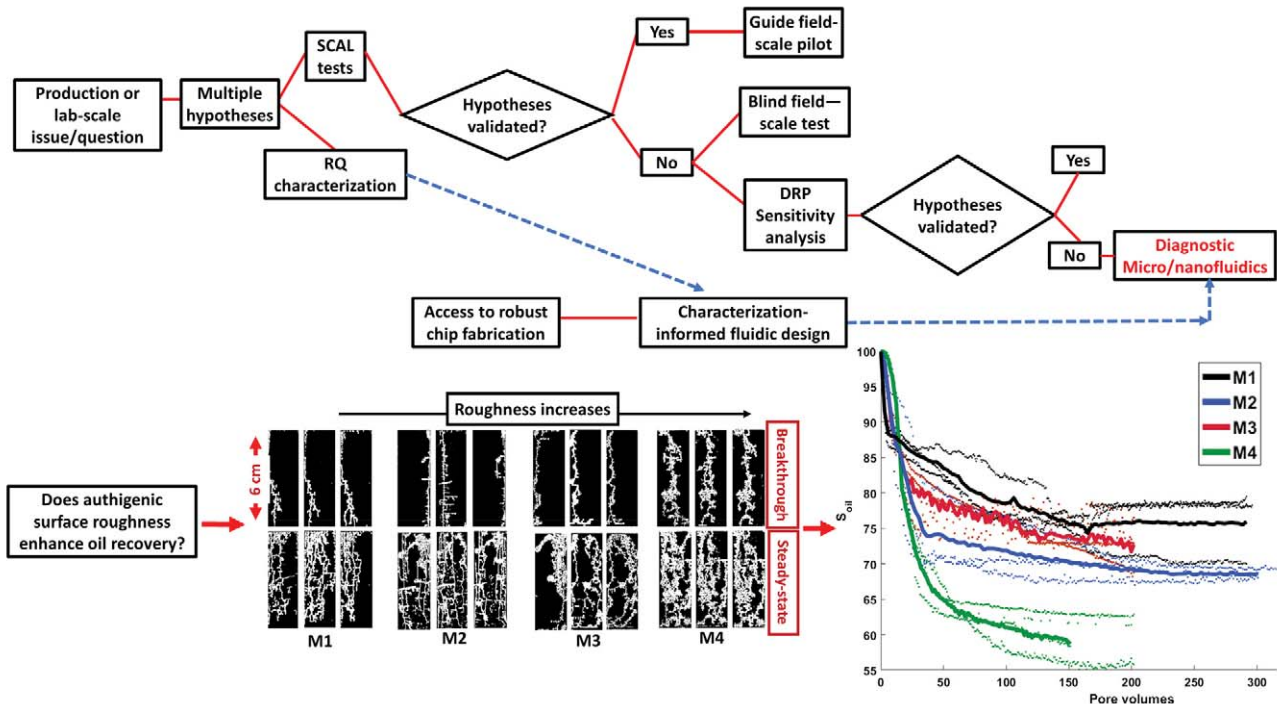


Fig. 9—(Upper) Roadmap for incorporation of micro/nanofluidic for hypothesis testing and reservoir characterization. (Lower) an example application of the roadmap for validating the hypothesis whether authigenic surface roughness can enhance oil recovery during gasflooding. Results are from Mehmani et al. (2019a).

Table 1—Main Advantages and Disadvantages of Micro/Nanofluidics, Digital Rock Physics, and Core Measurements

	Micro/Nanofluidics	Digital Rock Physics	Core Measurements
Key Advantages	Rapid Direct real-time visualization Small amounts of fluid required Repeatable	Convenient for probing the parameter space Wet laboratory and experimental costs avoided A robust software can be run without expertise in the algorithms Accuracy can be sacrificed depending on computational infrastructure	Most accurate representation of the subsurface and rock-fluid interaction phenomenon
Key Disadvantages	Two dimensional Synthetic systems Experience in fabrication and design is required Cleanroom access is typically needed	Requires benchmarking with experiments Depending on the application, simulations can be time consuming Algorithm development is nontrivial	Time consuming Core sample may not be available Reservoir fluids can be limited Pore-scale visualization is nontrivial

Ideally, such lab-on-a-chip devices can be implemented as fluid-transport calibration standards such that the aforementioned fluid behaviors can be mapped back to pore-size distributions and other matrix topology properties already quantified in petrophysical and reservoir quality workflows (e.g., via mercury porosimetry, nitrogen adsorption, NMR, petrography, etc.). In sum, use of fluidic devices as fit-for-purpose high-throughput diagnostic and upscaling tools has immense potential for the oil and gas industry and earth science research in general.

NOMENCLATURE

Abbreviations

CNT	= carbon nanotube
CT	= computed tomography
DWNT	= double-walled carbon nanotubes
EOR	= enhanced oil recovery
HSE	= health, safety and environmental
MD	= molecular dynamics
PC	= polycarbonate membrane
PDMS	= polydimethylsiloxane
PIV	= particle imaging velocimetry
PNM	= pore-network model
REA	= representative elementary area
REV	= representative elementary volume
SCAL	= special core analysis
UV	= ultraviolet

Symbols

q_{nw}	= flow rate of the nonwetting phase
q_w	= flow rate of the wetting phase
σ_{og}	= interfacial tension between oil and gas
σ_{ow}	= interfacial tension between oil and water
σ_{wg}	= interfacial tension between water and gas

ACKNOWLEDGEMENTS

Use of The University of Texas at Austin's Center for Nano and Molecular Science cleanroom was vital to some of the authors' reviewed works and we thank the Welch Foundation for supporting those facilities. We also thank The University of Texas at Austin Institute for Cellular and Molecular Biology and the Jackson School of Geosciences for the use of their microscopy equipment. This research was supported by the University of Texas at Austin Research Consortium on Formation Evaluation, sponsored by Anadarko Petroleum Corporation, Saudi Aramco, Baker Hughes, BHP Billiton, BP, China Oilfield Services LTD., ConocoPhillips, DEA, DET Norske, ENI, ExxonMobil, Hess, INPEX, Petrobras, Repsol, Paradigm, Schlumberger, Shell, Southwestern Energy, Statoil, Total, Wintershall, and Woodside Petroleum Limited. Carlos Torres-Verdín is thankful for the financial support provided by the Brian James Jennings Memorial Endowed Chair in Petroleum and Geosystems Engineering.

REFERENCES

- Akbarabadi, M., Saraji, S., Piri, M., Georgi, D., and Delshad, M., 2017, Nano-Scale Experimental Investigation of In-Situ Wettability and Spontaneous Imbibition in Ultra-Tight Reservoir Rocks, *Advances In Water Resources*, **107**, 160–179. DOI: 10.1016/j.advwatres.2017.06.004.
- Alfi, M., Banerjee, D., and Nasrabadi, H., 2016, Effect of Confinement on the Dynamic Contact Angle of Hydrocarbons, *Energy & Fuels*, **30**(11), 8962–8967. DOI: 10.1021/acs.energyfuels.6b01450.
- Armstrong, R.T., and Berg, S., 2013, Interfacial Velocities and Capillary Pressure Gradients During Haines Jumps, *Physical Review E*, **88**(4), 043010. DOI: 10.1103/PhysRevE.88.043010.
- Avraam, D.G., Kolonis, G.B., Roumeliotis, T.C., Constantinides, G.N., and Payatakes, A.C., 1994, Steady-State Two-Phase

- Flow Through Planar and Nonplanar Model Porous Media, *Transport in Porous Media*, **16**(1), 75–101. DOI: 10.1007/BF01059777.
- Avraam, D.G., and Payatakes, A.C., 1995, Flow Regimes and Relative Permeabilities During Steady-State Two-Phase Flow in Porous Media, *Journal of Fluid Mechanics*, **293**, 207–236. DOI: 10.1017/S0022112095001698.
- Bakli, C., and Chakraborty, S., 2012, Capillary Filling Dynamics of Water in Nanopores, *Applied Physics Letters*, **101**(15), 153112. DOI: 10.1063/1.4758683.
- Beskok, A., and Karniadakis, G.E., 1999, Report: A Model for Flows in Channels, Pipes, and Ducts at Micro and Nano Scales, *Microscale Thermophysical Engineering*, **3**(1), 43–77. DOI: 10.1080/108939599199864.
- Bhattacharya, S., Datta, A., Berg, J.M., and Gangopadhyay, S., 2005, Studies on Surface Wettability of Poly(Dimethyl) Siloxane (PDMS) and Glass Under Oxygen-Plasma Treatment and Correlation With Bond Strength, *Journal of Microelectromechanical Systems*, **14**(3), 590–597. DOI: 10.1109/JMEMS.2005.844746.
- Bryant, S.L., King, R., and Mellor, D.W., 1993, Network Model Evaluation of Permeability and Spatial Correlation in a Real Random Sphere Packing, *Transport in Porous Media*, **11**(1), 53–70. DOI: 10.1007/BF00614635.
- Bultreys, T., Van Hoorebeke, L., and Cnudde, V., 2015, Multi-Scale, Micro-Computed Tomography-Based Pore Network Models to Simulate Drainage in Heterogeneous Rocks, *Advances in Water Resources*, **78**, 36–49. DOI: 10.1016/j.advwatres.2015.02.003.
- Byrnes, A., Cluff, R., Webb, J., Victorine, J., Staider, K., Osburn, D., Knoderer, A., Metheny, O., Hommertzhaim, T., Byrnes, J., Krygowski, D., and Whittaker, S., 2008, Analysis of Critical Permeability, Capillary Pressure and Electrical Properties for Mesaverde Tight Gas Sandstones From Western U.S. Basins, U.S. Department of Energy, National Energy Technology Laboratory, Contract No. DE-FC26-05NT42660. DOI: 10.2172/971248.
- Chatzis, I., Morrow, N.R., and Lim, H.T., 1983, Magnitude and Detailed Structure of Residual Oil Saturation, Paper SPE-10681, *SPE Journal*, **23**(2), 311–326. DOI: 10.2118/10681-PA.
- Chen, Y., Li, Y., Valocchi, A.J., and Christensen, K.T., 2018, Lattice Boltzmann Simulations of Liquid CO₂ Displacing Water in a 2D Heterogeneous Micromodel at Reservoir Pressure Conditions, *Journal Of Contaminant Hydrology*, **212**, 14–27. DOI: 10.1016/j.jconhyd.2017.09.005.
- Conn, C., Ma, K., Hirasaki, G.J., and Biswal S.L., 2014, Visualizing Oil Displacement With Foam in a Microfluidic Device With Permeability Contrast, *Lab on a Chip*, **14**(20), 3968–3977. DOI: 10.1039/C4LC00620H.
- Datta, S.S., Chiang, H., Ramakrishnan, T.S., and Weitz, D.A., 2013, Spatial Fluctuations of Fluid Velocities in Flow Through a Three-Dimensional Porous Medium, *Physical Review Letters*, **111**(6), 064501. DOI: 10.1103/physrevlett.111.064501.
- De Haas, T.W., Fadaei, H., Guerrero, U., and Sinton, D., 2013, Steam-on-a-Chip for Oil Recovery: The Role of Alkaline Additives in Steam Assisted Gravity Drainage, *Lab on a Chip*, **13**(19), 3832–3839. DOI: 10.1039/C3LC50612F.
- Dehghan, A.A., Ghorbanizadeh, S., and Ayatollahi, S., 2012, Investigating the Fracture Network Effects on Sweep Efficiency During WAG Injection Process, *Transport in Porous Media*, **93**(3), 577–595. DOI: 10.1007/S11242-012-9970-7.
- Dehghanpour, H., Lan, Q., Saeed, Y., Fei, H., and Qi, Z., 2013, Spontaneous Imbibition of Brine and Oil in Gas Shales: Effect of Water Adsorption and Resulting Microfractures, *Energy & Fuels*, **27**(6), 3039–3049. DOI: 10.1021/Ef4002814.
- Dendukuri, D., Gu, S.S., Pregibon, D.C., Hatton, T.A., and Doyle, P.S., 2007, Stop-Flow Lithography in a Microfluidic Device, *Lab on a Chip*, **7**(7), 818–828. DOI: 10.1039/B703457A.
- Dong, M., Dullien, F.A.L. and Chatzis, I., 1995, Imbibition of Oil in Film Form Over Water Present in Edges of Capillaries With an Angular Cross Section, *Journal of Colloid and Interface Science*, **172**(1), 21–36. DOI: 10.1006/jcis.1995.1221.
- Doorwar, S., and Mohanty, K.K., 2014, Extension of the Dielectric Breakdown Model for Simulation of Viscous Fingering at Finite Viscosity Ratios, *Physical Review E*, **90**(1), 013028. DOI: 10.1103/PhysRevE.90.013028.
- Doorwar, S., and Mohanty, K.K., 2017, Viscous-Fingering Function for Unstable Immiscible Flows, Paper SPE-173290, *SPE Journal*, **22**(1), 19–31. DOI: 10.2118/173290-PA.
- Du, Y., Xu, K., Mejia L., Zhu, P., and Balhoff, M., 2019, Microfluidic Investigation of Low-Salinity Effects During Oil Recovery: A No-Clay and Time-Dependent Mechanism, Paper SPE-197056, *SPE Journal*, preprint, DOI: 10.2118/197056-PA.
- Fadaei, H., Scarff, B., and Sinton, D., 2011, Rapid Microfluidics-Based Measurement of CO₂ Diffusivity in Bitumen, *Energy & Fuels*, **25**(10), 4829–4835. DOI: 10.1021/Ef2009265.
- Fisher, R., Shah, M.K., Eskin, D., Schmidt, K., Singh, A., Molla, S., and Mostowfi, F., 2013, Equilibrium Gas–Oil Ratio Measurements Using a Microfluidic Technique, *Lab on a Chip*, **13**(13), 2623–2633. DOI: 10.1039/C3LC00013C.
- Fogden, A., Olson, T., Cheng, Q., Middleton, J., Kingston, A., Turner, M., Sheppard, A., and Armstrong, R., 2015, Dynamic Micro-CT Imaging of Diffusion in Unconventionals, Paper URTEC-2154822 presented at the Unconventional Resources Technology Conference, San Antonio, Texas, USA, 20–22 July. DOI: 10.15530/urtec-2015-2154822.
- Ford, D.M., Simanek, E.E., and Shantz, D.F., 2005, Engineering Nanospaces: Ordered Mesoporous Silicas as Model Substrates for Building Complex Hybrid Materials, *Nanotechnology*, **16**(7), S458–S475. DOI: 10.1088/0957-4484/16/7/022.
- Frank, F., Liu, C., Scanziani, A. Alpak, F.O., and Riviere, B., 2018, An Energy-Based Equilibrium Contact Angle Boundary Condition on Jagged Surfaces for Phase-Field Methods, *Journal of Colloid and Interface Science*, **523**, 282–291. DOI: 10.1016/j.jcis.2018.02.075.
- Grate, J.W., Warner, M.G., Pittman, J.W., Dehoff, K.J., Wietsma, T.W., Zhang, C., and Oostrom, M., 2013, Silane Modification of Glass and Silica Surfaces to Obtain Equally Oil-Wet Surfaces in Glass-Covered Silicon Micromodel Applications, *Water Resources Research*, **49**(8), 4724–4729. DOI: 10.1002/wrcr.20367.
- Gruener, S., and Huber, P., 2009, Spontaneous Imbibition Dynamics

- of an N-Alkane in Nanopores: Evidence of Meniscus Freezing and Monolayer Sticking, *Physical Review Letters*, **103**(17), 174501. DOI: 10.1103/PhysRevLett.103.174501.
- Gruener, S., Sadjadi, Z., Hermes, H.E., Kityk, A.V., Knorr, K., Egelhaaf, S.U., Rieger, H., and Huber, P., 2012, Anomalous Front Broadening During Spontaneous Imbibition in a Matrix With Elongated Pores, *Proceedings of the National Academy of Sciences*, **109**(26), 10245–10250. DOI: 10.1073/pnas.1119352109.
- Hasham, A.A., Abedini, A., Jatukaran, A., Persad, A., and Sinton, D., 2018, Visualization of Fracturing Fluid Dynamics in a Nanofluidic Chip, *Journal of Petroleum Science and Engineering*, **165**, 181–186. DOI: 10.1016/j.petrol.2018.02.017.
- He, K., Xu, L., Gao, Y., Neeves, K.B., Yin, X., Bai, B., Ma, Y., and Smith, J., 2014, Validating Surfactant Performance in the Eagle Ford Shale: A Correlation Between the Reservoir-On-A-Chip Approach and Enhanced Well Productivity, Paper SPE-169147 presented at the SPE Improved Oil Recovery Symposium, Tulsa, Oklahoma, USA, 12–16 April. DOI: 10.2118/169147-MS.
- He, K., Xu, L., Gao, Y., Yin, X., and Neeves, K.B., 2015, Evaluation of Surfactant Performance in Fracturing Fluids for Enhanced Well Productivity in Unconventional Reservoirs Using Rock-on-a-Chip Approach, *Journal of Petroleum Science and Engineering*, **135**, 531–541. DOI: 10.1016/J.Petrol.2015.10.008.
- Head, D., and Vanorio, T., 2016, Effects of Changes in Rock Microstructures on Permeability: 3-D Printing Investigation, *Geophysical Research Letters*, **43**(14), 7494–7502. DOI: 10.1002/2016GL069334.
- Hele-Shaw, H.S., 1898, The Flow of Water, *Nature*, **58**, 34–36. DOI: 10.1038/058034a0.
- Herring, A.L., Gilby, F.J., Li, Z., McClure, J.E., Turner, M., Veldkamp, J.P., Beeching, L., and Sheppard, A.P., 2018, Observations of Nonwetting Phase Snap-Off During Drainage, *Advances in Water Resources*, **121**, 32–43. DOI: 10.1016/j.advwatres.2018.07.016.
- Hoffmann, F., Cornelius, M., Morell, J., and Fröba, M., 2006, Silica-Based Mesoporous Organic–Inorganic Hybrid Materials, *Angewandte Chemie International Edition*, **45**(20), 3216–3251. DOI: 10.1002/anie.200503075.
- Holt, J.K., Park, H.G., Wang, Y., Stadermann, M., Artyukhin, A.B., Grigoropoulos, C.P., Noy, A., and Bakajin, O., 2006, Fast Mass Transport Through Sub-2-Nanometer Carbon Nanotubes, *Science*, **312**(5776), 1034–1037. DOI: 10.1126/science.1126298.
- Islam, A., Chevalier, S., Ben Salem, I., Bernabe, Y., Juanes, R., and Sassi, M., 2014, Characterization of the Crossover From Capillary Invasion to Viscous Fingering to Fracturing During Drainage in a Vertical 2D Porous Medium, *International Journal of Multiphase Flow*, **58**, 279–291. DOI: 10.1016/j.ijmultiphaseflow.2013.10.002.
- Jacobs, T., 2019, Reservoir-on-a-Chip Technology Opens a New Window Into Oilfield Chemistry, Paper SPE-0119-0025-JPT, *Journal of Petroleum Technology*, **71**(1), 25–27. DOI: 10.2118/0119-0025-JPT.
- Javadpour, F., 2009, Nanopores and Apparent Permeability of Gas Flow in Mudrocks (Shales and Siltstone), *Journal of Canadian Petroleum Technology*, **48**(8), 16–21. DOI: 10.2118/09-08-16-DA.
- Joekar-Niasar, V., Hassanizadeh, S.M., and Dahle, H.K., 2010, Non-Equilibrium Effects in Capillarity and Interfacial Area in Two-Phase Flow: Dynamic Pore-Network Modelling, *Journal of Fluid Mechanics*, **655**, 38–71. DOI: 10.1017/S0022112010000704.
- Jones, B.R., Brouwers, L.B., and Dippenaar, M.A., 2018, Partially to Fully Saturated Flow Through Smooth, Clean, Open Fractures: Qualitative Experimental Studies, *Hydrogeology Journal*, **26**(3), 945–961. DOI: 10.1007/S10040-017-1680-3.
- Kalra, A., Garde, S., and Hummer, G., 2003, Osmotic Water Transport Through Carbon Nanotube Membranes, *Proceedings of the National Academy of Sciences*, **100**(18), 10175–10180. DOI: 10.1073/pnas.1633354100.
- Keller, A.A., Blunt, M.J., and Roberts, A.P.V. 1997, Micromodel Observation of the Role of Oil Layers in Three-Phase Flow, *Transport in Porous Media*, **26**(3), 277–297. DOI: 10.1023/A:1006589611884.
- Kelly, S., Torres-Verdín, C., and Balhoff, M., 2015, Shale Fluid Transport in Nanoscale Networks: The Competing Roles of Fluid Properties, Interfaces and Network Geometry, Paper URTEC-2154187 presented at the Unconventional Resources Technology Conference, San Antonio, Texas, 20–22 July. DOI: 10.15530/URTEC-2015-2154187-MS.
- Kelly, S., Torres-Verdín, C., and Balhoff, M., 2016a, Subsurface to Substrate: Dual-Scale Micro/Nanofluidic Networks for Investigating Transport Anomalies in Tight Porous Media, *Lab on a Chip*, **16**(15), 2829–2839. DOI: 10.1039/C6LC00613B.
- Kelly, S., Torres-Verdín, C., and Balhoff, M.T., 2016b, Anomalous Liquid Imbibition at the Nanoscale: The Critical Role of Interfacial Deformations, *Nanoscale*, **8**(5), 2751–2767. DOI: 10.1039/C5NR04462F.
- Kelly, S., Torres-Verdín, C., and Balhoff, M.T., 2018, Influences of Polarity and Hydration Cycles on Imbibition Hysteresis in Silica Nanochannels, *Physical Chemistry Chemical Physics*, **20**(1), 456–466. DOI: 10.1039/C7CP05833K.
- Khajepour, H., Mahmoodi, M., Biria, D., and Ayatollahi, S., 2014, Investigation of Wettability Alteration Through Relative Permeability Measurement During MEOR Process: A Micromodel Study, *Journal of Petroleum Science and Engineering*, **120**, 10–17. DOI: 10.1016/j.petrol.2014.05.022.
- Lee, H., Lee, S-G., and Doyle, P.S., 2015, Photopatterned Oil-Reservoir Micromodels With Tailored Wetting Properties, *Lab on a Chip*, **15**(14), 3047–3055. DOI: 10.1039/C5LC00277J.
- Lele, P., Syed, A.H., Riordon, J., Mosavat, N., Guerrero, A., Fadaei, H., and Sinton, D., 2018, Deformation of Microdroplets in Crude Oil for Rapid Screening of Enhanced Oil Recovery Additives, *Journal of Petroleum Science and Engineering*, **165**, 298–304. DOI: 10.1016/j.petrol.2018.02.009.
- Lenormand, R., Touboul, E., and Zarcone, C., 1988, Numerical Models and Experiments on Immiscible Displacements in Porous Media, *Journal of Fluid Mechanics*, **189**, 165–187. DOI: 10.1017/S0022112088000953.
- Lenormand, R., and Zarcone, C., 1984, Role of Roughness and

- Edges During Imbibition in Square Capillaries, Paper SPE-13264 presented at the SPE Annual Technical Conference and Exhibition, Houston, Texas, USA, 16–19 September. DOI: 10.2118/13264-MS.
- Lenormand, R., and Zarcone, C., 1985, Invasion Percolation in an Etched Network: Measurement of a Fractal Dimension, *Physical Review Letters*, **54**(20), 2226–2229. DOI: 10.1103/PhysRevLett.54.2226.
- Li, Y., Kazemifar, F., Blois, G., and Christensen, K.T., 2017, Micro-PIV Measurements of Multiphase Flow of Water and Liquid CO₂ in 2-D Heterogeneous Porous Micromodels, *Water Resources Research*, **53**(7), 6178–6196. DOI: 10.1002/2017WR020850.
- Li, S., Lowengrub, J.S., Fontana, J., and Palffy-Muhoray, P., 2009, Control of Viscous Fingering Patterns in a Radial Hele-Shaw Cell, *Physical Review Letters*, **102**(17), 174501. DOI: 10.1103/PhysRevLett.102.174501.
- Li, H., Zhong, J., Pang, Y., Zandavi, S.H., Persad, A.H., Xu, Y., Mostowfi, F., and Sinton, D., 2017, Direct Visualization of Fluid Dynamics in Sub-10 Nm Nanochannels, *Nanoscale*, **9**(27), 9556–9561. DOI: 10.1039/C7NR02176C.
- Ma, J., Sanchez, J. P., Wu, K., Couples, G. D., and Jiang, Z., 2014, A Pore Network Model for Simulating Non-Ideal Gas Flow in Micro- and Nano-Porous Materials, *Fuel*, **116**, 498–508. DOI: 10.1016/j.fuel.2013.08.041.
- Mason, G., and Mellor, D.W., 1995, Simulation of Drainage and Imbibition in a Random Packing of Equal Spheres, *Journal of Colloid and Interface Science*, **176**(1), 214–225. DOI: 10.1006/jcis.1995.0024.
- Martic, G., Gentner, F., Seveno, D., Coulon, D., De Coninck, J., and Blake, T.D., 2002, A Molecular Dynamics Simulation of Capillary Imbibition, *Langmuir*, **18**(21), 7971–7976. DOI: 10.1021/La020068n.
- Mehmani, A., Kelly, S., Torres-Verdin, C., and Balhoff, M., 2017, Quantification of Fracture-Matrix Fluid Transport in Unconventional Rocks Using Two-Scale Microfluidic Chips, Paper URTEC-2669314 presented at the Unconventional Resources Technology Conference, Austin, Texas, USA, 24–26 July. DOI: 10.15530/URTEC-2017-2669314-MS.
- Mehmani, A., Kelly, S., Torres-Verdin, C., and Balhoff, M., 2018, Impact of Authigenic Surface Roughness on Water Invasion and Flowback in Fractured Media: A Micromodel Study, Paper URTEC-2871486 presented at the Unconventional Resources Technology Conference, Houston, Texas, USA, 23–25 July. DOI: 10.15530/URTEC-2018-2871486-MS.
- Mehmani, A., Kelly, S., Torres-Verdin, C., and Balhoff, M., 2019a, Residual Oil Saturation Following Gas Injection in Sandstones: Microfluidic Quantification of the Impact of Pore-Scale Surface Roughness, *Fuel*, **251**, 147–161. DOI: 10.1016/j.fuel.2019.02.118.
- Mehmani, A., Milliken, K., and Prodanović, M., 2019b, Predicting Flow Properties In Diagenetically-Altered Media With Multi-Scale Process-Based Modeling: A Wilcox Formation Case Study, *Marine and Petroleum Geology*, **100**, 179–194. DOI: 10.1016/j.marpetgeo.2018.09.001.
- Mehmani, Y., Oostrom, M., and Balhoff, M.T., 2014, A Streamline Splitting Pore-Network Approach for Computationally Inexpensive and Accurate Simulation of Transport in Porous Media, *Water Resources Research*, **50**(3), 2488–2517. DOI: 10.1002/2013WR014984.
- Mehmani, A., and Prodanović, M., 2014, The Application of Sorption Hysteresis in Nano-Petrophysics Using Multiscale Multiphysics Network Models, *International Journal of Coal Geology*, **128–129**, 96–108. DOI: 10.1016/j.coal.2014.03.008.
- Mehmani, A., Prodanović, M., and Javadpour, F., 2013, Multiscale, Multiphysics Network Modeling of Shale Matrix Gas Flows, *Transport in Porous Media*, **99**(2), 377–390. DOI: 10.1007/S11242-013-0191-5.
- Mejia, L., Mehmani, A., Balhoff, M., and Torres-Verdin, C., 2019a, Process-Based Microfluidics: Tools for Quantifying the Impact of Reservoir Quality on Recovery Factor, Paper URTEC-2019-888 presented at the Unconventional Resources Technology Conference, Denver, Colorado, USA, 22–24 July. DOI: 10.105530/URTEC-2019-888.
- Mejia, L., Tagavifar, M., Xu, K., Mejia, M., Du, Y., and Balhoff, M., 2019b, Surfactant Flooding in Oil-Wet Micromodels With High Permeability Fractures, *Fuel*, **241**, 1117–1128. DOI: 10.1016/j.fuel.2018.12.076.
- Mostowfi, F., Molla, S., and Tabeling, P., 2012, Determining Phase Diagrams of Gas–Liquid Systems Using a Microfluidic PVT, *Lab on a Chip*, **12**(21), 4381–4387. DOI: 10.1039/C2LC40706J.
- Nghe, P., Tabeling, P., and Ajdari, A., 2010, Flow-Induced Polymer Degradation Probed by a High Throughput Microfluidic Set-Up, *Journal of Non-Newtonian Fluid Mechanics*, **165**(7), 313–322. DOI: 10.1016/j.jnnfm.2010.01.006.
- Nguyen, P., Fadaei, H., and Sinton, D., 2013, Microfluidics Underground: A Micro-Core Method for Pore Scale Analysis of Supercritical CO₂ Reactive Transport in Saline Aquifers, *Journal of Fluids Engineering*, **135**(2), 021203. DOI: 10.1115/1.4023644.
- Nguyen, P., Mohaddes, D., Riordon, J., Fadaei, H., Lele, P., and Sinton, D., 2015, Fast Fluorescence-Based Microfluidic Method for Measuring Minimum Miscibility Pressure of CO₂ In Crude Oils, *Analytical Chemistry*, **87**(6), 3160–3164. DOI: 10.1021/ac5047856.
- Niasar, V.J., Hassanizadeh, S.M., Pyrak-Nolte, L.J., and Berentsen, C., 2009, Simulating Drainage and Imbibition Experiments in a High-Porosity Micromodel Using an Unstructured Pore Network Model, *Water Resources Research*, **45**(2). DOI: 10.1029/2007WR006641.
- Nosek, B.A., and others, 2015, Promoting an Open Research Culture, *Science*, **348**(6242), 1422–1425. DOI: 10.1126/science.aab2374.
- Noy, A., Park, H.G., Fornasiero, F., Holt, J.K., Grigoropoulos, C.P., and Bakajin, O., 2007, Nanofluidics in Carbon Nanotubes, *Nanotoday*, **2**(6), 22–29. DOI: 10.1016/S1748-0132(07)70170-6.
- Oren, P.E., Billiotte, J., and Pinczewski, W.V., 1992, Mobilization of Waterflood Residual Oil by Gas Injection for Water-Wet Conditions, Paper SPE-20185, *SPE Formation Evaluation*, **7**(1), 70–78. DOI: 10.2118/20185-PA.
- Oyarzua, E., Walther, J.H., Mejía, A., and Zambrano, H.A., 2015, Early Regimes of Water Capillary Flow in Slit Silica

- Nanochannels, *Physical Chemistry Chemical Physics*, **17**(22), 14731–14739. DOI: 10.1039/C5CP01862E.
- Peters, E.J., 2012a, *Advanced Petrophysics: Volume 1: Geology, Porosity, Absolute Permeability, Heterogeneity, and Geostatistics*. Live Oak Book Company. ISBN: 978-1936909452.
- Peters, E.J., 2012b, *Advanced Petrophysics: Volume 2: Dispersion, Interfacial Phenomena/Wettability, Capillarity/Capillary Pressure, Relative Permeability*. Live Oak Book Company. ISBN: 978-1936909469.
- Piri, M., and Blunt, M.J., 2005a, Three-Dimensional Mixed-Wet Random Pore-Scale Network Modeling of Two- and Three-Phase Flow in Porous Media. I. Model Description, *Physical Review E*, **71**(2), 026301. DOI: 10.1103/PhysRevE.71.026301.
- Piri, M., and Blunt, M.J., 2005b, Three-Dimensional Mixed-Wet Random Pore-Scale Network Modeling of Two- and Three-Phase Flow in Porous Media. II. Results, *Physical Review E*, **71**(2), 026302. DOI: 10.1103/PhysRevE.71.026302.
- Porter, M.L., Jiménez-Martínez, J., Martínez, R., McCulloch Q., Carey, J.W., and Viswanathan, H. S., 2015, Geo-Material Microfluidics at Reservoir Conditions for Subsurface Energy Resource Applications, *Lab on a Chip*, **15**(20), 4044–4053. DOI: 10.1039/C5LC00704F.
- Qi, P., Ehrenfried, D.H., Koh, H., and Balhoff, M.T., 2017, Reduction of Residual Oil Saturation in Sandstone Cores by Use of Viscoelastic Polymers, Paper SPE-179689, *SPE Journal*, **22**(2), 447–458. DOI: 10.2118/179689-PA.
- Radenovic, A., Trepagnier, E., Csencsits, R., Downing, K.H., and Liphardt, J., 2008, Fabrication of 10 nm Diameter Hydrocarbon Nanopores, *Applied Physics Letters*, **93**(18), 183101. DOI: 10.1063/1.3012376.
- Raeini, A.Q., Bijeljic, B., and Blunt, M.J. 2014, Numerical Modelling of Sub-Pore Scale Events in Two-Phase Flow Through Porous Media, *Transport in Porous Media*, **101**(2), 191–213. DOI: 10.1007/S11242-013-0239-6.
- Riewchotisakul, S., and Akkutlu, I.Y., 2016, Adsorption-Enhanced Transport of Hydrocarbons in Organic Nanopores, Paper SPE-175107, *SPE Journal*, **21**(6), 1960-1969. DOI: 10.2118/175107-PA.
- Roof, J.G., 1970, Snap-Off of Oil Droplets in Water-Wet Pores, Paper SPE-2504, *SPE Journal*, **10**(1), 85–90. DOI: 10.2118/2504-PA.
- Roy, S., Raju, R., Chuang, H.F., Cruden, B.A., and Meyyappan, M., 2003, Modeling Gas Flow Through Microchannels and Nanopores, *Journal of Applied Physics*, **93**(8), 4870–4879. DOI: 10.1063/1.1559936.
- Saffman, P.G., and Taylor, G.I., 1958, The Penetration of a Fluid Into a Porous Medium or Hele-Shaw Cell Containing a More Viscous Liquid, *Proceedings of the Royal Society London A*, **245**(1242), 312–329. DOI: 10.1098/rspa.1958.0085.
- Sakhaee-Pour, A., and Bryant, S., 2012, Gas Permeability of Shale, Paper SPE-146944, *SPE Reservoir Evaluation & Engineering*, **15**(4), 401–409. DOI: 10.2118/146944-PA.
- Schmatz, J., Urai, J.L., Berg, S., and Ott, H., 2015, Nanoscale Imaging of Pore-Scale Fluid-Fluid-Solid Contacts in Sandstone, *Geophysical Research Letters*, **42**(7), 2189–2195. DOI: 10.1002/2015GL063354.
- Schneider, M.H., Sieben, V.J., Kharrat, A.M., and Mostowfi, F., 2013, Measurement of Asphaltenes Using Optical Spectroscopy on a Microfluidic Platform, *Analytical Chemistry*, **85**(10), 5153–5160. DOI: 10.1021/Ac400495x.
- Scholle, P.A., and Ulmer-Scholle, D.S., 2003, *A Color Guide to the Petrography of Carbonate Rocks: Grains, Textures, Porosity, Diagenesis*, AAPG Memoir **77**. DOI: 10.1306/M77973.
- Skoulidas, A.I., Ackerman, D.M., Johnson, J.K., and Sholl, D.S., 2002, Rapid Transport of Gases in Carbon Nanotubes, *Physical Review Letters*, **89**(18), 185901. DOI: 10.1103/PhysRevLett.89.185901.
- Song, W., De Haas, T.W., Fadaei, H., and Sinton, D., 2014, Chip-off-the-Old-Rock: The Study of Reservoir-Relevant Geological Processes With Real-Rock Micromodels, *Lab On A Chip*, **14**(22), 4382–4390. DOI: 10.1039/C4LC00608A.
- Song, W., and Kovscek, A.R., 2015, Functionalization of Micromodels With Kaolinite for Investigation of Low Salinity Oil-Recovery Processes, *Lab on a Chip*, **15**(16), 3314–3325. DOI: 10.1039/C5LC00544B.
- Song, W., and Kovscek, A.R., 2016, Direct Visualization of Pore-Scale Fines Migration and Formation Damage During Low-Salinity Waterflooding, *Journal of Natural Gas Science and Engineering*, **34**, 1276–1283. DOI: 10.1016/j.jngse.2016.07.055.
- Stokes, J.P., Weitz, D.A., Gollub, J.P. Dougherty, A., Robbins, M.O., Chaikin, M., and Lindsay, H.M., 1986, Interfacial Stability of Immiscible Displacement in a Porous Medium, *Physical Review Letters*, **57**(14), 1718–1721. DOI: 10.1103/PhysRevLett.57.1718.
- Sun, W., Qu, Z., and Tang, G.-Q., 2004, Characterization of Water Injection in Low Permeable Rock Using Sandstone Micro-Model, Paper SPE-86964 presented at the SPE International Thermal Operations and Heavy Oil Symposium and Western Regional Meeting, Bakersfield, California, USA, 16–18 March. DOI: 10.2118/86964-MS.
- Tomutsa, L., Mahmood, S.M., Brinkmeyer, A., and Honarpour, M., 1990, Application of Integrated Pore-to-Core Image Analysis to Study Fluid Distribution in Reservoir Rocks, Paper SPE-20478 presented at the SPE Annual Technical Conference and Exhibition, New Orleans, Louisiana, USA, 23–26 September. DOI: 10.2118/20478-MS.
- Ulmer-Scholle, D.S., Scholle, A., Schieber, J., and Raine, R.J., 2015, *A Color Guide to the Petrography of Sandstones*, AAPG Memoir **109**. DOI: 10.1306/M1091304.
- Valvatne, P.H., and Blunt, M.J., 2004, Predictive Pore-Scale Modeling of Two-Phase Flow in Mixed Wet Media, *Water Resources Research*, **40**(7). DOI: 10.1029/2003WR002627.
- Wan, J., Tokunaga, T.K., Tsang, C.-F., and Bodvarsson, G.S., 1996, Improved Glass Micromodel Methods for Studies of Flow and Transport in Fractured Porous Media, *Water Resources Research*, **32**(7), 1955–1964. DOI: 10.1029/96WR00755.
- Wang, S., Feng, Q., Javadpour, F., and Yang, Y.-B., 2016, Breakdown of Fast Mass Transport of Methane Through Calcite Nanopores, *Journal of Physical Chemistry C*, **120**(26), 14260–14269. DOI: 10.1021/acs.jpcc.6b05511.
- Wang, S., Feng, Q., Zha, M., Javadpour, F., and Hu, Q., 2017, Supercritical Methane Diffusion in Shale Nanopores:

- Effects of Pressure, Mineral Types, and Moisture Content, *Energy & Fuels*, **32**(1), 169–180. DOI: 10.1021/acs.energyfuels.7b02892.
- Wang, S., Javadpour, F., and Feng, Q., 2016a, Fast Mass Transport of Oil and Supercritical Carbon Dioxide Through Organic Nanopores in Shale, *Fuel*, **181**, 741–758. DOI: 10.1016/j.fuel.2016.05.057.
- Wang, S., Javadpour, F., and Feng, Q., 2016b, Molecular Dynamics Simulations of Oil Transport Through Inorganic Nanopores in Shale, *Fuel*, **171**, 74–86. DOI: 10.1016/j.fuel.2015.12.071.
- Wu, Q., Bai, B., Ma, Y., Ok, J.T., Yin, X., and Neeves, K., 2014, Optic Imaging of Two-Phase-Flow Behavior in 1D Nanoscale Channels, Paper SPE-164549, *SPE Journal*, **19**(5), 793–802. DOI: 10.2118/164549-PA.
- Xu, K., Zhu, P., Colon, T., Huh, C., and Balhoff, M., 2016, A Microfluidic Investigation of the Synergistic Effect of Nanoparticles and Surfactants In Macro-Emulsion-Based Enhanced Oil Recovery, Paper SPE-179691, *SPE Journal*, **22**(2), 459–469. DOI: 10.2118/179691-PA.
- Zhao, B., MacMinn, C.W., and Juanes, R., 2016, Wettability Control on Multiphase Flow in Patterned Microfluidics, *Proceedings of the National Academy of Sciences*, **113**(37), 10251–10256. DOI: 10.1073/pnas.1603387113.
- Zhong, J., Abedini, A., Xu, L., Xu, Y., Qi, Z., Mostowfi, F., and Sinton, D., 2018, Nanomodel Visualization of Fluid Injections in Tight Formations, *Nanoscale*, **10**(46), 21994–22002. DOI: 10.1039/C8NR06937A.
- Zhou, J., Ellis, A.V., and Voelcker, N.H., 2010, Recent Developments in PDMS Surface Modification for Microfluidic Devices, *Electrophoresis*, **31**(1), 2–16. DOI: 10.1002/Elps.200900475.

Carlos Torres-Verdín received a PhD in Engineering Geoscience from the University of California at Berkeley in 1991. During 1991–1997, he held the position of Research Scientist with Schlumberger-Doll Research. From 1997–1999, he was Reservoir Specialist and Technology Champion with YPF (Buenos Aires, Argentina). Since 1999, Dr. Torres-Verdín has been affiliated with the Hildebrand Department of Petroleum and Geosystems Engineering of the University of Texas at Austin, where he is currently Full Professor, and holds the Brian James Jennings Memorial Endowed Chair in Petroleum and Geosystems Engineering. Dr. Torres-Verdín is the founder and director of the Research Consortium on Formation Evaluation at the University of Texas at Austin, which has been in operation since 2000. He is the recipient of the Cockrell School of Engineering's 2016–2017 Lockheed Martin Aeronautics Company Award for Excellence in Engineering Teaching, the 2019 Anthony F. Lucas Gold Medal from the SPE, the 2017 Conrad Schlumberger Award from the EAGE, the 2017 Honorary Membership from the SEG, the 2014 Gold Medal for Technical Achievement from the SPWLA, the 2008 Formation Evaluation Award from the SPE, and the 2006 Distinguished Technical Achievement Award from the SPWLA.

ABOUT THE AUTHORS

Ayaz Mehmani is a research consultant for the oil and gas industry in Texas. He obtained his BS degree from Sharif University of Technology and PhD from The University of Texas at Austin, both in Petroleum Engineering. His research interests include digital rock physics, micro/nanofluidics, and machine learning.

Shaina Kelly is a Senior Petrophysicist in ConocoPhillips' Geoscience (Technology) group in Houston, Texas, where she works on technical service and technology development projects. Shaina obtained her bachelor's degree in Environmental Engineering from the University of Florida and her masters and PhD degrees in Petroleum Engineering from the University of Texas at Austin. Shaina's research interests include pore-scale petrophysics, imaging, and modeling as well as special core analysis, micro/nanofluidics, and fluid-rock interactions.

CORRIGENDUM

Addendum to Tutorial: Thomas, E.C., 2018, Capillary Pressure Tutorial Part 1—It's a Jungle in Here, *Petrophysics*, **59**(4), 421–427.

Let me begin by saying “mea culpa.” I did not provide the necessary references for this tutorial (at least it is not an erratum). The references I discuss below were provided by Professor Emeritus, Dr. George Hirasaki, Rice University. Dave Murphy provided the key directive pointing to Dr. Hirasaki. To both friends I give my thanks. These references reflect the exciting discoveries of Professor Geraldine L. Richmond, her post-docs and graduate students at the University of Oregon. Professor Richmond is not the only researcher delving into this new territory. Here are a few of the references I neglected to include:

1. Brown, M.G., Walker, D.S., Raymond, E.A., and Richmond, G.L., 2003, Vibrational Sum-Frequency Spectroscopy of Alkane/Water Interfaces: Experimental and Theoretical Simulations, *Journal of Physical Chemistry B*, **107**(1), 237–244. DOI: 10.1021/jp0218589.
2. Hore, D.K., Beaman, D.K., and Richmond, G.L., 2005, Surfactant Headgroup Orientation at the Air/Water Interface, *Journal of the American Chemical Society*, **127**(26), 9356–9357. DOI: 10.1021/ja51492o.
3. Walker, D.S., Hore, D.K. and Richmond, G.L., 2006, Understanding the Population, Coordination, and Orientation of Water Species Contributing to the Nonlinear Optical Spectroscopy of the Vapor-Water Interface Through Molecular Dynamics Simulations, *Journal of Physical Chemistry B*, **110**(41), 20451–20459. DOI: 10.1021/jp063063y.

Brown et al. (2003) provide a short, simplified explanation of the ingenious experimental apparatus. You have to supply foreknowledge of infrared spectroscopy;

one such fact is that allowed absorption transitions can only occur in molecules that possess a dipole moment.

Hore et al (2005) and Walker et al. (2006) presented me with a new fact, namely that not every water molecule in liquid water is hydrogen bonded with four other water molecules. As the title of the tutorial suggests, there is fierce in-fighting in the water jungle to achieve four hydrogen-bonded partners. At any given moment, a water molecule may have fewer than four coordinated water molecules in their sphere of influence. Think of it as a game of musical chairs; at any given time we wish to stop and count, not every water molecule has four hydrogen-bonded partners. Thus, the number of water molecules can exceed the number of hydrogen-bonded “seats” and the authors have named them “free” O-H (no hydrogen bond). It is these “free” O-H groups on water molecules that orient this “free” OH group into the vapor phase of a water/vapor interface.

Hore et al. (2005) show that there is a tendency in any surfactant with an alkyl hydrophobic tail to orient it into the vapor phase (or hydrophobic phase). The authors chose to work with sodium dodecyl sulfate, one of many such surfactants found in cleaners. The preferred orientation of the SO_4^- is for the sulfur to reside at the interface which places three S-O bonds in the hydrophilic phase leaving one S-O bond to reside in the hydrophobic phase, roughly oriented 16° from the normal to the interface. The alkyl group is bonded to the O and stretches out into the hydrophilic phase. Note, since all the alkyl bonds are single bonds, they are free to rotate at every C atom, producing innumerable twists and turns for the alkyl group. Of course, the head group does not have to be sulphate, but can be any organic acid or base.

Well, I hope I have not put you to sleep with this addendum. I am personally quite excited about learning more about the orientation of molecules at interfaces. They have started with simple systems and I anxiously await results on solid/liquid interfaces.

- Agostini, F., Egermann, P., Jeannin, L., Portier, E., Skoczlas, F., and Wang, Y., 2019, Loading Effects on Gas Relative Permeability of a Low-Permeability Sandstone, April, 326–334.
- Al-Saedi, H.N., and Flori, R.E., 2019, Novel Coupling Smart Water-CO₂ Flooding for Sandstone Reservoirs, August, 525–535.
- Almasoodi, M., and Reza, Z., 2019, Finite-Volume Computations of Shale Tortuosity and Permeability From 3D Pore Networks Extracted From Scanning Electron Tomographic Images, June, 397–408.
- Ansari, R., Merletti, G., Gramin, P., and Armitage, P., 2019, More Accurate Quantification of Free and Adsorbed Gas in Shale Reservoirs, October, 560–584.
- Badruzzaman, A., Schmidt, A., and Antolak, A., 2019, Neutron Generators as Alternatives to Am-Be Sources in Well Logging: An Assessment of Fundamentals, February, 136–170.
- Bennett, N., Donald, A., Ghadir, S., Nassar, M., Kumar, R., and Biswas, R., 2019, Borehole Acoustic Imaging Using 3D STC and Ray Tracing to Determine Far-Field Reflector Dip and Azimuth, April, 335–347.
- Bérard, T., Chugunoy, N., Desroches, J., and Prioul, R., 2019, Feasibility and Design of Hydraulic Fracturing Stress Tests Using a Quantitative Risk Assessment and Control Approach, February, 113–135.
- Berthet, H., Hebert, M., Barbouteau, S., Adriamanajaona, P., and Riveng, R., 2019, Pore-Scale Insights on Trapped Oil During Waterflooding of Sandstone Rocks of Varying Wettability States, April, 229–239.
- Blount, A., McMullen, A., Durand, M., and Driskill, B., 2019, Maintaining and Reconstructing In-Situ Saturations: A Comparison Between Whole Core, Sidewall Core, and Pressurized Sidewall Core in the Permian Basin, February, 50–60.
- Bolt, H., 2019, Correction of Driller's Depth: Field Example Using Driller's Way-Point Depth Correction Methodology, February, 76–91.
- Brazell, S., Bayeh, A., Ashby, M., and Burton, D., 2019, A Machine-Learning-Based Approach to Assistive Well-Log Correlation, August, 469–479.
- Chen, Z., Singer, P.M., Wang, X., Vinegar, H.J., Nguyen, S.V., and Hirasaki, G.J., 2019, NMR Evaluation of Light Hydrocarbon Composition, Pore Size, and Tortuosity in Organic-rich Shales, December, 771–797.
- Craddock, P.R., Miles, J., Lewis, R.E., and Pomerantz, A.E., 2019, Thermal Maturity-Adjusted Log Interpretation (TMALI) in Organic Shales, October, 540–559.
- Deng, T., Xu, C., Jobe, D., and Xu, R., 2019, A Comparative Study of Three Supervised Machine-Learning Algorithms for Classifying Carbonate Vuggy Facies in the Kansas Arbuckle Formation, December, 838–853.
- Elkatatny, S., Al-AbdulJabbar, A., and Mahmoud, A.A., 2019, New Robust Model to Estimate the Formation Tops in Real-Time Using Artificial Neural Networks, December, 825–837.
- Elshahawi, H., Huang, S., Pollack, J., and Veedu, V., 2019, Novel Composite Cement for Improved Well Integrity Evaluation, February, 61–69.
- Fokkema, E., and Visser, C., 2019, Connecting the Dots—The Relevance of Proper Depth Control in the Discovery of the Groningen Field, February, 73–75.
- Fu, D.-L., Xu, G., Tao, T., Qin, J.-G., and Yang, F., 2019, Composition of the Shales in Niutitang Formation at Huijunba Syncline and its Influence on Microscopic Pore Structure and Gas Adsorption, June, 373–383.
- Gong, B., Keele, D., Toumelin, E., and Clinch, S., 2019, Estimating Net Sand From Borehole Images in Laminated Deepwater Reservoirs With a Neural Network, October, 596–604.
- Gowida, A., Elkatatny, S., and Abdullaheem, A., 2019, Application of Artificial Neural Network to Predict Formation Bulk Density While Drilling, October, 660–674.
- Howard, J., Lin, S., and Zhang, S., 2019, Uncertainty Quantification in Image Segmentation for Image-Based Rock Physics in a Shaly Sandstone, April, 240–254.
- Howard, J.J., and Hester, K.C., 2019, Monitoring Core Measurements With High-Resolution Temperature Arrays, April, 297–304.
- Hulea, I.N., 2019, Perched Water Contacts: Understanding Fundamental Controls, June, 438–449.
- Kausik, R., Freed, D., Fella, K., Feng, L., Ling, Y., and Simpson, G., 2019, Frequency and Temperature Dependence of 2D NMR T₁-T₂ Maps of Shale, February, 37–49.
- Kennedy, D., and Garcia, F., 2019, Introduction to Resistivity Principles for Formation Evaluation: A Tutorial Primer, April, 208–227.
- Lawal, L.O., Mahmoud, M., Alade, O.S., and Abdullaheem, A., 2019, Total Organic Carbon Characterization Using Neural-Network Analysis of XRF Data, August, 480–493.
- Le, T., Liang, L., Zimmerman, T., Zeroug, S., and Heliot, D., 2019, A Machine-Learning Framework for Automating Well-Log Depth Matching, October, 585–595.
- Lei, T., Zeroug, S., Bose, S., Prioul, R., and Donald, A., 2019, Inversion of High-Resolution High-Quality Sonic Compressional and Shear Logs for Unconventional Reservoirs, December, 697–711.
- Li, P., Lee, J., Coates, R., Jin, J., and Wong, S.M., 2019, New 4.75-in. Ultrasonic LWD Technology Provides High-Resolution Caliper and Imaging in Oil-Based and Water-Based Muds, December, 712–732.

- Lin, Q., Bijeljic, B., Krevor, S.C., Blunt, M.J., Rücker, M., Berg, S., Coorn, A., van der Linde, H., Georgiadis, A., and Wilson, O.B., 2019, A New Waterflood Initialization Protocol With Wettability Alteration for Pore-Scale Multiphase Flow Experiments, April, 264–272.
- Looyestijn, W., 2019, Practical Approach to Derive Wettability Index by NMR in Core Analysis Experiments, August, 507–513.
- Masclé, M., Youssef, S., Deschamps, H., and Vizika, O., 2019, In-Situ Investigation of Aging Protocol Effect on Relative Permeability Measurements Using High- Throughput Experimentation Methods, August, 514–524.
- Mehmani, A., Kelly, S., and Torres-Verdin, C., 2019, Review of Micro/Nanofluidic Insights on Fluid Transport Controls in Tight Rocks, December, 872-890.
- Mendoza, A., Roininen, L., Girolami, M., Heikkinen, J., and Haario, H., 2019, Accelerated Whole-Core Analysis Optimization With Well-site Tomography Instrumentation and Bayesian Inversion, June, 384–396.
- Mitchell, J., and Valori, A., 2019, Application of a Fast NMR T_1 Relaxation Time Measurement to Sedimentary Rock Cores, June, 409–420.
- Newsham, K., Comisky, J., and Chemali, R., 2019, Organic-Mudstone Petrophysics: Workflow to Estimate Storage Capacity, February, 4–15.
- Newsham, K., Comisky, J., and Chemali, 2019, Organic Mudstone Petrophysics, Part 2: Workflow to Estimate Storage Capacity, April, 181–207.
- Newsham, K., Comisky, J., and Chemali, R., 2019, Organic Mudstone Petrophysics, Part 3: Workflow to Estimate Storage Capacity, June, 351–371.
- Nikitin, A., Durand, M., McMullen, A., Blount, A., Driskill, B., and Hows, A., 2019, Crushed-Rock Analysis Workflow Based on Advanced Fluid Characterization for Improved Interpretation of Core Data, December, 755-769.
- Pan, H., Li, H., Zhang, Y., Chen, J., Cai, S., and Geng, C., 2019, Joint Interpretation of Elastic and Electrical Data for Petrophysical Properties of Gas-Hydrate-Bearing Sediments Using Inverse Rock Physics Modeling Method, December, 854-871.
- Perry, S.E., and Hayes D., 2019, Presenting a Multifaceted Approach to Unconventional Rock Typing and Technical Validation—Case Study in the Permian Basin and Impacts on Reservoir Characterization Workflows, October, 641–659.
- Poedjono, B., Nwosu, D., and Martin, A., 2019, Wellbore Positioning While Drilling With LWD Measurements, June, 450–465.
- Reed, J., and Cense, A., 2019, In-Situ Saturation Monitoring (ISSM)— Recommendations for Improved Processing, April, 273–282.
- Reed, J., and Maas, J., 2019, Review of the Intercept Method for Relative Permeability Correction a Variety of Case Study Data, April, 283–296.
- Ruth, D., and Arabjamaloei, R., 2019, Reconsidering Klinkenberg's Permeability Data, June, 421–428.
- Sarkar, P.S., Chatterjee, S., Lal, M., Kumar, M., and Deo, P.O., 2019, Influence of Magnetic Susceptibility Contrast on NMR Studies—Experimental Analysis From Siliciclastic Reservoirs, December, 798-824.
- Schroeder, C., and Torres-Verdin, C., 2019, Experimental Method for Time-Lapse Micro-CT Imaging of Mud-Filtrate Invasion and Mudcake Deposition, October, 620–630.
- Se, Y., Villegas, M., Iskakov, E., Playton, T., Lindsell, K., Cordova, E., Turmanbekova, A., and Wang, H., 2019, 'Log-Soak-Log' Experiment in Tengiz Field: Novel Technology for In-Situ Imbibition Measurements to Support an Improved Oil Recovery Project, October, 605–619.
- Sheng, X., Shen, J., Shen, Y., Zhu, L., and Zang, D., 2019, Through-Casing Formation Conductivity Measurement Based on Transient Electromagnetic Logging Data, October, 675–691.
- Skalinski, M., Mallan, R., Edwards, M., Sun, B., Toumelin, E., Kelly, G., Wushur, H., and Sullivan, M., 2019, Defining Net-Pay Cutoffs in Carbonates Using Advanced Petrophysical Methods, February, 17–36.
- Stalheim, S.O., 2019, Deducing Electrical Permittivity of Formations From LWD Resistivity Measurements, December, 733-754.
- Tang, X., Su, Y., and Zhuang, B., 2019, A Through-Casing Acoustic Logging Tool Using Dual-Source Transmitters, October, 631–639.
- Theys, P., 2019, Depth: A Love and Hate Story, February, 71–72.
- Trans, H., and Sakhaee-Pour, A., 2019, The Compressibility Factor (Z) of Shale Gas at the Core Scale, August, 494–506.
- Valori, A., and Nicot, B., 2019, A Review of 60 Years of NMR Wettability, April, 255–263.
- Vandamme, T., Caroli, E., and Gratton, S., 2019, How the Invasion Zone Can Contribute to the Estimation of Petrophysical Properties From Log Inversion at Well Scale?, April, 306–325.
- Wang, D., and Peng, J., 2019, Determination of the Appropriate Value of m for Evaluation of Carbonate Reservoirs With Vugs and Fractures at the Well-Log Scale, June, 429–437.
- Wang, H., Stockhausen, E., Wyatt, D.F., Jr., and Gulick, D., 2019, Modeling of Azimuthal Gamma-Ray Tools for Use in Geosteering in Unconventional Reservoirs, February, 93–112.

